

14

Journal of
**Geophysical
Research**

VOLUME 66

JULY 1961

NUMBER 7

PUBLISHED BY

THE AMERICAN GEOPHYSICAL UNION

Journal of Geophysical Research

An International Scientific Publication

OFFICERS OF THE UNION

THOMAS F. MALONE, *President*
GEORGE P. WOOLLARD, *Vice President*
A. NELSON SAYRE, *General Secretary*
WALDO E. SMITH, *Executive Secretary*

OFFICERS OF THE SECTIONS

Geodesy

FLOYD W. HOUGH, *President*
CHARLES A. WHITTEN, *Vice President*
BUFORD K. MEADE, *Secretary*

Seismology

JAMES A. PEOPLES, JR., *President*
JACK E. OLIVER, *Vice President*
BENJAMIN F. HOWELL, JR., *Secretary*

Meteorology

MORRIS NEIBURGER, *President*
HENRY G. HOUGHTON, *Vice President*
WOODROW C. JACOBS, *Secretary*

Geomagnetism and Aeronomy

C. T. ELVEY, *President*
E. H. VESTINE, *Vice President*
J. HUGH NELSON, *Secretary*

Oceanography

DONALD W. PRITCHARD, *President*
ROBERT S. ARTHUR, *Vice President*
ARTHUR E. MAXWELL, *Secretary*

Volcanology, Geochemistry, and Petrology

HATTEN S. YODER, JR., *President*
EDWARD D. GOLDBERG, *Vice President*
DAVID R. WONES, *Secretary*

Hydrology

WILLIAM C. ACKERMANN, *President*
DAVID K. TODD, *Vice President*
RALPH N. WILSON, *Secretary*

Tectonophysics

LOUIS B. SLICHTER, *President*
DAVID T. GRIGGS, *Vice President*
IRIS BORG, *Secretary*

BOARD OF EDITORS

Editors: PHILIP H. ABELSON and J. A. PEOPLES, JR.

ASSOCIATE EDITORS

1959-1961

HENRI BADER	T. NAGATA
K. E. BULLEN	FRANK PRESS
CONRAD P. MOOK	A. NELSON SAYRE
WALTER H. MUNK	MERLE A. TUVE

JAMES A. VAN ALLEN

1960-1962

JULIUS BARTELS	L. A. MANNING
V. V. BELOUSSOV	TOR J. NORDENSON
E. G. BOWEN	E. N. PARKER
JOHN E. CHAPPELEAR	GEORGE P. RIGSBY
G. D. GARLAND	WALTER O. ROBERTS
GORDON J. F. MACDONALD	C. N. TOUART

JAMES R. WAIT

1961-1963

FRANKLIN I. BADGLEY	ROBERT O. REID
HENRY G. BOOKER	BRUNO ROSSI
JOSEPH W. CHAMBERLAIN	GEORGE H. SUTTON
HERBERT FRIEDMAN	DAVID K. TODD
MARK F. MEIER	VICTOR VACQUIER

ARTHUR H. WAYNICK

The Editors of the *Journal of Geophysical Research* welcome original scientific contributions on the physics of the earth and its environment.

Manuscripts should be submitted in triplicate to J. A. Peoples, Jr., Department of Geology, University of Kansas, Lawrence, Kansas. Authors' institutions if in the United States or Canada, are requested to pay a publication charge of \$25 per page, which, honored, entitles them to 100 free reprints.

Subscriptions to the *Journal of Geophysical Research* and *Transactions, AGU*, are included in membership dues.

Nonmember subscriptions, *Journal of Geophysical Research*, \$30 for back volume of 1959, \$42 for back volume of 1960, \$4 for this issue; \$20 for the calendar year 1961.

Nonmember subscriptions, *Transactions, AGU*, \$4 per calendar year, \$1.25 per copy.

Subscriptions, renewals, and orders for back numbers should be addressed to American Geophysical Union, 1515 Massachusetts Ave., Northwest, Washington, D. C. Suggestions to authors are available on request.

Advertising Representative: Howland and Howland Inc., 230 Park Ave., New York 17, N. Y.

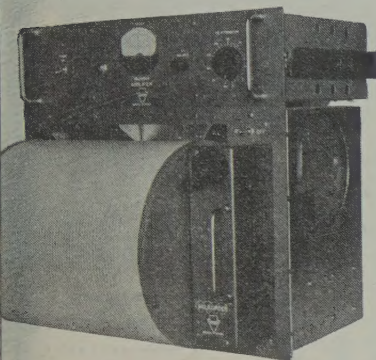
Since January 1959 (Vol. 64, No. 1) the *Journal of Geophysical Research* has been published monthly by the American Geophysical Union, the U. S. National Committee of the International Union of Geodesy and Geophysics organized under the National Academy of Sciences-National Research Council as the U. S. national adhering body. Publication of this journal is supported by the National Science Foundation and the Carnegie Institution of Washington. The new monthly combines the type of scientific material formerly published in the bi-monthly *Transactions, American Geophysical Union*, and the quarterly *Journal of Geophysical Research*. The *Transactions, American Geophysical Union* will continue as a quarterly publication for Union business and items of interest to members of the Union.

Published monthly by the American Geophysical Union from 1407 Sherwood Avenue, Richmond, Virginia. Second class postage paid at Richmond, Virginia.

PRECISION INSTRUMENTS for SEISMOLOGY — GEOPHYSICS

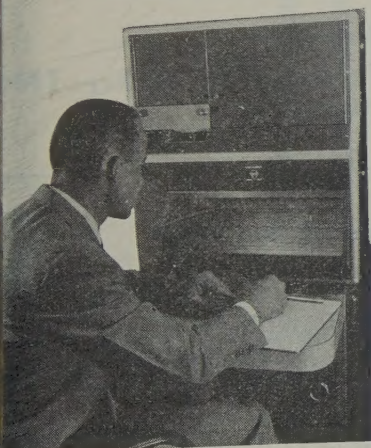
HELICORDER

1127 H
An immediate data display, and up to 72 hours of data recorded on one 12" x 36" record are featured by this precision recorder. The penmotor(s) translates as the drum revolves, recording data on heat sensitive paper in helical fashion. Significant data is easily identified with one glance at the entire record. No dark room or delay for photo processing is necessary, and there is no ink to clog. One- and three-trace models are available. Drum speed is adjustable, and 8 to 72 hours of analog data in a band pass of 0 to 24 cps can be recorded on one permanent record. The companion amplifier shown is also available. The recorder can be rack-mounted or furnished with a cabinet for table mounting. Dependability is proven through years of trouble-free operation under extreme field conditions.



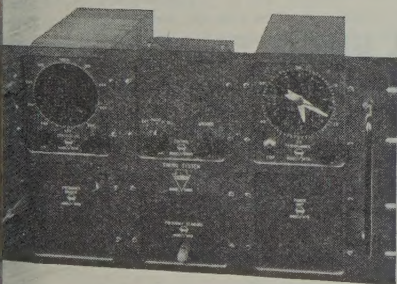
DEVELOCORDER

This is a combination 16 mm film recorder, automatic film processor, and film viewer. With 1 to 16 miniature Geotech galvanometers installed, Model 4000 will record up to 120 hours of data on a 200 ft. roll of film. Band pass is 0 to 120 cps depending upon film speed and galvanometers selected. With a cathode ray tube installed, Model 4000A will also record data across the film, as well as intensity-modulated spectrograms, Lissajous patterns, and other presentations. A film speed of 3 cm/min is standard, and speeds from 0.6 to 20 cm/min are available on special order. Self-contained chemicals process the film internally. Data is displayed magnified 10X on the 6" x 17" view-screen within 2 to 20 minutes after recording. A 2-directional, variable-speed drive is provided for viewing. Date and time are printed on the film at regular intervals.



PORTABLE STATION TIMING SYSTEM

This is a complete station timing system for precision recording and timing applications which has been transistorized and packaged in miniature modules for dependable, portable field use. It provides accurate clock time and programmed time marks, and 15 va of 60-cps power output, all with a stability of at least 5 parts in 10⁷ per week. Individual modules, which can be obtained separately, are: an oven- and crystal-controlled frequency standard, a frequency divider, a strobe unit for comparing and adjusting system time with external time, a clock and time-mark programmer, a speaker for radio time signals, and an amplifier providing the output power for recorder drives and other devices. Dimensions are 19"W x 10.5"H x 9"D. Weight is 25 pounds. Power required is 2 amps, 24 volts, DC. These systems have operated in the field for over a year.



For detailed specifications, price, or delivery, write to:

THE GEOTECHNICAL CORP.

01 SHILOH ROAD

GARLAND, TEXAS

Please mention JOURNAL OF GEOPHYSICAL RESEARCH, when writing to advertisers

PORTABLE, ACCURATE, EASY TO OPERATE Sprengnether's Blast and Vibration Seismograph

Ideal for recording all types of vibrations caused by blasting, pile driving, heavy industrial machinery and other sources of strong motion vibrations.

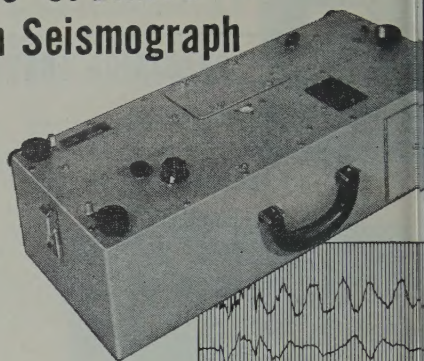
Portability (38 lbs. — 25 x 10 x 8 in.) Unit is self contained and free from external power source.

Extremely Accurate To guard against error, each instrument is tested and calibration data furnished. Frequency response, 3 to 200 cycles per second. Timing lines are across record at intervals of 0.02 seconds with accuracy of 0.1%.

Easy to Operate: All controls are easily accessible. Instrument can be set up, leveled and made ready to operate within minutes.

Seismometer System: A mechanical, optical seismometer employing three independent pendulum systems with magnetic damping. System is contained within unit, hence, no need for external geophones.

Recording System: Photographic recording of all three components appearing on 2¾ inch wide paper. Cartridge type cameras are replaceable and can be pre-loaded to facilitate in the field camera replacement.



Write today for
complete
information.

OTHER SPECIFICATIONS

Natural Period (All Components).....	0.77
Damping (Fraction of Critical).....	.58
Static Magnification.....	**

*May be specified by purchaser from 50 to 200.
Two ranges in one instrument available.

Internationally Known Mfrs. of Seismological, Geophysical Instruments.

W.F. SPRENGNETHER INSTRUMENT CO., INC.
4567 SWAN AVENUE • ST. LOUIS 10, MO.

GEODESY AND CARTOGRAPHY, 1959 and 1960

(Geodezia i Kartografiya)

The leading monthly journal of Geodesy and Cartography in the USSR is being translated and published in an English edition, *for the years 1959 and 1960*, by the American Geophysical Union, aided by a grant from the National Science Foundation.

Subscription price, \$20.00 for each volume of 12 numbers

Send subscription requests to

AMERICAN GEOPHYSICAL UNION

1515 Massachusetts Avenue, N.W.

Washington 5, D. C., U.S.A.

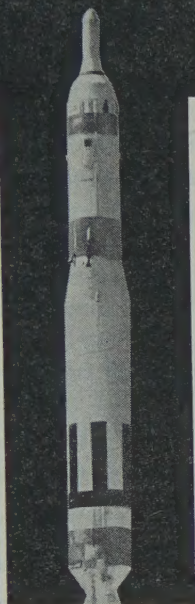
Other publications of the AGU include

- JOURNAL OF GEOPHYSICAL RESEARCH (monthly), 4800 pages anticipated for 1961, subscription \$20.00
- TRANSACTIONS (quarterly), \$4.00 per calendar year
- GEOPHYSICAL MONOGRAPH SERIES (occasional volumes), No. 5 (issued in 1960) *Physics of Precipitation* (proceedings of the Cloud Physics Conference, Woods Hole, Massachusetts, June 3-5, 1959), 435 pp., \$12.50
- IZVESTIYA, Academy of Sciences, USSR, Geophysics series, English edition (monthly), \$25.00 per calendar year, available for 1957, 1958, 1959, 1960, and 1961.

Please mention JOURNAL OF GEOPHYSICAL RESEARCH, when writing to advertisers

TITAN—newest triumph of Space Technology Leadership

May 3, 1961—Giant Stride toward ICBM Invulnerability



The nation's first in-silo launch of an ICBM marks a major milestone in the timely development of USAF Titan—and a signal success for an industrial team led by scientists and engineers of Space Technology Laboratories, Inc., under Air Force program management. This successful test confirmed the STL design solution to the unparalleled vibration problems created by the roar of Titan's 300,000-pound thrust booster engine within the confines of its 10-story underground silo. ■ Two years ago, studies by STL as contractor to the Air Force for systems engineering and technical direction of the Titan program, indicated that in-silo launching which provided invulnerability and enormous economy was technically attainable. But one major problem had yet to be solved: proper control of the noise-created vibration during the first few seconds of in-silo firing which, if uncontrolled, could literally shake apart the 97-foot Titan. Research and analysis by STL produced the solution, verified by the dramatically successful test at Vandenberg Air Force Base on May 3, 1961. ■ The successful launch of Titan I demonstrated the soundness of STL silo design concepts for the Air Force Titan II program. Titan II is a fast reacting, highly flexible weapon of maximum range and destructive capability—a new and potent element in deterring aggressor attack. ■ Today STL scientists and engineers are actively engaged in the program that is producing soon-to-be-operational Titan I and quick-reacting Titan II. Their responsibilities in this, as well as in the Atlas and Minuteman programs, create career opportunities for additional numbers of outstanding scientists and engineers. For opportunities with STL in Southern California or at Cape Canaveral, please write to Mr. R. C. Potter, Manager of Professional Placement and Development, at either location.

TITAN TEAM. Program Management: Ballistic Systems Division, Air Force Systems Command. **Major Associate Contractors:** Space Technology Laboratories, Inc., systems engineering and technical direction; The Martin Co., airframe, assembly, and test; Bell Telephone Laboratories and Remington-Rand UNIVAC, radio guidance; AC Spark Plug, all-inertial guidance; Aerojet General, propulsion; Avco Corp. and General Electric, re-entry vehicles; American Machine & Foundry, silo-lift launcher system; D. Little, propellant loading system; Daniel, Mann, Johnson, Mendenhall & Assoc. and Ralph M. Parsons Co., architects and engineers; Kellogg Switchboard & Supply Co. and Stromberg-Carlson, communications.

SPACE TECHNOLOGY LABORATORIES, INC. P. O. BOX 95005 JK, LOS ANGELES 45, CALIFORNIA

subsidiary of Thompson Ramo Wooldridge Inc.

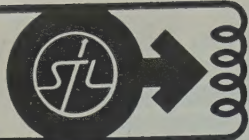
Los Angeles • Santa Maria • Cape Canaveral • Washington, D. C.



P. O. BOX 4277 JK, PATRICK AFB, FLORIDA
Boston • Dayton • Huntsville • Edwards AFB • Canoga Park • Hawaii

All qualified applicants considered regardless of race, creed, color, or national origin.

Please mention JOURNAL OF GEOPHYSICAL RESEARCH, when writing to advertisers



ELECTROMAGNETIC SYSTEMS

Division of Space Technology Laboratories, Inc.

*Offers Immediate Assignments
in Southern California*

The continuing growth and diversification of Space Technology Laboratories, Inc. creates immediate career openings in the Radio Physics and Signal Equipment Laboratories of STL's Electromagnetics Division, located in the community of Canoga Park in Los Angeles' San Fernando Valley.

This division is engaged in developing advanced communication, radio direction finding, electro-optical, and penetration and reconnaissance systems; and in investigating advanced signal processing, electronic and anti-submarine warfare techniques.

Outstanding engineers and scientists who can qualify to perform advanced work in these areas are invited to communicate with Dr. R. C. Potter, Manager of Professional Placement and Development. All qualified applicants considered regardless of race, creed, color or national origin.

SPACE TECHNOLOGY LABORATORIES, INC.

a subsidiary of Thompson Ramo Wooldridge, Inc.

P. O. Box 95005JK, Los Angeles 45, California

BULLETIN (IZVESTIYA), ACADEMY OF SCIENCES, U.S.S.R. GEOPHYSICS SERIES

Subscriptions for 1961 series now available

This monthly Russian publication, perhaps the leading journal of Geophysics of the U.S.S.R., is being translated and published in an English edition for the year 1961 by the American Geophysical Union. The twelve numbers in Russian cover about 2000 pages. Published with the aid of a grant from the National Science Foundation.

Send subscriptions now to

**AMERICAN GEOPHYSICAL UNION
1515 Massachusetts Avenue, N.W.
Washington 5, D. C., U.S.A.**

Subscription rates: \$25.00 for the volume of 12 numbers (\$20.00 to individual members of AGU subscribing for personal use)
Numbers will be mailed as issued.

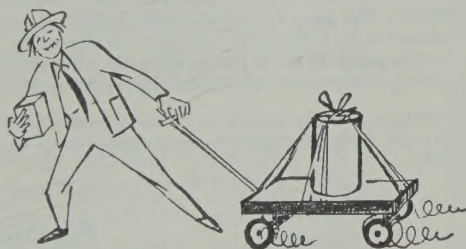
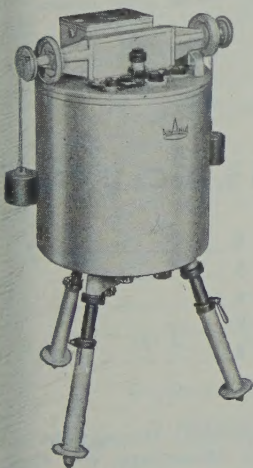
The English edition of this publication for 1957 has been translated and published for the American Geophysical Union by Pergamon Press. This volume may be ordered through the American Geophysical Union at a price of \$25.00. The 1958, 1959, and 1960 series are available at a price of \$25.00 for each volume of 12 numbers. Titles and authors of the papers contained in the series have been published in recent issues of the *Transactions*, AGU.

Please mention JOURNAL OF GEOPHYSICAL RESEARCH, when writing to advertisers

IAGA stresses the importance of having correct measurements (by *variographs*) at some special "variation repeat stations" for periods of several days. Such repeat stations are particularly needed in regions where the magnetic field is anomalous because of geological conditions, or where it is varying rapidly because of the nearness of the station to the auroral zone. . . .



Recommended by JAGA, JUGG
Meeting resolution taken at Helsinki in August 1960



The MOVABLE OBSERVATORY Askania Variograph type Gv-3

other instruments:

Torsion Magnetometers
Gravimeters, Station
Seismographs for local
and remote earthquakes

Write for detailed information!

ASKANIA-WERKE
Division of Continental Elektroindustrie AG

J. S. Branch

4913 Cordell Avenue

Bethesda 14, Maryland

Please mention JOURNAL OF GEOPHYSICAL RESEARCH, when writing to advertisers

GEOPHYSICAL MONOGRAPH SERIES

AMERICAN GEOPHYSICAL UNION

1515 MASSACHUSETTS AVENUE, N.W.

WASHINGTON 5, D. C., U.S.A.

Antarctica in the International Geophysical Year—Geophysical Monograph No. 1 (Publication No. 462, National Academy of Sciences—National Research Council); Library of Congress Catalogue Card No. 56-60071; 133 pp. and large folded map of the Antarctic, 1956, 7" x 10", \$6.00. Contains 16 pages by various American authorities on the Antarctic under the headings: General, Geographic and Meteorological, Geological and Structural, Upper Atmospheric Physics, and Flora and Fauna. Map (41" x 41") compiled by the American Geographical Society. Introduction by L. M. Gould.

Geophysics and the IGY—Geophysical Monograph No. 2 (Publication No. 590, National Academy of Sciences—National Research Council); Library of Congress Catalogue Card No. 58-60035; 210 pp., 1958, 7" x 10", \$8.00. Contains 30 papers by leading American authorities under the headings: Upper Atmospheric Physics, The Lower Atmosphere and the Earth, and The Polar Regions. Preface by Joseph Kaplan.

Atmospheric Chemistry of Chlorine and Sulfur Compounds—Geophysical Monograph No. 3 (Publication No. 652, National Academy of Sciences—National Research Council); Library of Congress Catalogue Card No. 59-60039; 129 pp., 1959, 7" x 10", \$5.50. Based on a symposium held jointly with the Robert A. Taft Sanitary Engineering Center of the U. S. Public Health Service in Cincinnati in November, 1957. Contains 23 papers (some as summaries) with discussion. Preface by James P. Lodge, Jr.

Contemporary Geodesy—Geophysical Monograph No. 4 (Publication No. 708, National Academy of Sciences—National Research Council); Library of Congress Catalogue Card No. 59-60065; 96 pp., 7" x 10", 1959, \$5.50. Based on a Conference held at Cambridge, Massachusetts, in December 1958 jointly by the AGU with the Smithsonian Astrophysical Observatory and the Harvard College Observatory. Contains 14 papers by leading authorities, with verbatim discussions on topics ranging from classical geodesy to trilateration by underwater sound to space navigation in the solar system. Edited by Charles A. Whitten and Kenneth H. Drummond.

Physics of Precipitation—Geophysical Monograph No. 5 (Publication No. 746, National Academy of Sciences—National Research Council); Library of Congress Catalogue Card No. 60-60010; 435 pp., 7" x 10", 1960, \$12.50. Based on a Conference held at Woods Hole, Massachusetts, in June 1959. Contains 48 papers by leading authorities, with verbatim discussions on topics ranging from planetary-scale phenomena to microanalysis including hail formation and precipitation control. Edited by Helmut Weickmann.

Postage is to be added to prices shown unless payment accompanies order. Quantity discounts (count each Monograph separately): 5-19 copies, 10%; 20-49 copies, 15%; 50 or more copies 20%.

Purchase Order

TO AMERICAN GEOPHYSICAL UNION

1515 Massachusetts Avenue, N.W., Washington 5, D. C., U.S.A.

Please enter our order for the following:

_____ copies of Geophysical Monograph No. 1, at \$6.00 *	\$ _____
_____ copies of Geophysical Monograph No. 2, at \$8.00 *	\$ _____
_____ copies of Geophysical Monograph No. 3, at \$5.50 *	\$ _____
_____ copies of Geophysical Monograph No. 4, at \$5.50 *	\$ _____
_____ copies of Geophysical Monograph No. 5, at \$12.50 *	\$ _____

- ☐ Payment of \$ _____ is enclosed.
- ☐ Please send invoice, adding postage charges.
- ☐ Enter our standing order for _____ copies of subsequent Geophysical Monographs at the special prepublication rates, e.g., prepublication rate for Monograph No. 4 for non-members was \$4.00, payment in advance, or \$4.75 (plus postage) on invoice.

* List price is net for quantities up to four; see above for discounts on quantity purchases. Special discounts to members.

Typed name _____ Signature _____

Address _____

Space Physics at

AEROSPACE CORPORATION

The scientists and engineers of Aerospace Corporation are the critical civilian link uniting government and the scientific-industrial team developing space systems and advanced ballistic missiles. These men, highly skilled in at least one discipline, are also knowledgeable in inter-disciplinary problem solving.

In space physics their specific activities include extensive studies of particle measurement in auroral zones; space plasma physics; solar physics and solar-terrestrial interactions; Van Allen belts and solar flares; magnetic and electric field measurements; analysis of planetary atmospheres, surfaces and magnetic fields; micrometeorite investigations; space probe instrumentation; and space data processing and evaluation.

These studies, conducted in close association with Air Force space and missile experimental flight programs, are enhanced by the stimulating environment made possible by Aerospace Corporation's stable funding.

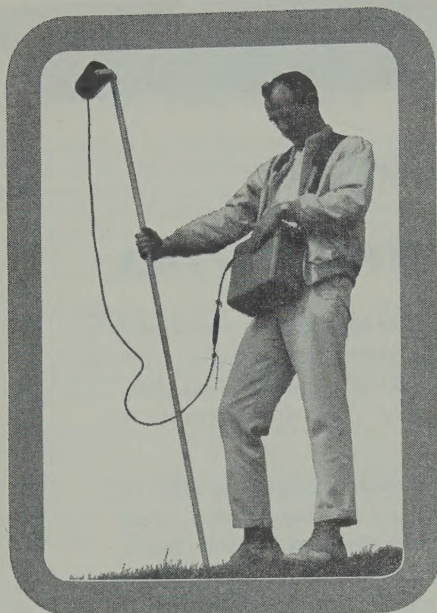
Today more men of superior ability and advanced education are needed to meet Aerospace Corporation's growing responsibilities in the area of space physics. Immediate assignments exist for qualified physicists interested in theoretical and experimental investigations of the space environment.

Such men are urged to contact Mr. George Herndon (OSborne 9-4661, Extension 1171), Aerospace Corporation, Room 193, P.O. Box 95081, Los Angeles 45, Calif. All qualified applicants will receive consideration for employment without regard to race, creed, color or national origin.



AEROSPACE CORPORATION

*Organized in the public interest and dedicated to providing objective leadership
in the advancement and application of space science and technology
for the United States Government.*



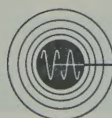
**M-49A PORTABLE
MAGNETOMETER
AVAILABLE NOW AT
\$3,950**

**PROVIDES FAST, ACCURATE
MAGNETIC SURVEYS
AT STILL LOWER COST**

World-wide acceptance of Russell Varian's *proton free precession principle* and wide usage of the M-49 portable magnetometer have now made it possible for Varian Associates to price the improved M-49A within the budget of most exploration programs.

PORTABLE The Varian M-49A, a complete proton magnetometer weighing only 22 pounds, furnishes direct readings in gammas every six seconds. Sensitive to better than ± 10 gammas, it requires no calibration or levelling and is so versatile it can make equally accurate field surveys on land, in the air, or over water — throughout the world.

Immediate delivery, parts, and service available in many countries of the free world. Technical data, sales, and lease information from Instrument Division:



VARIAN associates
PALO ALTO 43, CALIFORNIA

NEW REPRINT

American Geophysical Union: Transactions

(Reproduced with the permission of the American Geophysical Union)

Now Available

Volumes 13-15, 1932-1934

Volume 13, 1932, paper bound
Volume 14, 1933, paper bound
Volume 15, 1934, paper bound

Previously Reprinted

Volumes 1-12, 1920-1931

(Volumes 3 and 5 were never published)

Paper bound set (in 9 volumes)	\$110.00
Volume 1, 1920, paper bound	5.00
Volume 2, 1921, paper bound	10.00
Volume 4, 1923, paper bound	15.00
Volume 6, 1925, paper bound	5.00
Volume 7, 1926, paper bound	15.00
Volume 8, 1927, paper bound	20.00
Volume 9, 1928, paper bound	15.00
Volume 10-11 1929-1930, paper bound	20.00
Volume 12, 1931, paper bound	15.00

(Volumes 2, 4, and 6-9 published in National Research Council Bulletin)

Volumes 16-34, 1935-1953, will be reproduced by photo-offset as soon as there is sufficient demand to warrant the understanding of a reprint edition.



**JOHNSON
REPRINT CORPORATION**

111 FIFTH AVENUE
NEW YORK 3, NEW YORK

Please mention JOURNAL OF GEOPHYSICAL RESEARCH, when writing to advertisers

Journal of GEOPHYSICAL RESEARCH

VOLUME 66

JULY 1961

No. 7

The National Program for Lunar and Planetary Exploration

A. R. HIBBS

*Jet Propulsion Laboratory, California Institute of Technology
Pasadena, California*

Abstract. The National Aeronautics and Space Administration has assigned to the Jet Propulsion Laboratory the responsibility for design and development of spacecraft for the exploration of the moon, the planets, and interplanetary space. In carrying out its assignment, JPL, the United States' oldest guided-missile and rocket-research laboratory, is designing and fabricating spacecraft to be flown past the moon and to land scientific equipment on the surface of the moon. Designs have also begun for spacecraft to fly past the planets and land capsules of scientific instruments on the planetary surfaces. This paper describes the Ranger spacecraft, now undergoing assembly, which will initiate the lunar exploration program; the Mariner, now being designed, which will initiate the planetary program with a flight past Venus; and the Surveyor, in which packages of scientific instruments will be soft-landed on the moon.

Introduction. The Jet Propulsion Laboratory (JPL) of the California Institute of Technology was established more than 20 years ago to undertake the research and development of guided missiles. Until 1958, the end products of these activities were military weapons systems: for example, the Corporal—the nation's first operational guided missile—and its successor, the Sergeant—now entering operational status as a second-generation successor to the Corporal. The Laboratory was also responsible for numerous fundamental developments in rocketry, guidance, communication, instrumentation etc. These skills, which the Laboratory had developed as the founder of United States guided-missile technology, were used in the design and construction of this country's first successful artificial satellite, Explorer I. At the time of launching of Explorer I, January 31, 1958, the Laboratory, under contract to the United States Army, joined with its companion organization, the Army Ballistic Missile Agency (ABMA), under the technical leadership of Dr. Wernher von Braun, in the launching of this satellite.

In addition to a series of successful launchings of artificial satellites, JPL and ABMA launched

two probes intended for lunar exploration, Pioneers III and IV. Neither of these came sufficiently close to the moon to be considered a lunar probe; nevertheless, Pioneer IV successfully escaped from the gravitational field of earth to take up its independent orbit around the sun as this country's first artificial planet.

This successful launching occurred in March 1959, 3 months after the Laboratory had been transferred to the direction of the National Aeronautics and Space Administration (NASA). The successful team that launched the Explorers and the first successful Pioneer has been kept intact. Dr. Wernher von Braun's group at Huntsville, Alabama, also has been transferred to the auspices of NASA and has been given the new name of the Marshall Space Flight Center. The third space flight center has been organized by NASA in Greenbelt, Maryland, under the name of the Goddard Space Flight Center.

Each of the three space flight centers has a particular role in the space flight program. The Goddard Space Flight Center is developing payloads for earth satellites and sounding rockets. The Marshall Space Flight Center has been given the assignment for development and opera-

	61	62	63	64	65	66	67	68	69	70
SPACECRAFT DEVELOPMENT	2									
RANGER ROUGH LANDING		3								
CENTAUR SOFT LANDING			2	2	3					
CENTAUR LUNAR ORBITERS				1	1					
SATURN SOFT LANDINGS							2	2	2	3

Fig. 1. Planning schedule for lunar program.

tion of the launching rockets, and the Jet Propulsion Laboratory in Pasadena is developing spacecraft for lunar and planetary exploration.

The lunar and planetary program. The lunar program (for which a 10-year planning schedule is given in Fig. 1) is characterized by a steady increase in the complexity of exploring spacecraft. The lunar program begins in 1961 with spacecraft development flights and continues in 1962 with 'rough landing' missions. Next, lunar orbiters, capable of photographing the moon

from a few hundred kilometers above it, and lunar soft landers, capable of exploring the immediate environs, occur in the period from 1963 to 1965.

In the second half of the decade, more complicated and larger lunar vehicles are employed. These vehicles are capable of returning samples of lunar material to earth and roving over the surface to extend the exploration program to a much more diversified type of lunar material and surface.

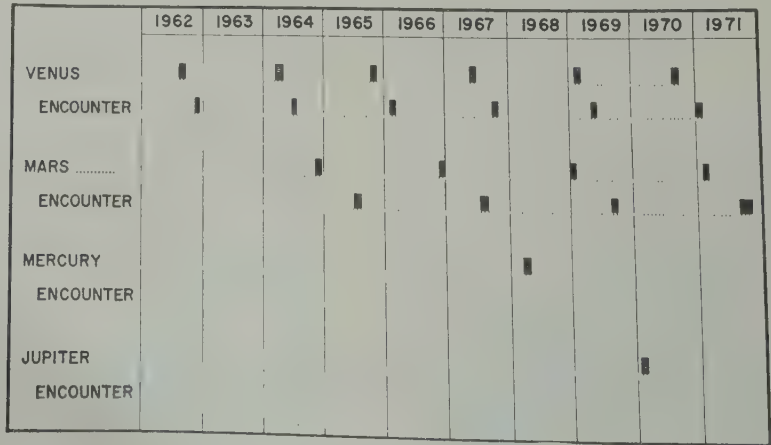


Fig. 2. Schedule of planet availability.

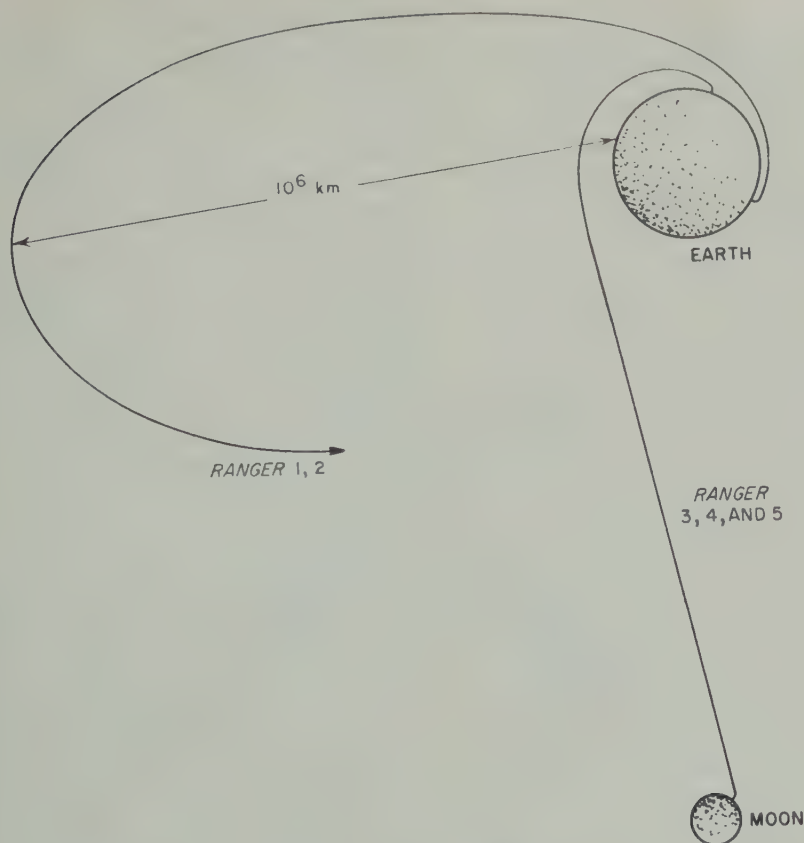


Fig. 3. Ranger trajectories.

The flight schedules to the planets are limited by the motions of the planets in their orbits. Figure 2 lists the years in which flights to the planets are planned over the next decade.

The planetary program will begin in 1962 with a Venus fly-by passing close enough to the planet to obtain better resolution in planetary measurements than could be obtained either from earth or an earth satellite in this same time period. The second flight, later in 1962, will gather only interplanetary data. Similar flights past Venus will be made in 1964 and possibly in 1965.

In 1963, a Mars spacecraft will be flight-tested, and in 1964 it will be flown on a mission to observe Mars. Availability of the Saturn booster in the second half of the decade will permit experiments with spacecraft put in orbit around the target planets and landed on the surface of Mars and possibly on Venus, if continued temperature measurements indicate that this is practical.

The increased capability of Saturn vehicles will provide spacecraft flexibility in the exploitation of new discoveries, and will allow such special missions to be flown as fly-bys of Mercury and Jupiter and a flight considerably out of the plane of the ecliptic to be flown near the end of the decade.

Spacecraft. Only the very earliest spacecraft involved in the lunar and planetary programs are described here since only for these is sufficient design detail available to make such a description valuable.

Two vehicles, Ranger 1 and 2, will be launched in the last half of 1961 to begin the interplanetary exploration program. As can be seen in Figure 3, each will be sent on a long elliptical trajectory whose apogee is approximately 1 million kilometers from earth. This means that they will be launched with a speed only slightly less than escape speed. As a result, they will spend about 1 to 2 months measuring the characteristics of

TABLE 1. Scientific-Experiment Plan for Ranger 1 and 2

Experiment	Sponsoring Agency	Experimenter(s)
Triple-coincidence telescopes	University of Chicago	C. Y. Fan, P. Meyer and J. A. Simpson
Integrating ionization chamber	California Institute of Technology and JPL	H. V. Neher and H. R. Anderson
Medium-energy-particle detectors		J. A. Van Allen
(a) Geiger tubes and CdS detectors	(a) State University of Iowa	
(b) Au-Si detectors	(b) University of Chicago	C. Y. Fan, P. Meyer and J. A. Simpson
Electrostatic analyzers	JPL	M. Neugebauer and C. W. Snyder
Magnetometer	NASA Goddard Space Flight Center	J. P. Heppner
Lyman α telescope	Naval Research Laboratory	T. A. Chubb and R. W. Kreplin
Cosmic-dust detectors	NASA Goddard Space Flight Center	W. M. Alexander

space at the order of several hundred thousand to a million kilometers from earth. Ranger 3, 4, and 5 will be sent on trajectories toward the moon and will carry with them a capsule containing a seismometer. This capsule will be detached from the main bus of the spacecraft, slowed by a retrorocket, and landed on the surface at a speed of a few hundred miles an hour.

Table 1 lists the scientific experiments which will be carried out by the first two Ranger spacecraft and the scientists assigned responsibility for them. Most of the experiments are directed toward the objectives of measuring interplanetary fields and charged particles. There are two exceptions to this category; namely, a measurement of the density of interplanetary dust, and an observation of the neutral hydrogen geocorona.

The charged particle measurements will be carried out by instruments covering a range of energies. At the lowest energy range, there are electrostatic analyzers capable of examining the spectrum of protons from 0 to 5000 electron volts and the spectrum of electrons up to a few hundred electron volts. These analyzers will thus be the first flown that extend their measurements into this very low region, characteristic of the hypothesized solar wind. Medium-range particles will be detected by a group of counters relying both on the solid-state property of semiconductors and on traditional Geiger tubes. Ionization chambers, such as those flown on balloons in the earth's atmosphere, and triple-coincidence telescopes, such as those that were used on Pioneer V, will complete the charged particle measurements by covering the highest energy range in

the neighborhood of 10 to 100 Mev for protons.

Closely associated with the behavior of charged particles is, of course, the behavior of the interplanetary and magnetic field. This will be measured with a rubidium vapor magnetometer which will detect the strength of the field by measuring the Larmor frequency separating the rubidium vapor lines whose fine structure has been split by an amount proportional to the strength of the field.

The neutral hydrogen cloud around the earth will be observed by a scanning telescope that detects scattered radiation of the Lyman α frequency. As the spacecraft recedes from earth, this telescope will repeatedly scan the vicinity of the earth, including in its successive pictures a larger and larger field of view.

The micrometeorite detectors on the Ranger will give information on both the energy and momentum of the particles striking it.

Figure 4 shows a photograph of a model of the spacecraft for Ranger 1 and 2. The rubidium vapor magnetometer is located near the front end, where it is as far removed as possible from those parts of the spacecraft that may introduce a spurious magnetic field. The ionization chamber is below it, located in a position where it will be shielded as little as possible by the structure of the spacecraft. The six electrostatic analyzers are positioned in such a way that they can see freely along opposite directions of each of three coordinate axes.

The spacecraft itself is powered by solar panels that operate after the attitude-control system has successfully aimed the spacecraft directly at

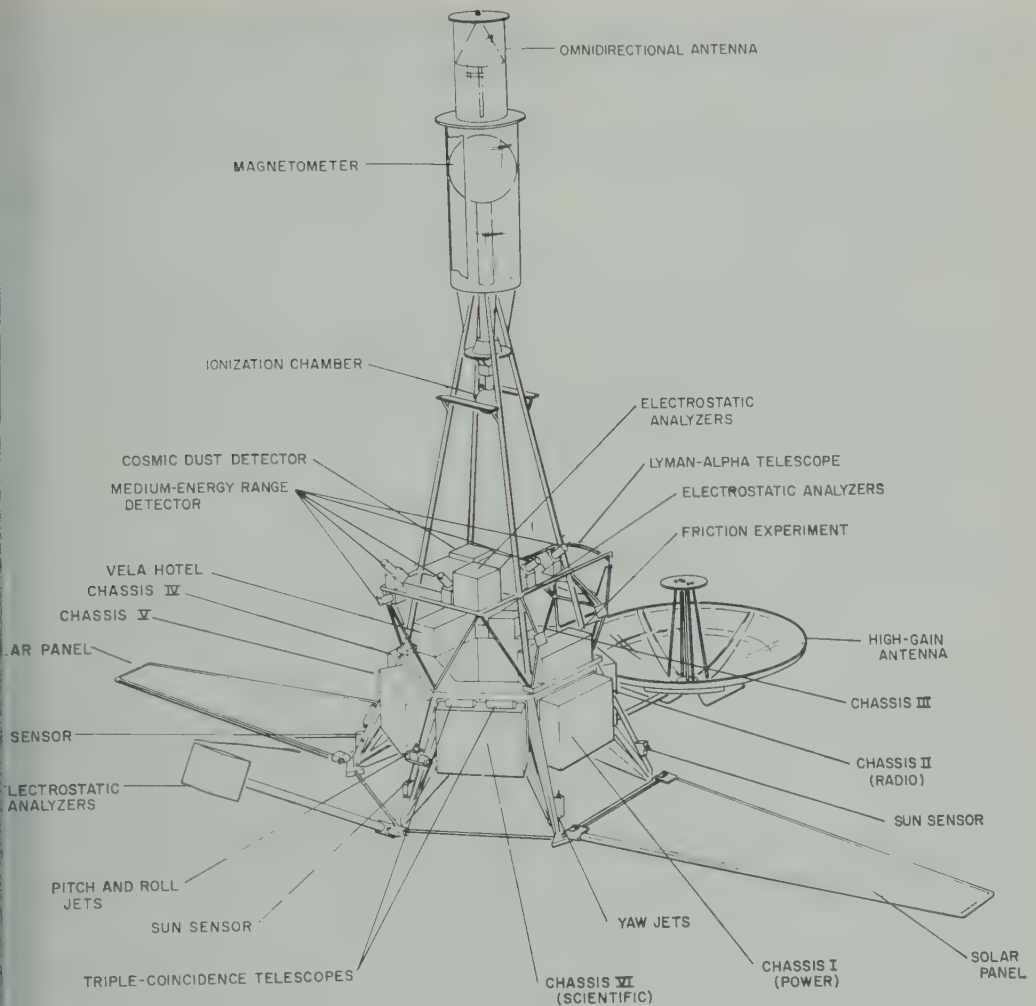


Fig. 4. Ranger 1 and 2.

sun. The attitude-control system will there-
 er maintain this aiming direction throughout
 e lifetime of the experiment. The directional
 abolic antenna will be aimed at earth with
 e same attitude-control system by means of
 ling the spacecraft around its longitudinal axis
 er the sun direction has been fixed. In this
 y, and by hinging the antenna out from the
 spacecraft to the appropriate angle, the antenna
 can be made to point at earth.

Figure 5 shows the proof-test model of Ranger
 a device identical in every way to the flight
 model but one which will be subjected to much
 ore rigorous testing than that employed to
 ck out the actual flight version. The rubidium

vapor magnetometer is inside the fiberglass
 casing at the top of the structure; on a platform
 near the base, several of the charged-particle
 detectors can be seen in this figure.

Figure 6 shows a mating test underway to
 ascertain that the nose cone of the Atlas-Agena
 B fits properly around the base of the spacecraft
 and onto the mating structure. The hexagonal
 base of the spacecraft can be seen between the
 nose cone and the base structure. The six boxes
 positioned around this hexagonal base contain
 all the electronic parts required for the successful
 operation of the spacecraft and its scientific
 instruments.

The second group of Ranger spacecraft, 3, 4,

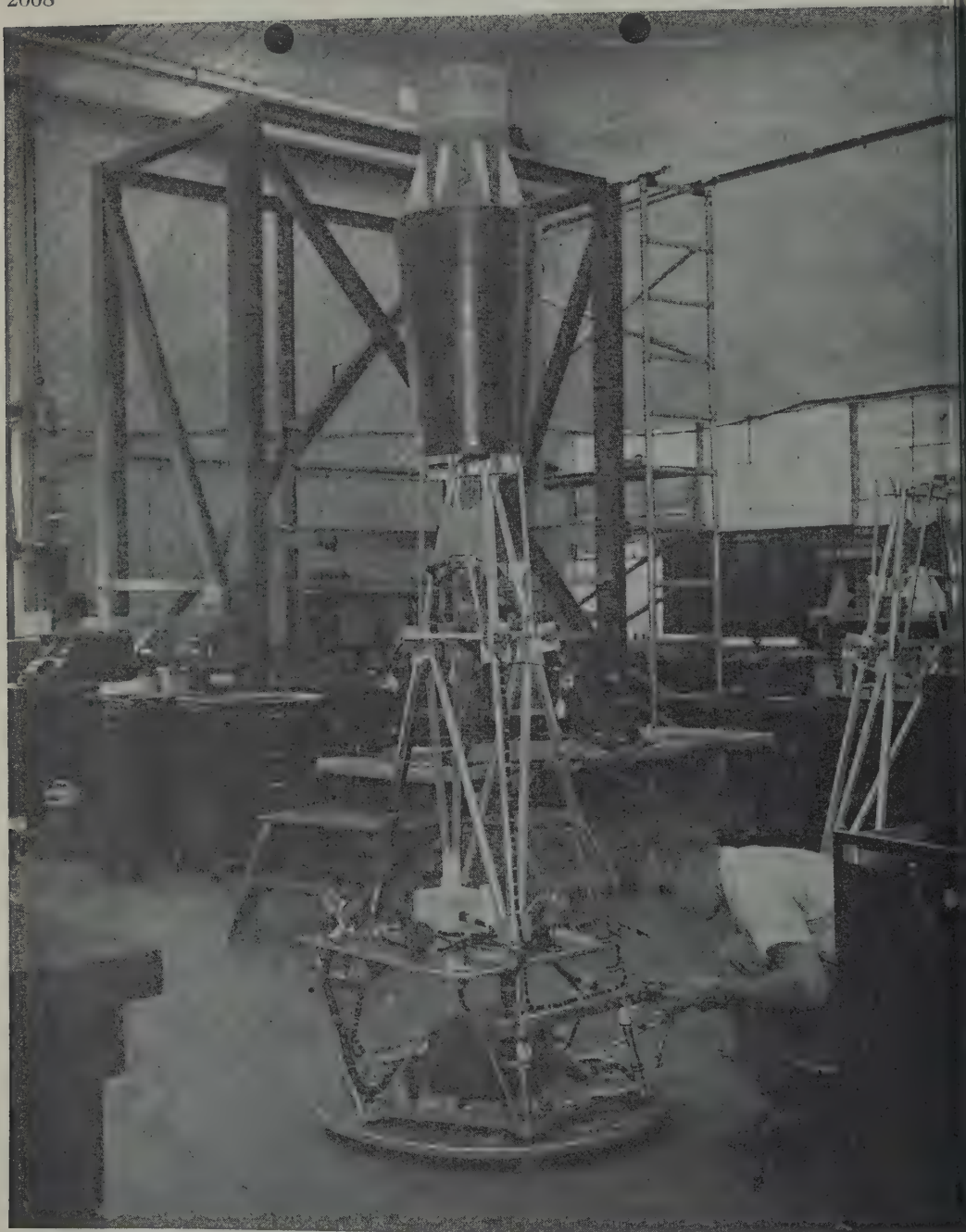


Fig. 5. Proof-test model of Ranger 1.

and 5, are intended for lunar exploration. Table 2 lists the experiments selected for these flights. As the spacecraft approaches the moon, a succession of photographs will be taken by a vidicon camera which is aimed toward the lunar surface.

The vidicon tube will employ a 200-line scan, and the optics will be such as to take a picture measuring approximately 40 kilometers on a side at the initiation of the picture-taking sequence and decreasing steadily to 600 meters on a side

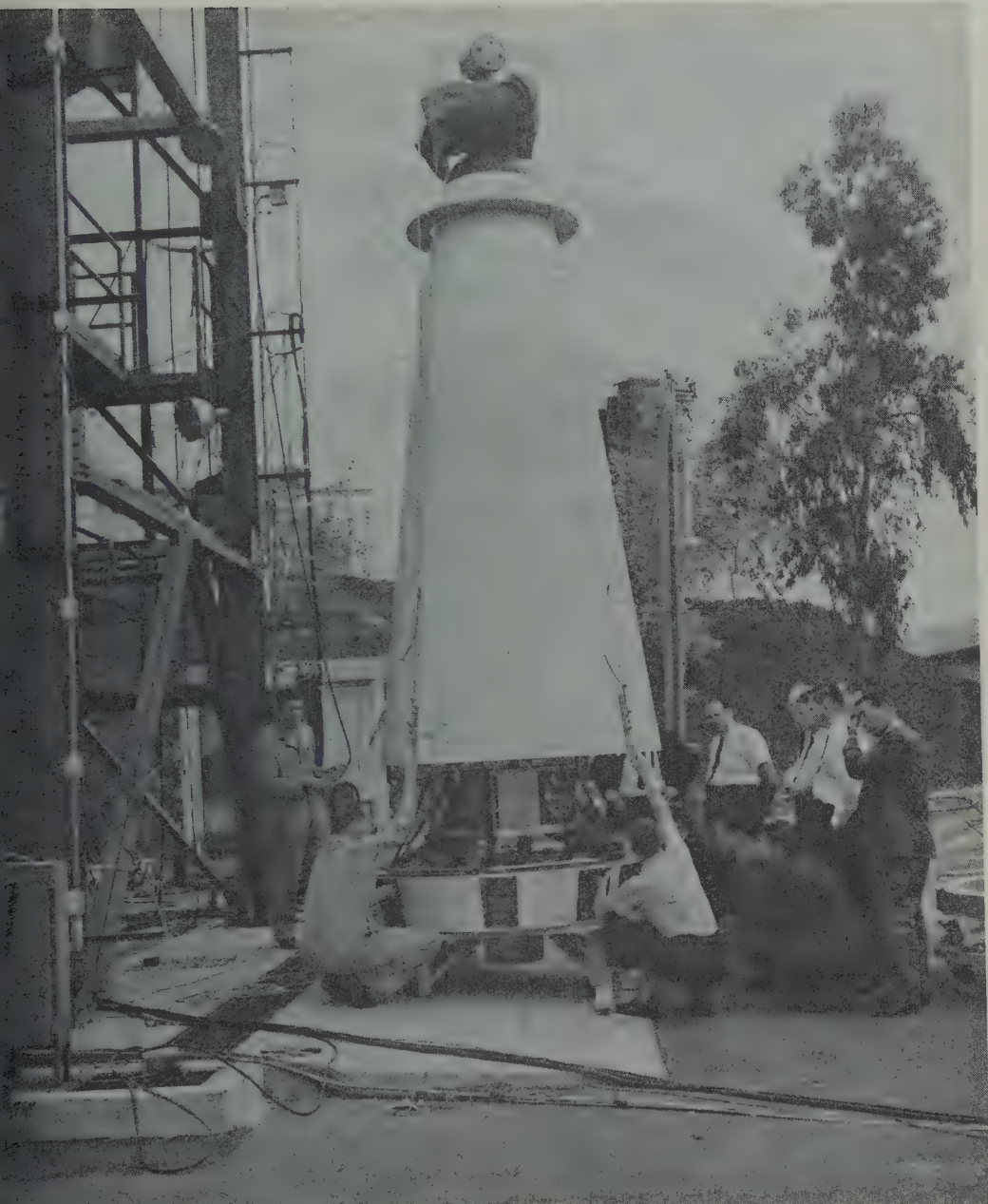


Fig. 6. Mating test of Ranger and Atlas-Agena B nose cone.

or the last picture expected to be successfully recovered from the data. While the vidicon is in operation, a gamma-ray spectrometer, positioned far from the spacecraft so as to avoid the effect of secondaries, will measure the ambient radioactivity in the region of the spectral line associated with the decay of potassium 40. This

experiment has been so designed that, even if the moon is composed of material as low in natural radioactivity as the chondritic meteorites, the detector will observe the lunar potassium 40 line above the background expected from interplanetary and cosmic-ray sources.

Figure 7 shows a model of the Ranger 3, 4,

TABLE 2. Scientific-Experiment Plan for Ranger 3, 4, and 5

Experiment	Sponsoring Agency	Experimenter(s)
<i>Capsule</i>		
Seismometer	California Institute of Technology	F. Press and M. Ewing
Capsule temperature measurement	and Columbia University	
<i>Bus</i>		
Vidicon television	JPL	E. F. Dobies
Gamma-ray spectrometer	University of California, Los Alamos Scientific Laboratory, and JPL	J. R. Arnold, M. A. Van Dilla, E. C. Anderson, and A. Met

and 5 spacecraft, which is similar in many ways to that which was used for Ranger 1 and 2. However, the superstructure containing the scientific instruments has been replaced by a superstructure supporting an omnidirectional antenna and surrounding the lunar capsule together with its retrorocket, being developed by Aeronutronic Corporation under subcontract to the Laboratory. This spacecraft is also powered by solar panels and communicates with earth by means of a directional parabolic antenna.

Approximately 30 kilometers above the lunar surface, after the spacecraft has been properly positioned, the capsule, together with its retrorocket, will be detached from the parent spacecraft. The capsule is spun to maintain its aim direction. Thereafter, the retrorocket is ignited which slows down the capsule to a zero speed relative to the lunar surface at an altitude of about 400 meters. The capsule then falls free from this altitude to impact with a speed of about 30 meters per second.

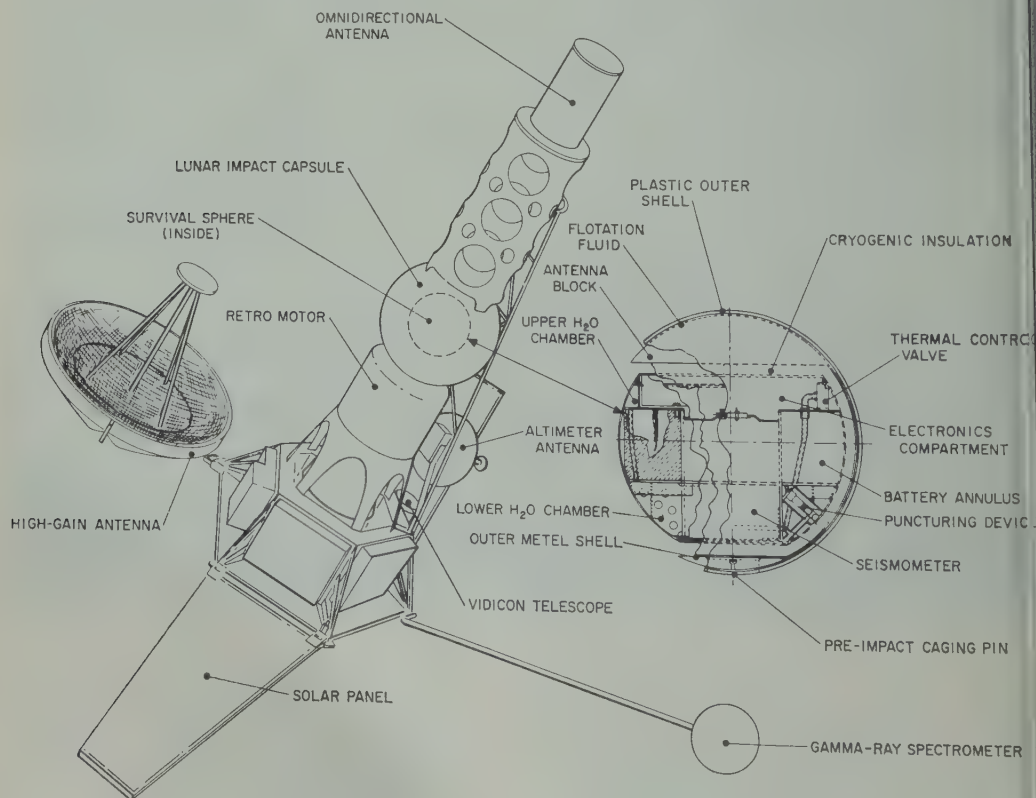


Fig. 7. Ranger 3, 4, and 5.



Fig. 8. Seismometer impact test.

Variations in retromotor performance will, of course, result in a variation of landing speeds. The expected standard deviation of landing speeds is approximately 30 to 40 meters per second. The landing capsule and all the instrumentation within it—that is, the seismometer, its amplifier, transmitter, and antenna, and power supply, righting mechanism, temperature control device, zeroing motor, and automatic calibration device—have been designed to withstand several thousand G's of impact acceleration.

Figure 8 shows the results of one of the numerous tests that have been conducted to ensure that this design objective has been met. This is not a lunar crater but rather a terrestrial crater produced in blacktop by the impact of a seismometer dropped from a helicopter at 1000 feet. The seismometer, lying on the ground beside the crater, operated properly after this drop test.

The seismometer carried in the capsule of

Ranger 3, 4, and 5 is designed to operate for a period of 30 to 60 days. Even if no internal seismic activity occurs on the moon, it is likely that the impact of meteorites on the moon will create sufficient seismic disturbances to be detected by this device.

Detailed lists of experiments for the first flights in the planetary exploration program have not yet been fully formalized. However, committees of the National Academy of Sciences Space Science Board, as well as groups of consultants working with NASA personnel to advise the Space Sciences Steering Committee of NASA Headquarters, have considered in some detail the most pressing problems of planetary science that should be investigated with our earliest probes.

Among the experiments that would be appropriate for a spacecraft designed to make a single pass in the near vicinity of Venus are: Venus temperatures, atmospheric composition,

TABLE 3. Lunar-Surveyor-Instrument Studies

Instrument	Study Contractors
Drill	Armour Research Foundation Hughes Tool Co. Texaco, Inc.
Shaped-charge hole drill	Wells Survey, Inc.
Geophysical instrument package (sound speed, temperature, thermal diffusivity, density, hardness, magnetic susceptibility, electrical resistivity)	Wells Survey, Inc. Texaco, Inc.
Chemical Analysis	
1. Neutron activation	Wells Survey, Inc. Kaman Aircraft Corp.
2. X-ray spectrograph and diffractometer	Philips Electronics and Pharmaceutical Industries Corp.
3. Gas chromatograph	Aerojet-General Corp.
4. Mass spectrometer	The Bendix Corp.
5. Absorption spectrophotometer	Beckman Instruments, Inc.

magnetic field, and dust density and charged-particle spectrum. Some of the instruments for these experiments would be expected to produce their results only during the period of the near-pass of the planet. Others would operate all the way from earth to Venus. The magnetometer, for example, is in this latter class and, consequently, would have to be designed to measure not only the fields of the order of a few gammas, which are expected to occur in interplanetary space, but also fields of the order of a gauss that may occur in the close vicinity of Venus.

A spacecraft designed to pass close to the planet Mars would carry very nearly the same instruments; however, their order of priority would differ. A difference which obviously affects the selection of instruments is the fact that the surface of Venus, unlike the surface of Mars, is not available to optical instruments.

Although no selection has been made for the experiments to be carried out by the first spacecraft to be soft-landed on the moon, design studies of possible instruments have been completed. Table 3 lists these instruments and the companies engaged in their study. Although a drill to penetrate a few feet into the lunar surface is not a scientific instrument, it is considered so much a part of the scientific-instrument payload that it is listed along with those devices whose operation it will make possible. In addition to the devices listed in this table, the spacecraft will contain several television cameras with the total capability of a complete panoramic sweep of the vicinity of the spacecraft as well as close-up observation of the material in the immediate neighborhood of the spacecraft.

Conclusions. The instrumentation and the spacecraft described in this report will initiate this nation's program for the exploration of the moon and planets. The successful development of this exploration program will yield, for example, geophysical and geochemical information about the moon which will help us to understand not only the nature of our sister planet but, perhaps, also something of the origin of the solar system, since the moon may still retain on its surface the five-billion-year-old record of these early processes. It is possible that the biological exploration of Mars may reveal extraterrestrial life forms. The chemical analysis of such life developing in an ecology completely separate from earth, may bring us closer to the understanding of the origin of life. But even the excitement inherent in such possibilities as these will undoubtedly be surpassed by the reality of the discoveries which lie before us.

Acknowledgment. This paper presents the results of one phase of research carried out at the Jet Propulsion Laboratory, California Institute of Technology, under contract NASw-6, sponsored by the National Aeronautics and Space Administration.

(Manuscript received February 16, 1961;
revised April 12, 1961.)

Characteristics of the Van Allen Radiation Zones as Measured by the Scintillation Counter on Explorer VI

ALAN ROSEN AND THOMAS A. FARLEY

*Space Technology Laboratories, Inc.
Los Angeles 45, California*

Abstract. A scintillation counter responding principally to direct electrons has been flown on the Explorer VI earth satellite in an elliptical orbit extending to 48,600 km. The instrument measured fluxes of electrons above 200 kev and protons above 2 Mev. After a week of magnetically quiet observations, a geomagnetic storm occurred, and an immediate increase in the counting rate of this instrument was detected; other radiation instruments showed a decrease in counting rate at this time. Gross fluctuations in particle intensity were observed at the edge of the outer zone of the Van Allen radiation belt during the storm, and these fluctuations are closely related to simultaneous geomagnetic activity. The increased particle intensity in the outer zone declined quite slowly after the storm until the next period of magnetic activity about two weeks later. This paper presents a detailed summary of the observations made by the scintillation counter during the period of data reception from the satellite.

Introduction. Space Technology Laboratories, Inc., has constructed, calibrated, and flown a scintillation counter on the Explorer VI earth satellite. The object of the experiment was to make direct observations of electrons in both the inner and outer zones of the radiation belt with a detector insensitive to bremsstrahlung.

The Explorer VI satellite, constructed by Space Technology Laboratories, Inc., was launched at 14:23 GMT on August 7, 1959, into an elliptical orbit having an apogee 48,600 km from earth center and a perigee at 6,600 km (230 km altitude). The period of the satellite was 12 hours and 42 minutes, and the payload spun about its own axis at a rate of 2.8 cps. The orbit was inclined 38° with respect to the plane of the ecliptic. Perigee took place at about 9:30 AM local time at the approximate latitude of Florida, and apogee took place at approximately 9:00 PM local time in high southern latitudes. The satellite did not go into the earth's shadow in the 6-week period during which the analog transmitter broadcasting the scintillation counter data was operating.

The geomagnetic storm that is frequently referred to in this paper, and that produced such profound effects on the trapped radiation, began with a sudden commencement at 0404 GMT on August 16, 1959. The initial phase lasted approximately 2 hours. The main phase decrease in horizontal intensity began at about 0600 GMT, and the storm main phase ended late on August

17, and was designated moderately severe at most ground station observatories.

Instrumentation. The detector used in this experiment consisted of a cylindrical plastic scintillator, approximately 1 inch in diameter and $\frac{1}{4}$ inch thick, cemented to a Dumont 6467 photomultiplier tube. Figure 1 shows a photograph of the photomultiplier tube package and associated circuitry. The output pulses of the photomultiplier were amplified and fed into a binary register having a capacity of 2^{20} pulses. Voltages representing the state (on or off) of the ninth, fourteenth, and twentieth binaries were added and used to modulate a subcarrier oscillator, so that transitions between the states of these binaries could be used to determine the counting rate. The output of the 2^{20} binary was also fed into a digital register whose contents were broadcast in digital form by a second transmitter.

The detector was covered with a foil having a thickness of 3.3 mg/cm². An electronic bias was used in order to count only particles losing 100 kev or more of energy in the scintillator; this bias was adjusted by using the 624 kev electron conversion peak of Cs¹³⁷ as an energy standard. This instrument, mounted inside the shell of the satellite, responded to radiation penetrating a 3.3 mg/cm² foil-covered window, and to more energetic particles passing through the payload shell. The minimum energy detectable, determined by the foil thickness, the permitted angle

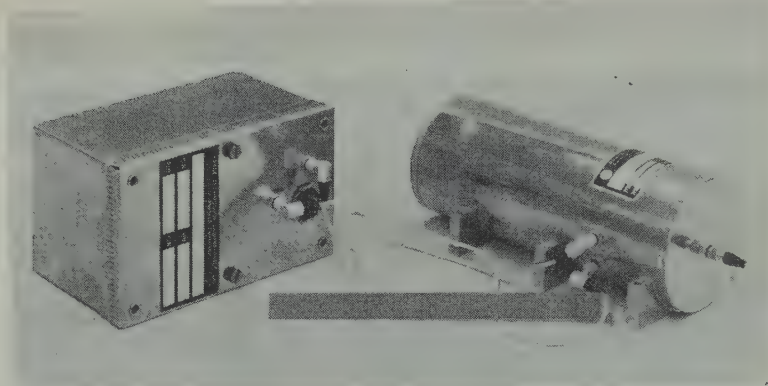


Fig. 1. Photograph of flight instrument showing photomultiplier housing and associated circuitry.

of penetration of the foils, and the electronic bias of 100 kev, was 200 kev for electrons and 2 Mev for protons.

The omnidirectional geometrical factor¹ of this instrument for the direct observation of electrons and protons was estimated from geometrical considerations to be approximately $2 \times 10^{-4} \text{ cm}^2$ for 200–500 kev electrons and 2–10 Mev protons. Five hundred kev electrons and 10 Mev protons could just penetrate the shell and be detected, and at these energies the omnidirectional geometrical factor was estimated to be $4 \times 10^{-2} \text{ cm}^2$. The geometrical factor rose slowly to a maximum value of 3.5 cm^2 for very penetrating particles.

The saturation characteristic of the entire detector system, including flight power supply and all flight electronics, was determined before the satellite was launched by tests made on the actual flight instrument. The results of this test are shown in Figure 2. A 1 millicurie source of Sr^{90} was used for this test, and the incident intensity was increased by decreasing the source to detector distance. The observed count rate continued to rise slowly, even for very high incident intensities, because the potential across the later dynode resistors of the photomultiplier dropped, the output pulse height and width

decreased, and a higher count rate could be handled by the succeeding electronic circuitry.

The scintillation counter was relatively insensitive to bremsstrahlung, and the counting rate of this instrument due to electrons of a given energy must considerably exceed the count rate due to bremsstrahlung from electrons at the same incident energy. The only photon interaction of importance in a plastic scintillator is the Compton interaction, and because of the electronic bias of 100 kev, the theoretical threshold for photon detection was about 220 kev. Electrons having energies below the threshold could not produce bremsstrahlung that would be registered by the detector. Because a plastic scintillator has a low efficiency for detection of photons above 220 kev, and because electrons having energies of several hundred kev have a small probability of producing 220 kev photons, the instrument responded principally to direct electrons at all energies.

The calculated estimates of the efficiency and geometrical factor for bremsstrahlung detection were confirmed by measurements after Explorer VI was launched on a similar instrument with the same bias level. An entire payload, identical to Explorer VI, was subjected to an electron bombardment at the High Voltage Engineering Corporation in order to measure the response of the various radiation instruments to electrons at 1 Mev, and to bremsstrahlung from monoenergetic electrons at 500, 350, and 250 kev. At 1 Mev the electrons were permitted to strike the payload directly, whereas at 500, 350, and 250 kev the electron beam was absorbed in an aluminum plate placed near the payload allowing only bremsstrahlung to reach the satellite. The

¹ The omnidirectional geometrical factor G , which depends on the counter surface area and the solid angle through which radiation can reach the counter, is defined by $\epsilon G = R/J$. R is the corrected counting rate of the detector and J , the omnidirectional intensity of isotropic radiation, is the flux per unit time of particles from all directions through a sphere of unit cross-sectional area (J is measured in $\text{cm}^{-2} \text{ sec}^{-1}$). ϵ , the detection efficiency for the radiation in question, is assumed to be 100 per cent for electrons and protons.

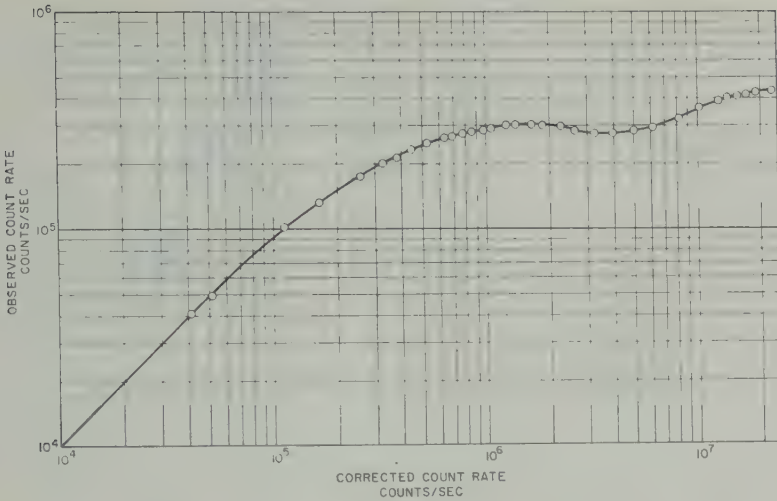


Fig. 2. Observed count rate of the flight instrument as a function of incident intensity of Sr^{90} source. The data points were obtained before flight in a laboratory measurement on the actual detector, power supply, and electronics that were used in the satellite. This curve has been used to correct the count rate for saturation effects.

boardment was made from a variety of sections, and the response was integrated over surface of the payload to measure the product for each of these energies. These measurements represent the bremsstrahlung efficiency even at 1 Mev, for the scintillation counter was never directly in the rather narrow electron beam. These results are shown in Figure 3 together

with the estimated geometrical factors for direct detection of electrons. The total response of the detector for measurement of electron flux is the sum of these two curves, and is also shown in the figure. It is this total response curve that must be used to interpret the counting rate of the instrument in orbit.

While bremsstrahlung from electrons below

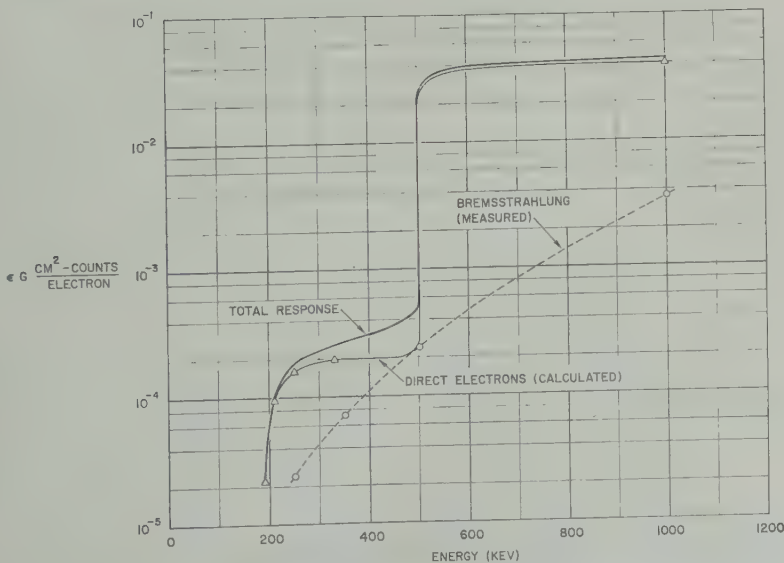


Fig. 3. A representation of the over-all efficiency of the scintillation counter for the detection of electrons, both directly and by means of bremsstrahlung from the electrons.

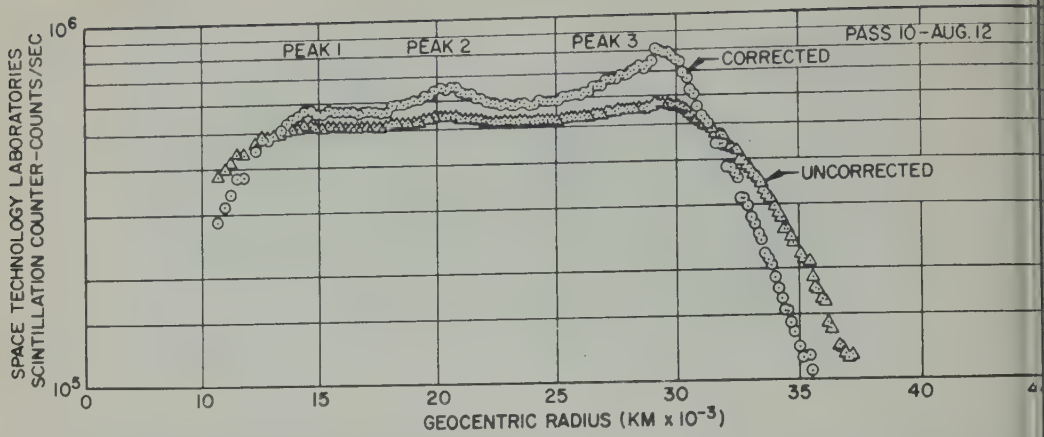


Fig. 4. Typical observed and corrected count rate curves in the outer Van Allen zone before the geomagnetic storm of August 16, 1959.

about 220 kev could not in theory produce counts in the detector, sufficiently high intensities of low-energy photons could cause pulse pile-up above the threshold of the scintillation counter. The spare Explorer VI payload was bombarded with low-energy electrons from an electron gun at the University of Minnesota, and the duplicate scintillation experiment count rate was observed.

The omnidirectional electron fluxes required to produce the count rates observed in the outer zone on a quiet, prestorm day were calculated from these measurements, and were as follows: at 40 kev, 2×10^{12} electrons/cm² sec; at 60 kev, 6×10^{11} electrons/cm² sec; at 85 kev, 3×10^{10} electrons/cm² sec. The fluxes would have to be more than an order of magnitude higher if

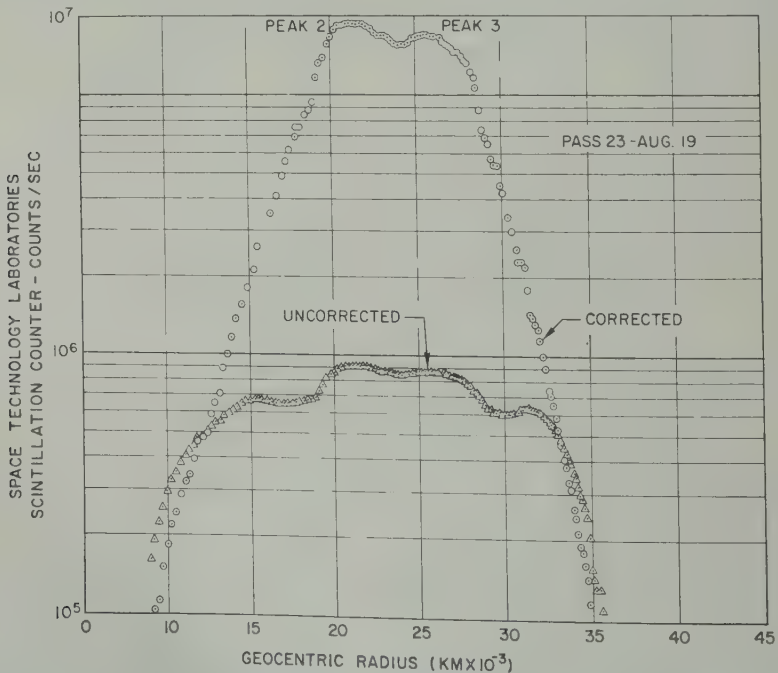


Fig. 5. Typical observed and corrected count rate curve in the outer Van Allen zone after the geomagnetic storm of August 16, 1959.

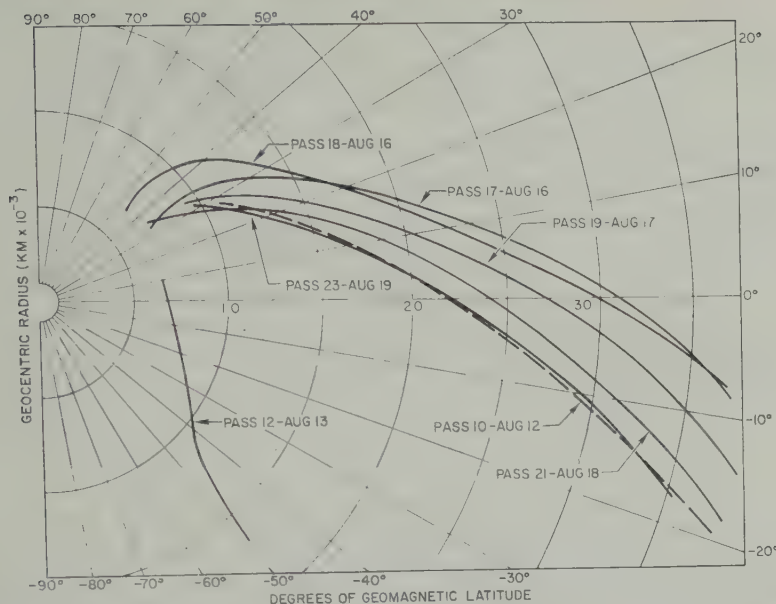


Fig. 6. Radial distance and geomagnetic latitude for the trajectory portions used in this paper.

duce the counting rate observed after the geomagnetic storm. Because the required fluxes are so large, it is unlikely that pulse pile-up due to bremsstrahlung from low-energy electrons contributed more than a minor fraction of the count rate in the outer zone.

Two examples of the data as reduced from the telemetry records, one taken before and one taken after the great increase in count rate during the geomagnetic storm beginning August 16, 1959, are shown in Figures 4 and 5. The corresponding trajectories are shown in Figure 6, together with the trajectories of other traversals of the radiation belts discussed in this work. The trajectories are plotted in a geomagnetic coordinate system based on an earth-centered magnetic dipole axis intersecting the earth's surface at 78.5°N latitude and 291°E longitude. The high observed count rates plotted in Figures 4 and 5 clearly indicate that the true radiation intensity saturated the instrument at the peak of the outer Van Allen zone. Furthermore, the observed count rates were considerably higher than those obtained with very high intensities of Sr^{90} in the laboratory with the flight instrument.

Figure 5 illustrates a condition common to all traversals of the high intensity radiation regions after August 18: there are maxima at approximately 620,000 to 640,000 counts per

second on both sides of the region of highest intensity. These 'shoulders' have been identified as the characteristic maximum in the saturation curve shown in Figure 2. Since these maxima always appear at just double the 310,000 counts per second maximum in the saturation curve, the very high count rates have been attributed to a binary failure that resulted in a doubling of all observed count rates. This conclusion is supported by a count rate outside the radiation zones that consistently indicated an interplanetary cosmic-ray flux of approximately twice the value observed by the other experiments on this vehicle. Approximate true intensity curves have been constructed, therefore, by halving the observed count rate, and by reading the true intensity from the saturation curve. The corrected count rates, calculated as described here, are also shown in Figures 4 and 5. All other particle intensities referred to or illustrated in this work have been corrected in this way. An analysis of the possible errors and uncertainties which may be introduced by this correction procedure has been placed after the data presented in the next section.

Data. The data from this experiment show systematic differences from that obtained by the bremsstrahlung detectors on the same satellite, and these differences must be due to the different energies to which the scintillation counter

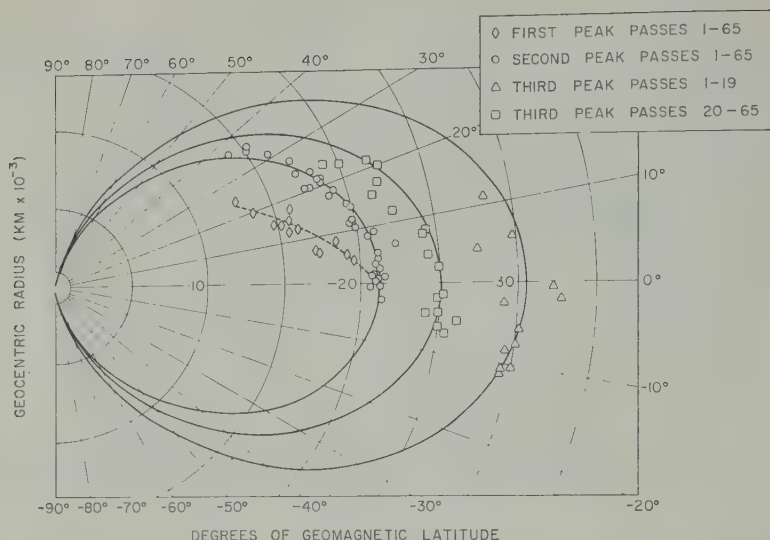


Fig. 7. Positions of the three peaks seen by the scintillation counter. The solid lines are magnetic dipole lines of force. The dotted line connects the points representing peak 1 that are not distributed along a line of force.

responds. The data are presented here in a way that facilitates comparison with the other instruments on this vehicle.

Pass 10 in Figure 4 has three identifiable peaks labeled 1, 2, and 3. This pass is representative of data taken between August 8 and 16, although peak 1 is never outstanding and is sometimes missing. None of these peaks are to be identified with the high energy proton 'inner belt,' since the counting rates are much too high, and the satellite passes too far north on the outward traversal to see these protons, according to *Fan, Meyer, and Simpson [1960]*. Pass 23 in Figure 5 illustrates the type of data obtained from August 18 to September 3. Peak 1 is never seen, and on the most northerly passes only one peak is observed.

The position of these peaks, both before and after the magnetic storm, are plotted in Figure 7 in the above-described geomagnetic coordinate system. This figure includes the magnetic lines of force along which peaks 2 and 3 are found. It also shows the large change in position of peak 3 after the occurrence of the geomagnetic storm, and the apparent merger of peak 3 with peak 2 at high latitudes after the storm.

The position of peak 2 appears to be essentially independent of the geophysical events that took place during the lifetime of the satellite. The points representing peak 1, unlike the other

peaks, do not fall along a line of force.

An indication of the substantial day-to-day variation in the outer Van Allen zone may be obtained from the data plotted in Figure 8. This figure shows the count rate at 10° south geomagnetic latitude using data taken from each pass when the satellite was within 1° of this latitude.

Figures 9, 10, and 11 show comparison between simultaneous measurements made by the STL scintillation counter, the University of Minnesota Geiger counter and ion chamber [Arnoldy, Hoffman, and Winckler, 1960]; and the University of Chicago proportional counter [Fan, Meyer, and Simpson, 1960]. Figure 9 shows data taken on August 16 immediately before the geomagnetic storm. Figure 10 shows the remarkable changes that had occurred by August 17: the scintillation counter peak intensity had increased while the instruments sensitive to bremsstrahlung show a decrease.

After passing through apogee at approximately 48,000 km from earth center, the satellite spent several hours at high southern latitude outside the radiation zones, and then re-entered the outer belt at fairly low altitude, passing rapidly through a region of depressed intensity, and the inner zone containing the high-energy protons. Figure 11 shows typical scintillation counter results during this period and compares

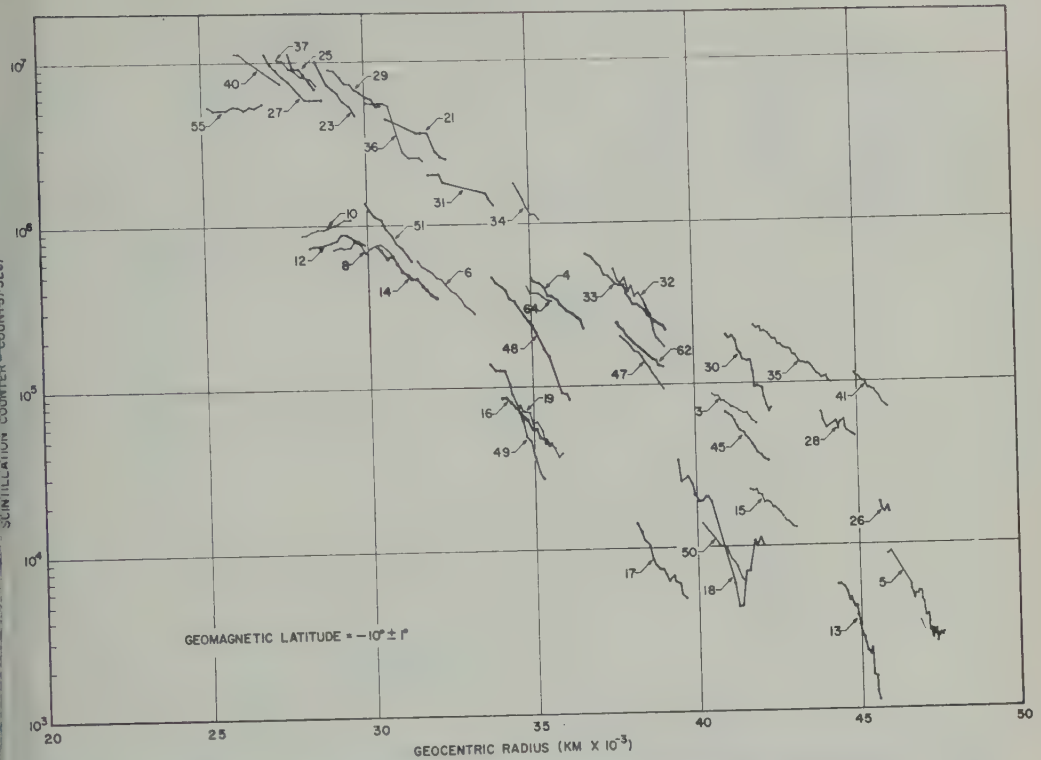


Fig. 8. Count rates from different passes at various radial distances, always within $\pm 1^\circ$ of 10° south geomagnetic latitude. The count rate shows a radial dependence of approximately $r^{-1.5}$.

em with simultaneous measurements made by the proportional counter of the University of Chicago. There was never more than one peak in the scintillation counter results while passing through the outer zone at these distances.

The systematic discrepancies in the position and behavior of the peak intensities between the scintillation counter and the instruments sensitive to bremsstrahlung raise important questions concerning the type and energy of the particles to which each instrument is responding. These questions will be considered more fully in the next section.

Figure 12 shows the results of three day-by-day passes beginning immediately before the geomagnetic storm of August 16 and continuing through pass 21 on August 18 when the increase due to the storm was over. The initial increase seems to be mostly in peak number 2, with the decrease and change in position of peak 3 occurring between passes 19 and 21. Although the trajectory of the satellite was not identical for these four passes (see Fig. 6), the increase certainly cannot be attributed to a change in

the trajectory, for even on pass 18 the intensity rose to a higher value than any seen between August 8 and August 16. There is, therefore, no decrease in the peak intensity of either peak in the outer Van Allen zone of particles to which the scintillation counter responded. Figure 8, however, shows that the intensity far out in the outer zone did show a tendency to decrease during the early stages of the storm on passes 18 and 19.

Figure 13 shows the maximum peak intensity in the outer zone for essentially all the available passes. Sometimes the maximum intensity is at peak 2 and sometimes it is at peak 3, although the difference in peak heights is always small. While the uncertainties in the reconstruction of the intensity curves and the uncertainty in the estimate of the efficiencies for particles of various energies do not permit accurate measurements of the particle flux, the relative day-to-day changes are probably quite well represented in Figure 13. For example, the alternate increase and decrease in peak intensity starting with pass 20 was at least partly the result of traversals

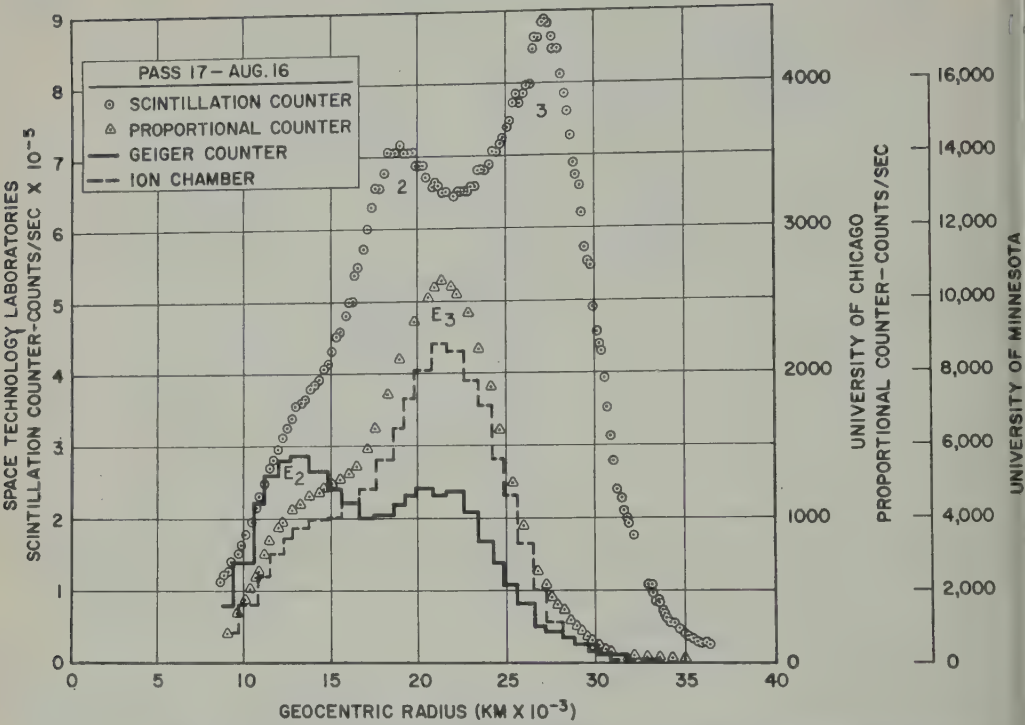


Fig. 9. Results from the four radiation detectors aboard the Explorer VI satellite immediately before a geomagnetic storm.

alternately at high and low geomagnetic latitudes. Since the period of the satellite was just slightly greater than 12 hours, consecutive passes differ in geographic longitude by approximately 180°. Therefore, the magnetic dipole axis was alternately tipped toward the satellite (high geomagnetic latitude pass) and away from the satellite (low latitude pass). A few days later, because

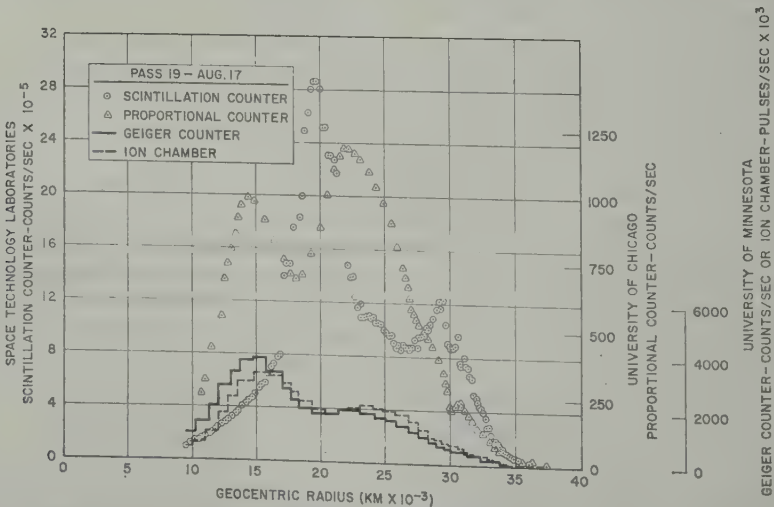


Fig. 10. Results from the four detectors approximately 20 hours after a geomagnetic storm sudden commencement. Note the contraction of the scintillation counter scale, and the expansion of the other scales from those used in Figure 9.

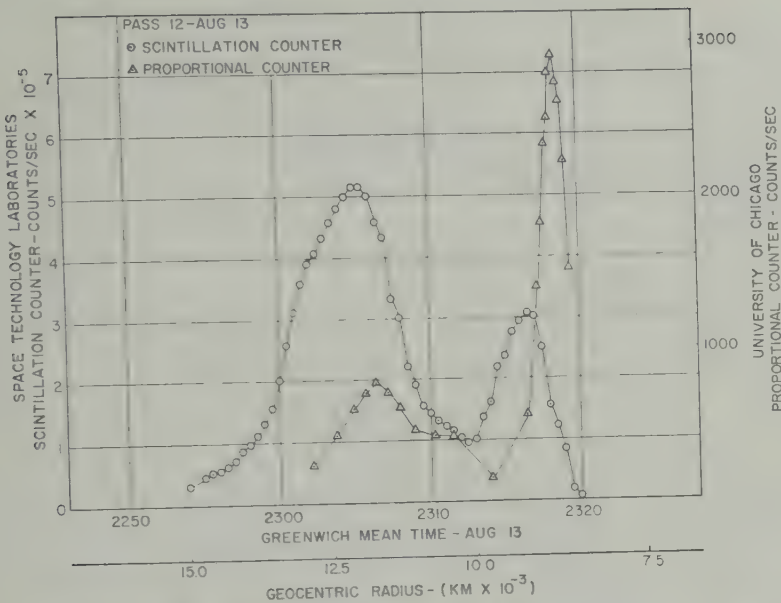


Fig. 11. A typical traversal of the outer and inner Van Allen zones while the satellite approaches perigee, comparing the scintillation counter and proportional counter results.

satellite period was incommensurate with the day's period, the magnetic axis was tipped to the side on each traversal, and both passes were at intermediate geomagnetic latitudes. The low latitude passes produced the high count rates, and the high latitude passes, the low ones. The appearance of such expected effects supports the validity of the reconstruction of the peak intensities from the saturation curve.

At radial distances of about 7 earth radii, the trapped radiation intensity decreased to a low value, presumably the interplanetary cosmic-ray flux. The decrease in intensity was quite rapid, varying approximately as the inverse twentieth power of the radial distance at constant latitude, as shown in Figure 8. On several occasions during periods of magnetic activity observed at surface observatories, large fluctuations indicative of very disturbed conditions in the radiation field have been seen at the outer edge of the outer Van Allen zone. The three best examples of these fluctuations are shown in Figures 14, 15, and 16, together with some simultaneous data from the University of Minnesota Geiger counter in Figures 14 and 15. The data shown in Figures 14 and 15 were taken during the main phase of the August 16 geomagnetic storm. The data in Figure 16 were taken during a period of irregular magnetic activity

that lasted from September 2 to September 4.

The authors have shown in a separate work [Farley and Rosen, 1960] that the scintillation experiment count rate is negatively correlated with the magnetic field for at least a 20 minute period during these fluctuations. The magnetic field was measured by the Space Technology Laboratories' magnetometer [Sonett, Smith, and Sims, 1960; Smith, Coleman, Judge, and Kelso, 1960] carried on the vehicle. The correlation is probably typical of all the fluctuations shown in these figures, in sharp contrast to the quiet-day positive correlations found between these same two instruments by Judge and Coleman (private communication), which they have identified as a betatron-type acceleration of trapped particles.

A continuing investigation is being carried out to see what connection these fluctuations may have between distant and ground station magnetic disturbances, and what relation they may have to hydromagnetic waves propagating in the geomagnetic field.

The count rate outside the radiation belt at high southern latitudes varied from about 5.5 to 10 counts/sec (corrected) from day to day, although it often seemed quite steady over several hours' time. This count rate corresponded to an omnidirectional flux of 1.6 to 2.9 par-

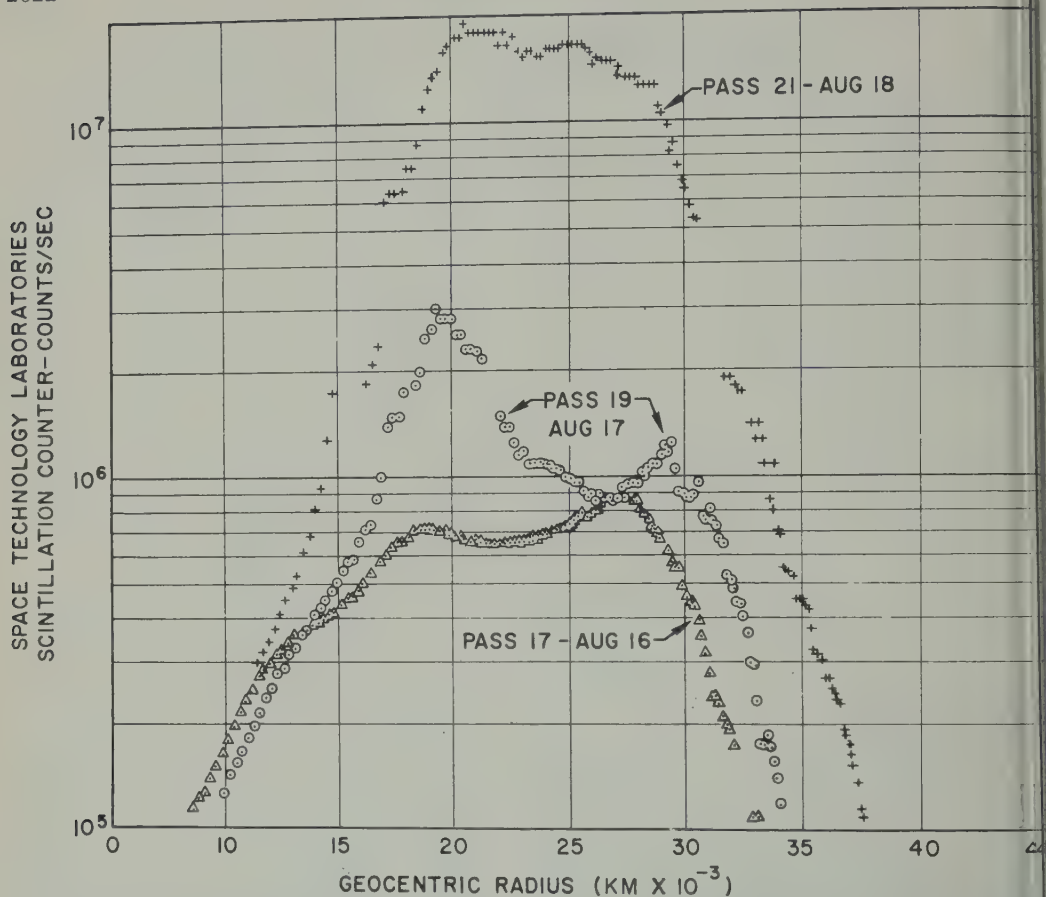


Fig. 12. Three traversals of the outer Van Allen zone at approximately 24-hour intervals during a geomagnetic storm, showing a continuous increase in count rate.

ticles/cm² sec if it was caused by particles having sufficient energy to penetrate to the scintillator from all directions. During the period of the geomagnetic storm this count rate rose to 50 counts/sec and more, probably owing to low-energy particles in this region as a result of the storm.

It is now appropriate to consider to what extent these results, differing markedly in some respects from those of the bremsstrahlung instruments, have been affected by the saturation and binary failure corrections applied to the STL data. Perhaps the most noticeable difference in this experiment was the appearance of three peaks, none of which was located at the positions of peaks observed by the other experiments. We offer the following arguments that the peaks indicated by the scintillation counter are real and are located correctly:

1. The peaks indicated by the scintillation counter show a systematic distribution in space and have a time behavior that can be related to that of the bremsstrahlung detector peaks. The observation of a peak depends on the ability to tell when the true incident intensity stops increasing and starts decreasing. A false indication of a change from increasing to decreasing intensity might be given by a maximum in the saturation curve, or by a failing binary starting to function normally. Both of these effects would produce a false peak appearing at a given count rate, or perhaps appearing randomly for a binary failure not related to the count rate. But this certainly does not occur. Peak 2, for example, falls along the same line of force (Fig. 7) after the storm of August 16 as it did before, even though the observed counting rates are quite different. Peak 3 does change position after

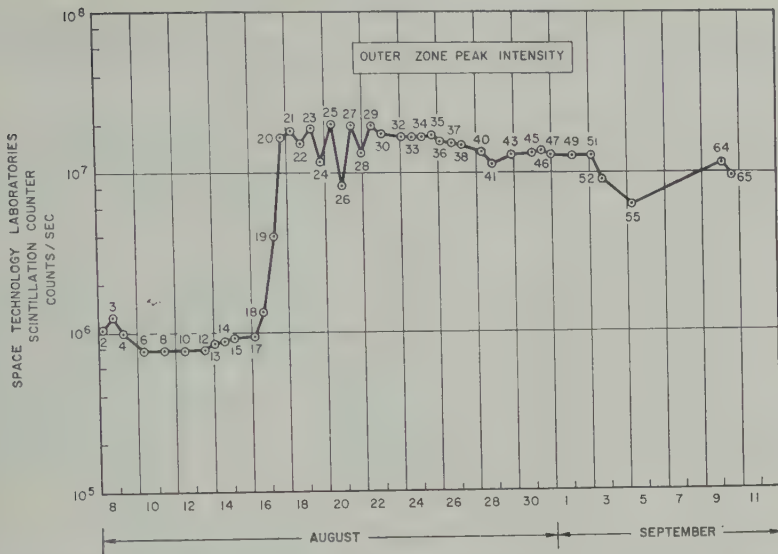


Fig. 13. Approximate maximum count rate of the scintillation counter for all passes on which data are available.

the storm, but it moves inward about 5000 km a way quite similar to the outermost peak of the bremsstrahlung counters, and certainly is not found at the same observed counting rates. In short, the peaks observed by this detector and described as real in this paper are not systematically correlated with the observed count rate, nor are they randomly sprinkled over the outer radiation zone.

2. A careful examination of the data in Figure 10 at the position of the outermost scintillation counter peak reveals significant changes in the slope of the proportional counter count rate which indicates that the proportional counter responds in some degree to the particles in peak 3. Although peak 3 is not seen in this position hereafter (because of the storm increase), there are significant slope changes in both the scintillation counter and proportional counter count rates at this position in space on subsequent passes. Such correlations could hardly be expected if peak 3 of the scintillation counter were a spurious peak due to saturation or binary failure effects.

3. There is evidence for total failure of the binary involved. If the observed count rates on a quiet day outside the radiation belt are accepted without correction, this results in an interplanetary flux of approximately twice the value of 1.8 particles/cm² sec reported by *Fan, Meyer, and Simpson* [1960]. There is evidence, therefore, of

a factor of 2 error both at 11 counts per second and at 640,000 counts per second, indicating that the binary failure is total and not count rate dependent.

Besides the establishment of the peaks and their locations, the authors have made flux estimates that are affected by the saturation and binary failure corrections. Before the storm, a typical correction at peak 3 is a factor of 2 decrease for binary failure, and a factor of 3 increase for saturation. After the storm the correction is a factor of 2 decrease for binary failure and about a factor of 40 increase for saturation. As a result of these large corrections, as well as of some uncertainties in the geometrical factors, the authors claim only an order of magnitude accuracy for their flux estimates, although they may be somewhat better than this before the storm. It is important to point out that if the fluxes of electrons above 200 kev were not of the order estimated in this paper the scintillation counter simply would not have saturated.

Discussion. A comparison of the results of this experiment with the results of the other radiation experiments on the same satellite gives important information on the type and energy of the particles in the outer Van Allen zone. There are several remarkable differences in spatial distribution and behavior during the magnetic storm that indicate that the scintillation counter is at times responding to particles

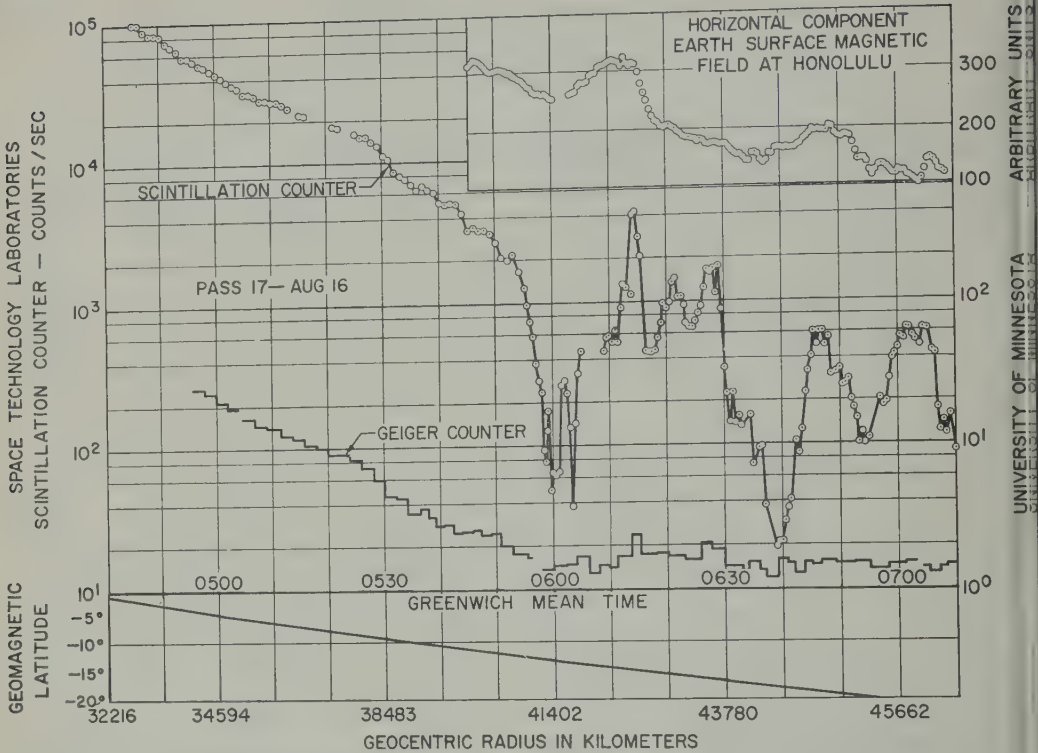


Fig. 14. Gross fluctuations observed at the edge of the outer Van Allen zone, commencing approximately at the start of the main phase of a geomagnetic storm.

other than those to which the proportional and Geiger counters are sensitive.

These differences can probably be explained by the different sensitivities of the instruments to electrons of varying energies. The scintillation counter, unlike the bremsstrahlung instruments, has a rather sharp low-energy cutoff at 200 kev for electrons, and except when the electron spectrum is quite steep between 200 and 500 kev, it responds principally to electrons above 500 kev. The scintillation counter also has a proton sensitivity that extends to considerably lower energies (2 Mev) than the other radiation detectors. The differences between the results of the scintillation counter and the bremsstrahlung instruments have been discussed below with the assumption that they are caused by the different sensitivity of the scintillation counter.

The spatial distribution differences are obvious from Figures 9 and 10. The scintillation counter peaks 2 and 3 are not readily identifiable as the electron peaks E_2 and E_3 [Fan, Meyer, and Simpson, 1960]. The correlations between peak 3 and the slope changes in the proportional counter

on Pass 19 mentioned in the last section indicate that the proportional counter was responding inefficiently to particles observed by the scintillation counter, and that this response is superimposed on a considerably greater count rate due to other particles. The counts registered by the proportional counter telescope in the outer Van Allen zone have been identified unambiguously as bremsstrahlung from electrons because of the absence of triple counts [Fan, Meyer, and Simpson, 1960]. Since this counter was shielded with 5 g/cm² of lead, it was least sensitive to bremsstrahlung from low-energy electrons, and it seems most reasonable to identify peak 3 of the scintillation counter as electrons having energies significantly below those that caused most of the proportional counter response. We conclude, therefore, that there were large fluxes of electrons above 200 kev in peak 3 whose distribution and storm behavior were noticeably different from those electrons detected by the other instruments.

Throughout the period of observation by the scintillation counter, peaks 2 and 3 appear to be closely related. They were of approximately the

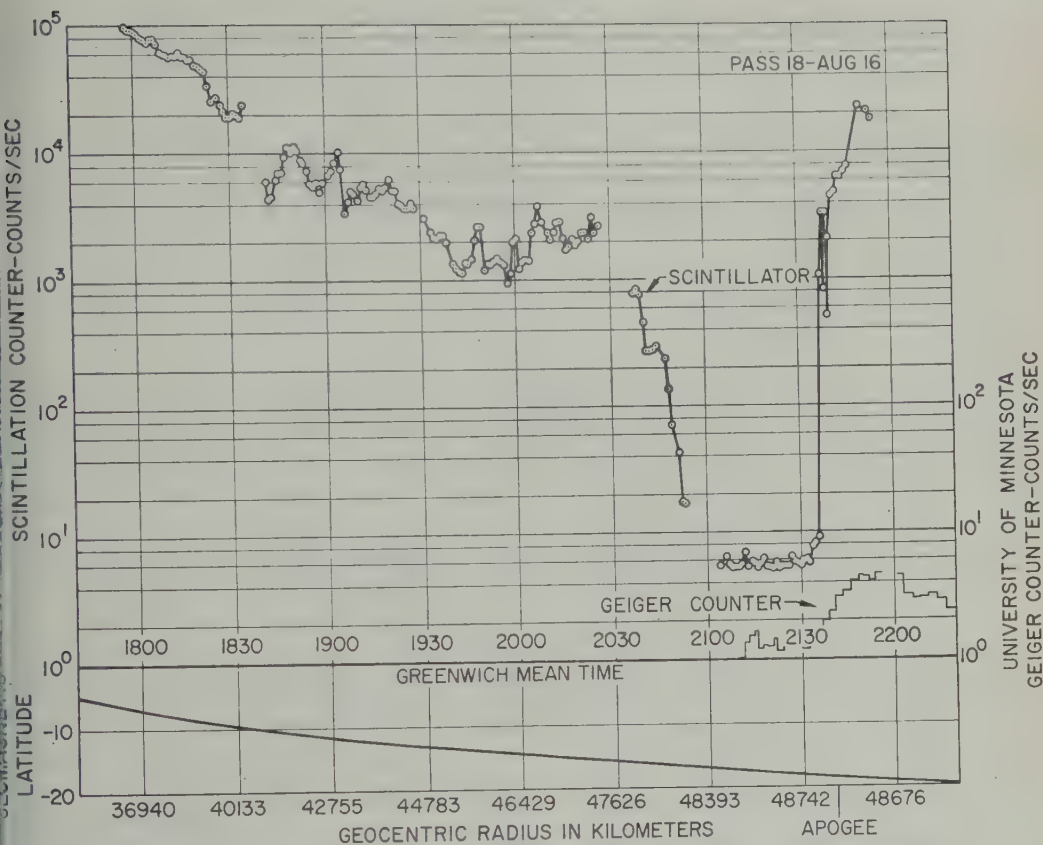


Fig. 15. Gross fluctuations are still present some 12 hours after the sudden commencement.

me intensity before the magnetic storm, and they both underwent a 20-fold increase in intensity during the storm. The intensity of both peaks decreased slowly at the same rate after the storm. Furthermore, they appeared to merge at high geomagnetic latitudes after the storm, and only one peak was seen on passes at these latitudes. It seems reasonable, therefore, to assume that peaks 2 and 3 were both caused by electrons of several hundred kev energy, and that the intensity of these particles decreased slightly between peak 2 and peak 3.

The ion chamber to Geiger counter ratio reaches a peak near the E_s maximum, and this has been interpreted to indicate a very soft electron spectrum at E_s [Arnoldy, Hoffman, and Winckler, 1960]. The dip between peaks 2 and 3 of the scintillation counter may be the result of an electron spectrum at E_s so soft that it cannot be detected by the scintillation counter. At the same time there must be sufficient high-energy elec-

trons (500 kev–1 Mev) to account for the proportional counter response. If the scintillation counter is responding to electrons above 500 kev at the position of E_s , the count rate (pass 17) corresponds to an isotropic flux of approximately 2×10^7 electrons/cm² sec, and this is in quite good agreement with the spectrum proposed by J. A. Simpson (Space Science Research Conference, California Institute of Technology, January 24, 1961) to account for the proportional counter response at E_s .

The simplest electron spectrum that would be consistent with all the instruments on this satellite would have large fluxes of soft electrons (20–100 kev) which dominate the Geiger-counter and ion-chamber response, but are not seen by the scintillation counter and the lead-shielded proportional counter. It would also have a much smaller group of high-energy electrons (500 kev–1 Mev) which would cause the proportional counter and scintillation counter response at the E_s .

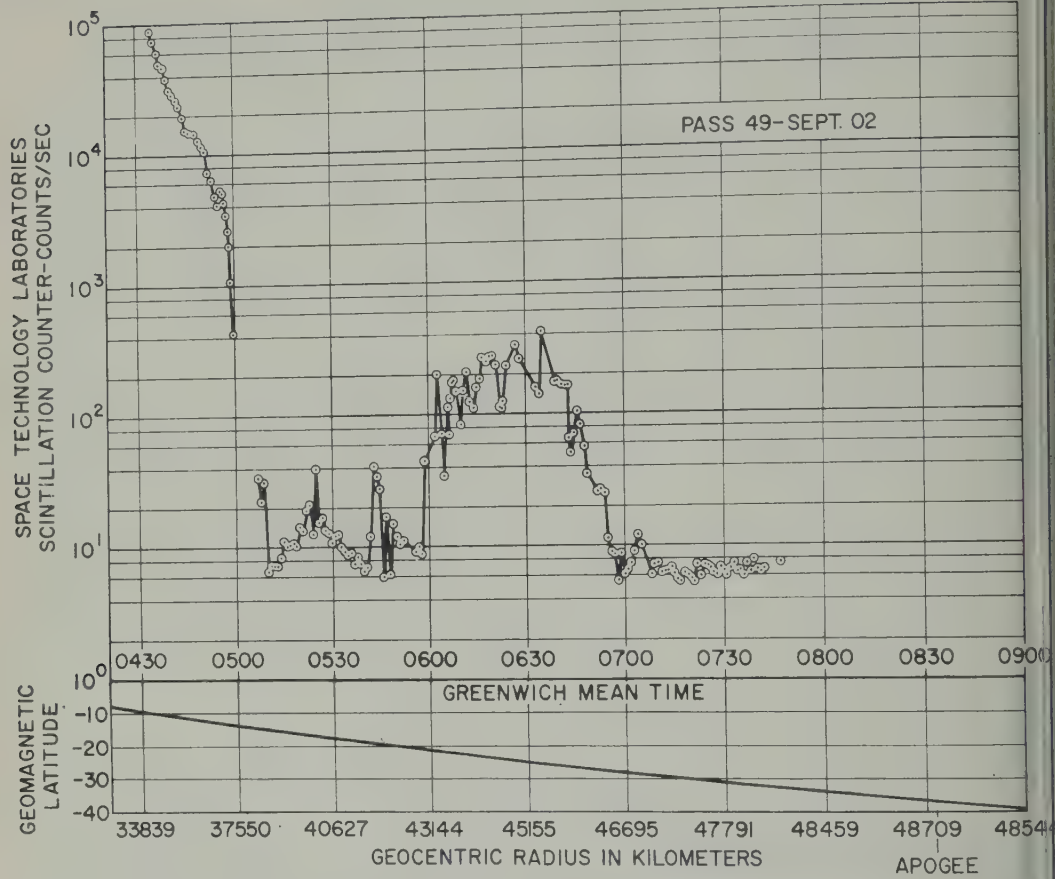


Fig. 16. Particle fluctuations during a period of irregular magnetic activity on September 2, 1959.

maximum. It does not seem possible to represent this electron spectrum by an energy distribution function of the form $E^{-\gamma}$ over the whole range from 20 kev to 1 Mev. Indeed, Vernov and Chudakov [1960] have suggested that the particles comprising the outer zone are electrons which appear to be in two energy groups. According to their investigation, the first group consists of electrons of 10–100 kev whose maximum intensity is 10^3 electrons/cm² sec sterad above 20 kev. The second group consists of electrons of energy of the order of 1 Mev whose maximum intensity is 10^5 electrons/cm² sec sterad. It may be possible to construct a detailed spectrum when the efficiencies of all the instruments as a function of energy have been determined.

It is possible that at some times and some places in the outer zone, the scintillation

counter—and perhaps the Geiger counter and ion chamber—responded to protons instead of electrons. In particular, the authors have suggested [Farley and Rosen, 1960] that the increase in intensity (for example, pass 19) observed during the main phase of the storm must be the result of protons because the bremsstrahlung instruments observed a decreased count rate during this period. If it can be determined that the bremsstrahlung counters cover the entire electron energy range to which the scintillation counter is sensitive, then there appears to be no alternative to the proton hypothesis. However, the ion-chamber to Geiger-counter ratio indicates a considerable hardening between passes 17 and 19, while both the Geiger counter and lead shielded proportional counter have approximately equal (60 per cent) decreases in count

TABLE 1.

	Count Rate	$\beta = \frac{v}{c}$	Flux, part./cm ² sec	Particle Density, part./cm ³	Particle Energy Density, ergs/cm ³	Magnetic Field, gauss	Magnetic Energy Density, erg./cm ³	Gyroradius, km
Peak 1								
2 Mev protons	5.8×10^5	6.6×10^{-2}	2.9×10^9	7.4×10^{-1}	2.4×10^{-6}	3.05×10^{-2}	3.7×10^{-6}	68
10 Mev protons	5.8×10^5	1.5×10^{-1}	1.5×10^7	1.7×10^{-3}	2.7×10^{-8}	3.05×10^{-2}	3.7×10^{-5}	150
Peak 2								
200 kev electrons	6.5×10^5	7.0×10^{-1}	2.2×10^9	5.2×10^{-2}	1.7×10^{-3}	9.90×10^{-3}	3.9×10^{-6}	1.7
500 kev electrons	6.5×10^5	8.6×10^{-1}	1.6×10^7	3.2×10^{-4}	2.5×10^{-10}	9.90×10^{-3}	3.9×10^{-6}	3.0
Peak 3								
200 kev electrons	8.0×10^5	7.0×10^{-1}	2.7×10^9	6.4×10^{-2}	2.0×10^{-8}	3.50×10^{-3}	4.9×10^{-7}	4.7
500 kev electrons	8.0×10^5	8.6×10^{-1}	2.0×10^7	3.9×10^{-4}	3.1×10^{-10}	3.50×10^{-3}	4.9×10^{-7}	8.4

rate. Until this apparently contradictory situation can be explained, there still exists the possibility that an electron component of the radiation can cause an increase in the scintillation counter without being observed by the other counters.

It seems rather unlikely that peak 2 can be caused by protons, except perhaps on pass 19, because of the previously mentioned similarities with peak 3, and because of recent calculations by *Dragt* [1960] which indicate a sharp cutoff of proton intensities with radial distance, even at low energies. Furthermore, the energy densities computed from that possibility seem improbably large. Peak 1, however, is considerably closer in, and it is possible that protons of lower energy than those detectable by the Geiger counter (~ 25 Mev) are responsible for this peak. It should be noted that the points representing the position of this peak in Figure 7 do not fall along a line of force, suggesting that these particles are trapped more closely to the geomagnetic equator with increasing radial distance. Several possibilities for peak 1, and the previously mentioned possibilities for peak 2 and 3 are shown in Table 1, together with the corresponding particle and field energy densities, using data from pass 10 (Fig. 4).

The fluctuations in count rate starting at about 7 earth radii in Figures 14, 15, and 16 are the result of some dynamic mechanism which occurred during stormy periods. Correlations with the STL magnetometer carried aboard Explorer VI have yielded information on this mechanism [Farley and Rosen, 1960]. The earth-surface horizontal component of the magnetic field at Honolulu has been included in Figure 14. The correlation suggested in this figure has not been borne out in subsequent comparisons with data at the ground stations, and it must be concluded that any correlation that does exist is obscured by local effects either at the vehicle or near the individual ground stations.

Conclusions. The scintillation counter on the Explorer VI earth satellite monitored the particle intensity in the earth's radiation belt for a period of 4 weeks. The experiment demonstrated the presence of large fluxes of several hundred kev electrons in the outer zone whose distribution differs somewhat from the particles observed by the bremsstrahlung detectors on the same vehicle.

This detector observed an increase in counting

rate in the outer zone during the early stages of the geomagnetic storm of August 16, 1959, while the bremsstrahlung detectors observed a decrease. This increase must be attributed to particles other than those to which the bremsstrahlung instruments were principally responding. The scintillation counter rate rose by a large factor after the geomagnetic storm, as did the rates of the other instruments on the vehicle.

Gross fluctuations in particle intensity at the edge of the outer zone were observed during the geomagnetic storm. These fluctuations are evidently caused by some dynamic process that takes place at the edge of the trapped radiation belt during a geomagnetic storm.

Acknowledgments. We are indebted to Charles P. Sonett for many discussions of the data and for his continued support of this experiment. Stuart Baker has conceived special instrumentation for reduction of the data, and John McGehee has spent many careful hours reading and plotting data from the records.

This work was carried out under the direction of the National Aeronautics and Space Administration.

REFERENCES

- Arnoldy, R. L., R. A. Hoffman, and J. R. Winckler, Observations of the Van Allen radiation region during August and September 1959, Part II, *J. Geophys. Research*, **65**, 1361-1376, 1960.
- Dragt, A. J., Effect of hydromagnetic waves on the lifetime of Van Allen radiation protons, *J. Geophys. Research*, **66**, 1641-1649, 1961.
- Fan, C. Y., P. Meyer, and J. A. Simpson, Trapped and cosmic radiation measurements from Explorer VI, *Proceedings of the First International Space Science Symposium*, p. 951, North Holland Publishing Company, Amsterdam, 1960.
- Farley, T. A., and A. Rosen, Charged particle variations in the outer Van Allen zone during a geomagnetic storm, *J. Geophys. Research*, **65**, 3494-3496, 1960.
- Smith, E. J., P. J. Coleman, Jr., D. L. Judge, and C. P. Sonett, Characteristics of the extra terrestrial current system: Explorer VI and Pioneer V, *J. Geophys. Research*, **65**, 1858-1861, 1960.
- Sonett, C. P., E. J. Smith, and A. R. Sims, Survey of the distant magnetic field: Pioneer I and Explorer VI, *Proceedings of the First International Space Science Symposium*, p. 921, North Holland Publishing Company, Amsterdam, 1960.
- Vernov, S. N., and A. E. Chudakov, Terrestrial corpuscular radiation and cosmic rays, *Proceedings of the First International Space Science Symposium*, p. 751, North Holland Publishing Company, Amsterdam, 1960.

(Manuscript received December 1, 1960;
revised March 31, 1961.)

Cosmic-Ray Production of Low-Energy Gamma Rays

FRANK C. JONES¹

*Enrico Fermi Institute for Nuclear Studies
University of Chicago, Chicago 37, Illinois*

Abstract. An attempt has been made to detect and measure any vertically incident flux of low-energy (0.25 to 10 Mev) gamma rays that might be present at high altitudes. The experiment consisted of a series of balloon flights carrying a phoswich gamma spectrometer with pulse height recording to altitudes of about 5.5 g/cm² atmosphere depth. Directional sensitivity was obtained by placing a lead collimating shield around the detector and by periodically opening and closing a lead shutter above the opening of the shield. At altitudes between 5.4 and 6.0 g/cm² atmospheric depth the experiment yielded a value of 0.000 ± 0.034 photons sec⁻¹ cm⁻² sterad⁻¹ for the vertical flux of gamma rays in the vicinity of 0.5 Mev energy. This is a null result; however, it places a new upper limit on the vertical gamma-ray flux that is lower than any previously reported for this energy region. At lower altitudes it was observed that gamma rays are generated by cosmic rays in the atmosphere and in the collimating lead shield. At an atmospheric depth of 300 g/cm² the flux of gamma rays from the atmosphere was about 0.3 photons sec⁻¹ cm⁻² sterad⁻¹. Convincing evidence was found that the gamma rays of atmospheric origin were generated by the secondary nucleonic component, and that they are not genetically related to the electromagnetic or 'soft' component of the secondary cosmic rays.

I. INTRODUCTION

Table 1 gives a summary of previous measurements of low-energy gamma radiation both within and above the atmosphere. As can be seen from the table, these experiments either employed GM counters which, owing to the approximately linear variation of their detection efficiency with photon energy, measure energy rather than photon flux, or used scintillation counters with no provision for excluding the effects of the charged-particle radiation that was certainly present.

The present experiment is an exploration of low-energy gamma radiation generated in the atmosphere by cosmic radiation and, in addition, an attempt was made to detect any vertical flux of low-energy gamma rays that might be present at high altitudes (5-6 g/cm² residual atmosphere) and, therefore, possibly of extraterrestrial origin. The detector was designed to give spectral information about the photon flux, and in addition provisions were made to exclude charged particles from the measurement. The attempt to detect a vertical flux of gamma rays at high altitude yielded a null result, but it did establish an upper limit that was derived from the result considerably lower than that established in

previous experiments. Strong evidence was obtained that the majority of the low-energy gamma radiation generated in the atmosphere is genetically related to the low-energy nucleonic component rather than the 'soft' electromagnetic component. It is suggested that the gamma radiation originates in the small nuclear stars arising from collisions of the secondary nucleonic component of the cosmic rays with nuclei of the atmosphere. This is the same type of collision that generates the free neutrons found in the atmosphere. There is good evidence that the gamma radiation does not result from multiple Compton-scattering of higher energy photons emitted from decaying neutral π mesons.

II. INSTRUMENTATION

In designing a suitable detector for low-energy photons at high altitudes one of the first problems encountered was the large background of charged cosmic-ray particles of both primary and secondary origin. To keep this charged radiation from being included in the measurement, some form of guard counter arrangement is needed. A separate guard counter that would give protection in all directions would be very large and would require several photomultiplier tubes to obtain sufficient light collection. Space and weight would be saved if this guard counter could be incorporated as a part of the basic

¹ Present address: Palmer Physical Laboratory, Princeton University, Princeton, New Jersey.

TABLE 1. Summary of Low-Energy Gamma Ray Flux Measurements

Detector	Energy Range	Altitude	Flux
Pb shielded GM telescope with anticoincidence guard counter*	≥ 3.4 Mev	1.8 g/cm ²	≤ 0.46 Mev sec ⁻¹ cm ⁻² sterad ⁻¹
GM counter with anticoincidence guard counters†	0.1 to 15 Mev	80 Km	0.3 Mev sec ⁻¹ cm ⁻²
GM counter with anticoincidence guard counters‡	≤ 4 Mev	300 g/cm ²	3.4 photons sec ⁻¹ cm ⁻²
Anthracene scintillator with pulse height recording§	0.1 to 1.7 Mev	300 g/cm ²	3.8 photons sec ⁻¹ cm ⁻²
NaI scintillator in 3rd Soviet satellite	10 Kev 30 Kev 50 Kev		< 1 erg sec ⁻¹ cm ⁻² $< 10^{-4}$ erg sec ⁻¹ cm ⁻² $< 10^{-6}$ erg sec ⁻¹ cm ⁻²
This experiment	0.2 to 10 Mev	300 g/cm ²	≈ 0.3 photons sec ⁻¹ cm ⁻² sterad ⁻¹
	≈ 0.5 Mev	5.2 to 6.0 g/cm ²	$0.000 \pm .034$ photons sec ⁻¹ cm ⁻² sterad ⁻¹

* Perlow and Kissinger, 1951a
† Perlow and Kissinger, 1951b
‡ Rest, Reiffel, and Stone, 1951
§ Reiffel, Stone, and Rest, 1951
|| Vernov, Chudakov, Gorchakov, Logachev, and Vakulov, 1959

gamma-ray detector. By developing the 'phoswitch' technique suggested by *Wilkinson* [1952] it is possible to construct a compact detector using only one photomultiplier that combines the functions of a gamma-ray spectrometer and a charged-particle guard counter.

The details of the construction and operation of the phoswitch detector for use in this experiment have been reported in a previous paper [*Jones*, 1960]. It is essentially a CsI(Tl) scintillation spectrometer whose sensitive volume (98 cm³) is completely surrounded by a plastic scintillator guard counter. Any charged particle

that penetrates the guard counter will trigger a blanking circuit and prevent any signal from the CsI(Tl) crystal being recorded. Figure 1 shows a block diagram of the recording and guard count circuits. The slow output is for the CsI(Tl) crystal pulse height information, and the fast output is for the plastic scintillator guard counter pulse. The screen of the cathode-ray-tube (CRT) is continuously photographed by a 35-mm camera whose film is transported at a constant rate.

This detector system records only events where the CsI(Tl) crystal initiated by a neutral particle

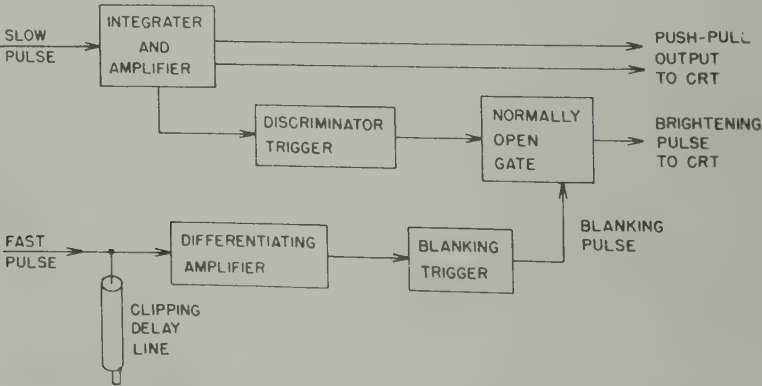


Fig. 1. Block diagram of pulse shape determination and recording circuits.

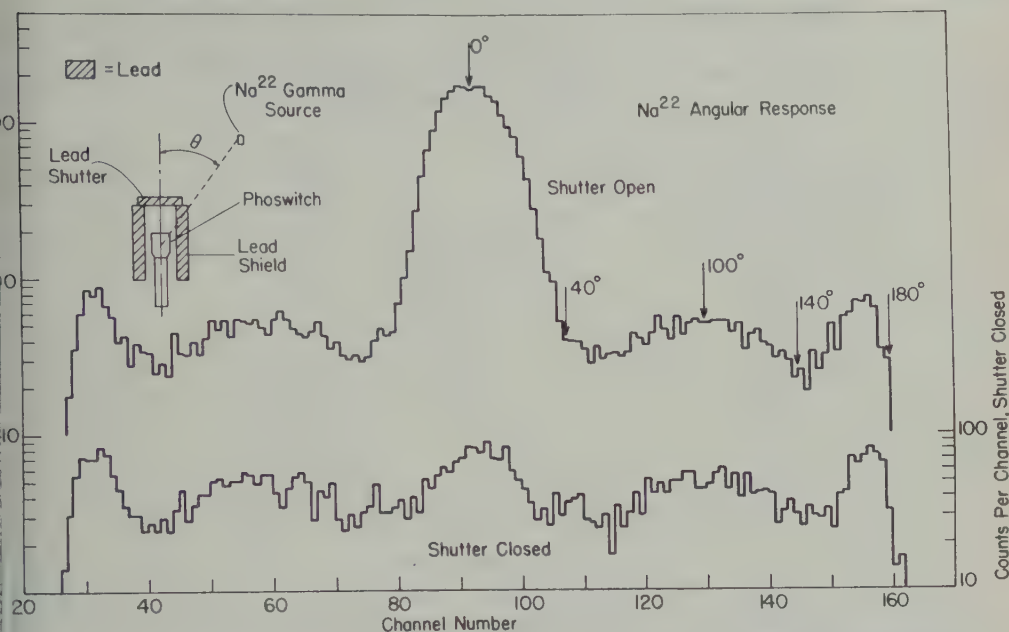


Fig. 2. Angular response of shielded phoswitch for gamma rays of Na^{22} showing the dependence of the response curve on shutter position.

Charged particles will be effectively ignored by the detector. Photons that are part of an iron-photon shower will also not be recorded since the electrons in the shower will trigger the guard counter, causing the event to be vetoed.

In order to give the phoswitch a directional sensitivity, so that vertically incident photons could be separated from a background flux of radiation from the atmosphere, it was placed in a lead shield. The shield consisted of a cylinder of 21 cm high with walls 4 cm thick. The part of the phototube that extended below the bottom of the shield was wrapped with $\frac{1}{4}$ -inch-thick lead sheets and a 3-cm-thick block of lead was placed below the phototube socket. A 3-cm-thick lead shutter was mounted above the shield with a spring drive mechanism that would periodically open and close it during the flight. To determine the angular response of the phoswitch and shield, a device was constructed in this laboratory that continuously rotated a Na^{22} gamma-ray source in a vertical circle about the shield. A potentiometer connected to the rotating device determined the channel address of the detector pulses in a 200-channel analyzer. The resulting distribution could then be easily con-

verted into an angular response function for the shielded phoswitch. This response function could then be used to predict the count rate of the phoswitch for various combinations of photon flux distributions and shutter positions. Extensive use is made of such calculations in section IV. Figure 2 shows typical distributions for the shutter in the open and closed positions, respectively, where the rotating source was a Na^{22} gamma-ray source ($E = 0.511$ Mev, 1.27 Mev).

The entire flight equipment was placed in a cylindrical gondola of 1/16-inch aluminum and maintained at atmospheric pressure throughout the flight. During flight, the gondola was wrapped with fiberglass housing insulation to minimize solar heating of the gondola.

III. BALLOON FLIGHTS

Three flights were launched in the summer of 1959 from Brownwood, Texas (geomagnetic latitude, 41°N). Only one flight, T59-3, yielded suitable data; therefore only this flight will be reported here. Flight T59-3 was launched at 0632 CST on August 30, 1959, and data was recorded for approximately 4 hours. It reached a maximum altitude of 5.4 g/cm² atmospheric depth in 2 hours and maintained fairly constant

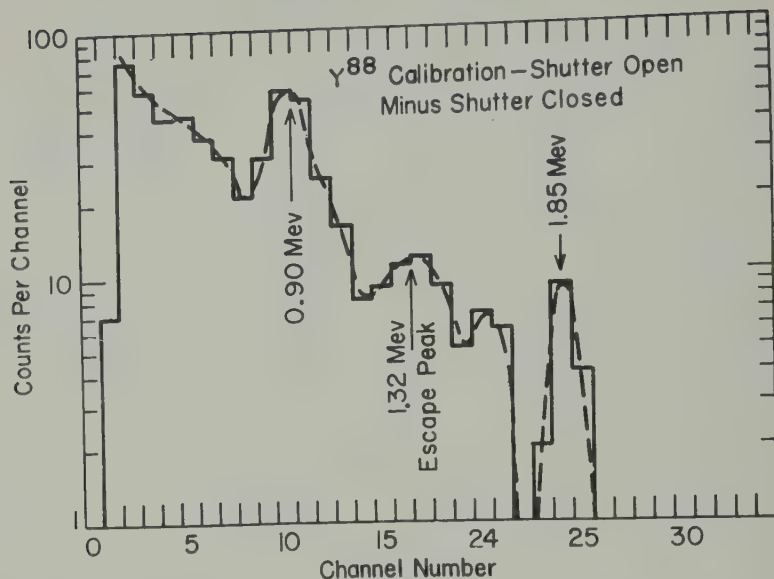


Fig. 3. Preflight calibration of flight T59-3. The Y^{88} source was placed on top of the gondola and the pulse height spectrum for the shutter-closed intervals was subtracted from that for the shutter-open intervals.

altitude for the next 2 hours, having dropped only to 6.0 g/cm^2 atmospheric depth by the time data recording ended.

The flight equipment was given an over-all calibration by placing a Y^{88} gamma-ray source above the gondola just before launching the flight. The calibration for flight T59-3 is shown in Figure 3.

IV. RESULTS

A. Origin of Gamma-Ray Flux in the Atmosphere

1. *Intensity of gamma-ray flux as a function of altitude (position of intensity maximum).* Figure 4 shows the phoswitch count rate for the intervals when the shutter was open as a function of time for flight T59-3. The most obvious characteristic of this curve is the pronounced maximum occurring between 60 and 70 g/cm^2 atmospheric depth.

The position in the atmosphere of the intensity maximum is characteristic of the low-energy nucleonic component of the cosmic rays. Since the soft component is only indirectly related to the high-energy nucleonic component (the electron-photon cascade process contributes greatly to the build-up in the atmosphere of the soft component) it exhibits a broad intensity maxi-

mum at about 160 g/cm^2 atmospheric depth, whereas the low-energy nucleonic component, detected by ion-chamber bursts [Whyte, 1950], nuclear stars in emulsions [Lord, 1951], and neutron flux measurements [Yuan, 1951; Meyer, 1955], exhibits an intensity maximum at high altitudes (48 to 100 g/cm^2).

The lead shield surrounding the detector is 4 cm thick, and the shutter is 3 cm thick (3.2 and 5.2 radiation lengths, respectively). It might appear that this thickness of lead, being adequate for the development of a cascade shower, could shift the soft component intensity maximum to higher altitudes, specifically, to the altitude observed in this experiment. That this is not the case can be seen from the following three points.

First, if a photon, incident on the lead shield, were to initiate a cascade shower, it would be recorded as a single event owing to the finite time resolution of the detector. The probability of detection of the event would be increased only slightly since this would be effected primarily by the lateral spread of the shower, and for lead thicknesses of only 3 or 4 cm this would not be large.

Second, since there is a finite probability that a photon will interact in the plastic scintillator guard counter, there is a good chance that

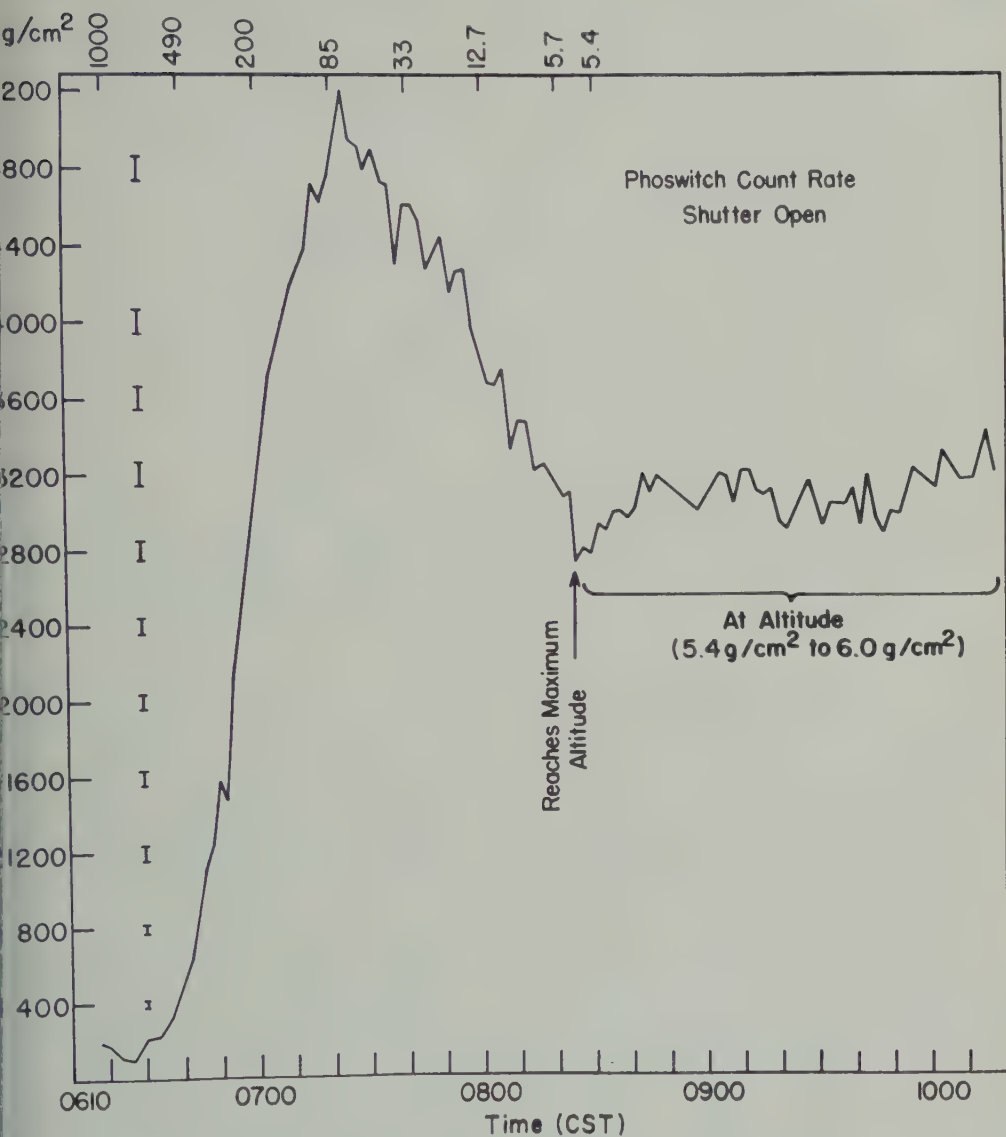


Fig. 4. Count rate of phoswitch as a function of time and residual atmosphere for flight T59-3 at $\lambda = 41^\circ\text{N}$ geomagnetic.

one of the photons in a shower will trip the guard counter and cause the event to be rejected. is the probability that a photon striking the detector will trip the guard counter, the probability that N photons can strike the detector and not trip the guard counter is given by $(1 - p)^N$. For Co^{60} gamma rays incident on the detector used in this experiment $p \approx 0.14$ and $Q_{10} \approx 0.23$.

third, any cascade shower that might develop

in the lead shield will contain roughly equal numbers of electrons and photons. The electrons in the shower will trip the guard counter and cause the event to be rejected.

2. *Absorption length in the atmosphere of gamma-ray producing radiation.* Figure 5 shows the count rate of the phoswitch as a function of residual atmosphere between 200 and 600 g/cm² for flight T59-3. The intervals during which the shutter was open and during which it was closed

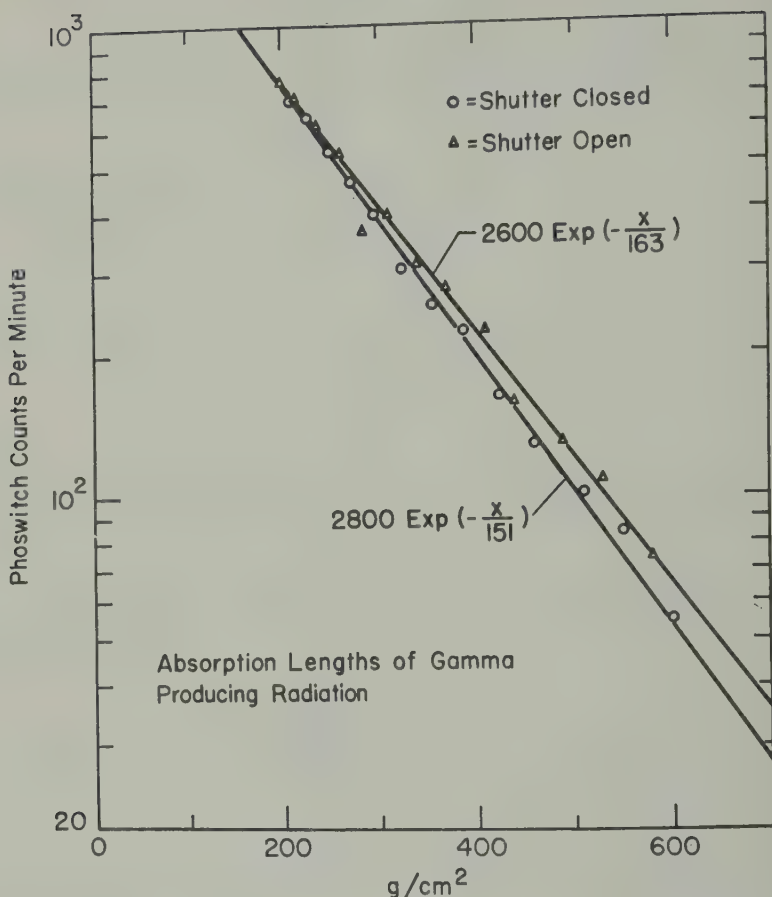


Fig. 5. Absorption lengths of gamma producing radiation for flight T59-3.

have been plotted with different symbols, and a least-squares fit for a curve of the form $A \exp(-X/L)$ has been calculated for each group separately. The absorption length L for the shutter-open intervals is greater than for the shutter-closed intervals. The count rates shown in this figure are scaled by a factor of 4 and should be multiplied by this factor to obtain the observed count rates. This factor has been taken into account in computing the statistical errors for each point. This procedure was also employed to obtain values of L for the count rates of the plastic guard counter during shutter-open and shutter-closed intervals. No significant difference was found between the value of L during shutter-open intervals and that during the shutter-closed intervals for the guard counter count rate.

Figure 6 shows the various absorption lengths

measured in flight T59-3 and those of other secondary cosmic-ray components of interest. The error bars for the data from the present experiment are 90 per cent confidence limits for the parameter, and the maximum likelihood value is shown. For the phoswitch count rate with shutter open, the points at $X = 284 \text{ g/cm}^2$ were excluded in calculating the confidence limits. It was felt that this point was far enough outside the line to be suspect and would have made the 90 per cent confidence limits $153.6 \leq L \leq 177 \text{ g/cm}^2$ if it had been included. For the value of L for neutrons in the free atmosphere the quoted error was doubled to compare it more easily with the 90 per cent confidence limits.

We see from the diagram that the absorption length with the shutter closed agrees quite well with that measured by *Simpson and Uretz* [19] for local neutron production in lead at 41

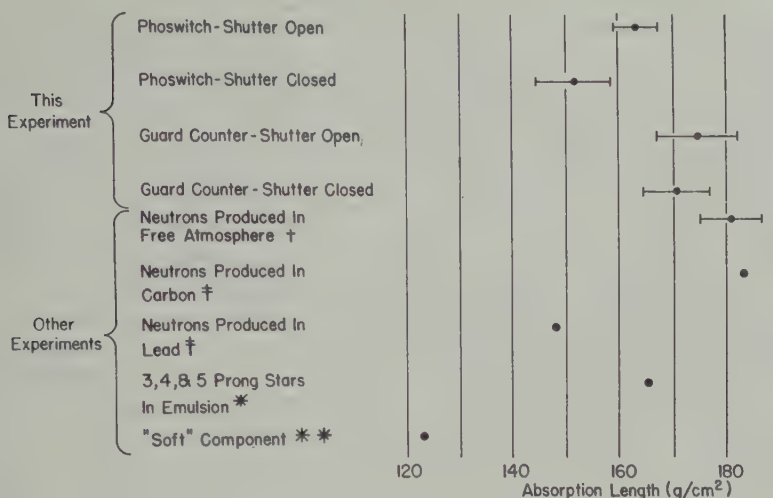


Fig. 6. Comparison of absorption lengths measured in this experiment with absorption lengths previously measured for other cosmic-ray components. Errors shown for this experiment are 90 per cent confidence limits and for neutrons in the free atmosphere double the quoted error is shown. † J. Simpson, 1951; ‡ Simpson and Uretz, 1953; * Lord, 1951; ** Puppi and Dallaporta, 1952.

magnetic latitude, and that when the shutter open the absorption length is longer, as is the absorption length for neutrons produced in the air [Simpson, 1951] and in carbon [Simpson and Uretz, 1953]. We also see that radiation measured by the phoswitch is considerably more penetrating in the atmosphere than is the electron-photon or 'soft' component as defined in cosmic-ray research which has an absorption length of 123 g/cm² [Puppi and Dallaporta, 1952].

Direct effect of neutrons. The plastic scintillator guard counter is effective in preventing direct detection of charged particles by the phoswitch. Neutrons, however, are uncharged and therefore are able to enter the CsI crystal through the phoswitch without being detected by the guard counter. Thus neutrons are capable of directly contributing to the count rate of the phoswitch by means of nuclear interactions in the CsI crystal. The two important reactions of neutrons may initiate in CsI are (a) capture of thermal neutrons with the subsequent emission of gamma rays, and (b) production of nuclear fission by energetic neutrons. Of the two effects, capture of thermal neutrons should be the more pronounced, since the flux of thermal neutrons is high in some regions of the atmosphere [Hess, Peterson, Wallace, and Chupp, 1959; Haymes and Korff, 1960] and the thermal neutron capture

cross section is large for Cs and I. It is difficult to calculate the probability that a neutron capture event in the crystal will be recorded since such an event is detected by absorption of the accompanying gamma ray. The thermal neutron capture cross sections are 29 barns for Cs and 7 barns for I giving a total of 36 barns per CsI molecule [Hughes and Schwartz, 1958]. It is known, however, that no more than 16 per cent of the neutron capture events in Cs are accompanied by a gamma ray of energy greater than 0.2 Mev [Groshev, Lutsenko, Demidov, and Pelikhov, 1959], so we may reduce the Cs capture cross section to 4.6 barns, giving 11.6 barns per CsI molecule. It is likely that the cross section for I should be reduced in a similar manner but the pertinent data are uncertain. We therefore have a total effective cross section of 0.048 cm² per cc of CsI or 4.7 cm² for the entire crystal.

Since neutrons in the atmosphere are captured by nitrogen before they are completely thermalized, their velocity spectrum is not accurately known, and the capture rate cannot be calculated directly from the value of the cross section at 2200 m/sec. However, since the absorption cross sections for Cs and I vary as 1/v, the capture rate in CsI may be calculated if the capture rate of atmospheric neutrons in some other '1/v' absorber is known. Such data are available from

the balloon flight of *Haymes and Korff* [1960] on August 24, 1959, from South St. Paul, Minnesota (geomagnetic latitude = 55.1°N). Using two proportional counters filled with BF_3 , each counter having different proportions of B^{10} , the capture rate in pure B^{10} was determined by the method of *Staker* [1950] and *Davis* [1950]. Comparing the cross section of B^{10} with that of our CsI crystal, the capture rate in the crystal may be computed. Using the results of *Simpson* [1951] and later measurements of *Soberman* [1956] it appears that the value of the thermal neutron flux should be reduced by a factor of 1.3 to be correct for geomagnetic latitude of 41°N .

We finally obtain the result that the count rate due to thermal neutron capture in the CsI crystal should be at most 1.6 per cent of the total count rate.

The effect of the star-producing flux of neutrons may be calculated using the measurements of *Lord* [1951]. From the flux of star-producing neutrons measured at geomagnetic latitudes of 54° and 28° we may estimate the flux at $\lambda = 41^\circ$ to be $0.3 \text{ neutrons cm}^{-2} \text{ sec}^{-1}$ at an altitude of 35 mm of Hg where this radiation reaches a maximum intensity. Using the average geometrical cross section² ($\sigma = 1.49$ barns) we obtain a cross section of 3.04 cm^2 for the crystal. This gives a star production rate of 55 stars per minute at the intensity maximum, which is only about 1 per cent of the phoswich counting rate at this altitude.

We can now see that although neutrons produce a direct contribution to the phoswich count rate such a contribution is at most a small fraction of the observed count rate.

4. *Relation to nucleonic component.* The facts that have been presented above strongly indicate that the gamma rays observed in this experiment are generated primarily by the low-energy nucleonic component. The over-all shape of the intensity vs. altitude curve is very similar to the corresponding curve for the nucleonic component. In addition, it exhibits features that are at variance with an assumption of an electromagnetic cascade as the origin of the observed

gamma rays. The most important such feature is the position in the atmosphere of the intensity maximum. It is difficult to understand how a flux of low-energy photons could exhibit an intensity maximum at a higher altitude than does the radiation that generates it. Such would have to be the case if one supposes that the low-energy gamma rays observed in this experiment are genetically related to the electromagnetic cascades of the soft component.

The fact that the absorption length between 200 and 600 g/cm^2 is similar to the nucleonic component, rather than the soft component, is suggestive of a nucleonic origin of the gamma rays but not conclusive. It is well known that the lower energy secondary nucleonic component of the cosmic rays exhibits a longer atmospheric absorption length than does the highly energetic primary component. The same type of relationship could exist between the low-energy gamma rays and the more energetic photons of the soft component.

The manner in which the absorption length depends on the shutter position, however, is more convincing. In their investigation of cosmic ray production of neutrons in various materials *Simpson and Uretz* [1953] discovered that the radiation responsible for the neutron production in lead exhibited an anomalous absorption length at geomagnetic latitude 40°N , being shorter than that of the radiation responsible for neutron production in carbon and the free atmosphere (see Fig. 5). It is evident from the data taken at maximum altitude and the calculation of the atmospherically produced radiation that the majority of the radiation detected by the phoswich was generated in the lead shield. When the shutter is closed the radiation is almost entirely from this source, but when the shutter is open the phoswich is exposed to a greater amount of gamma radiation generated in the free atmosphere.

It is suggested that the dependence of the absorption length on the shutter position observed in this experiment is another manifestation of the effect discovered by *Simpson and Uretz*. This implies that not only is the radiation responsible for the generation of soft gamma radiation the same as that responsible for neutron production but also that the nuclear reactions which the two 'secondary' radiations are generated are the same, or at least similar.

² This appears to be the correct cross section to use [*Carlson, Hooper, and King*, 1950]. However, since this assumption was used by *Lord* to calculate the flux from the emulsion star rate, it would yield the correct value as long as the suitable cross sections vary as $A^{2/3}$ from one element to another.

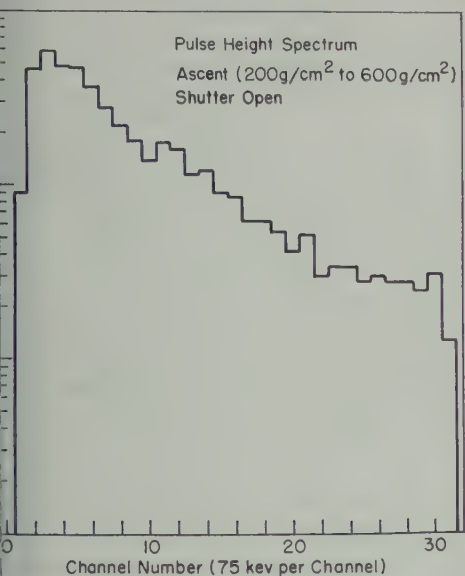


Fig. 7. Pulse-height spectrum for shutter-open intervals during ascent (200 to 600 g/cm²) of flight T59-3.

Energy Spectra and Photon Flux Between 200 g/cm² and 600 g/cm² Atmospheric Depth

It is evident that the pulse height spectrum of a scintillation counter will not have a one-to-one relationship with the energy spectrum of the incident gamma rays but will instead be representative of the energy loss in the crystal. There

are several methods of constructing the gamma-ray spectrum from the pulse height spectrum. Most of them are rather lengthy and often must be performed by computing machines, and, since the pulse-height spectra obtained in the present experiment exhibited no features of particular interest, an analysis of this type was not attempted. Any pronounced peaks in the gamma-ray energy spectrum would have shown up as peaks in the pulse-height spectrum, but no such peaks appeared. The energy units of the pulse-height spectra reported in this paper, therefore, represent energy loss in the crystal and not necessarily total gamma-ray energy.

Figure 7 shows the pulse-height spectrum obtained in the equilibrium region of the atmosphere for the intervals when the shutter was open. The spectrum for the shutter-closed intervals is so similar to the one shown that only when the actual shutter-open minus shutter-closed spectrum is plotted as in Figure 8 can the difference be seen. A correction has been applied to the difference spectrum; i.e. although an equal number of shutter-open intervals and shutter-closed intervals were selected, each shutter-closed interval was displaced 1 minute later in time with respect to the corresponding shutter-open interval. This, coupled with the fact that the count rate was increasing rapidly with time during this period, introduced a bias in favor of a higher average count rate for the shutter-closed intervals. To compensate this

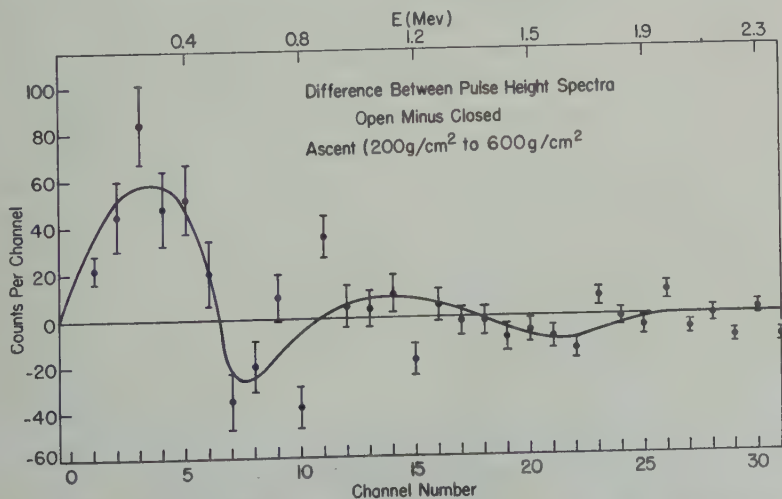


Fig. 8. Difference between shutter-open pulse-height spectrum and shutter-closed pulse-height spectrum for ascent (200 to 600 g/cm²) of flight T59-3. Standard deviations are shown.

bias, $\frac{1}{2}$ minute of data was subtracted from the later end of the shutter-closed intervals and $\frac{1}{2}$ minute of data added to the earlier end. This made the mean time of the shutter-closed intervals coincide with that of the shutter-open intervals.

As can be seen in Figure 8 the atmospheric radiation is most evident in the first few channels ($E \approx \frac{1}{2}$ Mev). As a result of the poor statistics in the higher channels, however, it is not possible to say whether this represents a peak in the spectrum of the atmospheric radiation or is just the low energy end of a steep spectrum extending to higher energies. The total pulse-height spectrum looks quite similar to the pulse-height spectrum of gamma rays emitted when lead is irradiated by 14.2 Mev neutrons [Sherrer, Theus, and Faust, 1953].

The high value (≈ 1) of the shutter-closed to shutter-open count rate ratio and the fact that the difference spectrum for these intervals exhibits several channels with negative values indicate that a considerable portion of the radiation detected by the phoswitch originated in the lead shield and shutter. Although closing the shutter reduces the amount of radiation falling on the phoswitch from outside the shield, the addition of the radiation originating in the shutter tends to cancel the effect, and in some cases, as we shall see, can make the shutter closed-shutter open ratio greater than one. These effects may be separated, however, and in Appendix 1 we calculate, for 300 g/cm², the flux of photons generated in the atmosphere.

Thus

$$f_{01} = 0.3 \text{ photons sec}^{-1} \text{ cm}^{-2} \text{ sterad}^{-1}$$

at

$X = 300 \text{ g/cm}^2$ and at $\lambda = 41^\circ \text{N}$ geomagnetic.

This value of f_{01} must be considered as an estimate based on the experimental data rather than a direct measurement. The omnidirectional photon flux of 3.4 photons cm⁻² sec⁻¹ reported for this altitude and energy region reported by Rest, Reiffel, and Stone [1951] is of the same order as our value. It is difficult to compare these two values, however, because, as has been remarked previously, Geiger counters measure gamma-ray energy flux rather than photon flux, and Rest, Reiffel, and Stone do not give the energy spectrum that was assumed in calculating the photon efficiency of their Geiger counters.

In Appendix 2 we make an estimate of the

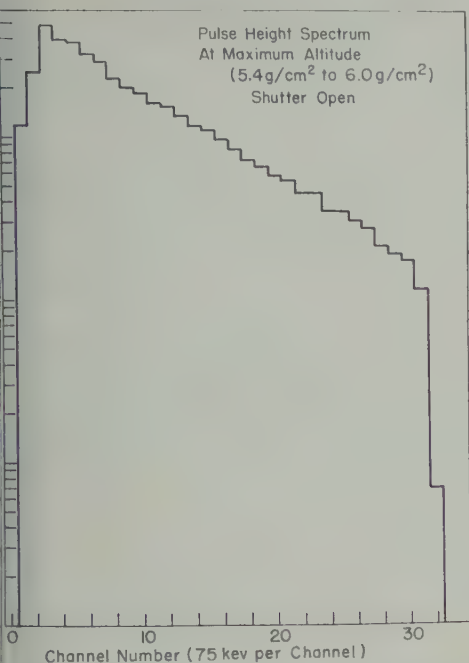
count rate due to photon generation in the lead shield by neutrons between 1 and 100 Mev energy. The calculation yields a count rate of 222 counts per minute at a pressure altitude of 200 g/cm². At this altitude the count rate with the shutter closed is 3000 counts per minute. The calculation, therefore, yields a value that is too small by an order of magnitude. Similar calculations show that including thermal neutron capture and star production in the lead would only increase the calculated value by a factor of 1.09. This calculation, however, is based on the assumption of only one photon generated per interaction. It has been shown [Sherrer, Theus, and Faust, 1953] that the cross section for gamma ray production in various materials by 14.2 Mev neutrons is greater than the corresponding inelastic cross section, indicating that the multiplicity of photons emitted per inelastic collision is greater than one. It is also quite possible that the spallation fragments from nuclear stars each radiate photons with a high multiplicity.

C. Photon Flux at Maximum Altitude

When the data for the 2-hour period that the balloon was at maximum altitude were collected and grouped according to shutter-open or shutter-closed intervals, it was found that the ratio of the shutter-closed count rate to the shutter-open count rate for the phoswitch was

$$k = \frac{44737 \pm 106}{43649 \pm 105} = 1.025 \pm 0.005$$

(Errors given in this section are standard deviations.) This is the value derived for radiation generated entirely within the lead shield and shutter. A flux of gamma rays falling on the detector from outside the lead shield and shutter would reduce this ratio, unless there were present at the same time some compensating effect that would tend to increase the ratio. The only way this ratio could be increased would be for the shutter to be more effective in irradiating the phoswitch than the rest of the shield. A collimated vertical flux of electrons could cause such an effect by emitting bremsstrahlung in the shutter provided their energy was insufficient to enable them to penetrate the shutter and enter the plastic guard scintillator. However, if such an electron flux existed, the count rate of the plastic counter should show a pronounced difference between shutter-open and shutter-closed with



g. 9. Pulse-height spectrum for shutter-open intervals during time at maximum altitude (5.4 to 6.0 g/cm²) for flight T59-3.

shutter-open count rate being larger. Such difference is not seen; in fact the closed-to-open count-rate ratio for the guard counter during the period is 1.010 ± 0.005 .

If we assume that the primary gamma radiation is isotropic from the upper hemisphere we can convert our measurement of the ratio k to a flux value f_{U2} . Using a calculation of the form given in Appendix 1 we obtain

$$= 0.000 \pm 0.034 \text{ photons sec}^{-1} \text{ cm}^{-2} \text{ sterad}^{-1}$$

assuming once again that the radiation is similar to that of Na²² ($E \approx 0.5$ Mev).

Comparing this gamma-flux value with the values reported by *Perlow and Kissinger* [1951b] we face the difficulty of comparing a photon flux with an energy flux. For the energy region 0.1 to 1.5 Mev these authors report an energy flux of $0.3 \text{ Mev sec}^{-1} \text{ cm}^{-2} \text{ sterad}^{-1}$; however, they state that there is a strong possibility that this is entirely due to albedo radiation from the atmosphere. The present experiment yields a value for 0.5 Mev photons that is an order of magnitude below the value of *Perlow and Kissinger*, and it is unlikely that the flux of

more penetrating, higher energy photons would be greater than this. In another experiment *Perlow and Kissinger* [1951a] measured a flux $0.46 \text{ Mev sec}^{-1} \text{ cm}^{-2} \text{ sterad}^{-1}$ for photons of an energy greater than 3.4 Mev/photon, although they state that the result was possibly a null one.

The present experiment, therefore, places a new upper limit of $0.034 \text{ photons sec}^{-1} \text{ cm}^{-2} \text{ sterad}^{-1}$ on a flux of low energy photons at high altitudes.

Figure 9 shows the pulse-height spectra for the shutter-open intervals for the period the balloon was at maximum altitude. The open minus closed pulse-height distribution exhibits a large number of negative values, since the count rate for the shutter-closed intervals was greater than that for the shutter-open intervals and therefore is not shown.

V. CONCLUSION

To within statistical accuracy the present experiment yielded a null result for the flux of gamma rays incident from the upper hemisphere at an altitude of 5.4 to 6.0 g/cm² atmospheric depth. The standard deviation of $\pm 0.034 \text{ photons sec}^{-1} \text{ cm}^{-2} \text{ sterad}^{-1}$ establishes an upper limit on the flux of gamma rays in the energy region about 0.5 Mev. The earlier measurements in this energy region and at comparable altitudes by *Perlow and Kissinger* [1951a, b] are difficult to compare with the present value since these authors report an energy flux rather than a photon flux. If it is assumed that the mean energy per photon detected by *Perlow and Kissinger* is about 1 Mev, one obtains a flux of $\leq 0.02 \text{ photons sec}^{-1} \text{ cm}^{-2} \text{ sterad}^{-1}$ between 0.1 and 1.5 Mev energy and 80-km altitude, a value comparable with the present one. At an altitude of 1.8 g/cm² atmospheric depth they have a flux of $0.115 \text{ photons sec}^{-1} \text{ cm}^{-2} \text{ sterad}^{-1}$ if one assumes a mean energy of 4 Mev per photon. It is easily seen that these values cannot be compared with the one from the present experiment unless a particular energy spectrum is assumed, and there is no information of this type known to the author.

At an atmospheric depth 300 g/cm² the present experiment yields a value for the gamma flux in the atmosphere of $0.3 \text{ photons sec}^{-1} \text{ cm}^{-2} \text{ sterad}^{-1}$ or $3.8 \text{ photons sec}^{-1} \text{ cm}^{-2}$ assuming isotropy. This value agrees with the result of *Reifel, Stone, and Rest* [1951] for the same altitude and energy

region 0.1 to 1.7 Mev. These authors, however, employed a scintillation counter with no provision for charged particle rejection and the contribution of charged particles. These same authors [Rest, Reiffel, and Stone, 1951] obtain a value of $3.4 \text{ photons sec}^{-1} \text{ cm}^{-2}$ for this altitude and energies $\leq 4 \text{ Mev}$. This measurement, however, employed an anticoincidence shielded Geiger counter and therefore measured an energy flux. The authors do not state what energy spectrum was assumed to obtain their value for the photon flux.

This experiment, therefore, while agreeing with previous measurements in the vicinity of 300 g/cm^2 atmospheric depth sets a new upper limit for the photon flux at high altitudes. While it is difficult to say whether or not this upper limit is significantly lower than that given by earlier measurements, it is certainly a different kind, being an upper limit for the photon flux rather than for the energy flux. The establishment of the connection between the low-energy gamma radiation in the atmosphere and the nucleonic component, in particular the similarity between processes which produce gamma rays and those which produce neutrons, is a new result.

Further balloon flights with a phoswitch detector widely separated from local material in the balloon gondola would be helpful in determining more accurate values for the flux of low-energy gamma rays within the atmosphere and their behavior as a function of altitude.

APPENDIX 1

Photon flux in the atmosphere. From the measured angular response of the shielded phoswitch (Fig. 2) we may deduce the ratio of the counting rates for the shutter open and closed owing to an isotropic flux of gamma radiation external to the shield.

$$a = \frac{(\text{count rate shutter closed})}{(\text{count rate shutter open})} = 0.48$$

In considering the effect of gamma radiation generated in the lead shield, the actual thickness of the lead in a given direction is not too important since the quantity that enters into the calculations is the 'effective' thickness

$$1/\mu [1 - \exp(-\mu r)]$$

where r is the actual thickness and μ is the gamma ray attenuation coefficient for lead. Picking a value of $\mu = 0.042 \text{ cm}^2/\text{g}$, we see from Figure 1 that the 'effective' thickness is essentially the same in all directions. The ratio of the counting rates for the shutter closed and the shutter open from radiation generated in the lead is just the ratio of the solid angles subtended by the lead in the two cases (with a minor correction) and we have,

$$b = \frac{(\text{count rate closed})}{(\text{count rate open})} = 1.025$$

The problem now reduces to finding what mixture of these two effects is required to give the observed closed-to-open ratio k . By simple algebra we obtain the result

$$\begin{aligned} & \left(\begin{array}{l} \text{shutter open count rate} \\ \text{from external radiation} \end{array} \right) \\ &= \left(\begin{array}{l} \text{shutter open count rate} \\ \text{observed} \end{array} \right) \left(\frac{b - k}{b - a} \right) \end{aligned}$$

This value may be converted to a flux value in a straightforward manner.

It is difficult to obtain an accurate value for k during the period that the balloon was ascending since the statistical uncertainty in the counting rates is large. The difference in the counting rates for the shutter-open and shutter-closed intervals is greatest in the region of 300 g/cm^2 so the derived value of $(b - k)$ is probably most accurate in this region. For 300 g/cm^2 $k = .922$ and we finally obtain

$$f_{U1} = 0.3 \text{ photons sec}^{-1} \text{ cm}^{-2} \text{ sterad}^{-1}$$

APPENDIX 2

Photon generation in lead shield. The expression for the photon flux due to the generation in the lead shield is

$$f = \frac{p}{4\pi\mu} [1 - \exp(-\mu r)] \text{ min}^{-1} \text{ cm}^{-2} \text{ sterad}^{-1}$$

where p is the production density of photons in lead per minute per gram, μ is the photon absorption coefficient in lead, and r is the thickness of the lead along the line of observation. Adopting the values

$$\mu = .042 \text{ cm}^2/\text{g}; \quad r = 45.4 \text{ g/cm}^2$$

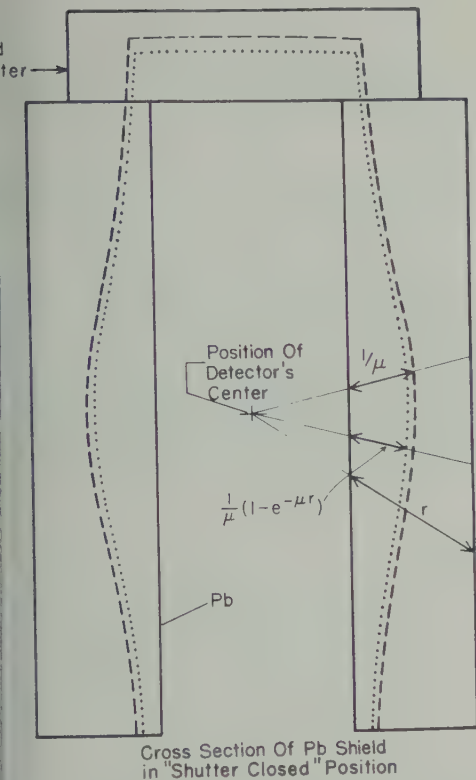


Fig. 10. Cross section view of lead shield with shutter in the 'closed' position showing 'effective' thickness.

obtain

$$F = \int f dw = 20.3P \text{ min}^{-1} \text{ cm}^{-2}$$

where $\int dw$ indicates integration over the entire solid angle. Applying the phoswitch cross section and detection efficiency factor we have

$$\text{count rate } Z_c = 284 P \text{ min}^{-1}$$

P may be estimated by performing the integral

$$P = N_{pb} \int \sigma_{ne}(E) f_n(E) dE \text{ min}^{-1} \text{ g}^{-1}$$

where $\sigma_{ne}(E)$ is the nonelastic cross section in barns for neutrons of energy E , $f_n(E)$ is the flux of neutrons of energy E , and N_{pb} is the number of lead nuclei per gram of lead. The above integral is performed approximately by fitting various simple analytic functions to the curves for $\sigma_{ne}(E)$ [Hughes and Schwartz, 1958] and to the spectrum $f_n(E)$ as measured by Hess, Patterson, Wallace,

and Chupp [1959] at an altitude of 200 g/cm² atmospheric depth. The result was

$$P = 0.898 \text{ min}^{-1} \text{ g}^{-1}$$

therefore $Z_c = 222$ counts per min.

Acknowledgments. I wish to thank Prof. J. A. Simpson for suggesting this problem and for many helpful discussions during the time the work was in progress. Special thanks are due Mr. E. C. Stone for invaluable assistance throughout all phases of the experiment. I also wish to thank Mr. G. Lentz, Mrs. D. Houston, and Mrs. L. Frisbie for their work in reading the films and reducing the data. For the design and construction of the lead shield and shutter mechanism thanks are due Mr. W. Mankawich and the men of the development shop of the University of Chicago Research Institutes. Thanks are due Mr. P. Yost, Mr. R. Keuser and all of the men of the Raven Industries field crew for their valuable work in launching, tracking, and recovering the balloon flights.

For aid in financing a portion of the balloon flights I wish to thank the Office of Naval Research. This research is supported in part by the Air Force Office of Scientific Research, Air Research and Development Command under contract AF18 (600)-666.

I should also like to express my appreciation to the Eastman Kodak Company for an Eastman Kodak Fellowship which I held during a part of the time this work was in progress.

REFERENCES

- Carlson, A. G., J. E. Hooper, and D. T. King, Nuclear transmutations produced by cosmic-ray particles of great energy, part V, The neutral mesons, *Phil. Mag.*, **41**, 701-724, 1950.
- Davis, W. O., Energy and density distribution of cosmic-ray neutrons, *Phys. Rev.*, **80**, 150-154, 1950.
- Groshev, L. V., V. N. Lutsenko, A. M. Demidov, and V. I. Pelikhov, *Atlas of Gamma-Ray Spectra from Radiative Capture of Thermal Neutrons*, translated by J. B. Sykes, Pergamon Press, New York, p. 127, 1959.
- Haymes, R. C., and S. A. Korff, Slow neutron intensity at high balloon altitudes, *Phys. Rev.*, **120**, 1460-1462, 1960.
- Hess, W. N., H. W. Patterson, R. Wallace, and E. L. Chupp, Cosmic-ray neutron energy spectrum, *Phys. Rev.*, **116**, 445-457, 1959.
- Hughes, D. J., and R. B. Schwartz, *Neutron Cross Sections*, BNL publication 325, 1958.
- Jones, F. C., Design of a gamma-ray spectrometer using the phoswitch technique for rejection of charged particles, *IRE Trans. on Nuclear Sci.*, **NS-7**, 175-177, 1960.
- Lord, J. J., Altitude and latitude variation in the rate of occurrence of nuclear disintegrations produced in the stratosphere by cosmic rays, *Phys. Rev.*, **81**, 901-909, 1951.

- Meyer, P., Zum Übergangseffekt der Hohenstrahl-neutronen in der Atmosphäre, *Z. für Physik*, **141**, 28-39, 1955.
- Perlow, G. J., and C. W. Kissinger, A search for primary cosmic gamma radiation I, *Phys. Rev.*, **81**, 552-554, 1951a.
- Perlow, G. J., and C. W. Kissinger, A search for primary cosmic gamma radiation II, Low energy radiation above and within the atmosphere, *Phys. Rev.*, **84**, 572-580, 1951b.
- Puppi, G., and N. Dallaporta, The equilibrium of the cosmic ray beam in the atmosphere, *Progress in Cosmic Ray Physics*, **1**, Interscience, New York, pp. 315-391, 1952.
- Reiffel, L., C. A. Stone, and F. G. Rest, Scintillation spectrum from cosmic rays at 30,000 feet, *Phys. Rev.*, **82**, 121-122, 1951.
- Rest, F. G., L. Reiffel, and C. A. Stone, Note on soft gamma component of cosmic rays, *Phys. Rev.*, **81**, 894, 1951.
- Sherrer, V. E., R. B. Theus, and W. R. Faust, Gamma rays from interaction of 14-Mev neutrons with various materials, *Phys. Rev.*, **91**, 1476-1478, 1953.
- Simpson, J. A., Neutrons produced in the atmosphere by the cosmic radiations, *Phys. Rev.*, **83**, 1175-1188, 1951.
- Simpson, J. A., and R. B. Uretz, Cosmic-ray neutron production in elements as a function of latitude and altitude, *Phys. Rev.*, **90**, 44-50, 1953.
- Soberman, R. K., High-altitude cosmic-ray neutron intensity variations, *Phys. Rev.*, **102**, 1399-1404, 1956.
- Staker, W. P., A determination of the high altitude latitude dependance in cosmic-ray neutron intensity, *Phys. Rev.*, **80**, 52-57, 1950.
- Vernov, S. N., A. E. Chudakov, E. V. Gorchakov, J. L. Logachev, and P. V. Vakulov, Study of the cosmic-ray soft component by the third Soviet earth satellite, *Planetary and Space Sci.*, **1**, 86-94, 1959.
- Whyte, G. N., Cosmic-ray bursts and the nucleon cascade, *Phys. Rev.*, **82**, 204-208, 1951.
- Wilkinson, D. H., The phoswich-a multiple phosphor, *Rev. Sci. Instr.*, **23**, 414-417, 1952.
- Yuan, L. C. L., Distribution of slow neutrons in free atmosphere up to 100,000 feet, *Phys. Rev.*, **81**, 175-184, 1951.

(Manuscript received February 27, 1961;
revised April 17, 1961.)

On the Interplanetary Magnetic Storm: Pioneer V

P. J. COLEMAN, JR.,¹ C. P. SONETT,¹ AND LEVERETT DAVIS, JR.²

*Space Technology Laboratories
El Segundo, California*

Abstract. During a period of intense solar activity between March 26 and April 6, 1960, measurements of the magnetic fields in interplanetary space were obtained with the space probe, Pioneer V. The measured component of the fields, associated with the solar plasma ejected during this period, attained strengths of 40 or more gammas (compared to an average value of 2.7 gammas during normal periods). It is argued that these comparatively high fields existed in interplanetary space for many hours. From estimates of the plasma velocity, the radial extent of these regions of high field is calculated to be 0.7 AU. The fields associated with these regions were observed to be quite regular. Similar results accompanied most of the more intense solar activity during the flight of Pioneer V. Possible implications of these results are discussed.

In a recent letter [Coleman, Davis, and Sonett, 1960] we have described an apparent steady interplanetary magnetic field observed by Pioneer V during periods of little solar activity. This field appeared to be approximately perpendicular to the ecliptic plane. Here we wish to describe the field measured during times of increased solar activity, with particular emphasis on the data obtained near the end of March and in early April 1960. The geophysical and interplanetary events produced by solar activity during this period were generally of unusual intensity and were well documented by satellite [Van Allen and Lin, 1960], balloon [Arnoldy, Hoffman, and Winckler, 1960], and surface observations [Leinbach, as quoted in Arnoldy, Hoffman, and Winckler, 1960], as well as by the instruments aboard Pioneer V. Of particular interest is a group of four solar flares of importance 2 that was emitted on March 31, and a subsequent flare of importance 3, emitted on April 1. The latter flare has been associated with a solar proton event. It was first observed spectrally at 0845 UT and continued until 1222 UT. The solar particles first arrived in the polar atmosphere at 0935 UT [Van Allen and Lin, 1960].

The magnetometer used for the measurements to be reported was similar to those carried on

Pioneer I and Explorer VI. Details of the apparatus have been previously published [Sonett, 1960]. It should be recalled that this instrument measures the magnitude of the magnetic field in the plane normal to the vehicle spin axis. This axis, fixed in inertial space, lay nearly in the plane of the ecliptic. Thus, the motion of the vehicle about the sun resulted in a rotation of the spin axis relative to the radius vector to the sun. The rate of this rotation was approximately 1° per day. At no time during the observations did the angle between the spin axis and radius vector from the vehicle to the sun exceed 27° . During the period from March 28 to April 6, this angle never exceeded 10° , and the vehicle was never more than 2×10^6 km from the line joining the sun and the earth. Thus, with the assumption that the propagation direction of solar plasma was outward from the sun, the vehicle geometry was such that fields normal to the direction of plasma propagation were measured.

The magnetometer data for the period of March 28 to April 6 are shown in Figure 1a. In this figure, each point of the data represents the average value of the measured component of the magnetic field taken over the period for which the vehicle transmitter was on (15 to 30 minutes). Figures 2a and b show the data received during portions of two separate transmissions. In these figures, each data point represents a single measurement of the field as transmitted by the vehicle, rather than an average. The rate at which these measurements were made during a

¹Now at NASA Headquarters, Washington 25, D. C.
²Permanent address: California Institute of Technology, Pasadena, California.

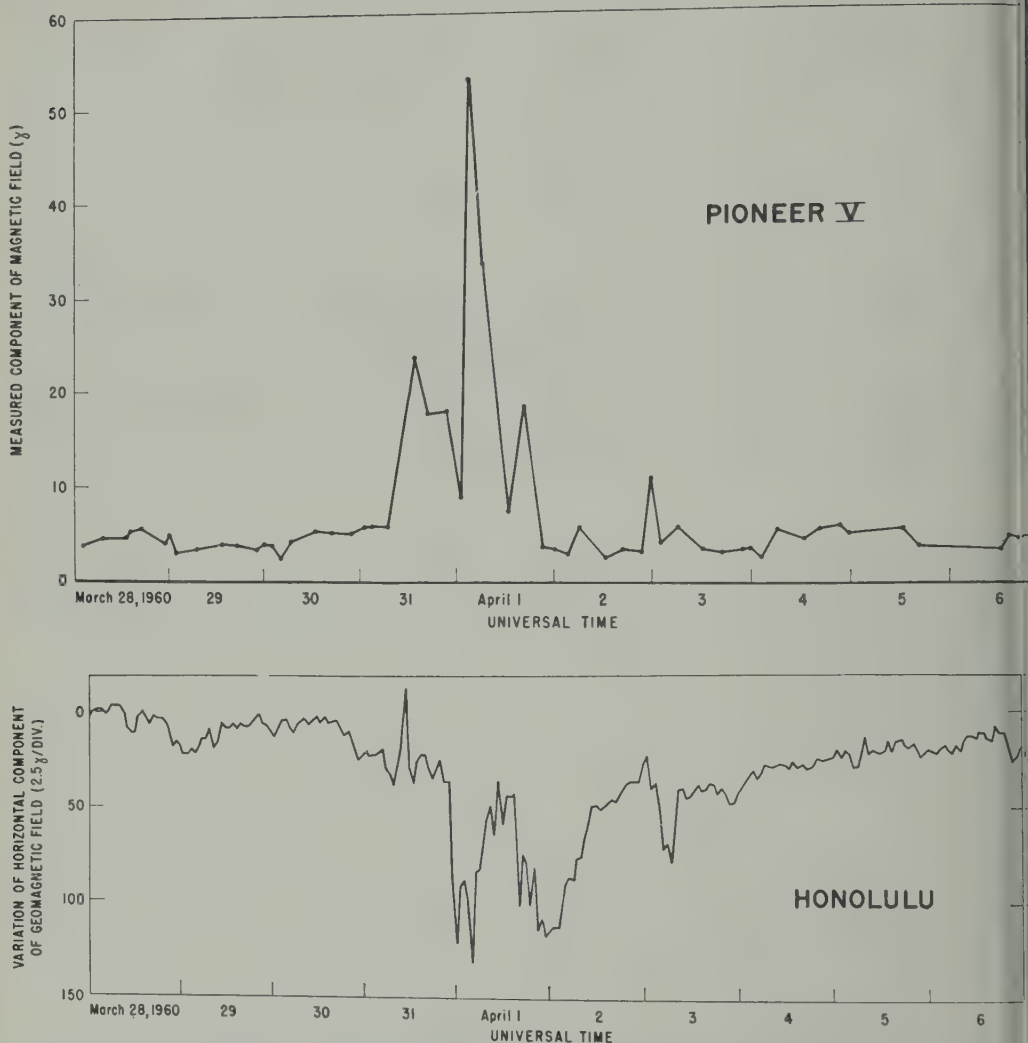


Fig. 1a. Intensity of the interplanetary magnetic field component normal to the earth-sun line. Each data point is an average over a transmitter-on period of between 15 and 30 minutes. Fig. 1b. Variations in the horizontal intensity of the geomagnetic field at Honolulu Magnetic Observatory.

given transmission depended upon communications factors, and varied from 45 per minute to 1 per 1.6 minutes.

The characteristics of the measured component of the interplanetary field during this period may be summarized as follows:

1. The magnitude was many times that observed during periods of low solar activity, i.e., 20 to 50 gammas as compared to an average quiet time field of approximately 2.7 gammas. Thus, during these periods, there exist large field

components perpendicular to the spin axis of the vehicle and, therefore, nearly perpendicular to the earth-sun line.

2. Usually these large amplitude fields seem to be quite regular, as shown in Figures 2a and 2b.

3. Occasionally, the amplitude displayed considerable irregularity. The fine structure within the flare gas is being investigated.

4. Reference to Figure 1a shows an enhanced magnetic field was observed during each of the successive transmission periods on April 1.

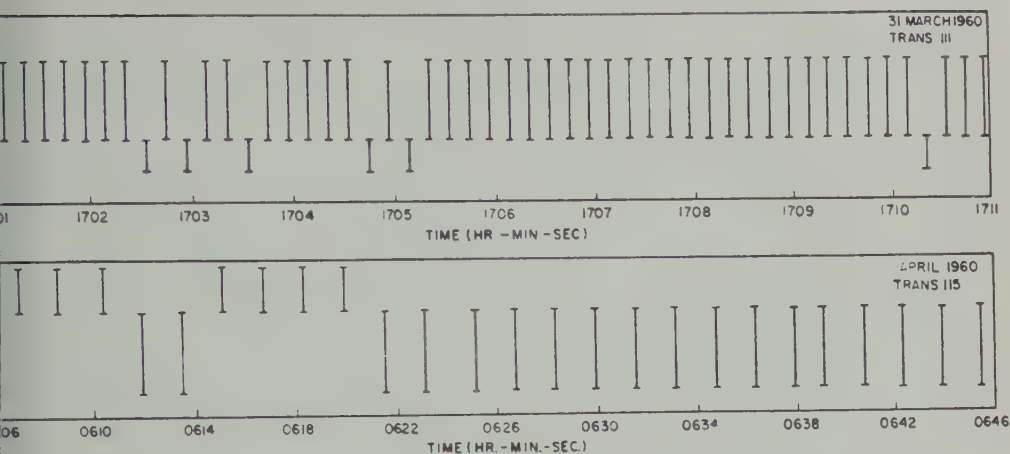


Fig. 2a, b. Intensity of the interplanetary magnetic field component normal to the earth-sun line. Each data point is a single digitized measurement. The flags indicate the width of the digitization levels within which the field value lies. Note that the sampling rates are different in these two figures. In relation to Figure 1, the upper plot corresponds to a portion of the fifth transmission on March 31, and the lower plot corresponds to the third transmission on April 1.

is likely that the interplanetary field at the vehicle remained at a high intensity for at least 12 hours on that day, i.e., for the periods between the three transmissions. This assumption is supported by the observation of large amplitude changes in the horizontal component of the magnetic field during this same series of transmissions as shown in Figure 1b, since there appears to be a correlation between the magnitudes of the magnetic field disturbances observed at Pioneer V and at the earth.

It is of particular importance to consider the structure of the interplanetary magnetic field on occasions, such as April 1, when high energy solar protons pass from the sun to the earth. The data of the magnetometer experiment show fields of magnitude 20 gammas normal to the earth-sun line during this time. This 20-gamma field is presumably associated with plasma traveling at 2×10^8 cm/sec outward from the sun as timed by Fan, Meyer, and Simpson [1960]. Taking this value of the velocity, and a duration of 14 hours for the intense field, we see that the radial scale of the disturbance is 1 AU. Further, this region of intense field must have existed between the sun and the vehicle before the emission of the high energy protons from the sun.

Next, a crude upper limit of the solar proton energy is estimated to be 300 Mev corresponding to a velocity of 2×10^{10} cm/sec.

We now inquire as to the manner in which the high energy protons, which leave the sun a day later than the plasma, can be observed to arrive at the vehicle and earth while both are immersed in this solar gas. (Since these particles reached both places, we assume that they fill the plasma cloud.) Diffusion of the protons through the plasma cloud might have occurred if the irregularities in the field had a scale small compared to 10^{10} cm, which is the radius of curvature of a 200-Mev proton in a field of 20 gammas. However, the data do not suggest this type of irregularity, and the fact that there was a Forbush decrease in the galactic cosmic rays shows that, even for these higher energy particles, diffusion into the regions occupied by fresh solar plasma was impeded. Similarly, escape of solar cosmic rays from the cloud would be impeded. Also, the solar protons must propagate into the high field regions mainly by traveling along lines of force with, at most, a small amount of diffusion across the lines. The relative absence of diffusion has been invoked previously to explain the storage of solar cosmic rays. In this case, for the protons associated with polar-cap absorption, the time of flight was two to three times the rectilinear flight time. These particles could have spiraled along a radially directed field, but, this would require the exclusion of small pitch angles for the higher energies. If small pitch angles are not to be excluded, and if the field were radial,

it is difficult to see why some protons did not arrive in times of the order of 20 minutes. Fan, Meyer, and Simpson [1960] conclude that the field between the sun and the earth at the time of the high energy proton event must have been of the order of 10^{-6} gauss rms or smooth and radial. These conclusions are not consistent with the data of the magnetometer, if, by 'radial' is meant an inclination to the geometrical radius of no more than the 10° suggested by a radial gas velocity of 2000 km/sec.

An argument against both the essentially zero field and the smooth radial field models is also provided by the data compiled by Arnoldy, Hoffman, and Winckler [1960]. As observed on Pioneer V, and as deduced from polar-cap absorption, solar protons were arriving throughout our neighborhood before and after the sudden commencement on March 31. The particles that arrive after have traveled through the high field region as discussed above. The protons that arrive before can scarcely have penetrated through the high field region. Conceivably, they could have been stored in the region ahead of the advancing magnetic plasma ever since it was emitted from the sun; or they could have detoured around it, perhaps by scattering, but most plausibly by spiraling along a curved line of force.

If the field is dipolar, as suggested by Elliott [1960], a line of force from the region of the sun to the earth will have a length of approximately 2 to 4×10^{13} cm, thus satisfying the time of flight requirement. On the other hand, propagation of the high energy protons along a magnetic field line having a limited connectivity between the sun and the earth is possible if the gaps are traversed by diffusion.

Although the particular mechanism for the propagation of the solar cosmic rays in such events is uncertain, it seems possible to establish

the fact that propagation of solar protons along a rectilinear path, or diffusion of these particles through a weak field, is not consistent with the Pioneer V magnetometer data obtained during this period.

Further, the observations of the solar cosmic rays, when considered in conjunction with the measurements of the interplanetary field, favor a model in which magnetic fields of solar origin are transported outward with the solar flare gas. This model is similar, in some respects, to one proposed by Gold [1959].

Acknowledgment. The space program was supported by the National Aeronautics and Space Administration.

REFERENCES

- Arnoldy, R. L., R. A. Hoffman, and J. R. Winckler, Solar cosmic rays and soft radiation observed at 5,000,000 kilometers from earth, *J. Geophys. Research*, **65**, 3004-3007, 1960.
- Coleman, P. J., Jr., Leverett Davis, and C. P. Sonett, The steady component of the interplanetary magnetic field, *Phys. Rev. Letters*, **5**, 4, 1960.
- Elliott, H., Cosmic ray intensity variations and the interplanetary magnetic field, *Nature*, **186**, 291, 1960.
- Fan, C. Y., P. Meyer, and J. A. Simpson, Rapid reduction of cosmic radiation intensity measurements in interplanetary space, *Phys. Rev. Letters*, **5**, 261, 1960.
- Gold, T., Plasma and magnetic fields in the solar system, *J. Geophys. Research*, **64**, 1665-1677, 1959.
- Sonett, C. P., Experimental physics using space vehicles, in *Advances in Space Science*, **2**, edited by F. W. Ordway, III, Academic Press, New York, 1960.
- Van Allen, J. A., and Wei Ching Lin, Outer radiation belt and solar proton observations with Explorer VII during March-April 1960, *J. Geophys. Research*, **65**, 2998-3003, 1960.

(Manuscript received March 16, 1961.)

Energy Spectrum of Electrons Trapped in the Geomagnetic Field

MARTIN WALT AND WILLIAM M. MACDONALD¹

*Lockheed Missiles and Space Division
Palo Alto, California*

Abstract. A Fokker-Planck equation for the distribution function of electrons trapped in a magnetic field in the presence of a scattering atmosphere is applied to the Van Allen electron belt. Solutions are obtained for the equilibrium flux resulting from an electron source of arbitrary energy for the cases where (a) loss of energy by collisions is neglected, and (b) loss by diffusion out of the trapping region is neglected; and an approximate solution is obtained for the actual case where both processes are important. The assumption that the electron source is supplied by decaying neutrons leads to an equilibrium electron flux whose energy dependence is qualitatively different from the observed spectrum.

Introduction. Experiments have shown that the numbers of electrons are trapped in the earth's magnetic field and many papers have appeared describing their behavior [Van Allen, 1958]. Although several source mechanisms for the electrons have been suggested, at the present time sufficient evidence is not available to show which, if any, of the postulated sources is the dominant one. Among the possible sources are (a) beta decay of neutrons or mesons, (b) ionization of solar plasma, and (c) local acceleration of low energy ambient electrons.

One of the most promising means of testing these hypotheses is to compare the observed electron flux and energy spectrum with calculated values derived from various source assumptions. However, several difficulties have restricted quantitative comparison; among these difficulties are uncertainties in the intensity and spectrum of sources *b* and *c*, and uncertainties in the mechanisms which remove or modify the spectrum of the trapped electrons. Comparison of calculated and observed quantities has also been somewhat limited by lack of definite experimental information on the energy spectrum and intensity of the electron flux.

Some time ago it was recognized that an accurate measurement of the electron spectrum would be crucial in evaluating possible source mechanisms. For this reason a magnetic spectrometer was constructed and flown to an altitude of 1000 km [Cladis, Chase, Imhof, and

Knecht, 1961; Walt, Cladis, Chase, Imhof, and Knecht, 1960]. The results of this flight indicated that the electron flux between 50 and 500 keV decreased monotonically with increasing energy, the dependence being approximately an exponential function of electron energy. Although the observed spectrum was qualitatively different from the neutron and meson β -decay spectra, it was suspected that interactions of the electrons with the atmosphere might reduce the average energy so that the equilibrium spectrum could be lower in energy than the source. In addition, preferential scattering of the lower energy electrons might lead to an enhancement of low energy electrons at the altitude where the measurement was made.

In order to examine these possibilities more completely, a Fokker-Planck formulation for the distribution function of electrons trapped in the earth's magnetic field in the presence of a scattering atmosphere was carried out [MacDonald and Walt, 1961]. Although it is not certain that scattering with the atmosphere is the only (or even the major) force perturbing the motion of the trapped electrons, this assumption will be made since direct evidence of the existence and magnitude of other forces is lacking. In the following paper the results of this calculation are compared with the measured electron spectrum.

Fokker-Planck formulation. In a previous paper, the Fokker-Planck equation for the distribution function of electrons trapped in a magnetic field in the presence of a scattering atmosphere was derived and an approximate solution, applicable to the case of the earth's

¹Permanent address: University of Maryland, College Park, Maryland.

atmosphere and a dipole field, was obtained. Since the details of the derivation are available elsewhere [MacDonald and Walt, 1961], only a brief outline will be given here.

The electron flux is described by a distribution function $f(\mu, T, t)$ which is the number of electrons at time t with kinetic energy T (in units of mc^2) within unit ΔT , and whose trajectory parameter μ is within unit $\Delta\mu$ at μ . The quantity μ is the cosine of the angle between the local magnetic field and the particle velocity vector measured at the instant the particle crosses the equatorial plane.

The general Fokker-Planck equation is

$$\frac{\partial f(\mu, T, t)}{\partial t} = -\frac{\partial}{\partial \mu} f(\Delta\mu) - \frac{\partial}{\partial T} f(\Delta T) + \frac{1}{2} \frac{\partial^2}{\partial \mu^2} f(\langle \Delta\mu \rangle^2) \quad (1)$$

+ higher order terms

where the brackets denote the average change per unit time of the enclosed increments. The bracketed quantities are evaluated for the case of coulomb collisions with the neutral and charged atmospheric constituents appropriate to a current atmospheric model [Johnson, 1960], the magnetic field line chosen for the evaluation being one which passes through the equatorial plane at a distance of 2 earth radii from the earth's center. With the assumption that the total distance traveled by an electron in one complete orbit is independent of μ equation 1 reduces to

$$\frac{\partial f}{\partial \tau} = \frac{M(\mu)}{n_0} \frac{\partial}{\partial T} \left[\frac{T+1}{T^{1/2}(T+2)^{1/2}} \ln \eta_D^{-1} f \right] + \frac{T+1}{2T^{3/2}(T+2)^{3/2}} \frac{\partial}{\partial \mu} \left[(1-\mu^2)\mu \frac{\partial}{\partial \mu} \ln \eta_D^{-1} \frac{f}{\mu} \right] \quad (2)$$

where τ is a dimensionless time variable and is equal to

$$\tau = 4\pi \frac{e^4}{m^2 c^2} n_0 t$$

where

- e = electronic charge.
- m = electron mass.

n_0 = density of protons at a distance of 2 earth radii from the center of the earth and

$$c = 3 \times 10^{10} \text{ cm sec}^{-1}$$

$M(\mu)$ is a function describing the atmospheric density causing energy loss to the trapped electrons. Specifically

$$M(\mu, T) = \tilde{n}_e + (\ln \eta_D^{-1})^{-1} \cdot (\tilde{n}_H \ln \sigma_H + 7\tilde{n}_a \ln \sigma_a)$$

where \tilde{n}_e , \tilde{n}_H , and \tilde{n}_a are the number density of free electrons, neutral hydrogen atoms, and neutral air atoms averaged over an orbit specified by the parameter μ . The scattering parameters η_D , σ_H^{-1} , and σ_a^{-1} are the minimum scattering angles possible for collisions with protons, neutral hydrogen and neutral air atoms. With current atmospheric models $M(\mu, T)$ for a field line passing through the equatorial plane at a distance of 2 earth radii from the earth's center will be relatively flat for $0 \leq \mu \leq 0.92$, and will be almost independent of T since the energy enters only in the arguments of the logarithms. For $\mu > 0.92$, $M(\mu, T)$ becomes very large because of the rapid increase in atmospheric density with decreasing altitude.

Equation 2 represents the time rate of change of the distribution function. The term containing the derivative with respect to energy represents the increase or decrease in the number of electrons of a given μ, T caused by collisions in which energy is lost. The term containing derivatives with respect to μ represents the change in the distribution function resulting from changes in pitch angles and can be considered a spatial diffusion term. This diffusion term differs from the one used in previous calculations [Wentzel, 1959; MacDonald, and Singer, 1959; Kellogg, 1960] in that the deflections introduced by scattering at any point in the orbit have been properly transformed into changes of μ . For electrons with energies in the range of interest the effects of energy loss and diffusion are comparable, so that both effects must be included.

In the presence of a continuous source of electrons, a source term must be added to the right-hand side of equation 2. To find the equilibrium spectrum for a given source let $f_s(\mu, T)$ be the number of electrons per unit energy that are injected into orbits that have pitch angle cosine μ within units $d\mu$. The equation

be solved is

$$= \frac{\partial f}{\partial \tau} = \frac{M(\mu)}{n_0} \frac{\partial}{\partial T} \left[\frac{T+1}{T^{1/2}(T+2)^{1/2}} \ln \eta_D^{-1} f \right] + \frac{T+1}{2T^{3/2}(T+2)^{3/2}} \frac{\partial}{\partial \mu} \cdot \left[(1-\mu^2) \mu \frac{\partial}{\partial \mu} \ln \eta_D^{-1} \frac{f}{\mu} \right] + f_s(\mu, T) \quad (3)$$

An approximate solution of (3) can be obtained by making use of the fact that $M(\mu)$ is very nearly constant until μ is sufficiently large that the electron begins to dip into the exponential atmosphere. The effect of the dense lower atmosphere can be simulated by requiring the distribution function to be zero at some value μ sufficiently close to the earth's surface. Since the actual flux does not fall rigorously to zero at this value of μ , the use of the artificial boundary condition implies that the flux values calculated in the region near the boundary are not accurate. In effect, this boundary condition establishes a slope to $f(\mu, T)$ and hence specifies the leakage of electrons out of the trapping region. For the present calculation the critical value of μ was chosen to be $\mu_c = 0.94$, corresponding to electrons that mirror at an altitude of about 800 km.

To solve equation (3) let

$$g(\mu, T) = \frac{T+1}{T^{1/2}(T+2)^{1/2}} \ln \eta_D^{-1} \frac{f}{\mu} \quad (4)$$

Expand $g(\mu, T)$ in a series of functions in which the energy dependence and spatial dependence are separated,

$$g(\mu, T) = \sum_{\lambda} a_{\lambda}(T) G_{\lambda}(\mu) \quad (5)$$

where the $G_{\lambda}(\mu)$ are an orthonormal set of functions satisfying the eigenvalue equation

$$\frac{\partial}{\partial \mu} \left[(1-\mu^2) \mu \frac{\partial G_{\lambda}}{\partial \mu} \right] + \lambda \mu G_{\lambda} = 0 \quad (6)$$

with boundary conditions

$$G_{\lambda}(\mu_c) = 0 \quad \frac{\partial G_{\lambda}(0)}{\partial \mu} = 0$$

Substituting (4) and (5) into (3), multiplying by G_{σ} , and integrating from $\mu = 0$ to $\mu = \mu_c$ results in

$$\sum_{\lambda} \frac{M_{\lambda\sigma}}{n_0} \frac{\partial a_{\lambda}}{\partial T} - \frac{\sigma a_{\sigma}}{2T(T+2)} + S_{\sigma}(t) = 0 \quad (7)$$

where

$$M_{\lambda\sigma} = \int_0^{\mu_c} \mu \, d\mu G_{\lambda}(\mu) M(\mu) G_{\sigma}(\mu)$$

$$S_{\sigma}(T) = \int_0^{\mu_c} f_s(\mu, T) G_{\sigma}(\mu) \, d\mu$$

Because of the slow dependence of $M(\mu)$ on μ over most of the range the matrix $M_{\lambda\sigma}$ is approximately diagonal, the off-diagonal elements being less than one-tenth the value of the diagonal elements. Neglecting the off-diagonal elements, the solution of the equation for the equilibrium flux is

$$f(\mu, T) = \frac{\mu T^{1/2}(T+2)^{1/2}}{(T+1) \ln \eta_D^{-1}} \cdot \sum_{\lambda} G_{\lambda}(\mu) \frac{n_0}{M_{\lambda\lambda}} \left[\frac{T+2}{T} \right]^{-\lambda n_0/4 M_{\lambda\lambda}} \cdot \int_{\tau}^{\infty} S_{\lambda}(T') \left[\frac{T'+2}{T'} \right]^{\lambda n_0/4 M_{\lambda\lambda}} dT' \quad (8)$$

It is instructive to consider solutions in which either the energy loss term or the diffusion term is neglected. If diffusion is neglected, the solution is

$$f(\mu, T) = \frac{T^{1/2}(T+2)^{1/2}}{(T+1) \ln \eta_D^{-1}} \frac{n_0}{M(\mu)} \cdot \int_{\tau}^{\infty} f_s(\mu, T') \, dT' \quad (9)$$

so that the energy spectrum is independent of μ . This equation 9 is equivalent to one derived more directly by Kellogg [1960] for the restricted case of electrons slowing down without leakage. For the case in which the energy loss is neglected and only diffusion is allowed, the equilibrium flux becomes

$$f(\mu, T) = \mu \frac{T^{1/2}(T+2)^{1/2}}{(T+1) \ln \eta_D^{-1}} \cdot \sum_{\lambda} G_{\lambda}(\mu) \frac{2T(T+2)}{\lambda} S_{\lambda}(T) \quad (10)$$

and the spectrum is again independent of μ . Equations 8, 9, and 10 give the equilibrium electron number for an arbitrary source. The

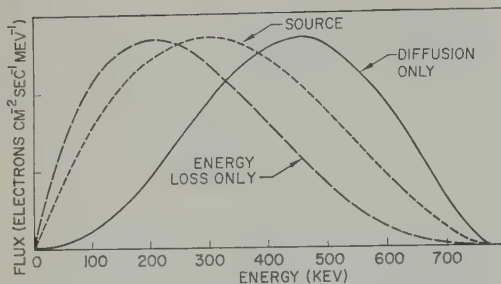


Fig. 1. Electron flux as a function of energy. The 'source' curve indicates the flux spectrum produced by β -decay of neutrons. The curves labeled 'diffusion only' and 'energy loss only' represent the steady state spectrum which would result if these two loss mechanisms are considered separately. The linear ordinate scale is in arbitrary units.

flux intensity is proportional to the product of $f(\mu, T)$ and the electron velocity.

The eigenvalue equation has been solved by analog computer for the first four eigenvalues and eigenfunctions. The first four eigenvalues are $\lambda_1 = 2.3$, $\lambda_2 = 18.5$, $\lambda_3 = 47.1$, and $\lambda_4 = 90.6$. Evaluation of the matrix $M_{\lambda\sigma}$ for the first four eigenfunctions, where the units are cm^{-3} , gives

$$M = \begin{pmatrix} 1122 & -76 & -26 & -68 \\ -76 & 1168 & 77 & 78 \\ -26 & 77 & 1177 & -94 \\ -68 & 78 & -94 & 1123 \end{pmatrix}$$

Of the possible source mechanisms, neutron decay offers the most favorable case for calculation since the energy spectrum of the source is well known. Assuming that the electron source from neutron decay is isotropic and uniform along the magnetic field line under consideration, Equations 8, 9, and 10 have been evaluated, and the results are given in Figures 1 and 2. In evaluating the case where both energy loss and diffusion are included, spectra for three values of μ are calculated. In the cases of diffusion without energy loss and of energy loss without diffusion, the energy spectrum is independent of μ .

Discussion of results. The influence of the two factors, energy loss and diffusion, upon the electron energy distribution is shown in Figure 1. The curve marked 'Source' is a plot of the neutron beta decay spectrum multiplied by the electron velocity. The curves labeled 'Energy

Loss Only' and 'Diffusion Only' are obtained from equations 9 and 10, respectively, after multiplying the value of $f(\mu, T)$ at each energy by the electron velocity at that energy. The effect of energy loss during collisions is to reduce the average energy. Diffusion, on the other hand, tends to raise the average energy by preferentially removing the lower energy electrons.

When both diffusion and energy loss are considered, the equilibrium flux is obtained using equation 8 and is plotted for three values of μ in Figure 2. For easier comparison these curves have been normalized to have the same maximum value; hence the values of the ordinate are arbitrary. The values of $\mu = 0.2, 0.5$, and 0.9 specify trajectories of electrons which mirror at altitudes above the earth's surface of 6.2×10^3 , 5.6×10^3 , and 2×10^3 km, respectively. Although the change in spectrum is small for this large change in mirror-point altitude, the trend is for the average electron energy to increase with decreasing mirror-point altitude, a condition produced by the more rapid leakage of low energy electrons near the boundary of the trapping region.

Also shown on Figure 2 is the observed spectrum of electrons measured on the same field line but at a somewhat lower altitude than that used in the calculations. It is apparent that the observed spectrum, even allowing for larger experimental uncertainties, is qualitatively different from any of the calculated curves. The agreement is not improved significantly by reasonable changes in the atmospheric density used or by restricting the neutron source loca-

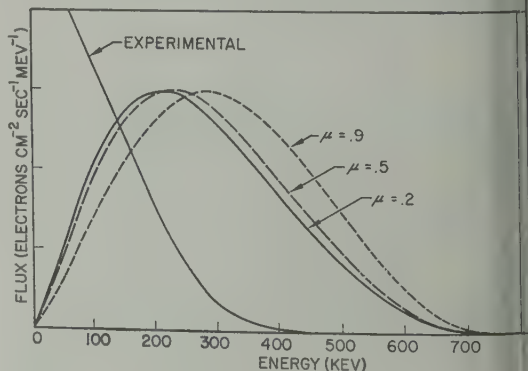


Fig. 2. Comparison of experimental and theoretical values of the electron flux in the outer radiation zone. Theoretical curves are shown for particles which mirror at three different altitudes.

to lower altitude. Since the average energy electrons produced by μ -meson decay is considerably higher than that of neutron decay products, the equilibrium spectrum for μ -meson decay would deviate even more strongly from the observed distribution.

This direct comparison of the calculated electron spectrum with the measured one requires some justification, since the measurement was made so close to the position of the arbitrary boundary that the diffusion theory results are questionable. A second concern is that anomalies in the earth's magnetic field introduce complications which are not included in the calculation. The effect, as trapped electrons drift eastward in altitude, the altitude distribution should be modified by magnetic anomalies that raise or lower the mirror points with respect to the atmosphere. These two conditions might lead to the suspicion that the measured flux at 10³ km is composed primarily of low energy electrons which have been scattered into low mirror point altitudes, and that the flux at altitudes above 10³ km, where the Fokker-Planck formalism is valid, might have a spectrum comparable to the theoretical curves of Figure 2.

However, there are several reasons for believing that the measured spectrum is also characteristic of fluxes at higher altitudes. Requiring the flux to become zero at a given altitude is equivalent to placing an absorbing barrier at that altitude so that any electron whose orbit carries it beyond this barrier will not return. Thus, the calculated value of $f(\mu, T)$ for μ sufficiently close to μ_c will be depleted by electrons which could have scattered into $f(\mu, T)$ on trajectories characterized by $\mu > \mu_c$. In the actual case of electrons in the earth's field, an absorbing layer does not exist, and the electron spectrum would be expected to vary in energy and altitude in a continuous manner. The diffusion calculations suggest that, although the change in spectrum shape with altitude is quite small, the trend is for the average energy to increase with decreasing mirror point altitude.

The effect of magnetic anomalies upon the low altitude spectrum is difficult to establish. As the electrons drift past an area of low field strength, the altitude of the mirror points will be lowered relative to the atmosphere, and the values of $f(\mu, T)$ near $\mu = \mu_c$ will be reduced. To the eastward of such magnetic anomalies the reduced

intensity of particles with $\mu \cong \mu_c$ would persist, and this relative void would be rapidly filled by the downward diffusion of electrons from higher altitudes. Since low energy electrons diffuse more rapidly than those with higher energies, the electron energy spectrum immediately east of a region of low magnetic field would be enriched in low energy electrons. It should be emphasized that this condition can only occur locally; on the average the spectrum at low altitude must be similar to that which obtains in an equilibrium condition.

Along the magnetic shell where the experimental curve of Figure 2 was measured, there are no pronounced magnetic anomalies immediately to the west of the flight position, the major area of low field strength being the region near South Africa, approximately 300° to the west. Hence, it is unlikely that the large intensity of low energy electrons could be attributed to inhomogeneities in the geomagnetic field.

These considerations are confirmed by the experimental data. Any boundary phenomenon or magnetic anomaly effect which would radically alter the energy spectrum at low altitude would introduce an altitude dependence to the spectrum. In the experiment it was found that the measured spectrum did not change noticeably in the altitude region between 600 and 1000 km, a region of high air density where any possible effects would be expected to be more pronounced than at higher altitude.

Conclusions. The severe disagreement between the measured energy spectrum and the equilibrium spectrum calculated by assuming a neutron decay source and atmospheric scattering leads to one or both of the following conclusions. Either the electrons at the inner edge of outer radiation belt are not produced by neutron decay or the dominant loss mechanism of electrons trapped in this region of the earth's magnetic field is not coulomb scattering with the atmosphere.

Acknowledgment. Work for this paper was supported in part by the Office of Naval Research under contract Nonr 1797(00).

REFERENCES

- Cladis, J. B., L. F. Chase, W. L. Imhof, and D. J. Knecht. *J. Geophys. Research*, 1961.
- Johnson, F. S., Lockheed Missiles and Space Division, *Tech. Rept. LMSD 895006*, 1960.

Kellogg, P. J., Electrons of the Van Allen radiation, *J. Geophys. Research*, 65, 2705-2713, 1960.
MacDonald, W. M., and M. Walt, *Ann. Phys.*, 1961.
Van Allen, J. A., State University of Iowa, Report SUI-60-18, 1960. (A comprehensive bibliography concerning geomagnetically trapped radiation.)
Walt, M., L. F. Chase, J. B. Cladis, W. L. Imhof, and D. J. Knecht, *Proceedings of the First Inter-*

national Space Science Symposium, Nice, 1960, edited by H. Kallmann, North Holland Publishing Company, Amsterdam, Holland, 1960.
Wentworth, R. C., W. M. MacDonald, and S. F. Singer, *Physics of Fluids*, 2, 499, 1959.

(Manuscript received March 17, 1961.)

Some Features of Magnetic Storms in High Latitudes

DAVID G. KNAPP

*U. S. Coast and Geodetic Survey
Washington, D. C.*

(Appendix 1 by D. G. Knapp and E. B. Fabiano)

Abstract. During a severe magnetic storm, observatory records obtained in high latitudes may show a type of disturbance here called a 'cusped bay,' characterized by a marked displacement of the trace, coupled with augmented short-period fluctuations. Several of these events registered during the IGY at stations near the northern and southern auroral zones, some with amplitudes approaching 2000 γ , were measured on all appropriate magnetograms and plotted on maps as equivalent overhead current vectors. They show some of the characteristics of systems based on hourly-value changes during storms. However, they afford almost no evidence of the afternoon eastward segment of the auroral electrojet, and the polar-cap effects are indicative of patterns having greater complexity than the one usually ascribed to this region. The author recommends the study of cusped bays as a supplement to the use of hourly values and a means of probing details of magnetic activity that are difficult to approach in other ways. A catalog of IGY storms is appended to the paper.

Background. Because of their affinity for high latitudes, magnetic storms can be studied effectively only by setting up networks of stations in the Arctic or Antarctic. A fairly extensive network was operated during the First International Polar Year of 1882-1883, but the records obtained were not particularly directed toward magnetic storm analysis and do not provide the requisite detail for close study of polar disturbances, although the term of operation fell at a peak of the sunspot cycle and included several severe storms.

The Second International Polar Year came at a sunspot minimum and included only one magnetic storm of any consequence, that of May 1, 1933. Because of the number of arctic stations then in operation, that storm has been more thoroughly studied heretofore than any other.

The third and most fruitful of these great cooperative endeavors was the recently completed International Geophysical Year. This was purposely set to coincide with another sunspot maximum. It proved to be the most active maximum yet recorded, in over 200 years of observing; and the expectations of strong magnetic activity were amply fulfilled. In the entire 18-month term, scarcely any intervals of more than a few weeks can be selected that were free from magnetic storms. Nine of the storms

surpassed the 1933 one in severity, and two or three of the nine can surely qualify for any list of the great magnetic storms of the century and more since recordings began. Furthermore, many of the cooperating agencies, forewarned by the shortcomings of the earlier programs, took pains to provide for wide-range, low-sensitivity installations in a special effort to capture the full progress of the more severe storm activity.

It is generally accepted that magnetic activity is produced by some mechanism involving ionized gaseous material within or beyond the ionosphere. There is a well-known drawing by Chapman [1935] which shows in somewhat idealized form a current system that might be invoked to account for some of the chief features of magnetic disturbance. On the basis of records of the moderate magnetic storm of May 1, 1933, Vestine [1940] and Fukushima [1953] have constructed series of patterns which incorporate some of the features of the Chapman scheme but which show the changing aspect of the field from hour to hour as it develops during the course of the storm. Figure 1 shows Vestine's diagram for a time about 24 hours after the beginning of the storm of April 30-May 1, 1933. It will be noted that this diagram places the maximum-current segment of the auroral electrojet some two or three hours earlier in local time than the 6 A. M. position of Chapman's original drawing.

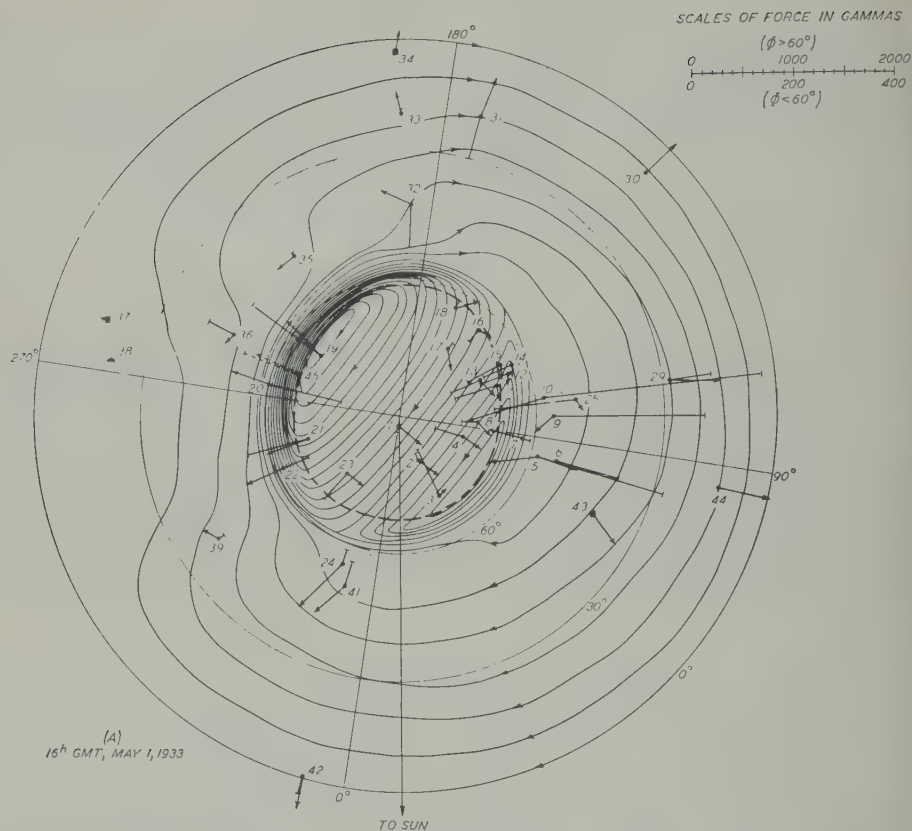


Fig. 1. Postulated current system for the storm of May 1, 1933, at 1600 UT. The vectors here represent the magnetic field data on which the current lines are based. Geomagnetic north pole (magnetic axis pole) in center; direction of sun toward lower edge of page. Current flow between lines 100,000 amperes. After Vestine [1940].

Figure 2 is a redrawn version of the central portion of Figure 1, with alternate lines omitted for clarity. In this and succeeding polar diagrams, the direction to the sun is upward throughout. The polar-cap return current flows toward the meridian of 10h local time, that is, along lines parallel to that meridian. (In Chapman's version, this flow is toward the noon meridian.) The corresponding antarctic system, seen from a point over the south geomagnetic pole, would be approximately the mirror image of this one.

These systems are constructed from hourly mean values. They build up in strength to a maximum during the main phase of the storm and then gradually fall off. However, so long as we limit ourselves to hourly values we are ignoring the violent short-period activity that is usually regarded as the most characteristic feature of magnetic storms. Furthermore, the hourly values give a somewhat watered-down

image of the storm effects, and, as one gets further in time from the prestorm quiet conditions that form the basis of reference, there is always a question how much of the observed disparity can be properly charged to the storm effect and how much is due to the normal quiet-day changes that would have occurred anyway. For these reasons, it is necessary to make the greatest possible use of those storms that are of outstanding violence, and to seek out any promising alternative means of obtaining detailed knowledge of the behavior of the current systems at different times in the course of the storm. It is therefore of considerable interest to look at some of the short-term features and see how their spatial patterns compare with the systems derived from hourly values. Fukushima has made a good beginning along these lines with his studies of bays. The wealth of magnetic storm material now becoming available from an

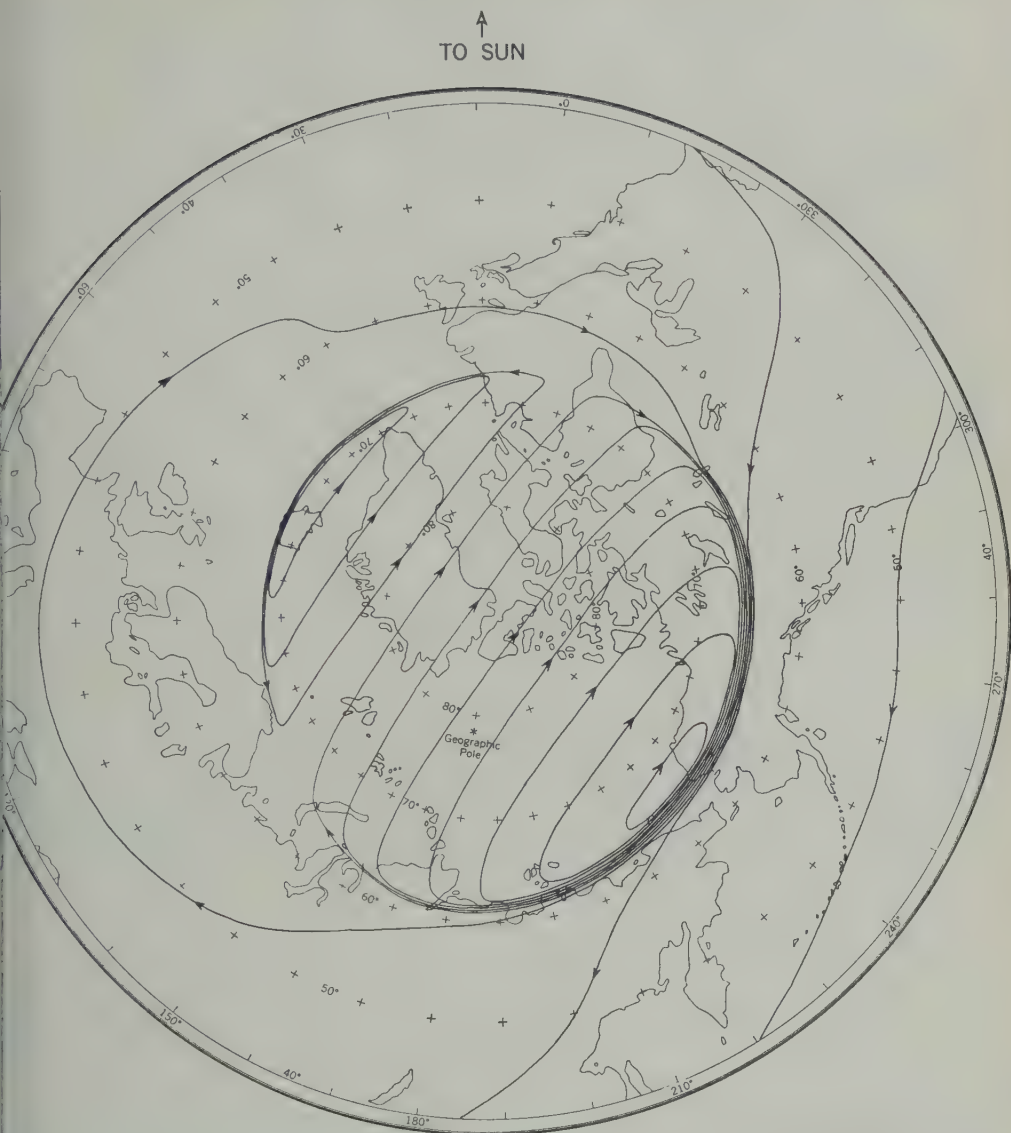


Fig. 2. Postulated current system for the storm of May 1, 1933, at 1650 UT. Geomagnetic north pole in center; direction of sun as indicated. Current flow between lines 200,000 amperes. After Fukushima [1953] and Vestine [1959].

anded coverage in both the Arctic and the Arctic suggests that further efforts along this direction would be fruitful.

Material and technique. The material available for this study was acquired over the 18 months of the International Geophysical Year, commencing with July 1, 1957. At the outset of study, a list was compiled (see Appendix 1) giving all the magnetic storms that occurred during the IGY span and classifying them into

six categories according to their relative severity. The list facilitated examination of magnetograms for the more severe storms from which specific events were selected for study. This scanning, devoted primarily to low-sensitivity records from the Coast and Geodetic Survey observatories, commenced with Fredericksburg and the mid-Alaskan stations and subsequently extended to Barrow, Sitka, and the antarctic stations.

When we examine the records of severe mag-

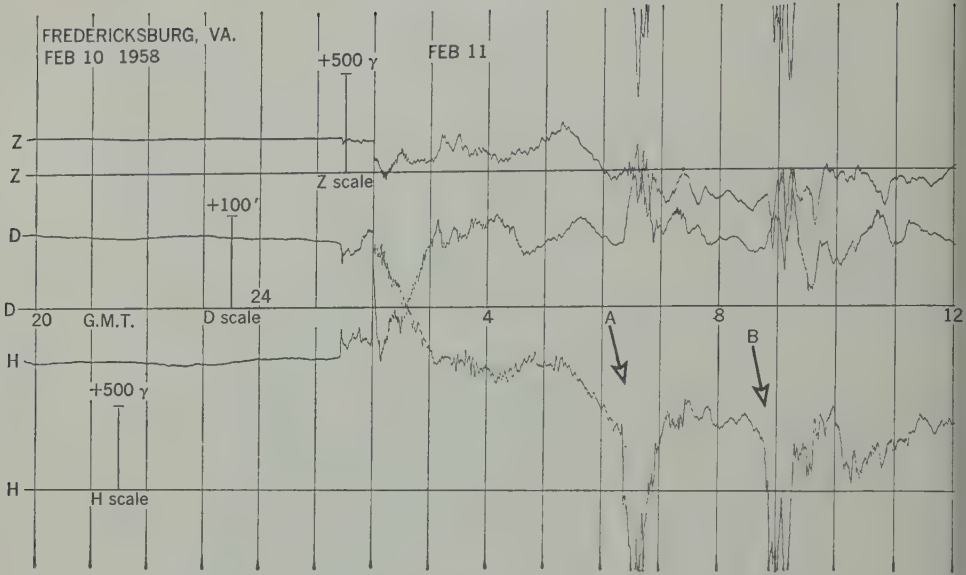


Fig. 3. Portion of low-sensitivity magnetogram from Fredericksburg (Virginia) Magnetic Observatory for February 10-11, 1958, showing two cusped bays at *A* and *B*.

netic storms we are struck by an occasional happening that may afford a suitable tool for studies along the lines outlined above. It is characterized by a large displacement in one or more of the traces, maintained for an interval

of from ten minutes to an hour or more. Beginning at about the same time as this general displacement (perhaps a little sooner), there is a surge of violent short-term fluctuations resembling the ordinary broad-spectrum background 'noise'

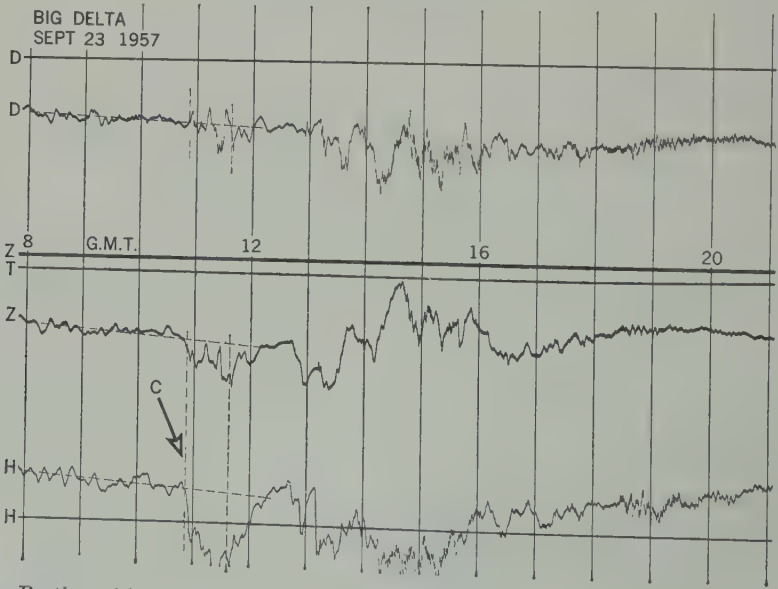


Fig. 4. Portion of low-sensitivity magnetogram from Big Delta Magnetic Observatory (IGY station) for September 23, 1957, showing method of scaling reference value for cusped bay at *C*.

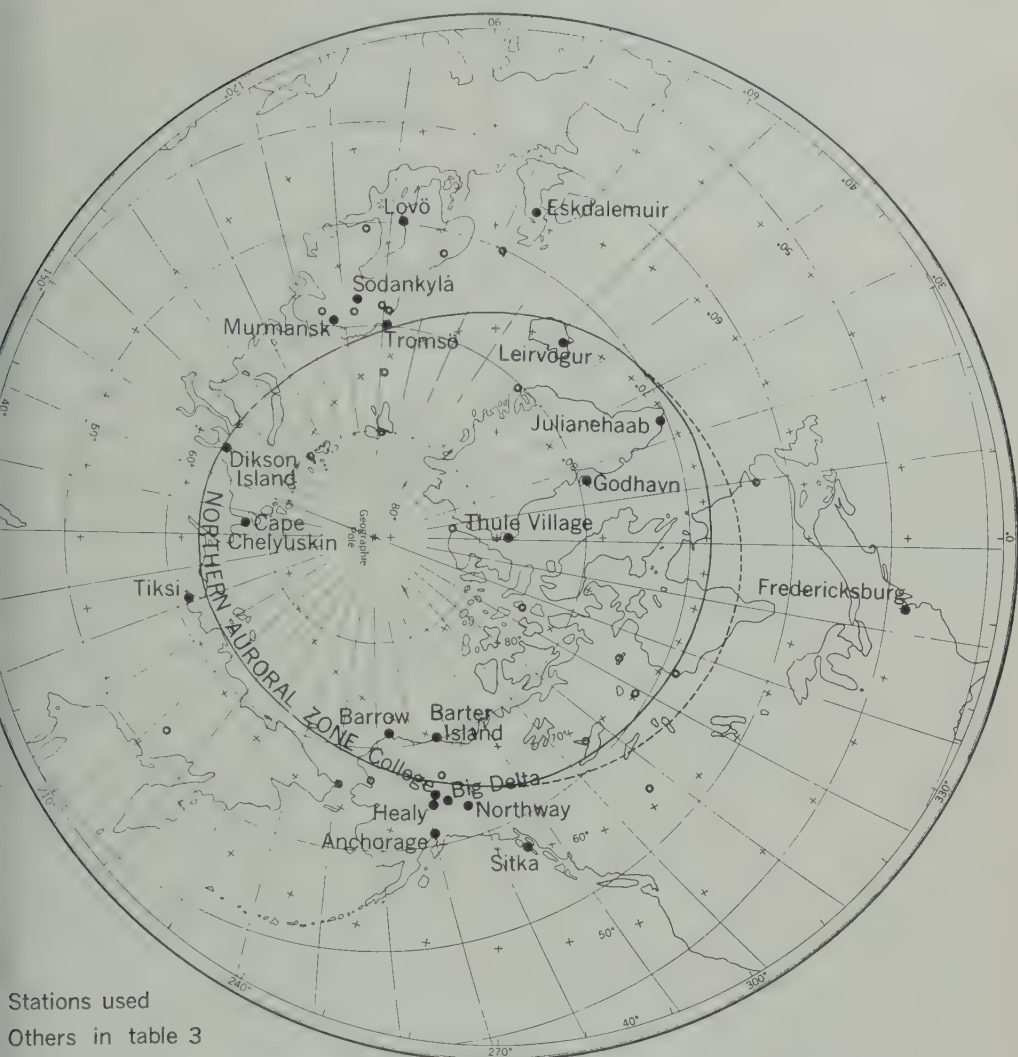


Fig. 5a. Regions north of 40°N geomagnetic latitude, on azimuthal equal-area projection centered on geomagnetic north pole, with auroral zone and high-latitude stations indicated. Full-line meridians and parallels are geographic; those indicated by intersections and numerals show geomagnetic coordinates.

netic activity but having greater amplitude. This noise may continue with a longer duration in the general displacement, and the form of the latter is so obscured and modified by the irregular activity as to warrant the term 'cusped' for these events. Figure 3 shows two of the events during the great storm of February 1958, one (pointer A) beginning at 6h 25m and the other (pointer B) at 8h 48m UT. It is thought a sudden new influx of solar plasma was added to the existing system so as to rein-

force the currents flowing—both the d-c or fairly regular flow and the a-c or background-noise flow.

Note the large amplitude of these events; this is a low-sensitivity magnetogram. Figure 4 shows another event, from the Big Delta records, for the storm of September 23, 1957. The Big Delta intensity traces (H and Z) were recorded at a lower sensitivity (higher scale value) than those at Fredericksburg, in the ratio of about 5/2. Note that in all three instances the occurrence

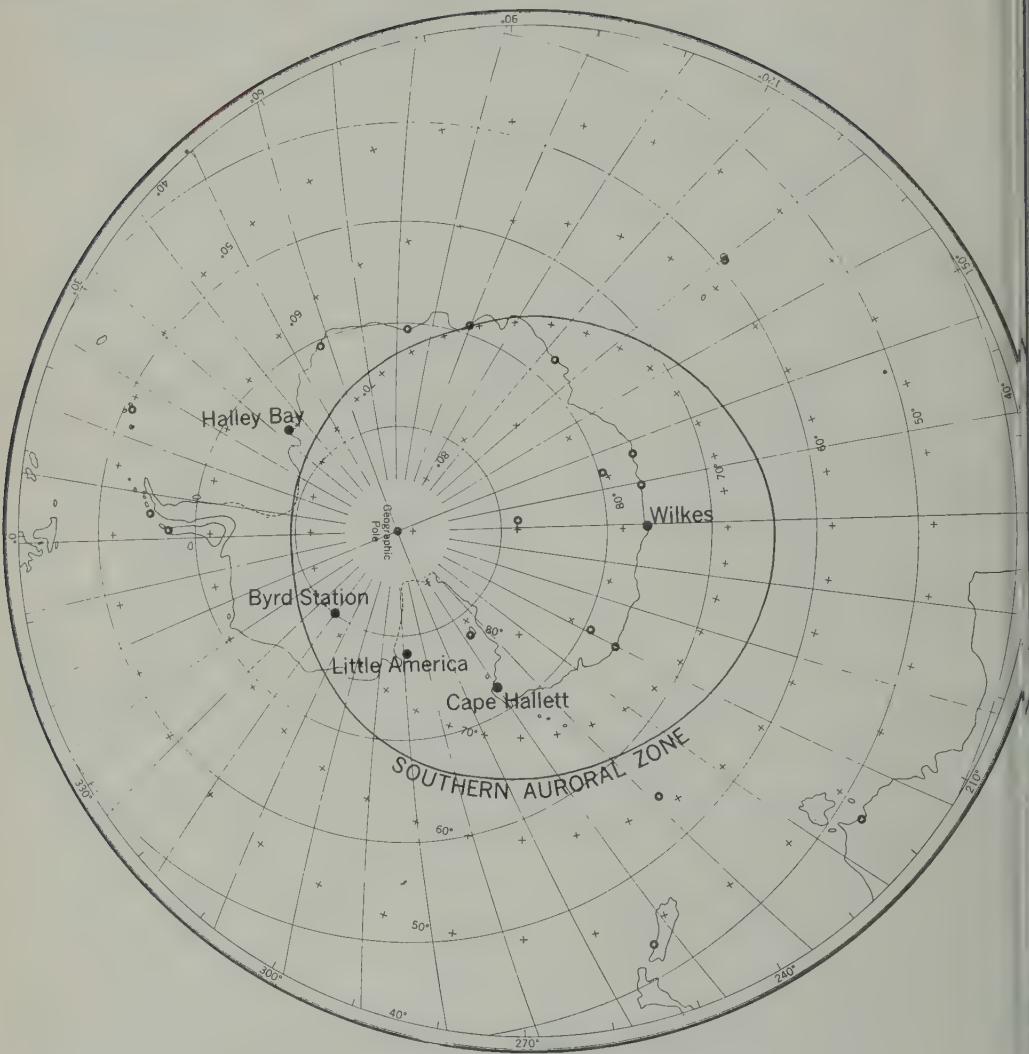


Fig. 5b. Regions south of 40°S geomagnetic latitude, as for Figure 5a.

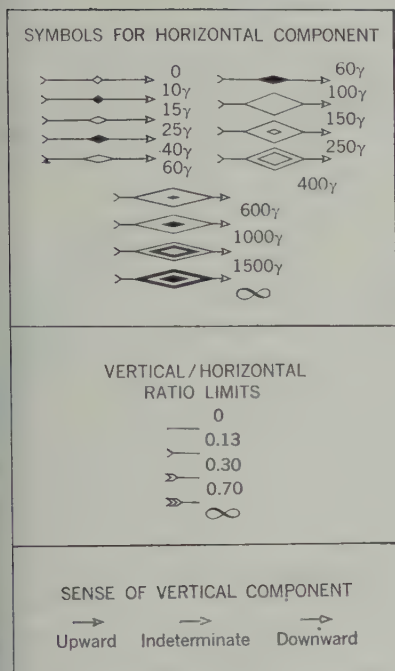
was during the main phase of the storm and showed a downward displacement of the *H* trace; this is typical of the events found.

The immediate objectives of this study are to examine these cusped bays at all available stations close to the auroral zones, to find out whether they can be attributed to the same current systems responsible for the slower manifestations of magnetic storms, and if so to ascertain what additional light they can throw on the probable nature of the causative currents.

Figure 5 shows all the stations that lie poleward of either auroral zone and a number that are close to the line but on the equatorward side.

Those actually used for this study are indicated by the heavier symbols and by the station names: Cape Chelyuskin, Tiksi, Barrow, Barter Island, Northway, Big Delta, College, Healy, Anchorage, Sitka, Fredericksburg, Thule Village, Godhavn, Julianehaab, Leirvogur, Eskdalemuir, Tromsø, Lovö, Sodankylä, Murmansk, and Dikson Island in the north, and Wilkes, Cape Hallett, Little America, Byrd Station, and Halley Bay in the south. Only one of the latter, Halley Bay, lies equatorward of the southern auroral zone; the other four are well inside the polar cap.

The base maps used in this paper are further discussed in Appendix 2. The full lines in Figure



6. Key to vector symbols in Figures 7 to 15.

show the auroral zones as laid down by Vestine [4] and by Vestine and Snyder [1945], whereas broken lines show the recently proposed revision [Hultqvist, 1959] based upon Gartlein's γ data on auroras. The revision is adopted for illustrations to follow and also for Figure 2. The procedure used in this study is illustrated in Figure 4. A straight line is drawn through the bay, conforming as well as possible to the trend published during the three or four hours preceding the cusped bay. The mean ordinate of the trace for the bay interval is compared with that of the straight line for the same interval. The interval scaled is typically somewhat shorter than the bay as manifested on an individual record, but is fixed so as to obtain large amplitude as many stations as possible. All three components are scaled for each bay. The declination and horizontal-intensity values are combined to find the direction and magnitude of the disturbance vector, and this is rotated 90° clockwise to obtain the corresponding equivalent current vector, which is appropriately plotted on a map. Each vector depicts the intensity of the overhead current that would be needed to account for the magnetic effect if it were due entirely to overhead current. This is, of course, a somewhat

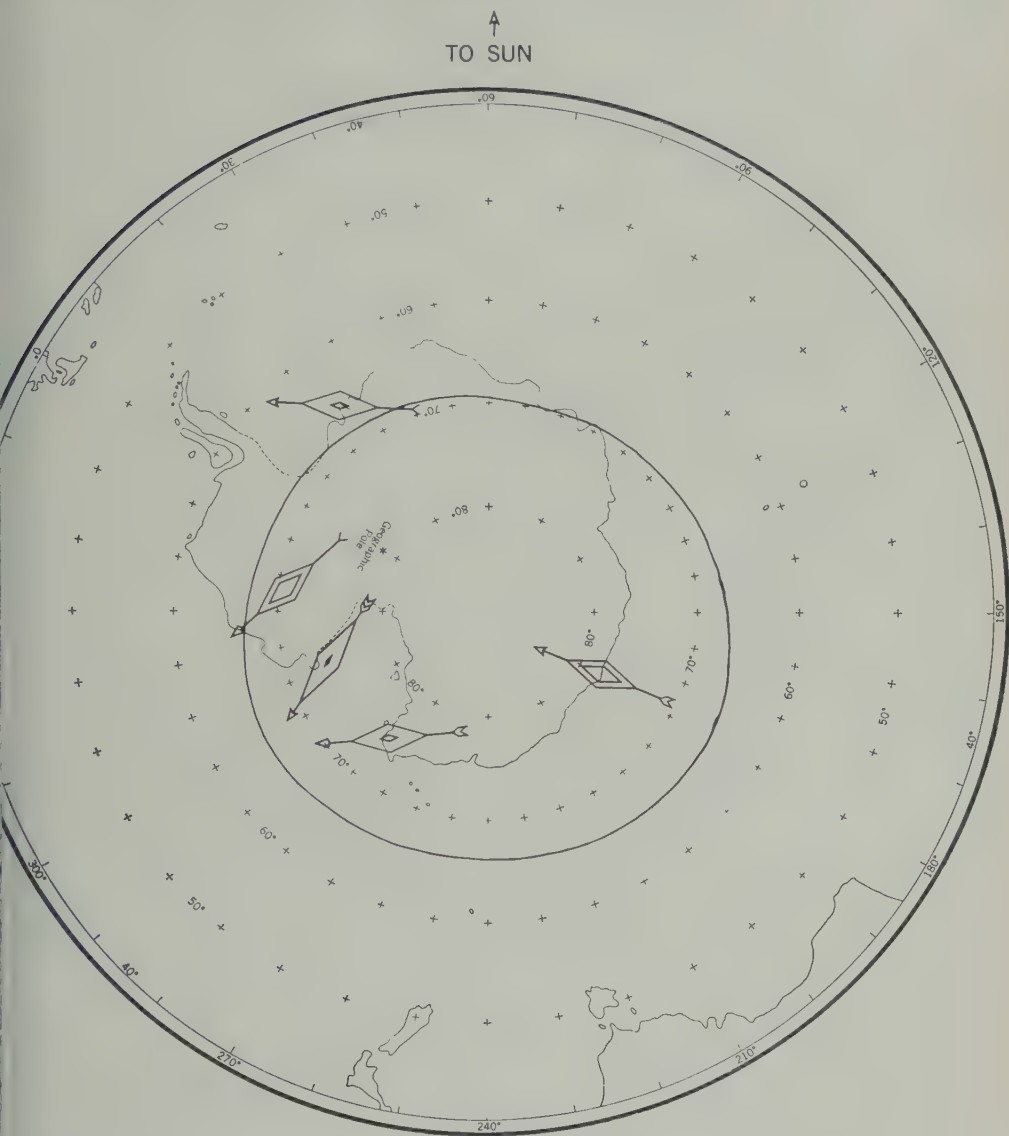
artificial assumption; the strong auroral electrojet must in fact be dominant for points situated some distance to the north and south of the line current. If we keep this limitation in mind, however, the vectors so determined permit a useful comparison between the cusped-bay disturbances and the current system derived from hourly values.

Referring again to Vestine's current pattern (Fig. 2), we note that there are two main segments of the auroral electrojet, each forming the principal feature of a 'cell' of electric current that is completed by a sheet flow across the polar cap. The main predawn cell, with clockwise current flow, is here concentrated over the Chuckchee Sea, and the smaller afternoon cell, having counterclockwise flow, centers over the North Atlantic. The approximate extent of each cell in longitude is governed by local time and hence may be noted on this figure and compared with the vectors shown on subsequent views of the area.

The circuits that will be set up in specific events may be expected to differ from the norm in various ways. For one thing, the auroral zone is generally considered to undergo a slight overall expansion or equatorward shift during severe magnetic storms.

To present the vectors in the most clear-cut relation to possible current systems, it is desirable to use polar projections and to take advantage of every recourse for simplifying the display. To this end, the graticule of geographic meridians and parallels may be omitted. And, in lieu of simple arrows graded in length, we may devise symbols of uniform length but graded in over-all impressiveness and place their centers instead of their root ends at the station sites. We thereby purchase a gain in clarity for both the very small vectors and those so big that their length would otherwise carry them far across the pattern. In addition, as Figure 6 shows, we can incorporate helpful information about the sense and magnitude of the vertical component of the disturbing field. An alternative method of presenting the latter information is exemplified by Figure 1, where the disturbance vectors have adjunct T segments to indicate the vertical contribution, those plotted radially outward corresponding to the positive sense of Z and inward the contrary.

The neat demarcation between the intense line current along the auroral-electrojet path and the



on September 3, 1957, centered at 1241 UT.

the three stations College, Healy, and Big Barrow is computed and shown at a mean position from a single station, it having been found that these three stations give results essentially the same for the purposes of this study. In each case, the southern polar cap is shown beside the northern one, corresponding geomagnetic latitudes being reflected about the midline of the figure.

Figure 7 shows the vectors for a cusped bay

that occurred during the magnetic storm of September 2-3, 1957, about 33 hours after the storm sudden commencement. We see that the vectors at most of the Alaskan stations show the dominance of the predawn main cell, although Barrow appears to be far enough north to be governed chiefly by the polar-cap return current—that is, by the eastward-flowing sheet current. Tiksi and Dikson Island, where we might expect a negligible or even an eastward-

↑
TO SUN

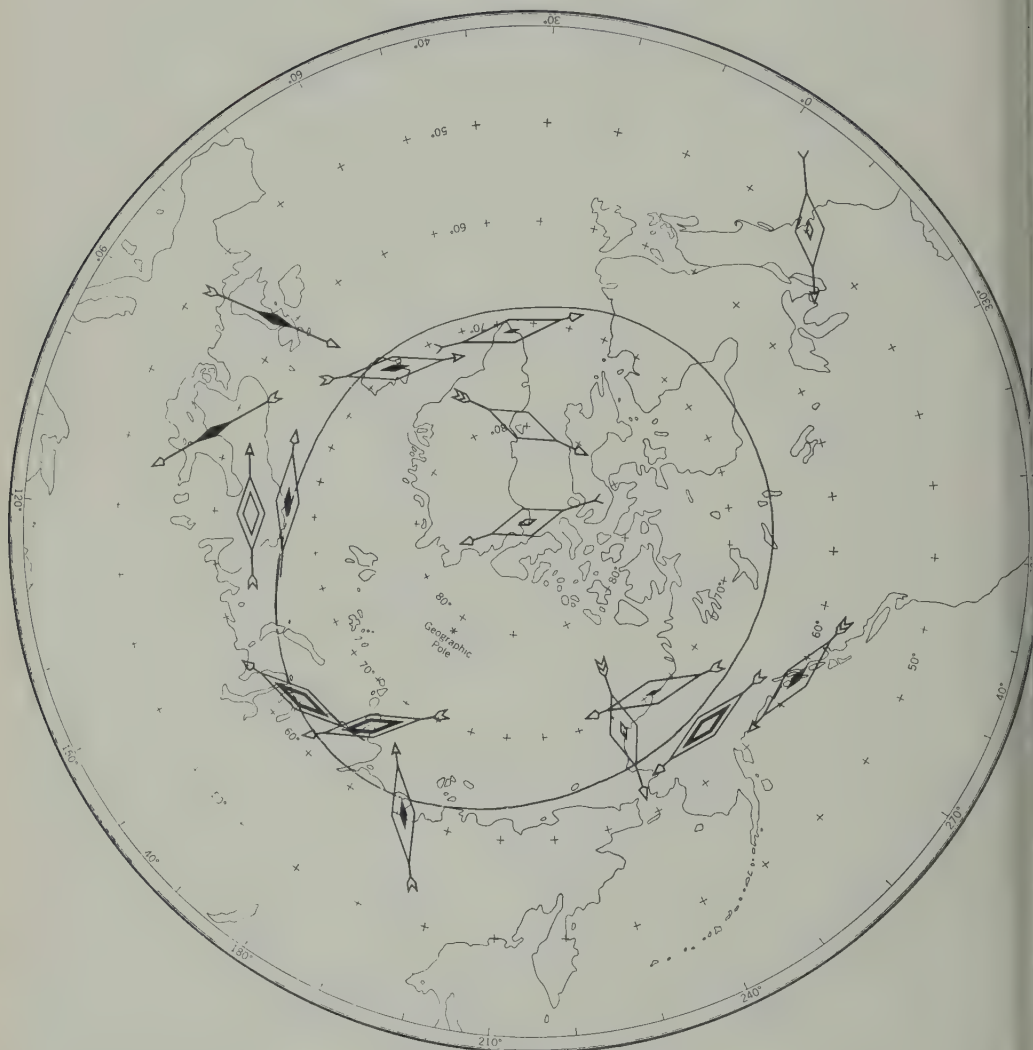
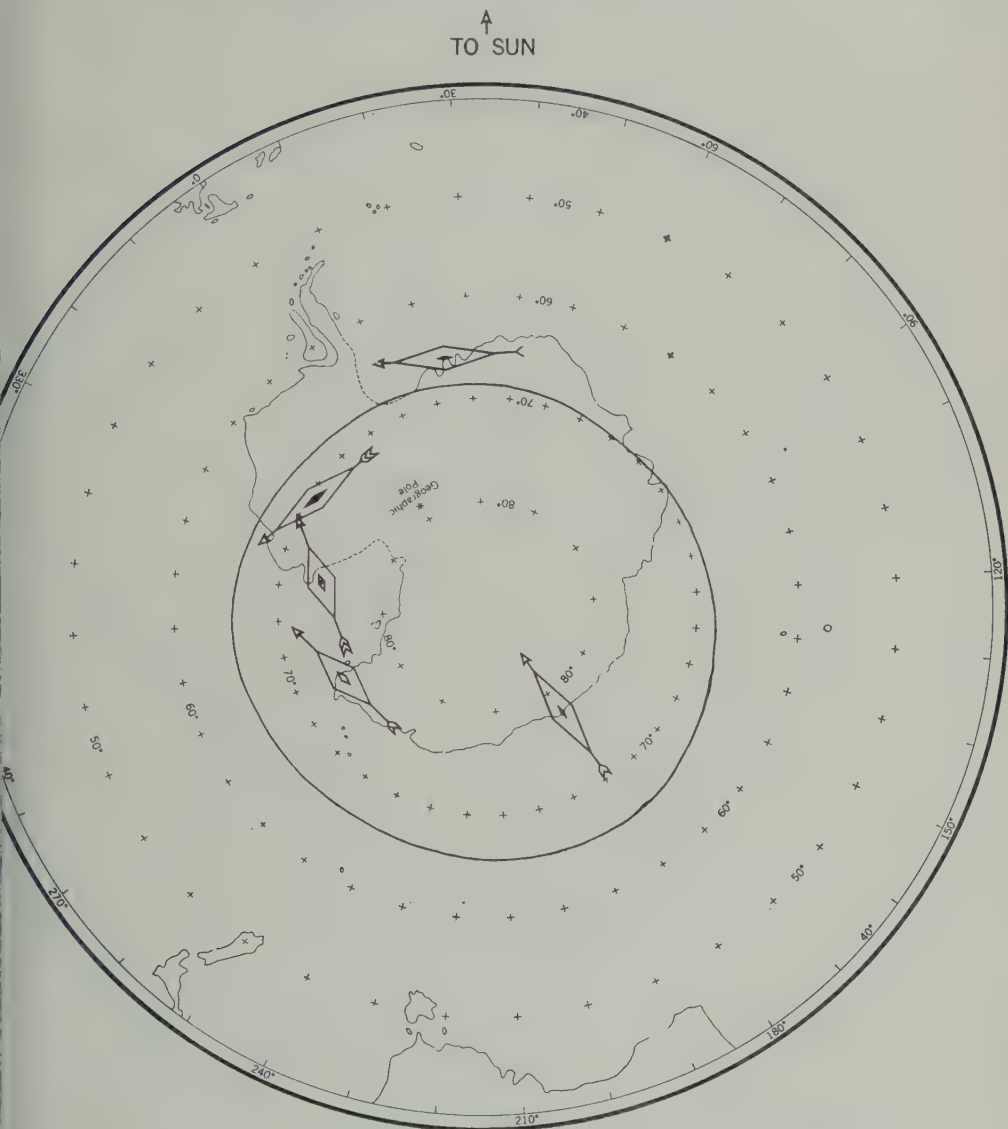


Fig. 8. Equivalent current vectors for a cusp.

flowing current, owing to the expected influence of the afternoon cell, seem to show rather a continuation of the main cell. Tromsø seems to reflect some anomalous condition, possibly associated with the polar-cap return current. Lovö is perhaps too far south of the auroral electrojet for definite conclusions to be reached; it seems to offer confirmation of the afternoon counterclockwise cell. However, we find no support for this idea at Eskdalemuir. This sta-

tion, as well as Godhavn, is anomalous as to the direction of the disturbance for this particular event, but it is too weak to be decisive.

In the Antarctic, the vectors suggest a northward current in the space between Byrd Station and Little America, notwithstanding their distance inside the polar cap. This could mean that the auroral electrojet followed a grossly distorted path, especially if the same circuit is invoked to account for the Halley Ba-



on September 22, 1957, centered at 1415 UT.

or. Wilkes and Cape Hallett show the polar effect, but with a rotation suggesting that pattern may be displaced even earlier, by an or so, than Vestine's results indicated.

he other feature of this view is worthy of ment. The sense of the vertical component he disturbance is downward at the interior kan stations but upward at Anchorage and itka. This suggests that the equatorward of the auroral electrojet was sufficient in

this storm to place it south of Healy but north of Anchorage and Sitka.

Figure 8 shows an instance registered only half an hour after the sudden commencement of a storm (somewhat more severe in general than the previous one) on September 22, 1957. Although this came much earlier in the storm, it is slightly later in terms of universal time than the September 3 event. We again see the dominance of the main cell at most of the Alaskan

↑
TO SUN

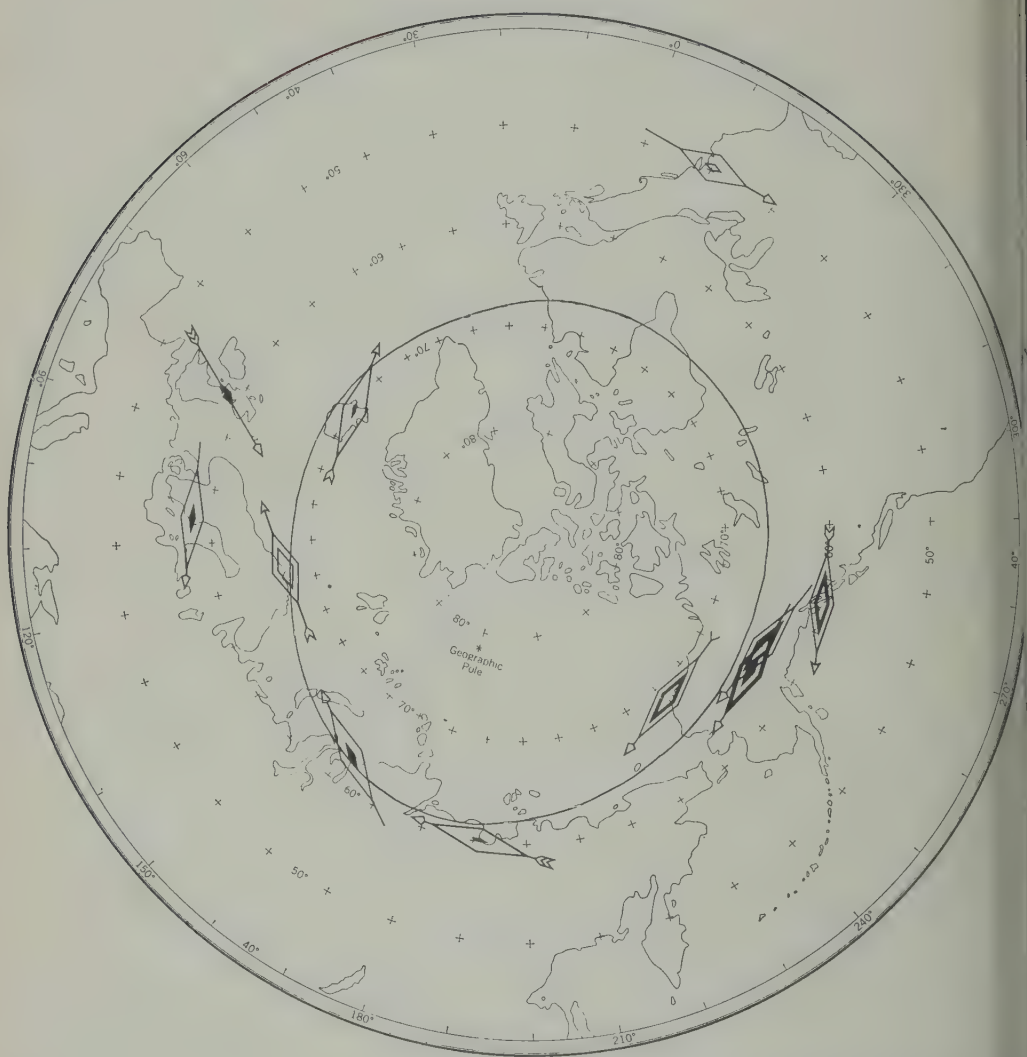
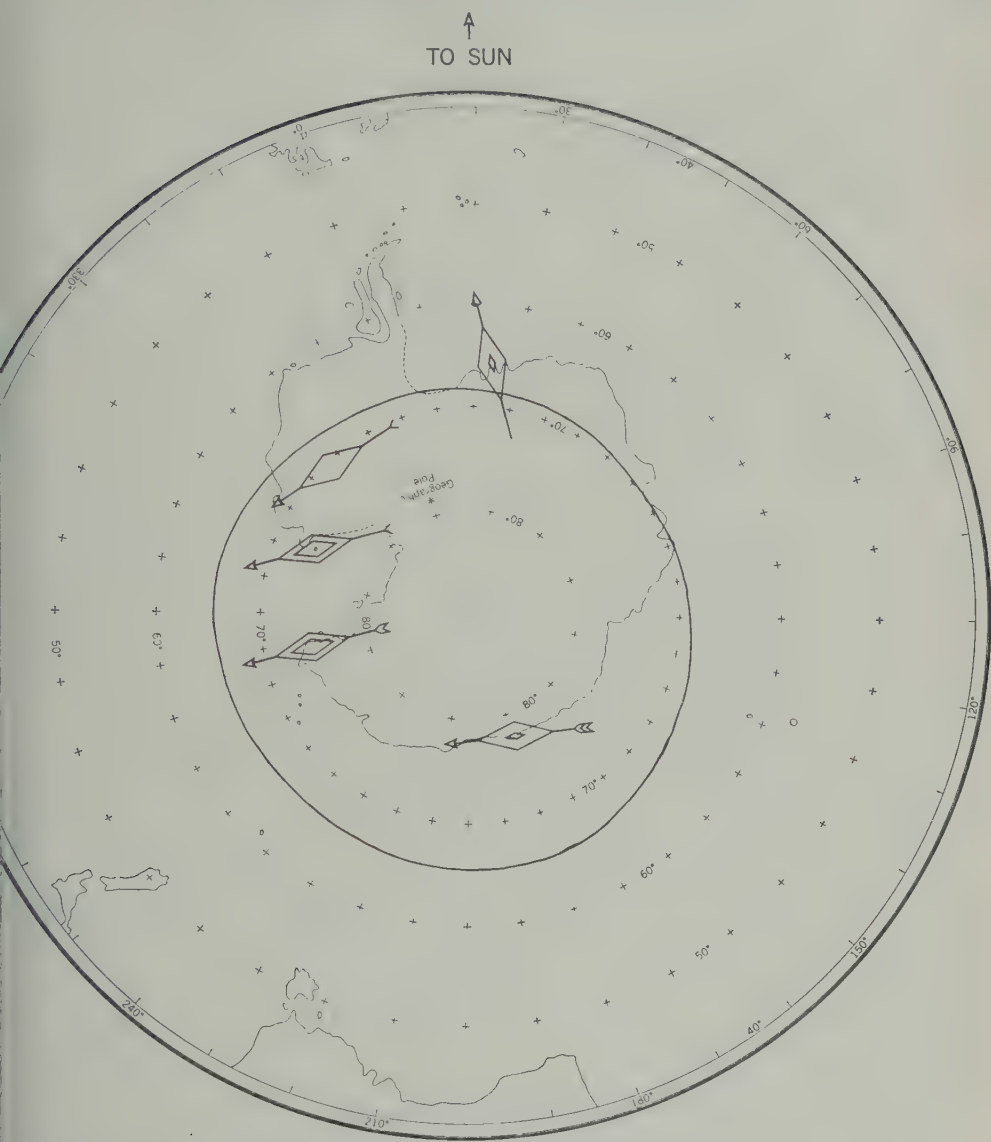


Fig. 9. Equivalent current vectors for a cusp

stations, with Barrow again showing a rather inconclusive result. Dikson Island shows a very strong influence of the electrojet (main cell) notwithstanding its situation at a segment of the auroral zone where the line current is supposedly weakest at this time of day. Cape Chelyuskin and Tiksi likewise show the dominance of the jet, though the anomalies of the direction are awkward. In Scandinavia and in the Atlantic area, where the afternoon cell

should be encountered, there is instead a strong further extension of the main-cell effect—Tromsø, Sodankylä, Leirvogur, and Julianehaab. Godhavn and Thule are contradictory as to the polar-cap flow.

This event was well registered in Antarctica and the record for Halley Bay is evidence against the existence of any afternoon cell. Byrd station suggests diversion of the main-cell jet current into the polar-cap region. Wilkes, Cape Halle



September 4, 1957, centered at 1521 UT.

little America seem to support the conventional view as to the polar-cap return current. Figure 9 we have an occurrence that fell two hours after the beginning of another severe storm, that of September 4, 1957. All the stations near the northern auroral oval show the dominance of the main cell. The Z component of the disturbance at Eureka and Leirvogur suggests that the electrojets shifted or branched into the polar-cap

realm in this region. The antarctic stations seem to suggest a polar current sheet that is rotated some 70° counterclockwise from that of the Vestine diagram. Halley Bay yields an anomalous vector for this event.

Turning next to Figure 10, we have an early cusped bay in the storm of September 2, from which a later instance has already been examined in Figure 7. This one is centered about 90 minutes after the onset of the storm, and the

↑
TO SUN

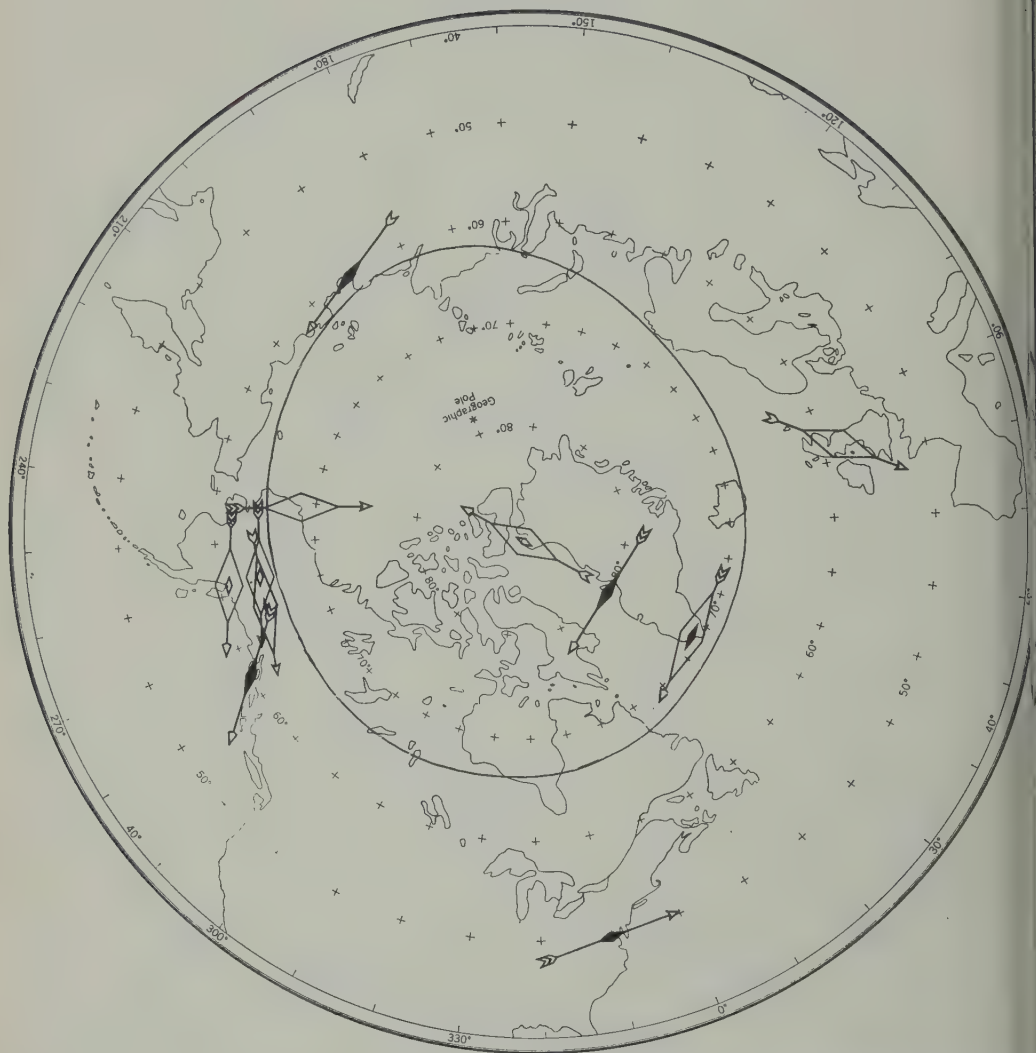
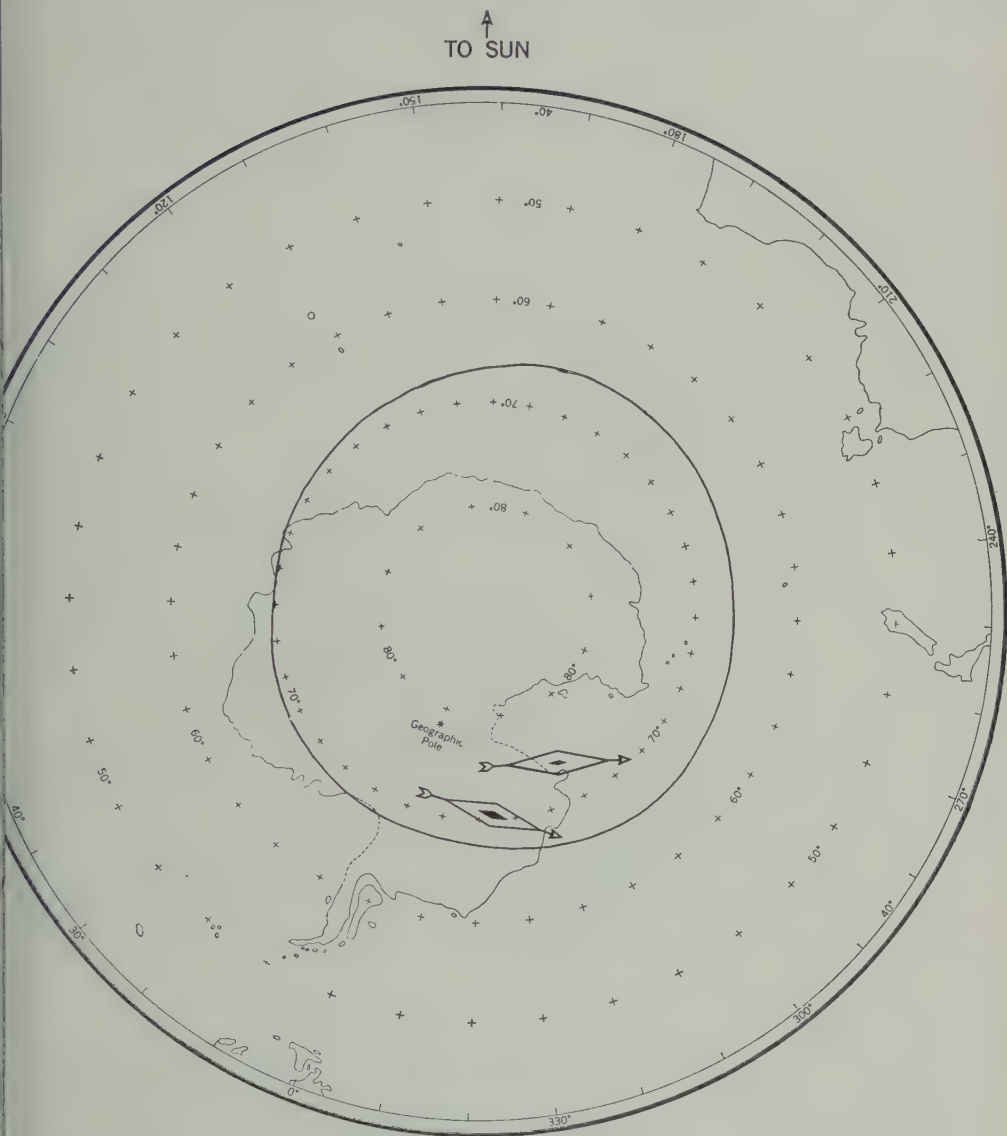


Fig. 10. Equivalent current vectors for a cusp.

vectors show an eastward current in the segment of the auroral zone centered over Alaska (approximately 7h local time). Julianehaab is the only station showing the main cell strongly for this event. Barrow and Thule Village give contradictory testimony as to the polar-cap effect. In the Antarctic, Byrd Station and Little America show strong effects suggestive of line currents, and their directions seem to be indicative of main-cell electrojet current displaced somewhat poleward from the norm.

Figure 11 shows an example registered about nine hours after the beginning of the storm on September 13, probably the second in rank in severity among the IGY storms. The main cell is well shown by Julianehaab and by the Alaskan stations, particularly by Sitka, suggesting that the southward displacement of the auroral zone was greater than usual. This is supported by the fact that the vertical-intensity displacement was in the same positive sense at Sitka as at the other Alaskan stations. In most of the other



on September 2, 1957, centered at 0445 UT.

At Sitka and Anchorage have the Z change opposite sign to the other Alaskan stations. The Barrow vector is here small and eastward, should be if the polar-cap local effect is to override that of the auroral electrojet. The Village and Godhavn are presumably in the polar cap, but the vectors at these stations are anomalous. The strong effect at Tromsø again suggests that the main cell extends to high latitude well beyond the limits shown in Figure 2. At Dikson Island and Tromsø, where

the afternoon cell would be expected to appear most strongly, the vectors are quite small and their directions inconclusive.

In Antarctica, the great intensity at Byrd Station is surprising; and in conjunction with the weak Z effect it suggests that the current which generated the bay was a line current situated almost directly over the station. If the path of the auroral electrojet was indeed this far south, we might expect Halley Bay to have a greatly reduced effect, and that is indeed the

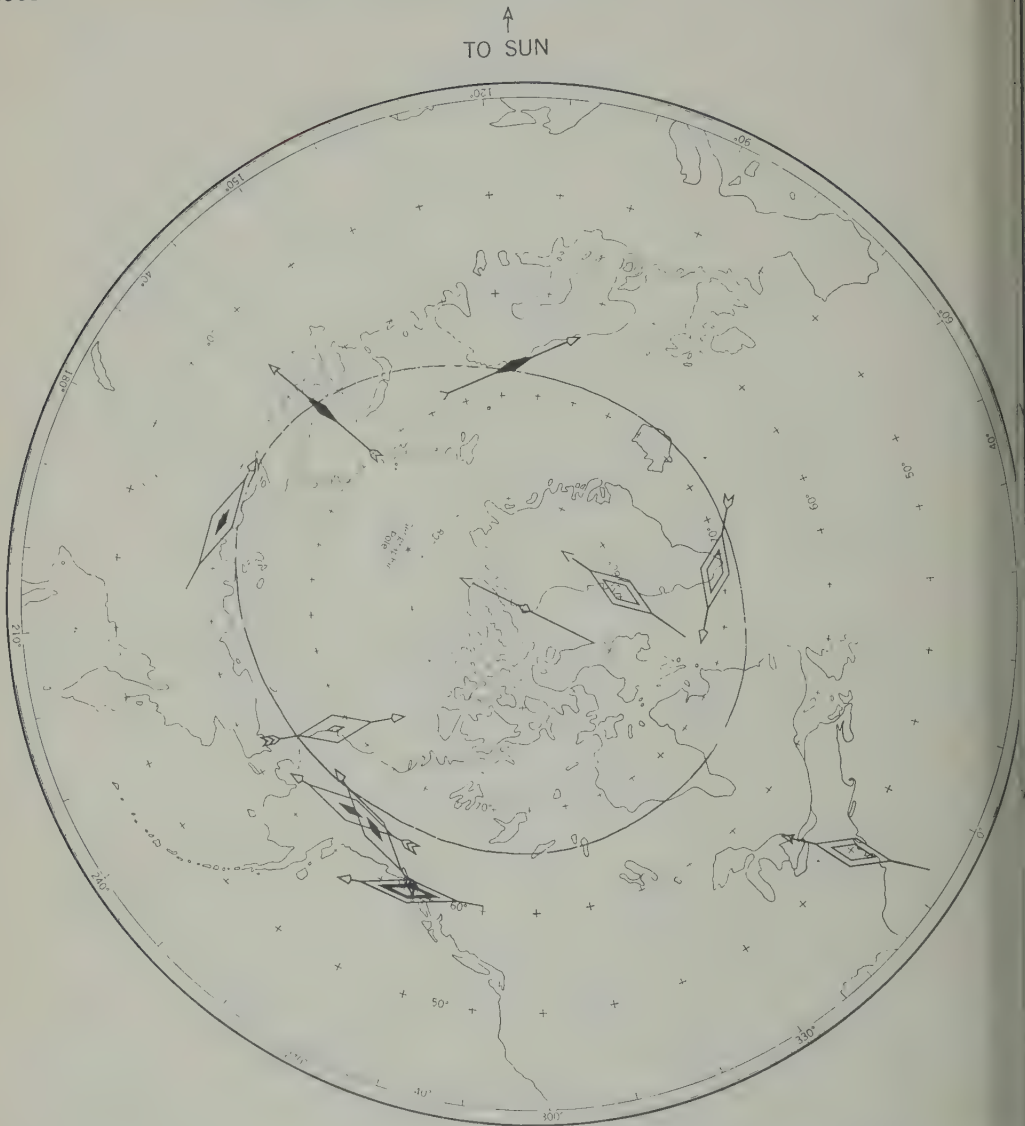
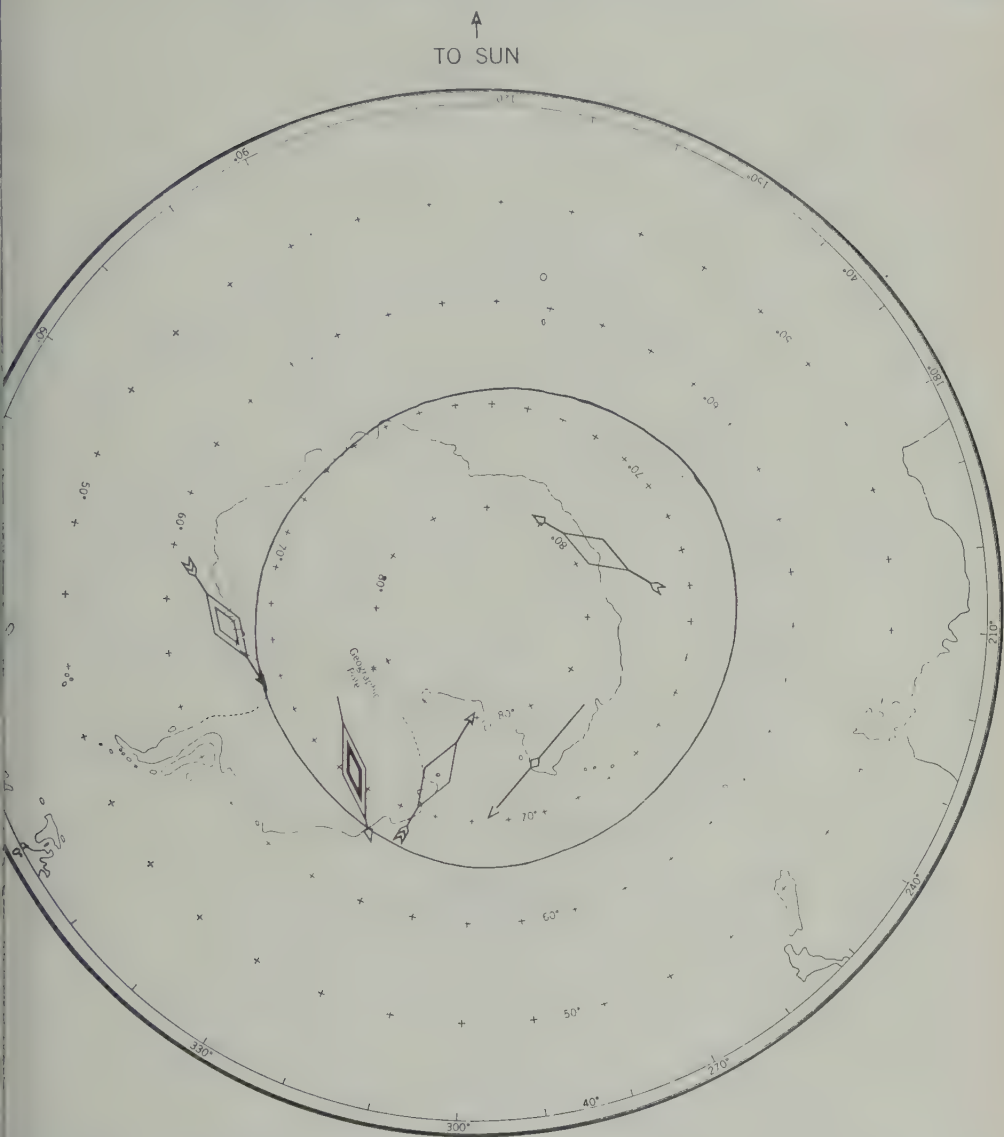


Fig. 11. Equivalent current vectors for a cusp

case, but the evidence is muddled by the presence of a Z component there, suggestive of a branch circuit to the north of Halley Bay. Wilkes is conformable to a conventional polar-cap current. Little America may have been under a mixed influence, and Cape Hallett showed too small an effect for fair evaluation.

We come next to Figure 12, obtained 6 hours after the beginning of the storm of June 30, 1957. This was a moderately severe one, ranking

not very much above the 1933 storm. Here again the dominance of the main cell is clear at the Alaskan stations. Sitka has practically no effect in this event, and Anchorage shows definite negative Z displacement, suggesting that the auroral electrojet passed almost directly over Sitka but a little to the north of Anchorage. Tromsø, situated well within the domain of the supposed afternoon cell, nevertheless appears to show the extension of the main predawn circle



September 13, 1957, centered at 0910 UT.

longitude. The antarctic stations are comparable with the conventional system; Halley and Little America show the main-cell effect (perhaps farther south than the red position) and Wilkes the polar-cap current.

Figure 13 we have a cusped bay registered at the same position shown in Figure 8 but about 10 hours later. The main cell is clearly dominant at most of the Alaskan stations, though Sitka is

rather weak and Barter Island still more so. The sign of the Z displacement still indicates that the auroral electrojet lies between Sitka and the interior Alaskan stations. None of the stations within the span of the supposed afternoon counterclockwise cell gives support to the occurrence of that feature. Leirvogur shows a quite strong effect indicative of westward flow. Julianehaab is rather anomalous as to direction, as are the other Greenland stations, supposedly

↑
TO SUN

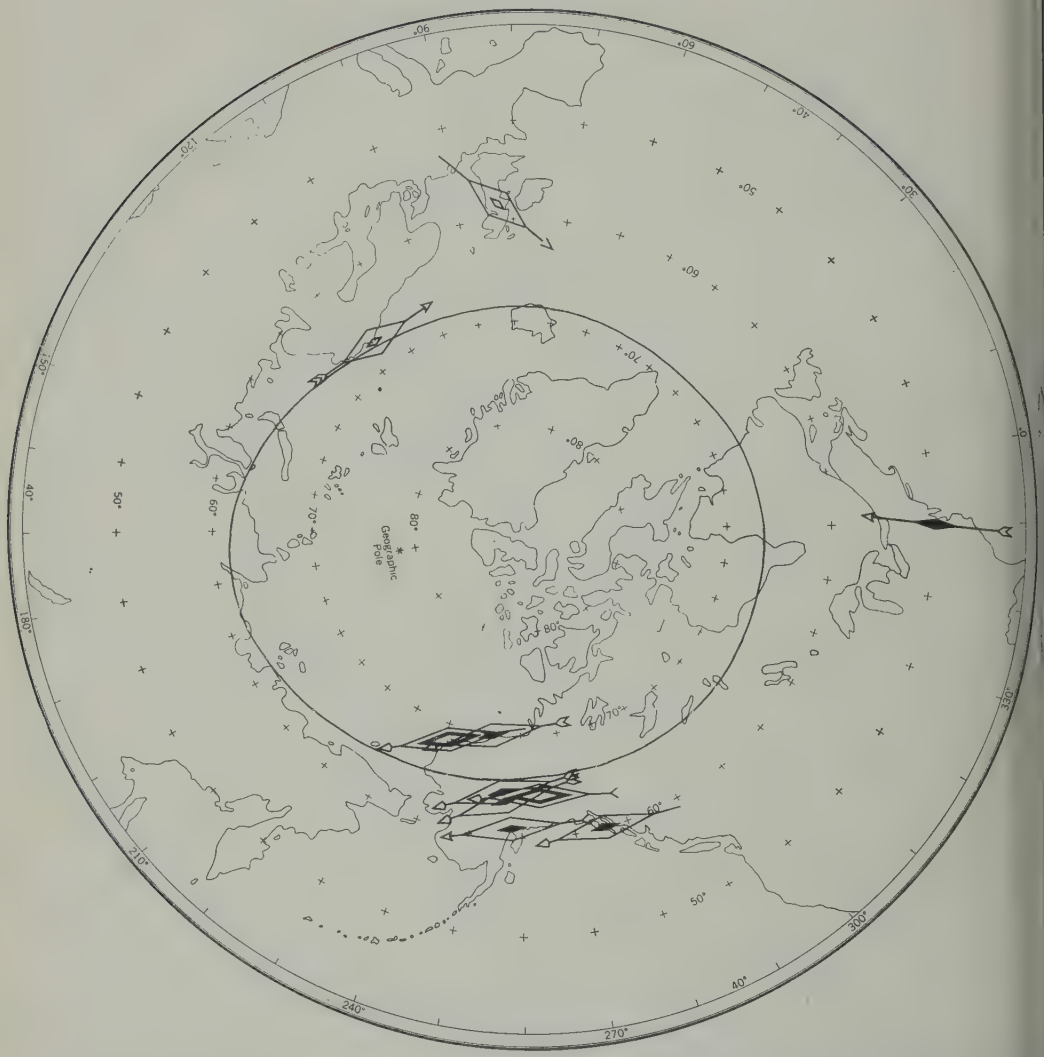
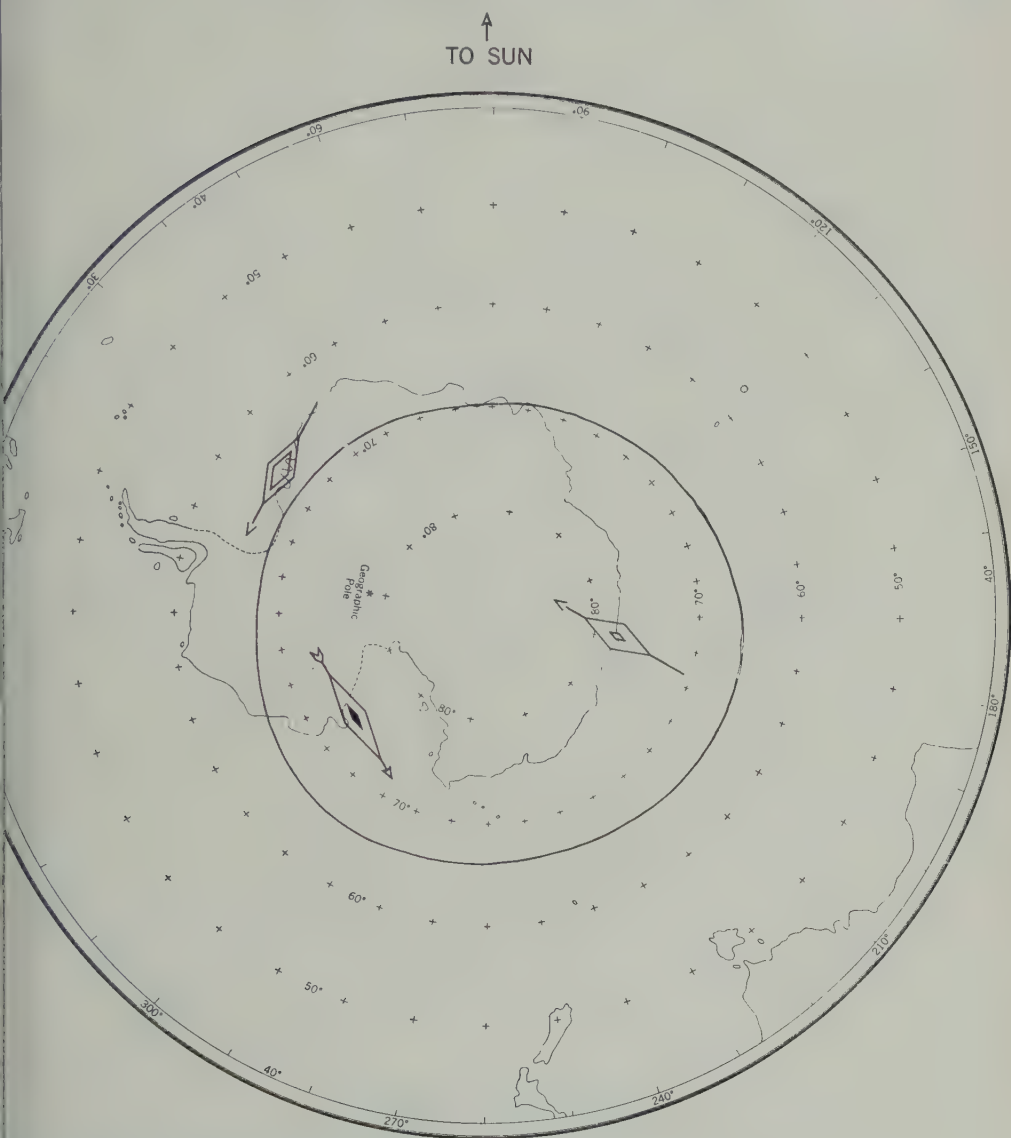


Fig. 12. Equivalent current vectors for a cusped

under the influence of the polar-cap system. Tromsø and Murmansk have rather small effects, but the direction of the indicated current is westward. The antarctic results are puzzling. The three larger vectors shown are all consonant with a substantial westward current. Byrd again shows a small Z effect as though the current were nearly overhead, while both Little America and Halley Bay have Z disturbances indicating the electrojet to be north of those stations. Wilkes is evidently in the polar-cap domain.

Figure 14 is included to show a somewhat different type of occurrence. This is a displacement during the initial phase of the storm of September 13, 1957, immediately following the sudden-commencement impulse. The main cell seems clear enough at Tromsø, Dikson Island, Leirvogur, Julianehaab, and Godhavn, with the Z disturbance suggesting a line current that was north of Leirvogur but south of all the other stations. Thule Village and Barrow seem to be registering the polar-cap effect, and the stations



on June 30, 1957, centered at 1143 UT.

mid- and southeast Alaska seem to support existence of an afternoon eastward current. In Antarctica, the main cell is rather sketchily at Halley Bay, while the other four stations to require a strongly developed polar-cap m.

Figure 15 shows another SC-linked world-wide placement. This one is taken from the storm February 11, 1958, by all odds the greatest recorded during the IGY and probably one of the six or eight all-time greatest. Here the

picture is indeed a puzzle. Tromsø has the usual westward flow indicative of the main cell, but Godhavn is anomalous. Barrow and Barter Island show a strong westward current flowing at a latitude north of both places (if the Z indication is trustworthy). Is this evidence for a counterclockwise afternoon cell with some striation or pinching of the polar-cap current? The peculiar vectors in middle and southern Alaska, though not so strong as the first two, would fit such an interpretation.

↑
TO SUN

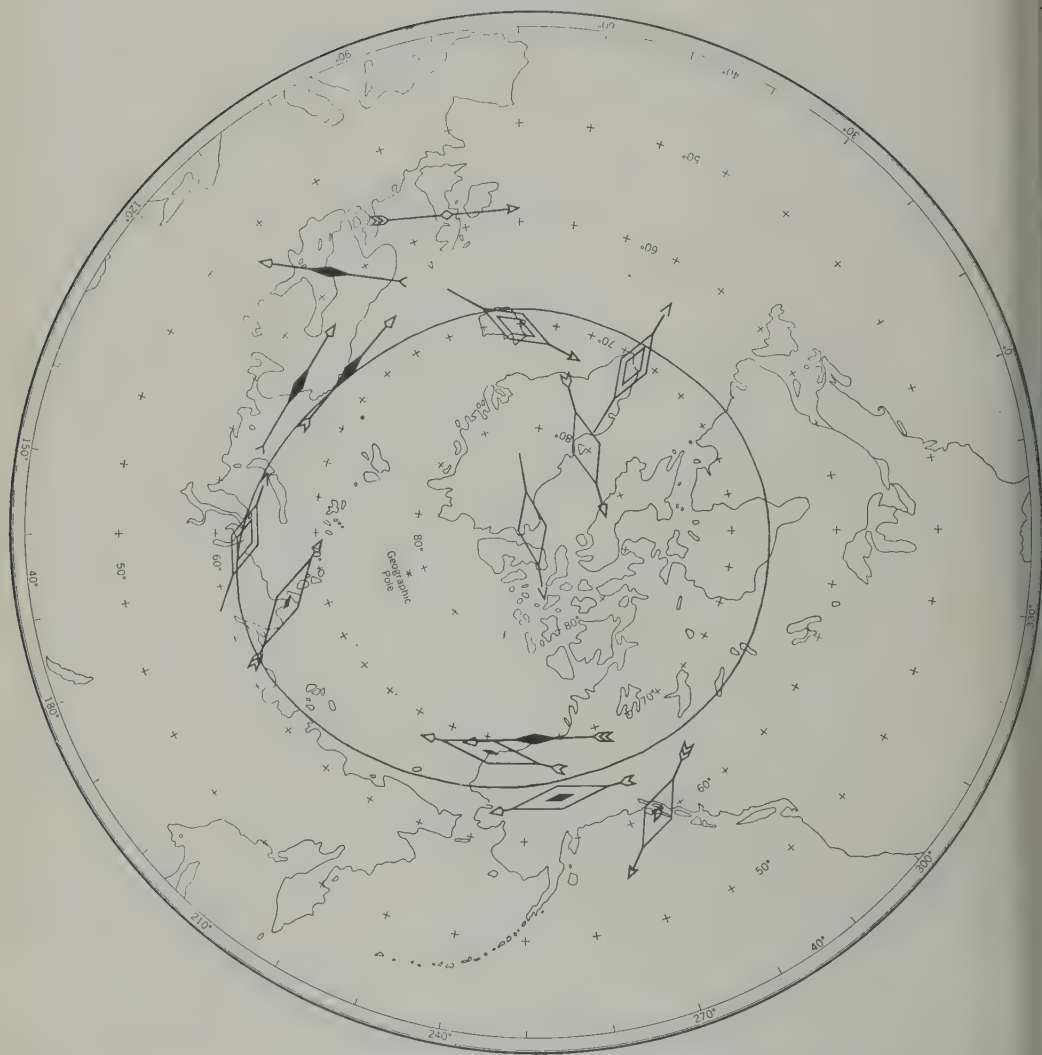
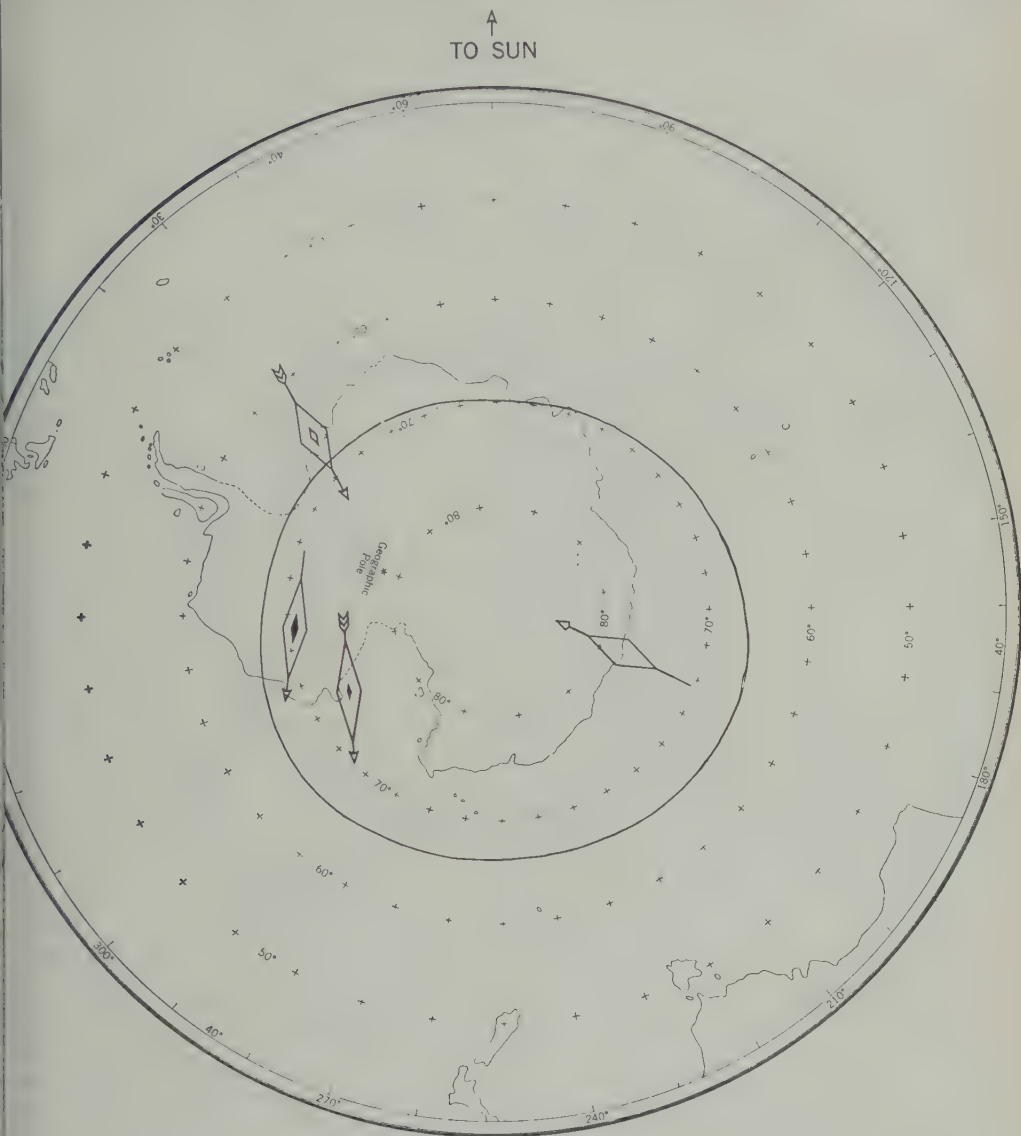


Fig. 13. Equivalent current vectors for a cusped bay on September 23.

The antarctic results too are unorthodox. A strong current at Halley Bay seems predominantly of the main-cell kind, but it is aimed considerably south of west, and it reappears at Byrd and Little America as though the auroral electrojet passed almost over those two places.

Conclusions. This study shows that the cusped bays, a striking feature of severe magnetic storms, are widespread events that may be observed simultaneously in the Arctic and the

Antarctic. It is clear that the effects are most strongly manifested in the neighborhood of the auroral zone and that they tend to fall into a pattern of strong westward current along the auroral zones. These resemblances to the major features of the more gradual storm fluctuations reflected in the hourly values seem to encourage some discussion of the detailed features observed and to warrant the tentative conclusion that the cusped bays and the hourly-value changes



, centered at 1149 UT. For Big Delta magnetogram see Figure 4.

represent modulations of one and the same current system.

In such an interpretation, the Z changes help pinpoint the latitude of the auroral electrojets; in particular, their equatorward shifting seems shown by the Alaskan stations on most of the occasions examined here—this despite the likelihood that induced ground currents play an important role in modifying the Z changes and the channeling of such currents by reason of

conductivity patterns will preclude simple interpretation of local gradients.

The polar-cap currents are not so clearly depicted as those along the auroral zones. In fact, it is the exception for polar-cap stations to concur in showing a more-or-less unidirectional sheet current in harmony with the conventional view. Sometimes there seem to be concentrations of current suggestive of striations or pinching of the return current or again of diversion or

↑
TO SUN

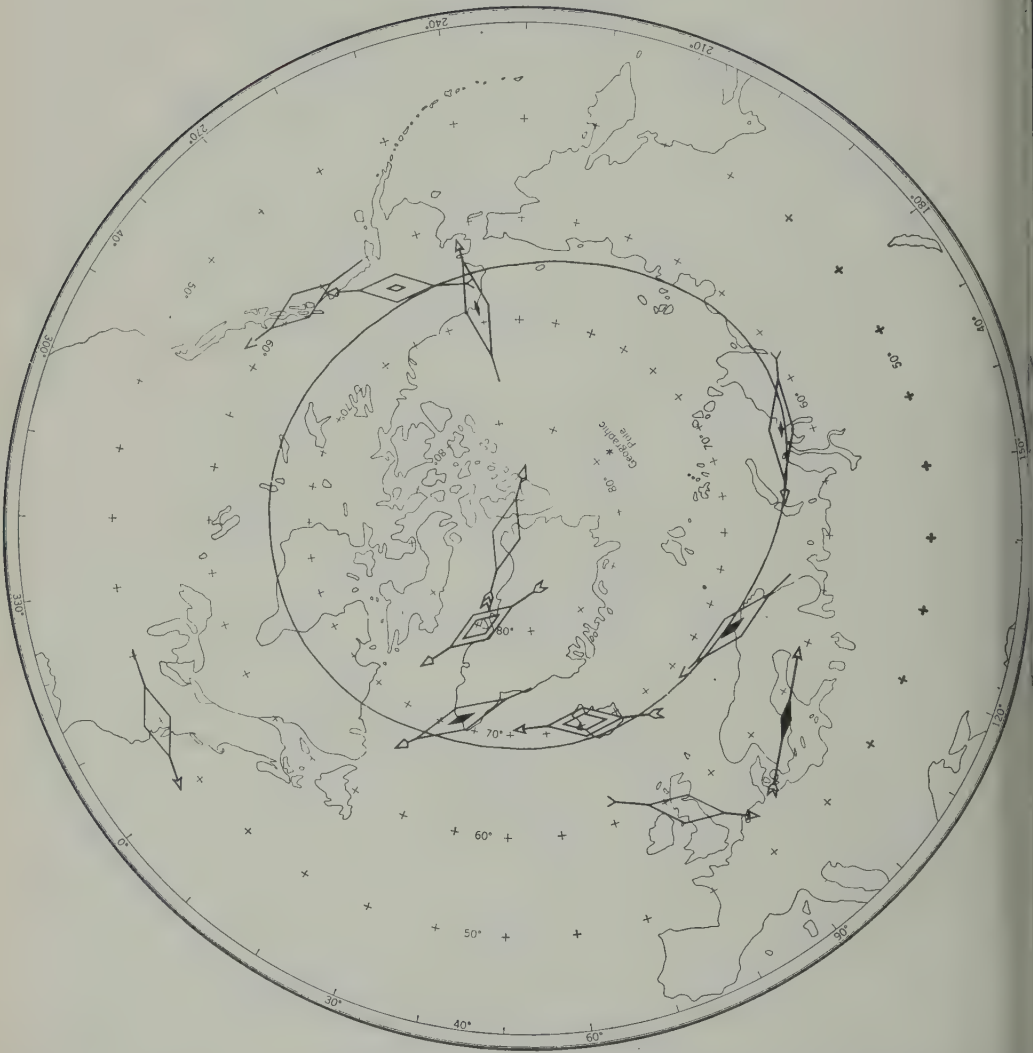
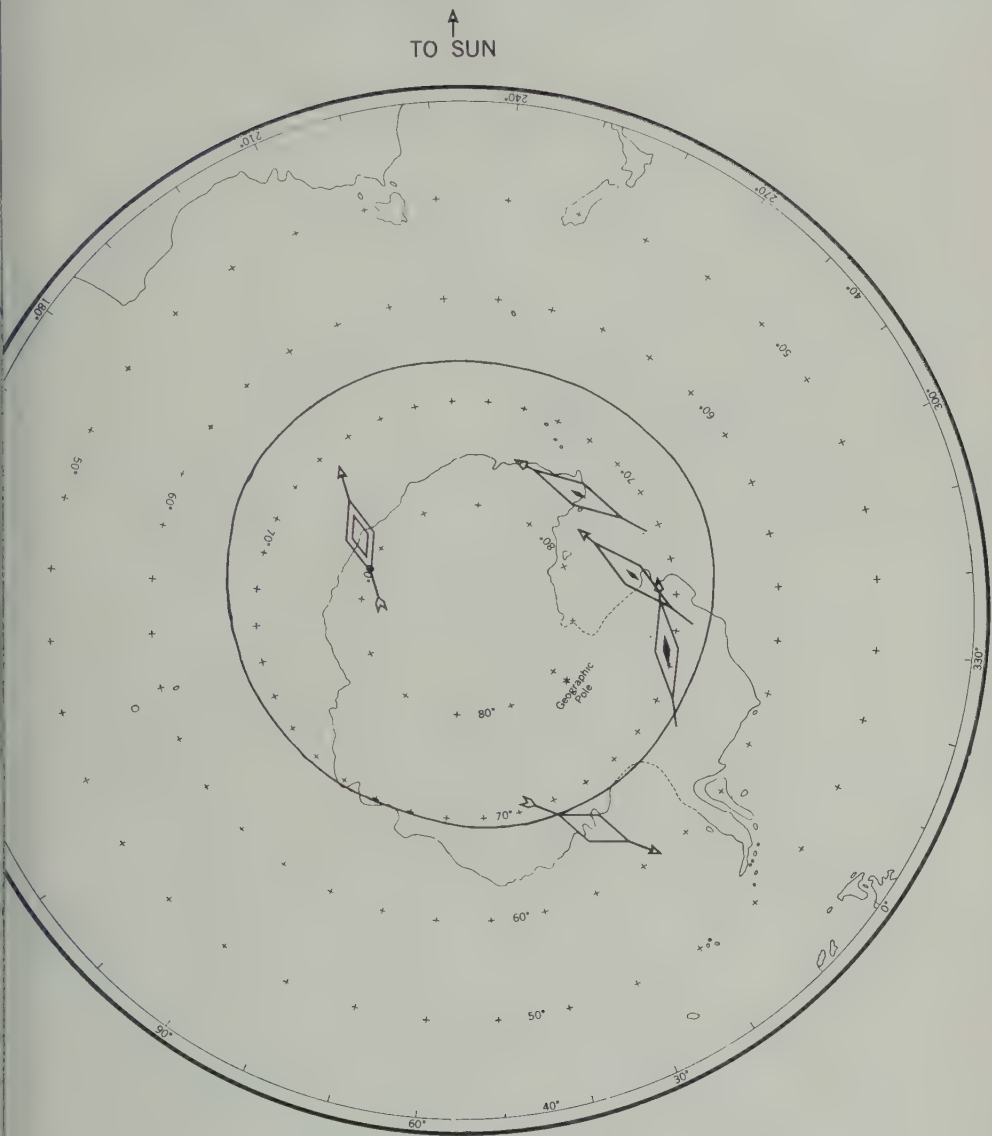


Fig. 14. Equivalent current vectors for an SCA

branching of the main auroral electrojet into the polar-cap area. The interpretation might be improved in the Antarctic by some revision of the adopted course of the auroral zone, but it is not likely that this would resolve many difficulties.

As to the existence of the midafternoon reverse cell, the evidence is negative except for the two events that were selected for times very near the onsets of storms. In the other cases,

the data for stations falling in the longitude zone where this eastward segment of the electrojet was to be expected show instead either a clear extension of the main westward segment or weak and inconclusive results. The interpretation of this outcome is not clear. The afternoon cell may be regarded as an artifact resulting from the superposition of separate S_D and D_{st} systems, and, if the relative magnitude of the two components is variable, the afternoon cell may be



September 13, 1957, centered at 0100 UT.

ned or extinguished as the storm progresses, and its occurrence may depend on the type of the storm.

In a general way, the patterns in the south may be expected to mirror those in the north, as implied in the discussions and in the chosen examples of Figures 7 to 15. Though a rough correspondence is obvious from the figures, the events studied do not seem to afford an adequate basis for examining this point in detail. In this

regard, a particular handicap is the paucity of stations along the segment of the antarctic coast where the auroral electrojet is dominant, between 60°W and 50°E geographic longitude, for example (or between 10° and 90° geomagnetic longitude).

Additional data from a few stations may still be forthcoming, and it may be that similar data could be assembled for other events occurring during the IGY and subsequently. Further study is also needed to compare the characteristics of

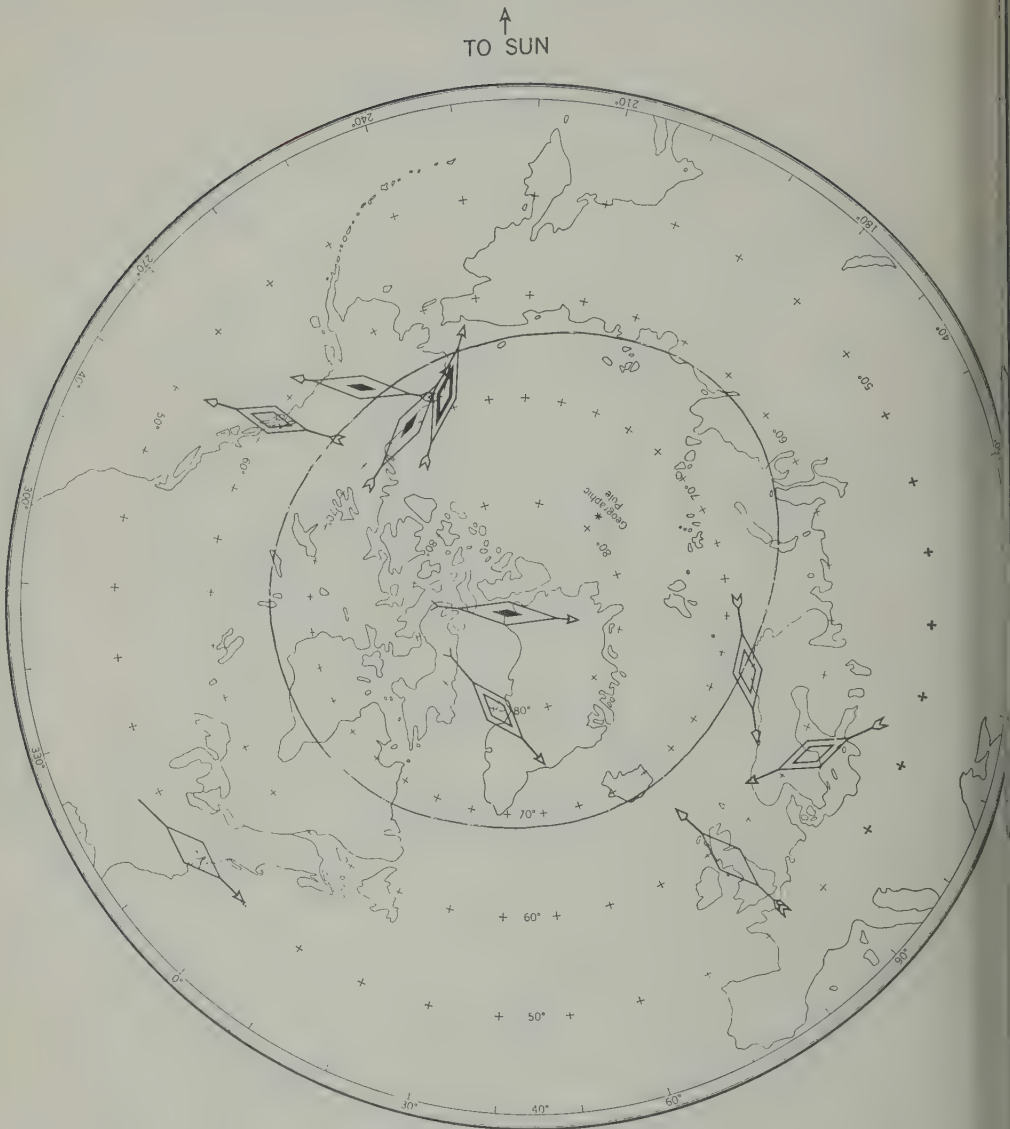
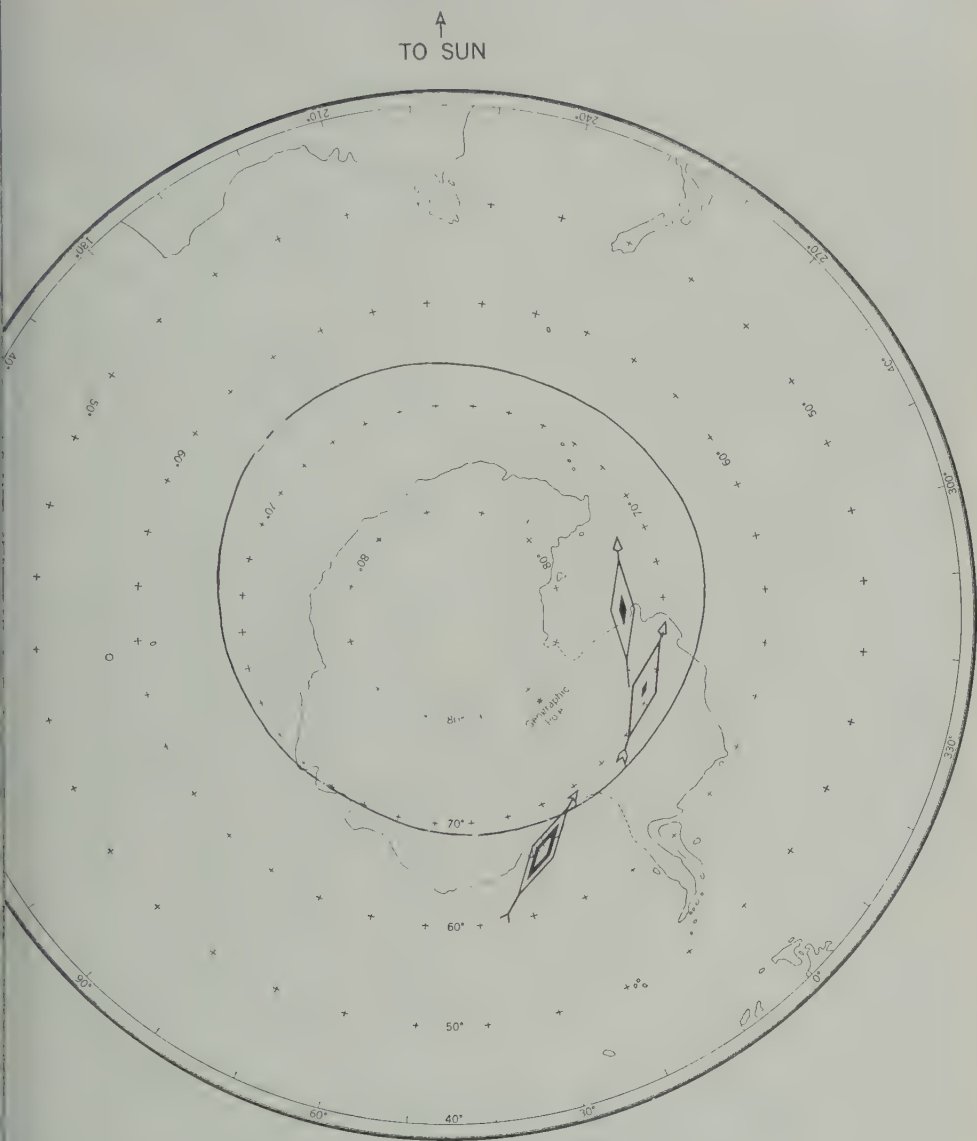


Fig. 15. Equivalent current vectors for auroral activity.

the cusped bays with those of the related but less violent 'polar elementary storms' discussed by Fukushima and other workers. It would be instructive to search also for coincident ionospheric and auroral events that might contribute further detail to the patterns here discussed.

Finally, we review some of the benefits to be sought through the continued study of cusped bays and related effects. When hourly values are used, they show a systematic progression, charac-

teristic of magnetic storms. This progression, of course, the basis of the recognized classification of the successive stages of storm development (initial phase, main phase, recovery phase). However, the progression is compounded by several effects, and in the present stage of understanding it is not at all certain that we can describe it satisfactorily. Three categories are usually adduced: (a) the storm-time change (which is usually considered to play the lead



February 11, 1958, centered at 0150 UT.

b) the disturbance-daily variation S_D , a new phenomenon; and (c) the irregular, fluctuations.

cannot evaluate S_D with any confidence for individual storm; and indeed we cannot know how the hourly values would have proceeded on the day in question had there been a storm. So the hourly values afford no clearly valid basis for separating the effects, much less deciding whether they correspond with

physically distinct aspects of the storm mechanism. The trouble is that the irregular fluctuations, though of course much attenuated in the hourly values, are typically so large as to produce serious disparities from hour to hour.

The cusped bays are a rather distinctive phenomenon of the third category. They can be evaluated and studied independently of the other storm effects. To the extent that the currents responsible for them seem to be geometrically

akin to those statistically invoked for slower changes, we may thus hope to combine information from the two kinds of data to improve our understanding of the current systems. On the other hand, there may be such significant differences that the cusped-bay patterns afford a relatively pure representation of a separate mechanism without the confusing admixture of the slower-moving effects. Every promising avenue for penetrating the obscurity surrounding magnetic storms needs to be fully explored, and the polar elementary storms and cusped bays seem to carry such a promise.

Acknowledgments. This study was conducted under grant 22-13/320 from the National Science Foundation, under the direction of James H. Nelson, Chief, Geomagnetism Branch, United States Coast and Geodetic Survey. Its progress was facilitated through planning sessions with E. O. Hulburt, E. H. Vestine, A. G. McNish, and S. E. Forbush, and the interpretation has benefited from helpful discussions with L. R. Alldredge and L. Hurwitz. The generous cooperation of the Directors of the many observatories from which data were used, and of the IGY World Data Centers, is gladly acknowledged. The preparation of the base maps described in Appendix 2 involved the programming by R. H. Gunst of the machine computation of geomagnetic coordinates and special drafting work ably executed by D. N. Forehand. Valuable assistance in examining the records, scaling the displacements, and computing the corresponding vectors has been rendered by E. B. Fabiano.

APPENDIX 1. A Catalog of Magnetic Disturbances Recorded during the IGY

Table 1 of this appendix is a catalog of 86 IGY disturbances, including (but not limited to) all those reported as having sudden commencements at two or more observatories. All times are expressed in UT. The last four columns contain evaluations of the severity of the storms, derived in four different ways. A_p' is the 'amplitude' in two-gamma units, corresponding to A_p as defined by Bartels and Veldkamp [1954], but instead of referring to a Greenwich day it refers to a continuous 24-hour interval satisfying stipulations that make it dependent on the time of incidence of the disturbance. These stipulations are: (a) the eight 3-hour intervals are K intervals (that is, the entire sequence begins and ends at a multiple of 3h, UT); (b) the first 3-hour interval includes part of the storm (not necessarily the initial part); (c) the largest value of K_p is definitely associated with the storm whose limits

are tabulated, rather than with a later one; (d) the selection is such as to yield the highest possible amplitude consistent with (a), (b), and (c). Where (b) and (c) are incompatible, (c) takes precedence over (b). The purpose of this departure from standard A_p was to insure that all the disturbances would be judged on the same basis whether their onset took place early or late in the Greenwich day.

It should be recognized that K_p and measures derived from it find their highest refinement in statistical measures rather than for close examination of individual 3-hour intervals. Consequently, the usefulness of A_p' as defined above is rather limited when it comes to evaluation and comparing individual storms. This is particularly pertinent near the upper limit of 9°, where the amount of information used to determine A_p' is so much smaller than that contained in the magnetograms that two storms having closely similar distributions of high K values may differ substantially in their actual severity. Furthermore, the inclusion of several lower ranking intervals to make up a 24-hour sequence may result in assigning higher rank to a protracted but moderate storm than to a brief but more violent one. This last is a very real drawback, since it is well known that the most violent storms tend to go through their phases more rapidly than others.

Another column of Table 1 shows A_p'' , which is derived from K_p in the same way as A_p' except that it is based on a 12-hour sequence. Still another contains ΔH_{Tu} , the Tucson H range (omitted for about 30 of the lesser disturbances). As a further aid in categorizing the stronger storms, the distribution of K_p for each storm was examined with reference to a working table arranged as in the following specimen entry:

Storm										
No.	Date	K_p	1	2	3	4	5	6	7	8
3	July 2, 1957	For A_p'' For A_p'						-	-	+
			+		-	+		-		

To assess the relative activity of the IGY storms as compared with notable storms of the past, we compiled another list (Table 2) containing 34 storms. This list was intended to cover all the very great storms that had occurred before the beginning of IGY. It also contains three less violent storms that are of special

TABLE 1. Magnetic Disturbance during the IGY

Date 1957	Begin h m	Date 1957	End h	A_p'	A_p''	$H_{Tu},$ γ	Category
Jun 30	5 28	Jul 1	10	182	214	333	4
Jul 1	17 47	1	22	33	56	90	2
2	8 57	3	15	67	98	117	3
3	1 50	3	15				
4	23 42	5	13	43	107	162	3
5	0 42	6	2				
16	7 14	17	1	18	22		1
19	13 44			22	33		2
22	4 19	23	6	31	38		2
27	19 59			12	16		1
Aug 3	15 57	Aug 4	12	32	58	146	2
6	5 08	6	24	37	37		2
9	13 47			16	18		1
12	13	13	13	33	47	111	2
13	6 17						
21	2 48	21	8	16	27		1
29	19 20	30	12	60	92	168	3
31	18 12	Sep 1	15	49	79	139	3
Sep 2	3 14	4	6	165	189	256	4
4	13 00	7	5	222	293	391	4
6	11 21	6	20				
12	21 54						
13	0 46	15	6	160	254	471	5
21	10 05	22	7	101	106	275	3
22	13 45	25	15	186	238	262	4
23	2 35						
29	0 16	Oct 1	5	152	238	288	4
Oct 14	4 40	15	1	51	60	120	2
21	22 41	23	2	30	45	105	2
Nov 3	6 21	Nov 3	22	11	17		1
6	18 21	7	12	49	81	203	3
24	9 01			33	34		2
26	1 55	29	8	79	103	159	3
26	14 54						
Dec 1	3 36	Dec 3	20	25	49	76	2
5	3 31	5	22	31	32		2
15	0 48	18	12	22	31		2
19	9 37	20	3	24	29		1
28	22 29	Jan 2	13				
30	4 10	Dec 30	21	66	77	140	3
31	5 14	Jan 2	14				
Jan 20	21 43	Jan 24	1	40	64	122	2
25	10 50	26	10	24	26		1
Feb 4	13 04	Feb 9	9	33	35		2
5	5 28						
11	1 25	13	15	199	293	546	6
	1 59						
16	16 42	23	21	31	33	127	2
28	13 11	Mar 1	4	11	22		1
Mar 3	9 31	8	15	48	52	111	2
5	5 37						
11	18	13	24	70	104	126	3
14	12 12	16	5	31	33		2
17	7 50	17	21	29	35	86	2
18	2 01	22	5	49	57	91	2
25	15 40	27	2	31	38		2
31	4 21	Apr 1	12	36	49		2
Apr 2	4 59	3	15	36	46	69	2
4	6	7	13	43	57	95	2

TABLE 1. Continued

No.	Date 1957	Begin h m	Date 1957	End h	A_p'	A_p''	H_{T_u} γ	Catego
47	14	9 12	20	10	54	65	117	3
	16	7 45						
48	26	12 47	27	3	14	21		1
49	27	17 28	May 2	9	38	40		2
	29	5 24						
50	May 6	20 10			9	11		1
51	8	20 41	12	1	20	26		1
52	12	12	16	2	42	54	138	2
	13	14						
53	17	9 16	19	9	19	22		1
54	20	23 11	21	7	7	10		1
55	25	15 31	28	9	38	56	115	2
56	29	0 36	30	9	53	64	90	3
57	31	16 52	Jun 2	21	63	165	189	3
58	Jun 7	0 46	8	1	77	134	177	3
59	8	17 28	13	6	38	51	115	2
60	14	18 28	15	11	31	37		2
	15	5 09						
61	21	2 06	25	15	74	94	124	3
	23	22 09						
62	28	7 13	29	24	136	163	245	3
		17 42						
63	30	4 02	Jul 1		17	24		1
64	Jul 7	7 41	Jul 8	7	18	26		1
65	8	7 48	10	15	216	309	503	5
65a	18	2 21	21	10	34	44	103	2
66	21	16 36	22	17	60	98	113	3
67	27	3	28	6	30	35		2
67a	31	15 29	Aug 2	1	20	23		1
68	Aug 17	6 23	18	15	91	133	255	3
69	22	2 27	22	13	34	56	127	2
70	24	1 40	25	15	92	145	212	3
71	26	9 42	27	23	64	88		3
	27	3 02			61	133	147	3
72	Sep 3	8 42	Sep 5	24	171	232	377	4
	4	13 39						
73	16	9 30	17	5	38	52	109	2
74	25	4 08	27	5	86	100	195	3
75	30	9 39	Oct 1	15	25	33		1
76	Oct 22	3 15	25	2	89	112	228	3
	24	7 31	25	6				
77	27	15 22			48	50	129	2
	28	6 50	29	1				
78	Nov 28	1 09	Nov 28	21	19	26		1
79	Dec 4	0 35	Dec 5	12	70	95	200	3
80	13	0 02	14	12	50	63	141	3
81	15	20 22	16	16	18	23		1
82	17	15 46	18	15	53	93	153	3
	17	18 17						

Explanation of Categories of Disturbance

No.	Description	Low-Latitude Range, γ
6	Extremely severe	>500
5	Very severe	400-500
4	Severe	300-400
3	Active	150-300
2	Moderate	70-150
1	Mild	30-70

TABLE 2. Notable Magnetic Storms prior to the IGY

Date	ΔH		A_p''	A_k'' Pots- dam	Cate- gory	Notes
	Abinger	Tucson*				
Sep 24	950				5	a
Sep 24	1100				5	a
Oct 23	1900				6	a
Nov 17	>550				4	a
Sep 2	>>625				6	abcd
Oct 25	1150				5	c
Feb 4	800				5	abcd
Apr 17	>455	477			5	
Nov 17	>1090	445			5	abd
Aug 12	540	403		118	4	
Jul 20	690	525		<333	5	
Aug 20	445	607		170	4	
Oct 31	1175	819		360	6	abd
Sep 25	1710			335	6	abcd
Aug 15	370	158		89	3	d
Aug 11	360	538		270	5	d
Mar 22	730	569		230	5	d
May 13	>>740	>488		360	6	abcd
Jul 8	>540	560		360	6	cd
May 1	215	218	150		3	
Jan 25	1055	443	232		5	a
Apr 16	1375	>819	230		5	abd
Mar 24	1370	>869	334		6	ad
Mar 29	640	318	252		5	
Mar 1	1650	>550	302		6	a
Jul 5	945	393	325		5	
Sep 18	1250	527	325		6	acd
Mar 28	1660	>550	284		6	a
Jul 26	925	495	302		5	
Sep 21	925	425	279		5	a
Jan 24	595	402	185		5	
Aug 18	305	325	215		4	c
Feb 25			153		3	
Jan 21		329	206		4	c

es [1955].

pman and Bartels [1940].

able aurora in low latitudes.

y and Howe [1945].

ges prior to 1917 from Bombay.

t. These storms occurred in 1918, 1933, 1956. The first was included among the 13 on the list by Ludy and Howe [1945], s because of a high Z range at Honolulu, gh according to the criteria used in the t study it was decidedly inferior to many that were not on the Ludy-Howe list. 1933 storm has the distinction of being ly the most exhaustively studied of all

magnetic storms, chiefly because it occurred during the Second International Polar Year and was therefore recorded much more extensively than any of the other storms listed in Table 2. The 1956 storm was the occasion of an unprecedented and extraordinary change in cosmic-ray intensity and is hence of special interest in cosmic-ray research. These three storms are, of course, only a small sample of the hundreds of

TABLE 3. Geomagnetic Coordinates of the Stations

Station	Lat.	Long.	Source	Station	Lat.	Long.	Source
Arctic							
Goose Bay	64.6	12.1	c	Resolute	83.0	289.6	b
Godhavn	79.9	32.5	b	Yellowknife	69.0	293.3	b, c
Julianehaab	70.8	35.6	b	Meanook	61.8	301.0	b, c
Leirvogur	70.2	71.0	b, c	Ennadai	70.1	311.1	c
Kap Tobin	75.6	81.8	b, c	Baker Lake	73.8	315.2	b
Eskdalemuir	58.4	82.8	c	Churchill	68.6	322.6	b
Lerwick	62.5	88.6	a, c	Alert	85.6	168.5	c
Dombås	62.3	100.1	a, c	Fredericksburg	49.6	349.9	c
Lovö	58.2	105.8	c	Thule Village	89.0	357.8	b, c
Nurmijärvi	57.9	112.6	a, c	Antarctic			
Abisko	66.1	115.0	c	Amundsen-Scott	78.5	0.0	c, d
Kiruna	65.3	115.9	c	San Martin	55.9	0.5	c
Tromsø	67.2	116.8	c	Argentine Is.	53.8	3.3	c
Sodankylä	63.7	120.0	c	Orcadas del Sur	50.1	18.2	c
Ivalo	64.6	121.9	c	Halley Bay	65.8	24.3	a, c
Bjørnøya	71.1	124.0	c	Norway Station	63.8	43.9	c
Murmansk	64.1	126.5	c	Roi Baudouin	67.9	62.0	c
Lovozero	62.8	127.3	b	Syowa Base	69.7	77.4	c
Murchison Bay	75.2	137.2	c	Vostok	89.2	92.6	b
Tikhaya Bay	70.9	156.5	b	Mawson	73.1	103.0	c
Dikson Island	63.0	161.5	a, c	Kerguelen	57.2	128.0	c
Chelyuskin	66.2	176.4	c	Mirny	77.0	146.8	b
Tiksi	60.1	191.1	b	Pionerskaya	80.3	146.6	b
Srednikan	53.2	210.5	c	Oasis	77.6	160.3	b
Uelen	61.8	237.0	a, c	Wilkes	77.8	179.1	d
Barrow	68.6	241.2	d	Toolangi	46.7	220.9	c
Kotzebue	63.6	242.3	d	Charcot	78.3	234.5	b, c
Barter Island	70.0	253.1	d	Dumont d'Urville	75.5	230.9	b, c
College	64.6	256.5	d	Macquarie I.	61.1	243.1	a, c
Healy	63.6	256.6	d	Amberley	47.6	252.6	c
Fort Yukon	66.6	256.8	d	Cape Hallett	74.7	278.2	d
Anchorage	60.9	258.1	d	Scott Base	79.0	294.4	a, c
Big Delta	64.3	259.3	d	Little America	74.0	312.1	d
Northway	64.1	263.8	d	Byrd Station	70.6	336.0	c, d
Sitka	60.0	275.4	d				

^a International Association [1957].

^b International Association [1959].

^c Nicolet and Doyen [1959].

^d Values derived from USC&GS mss. files, or from publications of observatory results in the press.

'ordinary' magnetic storms which would have been contained in Table 2 had the criteria for inclusion been similar to those used in Table 1.

Table 2 contains Abinger (or Greenwich) H ranges as well as those for Tucson (or Bombay). It also contains A_k'' for Potsdam, based on K indices reported by Bartels [1949] and by Fanslau and Thiele [1955], as a rough equivalent to A_p'' for storms recorded in the interval 1891-1932.

Finally, in both Tables 1 and 2, each disturbance has been assigned to one of six categories according to its relative severity. This classification takes into account all the measures thus far discussed, but it is chiefly determined by an independent comparison of H ranges at several widely dispersed places, special emphasis being given to low-latitude observatories. The assignment is necessarily somewhat subjective and

nal with respect to Table 2, particularly the lower portions, for which records are sparse. Nevertheless, it is our belief that this classification has real significance distinct from either of the amplitude measures A_p' and A_p'' . It is less than they by the drawbacks mentioned. There are admittedly two weaknesses in the use of over-all ranges for ranking storms. The method favors those storms in which the in-phase progression is slow enough to provide an opportunity for several bay-type disturbances to be registered during the low part of the trough. The other problem is that the range for a two-part disturbance will be less than that for either part taken separately, so that the ranking will depend on whether the event is regarded as two storms or one. Disturbances 41 and 42 have jointly a range of 142 γ , though the separate ranges were 86 and 91 γ . Such a difficulty is not encountered.

It appears that most of those disturbances for which A_p'' is less than 50 (or low-latitude ranges less than 100 γ) are too mild to be classed as magnetic storms. This would mean that about a half of the 'category 2' disturbances are entitled to be called magnetic storms, as of course are those in categories 3 and above.

It will be seen that the top-ranking category 6 includes only one IGY storm, and category 5 includes two. None of the IGY storms can match the intensity of those of March and September 1941 and May 1921, notwithstanding the fact that the IGY interval brackets a record-breaking incidence of solar and magnetic activity. There were at least nine IGY storms definitely more severe than the 1933 storm, the one that has recently been the basis of much of our detailed knowledge of the subject.

Added in proof. M. Sugiura and S. Kamekura have made a valuable list of 346 geomagnetic commencement storms for the years 1900 to 1945 as material for describing the general morphology of such storms (Abh. Akad. Wiss. Göttingen, Sonderheft 4, 53 pp., 1960). This list avowedly emphasizes abruptly beginning storms and rejects or subordinates other disturbances, such as the epochal storms of 1859, 1903, May 13, 1921, and March 24, 1933. These three certainly had gradual onsets, but each included at least one clear SSC according to present norms. Until rather recently,

recognition of SSC's occurring after the beginnings of storms has been sporadic.

APPENDIX 2. Azimuthal Maps for Geomagnetic Applications

The two base maps used for Figures 2, 5, and 7 to 15 are considered to embody an optimum choice for this application, as to projection and amount of detail. They are drawn on the azimuthal equal-area projection, each of them being centered on one of the geomagnetic poles. The chosen positions of the poles, at 78.5°N and 69.0°W, and at 78.5°S and 111.0°E, are in accordance with the conventional scheme of geomagnetic coordinates in relation to a centered-dipole approximation to the earth's main field. The shore lines correspond approximately with those shown on similar maps introduced by Fukushima [1953], but in order to depict with maximum clarity the auroral region and the subauroral belts we set the limit of each map at geomagnetic latitude $\pm 40^\circ$, thereby excluding most of the minauroral belt [Chapman, 1957].

As a further aid to legibility, the geomagnetic graticule is reduced to intersection marks only. The meridians of this graticule consist of uniformly spaced rays, and the parallels are concentric circles with radii given (for the arctic version) by

$$s = k \sin \frac{1}{2}(90^\circ - \Phi) \quad (1)$$

where Φ is the geomagnetic latitude of a given parallel and k is the radius of the implied bounding circle for geomagnetic latitude -90° . (The equation for the antarctic version is the same except that the negative sign is changed to positive.)

The choice of this projection was influenced by the circumstance that the phenomena of greatest interest occur in the higher latitudes. For all the well-known azimuthal projections except the orthographic, the tangential scale becomes larger in the margins than near the pole of projection. When we impose the equal-area condition, the increasing tangential scale must be offset by a diminishing radial scale; hence the parallels become closer together in lower latitudes. This means that the low-latitude zones are not magnified at the expense of the zones of the circumpolar region, as they otherwise would be. This magnifying effect, which is present in the equidistant projection with its uniformly spaced

parallels, is more noticeable in the stereographic with its spacing of parallels increasing in lower latitudes and reaches an extreme in the gnomonic. The orthographic is at the other extreme; it has a uniform tangential scale, but along the meridians there is a consequent compression that produces severe marginal distortion.

The fact that the construction of the maps begins with a geomagnetic graticule permits a simplified empirical procedure for superimposing the geographic graticule as in Figure 5. First we compute the geomagnetic coordinates of a network of intersection points corresponding to the proposed geographic meridians and parallels. These intersection points are then located by their geomagnetic coordinates and connected by curves smoothed by ordinary drafting techniques. The geomagnetic coordinates of the intersection points were computed with an IBM model 650 digital computer, for a total of 2520 intersections, covering the earth at a spacing of 5° in latitude and longitude, each result being computed to 0.01° . (The formulas are well known and need not be repeated here.) Extant tables of these coordinates were examined [Vestine, Laporte, Lange, Cooper, and Hendrix, 1947], but the number of significant figures given did not fully satisfy present requirements. In addition to geomagnetic latitude and longitude, the 'geomagnetic declination' was also computed, although not needed for the maps; this is defined as the angle between the geomagnetic and the geographic meridians at a point. (The resulting tabulations have been preserved as machine listings, and microfilm copies can be supplied to interested readers at a nominal cost.)

The projection used is not a conformal one. This means that in plotting vectors there may be significant angular distortion. It turns out that a line on the earth with geomagnetic azimuth α at a given point would be depicted on the map by a line having an apparent azimuth α_1 given by

$$\cot \alpha_1 = \cos^2 0.5(90^\circ - \Phi) \cot \alpha \quad (2)$$

An alternative form expressing the same relation is

$$\tan(\alpha_1 - \alpha) = \frac{\tan \alpha \sin^2 0.5(90^\circ - \Phi)}{\tan^2 \alpha + \cos^2 0.5(90^\circ - \Phi)} \quad (3)$$

Since most of the stations are near the aurozone, the values of Φ are large enough so that this azimuth error is nearly always less than 1° . No correction has been allowed in Figures 7 to 9.

For a map centered on the geomagnetic pole but prepared on a different azimuthal projection see Pollak [1938].

APPENDIX 3. Geomagnetic Coordinates of the Stations

In order to place the vector symbols in the correct locations on the maps (Figs. 7-15) it was decided to use geomagnetic coordinates conforming of course to the appropriate reference axis, as defined in Appendix 2. Table 3 shows the values used, encompassing all those observatories and temporary IGY stations that were regarded as potential sources of data for this study. Those listed are marked with symbols on Figure 5, as already explained.

Many of the stations could not be used for a study of this kind because their equipment did not include a storm magnetograph; the records from instruments of normal sensitivity were usually too confused to be useful during the severe disturbances under study. In other cases the registrations either were lacking for the time in question or were not available in time to be used.

REFERENCES

- Bartels, J., Three-hour range indices, K , for Potsdam-Seddin-Niemegk, 1900-1936, *Intern. Assoc. Geomag. Aeronomy, Bull.* 12b, 82-96, 1949.
- Bartels, J., and J. Veldkamp, International data on magnetic disturbances, first quarter, 1954, *J. Geophys. Research*, 59, 423-427, 1954.
- Chapman, S., The electric current system of magnetic storms, *J. Geophys. Research*, 40, 1935. (See especially Figures 14-15, p. 369.)
- Chapman, S., Visual auroral observations, *Ann. Intern. Geophys. Yr.*, 4, 41-103, 1957.
- Chapman, S., and J. Bartels, *Geomagnetism*, Oxford University Press, London, 2 vols. (esp. p. 328) 1940.
- Fanslau, G., and E. Thiele, *Geomagnetischen Kennziffern 1890 bis 1907 (nebst einigen Ergänzungen)*, *Geomag. Inst., Potsdam-Niemegk, Abh.* 17, 1955.
- Fukushima, N., Polar magnetic storms and geomagnetic bays, *J. Fac. Sci. Univ. Tokyo, sect. II*, 8, 293-412, 1953. (See especially Figure 12 on p. 353, which was the basis of Figure 2 of the present paper, along with a version by Vestine [1959].)

- vist, B., Auroral isochasms, *Nature*, 188, 3-1479, 1959.
- ational Association of Geomagnetism and onomy, Committee on Observatories, *Description des observatoires géomagnétiques*, Brussels, 1957; and Washington, v. 3, 1959.
- H. Spencer, *Sunspot and Geomagnetic-Storm Data Derived from Greenwich Observations 1874-1944*, Royal Greenwich Observatory, H. M. Stationery Office, London, 106 pp., 1955.
- A. K., and H. H. Howe, *Magnetism of the Earth*, U. S. Coast Geod. Survey Serial 663, Washington, 79 pp. (esp. p. 30), 1945.
- et, M., and P. Doyen, eds., Geographical distribution of the International Geophysical Survey stations, *Ann. Intern. Geophys. Yr.*, 8, 1959 (esp. pp. 155-168).
- k, M. J., The construction of an azimuthal distant map centered about the geomagnetic north pole, *J. Geophys. Research*, 43, 473-475, 1938.
- Vestine, E. H., The disturbance field of magnetic storms, *Intern. Assoc. Geomag. Aeronomy, Bull.* 11, 360-381, 1940.
- Vestine, E. H., The geographic incidence of aurora and magnetic disturbance, northern hemisphere, *J. Geophys. Research*, 49, 77-102, 1944.
- Vestine, E. H., Magnetic storms, *Science*, 130, 897-901, 1959.
- Vestine, E. H., and E. J. Snyder, The geographic incidence of aurora and magnetic disturbance, southern hemisphere, *J. Geophys. Research*, 50, 105-124, 1945.
- Vestine, E. H., L. Laporte, I. Lange, C. Cooper, and W. C. Hendrix, Description of the earth's main magnetic field and its secular change 1905-1945, *Carnegie Inst. Wash. Publ.* 578, 1947.

(Manuscript received February 13, 1961;
revised April 17, 1961.)



Some Studies of Geomagnetic Micropulsations

R. A. DUNCAN¹

*Upper Atmosphere Section
Commonwealth Scientific and Industrial Research Organization
Camden, N.S.W., Australia*

Abstract. Oscillations of the geomagnetic field with periods between 1 second and a few minutes have been studied by means of large ground loops at Hobart, Adelaide, Camden, and Townsville, Australia. Records have been made both on charts and on slowly moving magnetic tape; the tape recordings have been analyzed for frequency components on a 'Sonagraph' sound spectroscope. The period of the continuous oscillations known as *Pc*'s shows a diurnal variation and a marked dependence on latitude, shorter periods occurring at lower latitudes. The damped trains of oscillations, occurring predominantly around local midnight, known as *st*'s are followed by magnetic bays with an average delay of about 15 minutes. During storms, 'sweepers'—oscillations with a progressive change of frequency and sometimes with aharmonic overtones—are observed.

INTRODUCTION

Micropulsations, oscillations of the geomagnetic field with periods of a few seconds to a few minutes, were recorded on paper charts by these stations at Hobart (geomagnetic latitude 43°), Camden (43°), and Townsville (29°) from November 1959 till May 1960. These records have been described by Ellis [1961]. The work has now been extended by recordings at Camden and Adelaide (45°) from August 1960 to February 1961, both on charts as before and on slowly moving magnetic tape. This new work, a new study of the old records from Hobart and Townsville, will be presented here. Camden and Adelaide have been largely neglected because of high local noise level. The magnetic tapes have been analyzed on a 'Sonagraph' sound spectrograph.

RECORDING METHODS

The micropulsations were picked up on loops buried in the ground; that at Camden had three loops 200 meters in diameter. The signal was amplified 400-fold by a galvanometer-photocell system [Valley and Wallman, 1948, p. 487] and fed simultaneously onto a recording millivoltmeter and a magnetic tape, both the chart and tape moving at 6 inches per hour. Full scale deflection of the recorder occurred for a rate of change of field (dH/dt) of 1.3 γ /second, the minimum detectable signal being about 1/25 of full scale. The work was done at the High Altitude Observatory, Boulder, Colorado, until March 1962: High Altitude Observatory, Boulder, Colorado.

The response was linear from d-c to 7-second period oscillations but fell off rapidly for periods shorter than this. The apparatus at the other stations was essentially similar.

RESULTS

At the middle-latitude stations, in the absence of magnetic storms, the oscillations almost always fell approximately into the usual classes, the persistent irregularly fading sinusoidal oscillations known as *Pc* and the impulsive damped trains of oscillations known as *Pt*.

Occasionally other modes were seen; in the sound spectrogram reproduced in Figure 4, in addition to the dominant *Pc* mode, a mode and associated overtones with a frequency of 8 cycles/minute at 09 hours dropping progressively to 2 cycles/minute at 17 hours can be seen. At Hobart complex records were often observed, and this complexity extended to all stations during severe magnetic storms. The record of Figure 4 was taken on the day following a storm.

Persistent irregularly fading sinusoidal oscillations—Pc. Examples are shown in Figures 1, 2, and 3. These oscillations were almost completely confined to daylight hours, thus conforming to the pattern found by earlier workers [e.g., Campbell and Nebel, 1959]. At Adelaide, where the local noise level was particularly low, they were detected on 85 per cent of observing days, the median amplitude of each day's strongest burst being about 2 γ .

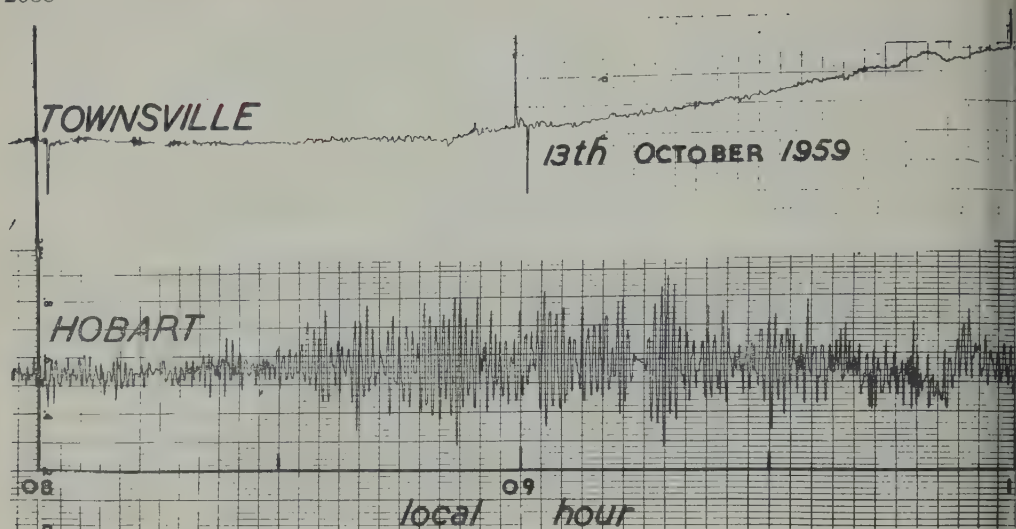


Fig. 1. Simultaneous induction magnetometer records from Hobart and Townsville showing strong *Pc* oscillations at Hobart. The slow drift at Townsville is instrumental.

A diurnal variation of period was found. *Kato and Saito* [1959] found a diurnal variation in the period of the highest frequency oscillations of any type present during each hour. Their variation passed through a maximum of 20 seconds at midday and a minimum of 8 seconds at 03 hours. Such a variation is compatible with the daytime and nighttime *Pc* periods found by *Yanagihara* [1959] and *Maple* [1959]. Some commentators have questioned whether these results refer to a continuous variation, and have suggested instead that they result statistically from the occurrence distribution of discrete classes of oscillations.

The tape recordings made in Australia show that during daylight hours a continuous change of period does occur; such tapes played back at high speeds produce a gliding note, the shorter period oscillations occurring at dawn. Sonagrams of tapes are reproduced in Figures 4 and 5.

Persistent oscillations are rare at night but the eight examples found on the Adelaide channel all had periods greater than 40 seconds, that is, contrary to *Yanagihara* and *Maple*, much greater than during the day. The sonagrams suggest a resolution of the conflict. Both the long period component and *Pc* component are found day and night, but at night the long period component is stronger. Nevertheless the period of the corresponding modes seems to be shorter.

The only oscillations commonly found at night are impulsive disturbances, or *Pt*'s; the spectra of these, however, seem to correspond to that of the persistent oscillations occurring during the day. An example occurring at 2133 hours on September 7, 1960, and illustrating all these points is seen in Figure 5.

Yoshimatsu [1950], *Kato and Watanabe* [1952] and *Maple* [1959] found the periods of *Pc* oscillations.

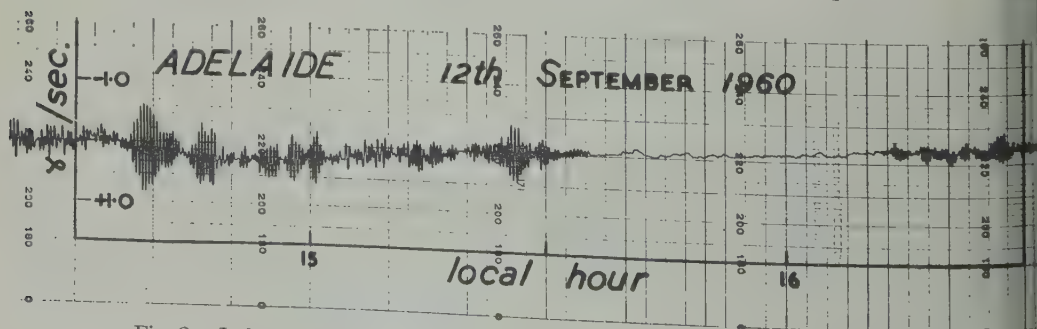


Fig. 2. Induction magnetometer record from Adelaide showing *Pc* oscillations.

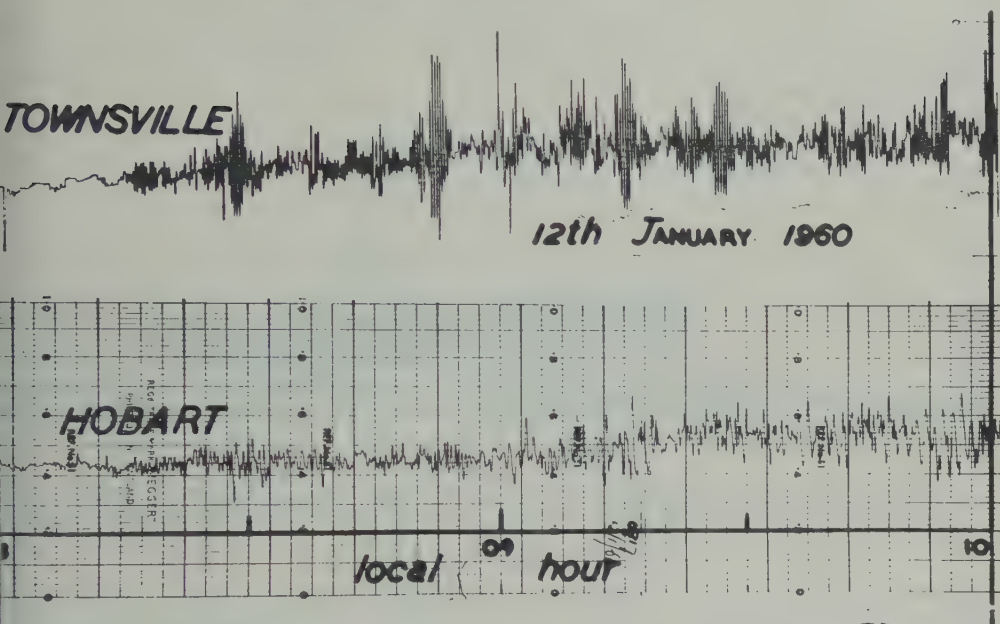


Fig. 3. Simultaneous induction magnetometer records from Hobart and Townsville showing strong P_c oscillations at Townsville in the absence of any remarkable behavior at Hobart.

to be shortened at times of magnetic disturbance. We have found the situation during a magnetic disturbance complex. In the post-storm period, however, typical P_c oscillations do appear, with enhanced amplitude and shortened period; shortening of the period is most pronounced in the morning hours, so that a magnetic disturbance increases the range of the daily variation (6).

The distributions of midday periods observed at each station are shown in Figure 7. In compiling these only cases of pure sinusoidal signals lasting at least $2\frac{1}{2}$ minutes were used. This criterion had little effect at Townsville and Adelaide, but it resulted in the rejection of about 60 per cent of the Hobart records. Most of the rejected Hobart records looked like a fundamental oscillation plus overtones and parasitics,

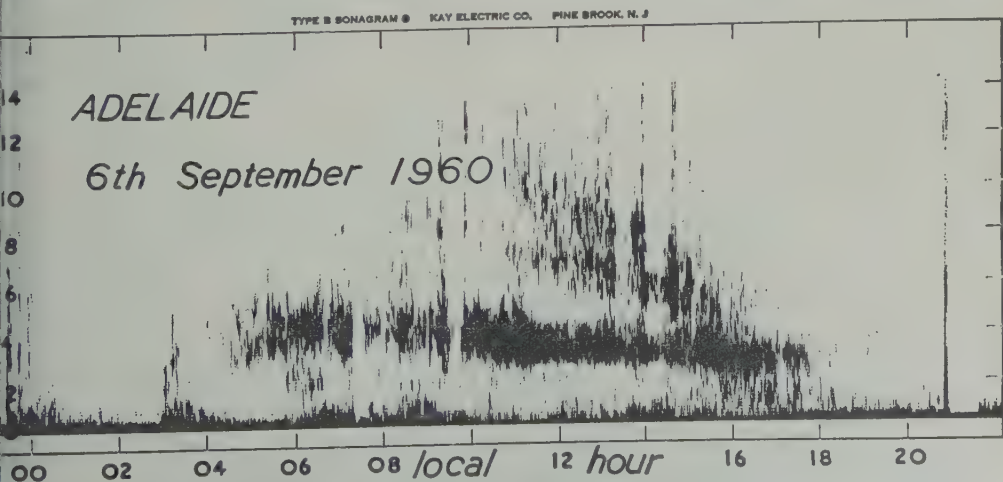


Fig. 4. Sonagram of the Adelaide tape record for September 6, 1960, showing P_c oscillations plus an additional mode.

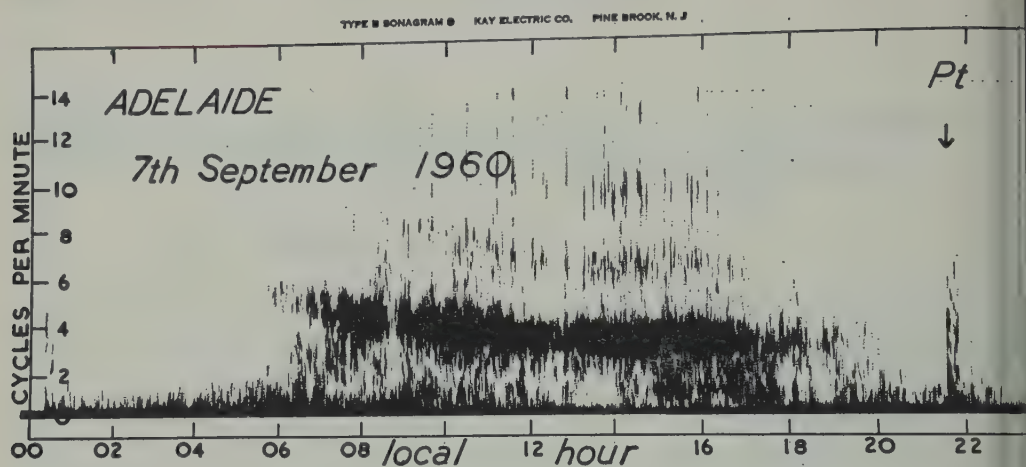


Fig. 5. Sonagram of the Adelaide tape record for September 7, 1960, showing P_c oscillations during the day and an impulsive disturbance or P_t at 2133 hours. A simultaneous chart recording of this P_t is reproduced in figure 8.

but it is very difficult to make quantitative studies of such phenomena from a paper chart; no tape recorder was installed at Hobart.

It will be seen from Figure 7 that the median midday period varies from 19 seconds at Townsville, to 23 seconds at Adelaide, and 27 seconds at Hobart. This result conflicts with the conclusion of Ellis [1961] from a study of the same data, but a survey of the literature shows that periods measured by other workers at various stations consistently show the same trend, shorter P_c periods at lower latitudes (Table 1). Jacobs and Sinno [1960] have noted this; Obayashi and Jacobs [1958] found a similar trend for giant

micropulsations—storm time oscillations with periods of 50 to 200 seconds.

It has been suggested [Ellis, 1961] that the oscillations arise in the auroral zones and propagate to lower latitudes; more effective propagation at shorter periods would then explain the mixed frequencies seen at Hobart and the pure short-period oscillations at Townsville. However, this explanation cannot explain much of the observed behavior; strong oscillations were sometimes observed in Townsville in the absence of strong oscillations at Hobart (Fig. 3); good Camden records are few, but we have one example (October 7, 1959) of simultaneous bursts

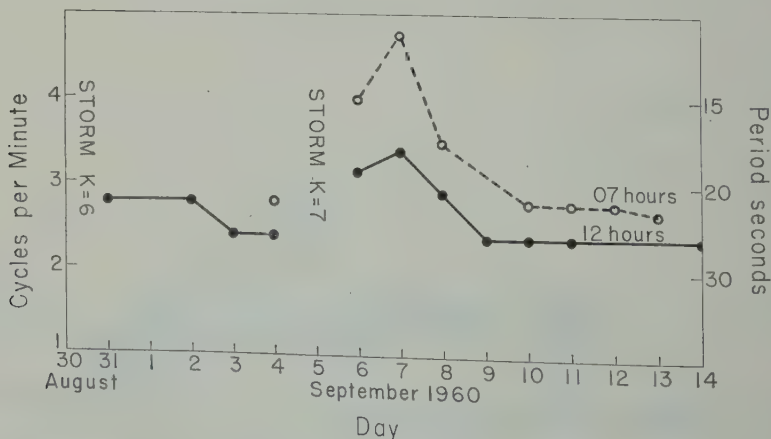


Fig. 6. The secular variation of the midday (solid line) and dawn (broken line) P_c period at Adelaide from August 30 to September 14, 1960. Only irregular oscillations with periods, greater than 2 minutes were observed during the moderate storms of August 30 and September 5.

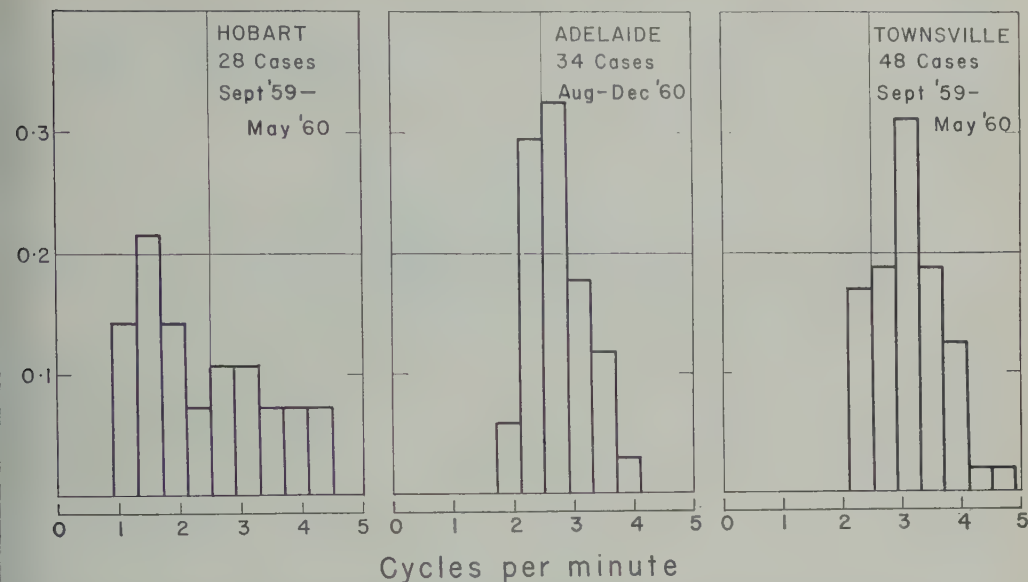


Fig. 7. The distribution of the periods of clean sinusoidal oscillations, lasting at least $2\frac{1}{2}$ minutes and occurring within half an hour of midday, for Hobart, Adelaide, and Townsville, respectively.

strong oscillations at Hobart, Camden, and Townsville with the same amplitude envelope and a marked latitude gradient of frequency.

Obayashi and Jacobs [1958] suggested that micropulsations—storm time oscillations with periods from 50 to 200 seconds—were riding Alfvén waves on the geomagnetic field lines, the vibrating string model. *Pc* oscillations have some properties in accord with this model. The short period at low latitudes where the field lines are short suggests it; the variable period at high latitudes (Fig. 7) could be due to the penetration of high latitude field lines into the disturbed exosphere. We have also the shortening of the daytime period after magnetic disturbance which plausibly could be attributed to the compression of the earth's field by a solar gas stream, and the additional shortening of the period at dawn in the vanguard of the earth's orbital motion through the gas. On this model, however, field lines on the night side of the earth could be stretched and the nighttime periods lengthened. This does not appear to be the case. As we have said, the little evidence available suggests that the period of corresponding modes is shorter at night than by day.

Impulsive damped trains of oscillations—Pt. Examples are shown in Figure 8, and they appear to be on the sonagram (Fig. 5). The sudden

commencements observed by the induction magnetometers were always oscillatory, and we have found no clear dividing line between the two phenomena; the oscillations usually termed *Pt* seem to be weak sudden commencements. In agreement with earlier workers [Meyer, 1951; Scholte and Veldkamp, 1955; Kato and Wantanabe, 1958], *Pt*'s were found to have a peak occurrence

TABLE 1. The Variation of *Pc* Period, as Determined by Various Workers, against Geomagnetic Latitude

Observer	Station	Geo-magnetic Latitude	Period, sec.
Kato and Saito 1959	Onagawa	28°	20
Duncan	Townsville	29°	19
Campbell 1959	Los Angeles	39°	22
Maple 1959	Tucson	40°	20
Berthold, Harris, and Hope 1960	Arizona	41°	35
Duncan	Adelaide	45°	23
Duncan	Hobart	52°	27
Scholte and Veldkamp 1955	Witteveen	54°	45
Duffus and Shand 1958	Victoria	54°	50

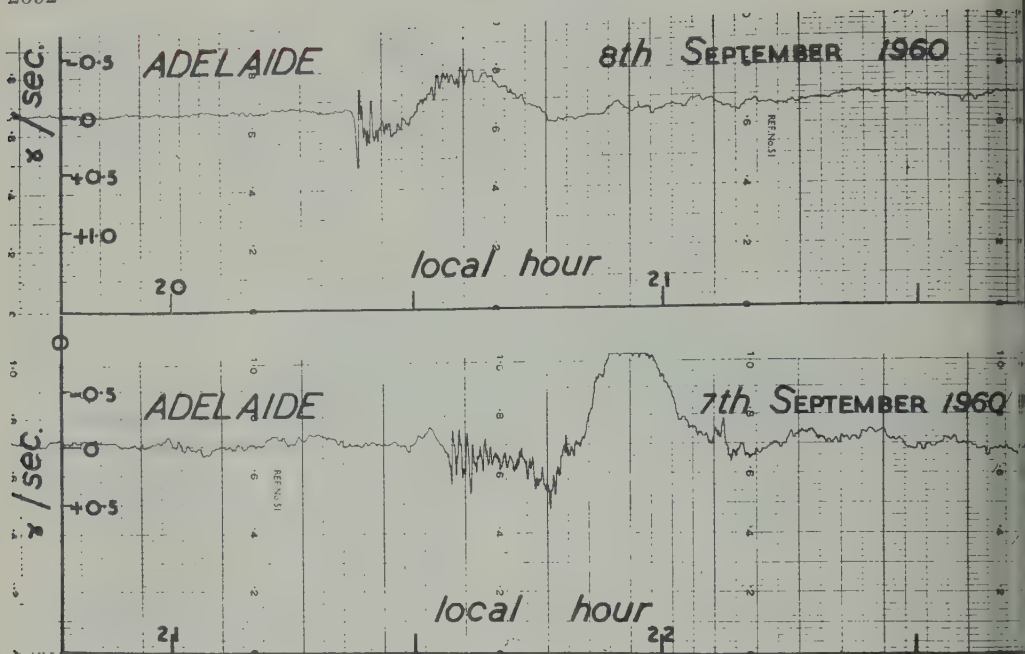


Fig. 8. Two examples of impulsive damped oscillations, or *Pt*, at Adelaide, showing the development of a bay about 15 minutes later. The *Pt* in the lower record is the one seen on the Sonagram reproduced in Figure 5.

at midnight and to precede magnetic bays, the average delay between the onset of oscillations and the peak build-up of the bay being about 15 minutes (see Fig. 8). Bless, Gartlein, Kimball, and Sprague [1959], Bhattacharyya [1960], and Stagg and Paton [1939] found a similar delay between auroral bursts and magnetic bays, suggesting that the two phenomena are closely linked.

Giant pulsations and other storm phenomena. The oscillations observed during magnetic storms have extremely varied and sometimes complex

frequency spectra. During moderate storm strong irregular long period oscillations are found and these seem to supplant shorter period oscillations; on September 5, 1960, for example, oscillations with a period less than 2 minutes were conspicuously absent at Adelaide although the normal *Pc* oscillations with a period of about 20 seconds were strong on the surrounding day (Fig. 6).

At Hobart, and at the lower latitude stations during severe storms, complex frequency spectra are observed, periods ranging from 2 seconds to

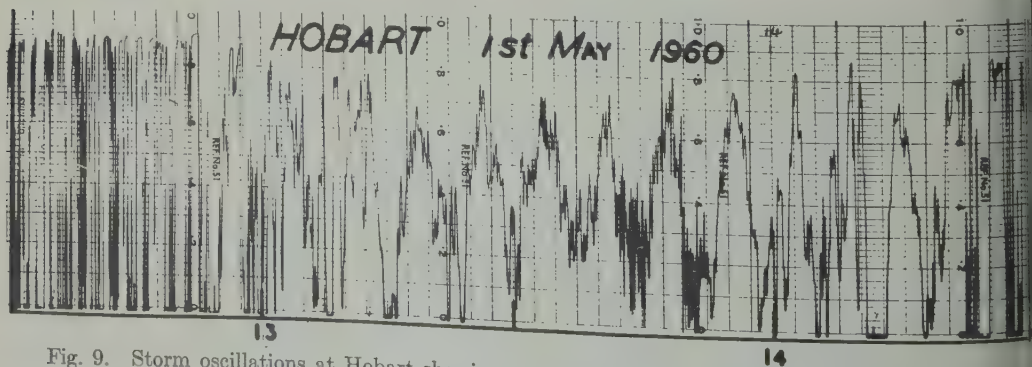


Fig. 9. Storm oscillations at Hobart showing, among other components, giant pulsations with a period of 7 minutes.

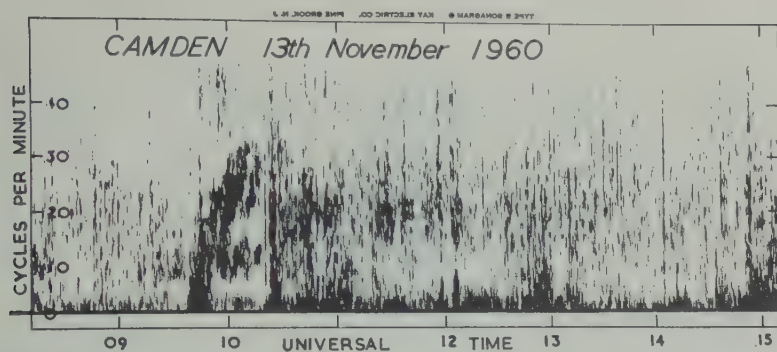


Fig. 10. Sonagram of a 'sweeper' recorded in the course of a storm on November 13, 1960.

minutes. It is probable that even shorter period oscillations occur; the recording apparatus, incorporating as it does a galvanometer, has a sensitivity rapidly as periods fall below 7 seconds. In Figure 9 oscillations of period 7 seconds can be seen, together with many higher frequencies. It is only the long period oscillations that are resolved on a normal magnetometer; it is these that are termed 'giant pulsations.' Recording on magnetic tape and subsequent spectral analysis enables us to study the higher frequencies also. *Duffus, Nasmyth, Shand, and Wright* [1958] using this technique discovered a long oscillation with a progressive change of frequency; they termed it a 'whistler.' We shall give two examples of oscillations recorded at Camden during the great storm which began on November 12, 1960. These differ considerably from each other and from the aforementioned whistler; the phenomena occurring during severe storms are evidently diverse.

Figure 10 is a sonagram of a swept frequency oscillation which began suddenly at 0937 UT on November 13, 1960, and accompanied a very

severe bay. As Duffus and his co-workers have remarked in connection with their phenomenon, the tape recording of this phenomenon when played back at high speed sounds similar to the whistlers of the audio frequency spectrum. The frequency swept from less than 2 cycles/minute to 35 cycles/minute in about half an hour. There is also a constant frequency component of about 11 cycles/minute. The sweeper was terminated by a very severe storm sudden commencement at 1022 UT; thereafter the frequency spectrum became more noisy. It will be noticed that many of the impulsive disturbances occurring during the surrounding hours have a discrete spectral structure.

Figure 11 is a sonagram of a storm sudden commencement at 2200 UT on November 15, 1960, following a very severe flare at 0220 hours on the same day. On a tape player this phenomenon sounds like a sharp crack followed by rumbling decaying echoes, such as a lightning stroke followed by thunder, for example. It will be seen (Fig. 11) that the noise begins at low frequencies and then extends to higher frequencies.

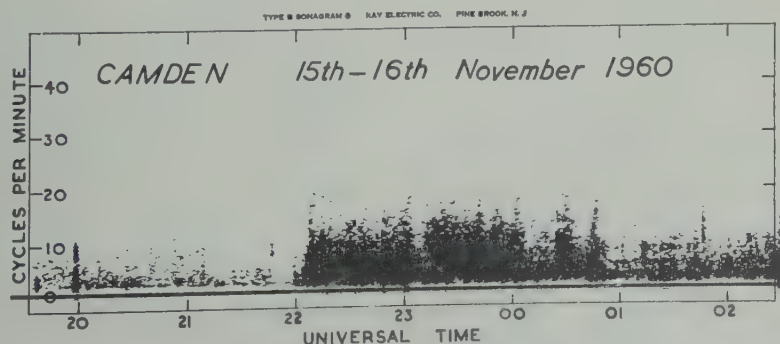


Fig. 11. Sonagram of a storm sudden commencement recorded on November 15-16, 1960, showing noise beginning at low frequencies and extending to high frequencies.

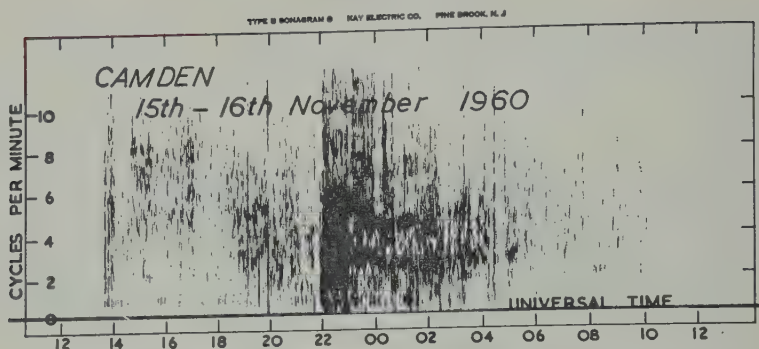


Fig. 12. Sonagram of a storm sudden commencement showing discrete spectral components, which are not harmonically related.

quencies; this is unlikely to be a dispersive effect as theory indicates that the higher frequencies have the greater velocity [Piddington, 1959].

In addition to the noise there are discrete frequency components; these do not show well in Figure 11 where we have used high contrast to emphasize the noise, but they may be seen more clearly in Figure 12. The oscillations sweep in frequency, in a manner and through a range similar to that of normal daytime *Pc* oscillations, and perhaps should be regarded as the same phenomenon. The overtones are not harmonically related; this might be anticipated as the upper atmosphere is a dispersive medium.

Acknowledgments. I am greatly indebted to Dr. G. R. Ellis for the suggestion that his earlier work be supplemented by recordings on magnetic tape, to T. W. Davidson for help in this project, and to Dr. D. F. Martyn for careful criticism of the paper. The Townsville recorder was operated by R. Conway of the Australian Ionospheric Prediction Service, and the Adelaide recorder by E. L. Murray of the University of Adelaide, to whom our thanks are due.

REFERENCES

- Berthold, W. K., A. K. Harris, and H. J. Hope, Correlated micropulsations at magnetic sudden commencements, *J. Geophys. Research*, **65**, 613-618, 1960.
- Bhattacharyya, B. K., Correlation studies of radio aurora, magnetic, and earth-current disturbances, *Canad. J. Phys.*, **38**, 624-637, 1960.
- Bless, R. C., C. W. Gartlein, D. S. Kimball, and G. Sprague, Auroras, magnetic bays and protons, *J. Geophys. Research*, **64**, 949-953, 1959.
- Campbell, W. H., Studies of magnetic field micropulsations with periods of 5 to 30 seconds, *J. Geophys. Research*, **64**, 1819-1826, 1959.
- Campbell, W. H., and B. Nebel, Micropulsations measurements in California and Alaska, *Nature*, **184**, Suppl. 2, 628, 1959.
- Duffus, H. J., P. W. Nasmyth, J. A. Shand, and C. Wright, Subaudible geomagnetic fluctuations, *Nature*, **181**, 1258-1259, 1958.
- Duffus, H. J., and J. A. Shand, Some observations of geomagnetic micropulsations, *Canad. J. Phys.*, **36**, 508-526, 1958.
- Ellis, G. R. A., Geomagnetic micropulsations, *Australian J. Phys.*, **13**, 625-632, 1961.
- Jacobs, J. A., and K. Sinno, World-wide characteristics of geomagnetic micropulsations, *Geophys. J. Roy. Astron. Soc.*, **3**, 333-353, 1960.
- Kato, Y., and T. Saito, Preliminary studies on the daily behaviour of rapid pulsations, *J. Geomagn. and Geoelect.*, **10**, 221-225, 1959.
- Kato, Y., and T. Watanabe, Studies on geomagnetic storm in relation to geomagnetic pulsations, *J. Geophys. Research*, **63**, 741-756, 1958.
- Maple, E., Geomagnetic oscillations at middle latitudes, *J. Geophys. Research*, **64**, 1395-1404, 1959.
- Meyer, O., Über eine besondere Art von erdmagnetischen Bay-Störungen, *Deutsche Hydrographische Zeitschrift*, **4**, Heft 1/2, 1951.
- Obayashi, T., and J. A. Jacobs, Geomagnetic pulsations and the earth's outer atmosphere, *Geophys. J. Roy. Astron. Soc.*, **1**, 53-63, 1958.
- Piddington, J. H., The transmission of geomagnetic disturbances through the atmosphere and interplanetary space, *Geophys. J. Roy. Astron. Soc.*, **2**, 173-189, 1959.
- Scholte, J. G., and J. Veldkamp, Geomagnetic and geoelectric variations, *J. Atmospheric and Terrestrial Phys.*, **6**, 33-45, 1955.
- Stagg, J. M., and J. Paton, Aurora and geomagnetic disturbance, *Nature*, **143**, 941, 1939.
- Valley, G. E., and H. Wallman, *Vacuum Tube Amplifiers*, McGraw-Hill Book Company, p. 74, 1948.
- Yanagihara, K., Some character of geomagnetic pulsation pt and accompanied oscillation s.p.t., *J. Geomagn. Geoelect.*, **10**, 172-176, 1959.
- Yoshimatsu, T., On the frequency of geomagnetic pulsation p.t., *J. Geomagn. Geoelect.*, **11**, 208-213, 1950.

(Manuscript received March 27, 1961;
revised April 24, 1961.)

Attempt to Measure Night Helium Glow—Evidence for Metastable Molecules in the Night Ionosphere

E. T. BYRAM, T. A. CHUBB, AND H. FRIEDMAN

*U. S. Naval Research Laboratory
Washington 25, D. C.*

Abstract. An Aerobee rocket flown from White Sands Missile Range at 1115 UT, November 29, 1960, included a first experimental attempt to measure the intensity of the helium glow in the night sky. The experiment has provided evidence that the brightness of this glow is less than one-tenth the brightness of the night Lyman α glow. The photoelectric detector produced signals that may be interpreted as evidence that a supply of metastable molecules exists in the night ionosphere at altitudes above 100 km.

Background. The search for a nighttime helium glow was undertaken as part of a continuing study of far ultraviolet emissions in the night sky. The first far ultraviolet study of the night sky [Byram, Chubb, Friedman, and Kupperman, 1957] was made in 1955 and resulted in the discovery of the night Lyman α glow. The Lyman α glow was shown later to have an average sky intensity at 140 km of $0.003 \text{ erg/cm}^2/\text{ster}$ with a minimum in the antisolar direction [Kupperman, Byram, Chubb, and Friedman, 1959]. In addition, the earth's atmosphere has been looking downward from 140 km was found to glow with a Lyman α albedo of brightness equal to about 42 per cent of the overhead Lyman α glow, in contrast to normal Lyman α emissions, showed no horizon brightening. These observations suggest that the overhead Lyman α glow is composed of scattered Lyman α , and that this overhead Lyman α radiation is rescattered by atomic hydrogen in the earth's atmosphere at the 100–120-km level. The next question to be resolved was that of the origin and location of the hydrogen doing the primary scattering: namely, is the primary scattering due to atomic hydrogen in the earth's atmosphere or to interplanetary neutral hydrogen? This was soon pointed out by F. S. Johnson [Johnson and Fish, 1960] that the hypothesis of interplanetary hydrogen could not easily explain the intensity of the earth's Lyman α albedo. The radiation scattered by interplanetary hydrogen would be in part Doppler-shifted relative to hydrogen in the earth's atmosphere because of the orbital velocity of the earth relative to the sun, and since cold telluric atomic

hydrogen scatters only a narrow line, an excessive amount of hydrogen at 120 km would be required to give the observed 42 per cent albedo. Hence, it was argued that the scattering must occur in a telluric hydrogen geocorona made up of neutral hydrogen enveloping the earth and arising from decomposition of water vapor and methane in the upper D region. In 1959 Purcell and Tousey [1960] obtained a profile spectrum of the solar Lyman α line showing that the central core of the incident line radiation had been partly removed by the time sunlight reached the 190-km level. The width of the missing core was consistent with that expected for exospheric H. From this profile the total amount of atmospheric H above 190 km was calculated to be $2 \times 10^{12} \text{ atoms/cm}^2$. This quantity of hydrogen was sufficient to cause considerable night Lyman α glow, but was about a factor of 3 below the amount needed to explain the measured glow as estimated by Johnson in his preliminary calculations. In 1960 an experiment was conducted in which the variation in the intensity of the night glow was measured between 350 and 1000 km. [Chubb, Friedman, Kreplin, and Mange, 1961]. The experiment was of relatively low accuracy, but indicated a drop of overhead brightness of only 20 per cent. This change in overhead brightness was sufficient to indicate a major contribution from earthly hydrogen. It did not resolve, however, the important question as to whether a significant contribution from interplanetary hydrogen does not also occur.

The search for 304 and 584 Å night helium glow was undertaken to determine whether neutral or partly ionized interplanetary gas

TABLE 1. Sensitivity of LiF Photocell

Wave-length, A	Quantum Yield	Basis for Value
1216	0.003	Calibration against ionization produced in gas mixture 3.5% CH ₃ I, 96.5% N ₂ by volume. Mixture assumed to have quantum yield 1.0.
584	0.45	Calibration against response of sodium salicylate-photo-multiplier detector with photo-multiplier calibrated at 1216 A. Fluorescent quantum yield of sodium salicylate assumed same at 1216 and 584 A.
304	0.45	Assumed.

occurs in sufficient concentration to backscatter to the earth measurable quantities of solar radiation. Such interplanetary He I and He II could arise from either recombination processes in dense solar plasma clouds or from the drift through the solar system of interstellar neutral gas. Helium glow appears to be a good radiation to look for since helium is present in high concentration in both the sun and interstellar space, whereas it is very scarce in the earth's atmosphere. Also, because of helium's high ionization potential, a far greater fraction of helium can be expected to occur in the He I or He II condition relative to the corresponding expected amount of H I [Rundle, 1960]. Since Hinteregger [1960] had measured solar line intensities of 0.1 erg/cm²/sec for the scatterable 584 A resonance line of He I and 0.25 erg/cm²/sec for the scatterable 304 A resonance line of He II, it appeared that easily measurable night fluxes of helium radiation were possible.

Design of experiment. The limiting factor in the design of a simple photometric experiment to measure the night helium glow was recognized to be the difficulty of eliminating detector sensitivity at the Lyman α line. To obtain a high level of sensitivity at 584 and 304 A while maintaining a high rejection ratio for Lyman α radiation, a photocell was designed using evaporated LiF as the photo-sensitive surface. The photocell was calibrated on an absolute basis at the Lyman α line. It was also calibrated relative to the fluorescence of sodium salicylate both at the Lyman α line and at the 584 A line of He I.

The results of these calibrations are shown in Table 1. The sensitivity at 584 A is calculated on the assumption that sodium salicylate has the same quantum yield at 584 A as at 1216 A. The sensitivity at 304 A was not measured; however, data by Lukirskii, Rumsh, and Smirnov [1960] on a similar LiF surface showed a quantum yield of 61 per cent at 113A. Also, results of Taft and Philipp [1957] for other alkali halide photosurfaces have always shown a monotonic increase in ultraviolet sensitivity with quantum energy.

The geometry of the experimental assembly flown is shown in Figure 1. To carry out a windowless photocell measurement in a rocket it is necessary to prevent response from collection of ionospheric ions and electrons. Electrons were excluded in this experiment by a magnetic shield that maintained a magnetic field of $H \geq 1$ gauss over the entrance aperture through which the detector looked. Collection of positive ions was prevented by operating the body and collection screen of the ion chamber at a potential +20 volts relative to the rocket body. The photocell operated in this fashion provided a sensitive surface of 8.2 cm² and viewed a solid angle of 0.6 steradian. The photocell was metered by an electrometer amplifier with a full scale sensitivity of 2×10^{-11} amps, corresponding to an incident 584 A flux at full scale of 1.9×10^6 ergs/cm²/sec/ster. The assembly was flown on an Aerobee rocket (NRL-59) which reached an altitude of 199 km. The rocket rolled at a rate of 0.26 rps while precessing in a yaw cone of 160° total angle. An accurate aspect solution for the detector view angle as a function of time was obtained from the star responses of various stellar photometers carried in the same flight. During most of the flight the rocket axis was within 30° of a plane perpendicular to the flight trajectory.

Experimental results: helium glow. The results of the above experiment were not exactly as anticipated, but we cannot attribute them to any instrumental malfunction. The response of the photocell appears to be made up of two components. The first component is a broad peaked response which has its maximum when the photocell is looking upward in the first half of the flight and when the photocell is looking downward in the second half of flight. This broad peak response appears to be a function of time.

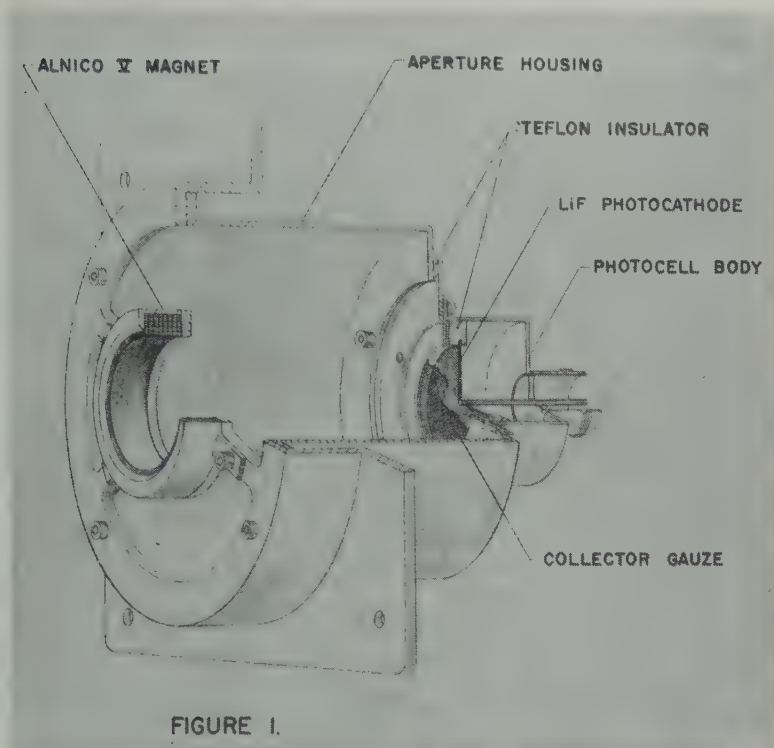


FIGURE 1.

Fig. 1. Open window photocell sensitive to helium glow radiation flown in Aerobee-Hi (NRL-59). The photocell was mounted inside an aperture housing maintained at rocket potential and viewed space through a set of open apertures at the left side of figure. A magnetic field of 30–200 gauss was established over these apertures by an Alnico V magnet, so as to provide an electron barrier. The photocell body and collector gauze were maintained at +20 volts relative to rocket body, so as to repel positive ions. The collector was an 80 per cent transmission 100-mesh electroformed nickel gauze. The photocathode, shown as the dark surface very close to the collector gauze, was a stainless steel plate coated with an evaporated film of LiF of about 0.7 mg/cm^2 surface density. The photocathode was mounted $1/8$ inch behind the collector gauze and was maintained at a potential of zero volts relative to the rocket body.

of attack of the photocell sensor, and the minimum signal occurs generally about 25° of after the detector looks at minimum angle of attack. The second component is a gradual rise with altitude of the background level from which the peaks rise. The base level is the d-c level of the detector response as measured mid-way between the peaked responses. This shift in minimum brightness level is interpreted as being caused primarily by a broadening of the roll maxima near peak altitude, where rocket velocity is high, but it may also contain a contribution from the helium glow.

In order to obtain a limit on the intensity of the helium glow, the background level of the photocell was measured on ascent and descent. The data points are shown in Figure 2.

The presence of helium glow should show up as an increase in the descent data near peak over the ascent data, since the descent background data were obtained when looking up and the ascent data were obtained when looking down. No significant differences between ascent and descent are evident. For the purposes of placing an upper limit on the helium glow intensity we have made use of the data at 187 km. Higher altitude data were not used in the calculation because of excessive spreading of the roll maxima. From the data shown in Figure 2, we conclude that at 187 km photoelectric emission is less than $0.51 \times 10^6 \text{ electrons/cm}^2/\text{sec}$. Using the value of quantum yield measured at 584 Å, i.e., 0.45, for both the 584 and the 304 Å calculations, we arrive at upper limits to the helium glow

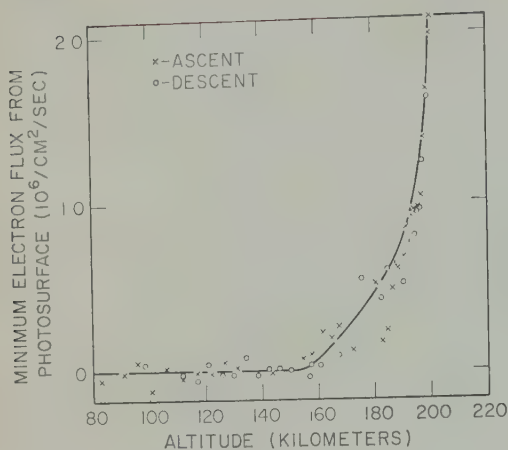


Fig. 2. Minima in electron current from LiF photocell as a function of altitude. Minima occur in downward direction during ascent and upward direction during descent.

intensity at 187 km as 7.9×10^{-5} ergs/cm²/sec/ster for 584 Å and 1.52×10^{-4} ergs/cm²/sec/ster for 304 Å. The results are summarized in Table 2. Corrections for atmospheric absorption are based on a model atmosphere by *F. S. Johnson* [1960; a pressure of 2.63×10^{-3} dynes/cm² at 187 km is given] for solar maximum and air absorption coefficients of 476 cm⁻¹ atm⁻¹ for 584 Å and 186 cm⁻¹ atm⁻¹ for 304 Å (Hinteregger, private communication). The detector view direction at 187 km was at an angle of 35° from vertical during rocket descent. However, since the field of view of the detector extended out beyond angles of 30° from normal, radiation 5° from zenith could strike the photosurface. Because of the relatively high optical depth at 187 km, the data are corrected for radiation arriving from a 25° zenith angle.

The measurements described in Table 2 indicate that the night helium glow is less than 10 per cent the intensity of the night Lyman α glow. This low limit to helium glow intensity lends additional indirect support to the view that the night Lyman α glow arises largely from a telluric hydrogen geocorona.

Evidence for metastable atmospheric molecules. Let us now consider the peaked responses observed by the open photocell. These peaks occur once per roll and they consistently occur 20 to 30 roll degrees (0.2–0.3 second) after the detector looks most closely parallel to the flight path. Thus all the maxima during ascent occur with

the detector looking upward, all the maxima during descent occur with the detector looking down. Although we cannot explain the slight delay in the peak response following minimum angle of attack, we are nevertheless forced to conclude that the response is caused by atmospheric particles hitting the photosurface rather than by any external radiation source. This interpretation is supported by the fact that the observed maxima are sharper at lower altitudes. At the lower altitudes the speed of the rocket is relatively greater than the speeds of the ambient molecules.

The analysis of the data has been carried out in the following fashion. The amplitudes of the individual roll maxima have been plotted as a function of altitude for both ascent and descent. The data uncorrected for angle of attack are shown in Figure 3. Next the angle of attack of the rocket axis was computed from knowledge of the rocket flight path, based on radar data and from a detailed solution of the rocket's orientation as a function of time, based on responses of stellar photometers carried in the vehicle. The amplitudes of the roll maxima were then multiplied by the secant of the minimum angle of attack of the view angle vector for the corresponding roll. This correction was not applied to the data above 195 km. Although the correction reduced the discrepancy between ascent and descent data, it still left relatively large variations. A single average curve was then drawn through the ascent and descent data. By dividing the data points derived in this fashion by the rocket velocity, the relative number of particles per cubic centimeter responsible for the electron emission was derived. The results of this data treatment are shown in Figure 4.

The particles responsible for the observed current are believed to be metastable molecules in the upper atmosphere. Both electrons and negative ions striking the photosurface would

TABLE 2. Upper Limits to Intensity of Night Helium Glow

Assumed Radiation, Å	Flux at 187 km, ergs/cm ² /sec/ster	Absorption Correction	Flux above Atmosphere, ergs/cm ² /sec/ster
304	1.52×10^{-4}	1.8	2.7×10^{-4}
584	7.90×10^{-5}	4.6	3.6×10^{-4}

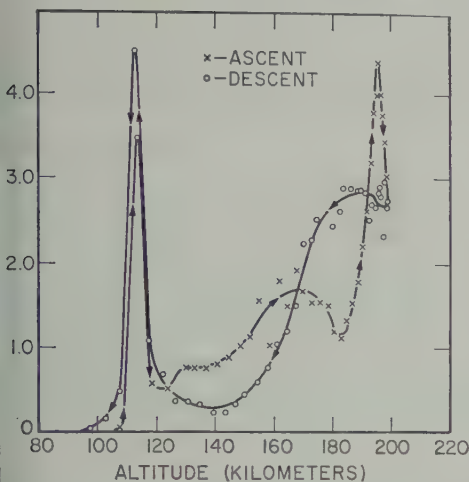


Fig. 3. Peak electron current from LiF surface as a function of altitude. Data not corrected for effect of attack.

...a deflection signal in a direction opposite that observed. In addition, the radius of curvature of a 1-ev electron in the 30-gauss minimum shielding field is 0.11 cm, so that penetration of the magnetic barrier could not occur. Positive ions could cause a deflection in the direction observed; however, it does not seem probable that they could override the +20-volt retarding potential applied between the photocell collection grid (an 80 per cent transmission fine-per-inch electroformed mesh) and the detector body. The motion of the rocket through the gas gives an impact energy of only 0.27 ev (mass $28 \text{ molecule at } 100 \text{ km}$, in contrast to energy required for strong photoelectric emission; therefore, it is most unlikely for ground state neutral molecular impacts to produce the observed emission. The most probable remaining alternative is that the observed emission is produced by impacts of metastable atmospheric molecules on the photosurface, with the metastable level more than 12 ev above the ground state. It seems possible that some such states may exist in the N_2 molecule. The other alternative which has been considered is that some sort of emission is associated with atomic oxygen recombination on the LiF surface might conceivably take place. The energy available from this process is only about 5 ev; nevertheless, it seems possible that surface energy states might exist on the LiF surface from which electrons could be obtained. We can be certain that the recombination process

should be ruled out as a possible explanation of the 110-km emission peak. It does appear to be unacceptable as an explanation of the high altitude rise since the number density of atomic oxygen is undoubtedly decreasing with altitude above 130 km.

If we accept the hypothesis that metastables are responsible for the detector response, Figure 4 shows that there are apparently two sources of metastable molecules. The data above 140 km resembles the variation with altitude of the density of O^+ ions at night [C. Y. Johnson, 1961]. It suggests diffusion of metastables from a reservoir in the F_2 region. Also, interestingly, the number of metastables in this region varies almost inversely with respect to the neutral particle density of the atmosphere. At lower altitudes the number density of metastables shows a sharp maximum at 113 km. The cause of the rapid rise in moving from 120 to 113 km is not understood. The rate of increase in the number of metastables in going from 120 to 113 km appears to be faster than the rate of increase of atmospheric molecules. It would appear, therefore, that the metastables must be created in this region rather than being carried down to lower altitude by a mixing process.

The final question to be discussed is the actual

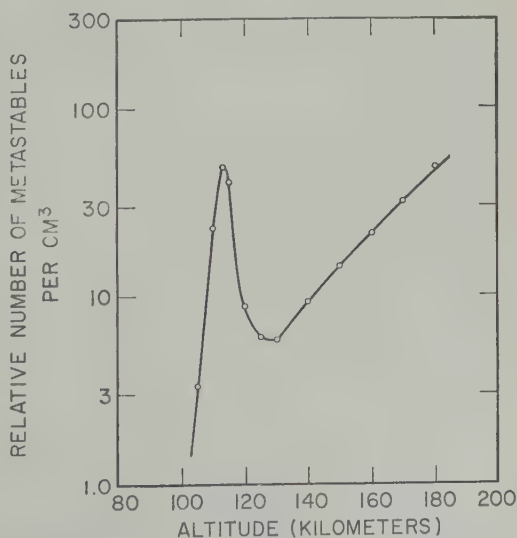


Fig. 4. Relative number density of metastable molecules vs. altitude. Plot gives absolute number of metastables per cubic centimeter assuming one electron emitted from the LiF surface for each metastable impact.

number of metastables present. Without knowing the efficiency of electron emission per metastable impact, it is impossible to provide a definite answer. The scale numbers shown in Figure 4 are the computed number of metastables per cubic centimeter, assuming that one free electron is emitted from the LiF surface for every metastable molecule striking the surface. The actual numbers of metastables may be much higher than indicated.

REFERENCES

- Byram, E. T., T. A. Chubb, H. Friedman, and J. E. Kupperian, Jr., *The Threshold of Space*, edited by M. Zelikoff, Pergamon Press, London, p. 203, 1957.
- Chubb, T. A., H. Friedman, R. W. Kreplin, and P. Mange, *Mémoire de La Société Royale des Sciences de Liège*, 1961.
- Hinteregger, H. E., *Ap. J.*, **132**, 801, 1960.
- Johnson, C. Y., *Ann. Geophys.*, **17**, 1, 1961.
- Johnson, F. S., ed., *Satellite Environment Handbook*, p. 1-1, Lockheed Company, Sunnyvale, California, 1960.
- Johnson, F. S., and R. A. Fish, *Ap. J.*, **131**, 563, 1960.
- Kupperian, J. E., Jr., E. T. Byram, T. A. Chubb, and H. Friedman, *Ann. Geophys.*, **14**, 329, 1959.
- Kupperian, J. E., Jr., E. T. Byram, T. A. Chubb, and H. Friedman, *Planetary Space Sci.*, **1**, 3, 1959.
- Lukirskii, A. P., M. A. Rumsh, and L. A. Smirnov, *Optics and Spectroscopy (Optüspektrask)*, **9**, 515, 1960.
- Purcell, J. D., and R. Tousey, *J. Geophys. Research*, **65**, 370, 1960.
- Rundle, H. N., *Planetary Space Sci.*, **2**, 86, 1960.
- Taft, E. A., and H. R. Philipp, *J. Phys. Chem. Solids*, **3**, 1, 1957.

(Manuscript received April 11, 1961.)

The Height and Geographical Position of the Red Auroral Arc of April 1-2, 1960

JAMES G. MOORE AND F. KIRK ODENCRANTZ

U. S. Naval Ordnance Test Station, China Lake, California

Abstract. Simultaneous observations of an auroral arc from Cactus Peak, California, and Fritz Peak, Colorado, on the night of April 1-2, 1960, have provided the information necessary to determine the height of maximum luminosity and the geographical position of the arc. Twenty pairs of measurements determine the average height to be 425 km with a standard deviation of ± 22 km from the average for a single pair of observations. The arc, observed from a point over the Pacific Ocean off the Oregon Coast to a point over the state of Mississippi, lay generally along a line of equal magnetic inclination.

Introduction. The existence of persistent red auroral arcs to the equator side of general auroral activity has been pointed out by *Barbier* [1958], *Roach and Marovich* [1959; 1960], *Duncan* [1959], and further by *Roach, Moore, Bruner, Cronin, and Silverman* [1960] who reported an average height of $412 \text{ km} \pm 23 \text{ km}$ for the arc of November 27-28, 1959. A résumé of current information regarding monochromatic arcs in the night sky can also be found in the *IGY Bulletin No. 36* [1960].

Observations. The magnetic observatory at College, Alaska, reported that a severe magnetic storm, *K*-index 9, began at 0430 UT, March 31, 1960. The intense solar activity caused a three-day Special World Interval to be called. Many evening auroral displays were reported on April 1 and 2-3 from observers over a large part of the North American continent. Photometric observations of the aurora began at 0240 UT, April 2, at Fritz Peak in Colorado, and at 0715 UT, April 2 at Cactus Peak, California. Table 1 contains the coordinates of the two observing stations. These observations continued until 0155 UT, April 2. This paper is concerned then with the determination of the effective height of the arc during the period when it was observed

from these two stations (the 4-hour period commencing at 2315 PST, April 1, 1960).

The arc structure was definitely distinguishable from a more general auroral activity further to the north during this 4-hour period. The geographical position of the arc was remarkably constant during this period.

Results. The method of height determination was the same as employed by *Roach, Moore, Bruner, Cronin, and Silverman* [1960] in their height determination of the red arc of November 27-28, 1959. This method involves the plotting of azimuth and zenith distance of the peak luminosity of the arc on a polar coordinate map for each station. The height of the arc is then deduced and is listed in Table 2 for twenty times during the night. The mean height is 425 km with a standard deviation of ± 22 km for the individual determinations. The deduced heights for the arc are plotted in Figure 1.

By combining this information with the mean coordinates of the arc as observed from Cactus Peak and Fritz Peak, the geographical longitude and latitude of the sub points of the arc were determined. These points are tabulated in Table 3 and are plotted on an Isoclinic Chart of the United States (see Figure 2).

TABLE 1. Coordinates of the Observing Stations

Station	Geographic Latitude	Geographic Longitude	Geomagnetic Latitude	Magnetic Isoclinic Latitude	Elevation above Sea Level, Meters
Cactus Peak	36°05'N	117°49'W	43.1°	42.0°	1650
Fritz Peak	39°54'N	105°29'W	48.7°	50.8°	2749

TABLE 2. Height of Monochromatic Arc
As a Function of Time

UT April 2	Height, km
0715	412
0730	456
0745	424
0800	443
0815	412
0820	412
0830	407
0845	430
0850	449
0900	456
0915	401
0930	381
0945	407
1000	437
1015	456
1030	407
1045	424
1055	437
1100	407
1115	437

Discussion. The determination of the height of quiescent auroral or airglow features by triangulation of photometric observations as suggested by *St. Amand, Pettit, Roach, and Williams* [1955] has been made for two subvisual red auroral arcs. The mean height determined for the arc of November 27–28, 1959, was 412 km [Roach, Moore, Bruner, Cronin, and Silverman, 1960] and that determined for the arc described herein was 425 km. Similar observations of the red arc of October 24–25, and 25–26, 1960, are now being reduced, and it is hoped that the results will be forthcoming shortly. On the basis of the observations of the subvisual auroral arcs already made, their presence can be correlated with intense magnetic storms (although not all magnetic storms give rise to these subvisual red auroral arcs). An attempt has also been made to correlate the existence of a subvisual red auroral arc to the dumping-out of particles from the outer Van Allen radiation belts [O'Brien, Van Allen, Roach, and Gartlein, 1960]. It has been hypothesized that this dumping-out of particles from the outer Van Allen zone causes local heating of the ionosphere and mixing of the atmospheric constituents, thereby starting a chemical reaction that yields 6300-Å radiation [King and Roach, 1960]. Since these correlations and hypotheses depend upon the effective height and the geographical distribution of the emitting region, it is suggested that a tentative value of

It is seen that the arc lies generally along a line of equal magnetic inclination and that it is about 1.5° south of Fritz Peak. This position corresponds to a geomagnetic latitude of approximately 47°, which is slightly lower than the proposed minimum of 48° [Roach and Marovich, 1960].

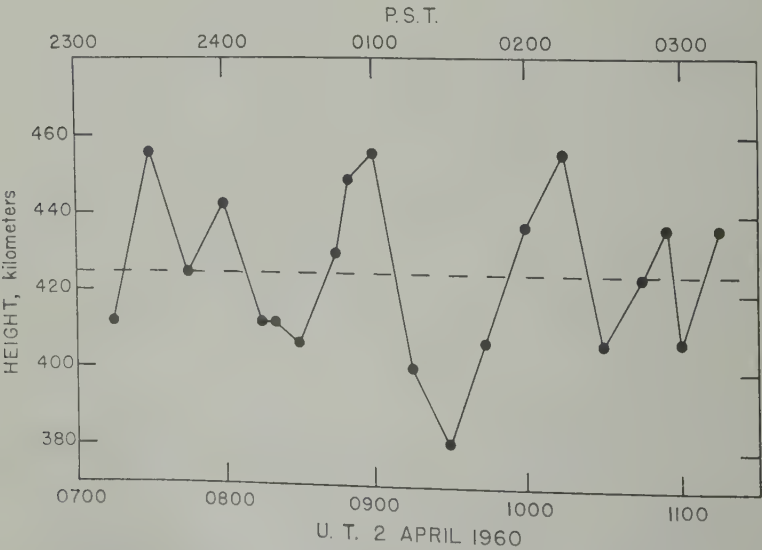


Fig. 1. Variation of the height of the 6300 Å arc with time.

TABLE 3. Average Values of the Latitude and Longitude of the Auroral Arc Subpoints as Determined Separately from Cactus Peak and Fritz Peak Data

Cactus Peak				Fritz Peak			
Zenith Distance, deg.	Azimuth, deg.	North Latitude, deg.	West Longitude, deg.	Zenith Distance, deg.	Azimuth, deg.	North Latitude, deg.	West Longitude, deg.
80	313	43.7	130.6	80	292	43.2	123.5
75	315	42.6	127.1	75	281	40.5	119.6
70	326	42.3	124.7	70	288	41.2	116.6
60	345	40.9	119.5	60	270	39.5	113.4
..	40	265	39.3	109.3
..	40	145	37.5	102.8
60	37	39.8	113.4	60	113	37.1	97.7
70	64	38.7	108.4	70	115	35.6	95.0
75	69	38.3	105.6	75	108	35.7	92
80	77	37.2	102.2	80	112	34.0	89.1

km be adopted for the mean height of these auroral forms, and that the geographical distribution is along a line of equal magnetic inclination. It is further suggested that rocket probes with charged-particle detectors, and D-A photometers aboard should be fired into the subvisual auroral arcs to make an independent determination of their height and of

their relationships to the charged-particle densities, as has been done for visible auroras [McIlwain, 1960].

Conclusions. From twenty measurements of the height of a subvisible red auroral arc, an effective mean height of 425 km with a standard deviation of ± 22 km has been obtained. The geographical distribution of the arc has been

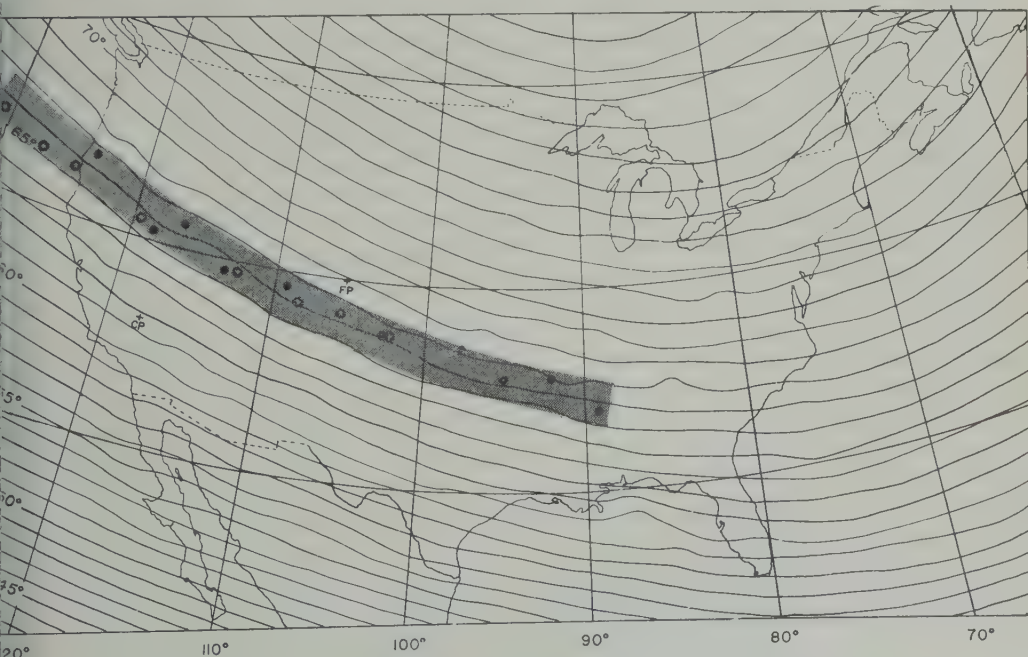


Fig. 2. Average position of the 6300 Å arc during the night of April 1-2, 1960, from observations at two stations. Open circles, Cactus Peak; closed circles, Fritz Peak. Geographical latitude and longitude are shown on the ordinate and abscissa, respectively, while the isoclinic lines are identified in the figure.

plotted and has been found to lie generally along a line of equal magnetic inclination ($i = 66^\circ$), extending about $\frac{2}{3}$ the distance across the United States. The dip latitude of the arc has been computed to be approximately 48.5° .

Acknowledgment. We are indebted to Dr. F. E. Roach, Boulder Laboratories, National Bureau of Standards, for making the Fritz Peak photometer records of April 1-2, 1960, available to us.

REFERENCES

- Barbier, D., L'activite aurorale aux basses latitudes, *Ann. geophys.*, **14**, 334-355, 1958.
- Duncan, R. E., Photometric observations of subvisual red auroral arcs at middle latitudes, *Australian J. Phys.*, **12**, (2), 1959.
- IGY Bulletin No. 36, Monochromatic arcs in the night sky, *Trans. Am. Geophys. Union*, **41** (2), 401-406, 1960.
- King, G. A. M., Roach, F. E., Relationship between red auroral arcs and ionospheric recombination, *J. Research NBS*, **65D** (2), 129-135, 1961.
- McIlwain, Carl E., Direct measurement of particles producing visible auroras, *J. Geophys. Research*, **65**, 2727-2747, 1960.
- O'Brien, B. J., J. A. Van Allen, F. E. Roach and C. W. Gartlein, Correlation of an auroral arc and a subvisible monochromatic 6300 Å arc with outer-zone radiation on November 28, 1959, *J. Geophys. Research*, **65**, 2759-2766, 1960.
- Roach, F. E., and E. Marovich, A monochromatic low latitude aurora, *J. Research NBS*, **63D**, 297-300, 1959.
- Roach, F. E., and E. Marovich, Aurora of October 22-23, 1958, at Rapid City, South Dakota, *J. Research NBS*, **64D**, 205-209, 1960.
- Roach, F. E., J. G. Moore, E. C. Bruner, Jr., H. B. Cronin, and S. M. Silverman, The height of maximum luminosity in an auroral arc, *J. Geophys. Research*, **65**, 3575-3580, 1960.
- St. Amand, P., H. B. Pettit, F. E. Roach, and D. R. Williams, On a new method of determining the height of the airglow, *J. Atmospheric and Terrestrial Phys.*, **6**, 189-197, 1955.

(Manuscript received April 8, 1961.)

Some Auroral Observations inside the Southern Auroral Zone

J. V. DENHOLM

*Antarctic Division, Department of External Affairs
Melbourne, Australia*

Abstract. Observations of the Australian National Antarctic Research Expedition at Wilkes in 1959 indicate two features of auroral behavior similar to that observed at other stations on the poleward side of the isoaurora of maximum frequency: (1) diurnal variation of overhead occurrence exhibits evening and morning maxima, and (2) homogeneous auroras tend to be aligned in the sun-earth line. The observations do not indicate the existence of an inner auroral zone within the field of view of Wilkes station. Directions of transverse movement of auroras tend to be westward, but velocities are not accounted for by a simple orientation-fixed model.

Introduction. Observations of the aurora at stations inside the southern auroral zone have been presented by *Malville* [1959] and by *Hatherton and Midwinter* [1960]. This paper presents other polar-cap observations, obtained at Wilkes (see Fig. 1) by the 1959 Australian National Antarctic Research Expedition. The observations were obtained with an all-sky camera, making one exposure of 40 seconds each minute on 16-mm Tri-X film. Supplementary visual observations were made, usually at 15-minute intervals.

General observations. Most auroras observed at Wilkes were arcs, bands, or rays. There was a complete absence of pulsating auroras, frequently observed near the maximum frequency isoaurora (ANARE logs, Macquarie Island), and of flaming aurora. To one who has observed auroras near the auroral zone there is a strong selective impression that, in general, auroras at Wilkes were much less bright, but of more variable form, than those farther north.

Auroras may appear in some part of the sky during any of the dark hours between 1600 and 0700 hours LT. A regular feature is that at midnight relatively bright green rays or red bands, sometimes accompanied by glow, appear near the horizon about azimuth 340° , which is the direction of the portion of the auroral zone closest to Wilkes (Fig. 1). The display then moves above the horizon and is usually as multiple rayed bands subject to frequent changes of shape, and sometimes accompanied by homogeneous bands. Parts of the display may occur over the station's zenithal region. The display sometimes becomes weaker in intensity, and after about an hour it may disappear completely.

Figure 2 shows the diurnal variation of frequency of occurrence of 'overhead' auroras (i.e., auroras whose plan position is within a great circle distance of 1.5° of the station, auroral lower border height assumed to be 105 km), calculated as the percentage of dark hours in which cloud cover was $\leq \frac{3}{8}$, and during which overhead aurora was observed. Also shown are diurnal variations for 1957 and 1958, obtained from a coded list of the original visual observations, made by observers from the United States, and supplied by Professor C. W. Gartlein.

Although the frequencies of occurrence for a given hour during 1957 and 1958 are greater than those for 1959, all three curves exhibit morning (0600–0700 hours) and evening (1600–1700 hours) maxima. Bimodal distributions for polar-cap stations have been reported for Scott Base and Hallett [*Hatherton and Midwinter*, 1960] and for South Pole [*Malville*, 1959], although in the latter instance the variation was calculated for all auroras visible from the station. *Davis* [1960] reported a bimodal diurnal variation for Resolute Bay, on the northern polar cap. *Mawson* [1925] found that at Cape Denison (Fig. 1) in 1912 and 1913 the diurnal variation of all auroras visible had maxima at 1800 and 0600 hours, and also at 2300 hours. In Figure 2 there is a suggestion of a near-midnight maximum, probably due to contributions from the previously described midnight display originating to the NNW.

In 1959 auroras were rarely observed farther than 2° from Wilkes in the region of the sky from south-west through south to south-east. Aurora that did occur in the southern sky was usually part of a form that also extended into the northern sky. *Aver'yanov* [1959] has suggested

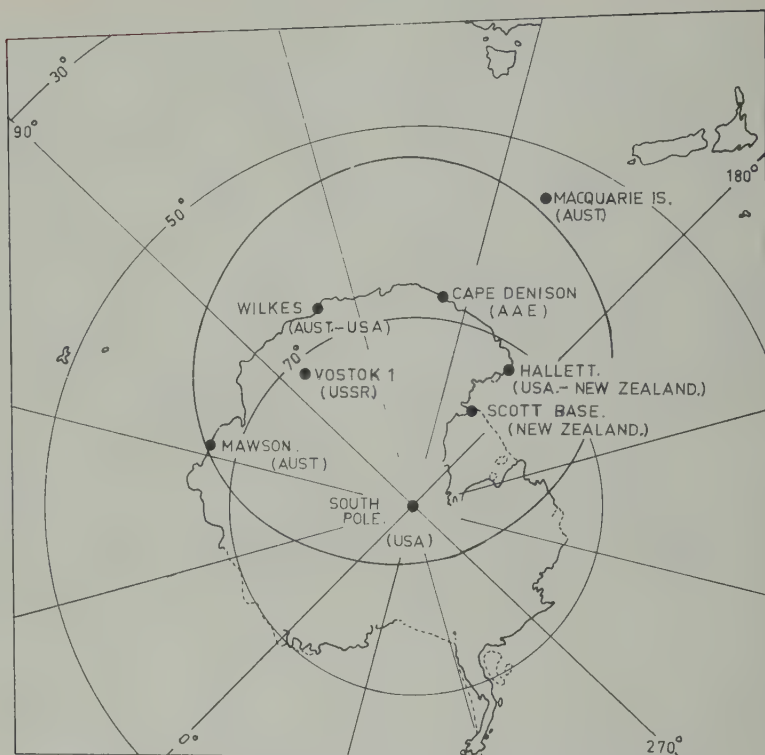


Fig. 1. Antarctic stations relative to maximum frequency isoaurora [Bond and Jacka, 1960].

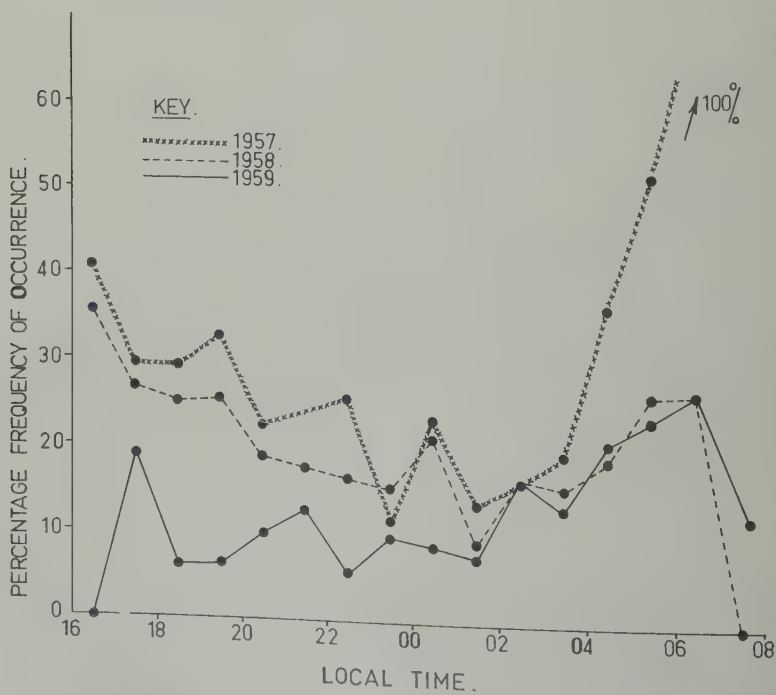


Fig. 2. Diurnal frequency of overhead aurora at Wilkes.

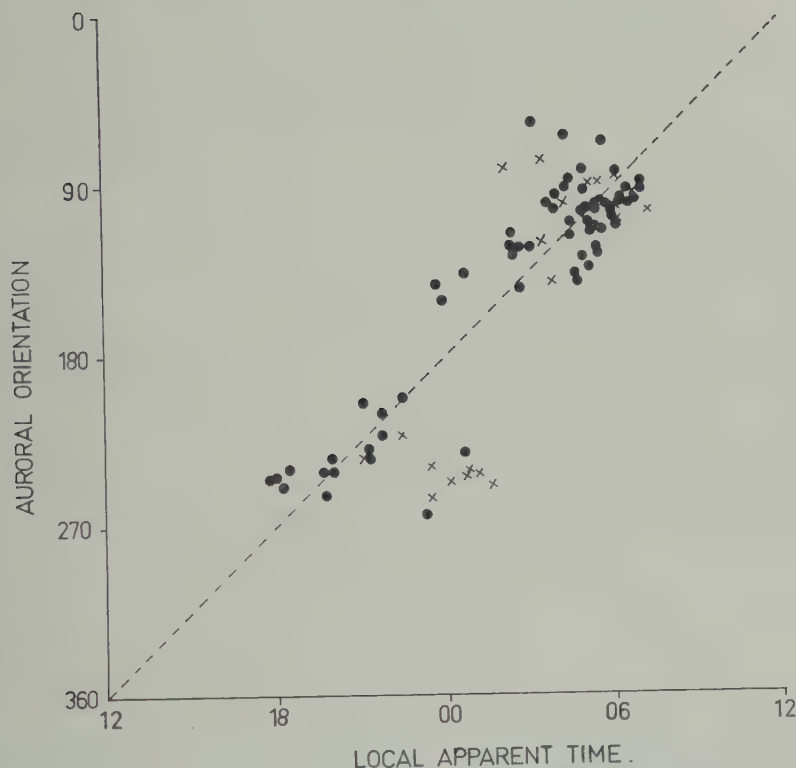


Fig. 3. Plot of auroral orientation against time, Wilkes 1959. Closed circles are orientations measured within 3° of Wilkes, crosses are observations measured farther than 3° from Wilkes. Dotted line represents annual mean azimuth of sun.

the observations at Vostok 1 ($72^\circ 08'S$, $5^\circ E$) in 1957 indicate an inner auroral zone at Vostok 1. The auroras in such an inner zone should be visible from Wilkes in the low northern and south-western sky, but in 1959 there was no auroral occurrence or behavior in this portion of the sky suggestive of an inner zone. Indeed, this region of the sky was remarkable for its paucity of auroras.

Color. When color was discernible it was usually the normal auroral green; weaker auroras appeared in the usual grayish-white. Red aurora was observed on two occasions. On July 1, 1959, between 1005 and 1100 UT, a bright 'diffuse surface' was present in the northern sky, and on May 8, 1959, between 1100 and 1115 UT, a faint red glow was observed near the NW horizon. At these times K_p was 9 and 5, respectively, and the local K indices 7 and 4, respectively.

At 1630 UT on August 7, 1959, a homogeneous aurora of unusual coloring was observed at about

5° elevation between azimuths 290° and 340° . This aurora was a brilliant white, with a red lower border (Type B) and of visual intensity comparable with that of the moon. (The observer has no defect of color vision.) A possible explanation for the bright white portion without visual trace of green or other coloration above the lower border is that the oxygen red doublet 6300/6364 Å, the violet nitrogen bands at 3914 and 4278 Å, and the green oxygen line at 5577 Å were present in such relative intensities as to appear white to the eye. The white appearance lasted only about 1 minute, then deteriorated into the usual auroral green. This bright green homogeneous band, without red lower border, persisted in the low NW sky until about 1745 UT.

An automatic patrol spectrograph (Perkin-Elmer, IGY model), aligned north-south, was operated at Wilkes during 1959 on nearly every night between February 18 and October 31. Two qualitative observations from the spectrograms are of interest.

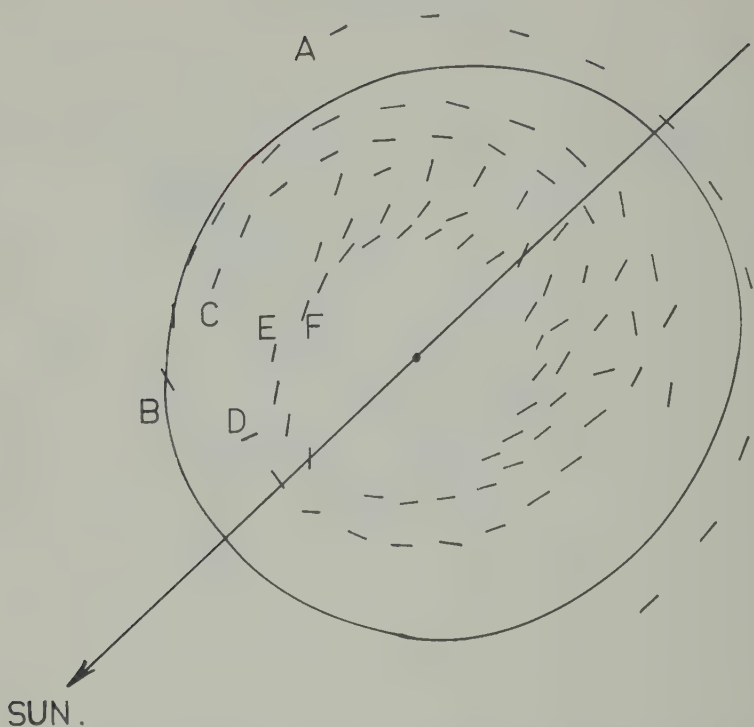


Fig. 4. Hourly mean orientations at Antarctic stations plotted in system centered on eccentric dipole axis and orientation-fixed relative to sun. Stations: A, Macquarie Island, 1957-1958; B, Mawson, 1958; C, Point 3° SE of Mawson, 1958; D, Hallett, 1957-1958; E, Scott Base, 1957-1958; F, Wilkes, 1959. The closed curve is the isoaurora of maximum frequency.

1. During auroras there was always enhancement of the nitrogen bands 3914 and 4278 Å.

2. H α was recorded on the following exposures only: April 14, 1959, between 1122 and 1302 UT; July 24, 1959, between 1212 and 1352 UT; August 1, 1959, between 2108 and 2248 UT. In the first and last instances H α was recorded over the whole field of view of the spectrograph ($180^\circ \times 2^\circ$). In the second instance H α was present only in the low north, below about 25° elevation. Auroral displays, consisting of homogeneous bands and rayed bands were present during the exposures.

Orientations. Following the earlier work of Mawson [1925] and Weill [1958], it has been shown [Denholm and Bond, 1961] that, at stations well inside the maximum frequency isoaurora, the orientation of homogeneous auroras tends to be toward the sun. The orientations of all simply shaped homogeneous auroras observed from Wilkes in 1959 are plotted against local apparent time in Figure 3. The orientations of

auroras within 3° of Wilkes are distinguished from those of auroras further away. The auroras have been plotted on synoptic maps, and orientation was measured as the angle from geographic north to the tangent to the plan position of the aurora, clockwise being taken as positive. It can be seen that most of the orientations are grouped about the sun-earth line, but near midnight there are a few points well off this line. Inspection of data shows that all except two of the points in this midnight group are about 5° from Wilkes and between Wilkes and the auroral zone. If the orientation variation phenomenon is a consequence of an auroral pattern fixed in orientation relative to the sun, then the anomalous orientation of these northerly auroras may be interpreted as being due to auroras lying along portions of pattern lines that are inclined at about 60° to the pattern lines over Wilkes.

In Figure 4 hourly mean orientations of auroras within 3° of Wilkes are plotted with hourly mean orientations at some other Antarctic

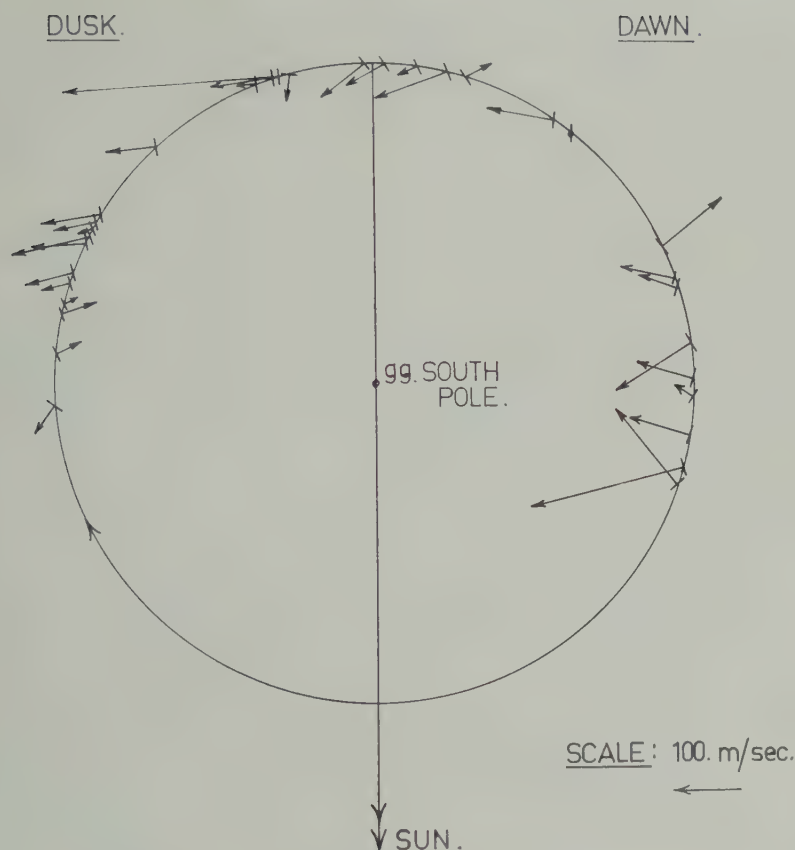


Fig. 5. Normal velocities of auroras plotted on path of Wilkes about South Geographic Pole.

ions. The diagram represents a system (in
mutual equidistant projection) fixed in orienta-
relative to the sun but centered on the
centric dipole axis (75°S , 120°E). The pattern
Figure 4 is consistent with one in which the
ora lies along lines of flow of a disturbance
rent system [Cole, 1960] similar to the current
tems given for the northern hemisphere by
tine, Lange, Laporte, and Scott [1947] and, in
alized form, by Chapman [1956] and is also
sistent with the pattern found near the
thern auroral zone by Davis [1960]. The plot
Figure 4 suggests that the lines of the pattern
r the polar cap, at least as far inside the zone
Wilkes, are curved, whereas the polar-cap
s of flow in the systems of Vestine, Lange,
orte, and Scott [1947] are straight lines (in
jection). The proposed current systems in
s region were, however, based on sparse
agnetic data.

Transverse velocities of auroras. In Figure 5
the observed velocities v of overhead quiet forms
in directions normal to their alignment are
plotted on the path of Wilkes station about the
geographic South Pole. Only 29 records suitable
for velocity measurement were found in the 1959
data, so the 1960 records were examined with
the hope of increasing the sample; however, only
3 more suitable records were found. These have
been included in the velocity analysis. Of the
32 measured velocities 27 are in the sense con-
trary to the earth's rotation, 4 are in the same
sense as the earth's rotation, and 1 is zero.

If an orientation-fixed auroral pattern such
as that discussed in the previous section is
centered on a fixed pole G , the (normal) auroral
velocity v (in degrees of arc/min) is given by

$$v = \omega \sin \phi \cos \alpha = \omega \sin \phi \cos (\beta + \theta)$$

where ω is the angular velocity of earth's rota-

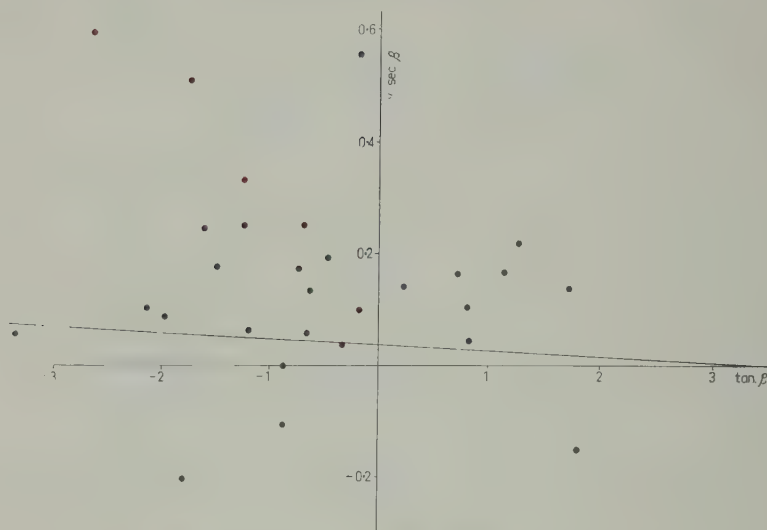


Fig. 6. Plot of $v \sec \beta$ against $\tan \beta$ (β = auroral orientation, v = normal velocity). Straight line is that expected for orientation-fixed pattern centered on eccentric dipole axis. (Note: four available points are not plotted owing to their great distance from the origin.)

tion, ϕ is the aurora's colatitude measured from the pole G , α is the auroral orientation relative to the meridian through the pole G , β is the auroral orientation relative to the geographic meridian, and θ is the angle between the two meridians. We find then

$$v \sec \beta = C + S \tan \beta$$

where $C = \omega \sin \phi \cos \theta$, and $S = \omega \sin \phi \sin \theta$.

In Figure 6 $v \sec \beta$ is plotted against $\tan \beta$. The straight line represents the expected relation for an orientation-fixed auroral pattern with its center G on the eccentric dipole axis. It is apparent that the observations do not fit this simple model. The observed velocities are on the whole substantially greater (westward) than expected.

Discussion. It is difficult to compare in detail the various published diurnal variations of auroral occurrence at polar-cap stations, because different authors have used different criteria. The diurnal variation at Wilkes agrees qualitatively, however, with published observations from other polar-cap stations in exhibiting evening and morning maxima. It seems likely that the times of maximum occurrence may be different at different stations.

The restriction of considering only the region within 1.5° of the zenith brings out the bimodal nature of the local diurnal variation; a diurnal

variation of *all* auroras visible would exhibit an additional maximum near midnight due to auroras between Wilkes and the auroral zone. The diurnal variation of all auroras observed at Cape Denison [Mawson, 1925], which is at about the same distance as Wilkes from the maximum frequency isoaurora, exhibits a pronounced near-midnight maximum in addition to the evening and morning maxima. The azimuth distribution of aurora observed at Cape Denison shows that, by far, most auroras were observed between the station and the maximum frequency isoaurora. Few auroras were seen in the southern half of the sky.

The orientation data from Wilkes and other southern stations give further evidence in favor of an auroral orientation pattern similar in form to proposed disturbance current systems, although auroral velocities are not explained by this simple model. It should be noted that the lines of flow over the polar cap in these systems [Vestine, Lange, Laporte, and Scott 1947] can assume different orientations relative to the sun during different disturbances. This gives a possible interpretation of the scatter in the orientation-time plot (Fig. 3).

Curvature of the pattern lines would give rise to nonlinearity in the orientation-time plot.

Acknowledgements. I am grateful to Major F. R. Bond, Dr. F. Jacka, and K. D. Cole of this Division

ful discussion and criticism, and to Geos Division, D.S.I.R., New Zealand, for permission to use data from the Hallett and Scott Base logs. The all-sky camera at Wilkes is the property of the U. S. Air Force Cambridge Research Center which also supplied the film.

REFERENCES

anov, V. G., Preliminary auroral results from tok 1, *Bull. Soviet Antarctic Expedition*, 5, 46-49, 1959.

F. R., and F. Jacka, Distribution of auroras in the southern hemisphere, *Australian J. Phys.*, 13, 610-612, 1960.

nan, S., *Vistas in Astronomy*, 2, Pergamon Press, London, p. 912, 1956.

K. D., A dynamo theory of the aurora and magnetic disturbance, *Australian J. Phys.*, 13, 449-497, 1960.

T. N., The morphology of the polar aurora, *Geophys. Research*, 65, 3497-3500, 1960.

Denholm, J. V., and F. R. Bond, Orientation of polar auroras, *Australian J. Phys.*, 14, 193-195, 1961.

Hatherton, T., and G. G. Midwinter, Observations of the aurora Australis at New Zealand Antarctic stations during IGY, *J. Geophys. Research*, 65, 1401-1411, 1960.

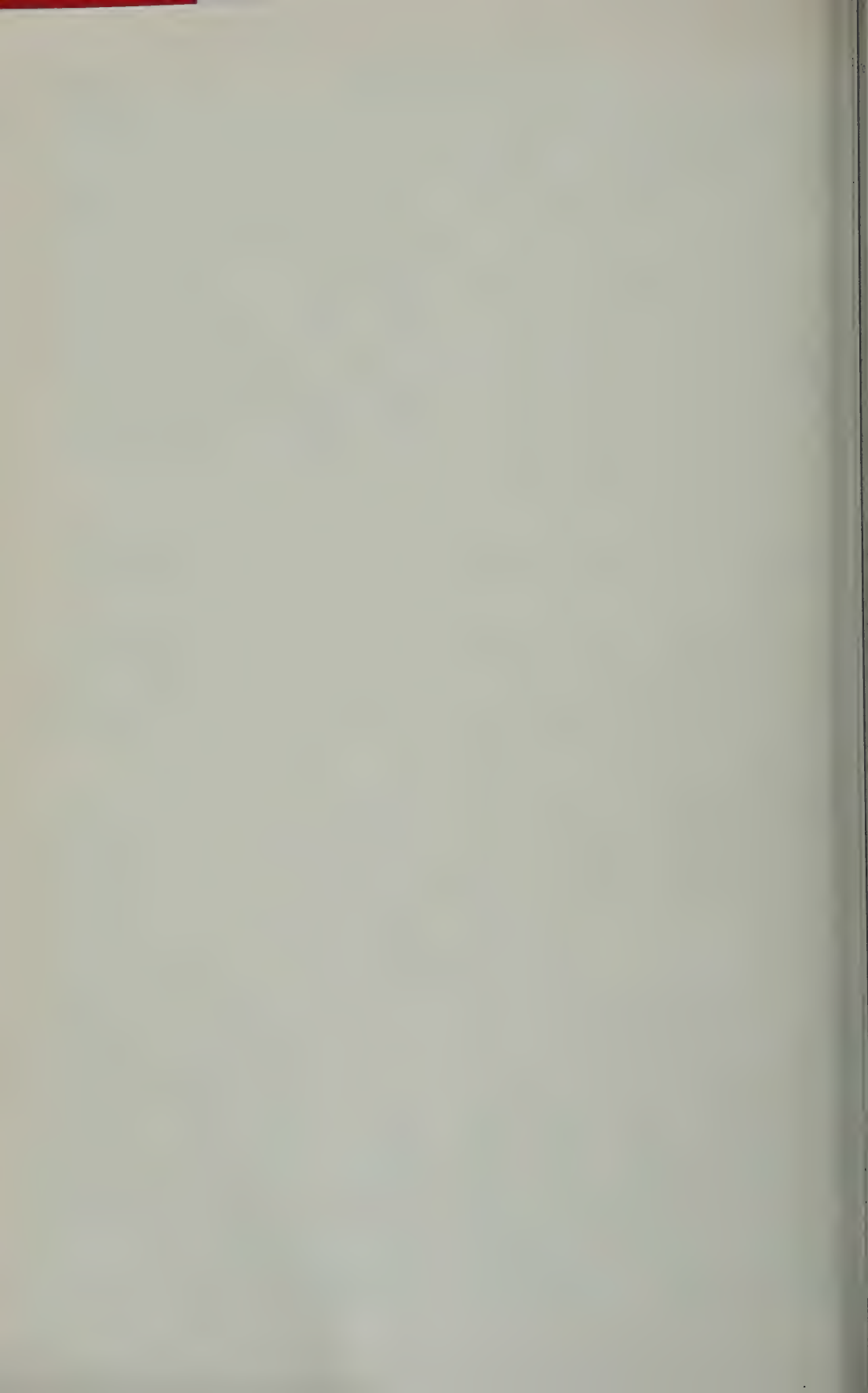
Malville, J. M., Antarctic auroral observations, Ellsworth Station, 1957, *J. Geophys. Research*, 64, 1389-1393, 1959.

Mawson, D., Records of the Aurora Polaris, Australasian Antarctic Expedition 1911-1914, *Sci. Rept. B*, 11, 1925.

Vestine, E. H., I. Lange, L. Laporte, and W. E. Scott, The geomagnetic field, its description and analysis, *Carnegie Inst. Washington Publ.* 580, Washington, D. C., 1947.

Weill, G., Aspects de l'aurore observée à la base Dumont d'Urville en Terre Adélie, *Comptes rend.*, 248, 2925-2927, 1958.

(Manuscript received April 14, 1961.)



Equatorial Spread F in Relation to Post-Sunset Height Changes and Magnetic Activity

M. S. V. GOPAL RAO AND B. RAMACHANDRA RAO

*Ionospheric Research Laboratories, Andhra University
Waltair, India*

Abstract. Equatorial spread F , magnetic activity, and post-sunset rise in $h'F$ are studied in detail as three parameters, and correlations in the variations in each of the three pairs are examined for all the seasons. Partial correlations are sought to examine the independent influence of magnetic activity and $h'F$ changes on spread F . It is observed that the time of maximum spread F on each night is effectively controlled by the magnitude of the $h'F$ change between 1800 and 1900 LT. The results are discussed in the light of the recent theory of spread F outlined by Martyn.

INTRODUCTION

Large changes in the F -region heights in the evening hours, especially during equinoctial months, are an important equatorial feature. In their early studies of Huancayo data, *Walker and Wells* [1938] observed that the onset of spread F was closely correlated with a marked rise of 100 km or more in the height of the F region between 1800 and 2000 LT. A significant positive correlation of the day-to-day variations in peak spread F index (read from the nocturnal spread- F curves of individual nights) with the rise in F -region height between 1800 and 1900 LT had been reported from the preliminary data of Waltair ($17^{\circ}43'N$, $83^{\circ}18'E$) by *Rao, Rao, and Martyn* [1960]. The occurrence of spread F has also been shown by *Lyon, Skinner, and Wright* [1958] to be closely associated with geomagnetic activity, the correlation being strong and positive at moderate to high latitudes and strong and negative at low latitudes. In a recent note, *Martyn* [1959a] has invoked the vertical drift of the ionized medium to explain the origin of E_s , spread F , and radio-star scintillations. He has outlined a preliminary theory for the origin of spread F based on the upward electrodynamic drift of the F region [*Martyn*, 1959b]. Further, he has indicated that the association of spread F with magnetic activity may be traced from the connection between the magnetic activity and F -region height changes.

In view of these recent developments leading toward a better understanding of the origin of the spread- F phenomenon, it is necessary that these effects be studied in greater detail at

different locations. The quantitative nature of the spread- F index (0-10) adopted by us for Waltair data permits such a study. This paper is intended to present some statistical estimates of the different parameters, utilizing the data accumulated from November 1958 through March 1960. The various parameters considered in this investigation are: $h'F$ (minimum virtual height of the F region measured at about 2 Mc/s); its changes, $\Delta h'F$, with time (1800 to 1900 LT); average spread- F index in the first half of the night; peak value of spread- F index before 0000 hours irrespective of its time of occurrence; and the three hourly indices of geomagnetic activity recorded at Colaba Observatory, Bombay (geomag. lat. $9.5^{\circ}N$). $h'F$ can also be considered a sensitive index for height variation of the F region as was pointed out by *Martyn* [1959b].

RESULTS OF PRELIMINARY ANALYSIS

The data for the total period are grouped into nights of 0 index or without spread F , and nights having average spread- F indices in the ranges 0-1, 1-2, 2-3, etc. The average $\Delta h'F$ (1800-1900 hours) connected with all these groups of days is presented in Figure 1. Similarly, the sum of the K indices of magnetic activity of the corresponding days averaged for all the connected groups of days is shown in Figure 2. These figures clearly indicate the relationship between spread F and the evening height changes of F region, on the one hand, and magnetic activity on the other. All nights free from spread- F incidence showed on the average only 29 km of

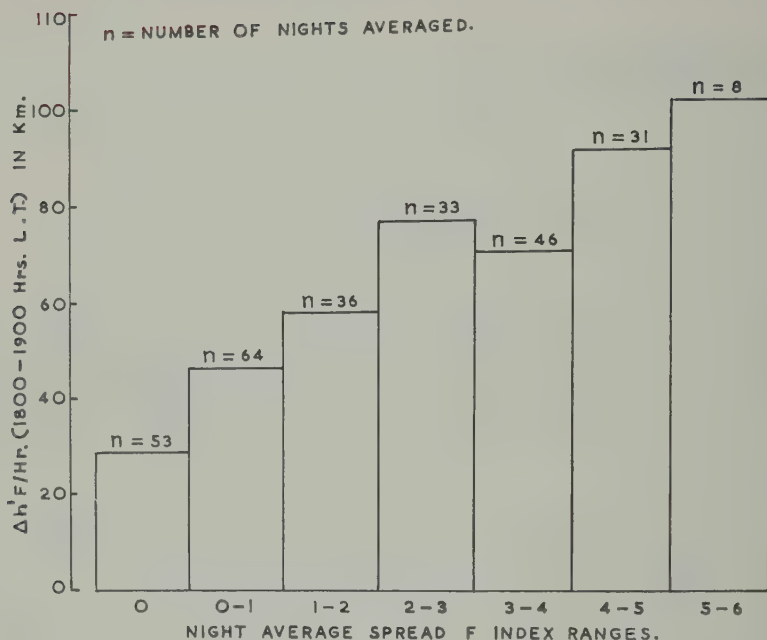


Fig. 1. Averaged values of $\Delta h'F$ (1800-1900 LT) vs. spread- F index.

$\Delta h'F$ (1800-1900 hours), and these nights are also associated with an average ΣK index of 25. The figures suggest fairly good linear relations. However, the diagrams are only indicative of the general trend and cannot be regarded as showing strong correlations, owing to the presence of large deviations of individual values from each of the mean values obtained. A detailed study of the correlations is therefore necessary; it is given in a later section.

INFLUENCE OF MAGNETIC ACTIVITY AND $\Delta h'F$ (1800-1900 HOURS) ON SPREAD- F NOCTURNAL VARIATION

From a survey of a number of nocturnal spread- F variation curves it appeared that, apart from the reduction or enhancement of spread F , on the average, with the changes in the above two parameters, the nature of the nocturnal variation showed some changes in the timing of the peak spread- F index.

With a view to studying this aspect, observations for some 12 nights having spread- F occurrence associated with relatively high magnetic K index have been separated out, and the averaged nocturnal variation has been obtained. Similarly, some 12 other nights with spread- F

occurrence, but associated with reduced magnetic activity, are also separated out, and the averaged nocturnal variation is obtained. Both curves are shown in Figure 3. It will be seen from this figure that the time of maximum spread F (which generally occurred in the first half of the night) on disturbed days is delayed by about 1 hour as compared with that on the quiet days. But this situation is reversed in the peaks occurring in the latter half of the night. These curves, however, are based on the data of only a few nights, and therefore are merely indicative, not conclusive. As there are enough data covering the premidnight period, detailed examination into this delaying action of the peak spread- F index is made separately for the two halves of the year from February 7 to August 7, 1959, covering vernal equinox and north solstice seasons, and from August 7, 1959, to February 7, 1960, covering autumnal equinox and south solstice seasons. The data are further divided into two groups of days according as K index over a day is less or greater than 17, to study the effect of low or high magnetic activity, respectively. Similarly the data are divided into two groups of days according as $\Delta h'F$ is less or greater than 60 km, to study the effect of this parameter on

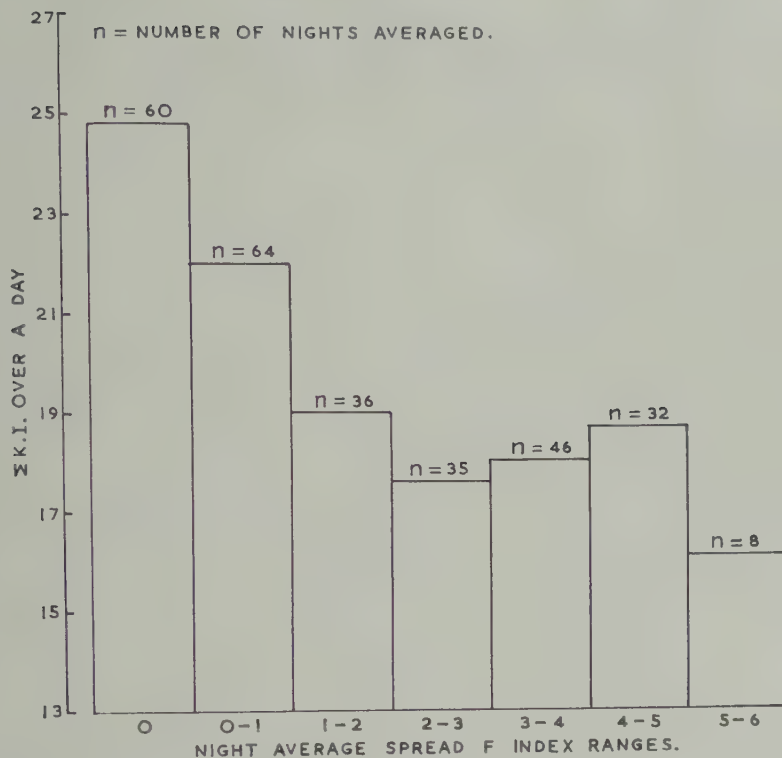


Fig. 2. Averaged values of ΣK index vs. spread- F index.

nocturnal spread- F variation. The results shown in Figure 4. The number of nights (n) to obtain each average variation is shown in the figure. From these comparisons it is clearly clear that the time of peak spread- F occurring in the first half of the night is closely connected with $\Delta h'F$ and not with magnetic activity. It can be safely concluded that peak spread F occurs earlier and later on nights showing larger and smaller rise, respectively, in $h'F$ in the evening hours and between 0 and 1900 LT.

DETAILED STUDY OF CORRELATIONS

In view of the distinct seasonal characteristics observed at this station, the data are analyzed by dividing them into the four seasons: vernal, summer, autumnal equinoxes, north and south solstices. For each period correlations were sought between the following pairs of variates:

1. Average spread- F index of first half of each night vs. $\Delta h'F$ of the corresponding evening.
2. The peak spread- F index attained on each

night (irrespective of the time of occurrence) vs. $\Delta h'F$.

3. Spread- F index attained at 2000 LT on each night vs. $\Delta h'F$.

4. Average magnetic K index corresponding to the first half of each night vs. spread- F index averaged for the same hours.

5. ΣK index over a complete day vs. average spread- F index of the corresponding night.

6. ΣK index over a day vs. peak spread- F index of the corresponding night.

7. ΣK index over a day vs. spread- F index at 2000 LT.

8. Average magnetic K index in the hours of the first half of night vs. $\Delta h'F$ of the corresponding evening.

9. ΣK index over a day vs. $\Delta h'F$.

10. ΣK index over a day vs. $h'F$ observed at 1900 LT on the corresponding evening.

11. $h'F$ at 1900 LT vs. average, or peak, or 2000 hours spread- F index, whichever gives best correlation coefficient in 1, 2, 3 with $\Delta h'F$.

To each of the observed values of correlation

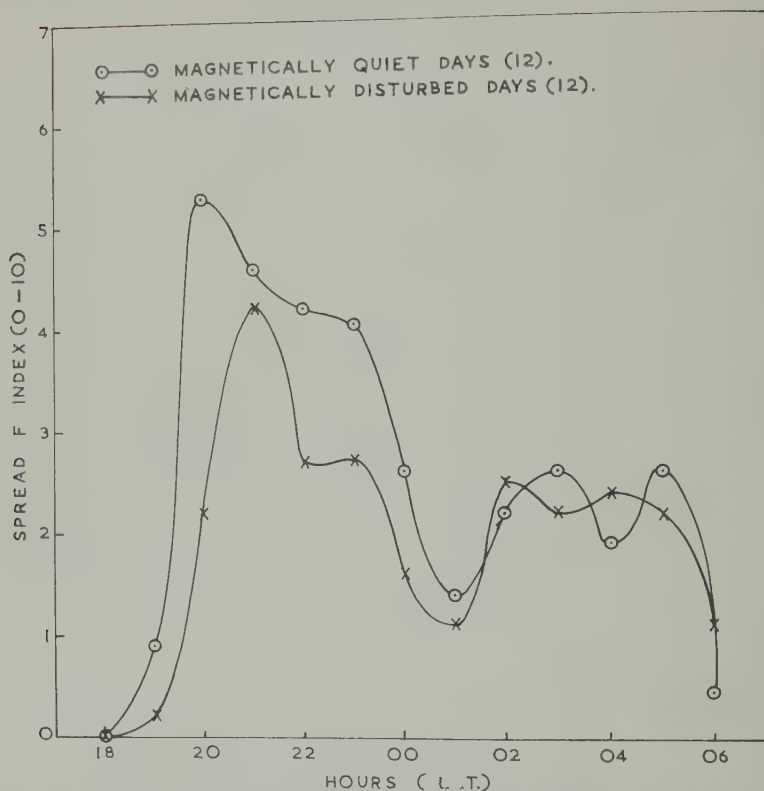


Fig. 3. Nocturnal variation of spread F on magnetically disturbed and quiet days.

coefficient (r) is attached a standard error σ obtained by $(1 - r^2)/(N - 1)^{1/2}$, where N is the total number of pairs considered in obtaining each r . Each correlation coefficient is tested for its significance at $P = 0.01$ and $P = 0.05$ levels following Fisher [1946]. All the coefficients are given in Tables 1 to 4. The serial numbers 1 to 11 in these tables correspond to the pairs described and listed above. The significant coefficients are indicated by asterisks and insignificant ones by dashes.

The results of all four periods may be summarized as follows.

1. *Vernal equinox.* (a) The value of $\Delta h'F$ is better correlated positively with the peak spread- F index as compared with either the night average or 2000 hours values of spread- F index. The difference between coefficients 1 and 2 is significant (as per Z transformation test), whereas that between 2 and 3 is insignificant.

(b) Coefficients 4 and 5 are insignificant although negative. From 6 and 7 it appears that the peak spread- F index is better correlated

negatively with ΣK index than 2000 hours spread- F index with ΣK index, although the difference is statistically insignificant.

(c) Coefficients 8 and 9 indicate that $\Delta h'F$ has significant negative correlation with magnetic activity.

(d) Coefficients 10 and 11 show that the value of $h'F$ observed at 1900 hours is also significantly correlated negatively with magnetic activity and positively with the peak spread- F index.

(e) Use of coefficients 2, 6, and 9 yields a partial correlation coefficient of 0.54 between $\Delta h'F$ and peak spread- F index eliminating the effect of magnetic activity, and a partial correlation coefficient of -0.43 is obtained between ΣK index and peak spread- F index eliminating $\Delta h'F$. Both these values are significant even at $P = 0.01$. These partial correlation coefficients are calculated using the expression

$$r_{12.3} = \frac{r_{12} - r_{13}r_{23}}{\sqrt{(1 - r_{13}^2)(1 - r_{23}^2)}}$$

where the suffixes 1, 2, and 3 indicate the three

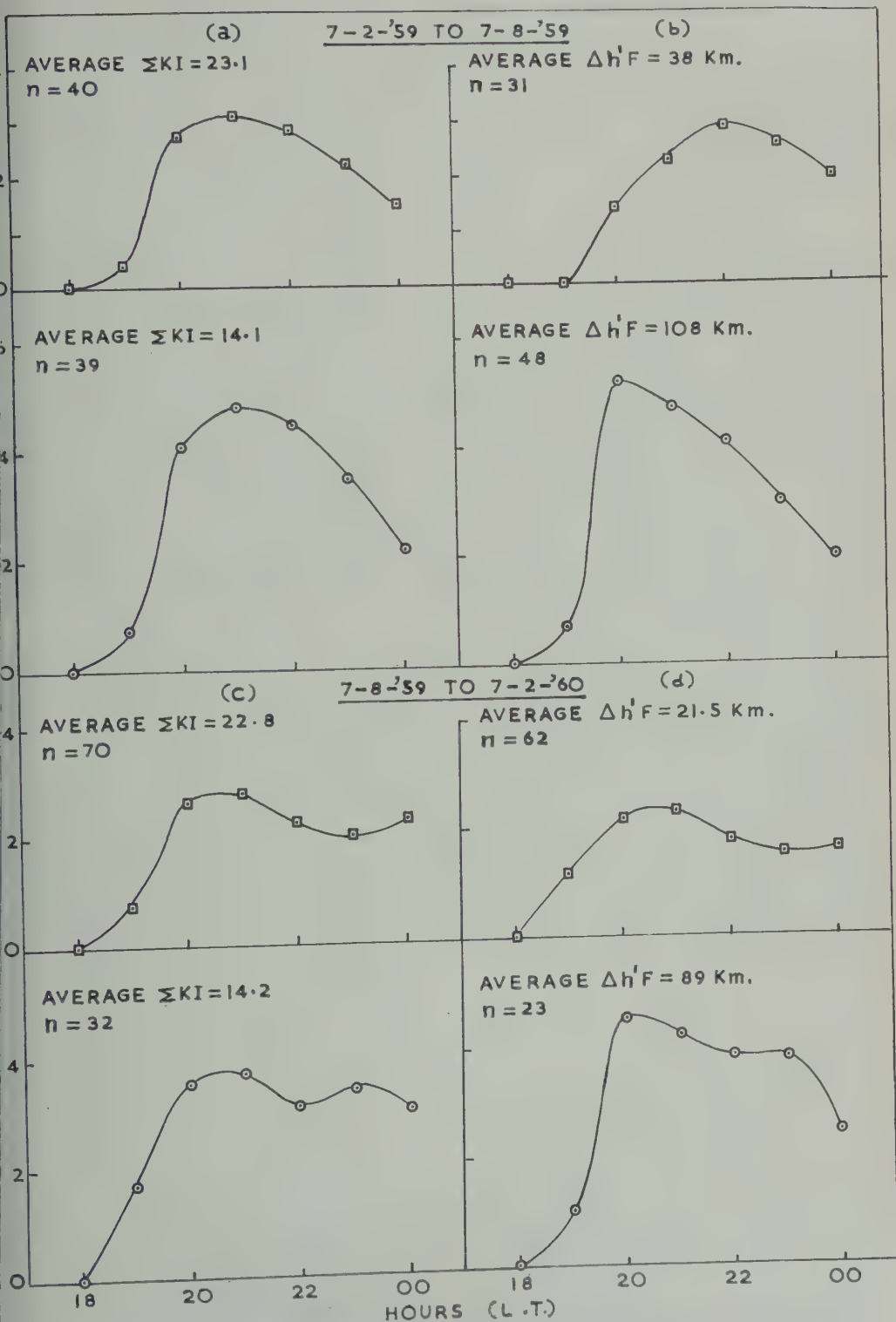


Fig. 4. Nocturnal variation of spread F as affected by magnetic activity and $\Delta h'F$ (1800-1900 LT).

TABLE 1. Vernal Equinox

Sl. No.	r	σ	$P = 0.01$	$P = 0.05$
1	+0.256	± 0.13	—	*
2	+0.610	± 0.09	*	
3	+0.498	± 0.11	*	
4	-0.224	± 0.12	—	—
5	-0.240	± 0.13	—	—
6	-0.520	± 0.10	*	
7	-0.420	± 0.12	*	
8	-0.392	± 0.12	*	
9	-0.330	± 0.13	*	
10	-0.440	± 0.10	*	
11	+0.560	± 0.10	*	

parameters of which any two have correlation coefficients r_{12} , r_{23} , r_{31} ; and $r_{12.3}$ denotes the partial correlation between 1 and 2 when 3 is eliminated.

2. *North solstice.* (a) Coefficients 1, 2, and 3 show that in this season $\Delta h'F$ is not significantly correlated with spread- F index.

(b) Correlation of spread F with magnetic activity, although negative, is not generally significant except in the case of 5 in which ΣK index is considered.

(c) Coefficients 8 and 9 show positive correlation between $\Delta h'F$ and magnetic activity; of these, only 8 is significant at $P = 0.05$.

(d) Although coefficient 11 is apparently better than 3, the difference between the two is insignificant.

(e) Using coefficients 1, 5, and 9, partial correlation of ΣK index vs. night average spread- F index is obtained as -0.405 (eliminating variations in $\Delta h'F$), which is significant at $P = 0.02$. The partial correlation of $\Delta h'F$ vs. spread F is obtained as 0.131 , which is insignificant.

3. *Autumnal equinox.* (a) Coefficients 1, 2, and 3 show that in this season, also, the correlation between $\Delta h'F$ and spread F is generally insignificant, although positive.

(b) Coefficients 4, 5, 6, and 7 indicate strong and significant negative correlation between spread F and magnetic activity. The difference between 4 and 7 is significant, showing that ΣK index is better correlated negatively with 2000 hours spread- F index than the average spread- F indices with average K index.

(c) Coefficients 8 and 9 are not significant, but slightly positive.

(d) Use of coefficients 2, 6, and 9 yields partial

correlation between ΣK index and peak spread- F index as -0.59 (eliminating $\Delta h'F$), and partial correlation between $\Delta h'F$ and the peak spread- F index is obtained as $+0.26$ (eliminating magnetic activity).

4. *South solstice.* (a) Coefficients 1, 2, and 3 indicate that, again, in this season, $\Delta h'F$ is showing strong positive correlation with spread- F index in general and with peak spread- F index in particular.

(b) Coefficients 4, 5, and 6 are quite insignificant, but the coefficient 7 indicates that ΣK index has somewhat significant negative correlation with 2000 hours spread- F index.

(c) Coefficients 8 and 9 suggest positive correlation between magnetic activity and $\Delta h'F$.

(d) The difference between 2 and 11 is not significant, although it is apparently better.

(e) Use of coefficients 3, 7, and 9 yields partial correlation of magnetic activity ΣK index with 2000 hours spread- F index as -0.42 (significant) and partial correlation of $\Delta h'F$ with 2000 hours spread- F index (eliminating magnetic activity) as $+0.4$.

DISCUSSION OF THE RESULTS

From the foregoing results it is clear that there are important differences in the strength of association between spread F and either magnetic activity or F -region height changes. Broadly speaking, at this station the negative correlation of spread F with magnetic activity is strong in autumnal and vernal equinoxes in order, and moderate during north solstice and poor during south solstice. The positive correlation of spread F with the evening rise in $h'F$ is strong during south solstice and vernal equinox (a continuous period of 6 months) and poor

TABLE 2. North Solstice

Sl. No.	r	σ	$P = 0.01$	$P = 0.05$
1	+0.057	± 0.17	—	—
2	-0.180	± 0.16	—	—
3	+0.210	± 0.16	—	—
4	-0.230	± 0.16	—	—
5	-0.390	± 0.14	—	*
6	-0.300	± 0.14	—	—
7	-0.170	± 0.16	—	—
8	+0.320	± 0.15	—	*
9	+0.160	± 0.16	—	—
10	+0.170	± 0.16	—	—
11	+0.380	± 0.14	—	*

TABLE 3. Autumnal Equinox

Sl. No.	r	σ	$P = 0.01$	$P = 0.05$
1	+0.098	± 0.14	—	—
2	+0.200	± 0.13	—	—
3	+0.180	± 0.14	—	—
4	-0.360	± 0.12	*	—
5	-0.600	± 0.09	*	—
6	-0.570	± 0.10	*	—
7	-0.760	± 0.06	*	—
8	+0.020	± 0.14	—	—
9	+0.030	± 0.13	—	—
10	+0.210	± 0.14	—	—
11	+0.099	± 0.14	—	—

g the remaining 6 months. Further, the ionizing action of magnetic activity on spread F could not be indirect, owing to its effect in changing $\Delta h'F$ as evidenced from the partial correlation coefficients. Thus, it is necessary to look for other ways in which the magnetic activity affects spread F .

Capman [1935] has shown that the spherical coordinate system D corresponding to the average magnetic disturbance may be analyzed into a symmetrical about the earth's axis, and an asymmetrical part S_D in which there will be a resultant flow along the circles of latitude. Viewed from the sun the resultant currents are stronger over the post-meridian than over the ante-meridian hemisphere at low latitudes. As the earth rotates in 24 hours each station on the earth can be considered to be moving under different portions of the relatively stationary magnetic field system. Thus, ΣK index over all the hours recorded at each station may be regarded as representing more of the symmetrical part of the disturbance field, whereas the average ΣK index corresponding to only a few hours, such as 1800 to 0000 hours, would represent the asymmetrical part as affected by only one phase of the S_D variations. This may cause differences in the correlations when considered separately.

It is strikingly obvious for the period of autumnal equinox when ΣK index has shown greater influence on spread F than the average ΣK index of the corresponding night hours. Thus, during this season, the suppression of spread F by magnetic activity may be predominantly due to the magnetic storms which are known to be widespread in character with a current system symmetrical about the earth's axis. Wright and Warner [1959] recently found that at Ibadan

and some five other African low-latitude stations the spread- F conditions are effectively inhibited only during the south solstice, and the effect is found to be less pronounced during equinoxes and negligible during north solstice. There is evidently some discrepancy between these and the results from Waltair. The causes for the discrepancy are not clear.

According to the recent theory of spread F outlined by Martyn [1959b], the ionization on the undersurface of the F layer is essentially unstable if it is moving upward under the influence of electrodynamic drift. A small initial inhomogeneity, ΔN , in the ionization contours gets amplified under these conditions, and the very large inhomogeneities necessary to explain spread F may be formed. The amplification of the original inhomogeneity is shown to be directly dependent on the velocity with which the ionized medium is drifting upward. The parameter $\Delta h'F$ /hour used in the present investigation represents this velocity only partly, because the heights considered are virtual heights, and the rise in the evening hours may not be completely of electrodynamic origin. The strong positive correlations of this parameter with spread F observed during at least half the year is consistent with this theory. If spread- F irregularities are produced only due to $\Delta h'F$ /hour, which is largest between 1800 and 1900 LT, its effect may be felt with greater correspondence at the nearest hour, such as 2000 LT, because during later hours the irregularities may be carried away from their place of origin by the general horizontal drifts. Further, there will be no scope for the production of irregularities after about 1900 LT, when the F region shows mainly downward movement, and in this case spread- F

TABLE 4. South Solstice

Sl. No.	r	σ	$P = 0.01$	$P = 0.05$
1	+0.350	± 0.12	—	*
2	+0.600	± 0.09	*	—
3	+0.360	± 0.12	*	—
4	-0.029	± 0.14	—	—
5	-0.080	± 0.13	—	—
6	-0.023	± 0.13	—	—
7	-0.380	± 0.14	—	*
8	+0.370	± 0.14	—	*
9	+0.030	± 0.14	—	—
10	-0.160	± 0.14	—	—
11	+0.730	± 0.07	*	—

irregularities are smoothed out, according to Martyn. In averaging spread- F index over all the hours of a night, a variety of temporal variations are included, and hence average spread F may not show a better correspondence with $\Delta h'F$ /hour at a given location. If the spread- F index at 2000 LT is also not correlating well with $\Delta h'F$ as compared with the peak spread- F index, in spite of its delayed occurrence on some days, this would suggest that the spread F at 2000 LT is still in the growth process and is completed only at the time of peak occurrence. The poor correlations between $\Delta h'F$ and spread F during half the year, and particularly during autumnal equinox, are suggestive of some difficulty in recognizing this upward movement of the F region as the only mechanism responsible for the production of spread- F irregularities. Yet it is not unlikely that there may be appreciable day-to-day changes in the magnitudes of the initial inhomogeneity which is said to originate from an irregular polarization potential communicated to the F layer from the lower dynamo region. If these changes are independent of the main polarization field, which will be responsible for the general vertical electrodynamic drift of the ionized medium, large values of $\Delta h'F$ may not be associated with larger values of spread- F index, and a poor correlation may result.

From a continuous observation of the F -layer echoes from 1800 to 1900 LT, on several occasions it was found that, even when the F -layer height was rising rapidly, spreading of the echo did not start during the rise of the layer but commenced only after it reached a fairly high level by about 1900 hours. So it is possible to consider the

actual higher level of the F layer at 1900 hours as creating favorable conditions for the onset of spread F . In this connection it may be noted from the results of Tables 1 to 4 that the actual values of $h'F$ at 1900 hours are also equally well correlated positively with spread- F activity.

The time of maximum spread F is almost always delayed with respect to the time of maximum $h'F$. This delay is further increased strikingly on the nights associated with smaller value of $\Delta h'F$. These peculiarities of the equatorial spread F are not directly explicable from the theory of spread F outlined by Martyn [1959b] unless it is suitably modified.

Acknowledgment. We are indebted to the Council of Scientific and Industrial Research of India for the financial support of these investigations. One of the authors (M. S. V. Gopal Rao) is grateful to the Council for the award of a Senior Research Fellowship.

REFERENCES

- Booker, H. G., and H. W. Wells, *Terrest. Magnetism and Atmospheric Elec.*, 43, 249, 1938.
- Chapman, S., *Terrest. Magnetism and Atmospheric Elec.*, 40, 351, 1935.
- Fisher, R. A., *Statistical Methods for Research Workers*, Oliver and Boyd, Edinburgh, 10th edition, 1946.
- Lyon, A. J., N. J. Skinner, and R. W. Wright, *Nature*, 181, 1724, 1958.
- Martyn, D. F., *Nature*, 183, 1382, 1959a.
- Martyn, D. F., *Proc. IRE*, 47, 153, 1959b.
- Rao, M. S. V. Gopal, B. R. Rao, and P. R. Panigrahi, *J. Atmospheric and Terrest. Phys.*, 17, 345, 1960.
- Wright, R. W., and N. J. Skinner, *J. Atmospheric and Terrest. Phys.*, 15, 121, 1959.

(Manuscript received February 27, 1961,
revised April 17, 1961.)

Theory of Overhead Nonblanketing Sporadic E

JACQUES RENAULT¹

Cornell University, Ithaca, New York

Abstract. We suggest a model for overhead nonblanketing sporadic E based upon scattering from a belt (1 or 2 km in thickness) of irregularities within a stratified E layer. Predicted $h'f$ curves are compared with observed data and found to be in good agreement.

Introduction. *Whale* [1951] presented a theory of sporadic E based on the hypothesis that the ionization density of the sporadic E layer consists of outward-thrusting 'ledges' in a parabolic E layer. This theory predicts results in good agreement with the main features of the observational data. However, there is one difficulty with *Whale's* model. To comment upon this difficulty, we note that the cutoff frequency of the sporadic E of the nonblanketing type must be 15 Mc/s or higher when the penetration frequency of the regular trace is about 3 or 4 Mc/s. Thus, it is necessary that the ratio of the electron density of the largest ledge to the mean electron density of the parabolic layer be as high as 5. Furthermore, if the ledge is to be transparent for a large frequency interval, the ledge thickness will have to be less than the smallest scattering wavelength. The ledge model of nonblanketing sporadic E , therefore, requires a thin region of a few meters in thickness with an electron density as high as twenty-five times the maximum background density of the E layer. *Best, Farmer, and Ratcliffe* [1938] had previously discussed the model later used by *Whale*, and had pointed out the difficulties involved in maintaining such an electron distribution. In the following paragraphs we suggest an alternative model for sporadic E based on a scattering mechanism, the model being only applicable to sporadic echoes returned from overhead.

The concept of scattering from ionized irregularities has been proposed previously in slightly different forms [*Best, Farmer, and Ratcliffe*, 1938; *Whale*, 1950; *Eckersley*, 1932; *Gallet*, 1951; *Whale, Ratcliffe and Pawsey*, 1933; *Smith*, 1956; *Whale and Weisskopf*, 1954; *Watson-Watt*, 1933]. In these papers, the ones published before

1950 envisaged the irregularities as 'clouds' of more intense ionization immersed in a horizontally stratified region. They explained the simultaneous appearance on an ionogram of the F -region normal trace and the sporadic- E echoes (nonblanketing type) as resulting from part of the wave proceeding through the 'holes,' while that part of the waves impinging on the clouds was reflected because of the opacity of the clouds. The cutoff frequency of sporadic E was due to the ionization density of the clouds, and the cutoff frequency increased if clouds of especially dense ionization were produced. On the other hand, the above cited papers published in and after 1950 proposed that the observed echoes, for frequencies higher than the penetration frequency, were due to scattered waves from ionized irregularities consisting of electron density fluctuations of no more than a few per cent from the surrounding mean electron density. The cutoff frequency of backscattered echoes could be related to the mean size of the smallest irregularities.

The authors proposing a scattering mechanism for sporadic E have not published a theoretical analysis of the $h'f$ curves that would result from their proposed models. The sole purpose of this paper is to present an analysis of the theoretical predictions of a particular scattering mechanism and to compare those predictions with observed ionograms.

Specifically our model consists of a belt, 1 or 2 km in thickness, containing small scale isotropic irregularities of electron density imbedded in a 'normal' E layer. *McNicol* [1949] has shown that at least 50 per cent of the time the 'normal' E -region echoes consist of a steady component plus a proportion of scattered signals. Therefore, we may consider the normal E layer consisting of large-scale weak irregularities throughout a parabolic electron density profile. For all transmitted wavelengths smaller than the large-scale

¹Now at Cornell Aeronautical Laboratory, Inc., Buffalo, New York.

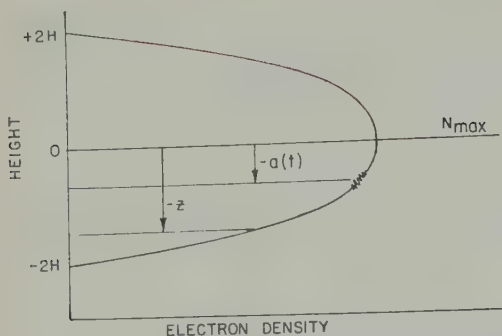


Fig. 1. Location of small scale irregularities $a(t)$ in the E layer.

irregularities, forward scattering will predominate, except at the level of reflection where backscattering will be enhanced. On the other hand, the belt of small-scale irregularities at a particular height is a good source of backscatter over the transmitted frequency range. The fluctuation of electron density of the small scale irregularities need be no more than the fluctuation associated with the large scale irregularities of the normal E region; in fact, less intense small-scale irregularities in the belt will still be sufficient. As expected, this model essentially leads to Whale's $h'f$ predictions of sporadic E . However, it is important to keep in mind that although both the belt scattering model and the ledge model used by Whale give similar results (since both models are designed to return echoes with no group retardation at frequencies high compared to the penetration frequency of the layer), the concept involved in the model adopted here differs fundamentally from the concept used by Whale. As to which of these models is more appropriate, this will have to be decided by experiment. According to the scattering model, the expected amplitude distribution of the echo will be Rayleigh-like, whereas the echo amplitude distribution based on Whale's model will be Rice-like.

Theoretical derivations of $h'f$ curves. Figure 1 is a diagram showing the belt of irregularities located at a height $a(t)$ inside a stratified E layer at a time t . We assume that the position of this scattering belt in the E region is slowly time dependent. Let the E layer have a parabolic electron density profile and the relative location of the irregularities be constant during a complete frequency sweep of the sounder (usually

15 seconds in modern ionosondes). Consider a ray of frequency f that travels in a vertical direction to a distance z inside the layer (z and $a(t)$ are measured from the height of the maximum electron density). If the operating frequency is such that the ray does not reach the height of the scatterers, then the virtual height of the ray neglecting the effect of the earth's magnetic field, is

$$ct = h_0 + 2H\rho \cdot \ln \frac{1 + \rho}{\frac{z}{2H} + \left[\left(\frac{z}{2H} \right)^2 - 1 + \rho^2 \right]^{1/2}} \quad (1)$$

where h_0 is the distance from the ground to the bottom of the E layer, $2H$ is the semithickness of the layer, and ρ is defined as the ratio of the operating frequency to the penetration frequency for that layer.

For low values of ρ the ray will travel up through the layer to a critical value $z_c \geq a(t)$ such that $(z_c/2H)^2 - 1 + \rho^2 = 0$ and 'specular reflection' will then take place. Note that z_c decreases as ρ increases. With increasing values of ρ the ray is reflected at higher and higher levels until finally it reaches the scatterers at a frequency

$$\rho_s = \left[1 - \left(\frac{a(t)}{2H} \right)^2 \right]^{1/2}$$

which depends, of course, on the position of the scatterers. For values of ρ such that $0 \leq \rho \leq \rho_s$ a normal trace will then be obtained from the layer as predicted by equation 1. For $\rho_s \leq \rho \leq \rho_{\text{max}}$ the virtual height of the $h'f$ curve will be double

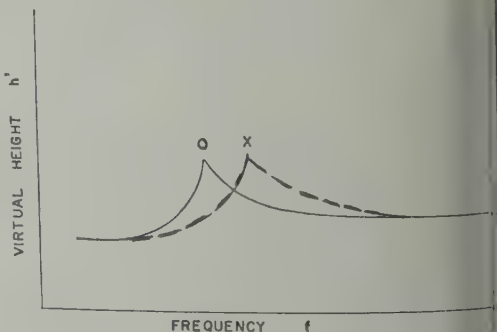


Fig. 2. Sketch of anticipated $h'f$ trace based on scattering model with scatterers at height corresponding to N_{max} .

d, one of its values being expressed by equation (1), and the other by

$$h_0 + 2H\rho \ln \frac{1 + \rho}{\frac{a(t)}{2H} + \left[\left(\frac{a(t)}{2H} \right)^2 - 1 + \rho^2 \right]^{1/2}} \quad (2)$$

is similar to equation (1) but z is replaced by $a(t)$ where $a(t)$ is constant during a frequency sweep. For $\rho_s \leq \rho \leq 1$, that part of the normal trace corresponding to echoes arriving from the belt of scatterers may not be seen if the scattering is sufficiently intense at the lower frequencies. When the operating frequency becomes lower than the penetration frequency ($\rho > 1$), the virtual height of the $h'f$ curve again becomes ρ -valued, and can be expressed by equation (2) since only the backscattered echoes contribute to the form of the $h'f$ curve.

When the scattering belt is confined to the region of maximum ionization density, no backscattering can take place until the transmitted frequency is such that $\rho \geq 1$. Only in this event the $h'f$ curve be single-valued and continuous for all values of ρ . Furthermore, when $\rho \gg 1$, the appreciable group retardation of the wave can take place; thus, the $h'f$ value of the trace corresponds to the actual distance h_s from the ground to the scattering region. The difference in height between h_s and h_0 is the height of the scattering region from the bottom of the ionospheric layer. The distance of the bottom of the E layer from the ground, h_0 , is found by taking the lowest height values of $h'f$ trace on the ionogram at the lowest value of ρ . When the scatterers are at the height of maximum electron density, the height difference, $h_s - h_0$, will then be the semithickness of the layer $2H$.

As a first approximation when the earth's magnetic field is introduced into the model, the curves bifurcate near the penetration frequency in the manner shown in Figure 2. The ordinary wave trace has been omitted from the calculations for the sake of clarity.

Comparison of theoretical predictions and observed virtual heights. Theoretical $h'f$ curves have been calculated, with scale size $H = 10$ km, for various heights of the scatterers, and the results have been plotted on an enlarged scale in Figures 3a, b, c, d, e, and f. Figure 3a is a plot for the case when the belt of scatterers is at the height of maximum ionization. Figure 3f is a plot

of the case when the scatterers have reached the bottom of the ionospheric layer. The rest of the plots correspond to intermediate positions of the belt.

We now turn to experimental data. With reference to Figure 4 the echoes arriving from a region about 100 km high have been referred to as overhead nonblanketing sporadic E . The ionograms of Figure 4 were photographed at the Panama Canal Zone Ionospheric Station on December 5, 1953. Although the phenomena lasted longer, the chosen sequence completes, for our purposes, the morphological study. The ionogram marked 1345 hours represents the case of backscattering from the level of maximum ionization density; the ionogram marked 1619 hours corresponds to the case when the scattering is from the lower region of the E layer. The ionograms photographed in the intermediate period represent intermediate positions of the scattering belt.

The ordinary penetration frequency of the E layer is clearly visible in the ionogram recorded at 1345 hours and is scaled as 3.1 Mc/s; the extraordinary penetration frequency is calculated to be approximately 3.7 Mc/s. The lower trace shown by the arrow is believed to be the extraordinary trace. The bottom of the E layer can be seen to be at about 100 km at 2 Mc/s, and the backscattered trace for frequencies greater than the penetration frequency approaches a constant height of 120 km. According to the theoretical results (Fig. 3a) the height difference of 20 km in the ionogram for 1345 hours represents the semithickness of the E layer, and the deduced scale height H of about 10 km corresponds well with the currently quoted values for the E region.

Since the descent of the scatterers from the level of reflection to the bottom of the layer takes, in this particular case, about $2\frac{1}{2}$ hours, the vertical velocity of the scattering belt is about 2.2 meters/sec relative to the E layer. During a single sweep of 15-second duration (a normal value), the relative height of the scatterers decreases by 33 meters. This then introduces an error of less than 0.1 per cent in the measurement, an error that is negligible compared with the error made in reading the heights from the observed ionogram.

Figure 5 is a further example illustrating most of the characteristics of this type of sporadic E , at a different station (Puerto Rico, December 2,

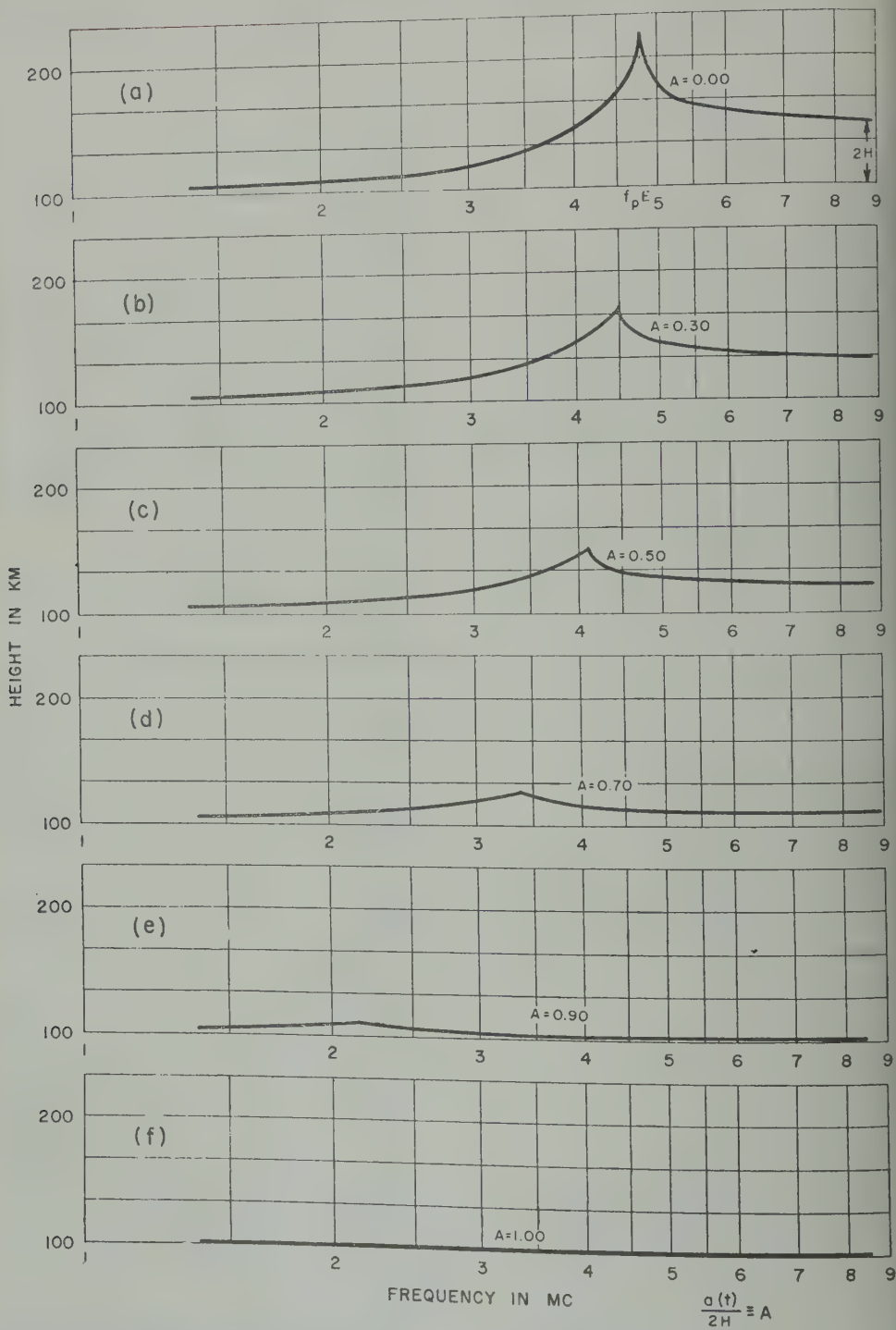


Fig. 3. Calculated nonblanketing overhead sporadic E for various heights of the small scale scattering irregularities.

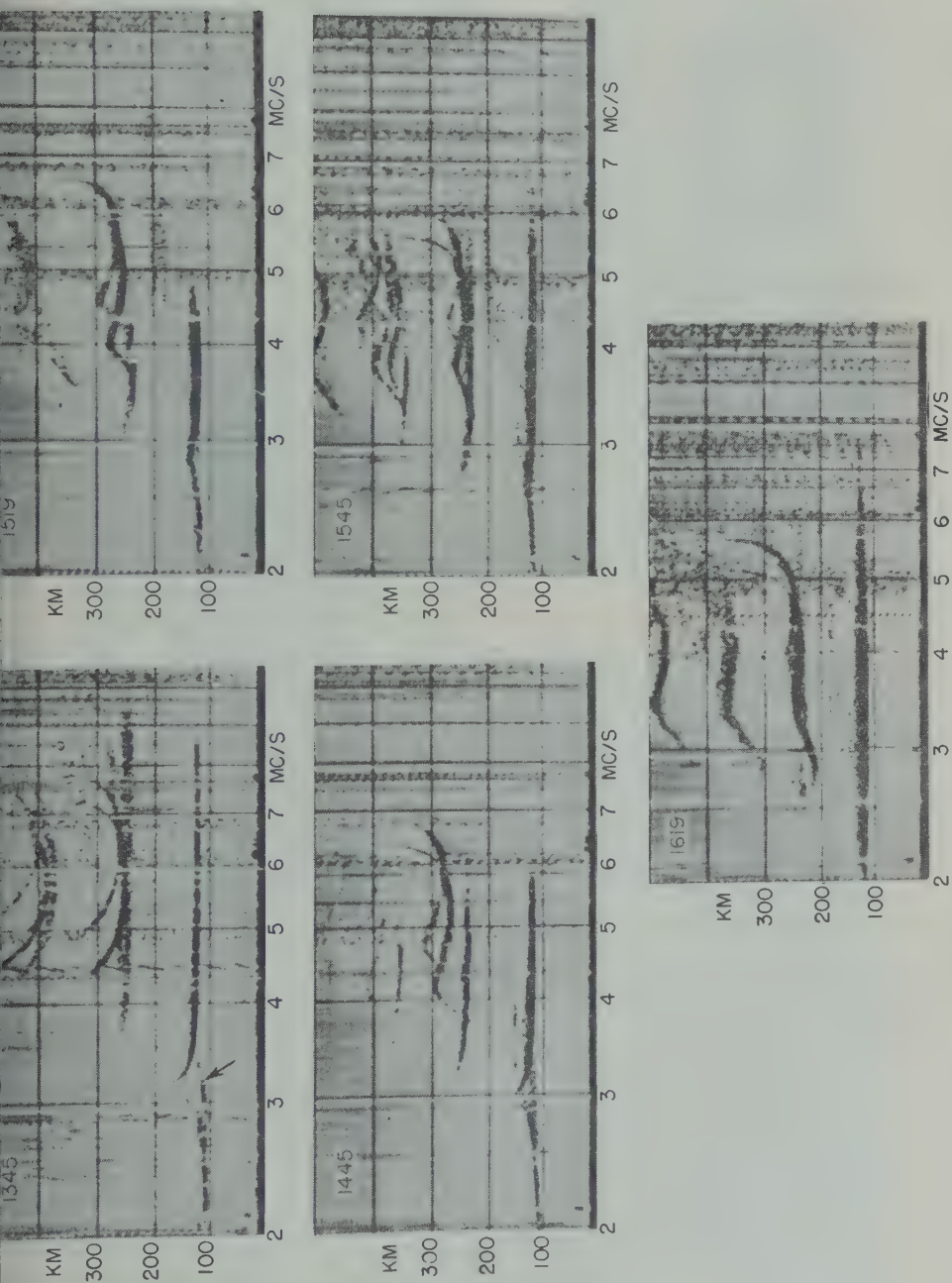


Fig. 4. Experimentally observed nonblanketing overhead sporadic *E*. Temporal sequence (Panama Canal, December 5, 1953).

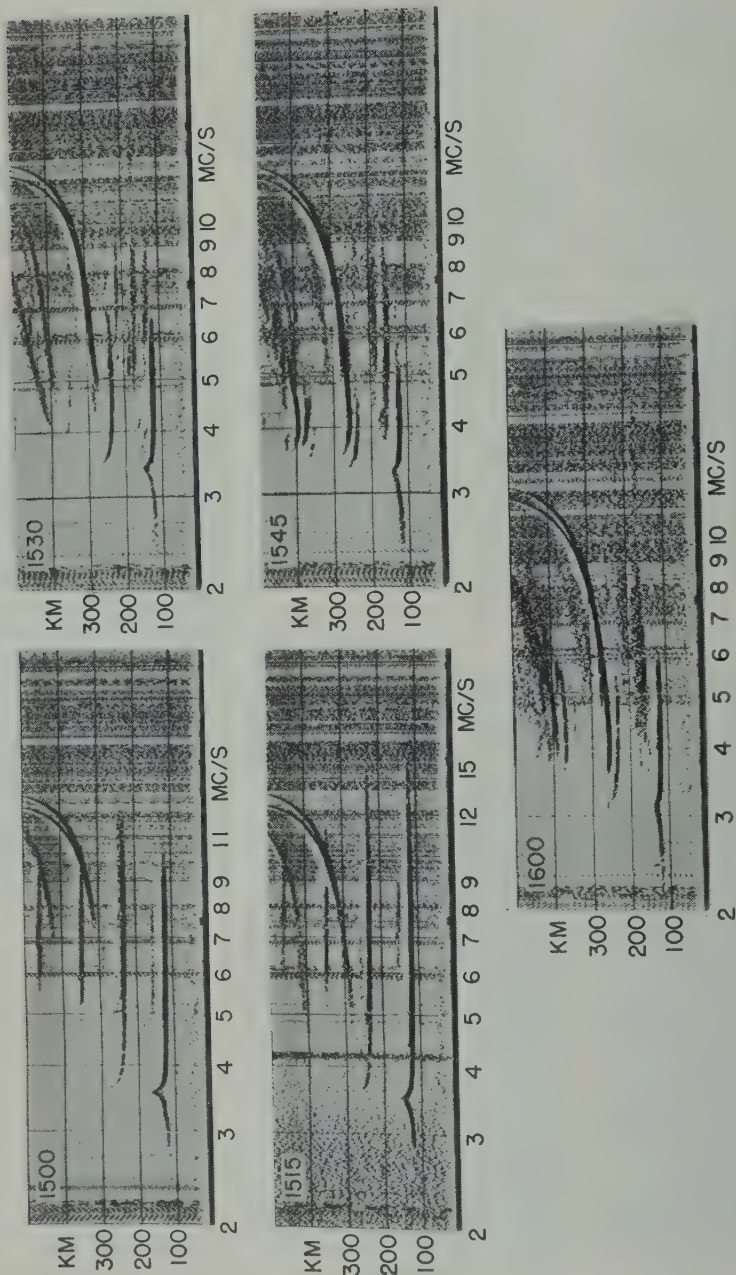
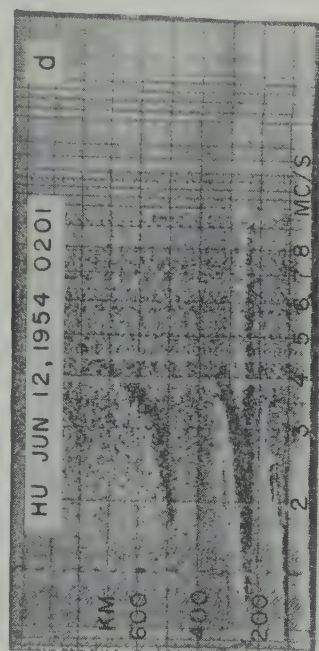
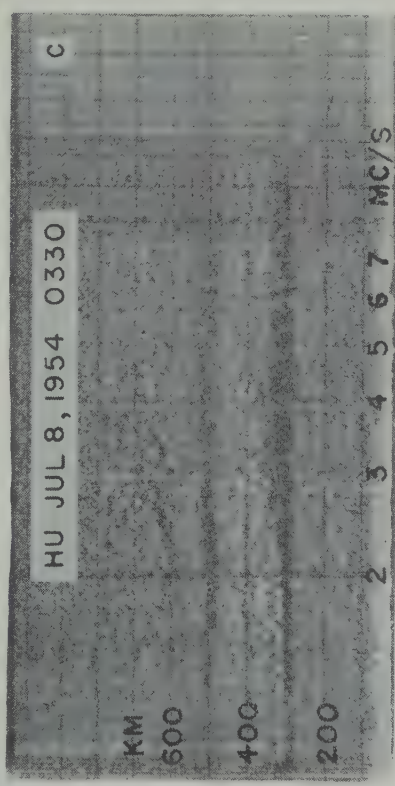
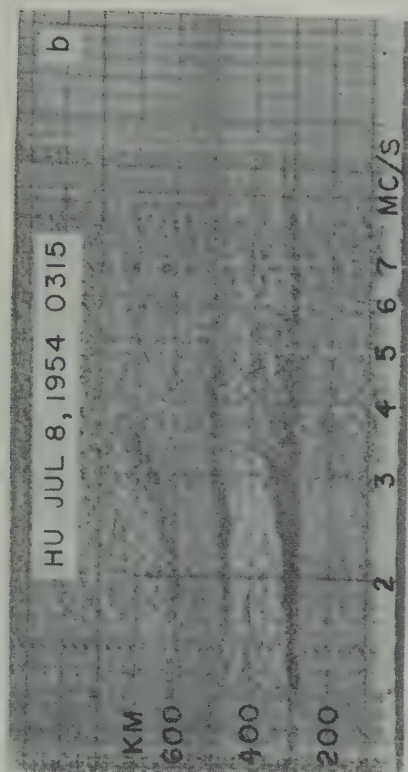
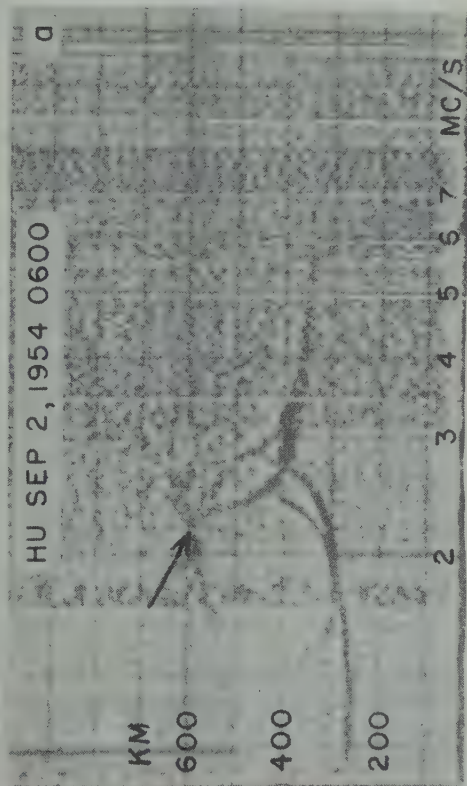


Fig. 5. Another example of data (Puerto Rico, December 2, 1959).

Fig. 6. Sporadic F at Huancayo.

1959). The theoretical curves of Figure 3 are in good agreement with the observed nonblanketing sporadic E of Figures 4 and 5. We conclude, therefore, that the observed ionograms can be explained by the model postulated in this paper, which is an alternative model from that of Whale's, and that the various ionosonde patterns represent the changing position of the scattering belt relative to the 'normal' E layer.

Although this paper is not concerned with F -region phenomena, we note that some ionograms from equatorial stations exhibit diffuse echoes from the F region bearing a strong resemblance to sporadic- E echoes of the type shown in Figures 4 and 5. Figure 6, photographed at Huancayo and coming from a height of about 250–300 km, could be referred to as sporadic F . Because of the reduced collisional frequency in the F region, the effect of the magnetic field in shaping the irregularities in this region is more pronounced. However, the anisotropy of the F -region scatterers can affect the intensity only and not the delay time of the echoes. Therefore, it is not unreasonable to assume that this type of sporadic F is an F -region manifestation of the simplified mechanism just described for the particular sporadic- E echoes.

Acknowledgments. I wish to thank the officials of the IGY Ionospheric Data Center, CRPL, Boulder, Colorado, for providing ionograms for this

study. Moreover, I am indebted to Professor H. G. Booker of Cornell University and to Dr. W. A. Flood of this Laboratory for several fruitful discussions. This material was supported by U. S. Signal Corps under contract DA-36-039-sc-78258.

REFERENCES

- Best, J. E., F. T. Farmer, and J. A. Ratcliffe, Studies of region E of the ionosphere, *Proc. Roy. Soc. A.*, **164**, 16, 1938.
 Booker, H. G., *Proc. Pennsylvania Conference on Ionosphere Phys. A*, p. 171, 1950.
 Eckersley, T. L., Studies in radio transmission, *J. Inst. Elec. Engrs.*, **71**, 405, 1932.
 Gallet, R. M., Sur la nature de la couche E sporadique et la turbulence de la haute atmosphere, *Compt. rend.*, **233**, 1649, Paris, 1951.
 Gallet, R. M., Aerodynamical mechanisms producing electronic density, *Proc. IRE*, **43**, 1240, 1955.
 McNicol, R. W. E., *Proc. IEE*, part 3, **96**, 517, 1949.
 Ratcliffe, J. A., and J. L. Pawsey, A study of the intensity variations of downcoming wireless waves, *Proc. Cambridge Phil. Soc.*, **29**, 301, 1933.
 Smith, E. K., World-wide study of sporadic E , Ph.D. thesis, Cornell University, 1956.
 Villars, F., and V. F. Weisskopf, The scattering of electromagnetic waves by turbulent atmospheric fluctuations, *Phys. Rev.*, **94**, 232, 1954.
 Watson-Watt, R. A., A discussion on the ionosphere, *Proc. Roy. Soc. A*, **141**, 715, 1933.
 Whale, H. A., Fine structure of the ionospheric region E , *J. Atmospheric and Terrest. Phys.*, **1**, 233, 1951.

(Manuscript received April 6, 1961.)

Seasonal and Latitudinal Variations of Air Density in the Mesosphere (30 to 80 Kilometers)

RODERICK S. QUIROZ

*Climatic Center, USAF
Washington, D. C.*

Abstract. The detailed density data for 69 soundings of the mesosphere are analyzed statistically. The soundings, obtained at latitudes from the equator to 75°N during 1947–1958, were taken by four methods of observation—rocket with pressure gages, rocket grenade, rocket and falling sphere, and the searchlight technique. Mean and extreme densities for the summer and winter half-years are presented for three latitude bands, for every 2 km from 30 to 80 km, along with means and extremes for the entire data sample. Standard deviations of density are given for every 10 km. A tentative model of the seasonal variation of density from near the ground to a height of 200 km is included. Various aspects of the variability of density in the mesosphere are discussed, with special emphasis on the large seasonal variation in northerly latitudes, especially at altitudes of around 60 to 70 km.

INTRODUCTION

The requirements of missile designers for data on upper-atmosphere density have been made known in various government publications. A report of the *U. S. Naval Ordnance Laboratory* [1959], for example, indicates that values of the density at 100,000 to 200,000 feet, accurate to within 5 to 20 per cent, will be needed in connection with certain specified programs. Besides lowering the practical needs of designers, values of air density are a promising aid in the investigation of relations between synoptic processes in the troposphere and stratosphere and disturbances in the upper atmosphere. Already, an apparent relation between large changes in density and temperature shown by rocket data at 45 and 65 km and an abrupt warming at balloon altitudes (20 and 30 km) has been demonstrated by Jones, Peterson, Schaefer, and Schulte [1959], for Fort Churchill, Canada, during January–February 1958.

The Air Weather Service recently published a report [Quiroz, 1961] containing the detailed density values for 65 soundings of the mesosphere (approximately 30 to 80 km). The report also included a description of the pertinent observational methods and an appraisal of the observational errors, with full documentation of the data sources used. The soundings, compiled from a wide variety of published and unpublished sources, were taken during 1947–1958, at latitudes from the equator to 75°N.

In this report the results of a statistical analysis of those data are presented, together with the data of four soundings not previously available. Seasonal means and extremes of density for three latitude bands, the annual means and extremes for the data sample as a whole, and standard deviations at selected levels are included. Various aspects of the variation of density in the mesosphere are discussed, and a tentative model of the seasonal variation of density at heights from near the ground surface to 200 km is presented.

OBSERVATIONAL METHODS AND ERROR ANALYSIS

Valuable density data for the mesosphere have been obtained mainly by six observational methods: (1) pressure gages on rockets, (2) grenades ejected from rockets, (3) falling spheres ejected from rockets, (4) searchlight scanning of night sky, (5) photographic and radio observations of meteors, and (6) photometric measurement of intensity of zenith skylight during twilight.

Concise descriptions of the first four methods listed above are given by Quiroz [1961]. Detailed descriptions have been given by Newell [1955], Stroud, Nordberg, Bandeen, Bartman, and Titus [1960], Jones, Peterson, Schaefer, and Schulte [1959], and Elterman [1954]. Densities derived by the fifth method listed above, for example, those reported by Jacchia [1952], start at moderately high levels (near 50 km) and include

TABLE 1. Frequency Distribution of Probable Errors

Height, km	Error in Reported Density Value				Total Cases	Mean Error, %*
	2-5%	6-10%	11-20%	Unknown		
30	42	7	1	0	50	5
40	47	5	5	0	57	6
50	49	5	0	0	54	5
60	52	5	2	1	60	5
70	27	2	3	1	33	6
80	15	8	2	0	25	8

* Computed from data for individual soundings. Mean errors obtained by multiplying frequencies by mid-cell values may differ by about 1 per cent.

errors comparable with some of the less accurate rocket data. These data were not included in the compilation of soundings. Also not included, owing to the apparently large observational error involved (factor of 2 or more), were molecular densities obtained from measurements of the intensity of the zenith skylight during twilight, reported by *Ashburn* [1952], among others.

On the basis of error information already presented by *Quiroz* [1961], an estimate of the probable error was assigned to each sounding, at each of the levels 30, 40, . . . , and 80 km. The distribution of probable errors is shown in Table 1. Since precise information on the error components and the degree of their independence was not available for many of the soundings, the individual probable errors represented in Table 1 should not be taken in a rigorous statistical sense (i.e., 0.67 times the standard deviation, for a normal distribution) but only as approximations of the true error.

In this table as well as in the tables which follow it will be noted that the total number of cases shown does not equal the total number of available soundings (69); this is explained by the fact that many soundings did not span the entire mesosphere.

The magnitude of the observational errors in upper-atmosphere density data is a factor which induced the author to consider the mesosphere primarily. At about 70 to 100 km, the errors inherent in most techniques of observation increases greatly. Appreciable molecular dissociation begins in the neighborhood of 80 km. Reduction methods that depend on the equation of state for deriving density may no longer be applied reliably, except with special knowledge of the molecular mass at the levels of interest. Throughout most of the mesosphere, however, the estimated observational errors are predominantly of the order of a few per cent. Thus a detailed statistical examination of the

TABLE 2. Distribution of Air Density Soundings

Location	Latitude	Longitude	Number of Soundings and Method of Observation*
Equator	00°11'N	161°25'W	1(†)
Guam, M. I.	13°37'N	144°51'E	7(‡)
White Sands, N. M.	32°24'N	106°20'W	2(†), 4(§)
Holloman AFB, N. M.	32°54'N	106°05'W	3(†)
Albuquerque, N. M.	~35°10'N	~106°30'W	18()
Wallops I., Va.	37°50'N	75°20'W	2(§)
Fort Churchill, Can.	58°46'N	94°10'W	11(†), 10(‡), 4(§)
Shipboard	49°-75°N	46°-94°W	4(†), 3(§)
Total			69

* Observational methods: (†) rocket with pressure gages, (‡) rocket grenade, (§) rocket and falling sphere (||) searchlight.

Note: Several rocket soundings at White Sands and at Fort Churchill which do not include data below 80 km are not reflected in this table.

TABLE 3a. Mean and Extreme Densities (g/m^3), Station Group I (0° – 14°N)

Height, km	Winter				Summer			
	<i>n</i>	Mean	Minimum	Maximum	<i>n</i>	Mean	Minimum	Maximum
30	7	16.4	15.0	17.5				
32	7	12.1	11.5	12.2				
34	7	8.97	8.9	9.1				
36	7	6.70	6.6	6.9				
38	7	5.00	4.9	5.3	1	7.5	7.5	7.5
40	7	3.80	3.7	4.1	1	4.7	4.7	4.7
42	7	2.91	2.8	3.3	1	3.1	3.1	3.1
44	7	2.23	2.1	2.5	1	2.3	2.3	2.3
46	7	1.73	1.63	1.94	1	2.0	2.0	2.0
48	7	1.33	1.26	1.44				
50	7	1.05	1.00	1.15				
52	7	0.821	0.78	0.88				
54	7	0.641	0.61	0.69				
56	7	0.487	0.48	0.55				
58	7	0.391	0.38	0.43				
60	7	0.310	0.30	0.34				
62	5	0.236	0.23	0.25				
64	5	0.182	0.175	0.195				
66	4	0.141	0.135	0.150	1	0.20	0.20	0.20
68	4	0.106	0.103	0.112				
70	3	0.0797	0.078	0.083				
72	2	0.0600	0.060	0.060				
74	2	0.0445	0.043	0.046				
76	2	0.033	0.031	0.035				
78	1	0.026	0.026	0.026				
80								

sity data appears feasible. Data on the standard deviation of density, presented later in report, bear out this hypothesis.

DATA PREPARATION

The original data sample consisted of 65 soundings compiled by Quiroz [1961], supplemented by four previously unavailable rocket soundings at Fort Churchill, Canada (AM 6.39, May 15, 1958; AM 4.12, October 15, 1958; AM 6.207, October 20, 1958; and AA 6.16, November 23, 1958). In addition, revised data were substituted for three soundings included in author's compilation, formerly regarded as provisional (AM 2.21, October 23, 1956; AM 7, February 24, 1958; and AM 6.38, March 1958). The total distribution of soundings is shown in Table 2.

The data were plotted on semilog graph paper, and values of density were derived for each sounding for even whole kilometers from 30 to 80 km. From an inspection of the curves for some of the more detailed soundings (e.g., the falling-sphere data), it appeared that interpolation or

extrapolation of data points lying between whole kilometers could be made without misrepresenting the true curves if the process were confined to layers approximately 2 km in thickness. Thus, in almost all cases, extrapolated values are removed from the original data points by not more than 2 km. The majority of the extrapolations were through height intervals smaller than 1 km (for example, to obtain a density at 58.0 km when the nearest reported value was at 57.6 km). Many of the data were originally reported at whole kilometers and thus did not require modification.

The complete data sample thus obtained is on file in the Climatic Center, USAF. A few doubtful data points were eliminated, and these were shown by an X in the tabulation. A large observational error, *per se*, was not a sufficient basis for eliminating data. In the falling-sphere soundings of December 11, 1952, and April 23, 1953, erratic fluctuations in the density curves, combined with a large observational error (>20 per cent), were considered a sufficient basis for eliminating the high-level data. Also omitted

TABLE 3b. Mean and Extreme Densities (g/m³), Station Group II (32°-38°N)

Height, km	Winter				Summer			
	<i>n</i>	Mean	Minimum	Maximum	<i>n</i>	Mean	Minimum	Maximum
30	7	17.63	17.0	18.0	15	17.85	16.5	19.5
32	7	13.01	12.5	13.5	15	13.13	10.9	15.2
34	8	9.73	9.2	10.2	15	9.49	8.3	10.4
36	8	7.20	6.8	7.7	16	6.94	5.7	7.6
38	8	5.36	5.0	5.9	16	4.91	4.2	5.7
40	8	4.03	3.7	4.5	16	3.89	3.1	4.4
42	8	3.03	2.7	3.4	16	2.98	2.1	3.5
44	9	2.26	1.85	2.5	16	2.27	1.95	2.5
46	9	1.71	1.45	1.90	16	1.78	1.55	2.1
48	1*	1.35	1.35	1.35	6*	1.50	1.32	1.60
50	9	1.04	0.86	1.20	17	1.08	0.94	1.29
52	9	0.838	0.71	0.97	18	0.869	0.74	1.00
54	9	0.667	0.51	0.80	18	0.677	0.41	0.80
56	9	0.539	0.41	0.66	17	0.542	0.45	0.66
58	9	0.469	0.36	0.60	17	0.435	0.37	0.52
60	9	0.388	0.28	0.55	18	0.348	0.26	0.44
62	9	0.296	0.22	0.42	17	0.278	0.21	0.35
64	8	0.256	0.178	0.35	17	0.235	0.157	0.36
66	8	0.207	0.137	0.30	16	0.182	0.120	0.25
68	9	0.170	0.107	0.26	16	0.151	0.082	0.22
70	2	0.106	0.082	0.129	4	0.0990	0.078	0.117
72	2	0.0810	0.062	0.100	3	0.0680	0.056	0.085
74	2	0.0605	0.046	0.075	2	0.0590	0.050	0.068
76	2	0.0460	0.035	0.057	2	0.0390	0.031	0.047
78	2	0.0340	0.026	0.042	2	0.0305	0.028	0.033
80	2	0.0243	0.0195	0.029	2	0.0200	0.0190	0.021

* Value for *n* is correct as stated.

were the complete data for the falling-sphere sounding of January 27, 1958, 1249 CST (Churchill), owing to an apparent disparity with the radiosonde data and with rocket grenade densities obtained in the same rocket firing. For this date and time the grenade sounding was used.

Revised unpublished data for several falling-sphere flights¹ were received from the University of Michigan High Altitude Engineering Laboratory in early February 1961, after the data on hand had been completely processed. A comparison with the earlier data for those flights indicated that the changes were nominal, except possibly in the upper reaches of the soundings. At the 70- and 80-km levels, the average change

amounted to 7 and 12 percent, respectively. With respect to the total data sample the effect is considered negligible. With respect to the winter densities in arctic latitudes the effect is to lower the average density by about 3 per cent at 70 km and 5 per cent at 80 km. In view of the large seasonal variation of density at these latitudes (discussed in a later section), this effect is considered unimportant; thus no change in the data sample was made.

MEAN AND EXTREME DENSITIES

The computed means and the observed extreme densities are shown in Table 3. Station group I, representing tropical latitudes, includes Guam and the shipboard location at 161°W, near the equator. Station group II, in middle latitudes, includes White Sands, Holloman AFB, Albuquerque (all in New Mexico), and Wallops Island, Va. Station group III, representing arctic and subarctic latitudes, includes Fort Churchill, Canada, and seven shipboard locations at latitudes 49° to 75°N. Winter and summer refer to

¹ Wallops Island, July 6, 1956; shipboard, November 2, 4, and 10, 1956; Fort Churchill, January 25, 27, and 29, 1958, and March 4, 1958. The revised data for these flights, together with data of the five earlier sphere flights, were subsequently published in a single report by Jones and Peterson [1961].

TABLE 3c. Mean and Extreme Densities (g m^{-3}), Station Group III (49° – 75°N)

Height, km	Winter				Summer			
	<i>n</i>	Mean	Minimum	Maximum	<i>n</i>	Mean	Minimum	Maximum
30	14	16.53	14.3	18.5	7	18.47	17.5	19.8
32	14	11.80	10.0	13.6	9	13.73	13.0	14.7
34	14	8.46	7.0	10.1	10	10.02	9.6	10.9
36	14	6.17	5.0	7.7	10	7.45	7.1	8.0
38	14	4.46	3.6	5.7	11	5.84	5.3	8.0
40	14	3.27	2.6	4.2	11	4.38	4.0	5.6
42	14	2.41	1.93	3.1	10	3.29	3.0	4.1
44	14	1.82	1.43	2.3	10	2.53	2.3	3.1
46	14	1.36	1.08	1.75	9	1.94	1.75	2.3
48	14	1.03	0.81	1.37	7	1.51	1.36	1.77
50	14	0.789	0.61	1.10	7	1.19	1.07	1.38
52	16	0.636	0.48	0.85	7	0.919	0.81	1.08
54	16	0.486	0.37	0.66	7	0.723	0.63	0.84
56	17	0.352	0.29	0.52	7	0.574	0.50	0.66
58	18	0.297	0.23	0.40	7	0.456	0.39	0.53
60	18	0.216	0.175	0.30	8	0.365	0.31	0.41
62	17	0.175	0.130	0.24	8	0.285	0.23	0.33
64	17	0.137	0.094	0.195	8	0.221	0.188	0.25
66	16	0.103	0.071	0.145	8	0.170	0.146	0.190
68	16	0.0784	0.055	0.105	7	0.133	0.116	0.150
70	16	0.0596	0.042	0.083	8	0.101	0.088	0.120
72	16	0.0468	0.033	0.068	8	0.0773	0.066	0.093
74	14	0.0344	0.025	0.055	7	0.0579	0.048	0.070
76	15	0.0267	0.0180	0.044	7	0.0429	0.035	0.053
78	14	0.0211	0.0141	0.036	7	0.0310	0.025	0.039
80	14	0.0173	0.0106	0.030	7	0.0229	0.0178	0.030

the winter and summer half-years, October–March and April–September, respectively.

In addition to the seasonal data by latitude groups, annual means and extremes are shown in Table 3d for all latitudes combined. Finally, the standard deviations of density for latitude groups II and III and for selected heights are given in Table 4.

Graphs of the data in Table 3 are shown in Figures 1 to 3. From Figure 1 it may be seen that the over-all mean density at 70 to 80 km is about 20 per cent less than the corresponding densities in the U. S. Extension to the Standard Mesosphere [U. S. Weather Bureau and AFCRC, 1958]. Below 70 km the departure becomes generally smaller with decreasing height.

VARIABILITY OF DENSITY

Early in the past decade Jacchia [1952] compared densities derived from the deceleration of meteors over New Mexico and Massachusetts and found a seasonal variation at heights from 60 to 85 km which was more than twice as large over Massachusetts as over New Mexico. Later

sources [Jones, Peterson, Schaefer, and Schulte, 1959; LaGow, Horowitz, and Ainsworth, 1960], based on limited series of rocket observations, have provided further evidence suggesting a large seasonal variation of the order of 10 to 40 per cent in the arctic mesosphere. These sources have also indicated an appreciable latitudinal gradient in the winter densities. These and other aspects of the variation of density will be discussed in the sections that follow.

Variations in the means. The most interesting features in the data for 1947–1958 are the low winter densities at arctic latitudes (curve IIIw, Fig. 2) and the large variability in the vicinity of 60 to 70 km. At these levels, the mean arctic density in winter is 60 per cent of the summer value and is one-half of the winter value for mid-latitudes (IIw). Below the mesopeak (the temperature maximum near 50 km), the seasonal variation diminishes greatly with decreasing height.

The seasonal variation in mid-latitudes amounts to only a few per cent near the base of the mesosphere; it is greatest at 66 km (13 per cent).

TABLE 3d. Mean and Extreme Densities (g/m³), Station Groups I, II, and III

Height, km	n	Annual		
		Mean	Minimum	Maximum
30	50	17.33	14.3	19.8
32	52	12.72	10.0	15.2
34	54	9.29	7.0	10.9
36	55	6.85	5.0	8.0
38	57	5.10	3.6	8.0
40	57	3.85	2.6	5.6
42	56	2.89	1.93	4.1
44	57	2.20	1.43	3.1
46	56	1.69	1.08	2.3
48	35	1.28	0.81	1.77
50	54	1.01	0.61	1.38
52	57	0.799	0.48	1.08
54	57	0.623	0.37	0.84
56	57	0.482	0.29	0.66
58	58	0.394	0.23	0.60
60	60	0.312	0.175	0.55
62	56	0.246	0.130	0.42
64	55	0.201	0.094	0.36
66	54	0.158	0.071	0.30
68	52	0.126	0.055	0.26
70	33	0.0790	0.042	0.129
72	31	0.0598	0.033	0.100
74	27	0.0450	0.025	0.075
76	28	0.0334	0.0180	0.057
78	26	0.0257	0.0141	0.042
80	25	0.0196	0.0106	0.030

At 70 to 80 km the data sample is too small to allow a precise determination of the amount of variation. A general decrease from the value at 66 km is indicated, possibly leading to a reversal in the sign of the variation near 80 km. Unlike conditions in the Arctic, the season of minimum density is not constant with height in the mesosphere. Our data indicate reversals in the sign of the variation at 33, 44, and 57 km.

A tentative model of the seasonal variation of mean density for the atmosphere from near the ground surface to a height of 200 km is shown in Figure 4. In this figure, the percentage departures from the annual mean densities at levels below 30 km are based on radiosonde data for geometric heights presented by *Sissenwine, Ripley, and Cole* [1958]. Data for St. Paul, Alaska (57°N), and Thule, Greenland (77°N) were used for arctic latitudes, and data for Washington, D. C. (39°N), were used for mid-latitudes. Data published by *Wege, Leese, Groening, and Hoffmann* [1958] in the form of seasonal isoline maps of mean density over the northern hemisphere are

constant-pressure data (200 to 20 mb) and are not directly comparable. To illustrate, the mean height of the 30-mb surface at 60°N, 90°W, varies approximately from 24.4 km in summer to 23.3 km in winter. The normal variation in density corresponding to this variation in height is about twice the seasonal variation at constant height; thus *Wege's* data show a winter density at 30 mb which is higher than the summer density, in contrast to the variation shown by the data of *Sissenwine, Ripley, and Cole* [1958].

For 30 to 80 km, the curves in Figure 4 are based on the means in Table 3.

In the region from 100 to 200 km, the values shown are based on limited data obtained from rocket soundings and are essentially consistent with theoretical curves deduced for the atmosphere from 100 to 500 km by *Nosenzo and Slezak* [1960]. The arctic rocket data examined were six winter soundings for Fort Churchill (November 17 and 20, 1956, February 21 and 24, March 24, and October 31, 1958) and one summer sounding for Fort Churchill (July 29, 1957). In view of the small data sample and the large observational errors involved, the curves were subjected to considerable smoothing, mainly in the region between 100 and 150 km. Near 125 km the density curve for July 29, 1957, coincides with the mean curve based on the six winter soundings; thus the percentage departure of the seasonal means shown by the available data is actually zero at this point. Above 100 km the mid-latitude curves were drawn symmetrically with the arctic curves, and they are in general agreement with the seasonal pattern suggested for 35°N by *Nosenzo and Slezak*. The few high-level rocket data available for White Sands are even less conclusive than the Fort Churchill data.

In interpreting Figure 4 it is useful to note

TABLE 4. Standard Deviation of Density (g/m³)

Height, km	Station Group II				Station Group III			
	n	s _p	s _p /ρ̄, %		n	s _p	s _p /ρ̄, %	
30	22	0.77	4		21	1.97	11	
40	24	0.33	8		25	0.71	19	
50	26	0.11	10		21	0.28	30	
60	27	0.066	18		26	0.10	39	
70	6	0.021	21		24	0.24	33	
80	4	0.0047	21		21	0.0059	31	

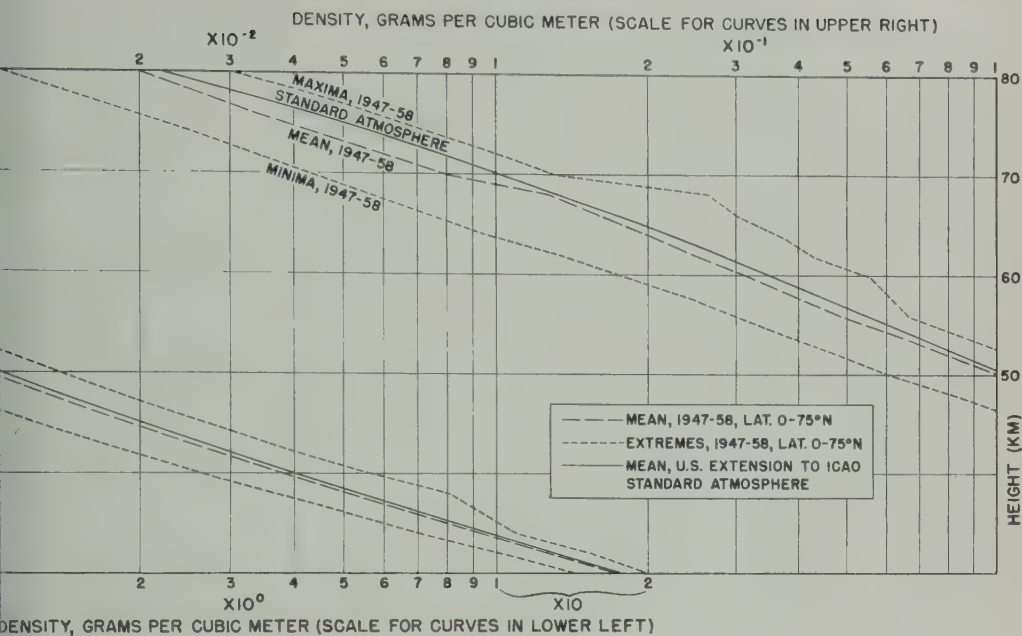


Fig. 1. Mean and extreme densities, 1947-1958, compared with U. S. Extension to ICAO Standard Atmosphere.

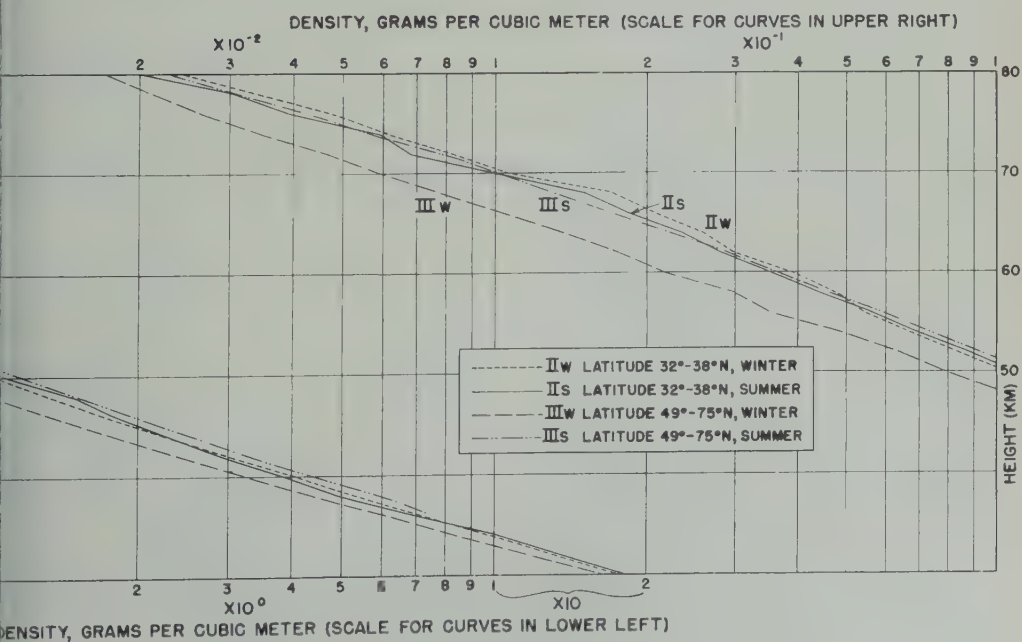


Fig. 2. Mean densities, 1947-1958, arctic and middle latitudes.

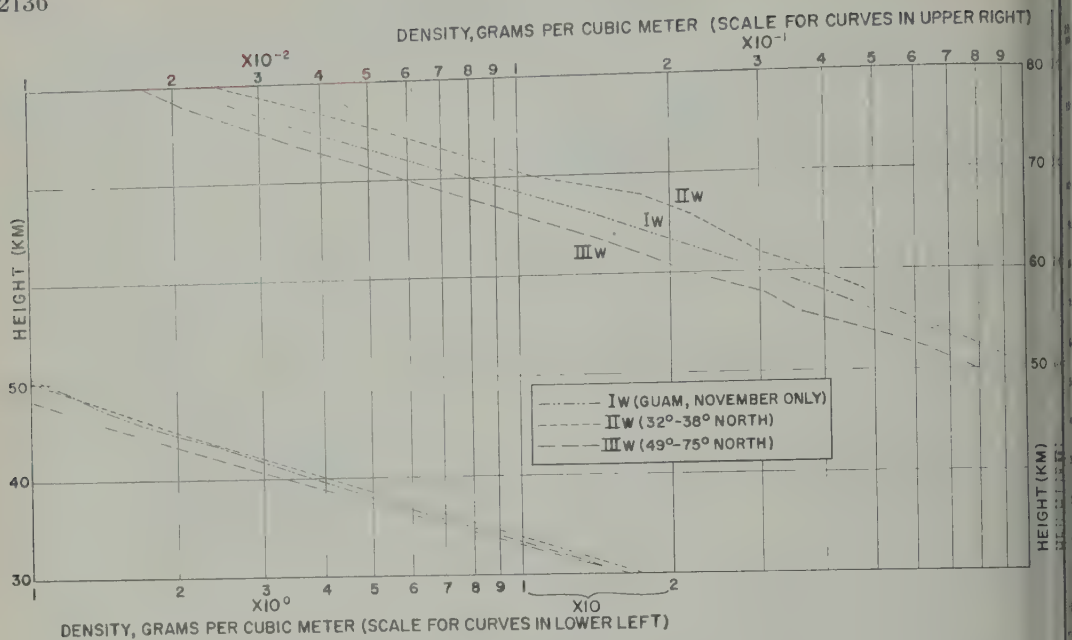


Fig. 3. Latitudinal variation of winter mean density.

that a departure of 33 per cent from the annual mean corresponds to a seasonal variation by a factor of 2 (at around 180 km the arctic summer density is twice the arctic winter density), a departure of 20 per cent corresponds to a variation by a factor of 1.5, and so on.

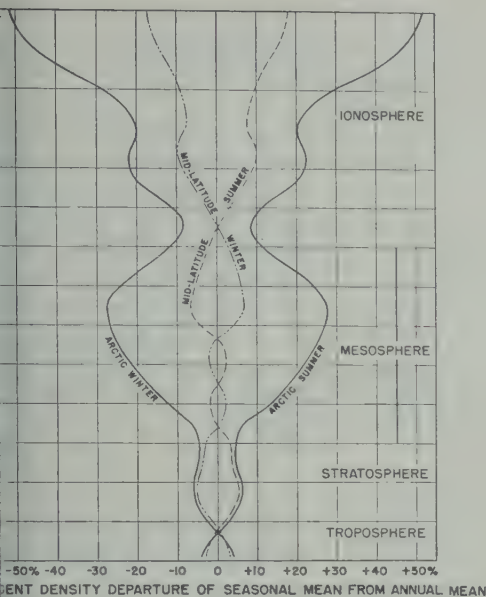
It should be emphasized that above 100 km, where the observational error for much of the rocket data is of the order of a factor of 2 or more, there are as yet insufficient data to define accurately the seasonal variation of density. Densities deduced from satellite orbital data fail to clarify the picture. According to *King-Hele and Walker* [1960], satellite densities at 200 to 300 km do not fall into a consistent pattern either seasonally or latitudinally. At these heights solar disturbances, which give rise to density variations of ± 20 per cent with a periodicity of about 28 days, appear to be the main factor influencing the air density.² King-Hele has further concluded that at heights near 220 km, at latitudes from 80°N to 65°S, the air density does not vary from its average value by a factor of more

than 1.5, i.e., 50 per cent of the annual average. This value is in good agreement with the percentage departure that would be inferred by extrapolating the arctic curves in Figure 4 to a height of 220 km.

The anomaly at 60 to 70 kilometers. The curious bulge above the mesopeak in curves IIw and IIs (Fig. 2), centered at 60–70 km, is of special interest. A straightedge placed along curve IIs clearly shows this feature to be present during the arctic summer also, although it is less pronounced.

Some of the bulging appears to be related to the peculiar temperature regime above the mesopeak. Below the mesopeak, temperature increases and pressure decreases with height, and, in accordance with the equation of state, temperature and pressure operate jointly to produce a fall in density. Above the mesopeak a general decrease in both temperature and pressure results in a reduced rate of fall in density. Furthermore, the curvilinear shape of the density profile appears to be an imperfect reverse reflection of the curvilinear temperature structure above the mesopeak present in some of the soundings for mid-latitudes and for the arctic summer. The shape of these soundings resembles

² At higher levels, the diurnal variation takes on increasing importance. At 650 km, according to *Nicolet* [1960], the diurnal effect is the principal factor in the variation of density.



4. Model of the seasonal variation of mean density to 200 km.

flattened S stretched along a straight line connecting 50 and 80 km, ascending diagonally to the left.

The temperature regime from 50 to 80 km above Fort Churchill differs radically from summer to winter. Rocket grenade experiments [Goud, Nordberg, Bandeen, Bartman, and Titus, 1950] have shown steep temperature lapse rates in summer, although winter, on the other hand, is characterized by stable lapse rates, with frequent inversions occurring above about 60 km. This seasonal variation may account for the different structure in density curves IIIw and IIIs.

While the general shape of curves II_s, II_w, and III_s (Fig. 2) is consistent with respect to temperature distribution, the marked degree of bulging is not readily explained. A detailed examination of temperatures and pressures in individual soundings, and their effect on the density, appears necessary. Other factors—for example, air motion—merit consideration. Upper-atmosphere wind data obtained in recent years point to the probability of very strong currents near 60 km; it is therefore reasonable to hypothesize that advective processes may strongly influence the density distribution above the tropopause.

Latitudinal gradient of mean density. The

winter mean density curves for Guam (14°N), latitude group 32°–38°N, and latitude group 49°–75°N have been plotted in Figure 3. Throughout most of the mesosphere, the maximum density in winter occurs in mid-latitudes. In the vicinity of 65 km, where the largest gradient is found, the density decreases northward from mid-latitudes at the rate of 2 per cent of the mid-latitude density per degree of latitude; equatorward, the density decreases at the rate of about 1½ per cent per degree of latitude. The only evidence for a gradient toward the equator consists of rocket grenade densities for Guam for November 1958. The one summertime sounding at 161°W, near the equator (see Table 3a), does not offer conclusive evidence about conditions in summer. When equatorial data at other longitudes and for other times of the year become available, it will be possible to learn more about the variation between densities in mid-latitudes and densities in the tropics.

Standard deviation of density. Standard deviations about the annual mean densities were computed from the density values in the individual soundings. A comparison of the standard deviations given in Table 4 with the probable error data of Table 1 indicates that the standard deviations, being only partially masked by the observational errors, should be expected to have statistical significance. At the base of the mesosphere the small values of the standard deviations, expressed as percentages of the mean annual densities, are consistent with values based on radiosonde data reported by Sissenwine, Ripley, and Cole [1958] and by the U. S. Army Ballistics Agency [1959]. The increase with height through the mesosphere is consistent with the wide spread of the means at higher levels. In arctic latitudes (station group III) the standard deviation reaches a maximum near 60 km and then falls off slightly in the upper reaches of the mesosphere. The general increase through the mesosphere is consistent with the large variability reported at ionospheric levels on the basis of densities deduced from high-altitude rocket flights and from satellite observations [Champion and Minzner, 1959].

Diurnal and interdiurnal variations. There is probably as yet insufficient observational material to establish the magnitude of diurnal and interdiurnal variations in density.

On the basis of rocket grenade firings at Guam

on several dates in November 1958, Nordberg and Stroud [1961] have reported significant day-to-day variations in temperature above the meso-peak, and a difference of 10°K between temperatures measured in two firings 7 hours apart. A variation in temperature of 10°K , assuming that the pressure is constant, results in a density variation of about 4 per cent at 60 km.

At Fort Churchill, a large variation in density over a period of several days in late January and early February 1958, at 45 and 65 km, has been reported by Jones, Peterson, Schaefer, and Schulte [1959].

For the New Mexico area, an analysis of the searchlight observations for May–October 1952 (several pairs of which were spaced 1 day apart) shows occasional day-to-day density changes exceeding 5 per cent in the vicinity of 40 and 50 km and several cases of more than 10 per cent at 60 km. Even if the sign of the observational error is assumed to vary, a significant interdiurnal variation remains after the error component is subtracted. These data suggest that in mid-latitudes the interdiurnal variation is at least as important as the seasonal variation.

SUMMARY

In an earlier report [Quiroz, 1961], the original density data for 65 soundings in the mesosphere were presented. From these data, together with data for four additional soundings not previously available, values for even whole kilometers from 30 to 80 km were obtained. An error analysis indicates that the mean probable error varies from 5 per cent at 30 km to 8 per cent at 80 km.

Means and extremes for the entire data sample and seasonal means and extremes for three latitude groups are presented in tables and graphs. Standard deviations were computed for every 10 km. Some conclusions reached are:

1. The lowest densities are found in winter in arctic latitudes. At 65 km, the mean winter density is 60 per cent of the mean summer density.

2. The seasonal variation in mid-latitudes is relatively small, amounting to less than 5 per cent below 50 km and reaching a maximum of 13 per cent at 66 km.

3. The latitudinal gradient is greatest in winter and greatest at around 65 km. The gradient is directed northward from mid-latitudes in the amount of 2 per cent per degree of latitude (at

65 km), and there is a smaller gradient directed equatorward from mid-latitudes.

4. At mid-latitudes the standard deviation of density varies from 4 per cent (of the mean density) at 30 km to about 20 per cent near 60 km, remaining nearly constant up to the top of the mesosphere. In arctic latitudes the standard deviation varies from 11 per cent at 30 km to a maximum of about 40 per cent near 60 km, decreasing to about 30 per cent at 80 km.

5. Although there are indications of significant diurnal and interdiurnal variations in density, the necessary observational material to establish the magnitude of these variations in the mesosphere is not yet available.

Though these conclusions are based on the best data available at the end of 1960, it is recognized that the statistical sample is still wanting in several respects, particularly above 70 km and in tropical latitudes. The initiation of the North American rocketsonde network in 1959 [Inter-Range Instrumentation Group, 1960] is an important step toward providing sufficient data to obtain a definitive climatology of the mesosphere. Some temperature soundings, in addition to numerous wind soundings, have already been taken. A falling-sphere arrangement to measure densities directly is contemplated. When the observational errors are fully evaluated, it will be possible to obtain temperature-derived and sphere densities that can be used to test the results presented in this report.

Acknowledgments. I wish to express my appreciation to Dr. Adam Kochanski and other members of the Climatic Center for helpful advice. The cooperation of various individuals in the National Aeronautics and Space Administration and at the University of Michigan is gratefully acknowledged. Special thanks are due L. M. Jones, W. Nordberg, N. W. Spencer, and D. R. Taesch for published and unpublished data provided during the course of this investigation. I am also indebted to Mrs. Constance Lincoln, who assisted materially in the clerical and computational phases of the work.

REFERENCES

- Ashburn, E. V., The density of the upper atmosphere and the brightness of the night sky, *J. Geophys. Research*, 57, 85–93, 1952.
- Champion, K. S., and R. A. Minzner, Atmospheric densities from satellite and rocket observations, *Planetary and Space Sci.*, 1, 259–264, 1959.
- Elterman, L., Seasonal trends of temperature, density, and pressure in the stratosphere obtained with the searchlight-probing technique, *Air Force*

- Cambridge Research Center, *Geophys. Research* paper 29, 1954.
- Long-Range Instrumentation Group, Initiation of the meteorological rocket network, *IRIG Doc. 65-60*, 1960.
- Stull, L. G., A comparative analysis of atmospheric densities from meteor decelerations observed in Massachusetts and New Mexico, *Harvard College Observatory Tech. Rept. 10*, 1952.
- Stull, L. M., and J. W. Peterson, Upper air densities and temperatures measured by the falling sphere method, 1961 review, *Rept. 03558-5-T*, contract AF 19(604)-6185, Dept. of Aeron. and Astron. Engineering, University of Michigan, February 1961.
- Stull, L. M., J. W. Peterson, E. J. Schaefer, and I. F. Schulte, Upper-air density and temperature: some variations and an abrupt warming in the mesosphere, *J. Geophys. Research*, 64, 2331-2340, 1959.
- Stull, L. M., D. G., and D. M. C. Walker, Variation of upper-atmosphere density with latitude and season: further evidence from satellite orbits, *Nature*, 185, 727-729, 1960.
- Stull, H. E., R. Horowitz, and J. Ainsworth, Results of IGY atmospheric density measurements above Fort Churchill, in *Space Research: Proc. First Internatl. Space Science Symposium, June, 1960*, North-Holland Publ. Co., Amsterdam, p. 164-174, 1960.
- Stull, H. E., Jr., Rocket data on atmospheric pressure, temperature, density, and winds, *Ann. Geophys.*, 11, 115-130, 1955.
- Stull, M., Structure of the thermosphere, *Sci. Rept. 134*, Ionospheric Research Lab., Pennsylvania State University, 1960.
- Stull, W., and W. G. Stroud, Results of IGY rocket grenade experiments to measure temperature and winds above the island of Guam, *J. Geophys. Research*, 66, 455-464, 1961.
- Nosenzo, L. V., and D. S. Slezak, Density variations in the upper atmosphere, M.S. thesis, Mass. Inst. Technol., 1960.
- Quiroz, R. S., Air density profiles for the atmosphere between 30 and 80 kilometers, *Air Weather Service Tech. Rept. 150*, 1961.
- Sissenwine, N., W. S. Ripley, and A. E. Cole, Behavior of atmospheric density profiles, *Air Force Cambridge Research Center, Survey in Geophys. 109*, 1958.
- Stroud, W. G., W. Nordberg, W. R. Bandeen, F. L. Bartman, and P. Titus, Rocket-grenade measurements of temperatures and winds in the mesosphere over Churchill, Canada, *J. Geophys. Research*, 65, 2307-2323, 1960.
- U. S. Army Ballistic Missile Agency, ABMA climatological ringbook, 2, Ambient density, *Rept. DA-TR-60-59*, 1959.
- U. S. Naval Ordnance Lab., Report on Phase I of the Feasibility Committee for 200,000 foot altitude instrumented HASP, *Rept. 6763*, 1959.
- U. S. Weather Bureau and Air Force Cambridge Research Center, U. S. Extension to the ICAO Standard Atmosphere, 1958.
- Wege, K., H. Leese, H. U. Groening, and G. Hoffmann, Mean seasonal conditions of the atmosphere at altitudes of 20 to 30 km and cross sections along selected meridians in the northern hemisphere, *Final Rept., contract DA-91-508-EUC-210*, Institut für Meteorologie, Berlin Free Univ., 1958.

(Manuscript received March 6, 1961.)



Wind and Temperature Measurements in the Mesosphere by Meteorological Rockets

JOHN E. MASTERSON,¹ WILLIAM E. HUBERT,¹ THOMAS R. CARR¹

Pacific Missile Range, Point Mugu, California

Abstract. Small, solid-propellant rockets carrying meteorological instruments to altitudes beyond the capability of conventional balloons have provided a relatively large number of direct measurements of wind and temperature in the mesosphere. Data are presented from 110 meteorological-rocket launches made at Point Mugu, California, during a 17-month period. They show (a) strong reversal in the mesospheric zonal flow from winter to summer; (b) temporary breakdown in the winter westerlies in late January; (c) reversal in the meridional flow between 40,000 and 70,000 feet from winter to summer; (d) at least three meridional circulation cells in the vertical; (e) large temperature fluctuations in the mesosphere but good correlation, in the mean, with the ARDC Model Atmosphere.

Introduction. Although popular attention is focused on satellites and large atmospheric probes, it is significant that small instrumented rockets are taking a large number of measurements in the mesosphere to an altitude of about 100 km. (The definition of the mesosphere as used in the glossary of meteorology is used throughout this report.)

The mesosphere, which heretofore has been little measured only by larger rockets such as Nike Cajun, the Aerobee, the Kappa, and others. Opinions expressed by the authors are their own and do not necessarily reflect the view of the U. S. Department.

the Russian meteorological rockets, is now open to measurement on a synoptic basis by the use of small meteorological sounding rockets. It is in the mesosphere near the altitude of 50 km that the first temperature maximum (approximately 270°K) occurs. This region is of further interest because of a known reversal of seasonal winds and sudden warmings first described by Scherhag [1952] for balloon heights, and later confirmed by rocket flights at Fort Churchill during the IGY [Stroud, Nordberg, Banteen, Bartman, and Titus, 1960]. The data presented in this paper for Point Mugu are typical of those that are being obtained on a quarterly

TABLE 1. Characteristics of Radars Used at Point Mugu to Track Wind-Responsive Targets Released from Meteorological Rockets

Type	AN/FPS-16	SCR 584/615	SCR 584 Mobile	M-33 Mobile	
				Tracking	Acquisition
Frequency band,					
Cycles	C(5400-5900)	S(2700-2900)	S(2700-2900)	X(8500-9600)	S(3100-3500)
Power,	1000	500	250	250	1000
Watts	341 & 682	680	321	1000	1000
Width,					
Microseconds	1 & 0.5	0.5	0.8	0.25	1.3
Antenna	4 horn monopulse 12' parabolic reflector	8' parabolic reflector	8' parabolic reflector	6' lens	pill box w/reflector
Antenna gain,					
	45	34.5	34.5	38.5	29
Width,					
Degrees	1.2	3	3	1.2	1.4 horizontal variable csc ² vertical

TABLE 2. Zonal (u) and Meridional (v) Wind Components of All Meteorological-Rocket Soundings at Point Mugu, California

Height, ft.	Oct. 13, 1959		Oct. 14		Oct. 20		Oct. 21		Oct. 26		Oct. 27		Oct. 28		Nov. 4	
	u	v	u	v	u	v	u	v	u	v	u	v	u	v	u	v
220,000	+39	-21	+28	+16												
210,000	+59	-13	+20	+56												
200,000	+55	-15	+51	-8	+153	+56	+107	+62	+134	0	+76	+2				
190,000	+24	+39	+54	+20	+136	+79			+150	-13	+102	+14				
180,000	+31	+3	+35	+30	+105	+51			+89	+16						
170,000					+109	+23										
160,000															+93	+
150,000													+94	+13	+95	
140,000													+69	+6	+74	-
130,000													+49	-13	+65	
120,000													+45	-7	+59	+
110,000									+36	0			+33	0	+69	+
100,000									+26	-4			+28	+2	+39	+
90,000					+20	-9			+11	+2			+10	+2	+15	-
80,000					+25	-3	+7	-9	-14	+2					+10	-
70,000					+4	-2	+6	-4	-4	-3					+6	-
60,000					+12	-2	0	-18							+23	-
50,000					+42	-12	+18	-21							+59	-
40,000							+23	-39							+74	-
	Nov. 10 1959		Nov. 12		Nov. 16		Nov. 18		Jan. 15, 1960		Jan. 18		Jan. 21		Jan. 22	
220,000																
210,000							+147	-25								
200,000			+175	0			+146	-25								
190,000			+163	+29			+130	+23								
180,000			+156	0	+106	+62	+115	0								
170,000			+154	-27	+119	+69	+134	+24			+12	+10			+83	+
160,000					+114	+66	+129	0			+16	-6			+79	+
150,000					+87	+51	+107	+15			+8	-13			+77	-
140,000					+69	+40					+8	+2			+84	+
130,000	+100	0			+75	+27					+14	-5			+78	+
120,000	+89	-15			+53	+45					+21	+2			+72	-
110,000	+85	0			+53	+45			+68	+25	+23	+17	+93	+34	+68	+
100,000	+70	0			+50	+9			+29	+5	+42	+11	+91	+33	+90	+
90,000	+34	+6			+41	0			+23	+4	+30	+11	+68	+25	+80	+
80,000	+25	+9			+23	-4			+15	+9	+15	-2	+39	+22	+30	+
70,000	+19	-7			+9	-11			+22	+13	+9	-3	+41	+7	+32	
60,000	+19	-7			+21	-11			+27	+5	+15	0	+35	+6	+41	-
50,000	+20	-3			+29	-5			+42	+16					+82	+
40,000	+74	-13														
	Jan. 25, 1960		Jan. 26		Jan. 28		Feb. 1		Feb. 2		Feb. 3		Feb. 4		Feb. 5	
220,000																
210,000	+211	+30														
200,000	+214	+38														
190,000	+176	+48														
180,000	+130	+52														
170,000	+96	+19														
160,000																
150,000																
140,000																
130,000											+36	-4	+68	-19		
120,000											+25	-16	+54	-4	+122	
110,000											0	-8	+32	-13	+90	-
100,000					-8	-9	-52	0	-41	0	-24	+4	+18	-6	+21	-
90,000			+31	+14	0	+13	-52	0	-43	-8	-32	+11	-10	-12	+8	-
80,000			+42	+14	+23	+27	-37	+6	-38	-7	-34	-6	-13	-10	+4	-
70,000			+21	0	+28	+10	-10	+1	-17	+6	-12	+1			+3	-
60,000			+19	+3	+17	+3	-11	-7	-12	0	-12	-2			0	-
50,000			+32	+6	+25	+9	+19	-16			+19	-11			0	-
40,000			+76	+28	+38	+7	+43	-36			+85	-3			+43	-
							+88	-73							+74	-

2143

TABLE 2. Continued

Feb. 8, 1960		Feb. 11		Feb. 15		Feb. 16		Feb. 17		Feb. 26		Mar. 2		Mar. 4	
u	v	u	v	u	v	u	v	u	v	u	v	u	v	u	v
				+164	+48			+115	-10	+131	+50	+80	0		
				+130	+40			+119	+21	+175	+31	+86	0		
				+101	+35			+114	+18	+164	+45	+104	0	+107	+4
+147	+11			+82	+30	+108	0	+96	+29	+188	+34	+103	+19	+104	+15
+120	+21			+79	-4	+104	-26	+86	+11	+153	+27	+66	-11	+63	-32
+112	+12			+81	+6	+82	-16	+73	+8	+76	+46	+36	+14	+42	+17
+104	+15			+93	+7	+96	-10	+82	+5	+58	+24	-16	+39	+17	+20
+97	+32			+69	+9	+60	-4	+65	-11	+55	+32	-17	+22	-16	+16
+69	+23	+92	-19	+44	+4	+45	0	+34	-7	+65	+30	-29	+10	-10	+10
+43	+16	+86	-23	+37	-4	+20	-9	+17	+3	+42	+20	-10	+3	-3	+5
+20	+8	+30	+2	+9	+14	+4	+7	+5	+6	+14	+5	+6	+4	+9	-3
+13	-9	-7	+3	+4	-3	+10	-13	+8	-8	+15	0	+12	0	+35	-6
+3	-11	-3	-8	+39	-1	+34	-20	+33	-12	+22	-4	+32	-7	+35	-6
+18	+3	+20	-34	+63	+10	+62	-41	+73	-12	+54	-9	+62	-10	+69	-3
+43	-24	+52	-71											+74	-11
+96	-66														
Mar. 8, 1960 (1809Z)		Mar. 8 (2230Z)		Mar. 10		Mar. 18		Apr. 8		Apr. 18		Apr. 20		Apr. 21	
+216	+54											-33	+19		
+140	0											-8	+22		
+144	+44							+66	0			-8	0		
+120	+12			+79	+31			+41	+23			-1	+6		
+112	+24	+109	-19	+94	+17	+49	+7	+23	+30			+2	+12		
+91	+11	+94	+10	+59	-11	+27	+7	+38	+45			+20	+7		
+101	+37	+81	+28	+38	-25	+17	-8	+20	+30			+28	+16		
		+77	-26	+4	-23	+13	-16	+30	+19	+19	+3	+36	0		
		+57	+11	-7	-16	+18	-15	+44	+22	+51	-2	+37	-3		
		+20	+34	+14	-20	+26	-2	+59	+2	+63	+3	+35	+13		
		-14	+26	+24	-9	+7	+7	+53	+2	+46	+9			+41	0
		-27	+15	-5	-14	-6	+10	+32	-22	+29	+12			+17	+14
		-33	+17	-10	-4	-17	+3	+11	-8	+18	+9			+3	+9
		-19	+12	-10	-3	-9	0	-21	+1	+3	+8				
		+2	-10	+4	-13	-18	-15	-19	0	+7	-2				
		+32	-11	+37	-9	-3	-15	-7	-3	+19	-1				
		+72	-12	+71	0	+7	-12	+28	+6						
				+62	-8	+9	-11	+41	+13						
Apr. 22, 1960		Apr. 25		Apr. 27		Apr. 29		May 3		May 4		May 9		May 10	
		+13	+15			-40	+10							-35	-45
		+11	+14			-46	+26							-52	+9
		+12	+16			-32	+16							-48	+2
		+14	+31	-14	-18	-23	+11							-54	+19
		+22	+6	+14	+34	+10	+22					-55	+9	-29	+11
		+9	-14	+14	+12	+21	-11					-26	+14	-40	+12
		+28	-6	+13	+16	+33	+18					-21	+8	-16	-12
		+42	+6	+40	+13	+30	+23					+20	+6	-6	-7
		+42	-2	+37	0	+11	+11	-18	-6			+7	+12	-2	-10
		+28	-4	+31	+4	+4	+5	-27	+4	-26	-1	+16	+6	-1	-10
+27	+22	+7	+3	+18	+2	+4	+3	-23	-1	-21	0	+3	+9	-6	-6
		-6	+1	+2	+7	+9	+3	-3	-5	-10	-8	-7	+5	-14	-6
		+2	-12	+5	+5	-1	-7	-3	-5	-10	-8	-8	+1	-11	-2
		+24	+3			+14	+2	+8	0	+14	-5	+4	-2	0	+10
						+50	-22	+34	-1	+40	-24	+30	-8	+44	-7
								+42	-29	+68	-38	+16	0		

TABLE 2. Continued

Height, ft.	Nov. 29, 1960		Jan. 17, 1961		Jan. 27		Jan. 31		Feb. 1		Feb. 3		Feb. 8		Feb. 14	
	u	v	u	v	u	v	u	v	u	v	u	v	u	v	u	v
220,000																
210,000																
200,000							+73	0								+180
190,000							+66	+16								+193
180,000	+80	-27	+255	+10			+78	+55			+16	+6	+81	+10		+156
170,000	+37	-5	+283	+45			+52	+30			+9	0	+65	+17	+128	+
160,000	+41	+9	+163	+23	+154	+96	+38	+23			+14	0	+42	+4	+120	+
150,000	+99	+27	+99	+14	+148	+92	+5	+34			+17	-10	+51	-9	+106	
140,000	+96	+9	+128	-4	+126	+73	0	+25			0	-48	+65	-17	+78	-
130,000	+68	+15	+40	-23	+99	+14	+19	-7	0	+21	0	-27	+40	-15	+48	
120,000	+60	-1	+14	0	+50	+11	+16	+34	+14	+24	+19	+4	+16	-9	+36	
110,000	+14	+6	-2	-10	+29	-2	+19	+53	+29	+29	+19	+16	+11	+9	+16	
100,000	-9	-11	-22	-2	+24	-14	+57	+27	+16	+6	+24	-8	-3	+5	+2	
90,000	-7	-17	-16	-3	-12	-6	+34	+5	+27	+2	+11	-4	-2	+5	0	
80,000	+9	+2	-27	-6	-19	-7	+10	+6	+10	-1	-1	-5	-2	+5	0	
70,000	+26	-1	0	0	-12	-16	+10	+2	+3	-8	0	-6	+3	+4	-2	
60,000	+28	+15	+4	-2	+9	-6	+32	+15	+16	-3	+26	-15	+12	-2	+10	
50,000	+52	+37	+27	+13	+52	-24	+48	+18			+34	-20			+20	
40,000					+89	-41	+49	-8								
	Feb. 15, 1961		Feb. 16		Feb. 17											
220,000																
210,000																
200,000																
190,000	+140	-24	+107	0	+79	-6										
180,000	+120	+21	+117	+21	+94	-6										
170,000	+110	+40	+90	0	+98	+8										
160,000	+156	-27	+116	0	+104	+5										
150,000	+183	0	+130	+23	+144	+8										
140,000	+120	+17	+94	+17	+101	+1										
130,000	+61	-16	+73	0	+73	-12										
120,000	+32	+3	+27	0	+38	+14										
110,000	+22	0	+22	-4	+13	+4										
100,000	-3	0	M	M	M	M										
90,000	-2	-2	M	M	M	M										
80,000	0	-5	M	M	M	M										
70,000	+9	+6	+5	-2	M	M										
60,000	+13	-6	+19	+3	+25	-10										
50,000	+41	+4	+28	0	+47	-8										
40,000	+58	+21	+28	-10	+51	-19										

synoptic basis from a number of rocket-firing sites throughout the North American continent [aufm Kampe, 1960; Webb, Hubert, Spurling, Miller, 1960]. A total of 110 successful launches have been made at Point Mugu to February 17, 1961; almost half of these occurred during the winter months. On some days a Loki I sounding was combined with an Arcas or a Loki II to obtain a more complete rocket wind profile.

Instrumentation. Three types of meteorological rockets are used to carry or catapult the payload to its apogee. The Loki I ejects an 8-foot (2.4 m) mular parachute as a target at an altitude of approximately 110,000 feet, whereas the Loki II ejects a payload of metallized S-band chaff at

about 210,000 feet [Newell, 1959; Masterson, 1959; Webb and Jenkins, 1959]. The Arcas rocket ejects at an altitude of about 206,000 feet a 15-foot- (4.57-m) diameter metallized silk parachute carrying a temperature instrumentation package [Houston, 1959; Masterson, Hubert, and Carr, 1960]. Horizontal wind speed and direction are determined from resolution of data plotted from real-time readout of the radar dials or from a reduction of the radar track penned on an automatic plotting board chart. For the convenience of researchers, some characteristic (which are not readily available) of the radar used at Point Mugu, are presented in Table 1. The temperature and reference signals are

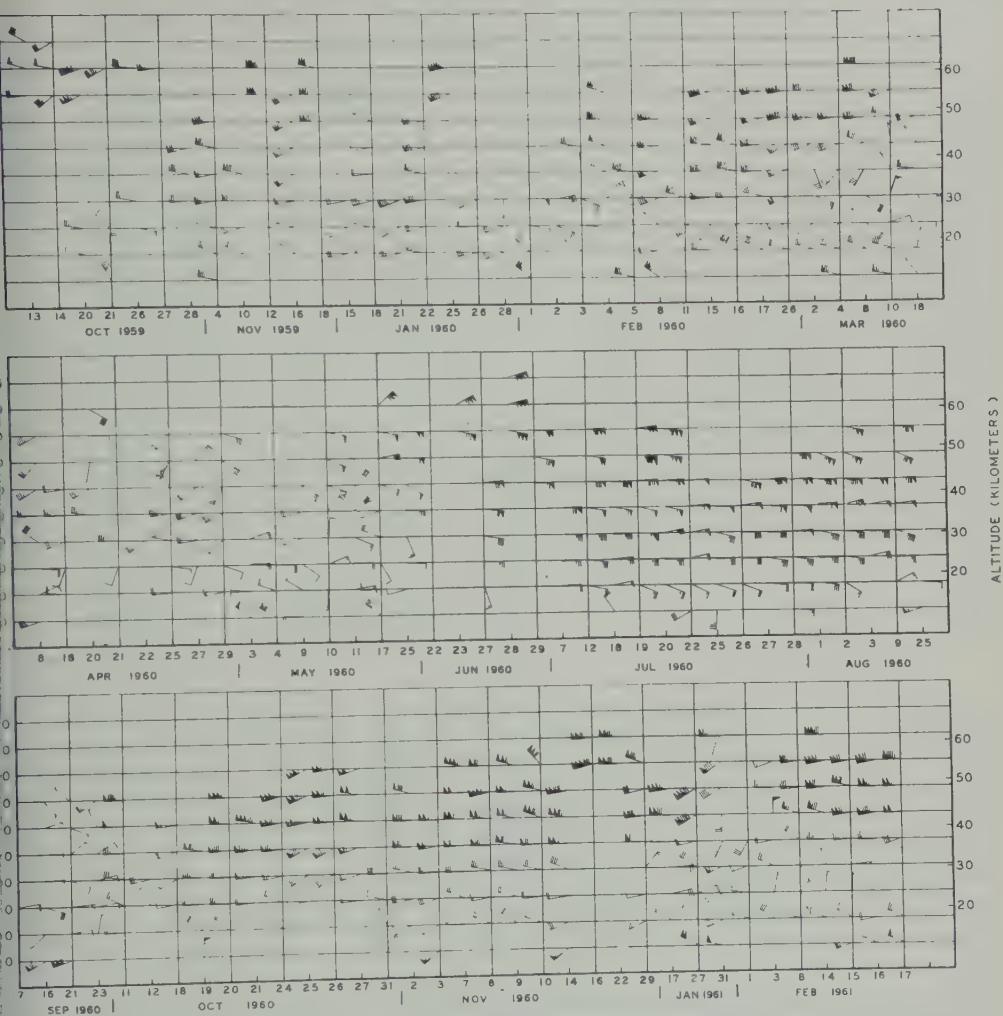


Fig. 1. Plot, on a nonlinear time base, of meteorological-rocket winds in knots at Point Mugu, California.

etered on 1680 Mc to a standard GMD-1 sonde receiver. The parachute presents a continuously coherent target for the radar to . The chaff, a shredded metallized radar-ative material, diffuses eventually into an erent target. Although it is expected to be accurate than the parachute, both the chute and the chaff are observed to be st immediately responsive to the wind. [1960] has shown that the response time haff is shorter than previously expected. Point Mugu, target movement of greater 150 knots at right angles to the launch uth within 20 seconds of parachute ejection een measured.

The temperature sensor flown in Arcas rockets at Point Mugu uses a 10-mil uncoated bead resistance thermistor externally inserted in the circuitry. The optimum exposure of the thermistor as it hangs from the parachute is not clearly known; however, data from those soundings in which the parachute-borne instrumentation has floated down to levels sampled essentially simultaneously by balloon-borne thermistors indicate that the temperatures obtained from the bead thermistor are compatible with those obtained by conventional radiosonde balloon-borne thermistor rods [Ogden and Swinton, 1960].

Point Mugu wind data. Table 2 is a compilation of the zonal (u) and meridional (v) wind

TABLE 3. Mean Meridional and Zonal Winds (Knots) over Point Mugu, California, during Four Major Flow Regimes

Height, ft.	Winter Regime			Spring Transition			Summer Regime			Fall Transition			Total C servatio N
	\bar{u}	\bar{v}	n	\bar{u}	\bar{v}	n	\bar{u}	\bar{v}	n	\bar{u}	\bar{v}	n	
220,000							-151	-46	1	+34	-2	2	3
210,000	+138	+16	7				-133	+18	1	+40	+34	2	10
200,000	+140	+11	12	-33	+19	1	-111	-55	3	+53	-12	2	18
190,000	+128	+17	20	+9	-2	4	-101	-3	4	+39	+30	2	30
180,000	+120	+14	30	-10	+11	5	-104	+5	10	+33	+16	2	47
170,000	+112	+16	34	-5	+14	7	-94	+12	10	+70	+12	2	53
160,000	+107	+13	36	-6	+17	8	-86	+14	10	+30	+4	4	58
150,000	+97	+8	40	-6	+12	9	-87	+10	12	+23	+1	4	65
140,000	+86	0	40	+3	+9	10	-77	0	16	+11	-2	4	70
130,000	+69	+2	44	+15	-1	10	-61	-2	16	+16	+1	4	74
120,000	+52	+7	44	+31	+3	10	-53	+1	17	+4	-2	4	75
110,000	+33	+8	52	+25	+6	10	-38	+4	18	-2	+4	4	84
100,000	+23	+3	54	+14	+2	12	-38	+2	17	+7	+1	5	88
90,000	+16	+2	52	-2	+2	12	-30	+1	17	-7	-4	6	87
80,000	+9	+1	52	-9	+2	12	-28	+1	17	-7	-2	6	87
70,000	+8	-3	51	-7	-4	11	-24	+4	17	-5	+2	5	84
60,000	+21	-4	46	+6	-1	10	-14	+4	16	0	+1	5	77
50,000	+43	-7	40	+33	-8	8	+1	+6	10	+35	+7	4	62
40,000	+55	-16	16	+35	-13	5	+12	+2	5	+76	+31	3	29

components obtained from all meteorological rocket firings at Point Mugu, California (34°07'N, 119°07'W). The speeds are in knots, with components from the west and south being positive. The table is presented for the convenience of researchers desiring to carry out quantitative investigations in mesospheric circulation problems. Figure 1 is a plot on a nonlinear time base of Point Mugu meteorological-rocket soundings of winds against height. The arrows indicate the direction from which the wind is blowing (north is at the top of the figure, and east to the right). Each flag represents 50 knots, each full barb, 10 knots, and each half barb, 5 knots.

The most predominant features revealed by the tabulation and time sections of individual wind soundings are:

- a. Strong mesospheric westerlies throughout most of the winter.
- b. A temporary breakdown in the upper flow in late January and early February.
- c. Deep mesospheric easterlies in summer.
- d. Chaotic winds during the spring and fall transition periods.

The breakdown in the flow mentioned above in (b) is clearly shown in the late January data for both 1960 and 1961. Apparently in late January there is an unsuccessful attempt of the wind to shift into the typical summertime

easterly flow. However, after a week or 10 days of unsteady conditions, the mesospheric westerlies predominate once more, with the complete reversal being delayed until March or April. The breakdown occurring in 1960 coincided with the period of 'unrest' in the upper flow over the Caribbean reported by *Riehl and Higgs* [1960] and was apparently limited in depth. The meteorological-rocket soundings of winds from February 3, 1961, on the other hand, indicate that the breakdown this year extended from the tropopause to at least 180,000 feet.

The summertime easterlies not only have greater depth but are relatively steady, both in direction and intensity. The observations show considerable evidence of waves in the westerlies in winter (e.g., November 1960), but the easterly flow is almost devoid of significant wind perturbations. In such an event, we should expect that the same quiet state would also apply to temperature conditions in summer.

A better picture of mean conditions is shown by grouping the wind data under four flow patterns (regimes) covering calendar periods as follows:

Winter regime	October 15–March 15
Spring transition	March 15–May 15
Summer regime	May 15–August 15
Fall transition	August 15–October 15

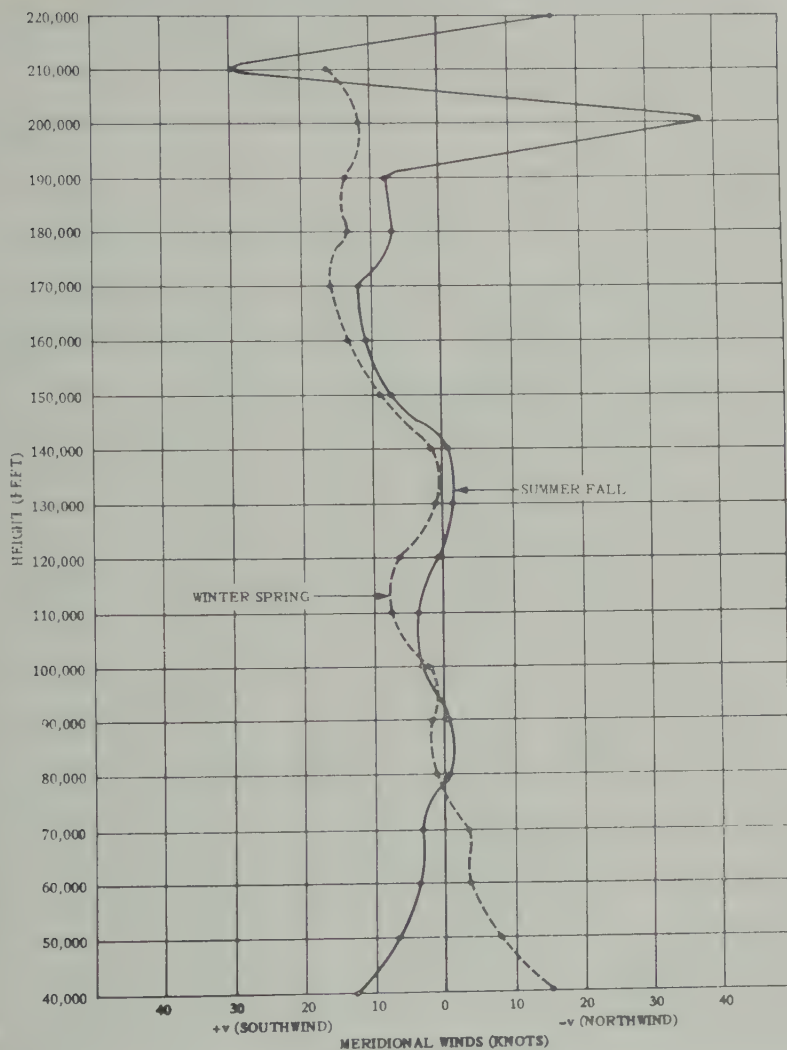


Fig. 2. Mean meridional winds in knots for winter-spring and summer-fall over Point Mugu, California.

Fig. 3 shows the mean zonal wind (\bar{u}), mean meridional wind (\bar{v}), and number of observations for the various regimes. The fall and winter data contain data from 2 different years; separate averaging revealed, however, that the results were quite similar, so they were combined to simplify the summary.

The mean zonal winds agree, in general, with those shown by Murgatroyd [1957]. Batten [1960] used some of the earlier Point Mugu data to construct a time section of mean zonal winds between latitudes 30° and 40°N. Both sets of data from Point Mugu show a zonal

minimum at an altitude of 70,000 feet, and comparable maximum near 200,000 feet.

Several interesting features appear in the mean meridional wind summaries. Above the tropopause to 70,000 feet, the mean meridional flow at Point Mugu was from the north in winter and spring, and from the south during summer and fall. Between 70,000 and 180,000 feet, the predominant meridional flow was from south to north, except in a narrow layer near 135,000 feet. All four regimes show a persistent tendency for weak southward flow at 135,000 feet. There is some evidence of another seasonal reversal

TABLE 4. Temperatures, °C, Obtained from Meteorological Rockets Launched at Point Mugu, California

TABLE 4. Temperatures, °C													
Height, ft.	Feb. 1, 1960	Feb. 5	Feb. 15	Apr. 27	Apr. 29	May 9	May 17	July 7	July 19	July 20	July 26	July 28	
200,000				+23									
190,000				+20									
180,000			+12	+17						-15			
170,000			+10	+13						-15			
160,000			-1	+10					-10	-16			
150,000			-3	+1		+1			-15	-22			
140,000	-2		-8	-12		-3			-15	-29	-23	+10	
130,000	-22	-30	-12	-27	-10	-6	+24	-30	-24	-33	-39	-15	
120,000	-32	-40	-22	M	-27	-13	+2	-34	-29		-42		
110,000	-27	-42	-32		-27	-21	-12	-41	-33		-54		
100,000	-45	-43	-41	-51	-39	-37	-25	-45	-39		-61		
90,000	-51	-52	-51	-52	-46	-43	-37	-50	-42		-69		
80,000	-55	-55	-56	-54	-53	-53	-47	-58	-48				
70,000		-58	-63	-56	-56	-60	-53	-61	-56				
60,000			-71	-57	-64	-73	-58	-70	-63				
50,000				-62	-63			-73					
40,000				-63				-53					
Height, ft.	Sept. 23 1960	Oct. 11	Oct. 17	Oct. 25	Oct. 26	Nov. 7	Nov. 8	Nov. 9	Nov. 10	Nov. 14	Nov. 29	Jan. 17, 1961	
200,000								+28					
190,000	+9	+28			+22			+27					
180,000	+5	+27			+14			+26	-8				
170,000	+6	+26			+12			+25	-9				
160,000	+3	+25			+8			+23	-9	+9	0		
150,000	-2	+23			+4		+18	+20	-10	-1	-6		
140,000	-10	+22			-8		+9	+15	-17	-12	-12		
130,000	-21	+17			-9	+21	+6	+6	-31	-26	-21		
120,000	-33	+7		-1	-29	-14	-4	-4	-36	-38	-30	-40	
110,000	-39	-8		-24	-45	-31	-20	-16	-45	-52	-40	-43	
100,000	-44	-28		-32	-49	-37	-36	-34	-47	-61	-49	-42	
90,000	-49	-46		-44	-57	-44	-50	-46	-52	-65	-55	-52	
80,000	-54	-52		-51	-64	-49		-50	-58	-67	-57	-61	
70,000	-58	-62	-57			-51		-54		-70	-61	-64	
60,000		-65	-62			-56		-60		-70	-65	-74	
50,000			-70					-61		-70	-65		
40,000			-62							-65			
Height, ft.	Jan. 26, 1961	Jan. 27	Jan. 30	Jan. 31	Feb. 1	Feb. 3	Feb. 8	Feb. 13	Feb. 15	Feb. 17	Mean \bar{T}	No. N	ARD Mod
200,000											+28	1	-19
190,000											+21	5	-7
180,000											+10	8	+4
170,000						+2				-12	+6	10	+9
160,000				+9		+3				-12	+3	14	+9
150,000				-3		-1				-14	0	16	+4
140,000				-10		-12		+7		-16	-5	18	-4
130,000				-29	-15	-26		-10		-21	-13	25	-13
120,000		-19	-23	-35	-33	-37		-24		-37	-24	30	-22
110,000		-41	-21	-30	-36	-31		-33		-50	-32	27	-31
100,000	-51	-45	-50	-46	-42	-40	-47	-48		-55	-43	30	-40
90,000	-62	-60	-60	-57	-50	-49	-52	-54	-53	-60	-52	31	-49
80,000	-67	-60	-70	-62	-60	-61	-58	-62	-60	-64	-58	30	-56
70,000	-69	-65	M	-70	-70	-71	-64	-68	-64		-62	24	-56
60,000	-70	-68	M	-70	-71	-71	-64	-69	-65		-66	22	-56
50,000	-67		-71	-69		-66	-61	-72	-66		-67	14	-56
40,000	-62		-60	-62		-64	-61	-73			-62	10	-56

190,000 feet. The principal meridional circulation features are shown in Figure 2.

From the data collected at Point Mugu, it appears that the mesosphere may be characterized by as many as three or four mean meridional circulation cells in the vertical at this latitude.

Point Mugu temperature data. Table 4 is a list of all the meteorological-rocket temperature soundings made at Point Mugu. Several different instrument packages were used to obtain these data; their relative merits are still being evaluated. No corrections have been made to make the rocket temperatures agree with radiosonde temperatures in regions of overlap. These observations represent only an attempt to study mesospheric temperatures; for this reason no discussion of accuracy will be given in this paper. The many problems involved in obtaining representative readings at high altitudes in the atmosphere have been covered quite thoroughly by Ney, Maas, and Huch [1961]. The dual temperature soundings (Table 3) are included for the use of those desiring to carry out additional investigation.

In general, the agreement with the ARDC Atmosphere is good, except near the tropopause (where the rocket temperatures are lower) and above 170,000 feet. The fact that rocket temperatures are much warmer at the highest levels may be explained by frictional heating of the nose cone during its ascent.

Conclusion. The data presented and discussed here have been typical of those obtained from the Meteorological Rocket Network sites. Similar data are obtainable from any location where small meteorological rockets can be fired. Where a GMD radiosonde and a tracking system are available. After the GMD-1 system is converted to a GMD-2, the system will be able to track and to reduce winds directly from the wind instruments; consequently, a tracking system will no longer be required. The measurements of the mesosphere on a synoptic basis by meteorological rocket systems, when adopted by a large number of stations throughout the Northern Hemisphere, will give new clues to the cause of warmings, the rapid reversals of wind in the mesosphere, and the mesospheric jet. It is

believed that these may all provide an insight to relationships and interactions between processes in the mesosphere and weather in the troposphere.

REFERENCES

- aufm Kampe, H. J., The meteorological rocket network, *J. Geophys. Research*, **65**, 501, 1960.
- Batten, E. S., Wind system in the mesosphere and lower ionosphere, *Engineering Division Rpt. P-2018-NSF*, The RAND Corporation, 1960.
- Houston, W. S., Program Report on ARCAS, presented at Semi-Annual Meeting, American Rocket Society, June 1959.
- Masterson, J. E., A review of meteorological sounding rockets, *International Symposium on Rockets and Astronautics, Proceedings*, Japanese Rocket Society, Tokyo, 1959.
- Masterson, J. E., W. E. Hubert, and T. R. Carr, Wind and temperature data measured by meteorological rockets, *Second International Symposium on Rockets and Astronautics, Proceedings*, Japanese Rocket Society, Tokyo, 1960.
- Murgatroyd, R. J., Winds and temperatures between 20 km and 100 km, a review, *O. J. Roy. Met. Soc.*, **83**, 417-459, 1957.
- Newell, H. E., Jr., *Loki-wasp* (chap. VIII), *Sounding Rockets*, McGraw-Hill, 1959.
- Ney, E. P., R. W. Maas, W. F. Huch, The measurement of atmospheric temperature, *J. Meteorol.*, **18**, 60-80, 1961.
- Odgen, D. E., and D. B. Swinton, ARCAS temperature data in the mesosphere, *Monthly Weather Review*, May 1960.
- Rapp, R. R., The accuracy of winds obtained by the radar tracking of chaff at high altitudes, *J. Meteorol.*, **17**, 507-514, 1960.
- Riehl, H., and R. Higgs, Unrest in the upper stratosphere over the Caribbean during January 1960, *J. Meteorol.*, **17**, 555-561, 1960.
- Scherhag, R., Die explosionsartigen stratosphärenwärmungen des Spät winters 1951/1952, *Ber. deut. Wetterdienstes in der U. S. Zone*, **38**, 51, 1952.
- Stroud, W. G., W. Nordberg, W. R. Bandeen, F. L. Bartman, and R. Titus, Rocket grenade measurements of temperatures and winds in the mesosphere over Churchill, Canada, *J. Geophys. Research*, **65**, 2307-2323, 1960.
- Webb, W. L., and K. R. Jenkins, Application of meteorological rocket systems, *J. Geophys. Research*, **64**, 1855-1861, 1959.
- Webb, W. L., W. E. Hubert, R. L. Miller, and J. F. Spurling, Initiation of the meteorological rocket network, *Bull. Am. Meteorol. Soc.*, **41**, May 1960.

(Manuscript received November 28, 1960;
revised March 21, 1961.)



On the Deduction of the Vertical Distribution of Ozone by Ultraviolet Spectral Measurements from a Satellite

SEAN TWOMEY

U. S. Weather Bureau, Washington, D. C.

Abstract. In a simple scattering atmosphere, containing an absorbing constituent that absorbs differently at different wavelengths, the spectral distribution of reflected energy depends on the vertical distribution of the absorbing constituent. In fact, if the vertical distribution is represented by expressing the pressure as an explicit function of the mass of absorbent between the top of the atmosphere and that pressure level, and the spectral energy distribution as an explicit function of the absorption coefficient, then, for a model with primary scattering only, the latter function is a Laplace transform of the former. This result can be utilized to obtain an approximate inversion and so to deduce the vertical distribution of the absorbing constituent. Some numerical computations are presented for the case of ozone distribution in the earth's atmosphere.

Introduction. The absorption coefficient of ozone varies rapidly with wavelength in the 200 to 3000 Å region of the ultraviolet: at 200 Å, for example, *Inn and Tanaka* [1956] give the exponential absorption coefficient as 1.5×10^{-4} (STP) at -44°C , whereas at 2992 Å the value is given as 10.7 cm^{-1} (STP). The variation into the atmosphere in this wavelength region consequently varies considerably in a relatively narrow spectral region. It has been suggested [*Singer*, 1956] that measurements from a satellite of the intensity of scattered light in this region might be used to determine the vertical distribution.

The present paper is concerned mainly with the problem of manipulating ultraviolet spectral measurements in order to deduce the ozone concentration. It is shown that the problem is equivalent to the inversion of a Laplace transform and that the inversion is possible if the spectral measurements are of sufficient sensitivity and precision. Although the entire ozone distribution curve cannot be obtained, it does appear that useful information about the distribution can be obtained down to, and somewhat above, the median ozone level (typically around 20 km), by simple spectral measurements in the 200 to 3000 Å region.

Rayleigh scattering in an atmosphere containing an absorbing constituent. Initially the following will be considered: An atmosphere containing a preponderance of molecules of polarizability α , containing also a small proportion of a highly absorbing constituent such as

ozone in concentration $\epsilon(p)$ cm (STP) per mb at the pressure level p . Attenuation by the scattering molecules and scattering by the absorbing molecules will be neglected; an infinitely deep atmosphere will be assumed at this stage, and the direction of illumination and of viewing will be assumed to be vertical. If the absorption coefficient at a wavelength λ is $k(\lambda) \text{ cm}^{-1}$, the energy flux per square centimeter at a level p is evidently, for this wavelength,

$$E_\lambda(p) = E_\lambda(0) \exp \left(-k(\lambda) \int_0^p \epsilon(p) dp \right)$$

if $E_\lambda(0)$ is the incident flux density at the top of the atmosphere at wavelength λ .

The theory of Rayleigh scattering shows that a molecule with polarizability α scatters an energy flux

$$\Delta F_s = \frac{1}{2} E_i (1 + \cos^2 \theta) (2\pi/\lambda)^4 |\alpha|^2 \Delta\omega \quad (1)$$

into an infinitesimal solid angle $\Delta\omega$ in a direction θ to the direction of propagation of an incident flux with flux density E_i ; the total flux scattered by a single molecule is found by integration of (1) over a sphere to be

$$F_s = E_i \cdot \frac{8\pi}{3} \cdot \left(\frac{2\pi}{\lambda} \right)^4 |\alpha|^2 = \frac{128\pi^5}{3\lambda^4} |\alpha|^2 E_i \quad (2)$$

Since, at this stage, attenuation due to scattering is neglected, the energy scattered backward, at vertical incidence, by the layer between the pressure levels p and $p + \Delta p$ is evidently,

at wavelength λ ,

$$\Delta E_p = E_\lambda(0) \exp \left(-k(\lambda) \int_0^p \epsilon(p) dp \right) \cdot \left(\frac{2\pi}{\lambda} \right)^4 |a|^2 (mg)^{-1} \Delta p \Delta \omega \text{ cm}^{-2}$$

if m = mass of a single molecule, g = acceleration of gravity. This backscattered light is further absorbed before emerging from the atmosphere. If the atmosphere is being viewed vertically by an optical system such that variations in path length and in scattering angle θ need not be considered, and if multiple scattering is neglected, the light in the wavelength interval $\lambda \rightarrow \lambda + \Delta\lambda$ reaching the optical system in a solid-angle increment $\Delta\omega$ from unit area between p and $p + \Delta p$ is

$$\Delta E = E_\lambda(0) \exp \left(-2k(\lambda) \int_0^p \epsilon(p) dp \right) \cdot \left(\frac{2\pi}{\lambda} \right)^4 |a|^2 (mg)^{-1} \Delta p \Delta \omega \Delta \lambda$$

This is equivalent to the statement that the layer between p and $p + \Delta p$ has a spectral steradiancy (brightness) of

$$E_\lambda(0) \exp \left(-2k(\lambda) \int_0^p \epsilon(p) dp \right) \cdot \left(\frac{2\pi}{\lambda} \right)^4 \frac{|a|^2}{mg} \Delta p \Delta \lambda$$

when viewed from above the atmosphere. It is well known that image brightness equals object brightness, regardless of distance, in a perfect optical system with no losses. Hence the scattered light falling on a detector at the wavelength for which the absorption coefficient is k is obtained by summing the equivalent steradiancy over all layers. Thus the response of the detector is proportional to the integrated steradiancy

$$\begin{aligned} B(\lambda) &= E_\lambda(0) \left(\frac{2\pi}{\lambda} \right)^4 \frac{|a|^2}{mg} \\ &\quad \cdot \int_0^\infty \exp \left(-2k(\lambda) \int_0^p \epsilon(p) dp \right) dp \\ &= 9.2 \times 10^{-23} \lambda^{-4} E_\lambda(0) \\ &\quad \cdot \int_0^\infty \exp \left(-2k(\lambda) \int_0^p \epsilon(p) dp \right) dp \end{aligned}$$

or, if the steradiancy $B(\lambda)$ multiplied by $mg\lambda^4/[16\pi^4|a|^2E_\lambda(0)]$ is denoted by $R(k)$, where $2k(\lambda) = k$, then, for an infinite atmosphere,

$$R(k) = \int_0^\infty \exp \left(-k \int_0^p \epsilon(p) dp \right) dp \quad (3)$$

The quantity $R(k)$ can be measured for a range of values of k by measuring the luminance of the atmosphere over the range of wavelength within which k varies in a known manner. The deduction of ozone distribution then rests on the deduction from $R(k)$ of some explicit functional relationship between ϵ and p .

Approximate solution. Taking a new variable

$$x = \int_0^p \epsilon(p) dp$$

(i.e., the total amount of ozone above the level p), equation 3 becomes

$$R(k) = p(0) + \int_0^\infty e^{-kx} \frac{dp}{dx} dx$$

Here the upper limit is taken as infinity. This arises from the conditions for the convergence of the integral in (3), which will converge only if

$$\int_0^p \epsilon dp \rightarrow \infty \quad \text{as} \quad p \rightarrow \infty$$

This implies that ϵ can be small, but must remain finite, as $p \rightarrow \infty$. (In practice an infinite atmosphere would never give an infinite value for the reflected energy even if $\epsilon = 0$ for $p > p_0$ but in such cases the attenuation by scattering would predominate for larger values of p and would produce the same effect as a positive nonzero value for ϵ .) Thus

$$\begin{aligned} R(k) &= p(0) + \int_0^\infty e^{-kx} \frac{dp}{dx} dx \\ &= p(0) + kL_k\{p\} \end{aligned} \quad (4)$$

where $L_k(y)$ denotes the Laplace transform $\int_0^\infty e^{-kx} y dx$. Physically the term $p(0)$ refers to scattering from any air molecules entirely above the ozone layer. Reference to the theory of Laplace transform shows that no two distinct functions can have identical transforms. Thus the uniqueness of a solution $p = p(x)$ of (4) is assured.

If the inversion of (4) gives p as an explicit function of x ($= \int_0^p \epsilon(p) dp$), it is then a simple

TABLE 1

cm^{-1}	20	30	40	60	100	150	200
(approx.)	3040	2970	2950	2915	2870	2840	2780
, mb	11.16	7.67	5.91	4.18	2.80	1.92	1.48
, $\text{erg cm}^{-2} \text{A}^{-1}$							
$\text{er}^{-1} \text{sec}^{-1}$	0.072	0.045	0.032	0.0192	0.0114	0.00747	0.00513

ter to deduce x as a function $x(p)$ of p , and
 ace p as a function of x , since, by definition
 the fact that $\epsilon \geq 0$, x is a monotonically
 easing function of p . It is preferable, how-
 , to retain the $p(x)$ or $x(p)$ curve to describe
 ozone distribution: this is physically the most
 nifingful description of the ozone distribution,
 n the point of view of ultraviolet absorption
 scattering (for the light intensity at a given
 sure level is determined primarily by the
 grated amount of ozone above that level).
 s quantity, and therefore the backscattered
 t, is inherently insensitive to large fluctua-
 s in very shallow layers. One cannot expect
 btain meaningful information about such
 tuations if they do not alter appreciably the
 e of integrated ozone versus pressure.

he Laplace transform of x^m can be derived
 t readily from the definition of the gamma
 ation:

$$\begin{aligned} \{x^m\} &= \int_0^\infty e^{-kx} x^m dx \\ &= k^{-(m+1)} \int_0^\infty e^{-kz} (kx)^m d(kx) \\ &= k^{-(m+1)} \Gamma(m+1) \end{aligned}$$

f m is an integer,

$$L_k\{x^m\} = m!/k^{m+1} \quad (5)$$

therefore, we approximate to $R(k)$ by a
 nomial in $(1/k)$ or any positive power thereof,
 can immediately write down the inversion of
 expansion: if

$$= a_0 + a_1 k^{-r_1} + a_2 k^{-r_2} + \dots$$

$$\begin{aligned} &= a_0 + a_1 \frac{x^{r_1}}{\Gamma(r_1 + 1)} \\ &\quad + a_2 \frac{x^{r_2}}{\Gamma(r_2 + 1)} + \dots \end{aligned}$$

t this stage it is worth mentioning that

quadrature tables for evaluation of Laplace
 transforms may be used to derive with fair
 accuracy the steradiancy of the model atmos-
 phere. For a typical ozone distribution, numerical
 integration gave the values in Table 1 for $R(k)$
 and the steradiancy $B(k)$, using for E_0 in the
 latter case the solar spectral irradiance values
 given in Allen [1955, p. 140].

The values in Table 2 were obtained for the
 same conditions by use of quadrature coefficients
 given by Salzer [1953] (a six-point quadrature
 was used with the transformation $p = bk$ and
 tabular points $x = 0, b, 2b, \dots, 5b$, taking
 $b = 0.05$ for $20 < k < 60$ and $b = 0.02$ for
 $60 < k < 200$).

Physically, the quantity $R(k)$ represents the
 thickness (in millibars) of an atmosphere which,
 if the ozone were removed, would have the same
 reflectivity as the actual (absorbing) atmosphere;
 it is therefore a measure of the effective penetra-
 tion of radiation into the absorbing atmosphere.

Determination of the coefficients. From the
 foregoing it is apparent that, if an expansion of
 the form $a_0 + a_1 k^{-1} + a_2 k^{-2} + \dots$ can be found
 for $R(k)$, a relationship between p and x can be
 obtained. In practice, of course, $R(k)$ will not be
 obtained in a functional form; it will be given as
 a graph or table of $R(k)$ covering a finite range
 of values of k . In practice, also, measurement of
 $R(k)$ at small values of k will be limited by
 penetration of the corresponding wavelengths
 to the surface (which gives rise to a large and
 erratic contribution from ground reflections). If
 $R(k)$ is considered to be known between $1/k = a$
 and $1/k = b$, and if a and b are chosen so that
 the ground-reflected contribution can be neg-
 lected, two procedures may be followed to esti-
 mate the value of the coefficients a_0, a_1, \dots , etc.

(a) Orthogonal polynomials. If we set $1/k = t$,
 Schmidt's process may be employed to con-
 struct from the set $1, t, t^2$ a set of polynomials
 $p_m(t)$ which are normal and orthogonal with
 respect to the interval (a, b) . These are, of
 course, analogous to the Legendre polynomials
 but with the interval $(-1, 1)$ replaced by (a, b) .

TABLE 2

	20	30	40	60	100	150	200
k							
$R(k)$	11.16	7.5	5.88	4.2	2.67	1.83	1.38
$B(\lambda)$	0.072	0.044	0.0318	0.0193	0.0109	0.00712	0.0048

The Schmidt process gives for $p_m(t)$

$$p_m(t) = \pi_m(t) \left\{ \int_a^b \pi_m(t) \pi_m(t) dt \right\}^{-1/2}$$

where

$$\pi_m(t) = t^m - p_{m-1}(t) \int_a^b t^m p_{m-1}(t) dt - \dots - p_0(t) \int_a^b t^m p_0(t) dt$$
$$p_m(t) = \alpha_{m,m} t^m + \alpha_{m,m-1} t^{m-1} + \dots + \alpha_{m,0}$$

and

$$\pi_0(t) = 1$$

Evidently

$$\int_a^b p_m(t) p_n(t) dt = 0 \quad (m \neq n)$$

$$= 1 \quad (m = n)$$

and

$$\int_a^b t^m p_n(t) dt = 0 \quad (m < n)$$

Once the orthogonal polynomials have been obtained, the coefficients a_n can readily be obtained. For any value of m , t^m may be expressed as a sum of the polynomials $p_m(t)$, $p_{m-1}(t) \dots p_0(t)$; hence, if

$$R(k) = a_0 + a_1(1/k) + a_2(1/k)^2 + \dots$$
$$= a_0 + a_1 t + a_2 t^2 + \dots$$
$$= b_0 + b_1 p_1(t) + b_2 p_2(t) + \dots = g(t)$$

evidently

$$b_0 = \int_a^b p_0(t) g(t) dt$$

$$b_1 = \int_a^b p_1(t) g(t) dt$$

$$\vdots$$

Once $g(t)$ has been expressed in terms of the $p_m(t)$ polynomials, the corresponding coefficients

in the series expressing $p(x)$ in powers of x can be obtained by collecting the terms in $t^0, t^1, t^2, \dots t^m$ and multiplying each by $1/m!$. Alternatively we may construct the inverse transform of each polynomial, and evaluate these for various suitable values of x . If

$$L_x^{-1}\{tp_m(t)\} = \frac{\alpha_{m,m}}{m!} x^m + \frac{\alpha_{m,m-1}}{(m-1)!} x^{m-1} + \dots + \alpha_{m,0}$$

and

$$p(x) = \sum_m b_m L_x^{-1}\{tp_m(t)\}$$

the construction of the orthogonal polynomial and the subsequent procedure are hardly suitable for manual computation but can be performed with facility by an electronic computer.

(b) Curve fitting. For manual computation it has been found convenient to transform the independent variable from k to ξ [$= (2abk^{-1} - a - b)/(b - a)$]; ξ is thus a decreasing function of k , linear in $1/k$, and takes the values ± 1 at $k = a$ and b , respectively. If $R(k) \equiv \rho(\xi)$ is then plotted against ξ , the resulting curve can be fitted by a series of the Chebychev polynomials $T_m(\xi)$ [Lanczos, 1952]. For, if the roots of the polynomial $T_{n+1}(\xi)$ are $\alpha_0, \alpha_1, \alpha_2, \dots, \alpha_n$, where

$$\alpha_j = \cos \frac{(2j+1)\pi}{2n+2}$$

then

$$\rho(\xi) \cong \frac{1}{2} c_0 + c_1 T_1(\xi) + c_2 T_2(\xi) + \dots + c_n T_n(\xi)$$

if

$$c_m = \frac{2}{n} \sum_{i=0}^{i=n} \rho(\alpha_i) T_m(\alpha_i)$$

Each Chebychev polynomial $T_m(\xi)$ is

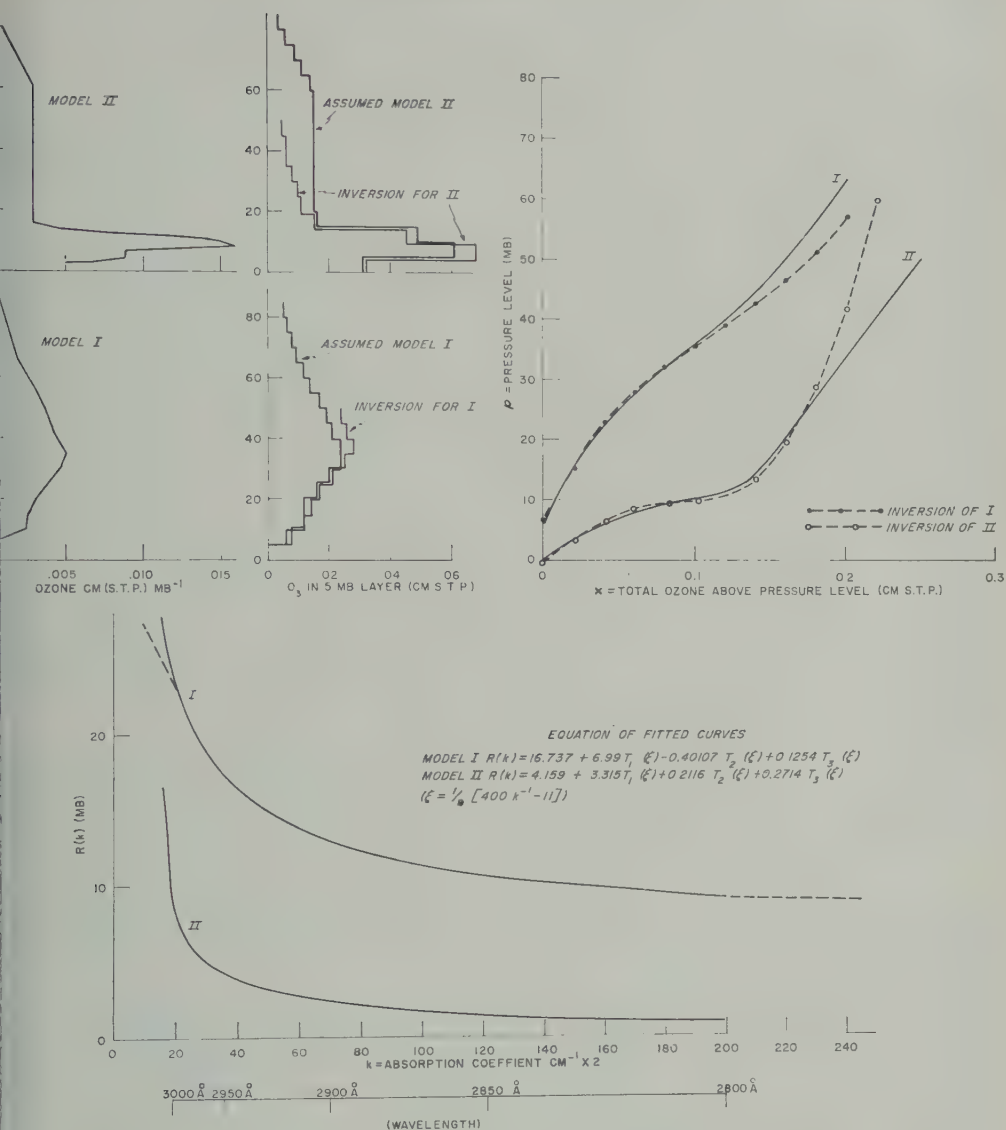


Fig. 1. (a) Initially assumed vertical distributions of ozone in continuous and histogram form, and deduced distribution (histogram form only); (b) assumed (solid) and deduced (broken) distributions in terms of integrated ozone column above a given pressure level; (c) equivalent reflectance of the model atmospheres in absorption band, as a function of absorption coefficient (from which the inversions in Figs. 1a and b were computed).

it polynomial in $1/k$, and the corresponding inversion $\theta_m(x)$ follows by application of equation 5; an approximate inversion for $\rho(\xi)$ is more readily obtained, being of the form

$$\begin{aligned} &\approx \frac{1}{2}c_0 + c_1T_1(\xi) + c_2T_2(\xi) + \dots \\ &+ c_nT_n(\xi) = L_k\{p'(x)\} \end{aligned}$$

$$\begin{aligned} p'(x) &= \frac{1}{2}c_0 + c_1\theta_1(x) + c_2\theta_2(x) + \dots \\ &+ c_n\theta_n(x) \end{aligned}$$

In applying this method it has been found necessary to truncate the Chebychev approximation [Lanczos, 1952, p. xviii]. The calculation of the coefficients c_m was usually carried out with

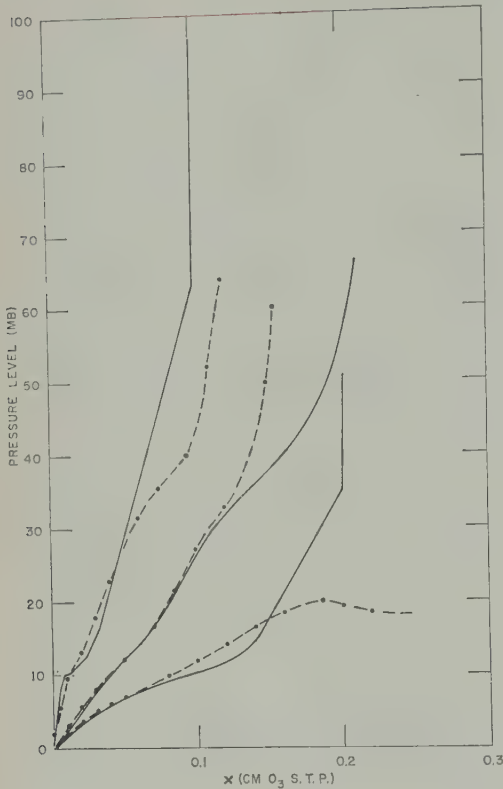


Fig. 2. Some initial (solid) and deduced (broken) distributions.

$n = 8$, but thereafter only such terms were retained as were necessary to fit the $R(k)$ curves within the accuracy of computation: dropping the higher, spurious, terms improved considerably the accuracy of the inversion process, for, whereas the polynomials T_m , although containing large individual terms, are bounded in the range $1 \geq \xi \geq -1$, the inversions $\theta_m(x)$ do not have this property, since they are formed by a term-by-term transformation. When this precaution was observed, satisfactory inversions of computed $R(k)$ curves were obtained, as shown in Figures 1 to 3. In Figure 1, two such inversions are illustrated in some detail: the assumed distributions, the equivalent $p-x$ curves, and the computed $R(k)-k$ curves are shown, together with the values obtained by inverting the $R(k)$ curve in the manner just described. The fitted polynomials are not shown, since within the range $200 > k > 20$ the differences between the fitted values and the original curve were less than 1 per cent—too small to be shown. Figures

2 and 3 show with less detail the result of several other inversion computations.

Limitations of the inversion procedure. The procedure just described related to an infinite atmosphere, and attenuation by scattering was neglected. The curve-fitting procedures that were followed took into account only the values of $R(k)$ in the range $200 > k > 20$, and the range of validity of the solutions obtained could have been extended merely by extending the range of k to lower values: this would, in effect, represent greater penetration of the atmosphere. In fact, however, the atmosphere and the ozone contained therein are finite, and any wavelength that penetrates to the lowermost part of the ozone will of necessity reach the ground, which has a higher reflectivity than the whole atmosphere and would contribute a large spurious component to the reflected energy at that wavelength. This is illustrated in Figure 4, which, for a representative ozone distribution, shows the reflected energy from atmospheric scattering (A), and from ground and/or cloud reflection

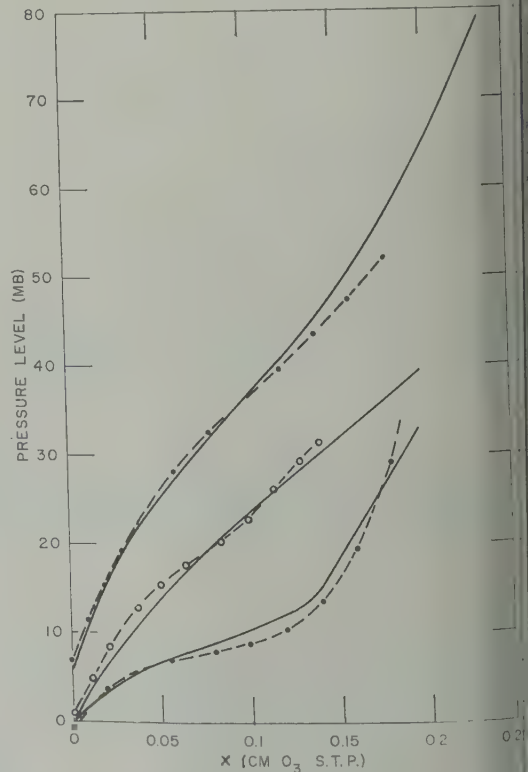


Fig. 3. Further initial and deduced ozone distributions.

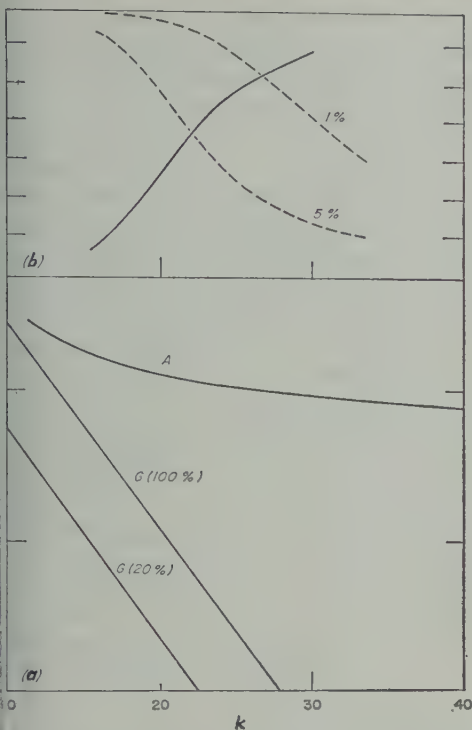


FIG. 4. (a) Comparison of relative magnitudes of atmospheric and surface reflection; (b) fraction of total ozone above level at which the upward-radiated flux equals the upward flux from surface reflection at 100 per cent surface reflectivity (solid line); the broken curves indicate the level at which upward flux from atmospheric scattering is 1 per cent, respectively, of the upward-scattered flux at the top of the atmosphere.

for ground reflectivities 100 and 20 per cent, respectively. The solid curve in Figure 4b shows, as a function of k , the total ozone lying above the level at which the scattered light from the surface just equals the 'noise' component due to surface reflection; the broken curves show the fraction of ozone above that level at which scattered light from below amounts to 1 and 5 per cent, respectively, of the total atmospheric scattering. If a measurement is to give information about conditions below a given level, two (dictating) criteria must be satisfied: (1) the portion of the atmospheric scattering originating below must be larger than the contribution to ground or cloud reflection, and (2) the portion of atmospheric scattering originating below must be larger than the experimental noise. Figure 4b shows that the lower one-fifth to one-third of the ozone column is virtually

inaccessible, since with increasing k the effective penetration of radiation into the atmosphere decreases whereas with decreasing k the ground reflection component increases more rapidly than the contribution from atmospheric scattering. In an actual experiment it would clearly be desirable to extend a spectral measurement to lower values of k (i.e., beyond 3000 Å), into the region where ground reflection predominates; the total ozone amount and the surface reflectivity could be deduced by measuring the reflected energy for two values of k ; these figures could then be applied to decide which value of k should be used as the lower limit of the range of k in the inversion procedure (for the useful lower limit it set by surface reflection, which depends on surface reflectivity and the total amount of ozone present).

Further extensions considerations. (a) Extension to oblique incidence and viewing. If a detector views a small solid angle in a direction ϕ with the local vertical in the area viewed, if the solar zenith angle in that area is ψ , and if the angle between the direction of view and the direction of illumination is θ , the steradiancy of the atmosphere is readily found to be, for any wavelength that is sufficiently absorbed to make the assumption of an infinite atmosphere valid,

$$B(\lambda) = \frac{\sec \phi}{2} E_{\lambda}(0) \cdot (1 + \cos^2 \theta) \left(\frac{2\pi}{\lambda} \right)^4 |a|^2 (mg)^{-1} \cdot \int_0^{\infty} \exp \left[(-k' \sec \psi - k' \sec \phi) \right] \cdot \int_0^{\infty} \epsilon dp \Big] dp$$

or

$$R(k) = p(0) + L_k \{ dp/dx \}$$

which is equivalent to (3), if R is now understood to denote the quantity

$$2mg(\lambda/2\pi)^4 |a|^{-2} (1 + \cos^2 \theta)^{-1} E_{\lambda}(0) \cos \phi$$

and k to denote $(\sec \phi + \sec \psi) k$. Thus only a change in the definition of R and k is needed to reduce the case of oblique incidence to that of vertical incidence. The fact that the angles ϕ and ψ enter into the definition of k shows, inci-

TABLE 3

$\lambda, \text{\AA}$	α, mb^{-1}	$k, \text{cm}^{-1} \text{ STP}$
2792	1.27×10^{-3}	216
2822	1.21×10^{-3}	163
2852	1.16×10^{-3}	123
2882	1.12×10^{-3}	86
2942	1.03×10^{-3}	42
2992	9.6×10^{-4}	21.5

dentally, that scanning in angle at a fixed wavelength produces a variation in k , and so could be used, in principle, as an alternative method for deducing the $R(k)$ function, and hence the ozone distribution. This method, however, appears inferior on two grounds: different regions would be viewed at different angles, so that all that could be deduced would be an average of the ozone distribution over a large horizontal area; and this average ozone distribution would not be a simple arithmetic average—it would be sensitive, for example, to horizontal changes in the vertical ozone distribution. It is doubtful whether the angle-scanning method would work at all if the vertical ozone distribution was not uniform over the area scanned.

(b) Attenuation by Rayleigh scattering. If the attenuating effect of Rayleigh scattering is to be included, an additional factor $e^{-\alpha p}$ should be written in the integrand in equation 3; α is evidently (see equation 2) given explicitly by

$$\alpha = \frac{128\pi^5 |a|^2 \cdot 10^3}{3\lambda^4 m g} = 7.7 \times 10^{-22} \lambda^{-4} \text{ mb}^{-1}$$

and takes the values shown in Table 3 at the wavelengths indicated.

In view of the uncertainty of our knowledge of the absorption coefficient, it would be pointless to include the effects of Rayleigh scattering in any computations of this kind. There would be no difficulty in doing so, however, for α is quite close to a linear function of k (of the form $Ak + B$) over the range of wavelengths under consideration. Under such conditions, it can readily be seen that the equation determining $R(k)$ can be written

$$R(k) = \int_0^\infty e^{-kx'} \cdot e^{-Bp} dp = \int_0^\infty e^{-kx'} g(x') dx'$$

if $g(x')$ is chosen so that

$$e^{-Bp} dp/dx' = g(x')$$

where $x' = x + Ap$. Thus an inversion of this transformation, instead of giving p as a function of x , would give g as a function of $x' (= x + Ap)$. The derivation of p and x explicitly is then a simple matter.

Discussion. The calculations made suggest that useful information about the distribution of atmospheric ozone could be gained by measuring the spectral steradiancy of the atmosphere and the incident solar energy spectrum as viewed from outside by a satellite-borne instrument, in the range 2800 to 3000 \AA . The calculations also show that the precision of the measurements must be high. An approximate indication of the error in the deduction of p as a function of x is given in Table 4, which relates the error in p to that in $R(k)$. This table was derived from the consideration that, if there is added to $p(x)$ a discontinuous error function $\delta(x)$ such that $\delta(x) = 0$ ($x < x_1$), $\delta(x) = A$ ($x_1 < x < x_2$), and $\delta(x) = 0$ ($x > x_2$), the resulting error in $R(k)$ is evidently

$$e(k) = k L_k \{ \delta(x) \} = A(e^{-kx_1} - e^{-kx_2})$$

Thus, for $k \geq k_1$,

$$|e(k)| \leq |A| |e^{-k_1 x_1}|$$

if x is real and positive; hence if $A = \epsilon e^{k_1 x_1}$,

$$|e(k)| \leq |\epsilon|$$

It follows that a constant error in p amounting to $\pm \epsilon e^{k_1 x_1}$ can be introduced from the point (p, x) onward without causing the corresponding error in $R(k)$ to exceed ϵ in the range $k \geq k_1$. It can also be shown that an error function of the form $(\beta - k_1)(2\beta - k_1) \epsilon e^{k_1 x}$, where $\beta > k_1$, can be added to $p(x)$ over the entire range of x without altering $R(k)$ by more than $|\epsilon|$ over the range $k > k_1$. The quantity $\epsilon e^{k_1 x}$ has been given

TABLE 4

Error in $R(k) =$	Error in p (mb) at Indicated Value of x				
	$x = 0.05$	0.1	0.15	0.2	0.25
0.01	0.03	0.07	0.2	0.5	1
0.05	0.14	0.37	1.0	2.6	7
0.1	0.3	0.7	2	5	15
0.5	1.4	3.7	10	26	75
1.0	2.7	7.4	20	50	150
Typical value of p (mb)	10	20	30	40	60

Table 4 for $k = 20$; it is not the absolute mathematical maximum error in p , but it is a useful measure of the size of slowly varying errors for given values of k_1 and x . The table shows that an accuracy of the order of 1 per cent is necessary if the ozone profile is to be deduced for beyond the median ozone level ($x \sim 0.2$ cm). There is no fundamental obstacle to the attainment of an accuracy better than 1 per cent in these measurements. The energy in the region of interest is of the order of $0.01 \text{ erg cm}^{-2} \text{ sec}^{-1} \text{ ster}^{-1} \text{ A}^{-1}$, so that with a detector of area 0.1 cm^2 , and an $F/1$ optical system, the incident photon flux would amount to about $10^8 \text{ cm}^{-2} \text{ sec}^{-1} \text{ A}^{-1}$, which, with an integrating time τ , a resolution of 1 A, and a quantum efficiency of 0.1, would produce a statistical (shot noise) uncertainty amounting to $10^{-2} \tau^{-1/2}$ of the signal; the statistical uncertainty would be about 3 per cent for an integrating time of 1 sec, 1 per cent for $\tau = 10^{-2} \text{ sec}$, and 3 per cent for $\tau = 10^{-4} \text{ sec}$. Scanning the spectrum from 2800 to 3000 A with a resolution of 1 A could thus be accomplished in 2 sec with an accuracy better than 1 per cent. Obviously, however, care should be taken to exclude from the detector any radiation outside the absorption band, for beyond the absorption band the reflected energy is several orders of magnitude greater than the detected energy in the absorption band.

The inversion procedure described can probably be improved in a number of ways. First, the use of integral powers of $1/k$ in deriving a polynomial approximation for $R(k)$ introduces large and higher terms in the polynomial approximation for $p(x)$; these terms increase more rapidly than is necessary or desirable; use of a fractional power of $1/k$, and inversion by means of the identity $L_k\{x^m\} = \Gamma(m+1) k^{-m-1}$, might be expected to give a more useful inversion. Second, the certainty (on physical grounds) that $p(x)$ must decrease monotonically with x has not been invoked to restrict the form of the approximating functions. Third, the bounded character of the Chebychev polynomials (which is lost when the term-by-term inversion is carried out) may be utilized, either by rearranging the power-series approximation for $p(x)$ in terms of the Chebychev polynomials of a suitably normalized variable y which is linear in x , or by constructing a set of orthogonal polynomials from the set of functions of $1/k$ obtained

by transforming the Chebychev polynomials in y . The possibility of improving the inversion method in these ways is being investigated.

The contribution of multiple scattering to the backscattered light in the ozone absorption band has not been fully evaluated at the present time. However, the increased ozone path traversed by any multiply scattered rays will evidently attenuate them considerably. Some very rough quantitative estimates suggest that the contribution due to multiple scattering in the region of high ozone absorption ($k > 20$) will be a small fraction of that due to primary scattering, and should not greatly affect any computation based on a model with primary scattering alone. Although accurate measurement of the $R(k)$ function was shown to be necessary, the inversion procedure is much less sensitive to systematic errors that do not affect the higher derivatives of the $R(k)$ function. For example, a systematic constant error of $+1$ in $R(k)$ evidently corresponds to an error of $+1 \text{ mb}$ in $p(x)$, while a hyperbolic error taking the values $+1$ at $k = 20$ and $+0.1$ at $k = 200$ would produce in $p(x)$ an error of $+20x \text{ mb}$, i.e., a few millibars over the range of x encountered in practice. Such errors, therefore, have less effect on the inversion than smaller errors of a random or oscillatory nature. Errors of the latter type, of course, may represent functions which are not Laplace transforms of any monotonic, increasing real function of x or even of any function of x , and it is the inclusion of such components that gives rise to the most serious inaccuracies in the inversion of the $R(k)$ function.

Conclusions. If the earth's atmosphere were viewed from outside by an instrument that accurately measured the spectral energy distribution of incident and reflected solar radiation in the strong ultraviolet absorption band of ozone, the vertical distribution of ozone, in the upper one-half to two-thirds of the total ozone column, could be deduced from this measurement. Calculations with assumed ozone distributions show that in most instances an adequate estimate of the ozone distribution can be obtained by polynomial expansion of the energy distribution (in terms of the reciprocal of the absorption coefficient), followed by a term-by-term inversion to obtain a corresponding expression for pressure in terms of total depth of ozone above that pressure.

Acknowledgment. This work has been supported by the National Aeronautics and Space Administration.

REFERENCES

- Allen, C. W., *Astrophysical Quantities*, Athlone Press, University of London, 1955.
- Inn, E. C. Y., and Y. Tanaka, Comparison of recently recorded ozone absorption coefficients in the visible and ultraviolet regions, *Conference on Ozone*, Armour Research Foundation, 1956.
- Lanczos, C., *Tables of Chebychev Polynomials*, National Bureau of Standards, Applied Mathematics Series 9, Government Printing Office, Washington, D. C., 1952.
- Salzer, H. E., *Tables of Coefficients for the Numerical Calculation of Laplace Transforms*, National Bureau of Standards, Applied Mathematics Series 30, Government Printing Office, Washington, D. C., 1953.
- Singer, S. F., Geophysical research with artificial earth satellites, *Advances in Geophysics*, 3, 301-367, edited by H. E. Landsberg, Academic Press, New York, 1956.

(Manuscript received March 29, 1961.)

Stratospheric Aerosol Studies

CHRISTIAN E. JUNGE AND JAMES E. MANSON

*Geophysics Research Directorate
Air Force Cambridge Research Laboratories
Bedford, Massachusetts*

Abstract. The stratospheric aerosol layer previously identified by balloon measurements has been studied extensively by means of recovered rod impactor samples obtained during aircraft flights at the 20-km level from 63°S to 72°N during March–November 1960. From a variety of physical and chemical measurements, which are presented in detail, the conclusion is drawn that this layer is stable, constant in time and space, and composed mainly of sulfate particles. The various questions raised by this result, particularly with respect to collection of micrometeorites, are presented and discussed.

1. INTRODUCTION

The work reported here is an extension of the study of stratospheric aerosols by *Junge, Mason, and Manson* [1961], henceforth referred to as I. This earlier study was based entirely on sampling by high-altitude balloons, which proved to be ideal vehicles for pioneering work in that regard, duration, and altitude of sampling could be varied over wide limits at the discretion of the experimenter. The work reported in this paper is based on sampling by the Lockheed C-130 aircraft.

This work was carried out with some urgency because of the desire to obtain results during theatorium on testing of atomic weapons. Thisatorium started in November 1958, and, thus, during the period of the earlier and also the recently reported study, the stratosphere received no additional injections of atomic debris.¹ Knowledge of the 'natural' aerosol content of the stratosphere is important in understanding the formation of radioactive particulate material during the transient period following large-scale injections of radioactive debris. It can be expected that such injections would interact with the ambient aerosol population and that the nature and origin of this ambient population could have an important bearing on the history of the injected debris, particularly of its highly dispersed fractions.

Although substantially correct, this statement should be qualified to allow for the slight addition of debris from the French test on February 13, 1960. See also footnote 3.

The general results of I were that particles of radius less than 0.1 micron diffuse upward from the troposphere, showing an average number concentration of about 100 cm^{-3} at the tropopause and less than 1 cm^{-3} at 20 km. The particles of radius between 0.1 and 1.0 micron are distributed with a maximum in number concentration of 1.0 cm^{-3} at approximately 20 km. The particles of radius greater than 1.0 micron were very low in number concentration and could be detected only occasionally, indicating a possibility of strong fluctuations in number concentration.

The particles of radius less than 1.0 micron have been studied for another year with no marked variations from the results in I. The particles of radius greater than 1.0 micron presented a serious problem for balloon-borne samplers, and could be studied only by use of a technique in which the sample volume of air is large and the ratio of sample volume to deposit area has a high value.

In all the balloon work, interpretation was hampered by the fact that the sample was obtained from a small volume of air taken at a specific time and position. Further, balloon operations tend to concentrate data points at geographic positions where launch and recovery of the balloon may be carried out. It was therefore very fortunate that participation in the High Altitude Sampling Program (Hasp) of the Department of Defense could be arranged.

In January 1960, a program of collection of particles by inertial impaction at altitudes of

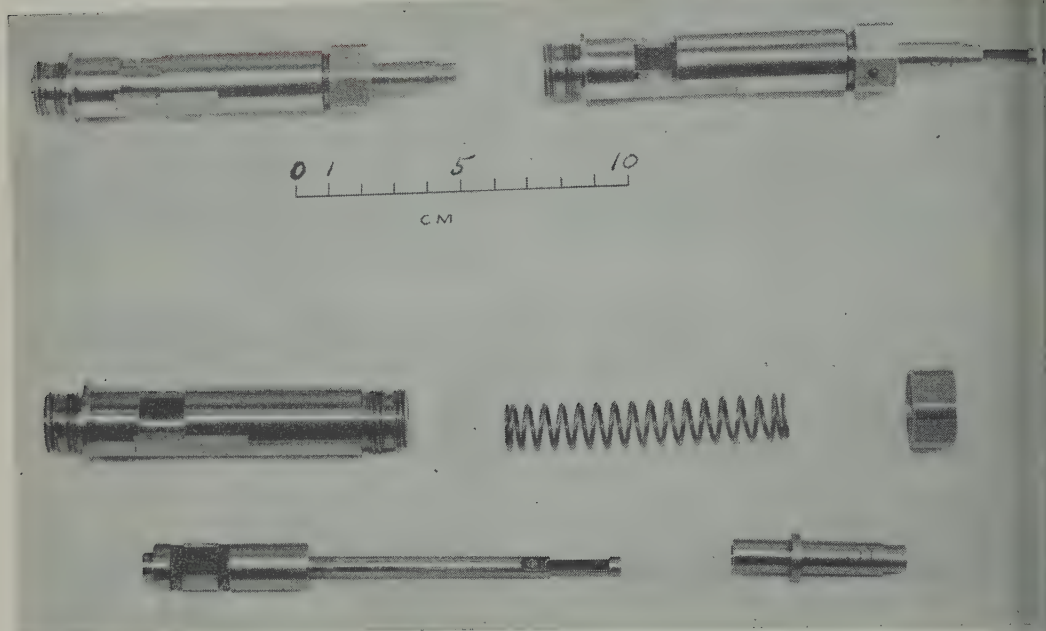


Fig. 1. The aircraft direct flow collector probe, shown closed, open, and disassembled.

40,000 to 70,000 feet (12 to 21 km) was initiated in close cooperation with Dr. James P. Friend of Isotopes, Inc. The flight paths were determined by the Hasp phase III and IV trajectories, and were up to 5000 km long, ranging in latitude from 40°S to 70°N [Stebbins, 1959]. Samples obtained from flights such as these could be expected to yield a sufficient concentration of particles to allow a reasonable extension of the previous work to the larger sizes. Further, the extended flight paths allowed a spatial average to be obtained for the data on particles of radius 0.1 to 1.0 micron with the possibility of checking our limited balloon data, and discovering the spatial extent of the sulfate layer at 20 km. The results of this program will be reported here.

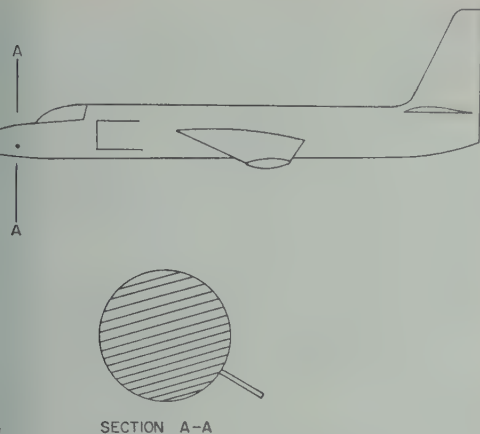
2. AEROSOL COLLECTION

In the collection and study of aerosols of such low concentration, the single most important factor is to make the distinction between collected particles and background contamination. Since the aircraft are flown from various bases scattered over South and North America, and since preparation of the collector probes must be done centrally in our laboratories, extreme care must be taken to protect the sampling surface from contamination during the period between

preparation and receipt of the collected sample. In this period shipment to and from the operating base must be made, as well as temporary storage at ground level. The necessary protection is achieved by use of a small, self-sealing collector which can be loaded at our laboratory and then mounted on a holder on the aircraft without breaking the seal. The sampling surface is protected before and after the collector is activated at the proper altitude. The design must be simple, reliable in operation over a wide range of temperature and pressure, and of such a nature that no particulate matter can be introduced by the activation process itself.

The collector which was developed to satisfy this set of requirements is shown in Figure 1. It contains two sample plates, one extending through the end nut, called the tip plate, and one exposed through the milled window in the side of the body, called the window plate. The dimensions were chosen to provide two collection efficiency characteristics, which are discussed below under Results. Henceforth we shall refer to those particles collected on the tip plate as the 'tip sample,' and to those collected on the window plate as the 'window sample.'

The cylindrical surfaces of the piston and the internal surfaces of the body and extension sleeve



2. The position of the collector probe on the Lockheed U-2 aircraft.

ground to individual fit. Stainless steel was used throughout, except for beryllium-copper re-clipper clips. The close tolerances and smoothness of the surfaces were such that after assembly the surfaces of the plates were completely isolated from the outside except for a very slow diffusion of air in or out in response to pressure changes. Initial models contained only a window plate, with no extension sleeve and tip plate. The tip plate was added during the course of the investigation and in no way changed the configuration at the window plate. The design of both of these sample zones provided a clear path, when the collector was closed, of approximately one-eighth of an inch parallel to the axis of symmetry. The mating cylindrical surfaces were machined to a tolerance of 0.0005 inch, and, as described below, were coated with a sticky film of silicone. Subsequent flight tests, during which the collector was opened only for a very short time, indicated that these design features completely excluded contamination during shipment, ground handling, and tropospheric flight. The position of this collector on the aircraft is shown in Figure 2. The mounting strut extends 15 cm from the skin of the aircraft on the port side, at an angle of 33° below the horizontal, and is located 132 cm back from the nose. The distance from the tip of the collector is, therefore, about 28 cm from the skin. The probe thus has free access to ambient air and a minimum of interference from the structure of the aircraft. The collector plates are oriented normal to the direction of flight.

The preparation of the collector plates turned out to be one of the most critical operations. Because of the small size of the glass plates and the surface tension of rinse water and solvents, it was very difficult to eliminate the last traces of background particles. The procedure for cleaning these plates was as follows.

The tip sample plate was carefully washed and then coated with germanium or gold, by vacuum evaporation when applicable. Because of the very dense deposit on this plate, no stringent requirements were necessary to eliminate scratches or occasional background particles. This plate was dipped in a 1 mg/ml solution of 250,000 centistokes silicone 200 fluid in hexane, or left dry. The window plate, on which it was desired to detect larger particles singly, was polished with 1/4-micron diamond paste to eliminate random pits and scratches. Following this, the plates were washed with organic solvents for the polishing binder and with detergent or chromic acid cleaning solution. The most critical step following such washing was a very thorough hot water rinse and a distilled water rinse, followed by draining on lens tissue and drying in a dust-free atmosphere. The plates were then coated by vacuum evaporation of gold or germanium following normal procedures for such coating. In all our metal coating, we planned for a metal deposit thickness of approximately 1 mg cm^{-2} . To secure an adhering, conducting coating of good optical quality and low reactivity, we were led to mint gold, even though this coating is far from ideal for the subsequent X-ray chemical analysis. For this analysis, later samples were collected on polished plates of solid aluminum or germanium. It has been found that polished germanium can be prepared such that only a few (0-5) background particles of radius greater than 0.5 micron are left on the exposed area of the window plate.

The parts of each collector were carefully cleaned by washing in carbon tetrachloride and hexane, and were then dipped in a 20 mg/ml solution of 250,000 cs silicone 200 fluid in hexane. Thus, the collector surfaces would retain any dirt coming in contact with them, and would prevent it from blowing off onto the plate during opening and closing of the collector. This thin silicone layer also prevented the friction of internal parts from producing particles that might have contaminated the plate.

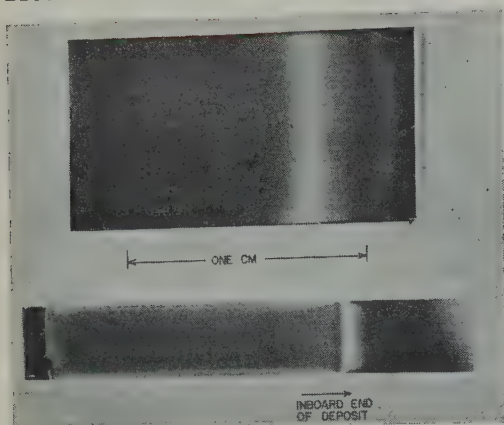


Fig. 3. Photograph in grazing incident light showing the typical band of heavy collection on the window plate and the heavier but more uniform collection on the tip plate.

The collectors were then ready to load. Each window plate was given a final dipping in from 1 to 5 mg/ml 250,000 cs silicone 200 fluid in hexane and immediately mounted in the collector. The collector was assembled as loading progressed. In this way the window plate could be protected by the body of the collector while the tip plate was being mounted. Finally, the

spring was carefully set in place and the extension sleeve placed over the tip plate.

These loaded and assembled collectors were sent by registered air mail to the various operating bases. For protection in the mail, a special container was devised which consisted of polyurethane foam inside one metal and one cardboard mailing tube. The collector probe itself was heat sealed in a polyethylene bag before being packed in the protective container. This container remained closed until a ground crew member opened it and installed the collector probe just before take off. The same ground crew member met the plane on return, demounted the collector, and repackaged it, using a new plastic bag and securing this around the collector with a rubber band. Obviously the success of the entire study rested on the care with which these collectors were handled during mounting and demounting, and on the attention of the pilot to the time of operation of the activator switch. The ground and flight support by the 4080th Strategic Reconnaissance Wing (SAC) left nothing to be desired in this respect.

3. RESULTS

A. *Size distribution.* As noted above, the

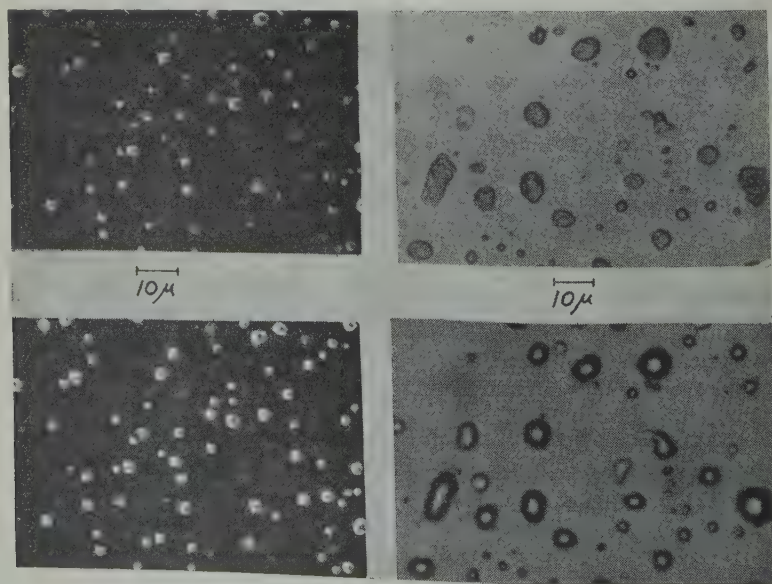


Fig. 4. Photomicrograph of typical heavy band deposit particles. On the left, the upper picture was taken at 50 per cent relative humidity, the lower at 95 per cent. On the right, the pictures were taken after several wet-dry growth cycles, the upper at 1 per cent relative humidity, the lower at 95 per cent. The onset of solution occurs below 85 per cent, the above high value being used to ensure clarity of presentation.

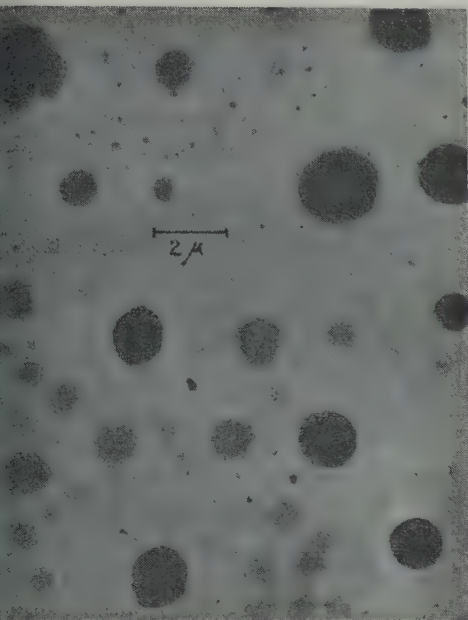


Fig. 5. Electron micrograph of particles in the window sample, collected directly on carbon-film-covered 200-mesh grids. Some of the particles show evaporation in the electron beam. Compare with Figure 13. (Electron micrograph taken by T. Turnbull of the M.I.T. Lincoln Laboratory.)

Window samples were collected on glass plates which were coated with germanium or gold and a thin film of silicone oil to insure adhesion of the collected particles. The metal coating was necessary for analysis with the electron probe; it also proved out to be very useful for observations of particles with the incident-light objective (Leitz) in dark-field illumination.

It soon became apparent that the cut of the window had an aerodynamic effect; the resulting deposit was not uniform but was concentrated in one or sometimes two parallel bands across the plate (Fig. 3). The deposition of particles in the band was ideal for evaluation of size distributions and electron micrographs because of the dense particle population at flights of several hours' duration. Figure 4 shows a photograph of a section of such a band, and Figure 5 shows an electron photomicrograph of a similar region of a similar band. These heavy, uniform deposits eliminated any problem of background particles, and the band structure gave assurance that these particles were collected during flight. The band was not in the center of

the plate; it was shifted to the inboard side because the mounting was such that the air stream was not quite normal to the plate.

The collection efficiency of the sampler can be computed from data available in the literature on impaction on cylinders or plane surfaces. The proper correction must be used for the Cunningham slip term for the main operating conditions of 20-km altitude and 770 km/hr (415 knots). Because the geometry of the window collector is more complicated and is neither a cylinder nor a plane surface, there is some doubt about which data should be applied. *Ranz and Wong* [1952] give collection efficiencies of cylinders (experimental and theoretical) and rectangular ribbons (only theoretical). In Figure 6 we calculated the size distributions of collected particles on the basis of an average size distribution obtained earlier (I) (see Fig. 7). The difference between cylinder and ribbon (curves 2 and 3) is considerable, but it is not serious with respect to the accuracies we can expect. We integrated the curves to obtain total numbers of collected particles (Table 1), which would correspond to the different collection devices.

Early in the program it became apparent that water condensation on and within the probe, due to the rapid rate of descent of the aircraft, was a problem. On a number of samples condensation on the plate occurred, partly dissolving the material collected and redistributing it after evaporation. Such samples could not be evaluated for size distribution and concentration. In some cases the condensation was only slight, resulting in droplet 'halos' around the particles, similar to those we found on the balloon samples (I). In other cases the collection was perfect. Some of these latter samples were used for size distribution evaluation by microscope. Because of the low collection efficiencies for particles of radius less than 0.3μ , we restricted this evaluation to sizes above 0.5μ and did the evaluation with a light microscope. The main emphasis in this aircraft sampling program was to obtain more precise information on the larger particles, since the balloon data covered primarily the range below 1μ . The results of this evaluation are shown in Figure 7. Curves 7 and 8 indicate the limits between which the size distributions obtained in our balloon flights (I) were located. The aircraft data were corrected according to curve 3 in Figure 6. The agreement between the two sets

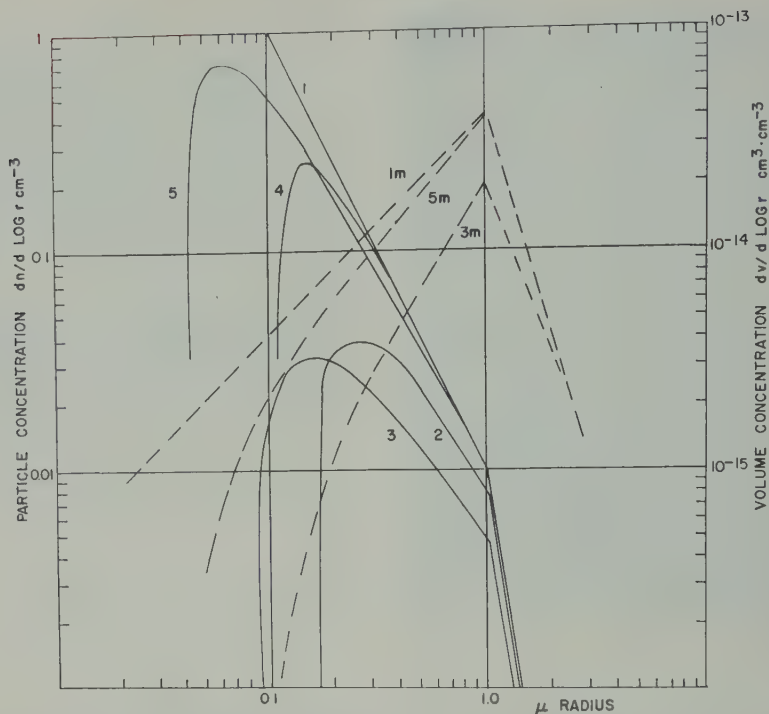


Fig. 6. Comparison of calculated number and volume distributions on various collectors at 20-km altitude. Curve 1, average size distribution from Figure 7; curve 2, size distribution deposited on a ribbon 1.59 cm wide at 770 km/hr, using theoretical efficiency data of *Ranz and Wong* [1952]; curve 3, same as curve 2, only on a cylinder 1.5 cm in diameter, using measured efficiency values of *Ranz and Wong*; curve 4, size distribution collected in the General Mills impactors used in I to measure the vertical profiles; curve 5, size distribution deposited on a ribbon 0.32 cm wide (tip collector); curves 1m, 3m, and 5m, volume distribution for the corresponding size distribution; scale on right.

of data in the overlapping area is surprisingly good, considering that the data were obtained with different methods and vehicles and at different locations and times. This implies that the methods of collection and evaluation are fairly accurate and also that this particle population in the size range between about 0.1 and 1.0 μ is indeed constant with time and space. In (I) we called these particles 'population two,' but for further reference we will call them 'large particles,' in agreement with the nomenclature for tropospheric aerosols.

In contrast to our balloon data, where too few particles larger than 1.0 μ were collected to permit reliable size distributions to be obtained, the aircraft sampled a sufficiently large volume of air to collect a statistically significant number of these particles. Figure 7 shows a very remarkable drop in concentration of particles larger than 1 μ . In four of the five samples, this drop is

a factor of 3000 over the radius range 1 to 3 μ . The total number of particles of all sizes counted in each case was required to be between 3000 and 6000 in order to obtain a significant number of particles larger than 3 μ . This sharp drop in the size distribution is obviously the upper limit of the large particles. On March 29, this limit was increased by a factor of 2, but it should be kept in mind that the measured particle sizes are not quite accurate because of their spread on the surface (see, for example, Fig. 5). Because of this and also because of inaccuracies in the assumed collection efficiencies (Fig. 6), we should consider the size distributions to be correct only within a factor of 2.

The three size distributions in Figure 7 which have a steep drop above a radius of 1 μ show a sudden change in slope above a radius of 3 μ . Particles in this size range are of special interest since it is here, with no other apparent source

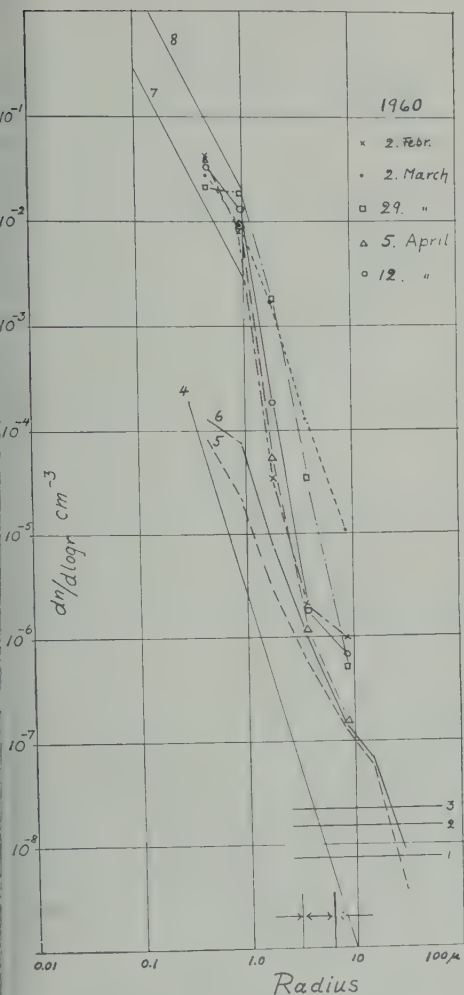


Fig. 7. Size distributions of aerosols at about 20 km altitude, from window samples collected on plates as shown. Curves 1, 2, and 3, concentration of particles which would result in 1, 2, or 3 particles/cm² being deposited during a flight of 4000 km at an altitude of 20 km; curve 4, calculated size distribution of extraterrestrial material at 20 km; curves 5 and 6, size distribution of background particles; curves 7 and 8, limits of size distribution data from balloon collections.

particles, that we may possibly detect particles of extraterrestrial origin. Though the substrates were very carefully prepared, it was impossible to avoid a certain background of particles. Curves 5 and 6 in Figure 7 make it clear that we were dealing with predominantly background particles above a radius of 3 μ in the three samples with the steep drop. These background counts were obtained on unexposed plates, pre-

pared in the same way as the others. Since it can be expected that the particles in the zodiacal dust cloud are similar in composition to stony meteorites, with only small fractions of nickel iron alloys, a reliable separation between background and collected particles will be difficult solely on the basis of chemical analysis. To minimize this problem, we have improved techniques to reduce and record the background particles. This raises the question of the possible detection of extraterrestrial material, which will be discussed later.

B. Latitudinal distribution of large particles. All the window samples which were not spoiled by condensation of water were evaluated in terms of total concentration of particles collected. No correction was made for the variation of collection efficiency with radius. This total concentration is simply the total number of particles on the window plate, divided by the volume of air which is geometrically intercepted by the plate during flight. Most flights were on north-south tracks at an altitude of about 20 km, at a speed of 770 km/hr, and of about 5 hours' duration. The flights took place during the period March–November 1960.

The results are plotted in Figure 8. With two exceptions, all values are in the same range of concentration, and there is no indication of a systematic variation with latitude. This indicates the presence of a huge, wide-spread, and fairly uniform layer of large particles. We have no explanation for the two deviating values.

We now have available a total of five vertical profiles of these particles collected at a latitude of 45°N over a period of one year [I, and Chagnon and Junge, 1961]. The size distribution of the particles collected in these balloon flights is given by curve 4, Figure 6. This distribution is seen to have a slightly smaller average size than

TABLE 1. Total Number of Collected Particles Obtained by Integrating Curves 2 to 5 in Figure 6

Type of Collector	Concentration of Particles, no. cm ⁻³
Window collector	
ribbon (2)	0.019
cylinder (3)	0.019
General Mills impactor (4)	0.088
Tip collector (5)	0.38

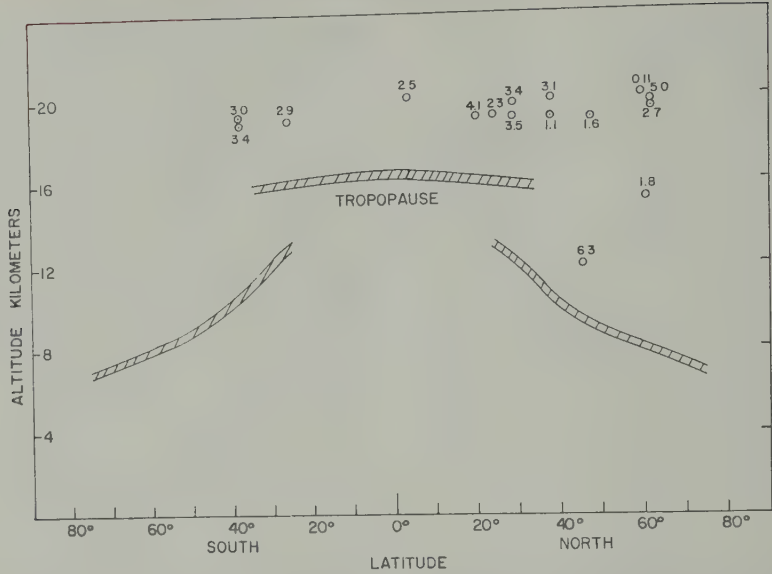


Fig. 8. Concentration of large particles as a function of latitude and altitude. The heavy lines indicate the average tropopause. The counts were not corrected for collection efficiency, and are in units of particles per 1000 cm³ volume at collection altitude.

that of the particles collected on the window plates (curves 2 and 3, Fig. 6), but both types of sample are representative of the same general population. All five balloon flight profiles are very similar in shape and absolute concentrations, so that the example presented in Figure 9 is quite representative. We see that a broad maximum

exists between 16 and 24 km at this latitude. By fortunate coincidence it so happens that the main collection altitude of the aircraft is right at this maximum. If we combine the balloon profiles with the aircraft data, we get the impression that these large particles form a continuous wide-spread layer in the stratosphere.

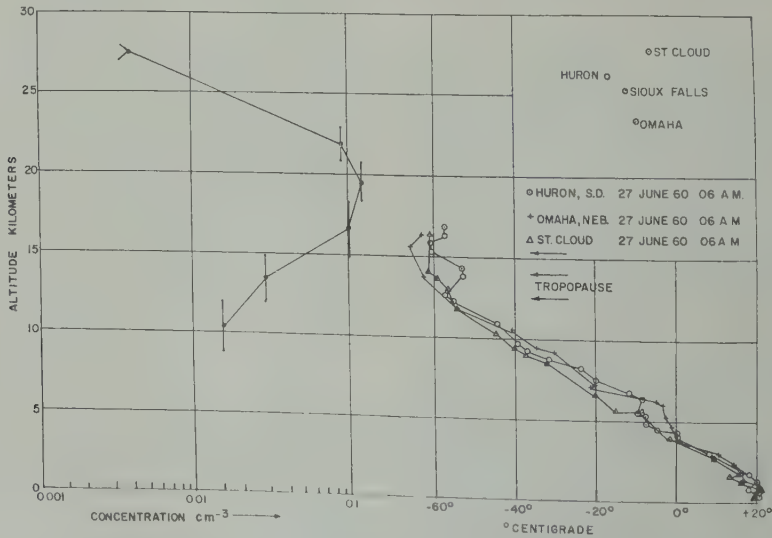


Fig. 9. Typical vertical profile of large particles (I). These particles are represented by curve 4, Figure 6.

layer is of considerable thickness and shows variation in time and space within the wide range of 40°S and 70°N. This phenomenon is certainly of general interest, particularly with regard to optical effects such as the 'purple haze,' and it merits further study.²

The absolute number concentrations obtained from our various collectors in the course of these investigations merit further comment. With the cascade impactors used in the early balloon flights, the total concentration was found to be about 1 cm⁻³. The impaction efficiency of these collectors is not well known, but it is close to 100 per cent for particles as small as 0.1 μ , and decreases for particles smaller than this. With a lower limit we indeed obtain from curve 1 of Figure 6 a total concentration of about 1 cm⁻³. According to Table 1, we should then expect the number concentration determined from the collectors used in the vertical profile study (curve 4 of Fig. 6), to have a value of 0.09 cm⁻³, in fair agreement with the sample profile in Figure 9. These balloon impactors were carefully calibrated with respect to collection efficiency as a function of radius under the relevant altitude conditions.

Table 1 indicates 0.02 cm⁻³ for the window sample, which is higher by a factor of from 4 to 10 than the values in Figure 8. If, however, only particles larger than 0.4 μ are counted for the distribution and corrected according to curve 1 of Figure 6, the agreement with our size distribution is satisfactory. This may be interpreted to mean that the cut-off size of the window collector is higher than was calculated with the aid of Ranz and Wong in curves 2 and 3 of Figure 6. This disagreement is probably due to a considerable distortion of the flow pattern in the window, as is indicated by the band structure of the window sample, and it has little influence on our previous conclusions drawn from Figure 8.

Chemical analysis. To perform the quantitative analysis of our samples we used two techniques. The first, electron microbeam probe

We are grateful for the following comment from J. Öpik, who reviewed this paper. 'From Figure 9, the total number of large particles per cm² column is $\sim 10^5$; the cross section $\pi r^2 \approx 3 \times 10^{-10}$ to 10^{-8} cm², average $< 10^{-8}$, and the geometrical coverage is only $10^5 \times 10^{-8} \sim 10^{-3}$. Daytime optical effects cannot be produced, but twilight effects can.'

analysis, has been described in (I), and will therefore be very briefly outlined here. A 30-kilovolt electron beam, from 1 to 60 μ in diameter, strikes the sample in vacuo. The X rays which are emitted by the sample are analyzed by a crystal spectrometer, and from this analysis the surface density of the elements can be determined. This technique is very well suited to the analysis of single particles larger than a few microns in diameter and can be made to yield very good data for a uniform deposit of smaller particles as well. Use of a beam with diameter of 60 μ provides a fairly good spatial average in a dense collection such as the tip sample. Analysis scans for sulfur, both lengthwise and across a typical sample, are illustrated in Figure 11. The ordinate, presented as surface density on the sample is related to counting rate in the spectrometer detector by

$$\sigma_x = k_x(I_x - I_x^b)/I_x^o \quad (3.1)$$

where

σ_x = surface density of element X in g cm⁻².

k_x = empirical constant with units of g cm⁻².

I_x = counting rate with spectrometer aligned for X, with the unknown in the specimen chamber.

I_x^b = same, with a sample of the substrate in the specimen chamber.

I_x^o = same, with a pure sample of element X in the specimen chamber.

Values of k_x were determined empirically for aluminum, sulfur, and nickel. In units of 10⁻³ g cm⁻², the values are 0.58, 0.63, and 0.75, respectively. These values were used for neighboring elements as well. In I a constant value of 1.0 mg cm⁻² was used, having been estimated from theoretical considerations. The discrepancy is caused by the fact that equation 3.1 represents the relationship between σ_x and $(I_x - I_x^b)/I_x^o$ only for low values of surface density. The actual curve has negative deviation from linearity; thus the empirical constant for low surface densities is less than that determined theoretically, assuming linearity.

A second method of analysis, X-ray fluorescence vacuum spectrometry, was used for this series of samples. This method is suitable for determination of the average composition of collections of many particles, since a large area may be analyzed at one time. For this reason it



Fig. 10. Photomicrograph of some of the unique particles collected on March 2, 1960. See Table 2.

is possible to calibrate the fluorescence equipment by preparation of known standards through use of a microsyringe and dilute solutions containing the desired elements. In our spectrometer the exciting radiation was limited to an area of 0.3 cm^2 . This area corresponds to the flat plateau region of the deposit shown in Figure 11. Direct comparison of the results of the fluorescence analysis with those of the electron probe analysis provided calibration of the latter for sulfur, the major constituent in our samples. The fluorescence technique has also been applied to the determination of silicon, chlorine, and calcium in those samples collected on solid aluminum.

The samples first subjected to analysis were the window samples. These contained two distinct groups of particles, those in the heavy band across the inboard end and those larger particles which were found distributed over the plate. The 'band' particles were hygroscopic and contained sulfur as the major constituent. These were the same particles that were collected on the tip sample plates; they will be discussed below.

As mentioned in section 3.A, we have reason to doubt that the large particles found in our early window samples were actually collected in

the stratosphere. Only one sample, collected on March 2, 1960, contained a sufficient number of particles of a unique appearance to provide a basis for assuming that they were collected in the stratosphere. A photomicrograph of several of these particles is shown in Figure 10. The analysis of ten of these particles is presented in Table 2. The maximum total surface density is consistent with a local deposit a few microns thick. It is considered significant that another sample, flown on March 4, 1960, over a total path 3200 km long at an altitude of 19.6 km between 29° and 50°N , contained no particles of a similar appearance. A normally dense deposit of the sulfate aerosol band was evident on both samples, however, indicating proper operation.

Any generalizations from this single sample seem premature. Our current efforts to identify positively every particle with radius greater than 2μ on the sample plate before and after collection yield a collected sample of from zero to three particles per flight, and, therefore, much work and many samples separate us from any reasonably accurate estimate of concentration of these particles and their average composition.

Between March and November 1960 twelve reliable tip samples were obtained. Of these, two were collected on a thin film of mint gold on glass, two on a film of germanium (intrinsic grade) on glass, and eight on solid pieces of 99.99 per cent pure aluminum. The tip sample plate shown in Figures 1 and 3, is 1.96 cm long and 0.32 cm wide, the collection area being about 1.1 cm long. By using the value of σ corresponding to the central region of the sample (Fig. 11), the end effects were minimized. Therefore, the theoretical impaction efficiency for an infinite ribbon, used to calculate curve 5 of Figure 6, could be assumed to apply. For the X-ray fluorescence work, a central area 1 cm long was

³ At the time of collection of this sample we considered the possibility that these particles could have originated in the French atomic tests in the Sahara on February 13, 1960. We rejected this idea on the basis of the large size of the particles which would imply rapid fall, and the low energy yield reported for these tests. Subsequently we have learned that at the time of collection of this sample, an increase in the short-lived fission products was observed at the same location and altitude, which indicated a coincidence in time of our sampling and the passage of the debris from the French tests. Further study of this sample is planned.

TABLE 2. Relative Analyses of Large Particles from the March 2, 1960, Sample (Collected at 30°N, 98°W. Flight path: 2400 km at altitude 18.2 km; 2400 km at altitude 19.8 km.)

Particle												$\Sigma \sigma, \text{g cm}^{-2} \times 10^{-6}$
Diam., microns	Mg	Al	Si	P	S	K	Ca	V	Ni	Fe		
12	2.5	2.5	94.	0.002	0.002	0.	0.	0.	0.	0.0006	103.	
27	4.	4.	0.	0.6	14.	10.	66.	0.	0.	1.1	17.4	
10	0.	13.	72.	0.6	4.5	1.2	5.7	0.	0.3	3.0	33.3	
6	0.	65.	0.	0.	19.	0.	0.	6.5	9.7	0.	3.1	
20	0.	26.	0.	1.2	12.	0.	17.	7.	0.	38.	16.2	
* 30	1.	0.7	98.	0.	0.4	0.	0.	0.	0.	0.	257.	
* 30	0.	5.	91.	0.	2.	0.	0.06	0.	0.	2.	37.4	
17	0.	0.9	97.	0.02	0.3	0.2	0.	0.	0.004	1.1	263.	
10	0.	49.	0.	0.	13.	0.	20.	4.	2.	11.	4.5	
15 × 40	0.	0.	0.	0.	100.	0.	0.	0.	0.	0.	0.03	
15 × 30	1.3	1.	98.	0.1	0.	0.	0.	0.	0.	0.2	166.	

* Two separate areas of the same large particle.

alyzed, thus eliminating the strong end peaks in this analysis as well.

Four of these samples, two on gold and two on minimum, were thoroughly analyzed. These are collected between 63° and 39°S, at 38°S, between 12° and 27°N, and at 72°N; they thus

provide a fair sampling of the entire stratosphere. The rest of the samples, including one transequatorial sample and several taken at middle north latitudes, were analyzed for silicon, sulfur, calcium, and iron, and in several cases other elements as well, as indicated in Table 3. All

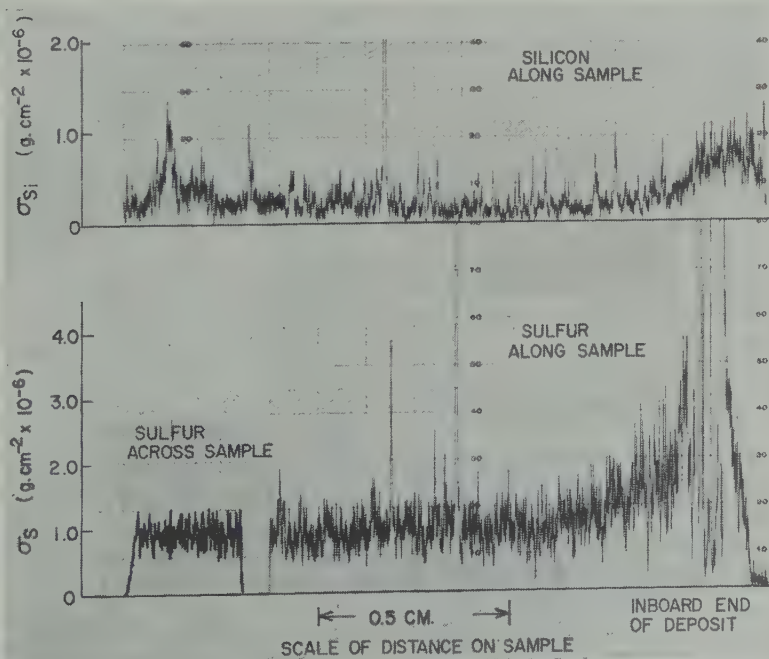


Fig. 11. Electron microprobe determination of the spatial distribution of surface density for silicon (top) and sulfur (bottom) on a tip sample plate. The two end peaks seen in the silicon curve correspond exactly to those noted on visual inspection of this sample. The scan across the sample for sulfur was located halfway along the deposit. The strip chart horizontal lines do not correspond to σ scales at left.

TABLE 3. Absolute and Relative Analysis of Tip Samples

Com- ponent	No. of Samples	ρ_{21}^* g cm ⁻³ $\times 10^{-15}$	C†	ΔC ‡
Mg	4	0.000	0.000	0.006
Al	4	0.43	0.056	0.006
Si	12	0.11	0.014	0.003
P	4	0.000	0.000	0.01
SO ₄	11	6.82	0.890	0.001
Cl	4	0.01	0.0013	0.0013
K	7	0.13	0.017	0.01
Ca	8	0.10	0.013	0.0005
Ti	3	0.000	0.000	0.05
V	4	0.000	0.000	0.01
Cr	4	0.000	0.000	0.01
Mn	4	0.000	0.000	0.005
Fe	12	0.071	0.0093	0.004
Co	4	0.000	0.000	0.006
Ni	7	0.000	0.000	0.01
Cu	4	0.000	0.000	0.01
Zn	4	0.000	0.000	0.02
Total	12	7.68		

* Density is in units of mass per unit volume of air at altitude.

† The concentration C is relative to the total ρ and expresses the relative composition of the condensed phase of the aerosol, the sulfur being assumed present as sulfate.

‡ ΔC refers to the detectability limits in terms of relative composition.

four samples on a nonaluminum substrate were analyzed for aluminum.

Several remarks concerning Table 3 are in order. The detection of aluminum and silicon is certain, although the quantitative measurement is not so positive. Detection is made quite definite for silicon by the characteristic inboard and outboard peaks shown in Figure 11, which were also evident from visual examination. However, the quantitative measurement of the silicon deposited in the central area is hampered by the presence of silicone oil. Further, the aluminum contained 0.001 per cent silicon as an impurity. In estimating the background, we have used the highest reasonable value, and thus the silicon concentration could be double that reported in Table 3. The aluminum analysis is likewise somewhat uncertain quantitatively because only four nonaluminum substrates were used, and the background intensity in the aluminum region was quite high relative to the net aluminum intensity. If these amounts of silicon and alumi-

num had a meteoritic origin, one would expect far greater densities of magnesium and iron, as well as a higher silicon-to-aluminum ratio. Tektites [O'Keefe, 1960] have silicon and aluminum as the major constituents aside from oxygen, and speculation along these lines is certainly justified on the basis of our findings. It will be noted that the heaviest deposits analyzed in Table 2, i.e., those having large values of $\Sigma \rho$, consist of silicon primarily, with variable amounts of aluminum.

Our explanation of the preponderance of sulfur in the aerosol is detailed in Section 4.A. To date the single most important result of the chemical analysis is the discovery that this stratospheric aerosol is primarily sulfur, which is present as a sulfate. This result, together with the essentially negative results for most elements in Table 3, has caused a revision in our early ideas about the origin of this material. It was thought that the massive injections of vaporized coral and sea water attendant in Pacific nuclear tests would produce an aerosol rich in chlorine and calcium. The threshold detection of chlorine and the relatively small amounts of calcium detected during 1960 (Table 3) with the negative results reported in I, allow one to discount such injections on a global scale, in comparison to the very large amount of sulfate present. The sulfur density is presented in Figure 12. The numbers refer to units of 10^{-15} g cm⁻³ of elemental sulfur, collected over the latitude ranges shown. As can be seen, no trend with latitude is evident.

As a spot check on these findings, one tip sample was destructively tested one year after collection for NH_4^+ and NO_3^- , which are not within the range of our X-ray methods. A direct comparison with known amounts of these ions made it possible to analyze small droplets of solution obtained from given areas of the sample. The ammonium ion was detected well within the sensitivity of the Nessler's reagent spot test, and the approximate concentration agreed with that calculated stoichiometrically from the SO_4 in Table 3. On the other hand, no nitrate ion was detected with the brucine test. This test was calibrated in the presence of $(\text{NH}_4)_2\text{SO}_4$ to be sensitive to 0.02 micrograms of NO_3^- , corresponding to an upper limit on $\rho \text{ NO}_3^-$ of 0.1×10^{-15} g cm⁻³ in the stratosphere. NH_4^+ and SO_4^{2-} analyses were performed on another

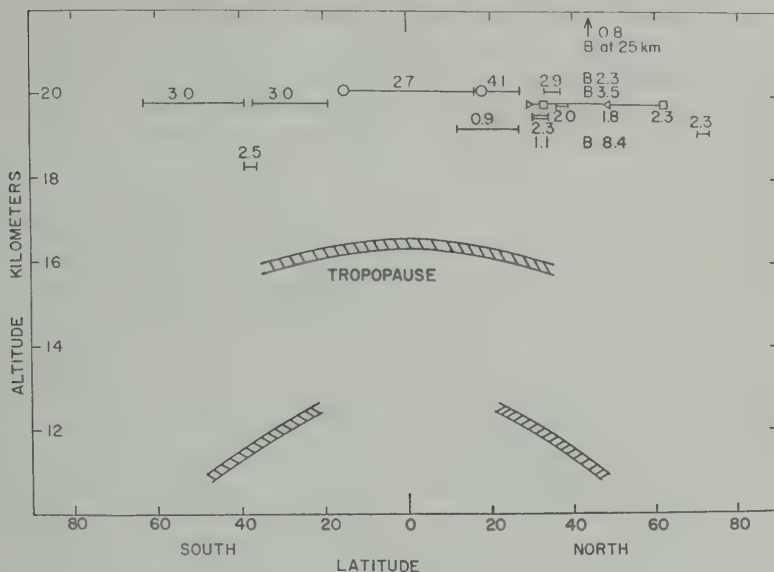


Fig. 12. Sulfur density as a function of latitude and altitude. The numbers refer to density in units of 10^{-15} g cm^{-3} . (From analysis of tip samples, represented by curves 5 and 5m of Fig. 6.)

ple 2 weeks after collection. The SO_4^{2-} concentration was in agreement with Table 3, but only one-fourth of the amount of NH_4^+ required $(\text{NH}_4)_2\text{SO}_4$ was detected. Thus it can be deduced that all the present evidence from chemical analyses indicates that the stratospheric aerosol layer is primarily ammonium sulfate or sulfuric acid, with small amounts of a few other substances as indicated in Table 3.

The average total density of this aerosol is 8×10^{-16} g cm^{-3} , as given in Table 3. If we assume an amount of mixed sodium and ammonium sulfate equivalent to the sulfate, this is increased to 9.2×10^{-16} g cm^{-3} . Let us see how this measured mass concentration compares with that calculated on the basis of our measured size distribution shown in Figure 6. The size distribution is given by

$$dn/dr = Cr^{-a} \quad (3.2)$$

The total curve is divided into two regions, as follows:

Region A $r_1 \leq r \leq r_2$

$$C = C_1; a = a_1$$

Region B $r_2 \leq r$

$$C = C_2; a = a_2 > 4$$

The dividing point, r_2 , is taken at 1.0μ in Figure

6, where the distribution is plotted logarithmically. The calculated mass distribution is related to the size distribution by

$$\frac{d\rho_c}{dr} = \frac{4}{3} \pi dr^3 \frac{dn}{dr} = \frac{4}{3} \pi dCr^{3-a} \quad (3.3)$$

where d is the average density of the condensed phase of the aerosol. Since the two regions join at r_2 , we have

$$K_1 r_2^{3-a_1} = K_2 r_2^{3-a_2} \quad (3.4)$$

where $K = (4/3) \pi d C$

Thus

$$K_2 = K_1 r_2^{a_2-a_1} \quad (3.5)$$

and the total mass per unit volume of aerosol is given by

$$\rho_c = K_1 \left[\int_{r_1}^{r_2} r^{3-a_1} dr + r_2^{a_2-a_1} \int_{r_2}^{\infty} r^{3-a_2} dr \right] \quad (3.6)$$

Since $a_2 > 4$, the 2nd term is finite, and we obtain

$$\rho_c = K_1 \left[\frac{r_2^{4-a_1} - r_1^{4-a_1}}{4-a_1} + \frac{r_2^{4-a_1}}{a_2-4} \right] \quad (3.7)$$

With the assumption that $d = 2$ g cm^{-3} , the constants in this expression are $a_1 = 3$,

TABLE 4. Aerosol Density ρ_c for Various Values of Distribution Parameters.* Units of 10^{-15} g cm $^{-3}$.

r_2 , microns	a_2				
	5	6	6.7	7	8
0.5	33	24	22	21	19
0.7	47	35	31	30	28
1.0	69	51	46	45	42
2.0	142	106	96	93	87
3.0	215	160	145	142	133

* $C_1 = 4.35 \times 10^{-11}$ cm $^{-1}$; $a_1 = 3$; $d = 2$ g cm $^{-3}$.

$K_1 = 3.6 \times 10^{-10}$ g cm $^{-4}$, $a_2 = 6.7$,
 $r_1 = 0.1 \times 10^{-4}$ cm, $r_2 = 1.0 \times 10^{-4}$ cm.

There are three major sources of error in this expression for ρ_c . First, the measured sizes must be corrected for whatever spreading factor applies; second, the exact 'knee point,' r_2 , is somewhat uncertain; and, last, the slope of region 2 is also uncertain because of the sparsity of particles of the larger sizes. In discussions of the size distribution, it has been suggested that the measured values may be uncertain by a factor of 2. This would imply a factor of 8 in ρ_c , and therefore the quantitative chemical analysis data, from which ρ is obtained directly, may be of some use in determining the magnitude of the necessary corrections.

If we consider the measured radius of a particle to be br , whereas the radius of the same particle as it exists in the atmosphere is r , then the density calculated, ρ_c , is related to the true density, ρ , by

$$\rho = \rho_c / b^3 \quad (3.8)$$

If we vary a_2 and r_2 in (3.6), keeping a_1 , r_1 , and K_1 constant, we obtain Table 4.

From Table 4 we see that variation of a_2 has little effect on ρ_c , and variation of r_2 causes an approximately proportionate variation in ρ_c , leaving the factor b in (3.8) as the most effective parameter in bringing the measured mass concentration into agreement with that calculated from size distribution data. The effect of allowing a_1 to be 4 instead of 3 causes (7) to become

$$\rho_c' = K_1' \left(\ln \frac{r_2}{r_1} + \frac{1}{a_2 - 4} \right) \quad (3.7a)$$

where $K_1' = 3.6 \times 10^{-14}$ g cm $^{-3}$.

If we choose $a_2 = 6.7$, $r_2 = 1.0 \mu$, and $r_1 = 0.1 \mu$, (7a) yields $\rho_c' = 96 \times 10^{-15}$ g cm $^{-3}$. In this

case, the value of ρ_c is very sensitive to the exact choice of r_1 , since most of the mass is concentrated in the smaller particles.

From these considerations we can draw the following conclusions. The measured aerosol density, assuming the sulfur to be present as ammonium sulfate and sodium sulfate, 9.2×10^{-15} g cm $^{-3}$. From (3.8) we find that a factor of $b = 1.7$ will force agreement between calculated and measured densities if we use the value $\rho_c = 46 \times 10^{-15}$ g cm $^{-3}$, corresponding to $a_1 = 3$, $a_2 = 6.7$, $r_1 = 0.1 \mu$, $r_2 = 1.0 \mu$, and $K_1 = 3.6 \times 10^{-10}$ g cm $^{-4}$. Since a droplet on a hydrophobic surface must be corrected by a factor of $b = 1.25$, the above correction seems quite reasonable. The result would be to shift the entire set of curves in Figure 6 to the left with the 'knee point' r_2 moved down to 0.6 μ . The other variations will not provide the necessary decrease in ρ_c without an unwarranted change in the shape of the size distribution.

D. Physical properties. It may be of interest to discuss briefly our observations about the water solubility of the particles in the heavy band of the window samples. These particles were found to be very hygroscopic, in full agreement with our previous observations of smaller particles on the balloon samples. A good demon-

TABLE 5. Relative Humidity at Room Temperature for Phase Transition of Various Salts and Stratospheric Aerosols

Salt	Calculated Phase Transition, %	Observed Phase Transition, %
Na_2SO_4	84	83-85
NaHSO_4	No data available	Between 20 and 25, but not well defined and up take of moisture slow. Particles extremely hygroscopic.
$(\text{NH}_4)_2\text{SO}_4$	82	81-83
$(\text{NH}_4)_2\text{S}_2\text{O}_8$	No data available	Fresh spray started at 87 and decreased to 83 after a few cycles. Conversion to $(\text{NH}_4)_2\text{SO}_4$?
$(\text{NH}_4)\text{HSO}_4$	No data available	45-55
Collected aerosol samples		72-80

tion is given in Figure 4, which shows photographs of particles in the band at various levels of relative humidity. Each pair of micrographs was taken under precisely the same conditions of illumination and development. One can see that almost all the particles are grown in volume than in diameter because, as the particles dry out, they have a tendency to become flat and do not shrink in diameter as much as in volume. For these photographs the sample was placed in a little curette and a stream of air of known and controlled humidity entered this chamber.

We tried to obtain more information on particle growth with humidity, especially on the humidity at which the dry particle becomes a liquid. Such a phase transition is very pronounced for pure substances, occurring at exactly the relative humidity which corresponds to that of a saturated salt solution at a given temperature. Such measurements of the phase transition must always be made by raising the humidity in small increments. If the humidity is lowered, the particles stay as supersaturated liquid droplets considerably below the equilibrium humidity. For $(\text{NH}_4)_2\text{SO}_4$, for instance, the phase transition at room temperature occurs at 72 per cent, but the particles remain liquid while the humidity is decreased down to 40 per cent, when they crystallize suddenly.

The stratospheric particles showed this phase transition between 72 and 80 per cent humidity, but the transition was more gradual than for the pure substances.

Since the sulfates of ammonium and sodium are most likely the ones present in the stratosphere (I), we made phase transition observations for corresponding salts. Table 5 gives the results. It appears that the transition humidity for the collected aerosols is compatible with that for Na_2SO_4 , $(\text{NH}_4)_2\text{SO}_4$, and $(\text{NH}_4)_2\text{S}_2\text{O}_8$, although a little bit lower, which may be accounted for by the increased solubility of particles of $1\ \mu$ as compared to particles of $20\ \mu$ and more which were used for the pure salts.

Another part of these investigations was to compare electron microscope pictures of spray aerosols of known composition with pictures of stratospheric aerosol samples. Figure 5 shows a picture of stratospheric aerosols, collected directly on an electron microscope screen in the heavy band. No kinds of particles can be distinguished, one

with little contrast and with indications of considerable evaporation under the electron beam, and the others with better contrast and possible evaporation only along the edges. Figure 13 shows several electron micrographs of spray samples which were produced in such a way that the particle size was compatible with the stratospheric particles. The pictures are sequences in time ranging over a few to 10 minutes, showing evaporation. It is evident that particles of the same material can look different but that the general appearance of these salt aerosols is very similar to that of the stratospheric particles. Unfortunately, the differences in appearance between some of the salts of interest are small and ambiguous and can hardly be used to help in precise identification. Our experience with spray aerosols does not exclude the possibility, for instance, that the two types of particles shown in Figure 5 are chemically identical but were collected under different conditions during the flight. The main results of these investigations is that the behavior of the stratospheric particles is quite compatible with that of ammonium sulfate, in agreement with the chemical analysis.

By an independent and simultaneous study, *Friend and Sherwood* [1961] identified $(\text{NH}_4)_2\text{SO}_4$ and $(\text{NH}_4)_2\text{S}_2\text{O}_8$ by electron diffraction analysis of stratospheric aerosols collected under similar conditions. This is the reason we included these salts in our study. The chemical literature indicates that ammonium persulfate is not stable and is slowly converted to the normal sulfate. Our phase transition study seems to confirm this.

4. DISCUSSION

A. Origin of the aerosol layer. Compared with other meteorological phenomena the variation in time and space of the aerosol layer is small. This strongly suggests that it is the product of a steady state between formation and removal. In I it was pointed out that the shape of the vertical profile (Fig. 9) makes it unlikely that these particles penetrate directly from the troposphere into the stratosphere by mixing or other exchange processes. Extraterrestrial origin, on the other hand, is practically excluded because of the chemical composition. It was therefore suggested that the particles are formed within the stratosphere by conversion of traces of H_2S or SO_2 into particulate material by oxidation. These gases are found in the troposphere in

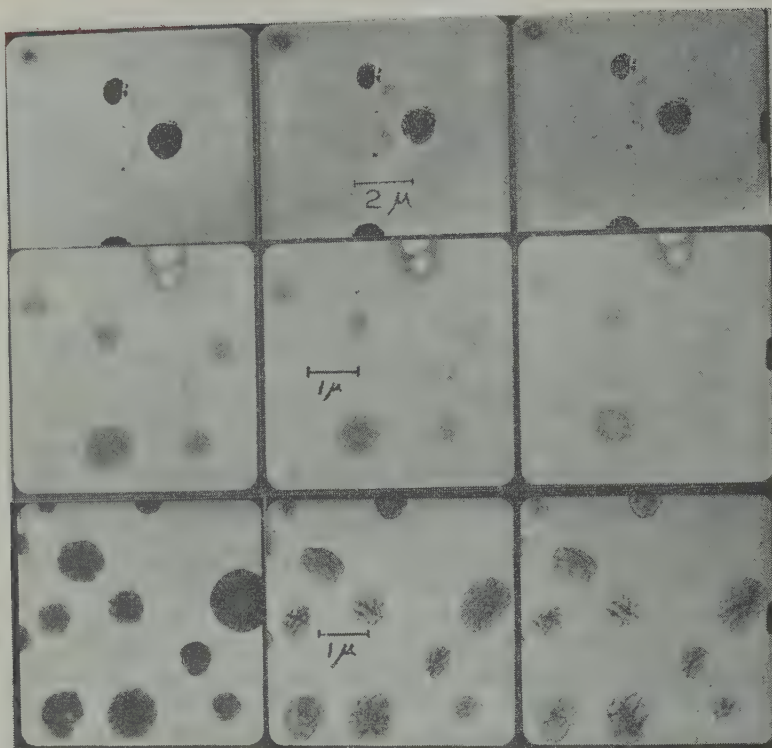


Fig. 13. Electron micrographs of particles collected at 20 km (top row) compared with ammonium sulfate particles prepared by atomizing a solution in the laboratory (center and bottom rows). All were supported on cast formvar films. The time of exposure of the sample to the electron beam increases from left to right, from a few seconds to several minutes.

sufficient concentration. It may be of interest to estimate the speed of this formation process.

It is most likely that the largest particles are removed exclusively by sedimentation and that the observed upper size limit of about $1\ \mu$ is controlled by this process. Under steady-state conditions these particles must be replaced by growth of the smaller particles. This growth can occur either by 'condensation' of sulfate as a result of SO_2 or H_2S oxidation. The speed of the coagulation process can be calculated by the well-known theory of Smoluchowsky. If we use our data for the size distribution and absolute concentration of particles, it turns out that replacement of $1\text{-}\mu$ particles by coagulation takes more than 100 years; coagulation is therefore ruled out as a possible mechanism. If our assumption of the origin of the particles is correct, growth by 'condensation' must thus be assumed. Perhaps it is possible to explain the inverse square law of

the logarithmic size distribution on the basis of such an equilibrium between sedimentation and growth by oxidation.

We will attempt to make an estimate of the time scales involved in these processes by considering the lifetime of the $1\text{-}\mu$ particles. We assume the thickness of the layer to be approximately 10 km (Fig. 9) and the average height to be 20 km. If the fall velocity of $1\text{-}\mu$ particles (density assumed to be 2 g cm^{-3}) is 0.07 cm sec^{-1} at 20 km, a column of 10 km height is removed in about 0.5 year. This should be the approximate maximum lifetime of these particles because air exchange with the surrounding layers would support the removal by sedimentation. During this time, the particles have to be replaced. In case sedimentation is not the limiting factor in particle growth, the alternative is replacement of air by exchange with the troposphere. From studies of radioactive fallout it is known that the residence time of stratospheric air at this

ude is about 1 year. We conclude, therefore, the sulfate aerosol is replaced once or twice ar.

The presence of extraterrestrial material in stratosphere, and its collection. It is now y well established that the zodiacal dust d is by far the most important source of aterrestrial material in our atmosphere. siderable information on concentration and distribution of this interplanetary zodiacal is available and was recently critically marized by Öpik⁹[1956]. The knowledge is ed on the observation of three optical phe- ena, i.e., the Fraunhofer corona around the the zodiacal light, and the Gegenschein, or aterglow. These three phenomena are now ight to be produced by light scattered at erent angles from the sun, and the dust acteristics derived on this basis give a fairly sistent picture. It is not our intention to at these derivations here, but rather to pt the following values, considered by Öpik most reasonable. If n is the concentration of icles per cm^3 and r their radius, we can write

$$dn/dr = Cr^{-p} \quad (4.1)$$

$5 \mu < r < 300 \mu$, $2.6 < p < 3.0$, $\bar{p} = 2.8$. mass density of the dust cloud in the nity of the earth is $\rho = 2 \times 10^{-21} \text{ g cm}^{-3}$ the density of the particulate material is imed to be $\delta = 3.5 \text{ g cm}^{-3}$. The value for ρ r vary by a factor of 3 either way, and δ is density of stony meteorites. From these es we may evaluate C as follows.

$$\rho = \frac{4}{3} \pi \delta C \int_r^R r^{+0.2} dr \quad (4.2)$$

h yields $C = 1.1 \times 10^{-20} \text{ cm}^{-1.2}$.

o compare this estimate with our collected ities in the stratosphere, we must calculate accretion rate of the earth, and this involves e difficulties. If the earth moves through the t cloud with a relative velocity u , and if the p of the capturing cross section to the geo- rical cross section of the earth is R , we have

$$R = 1 + (S^2/u^2) \quad (4.3)$$

re $S = 11.1 \text{ km sec}^{-1}$ is the escape velocity n the earth. It is apparent that R is very itive to u . Because the orbits of the dust icles differ somewhat, on the average, from

that of the earth in eccentricity and inclination, u will have a nonzero value. Under certain assumptions Öpik arrives at an 'effective' u of 4.4 km sec^{-1} , so that the accretion rate becomes

$$A = \frac{\rho}{4} u \left(1 + \frac{S^2}{u^2} \right) \\ = 1.6 \times 10^{-15} \text{ g cm}^{-2} \text{ sec}^{-1} \quad (4.4)$$

To estimate the size distribution which will result at stratospheric levels from such accretion in the exosphere, we shall assume that in this size range particles are neither created nor destroyed during transit to an altitude of 20 km. Further, we shall use a global average initial velocity of A/ρ for particles entering the atmosphere. Thus, F , the number of particles per unit horizontal area per unit time entering a vertical sedimentation column, will satisfy the following relations in the steady state:

$$\frac{dF}{dr} = \text{const.} = \left(\frac{dF}{dr} \right)_{z_1} = \left(\frac{dF}{dr} \right)_{z_2} \quad (4.5)$$

$$\frac{dF}{dr} = \frac{A}{\rho} \left(\frac{dn}{dr} \right)_{z_1} = W_{sc} \left(\frac{dn'}{dr} \right)_{z_2} \quad (4.6)$$

where Z_1 refers to the exosphere and Z_2 refers to the stratosphere, dn/dr is given in equation 4.1, W_{sc} is the Stokes-Cunningham fall velocity, and dn'/dr is the desired size distribution in the stratosphere and is given by

$$\frac{dn'}{dr} = \frac{A}{\rho W_{sc}} \left(\frac{dn}{dr} \right) = \frac{AC}{\rho W_{sc}} r^{-2.8} \\ \frac{dn'}{d \log r} = \frac{2.3 AC}{\rho W_{sc}} r^{-1.8} \\ = 2 \times 10^{-14} \frac{r^{-1.8}}{W_{sc}} \quad (4.7)$$

This relationship is given in curve 4, Figure 7. Because of the uncertainties of C and particularly of u , the values cannot be regarded as more accurate than one order of magnitude. It must be mentioned that the theory of micrometeorites shows that, in the size range below 10 to 50 μ , only a very small percentage of the particles will be heated enough to evaporate or to melt. Most of the dust particles will therefore come to rest in the atmosphere unaltered.

Rocket and satellite measurements of the influx of particles are now available, but these data are still very inaccurate for various reasons.

The sensors used respond either to the momentum or the impact energy of the particles, or some function of it. Calibrations are very difficult because of the difficulty in laboratory production of small particles with speeds in excess of 11 km/sec. Calibrations are therefore extrapolations over wide ranges, and, even if the momentum or impact energy were accurately known, one would have to make assumptions for the speed of the particles to obtain their size or mass. A most likely estimate of average influx in the size range between 1 and 10 μ is 10^{-7} particles per cm^2 per sec (H. Cohen, personal communication, 1959). If we assume a size distribution in this range with $p = 3.0$ (for simplicity), we obtain $dn'/d \log r = 4.6 \times 10^{-16} r^{-2}/W_{\infty}$ which is smaller by a factor of about 4 than the estimated size distribution. This good agreement must, however, be considered fortuitous. It does not reflect the reliability of the values.

The values of $dn'/d \log r$ were calculated under the assumption that sedimentation equilibrium exists in the atmosphere and that the earth's accretion rate is constant. For particles in the range of 10 μ , the fall velocities in the upper atmosphere must be considered equal to or larger than the turbulent velocities of the air, so that the assumption of sedimentation equilibrium is justified. It is, however, possible that the influx rate fluctuates considerably and that steady-state conditions are not always maintained. We see in Figure 7 that the stratospheric particles smaller than 2 μ have concentrations which are higher by about three orders of magnitude than the estimated concentration of the zodiacal particles. It will therefore be basically very difficult to detect and collect extraterrestrial particles in this size range, except perhaps for altitudes above 25 km, where the concentration of the large stratospheric particles starts to drop off. This basic result should be kept in mind by those who are interested in collecting only extraterrestrial material in the stratosphere.

For particles larger than 3 μ there is a fair chance of collecting and identifying such material, although this is by no means easy because of the extremely low expected concentrations. The problem involved is best illustrated by the horizontal lines 1 to 3 in Figure 7. These lines indicate concentrations which would result in the collection of 1, 2, or 3 particles/ cm^2 on a flight path of 4000 km at an altitude of 20 km.

(As we shall see later, collection by an aircraft impactor is superior to almost all other collection methods.) It is exceedingly difficult to produce substrate surfaces which have low background counts of this order. One possibility of overcoming this difficulty is to identify individual particles by making photomicrographs of the surface before and after collection, a method which is currently in use.

The cross-over of these lines with curve 4 in the vicinity of 6 μ . If curve 4 is correct it implies that above 6 μ it again becomes very difficult to collect extraterrestrial particles. The small 'window' for radii between about 3 and 6 μ appears to be the best chance for collection, the proper technique is applied.

These conclusions are important for the planning of future research in this area. They depend very much, however, on the reliability of curve 4. If the real influx were higher by a factor of 5 than that indicated by curve 4, the problem of extraterrestrial dust collection in the stratosphere could easily be solved. There is also the possibility that the influx rate is not constant. Indications of such fluctuations for larger particles, which can be observed as radar meteors, were recently obtained by *Gallagher and Eshelman* [1960]. Our most recent results for particles with radius of 2 to 4 μ , using full photomicrographic documentation, suggest that the low values given by curve 4 did apply to the stratosphere during October 1960.

On the other hand, on the flight of March 1960 (Fig. 7), the plate was covered with a large number of fairly large particles of peculiar structure (Fig. 10). These look as if they disintegrated into a large number of smaller spheres at impact. We observed similar particles, only very rarely, during other flights and were not able to identify them as a contamination. It is therefore possible that these particles are of extraterrestrial origin. We have discussed the data on their chemical composition above. If we are right about the origin of these 'splattered' particles, it implies that once in a while clouds of extraterrestrial dust enter the atmosphere.

Because of the considerable effort which has been devoted to the sampling of atmospheric particles and the very great interest in the collection of extraterrestrial particles in the atmosphere, we should like to present the quantitative evaluation from which we have determined our

TABLE 6. Comparison of Capacity and Collection Density for Various Stratospheric Collection Systems at About 20-Kilometer Altitude

General type of collector	Vehicle Used	Specific Instrument	Collection Area, cm ²	Flow Rate, cm ³ sec ⁻¹	Total Volume Collected, m ³	Density of Collection, L, km	Actual or Possible Duration of Exposure, hours
r (IPC)	Balloon	'Ash can' AEC	4700	2.4×10^5	850	1.8	1
r (IPC)	Balloon	Direct flow unit AEC	930	3.8×10^5	1360	15	1
r	Balloon	SMAC unit	9300	3.8×10^5	1360	1.5	1
(Microfiber)	Balloon	AFCRL					
le	Balloon	Large impactor					
impactor		First stage AEC, AFCRL	2.0	1.0×10^4	360	1800	10
le	Balloon	Small impactor					
impactor		AFCRL	0.04	2.4×10^2	5.2	1300	6
et flow	Aircraft	Rod impactor					
impactor		AFCRL	1	2.2×10^4	480	4800	6
mentation	Balloon	Exposed		3.0	0.11	1.1	10
		horizontal surface	1*	3×10^3	11	110	10

The surface area can of course be any size. We assumed 1 cm². We further assumed two particle sizes (1 and 100 μ) with a density of 2 g cm⁻³.

collection methods. Because of the difficulty in obtaining accurate calibration data for all sizes, gravimetric methods have not been considered. Thermal precipitators were rejected because of the generally low flow rates for reasonable sizes and heights. For the remaining methods, which depend on the dynamic characteristics of impactors, sedimentation, and filtration, the density of collection is given by $L = V/A$, where V is the total volume of air processed and A is the area of collection. L represents the length of the column swept by A and should be as large as possible. In Table 6 we have calculated L for the stratospheric collection systems used in recent times. Some of these systems were designed to collect radioactive material only, but they are included for comparison because they are characterized by very large total volumes.

It is apparent that even large volume filter systems are not comparable to impaction systems for the collection of nonradioactive particles of low concentrations if one wishes to determine their concentration or to identify them individually. Here we can distinguish between impactors and direct flow impactors. The first are used on balloons and the second on aircraft or rockets. It is our experience that it is more difficult to avoid contamination by a few large particles with balloon equipment than with aircraft, particularly when large balloons

are floated for hours at altitude. If the direct flow impactor is properly mounted on the aircraft, contamination of the sample during flight is excluded. In another technique a collecting surface was mounted on top of a large floating balloon and exposed at altitude. The collection is achieved by sedimentation. We see from Table 6 that, even for extremely large particles (100 μ), L for this sedimentation device is still smaller by one order of magnitude than for the direct flow impactor.

At the present time the ceiling for practical balloon operations is about 30 km, or 10 km greater than the 20 km reached by the U-2. Sedimentation equilibrium provides a good approximation for the vertical distribution of particles larger than a few microns. With sedimentation equilibrium the concentration of particles larger than about 3 μ will not vary much with altitude, in contrast to smaller particles the concentration of which is approximately proportional to the air density (1). Very little can be gained, therefore, by collecting particles larger than a few microns at 30 km instead of 20 km.

This discussion on methods for cosmic dust collection has been included because many workers in this field are not fully acquainted with the very special conditions which apply to particle collection in the stratosphere.

In summary, we conclude that collection by

direct flow impactors of proper design, mounted on aircraft, is the most promising method for stratospheric aerosol studies involving individual particle identification.

CONCLUSIONS

The observations presented in (I) and particularly in this paper show the presence of a world-wide stratospheric aerosol layer with the following characteristic features:

1. The particles range in radius from about 0.1 to $2\ \mu$. The upper limit is very pronounced; at the lower limit there is a transition to the Aitken nuclei (smaller than $0.1\ \mu$) which show an entirely different vertical profile.
2. The total particle concentration is about $0.1\ \text{cm}^{-3}$ and varies only by a factor of about 3. The size distribution ($dn/d\log r$) is about inverse to the square of the particle size.
3. The vertical profiles in middle latitudes show a broad maximum between 15 and 23 km with little change over the year.
4. The chemical analysis indicates that sulfur is the most prominent element between the atomic numbers of magnesium and zinc. The particles are very water soluble, and sulfur is most likely present in the form of sulfate. The cation could possibly be Na^+ , H^+ or NH_4^+ . There is an indication that it is NH_4^+ .
5. The form of the vertical profile in middle latitudes makes it unlikely that the particles are of direct tropospheric origin, unless they are injected by strong vertical motions into the tropical low stratosphere and spread to polar regions. On the other hand, their composition makes it very unlikely that they are directly or indirectly of cosmic origin. We feel that the most attractive explanation is particle formation within the stratosphere by oxidation of gaseous sulfur components such as H_2S and perhaps SO_2 . Such gases are present in the troposphere in concentrations sufficient to explain the stratospheric sulfate concentration. Gas traces, especially H_2S , can penetrate more easily into the stratosphere because they are not affected by tropospheric washout as strongly as aerosols.
6. The omnipresence of this cloud, except perhaps over the polar regions, makes it very

difficult to detect possible extraterrestrial particles of less size than $2\ \mu$ because the concentration of the native stratospheric particles is larger by about a factor of 1000. Above $3\ \mu$ the estimated concentration of extraterrestrial particles is already so low that the biggest problem in detecting cosmic dust is the particle background of any collection substrate. It is therefore necessary to use collection methods which allow the particles from a large volume of air to be concentrated on an area as small as possible.

Acknowledgments. We should like to thank Miss Susan Schur and Ralph Carnevale of the Advanced Metals Research Corporation for electron microprobe analysis and specimen preparation, respectively.

We are also indebted to the personnel associated with the High Altitude Sampling Program (HASP) of the Department of Defense. In particular, Major Albert K. Stebbins, III, of the Defense Atomic Support Agency, Dr. James P. Friend of Isotopes Inc., and the officers and men of the 4080th Strategic Reconnaissance Wing (SAC).

This work has been supported in part by the U. S. Atomic Energy Commission under contract AT(49-7)-1431.

REFERENCES

- Chagnon, C. W., and C. E. Junge, The vertical distribution of sub-micron particles in the stratosphere, *J. Meteorol.*, **18**, 1961.
- Friend, J. P., and R. D. Sherwood, The size distribution and composition of stratospheric particles, *Science*, **133**, 1961.
- Gallagher, P. B., and V. R. Eshelman, 'Sporadic shower' properties of very small meteors, *J. Geophys. Research*, **65**, 1846-1847, 1960.
- Junge, C. E., C. W. Chagnon, and J. E. Manson, Stratospheric aerosols, *J. Meteorol.*, **18**, 81-103, 1961.
- O'Keefe, J. A., The origin of tektites, *TN D-490*, National Aeronautics and Space Administration, Washington, D. C., 1960.
- Öpik, E. J., Interplanetary dust and terrestrial accretion of meteoritic matter, *Irish Astron. J.*, **4**, 84-135, 1956.
- Ranz, W. E., and J. B. Wong, Impaction of dust and smoke particles, *Anal. Chem.*, **44**, 1371-1381, 1952.
- Stebbins, A. K., III, Special report on the high altitude sampling program, *DASA 532B*, Defense Atomic Support Agency, Washington, D. C., 1960.

(Manuscript received March 23, 1961.)

Origin of Radioactive Fallout in the Northern Hemisphere after the Spring Maximum in 1959

J. F. BLEICHRODT, JOH. BLOK, AND E. R. VAN ABKOUDE

*Medical Biological Laboratory of the National Defence Research Organization TNO
Rijswijk, Z. H., The Netherlands*

Abstract. Evidence is presented that an insignificant fraction of debris from the Soviet nuclear test explosions in October 1958 was present in the lower stratosphere at the end of 1959 and that fallout during 1960 mainly originated from injections into the tropical stratosphere during 1958.

Introduction. Recently several attempts have been made to estimate the contribution of Sr^{90} originating from the Hardtack nuclear test explosions at Bikini (11°N , 165°E) and Eniwetok (16°N , 162°E) in May, June, and July, 1958, from the Soviet detonations north of the Tropic of Cancer in October 1958 to the total Sr^{90} at the end of 1959. It was estimated that since the autumn of 1958 [Lockhart, Patterson, Saunders, and Black, 1960a, b; Martell and Munn, 1960; Walton, 1960]. These estimates are possible because the unique tracer tungsten (^{185}W , half-life 75.8 days [Strominger, Hollander, and Seaborg, 1958]) was introduced into the stratosphere by some of the Hardtack explosions. The estimated value for the $^{185}\text{W}/\text{Sr}^{90}$ radioactivity ratio on an average explosion date was used to calculate the contribution of Hardtack debris to the total Sr^{90} from ^{185}W data. The percentage of Sr^{90} from the Soviet October tests was evaluated by means of the $\text{Sr}^{89}/\text{Sr}^{90}$ ratio after subtraction of the amount of Sr^{89} associated with Hardtack debris from the total Sr^{89} measured.

In studying atmospheric transport of debris from nuclear explosions in 1958, it is of importance to know the contribution of Sr^{90} of both tropical and polar origin to total Sr^{90} fallout. However, the reliability of the results of calculations as mentioned above is strongly dependent on the estimated $^{185}\text{W}/\text{Sr}^{90}$ ratio in Hardtack debris (the $\text{Sr}^{89}/\text{Sr}^{90}$ ratio at the moment of explosion is fairly well known). Moreover, knowledge of the percentage of Hardtack Sr^{90} in the total does not give information on the percentage of Sr^{90} originating from the tropical stratosphere. At least the contribution of the United States tests in April and September in the Johnston Island area (2°N , 167°W) should be taken into account.

Recent data suggest that the contribution of Sr^{90} of tropical origin to fallout in 1959 was substantially higher than the amount estimated from the ^{185}W fallout and that since the end of 1959 fallout originated mainly from injections into the tropical stratosphere. This means that essentially no debris from the Soviet October 1958 tests was left in the lower stratosphere at the end of 1959.

Experimental procedures. Sr^{90} (half-life 28 years) and Ce^{144} (half-life 285 days) were isolated from monthly rain-water samples collected by exposing pots with a diameter of about 45 cm and a height of about 40 cm. Inactive carriers were added to the pots before exposure. The amount of rainfall during the collection period was measured with a rain gage which was emptied three or more times a week. The nuclides were separated according to the method of Osmond, Owers, Healy, and Mead [1959]. Sr^{90} was purified radiochemically by the procedure of the same authors, Ce^{144} by that of Glendenin, Flynn, Buchanan, and Steinberg [1955]. Insoluble residues were analyzed separately for Ce^{144} , because it was found that sometimes about 25 per cent of Ce^{144} remained in the residue after extraction with nitric acid.

^{185}W was isolated from monthly rain-water samples similarly collected as described above, using the procedure of Welford, Collins, Sutton, and Morse [1959]. The $^{185}\text{W}/\text{Sr}^{90}$ ratios for October, November, and December, 1960, however, have been obtained by analyzing rain samples (80 to 100 liters) collected with a stainless steel tray of 1 m^2 .

The radioactivity of the purified nuclides was measured with a Geiger-Müller counting setup,

calibrated by means of standardized solutions of various nuclides with different β energies.

In the beginning of 1960, W^{185} activities had decreased to such low values that reliable activity measurements could not be carried out. Since that time the X radiation (about 57 kev) of the isotope W^{181} (half-life 126 days [Kreger and Lynn, 1960]), which was also produced during the Hardtack series, has been measured. By determining both the W^{181} and W^{185} activity (corrected for radioactive decay to a common date) in a number of fallout samples it was possible to determine the factor by which the W^{181} activity of a sample must be multiplied to obtain the W^{185} activity.

All measurements have been carried out in duplicate except W^{185}/Sr^{90} determinations in October, November, and December, 1960. Sr^{90} duplicates seldom differed more than 10 per cent; Ce^{144} duplicates showed larger differences. The standard error of the Ce^{144}/Sr^{90} ratios has been estimated by statistical analysis of the Ce^{144}/Sr^{90} duplicate values. The standard error of the W^{185}/Sr^{90} ratios is estimated at about 12 per cent.

Results and discussion. In Figure 1 Ce^{144}/Sr^{90} ratios at Rijswijk, Z. H. ($52^{\circ}3'N$, $4^{\circ}20'E$), have been plotted for the period 1958 through 1960, corrected for radioactive decay to the arbitrarily chosen date November 1, 1958. Data for Milford Haven ($51^{\circ}43'N$, $5^{\circ}2'W$) [Crooks, Osmond, Owers, and Fisher, 1959; Crooks, Osmond, Fisher, Owers,

and Evett, 1960] and for Washington, D. C. ($38^{\circ}50'N$, $77^{\circ}0'W$) [Lockhart, Baus, Patterson and Saunders, 1959], have been included for comparison.

After August 1958 the Ce^{144}/Sr^{90} ratio started to increase with the arrival of fresh debris from the Hardtack and Soviet October detonations. A maximum was reached during the spring of 1959 when most of the long-lived fission products originated from the Soviet series [Bleichrodt, Blok, and Dekker, 1961]. Then Ce^{144}/Sr^{90} decreased due to a diminishing contribution of Soviet debris. Since December 1959 the Ce^{144}/Sr^{90} ratio has remained approximately constant, suggesting either that the lower stratosphere in the northern hemisphere was well mixed or that fallout material was fed into the troposphere from two or more stratospheric sources at approximately proportional rates.

In Table 1 the W^{185}/Sr^{90} ratios in rain water at Rijswijk are given, corrected for radioactive decay to June 15, 1958. No large fluctuations are observed. This supports the conclusion drawn from the Ce^{144}/Sr^{90} ratios.

TABLE 1. W^{185} Fallout at Rijswijk, Z. H., Corrected for Decay to June 15, 1958

Sampling Period	W^{185} , pc/l*	Rainfall, mm	W^{185}/Sr^{90}
1959			
June	1000	27	72
July	380	63	54
August	280	44	60
September	1390	3.1	187†
October	98	91	74
November	113	50	81
December	81	74	66
1960			
January	70	89	42
February	187	33	77
March	420	15.5	90
April	143	36	42
May	129	49	40
June	187	36	54
July	98	58	48
October			49
November			58
December			30

* 1 pc/l = 10^{-12} curie per liter.

† Rainfall was extremely light during this month resulting in low radioactivity. The Cs^{137}/Sr^{90} ratio was 5.0. The average value for 1959, the September value not included, was 2.1. Therefore it seems probable that the Sr^{90} result was too low by a factor of about 2.5.

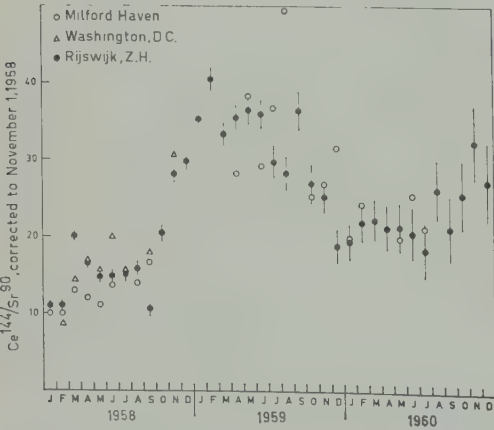


Fig. 1. Ce^{144}/Sr^{90} ratios in rain water at Rijswijk, Z. H., and Milford Haven, England, and in air at Washington, D. C., corrected for radioactive decay to November 1, 1958. The vertical lines represent one standard error.

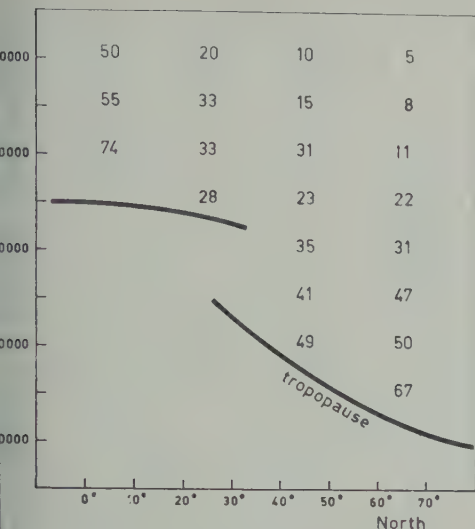


Fig. 2. W^{185}/Sr^{90} ratios in the lower stratosphere of the northern hemisphere during November-December 1959, corrected for radioactive decay to June 15, 1958. W^{185} and Sr^{90} data have been corrected from Figure 1 of Feely and Spar [1960].

the possibility that during 1960 radioactive debris was fed into the troposphere from two or three sources of different composition with approximately proportional rates must be excluded on the basis of stratospheric W^{185} and Sr^{90} . Feely and Spar [1960] recently published vertical profiles of W^{185} and Sr^{90} in the lower stratosphere for the period November-December 1959. Figure 2 shows W^{185}/Sr^{90} ratios in the lower stratosphere obtained from Figure 1 of Feely and Spar. The data have been corrected for radioactive decay (half-life $W^{185} = 75.8$ days) to June 15, 1958, in order to facilitate comparison with the data of Table 1.

It is apparent from Figure 2 that at the end of 1959 in the lower stratosphere of the northern hemisphere W^{185} and Sr^{90} were well mixed in layers which roughly parallel the tropopause. In the lower layers the W^{185}/Sr^{90} ratio is comparable with the ratio found in rain water during 1958. It may be concluded that fallout during 1958 consisted mainly of material residing in the lower 15,000 ft of the stratosphere during November-December 1959. This is in agreement with the view that vertical mixing is slow in the stratosphere.

According to Feely and Spar [1960] from September 1958 up to April 1960 at least, the

maximum W^{185} concentration in the stratosphere was found over the equator at about 70,000 ft. Changes in the distribution of W^{185} in the stratosphere during this period point to a transport of this nuclide by large-scale mixing in a layer sloping downward from the equatorial maximum towards the north pole. Above this layer the W^{185} concentration decreased with increasing altitude. As far as data were available for the southern hemisphere the situation was found to be roughly symmetrical about the equator with somewhat lower concentrations in the southern hemisphere.

The permanent W^{185} maximum in the equatorial stratosphere together with approximately constant W^{185}/Sr^{90} ratios in the layers of latitudinal mixing at the end of 1959 (Fig. 2) suggest that Hardtack Sr^{90} in the equatorial stratosphere has not been diluted appreciably by Sr^{90} from the Soviet detonations in October 1958. In case of dilution the W^{185}/Sr^{90} ratio would be expected to decrease with increasing latitude in the layers of mixing. Absence of dilution can also explain the stratospheric Sr^{89}/Sr^{90} ratio in the northern hemisphere. From November 1958 to November 1959 this ratio was found to be fairly uniform in the lower stratosphere between 5° and $65^{\circ}N$ and to decrease in accordance with the half-life of Sr^{89} [Stebbins, 1960]. It is highly improbable that such a uniform distribution of Sr^{89}/Sr^{90} at the end of 1958 resulted from mixing of equatorial debris and dust from the arctic tests in October 1958.

From these arguments it follows also that by the end of 1959 no dust from the Soviet October 1958 detonations was present in the lower stratosphere between 5° and $70^{\circ}N$.

The presence of Soviet October 1958 debris in the lower stratosphere north of 70° cannot be excluded from the data in Figure 2. It is to be expected that Sr^{90} from the Soviet tests still present in this part of the stratosphere at the end of 1959 would enter the troposphere during the spring of 1960 [Bleichrodt, Blok, and Dekker, 1961], causing a decrease in W^{185}/Sr^{90} and an increase in Ce^{144}/Sr^{90} in rain water. However, both ratios remained approximately constant during the spring of 1960.

Martell and Drevinsky [1960] assumed that the W^{185}/Sr^{90} ratio of stratospheric Hardtack debris was 380 on June 15, 1958; Lockhart and others [1960a] assumed a ratio of 500 for July 15, 1958. If these values reflect the true order of magni-

tude, this implies that Sr^{90} present in the equatorial stratosphere before the Hardtack tests commenced and Sr^{90} from the United Kingdom explosions diluted Hardtack Sr^{90} by a factor of 6 to 10 (Fig. 2). This is supported by measurements of Martell and Drevinsky at Pôrto Alegre (30°5'S, 51°3'W) during the period August 1958 to March 1959. The average $\text{Sr}^{89}/\text{Sr}^{90}$ ratio corrected for decay to June 15, 1958, was found to be 208 ± 48 , indicating fallout of recent explosions. The $\text{W}^{185}/\text{Sr}^{90}$ ratio, however, was 97 ± 17 .

In a recent calculation of the percentage of Sr^{90} originating from the Soviet October 1958 explosions in fallout during 1959 [Bleichrodt and others, 1961] all Sr^{89} in fallout since January 1959 was ascribed to the Soviet tests, because the contribution of Hardtack Sr^{89} estimated for a $\text{W}^{185}/\text{Sr}^{90}$ ratio of 500 [Lockhart and others, 1960a] was negligible. However, the arguments presented above suggest that, to estimate the amount of Sr^{90} of tropical origin, a much lower $\text{W}^{185}/\text{Sr}^{90}$ ratio should be used. Nevertheless it can be shown that, during the spring maximum in 1959, Sr^{90} originated predominantly from the detonations in October 1958.

An estimation of the contribution of equatorial Sr^{90} in 1959 can be made in a more accurate way on the basis of stratospheric $\text{Sr}^{89}/\text{Sr}^{90}$ ratios [Stebbins, 1960]. As was shown above, in 1959 Sr^{89} in the stratosphere between 5° and 65°N was of tropical origin. Extrapolation of $\text{Sr}^{89}/\text{Sr}^{90}$ to October 15, 1958, results in a $\text{Sr}^{89}/\text{Sr}^{90}$ ratio of about 60. If the $\text{Sr}^{89}/\text{Sr}^{90}$ ratio for October 1958 debris is assumed to be 180 on October 15, 1958, the fraction x of debris of tropical origin in fallout at any time during 1959 can then be calculated from

$$60x + 180(1 - x) = A$$

where A represents the measured $\text{Sr}^{89}/\text{Sr}^{90}$ ratio corrected to October 15, 1958.

In Table 2 results are given for Rijswijk, Abingdon, and Milford Haven, calculated from data of Bleichrodt and others [1961] and Crooks and others [1960]. It is seen that during the spring maximum in 1959 some 15 to 30 per cent of Sr^{90} fallout originated from equatorial explosions, so the more accurate calculation modifies the values given previously to a slight extent only. In the autumn of 1959, however, the contribution of

TABLE 2. Contribution of Sr^{90} from Explosions in Tropical Regions to Sr^{90} Fallout during 1959

Sampling Period	Tropical Sr^{90} (percentage of total)		
	Rijswijk	Abingdon	Milford Haven
1959			
January	45	77	47
February	43	51	47
March	48	29	43
April	15	27	17
May	17	21	26
June	21	23	42
July	24	40	47
August	45	63	62
September	27*	92	92
October	51	101	87
November	102	102	73

* Activities were low this month, due to low rainfall. Therefore the error may be relatively large.

equatorial Sr^{90} rose rapidly and approached values near 100 per cent.

In an attempt to calculate the relative amount of air from the polar and temperate stratosphere that brought Sr^{90} into the troposphere during the spring of 1959, Machta [1960] assumed that 60 per cent of tropospheric debris originated from the Soviet October 1958 explosions. This is somewhat lower than the result of the calculation mentioned above.

It is somewhat surprising that during the summer of 1959 the $\text{W}^{185}/\text{Sr}^{90}$ ratios were not significantly lower than the ratios found at the end of 1959 and in 1960, whereas the contribution from arctic tests diminished gradually to practically zero during the second half of 1959. A minimum in the $\text{W}^{185}/\text{Sr}^{90}$ ratio would have been expected at the time of the maximum percentage of fallout from the Soviet October 1958 tests. Such a minimum was indeed found in the northern hemisphere by Lockhart, Patterson, Saunders, and Black [1960b] and also, although less pronounced, by Walton [1960].

The $\text{W}^{185}/\text{Sr}^{90}$ ratio in equatorial debris might not have been constant in 1959. In this connection it is important to note that in November-December 1959 the W^{185} maximum over the equator resided at about 70,000 ft whereas the maximum $\text{W}^{185}/\text{Sr}^{90}$ ratio was found at 60,000 ft [Feely and Spar, 1960]. This may be due to the different altitudes reached by the clouds

atorial test explosions, resulting in a non-homogeneous distribution of W^{186} and Sr^{90} .

onhomogeneity of the equatorial debris with ect to W^{186} and Sr^{90} is suggested also by $^{85}Sr^{90}$ and Sr^{89}/Sr^{90} ratios found in the osphere [Lockhart and others, 1960b]. Whereas Sr^{89}/Sr^{90} ratio in ground-level air in the thern hemisphere, corrected for decay, in- used by a factor of about 4 during 1959, the rage W^{186}/Sr^{90} ratio remained approximately stant, showing a slight maximum in May.

he possibility of varying W^{186}/Sr^{90} ratios in ris from the equatorial explosions during 9 precludes a reliable assessment of the tion of equatorial Sr^{90} in fallout based on e data. Therefore, the Sr^{89}/Sr^{90} ratio in the osphere was used as a basis for the calcula- of the values in Table 2.

onclusion. There is evidence that no debris in the Soviet detonations in October 1958 was sent in the lower stratosphere at the end of 9 and that during 1960 fallout consisted nly of material from explosions in tropical s. This material was characterized by a $^{85}Sr^{90}$ ratio of 40 to 80 on June 15, 1958, and $^{144}Ce^{144}/Sr^{90}$ ratio of about 22 on November 1, 8 (Figs. 1, 2, and Table 1). The contribution quatorial explosions to fallout in 1959 is ngly underestimated when it is calculated h W^{186} data using a W^{186}/Sr^{90} ratio of 380 on e 15, 1958 [Martell and Drevinsky, 1960], or on July 15, 1958 [Lockhart and others, 1960a]. urtherless, during the spring maximum of 9 the contribution of Soviet debris from the ober 1958 explosions amounted to 70 to 85 cent (Table 2) in western Europe.

cknowledgment. We are indebted to Dr. M. ans for analyzing the Ce^{144}/Sr^{90} duplicates istically and to Mr. M. H. J. Huguenin for help the γ -ray spectrometer.

REFERENCES

chrodt, J. F., Joh. Blok, and R. H. Dekker, On e spring maximum of radioactive fallout from uclear test explosions, *J. Geophys. Research*, **66**, 135-141, 1961.
 Crooks, R. N., R. G. D. Osmond, E. M. R. Fisher, J. Owers, and T. W. Evett, The deposition of sion products from distant nuclear test explosions. Results to the middle of 1960, *AERE-R*

3349, United Kingdom Atomic Energy Authority, Harwell, 1960.
 Crooks, R. N., R. G. D. Osmond, M. J. Owers, and E. M. R. Fisher, The deposition of fission products from distant nuclear test explosions. Results to mid-1959, *AERE-R 3094*, United Kingdom Atomic Energy Authority, Harwell, 1959.
 Feely, H. W., and J. Spar, Tungsten-185 from nuclear bomb tests as a tracer for stratospheric meteorology, *Nature*, **188**, 1062-1064, 1960.
 Glendenin, L. E., K. F. Flynn, R. F. Buchanan, and E. P. Steinberg, Radiochemical determination of cerium in fission, *Anal. Chem.*, **27**, 59-60, 1955.
 Kreger, W. E., and R. L. Lynn, A measurement of the decay of ^{181}W , *Nuovo cimento*, **18**, 829-836, 1960.
 Lockhart, L. B., R. A. Baus, R. L. Patterson, and A. W. Saunders, Radiochemical analyses of air-filter samples collected during 1958, *NRL Rept. 5390*, U. S. Naval Research Laboratory, Washington, D. C., 1959.
 Lockhart, L. B., R. L. Patterson, A. W. Saunders, and R. W. Black, Contribution of Hardtack debris to contamination of the air during 1959, *Science*, **132**, 154, 1960a.
 Lockhart, L. B., R. L. Patterson, A. W. Saunders, and R. W. Black, Fission product radioactivity in the air along the 80th meridian (West) during 1959, *J. Geophys. Research*, **65**, 3987-3997, 1960b.
 Machta, L., An attempt to compute relative removal rates from the polar and temperate latitude stratosphere in the spring 1959, in *Fallout Program Quarterly Summary Report, HASL-95*, Health and Safety Laboratory, U. S. Atomic Energy Commission, New York, October 1, 1960.
 Martell, E. A., and P. J. Drevinsky, Atmospheric transport of artificial radioactivity, *Science*, **132**, 1523-1531, 1960.
 Osmond, R. G., M. J. Owers, C. Healy, and A. P. Mead, The determination of radioactivity due to caesium, strontium, barium and cerium in waters and filters, *AERE-R 2899*, United Kingdom Atomic Energy Authority, Harwell, 1959.
 Stebbins, A. K., editor, A special report on the high altitude sampling program, *Defence Atomic Support Agency, DASA 532*, Washington, D. C., 1960.
 Strominger, D., J. M. Hollander, and G. T. Seaborg, Table of isotopes, *Revs. Modern Phys.*, **30**, 585-904, 1958.
 Walton, A., Tungsten-185 in precipitation and the seasonal variations in fall-out, *Nature*, **188**, 220-221, 1960.
 Welford, G. A., W. R. Collins, D. Sutton, and R. Morse, The sequential analysis of ten nuclides occurring in long range fallout debris, *HASL-57*, Health and Safety Laboratory, U. S. Atomic Energy Commission, New York, 1959.

(Manuscript received March 13, 1961;
 revised May 5, 1961.)

Long-Range Sound Transmission in the Arctic Ocean¹

HENRY KUTSCHALE

*Lamont Geological Observatory, Columbia University
Palisades, New York*

Abstract. Strong hydroacoustic signals from underwater explosions as small as 2 pounds of TNT have been detected in the Arctic Ocean at distances up to 1150 km. Hydrophones at depth and geophones on the ice surface were used as listening devices. The signals propagate in the Sofar channel, whose axis in the Arctic Ocean occurs approximately at the surface, but the character of the signals differs markedly from that typical of the nonpolar oceans, largely because of the predominance of low-frequency waves in the Arctic. The character of the arctic Sofar signals is best explained by normal-mode wave propagation in a channel bounded by the surface and by the zone of increasing velocity in the upper several hundred meters of water. Irregularities in the ice boundaries apparently strongly attenuate the high-frequency waves but have a negligible effect on the amplitudes of the low-frequency waves. At least two normal modes were observed. In each normal mode the waves have a nearly sinusoidal appearance with periods decreasing from about 120 to 30 msec in the first mode and from 70 to 40 msec in the second mode. A good quantitative fit between experimental data and theoretical dispersion curves has been obtained. The signals were detected in both deep and shallow water.

Introduction. During July and August 1959, a series of experiments was conducted in cooperation with the U. S. Navy Underwater Sound Laboratory to study Sofar sound propagation in the central Arctic Ocean. Charges ranging in weight from 2 to 10 lb of TNT were fired from the ship's Ice Island (T-3), a drifting ice station, and the signals were detected with abundant signal strength by geophones and hydrophones at Drifting Station Charlie. The average distance between the stations was about 1100 km.

Waves corresponding to at least two normal modes were commonly observed. Waves of the first normal mode were normally dispersed (periods decreasing with decreasing velocity) and had a period from about 120 to 30 msec and a velocity from about 1445 to 1436 m/sec. Waves of the second normal mode were also normally dispersed and ranged in period from about 70 to 40 msec and in velocity from about 1445 to 1444 m/sec. The arrival of the waves of the second normal mode began at a group-velocity maximum, corresponding to an Airy phase. The waves of the first normal mode may be terminated at an Airy phase. The portions of the typical records on which waves of the first normal mode were recorded are shown in Figure 1. A tracing of a complete wave train, showing the first and second normal modes, is shown in Figure 2. The Lamont Geological Observatory Contribution

number for this work is 1445. The wave train shown in Figure 1 (shot 75, trace 8), showing waves of the first and second normal modes as well as some suggestion of waves of still higher normal modes is shown in Figure 2.

The waves observed in this work differ from those observed in the deep Sofar channel of the nonpolar oceans largely in that the character of the wave train is regular and oscillatory, in fact, almost sinusoidal, and the waves have relatively long periods. In the nonpolar oceans, the Sofar signal usually appears to consist of many discrete pulses and is relatively weak in waves in the period range of the arctic Sofar signals [Ewing and Worzel, 1948]. Because of these differences, the waves observed in this work are best explained by normal-mode theory rather than by ray theory, which is commonly used to interpret Sofar signals in the nonpolar oceans.

The sound channel controlling the propagation in the Arctic Ocean is bounded above by the surface and below by the zone of increasing velocity with depth within the water. For the waves observed in this work, only the upper several hundred meters of water are primarily involved. The effect of the ice layer on the velocity of propagation of the observed waves is apparently so small as to be negligible; however, the rough ice boundaries seem to affect the waves of periods shorter than those observed here,

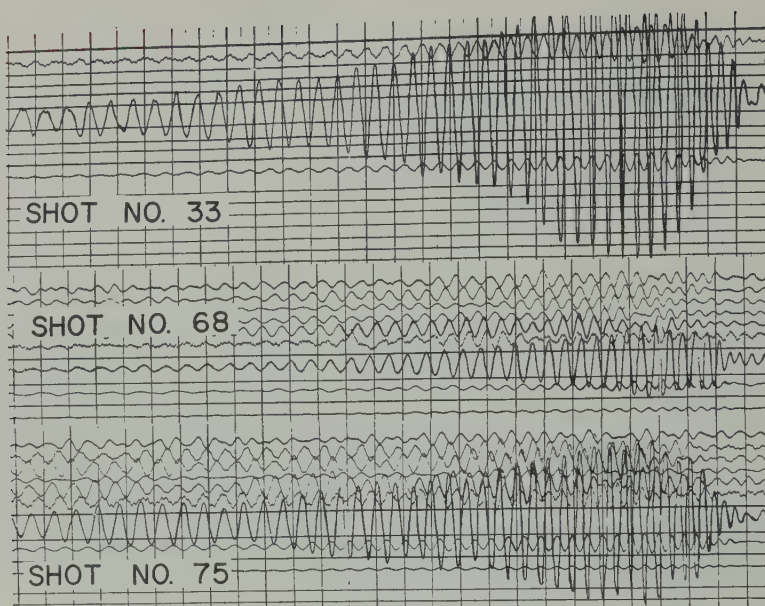


Fig. 1. Portions of three typical records showing waves of the first normal mode. The dark timing lines on the records occur every 100 msec. For shot 33, the upper, middle, and lower active traces correspond to hydrophones at depths of 40, 65, and 20 m, respectively. For shot 68, the upper six traces correspond to vertical-component geophones placed on the surface of the pack ice, and traces 8, 10, and 12 correspond to hydrophones at depths of 65, 20, and 40 m, respectively. The traces for shot 75 correspond to those for shot 68. The charges were 6 to 9 lb of TNT and were fired at depths of 130 to 200m. The distance between shot point and detectors was about 1100 km.

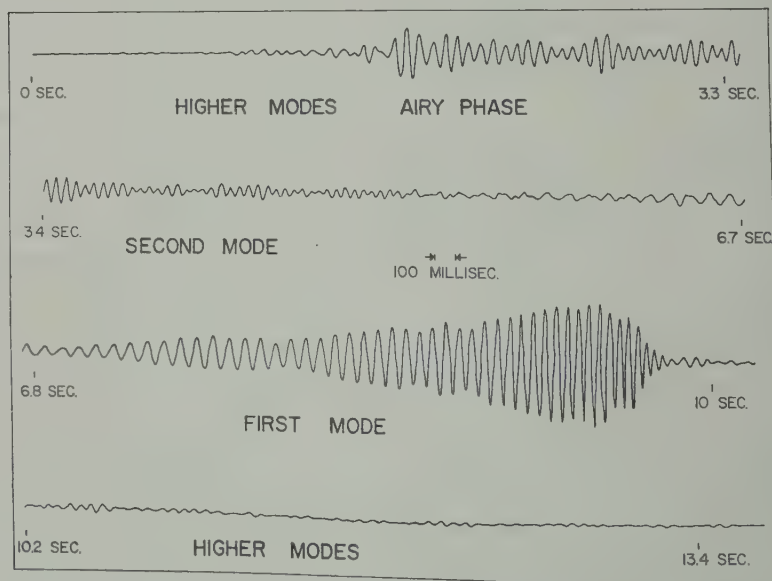


Fig. 2. A tracing of a complete wave train taken from one of the records shown in Figure 1 (shot 75, trace 8). The second normal mode starts about 1.5 sec after the waves begin (about 0 sec on the tracing). The first normal mode starts about 5 sec after the waves begin.

ably by scattering, so that they are not propagated within the waveguide to great distances. Certain periods in the wave train may have been enhanced as a result of the source spectrum associated with the initial explosion pulse and the succeeding bubble pulses.

In this work, the velocity and density structure within the pack ice and water was approximated by a model consisting of a series of homogeneous, isotropic, flat-lying layers in sufficient number to give a good representation of the physical situation. On the basis of this representation, phase- and group-velocity dispersion curves were computed. The results of these computations describe the velocities of the observed waves and the dispersion occurring in the wave train so well that it is virtually impossible that small disagreements between theory and experiment result from errors in position of drifting stations, due to weak navigational control.

Experimental work. The approximate drift tracks of the shooting and receiving stations during the experimental period are shown in Figure 3. The minimum distance between the stations during this period was about 1050

km, and the maximum distance was about 1150 km. The transmission path extended across the central Arctic Ocean, where water depths are generally greater than 3 km. During the course of the experiments, the receiving station drifted from deep water (2 km) into the relatively shallow water over the Chukchi rise, where the minimum recorded water depth was about 250 m. The maximum length of the shallow-water segment of propagation path was approximately 100 km. Water depths at the shooting station averaged about 1 km during the course of the experiments. A typical generalized bathymetric profile between the two stations is shown in Figure 4.

The experimental method used in this work was similar to that used in explosion seismology [see, for example, *Tatel and Tuve, 1955*]. The charges used as sound sources were detonated at depths from 30 to 330 m below the ice-water interface; about 80 shots were fired during the course of the experiments. Members of the U. S. Navy Underwater Sound Laboratory fired the charges as part of their program on Arctic Ocean acoustics. At the receiving station the recording apparatus consisted of a standard seismic ampli-

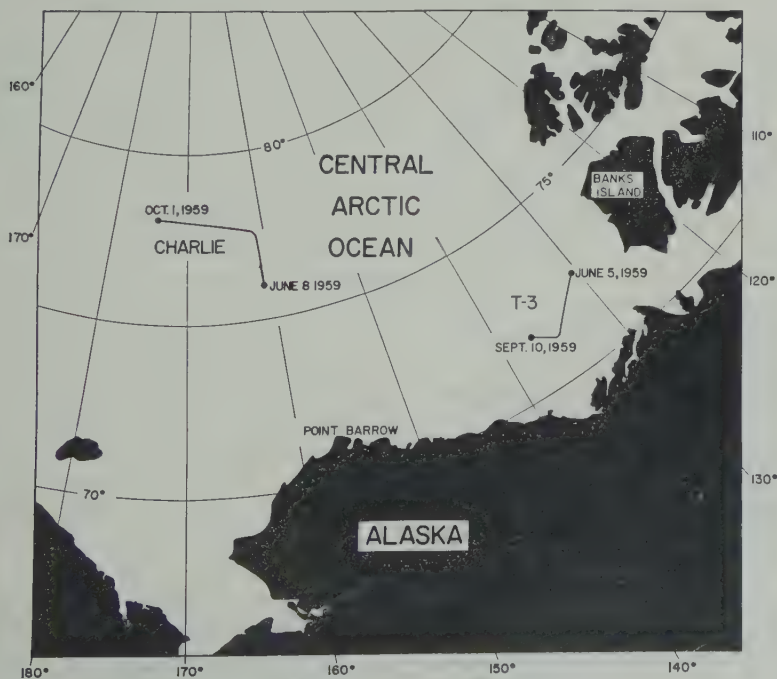


Fig. 3. Approximate drift tracks of the receiving station (Charlie) and the shooting station (T-3) during the experimental period.

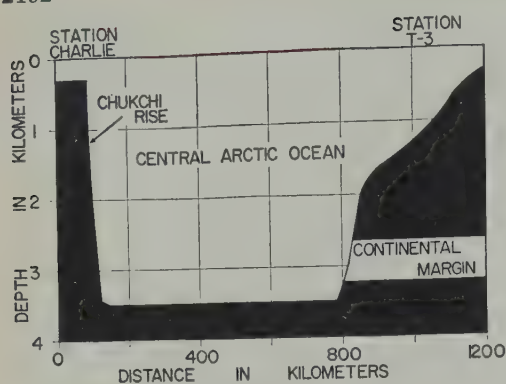


Fig. 4. Generalized bathymetric profile between the receiving station and the shooting station. Vertical exaggeration is 200 : 1.

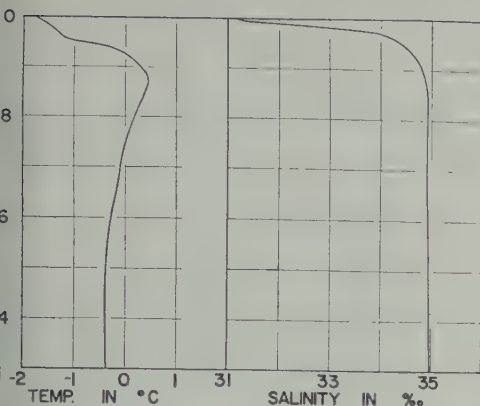
fier system and an oscillographic camera. Hydrophones suspended at depths from 20 to 65 m below the ice-water interface and a one- or two-dimensional horizontal array of vertical-component geophones placed on the surface of the pack ice were used to detect the waves. During one series of experiments, on a clear, windless day, weak low-frequency sounds were heard by ear almost simultaneously with the arrival of the waves at the geophones and hydrophones; these sounds may have corresponded to the leakage of some acoustic energy into the air. Detection by the unaided human ear of 6-lb explosive charges at a distance of about 700 miles (1100 km) is quite amazing and attests to the extreme efficiency of the natural waveguide. All shots were of necessity recorded with the camp generator running near the detectors, and many shots were recorded with other man-made background noise occurring at the receiving station. This man-made background noise generally set an upper limit to the sensitivity of the receiving system. However, all shots were always detected with abundant signal strength above background noise.

The general character of the waves remained fairly constant during the course of the experiments. Although shots were always detected whether the receiving station was in deep water or in shallow water, a slight decrease in signal strength was apparent for a long segment of shallow-water path. The waves corresponding to the first normal mode always arrived with ample signal strength for detection by the geophones and the hydrophones; the largest amplitudes

were observed by the deepest hydrophones (Fig. 1). The waves corresponding to the second normal mode were usually also well detected, particularly by the deepest hydrophone. On many records waves corresponding to higher normal modes were also identified. These waves occurred in the period range from about 40 to 90 msec, and they were generally detected only by the deepest hydrophone. No significant change was observed in the velocities of the waves or in the dispersion occurring within the wave train for records obtained at various times during the course of the experiments. Waves in the period range from about 35 to 80 msec were always the most strongly excited. The strongest signals were detected from the larger charges fired at the intermediate depths.

Theory. Because the velocity of sound in the central Arctic Ocean generally increases rapidly with depth to about 350 m and then continues to increase at a slower rate to the bottom, sounds are transmitted to great distances by a series of upward refractions in the water and multiple reflections at the ice-water and the ice-air interfaces. At a short distance from a non-directional underwater sound source, the sound field arriving at a detector can be conveniently interpreted by ray theory. However, when the ratio R/λ becomes sufficiently small, where R is the maximum depth of penetration of a ray and λ is the wavelength, and when the distance between source and detector becomes sufficiently large, a physical description of the sound field in terms of propagation along individual ray paths is not convenient, since the number of ray paths is too large and the sounds traveling along different ray paths overlap, giving rise to constructive and destructive interference. Therefore, rather than propagation along individual rays, the interference effects of the whole system of upward refracted sounds in the water and the multiply reflected sounds from the ice-water and the ice-air interfaces have been considered in this work. An analysis of this type leads to the normal-mode theory of sound propagation [see, for example, *Officer, 1958*].

Pekeris [1948] developed the normal-mode theory of shallow-water explosive sound transmission to explain the dispersive waves observed by *Worzel and Ewing* [1948]. The problem solved by *Pekeris* is somewhat similar to the problem encountered in the central Arctic Ocean. The



5. Vertical temperature and salinity profiles for the central Arctic Ocean.

low-water layer can be thought of as corresponding to the upper 350 m of water, while the half-space representing the sub-bottom elements can be thought of as corresponding to water beneath a depth of 350 m. In the central Arctic Ocean, however, each 'layer' is homogeneous since the speed of sound generally decreases with depth.

Typical vertical temperature and salinity profiles for the central Arctic Ocean are shown in Figure 5 [Farlow, 1958]. These profiles represent an average, but any particular set of observations taken at various times and locations in the central Arctic Ocean would not vary much from these [Crory, 1956]. On the basis of these temperature and salinity profiles, the vertical

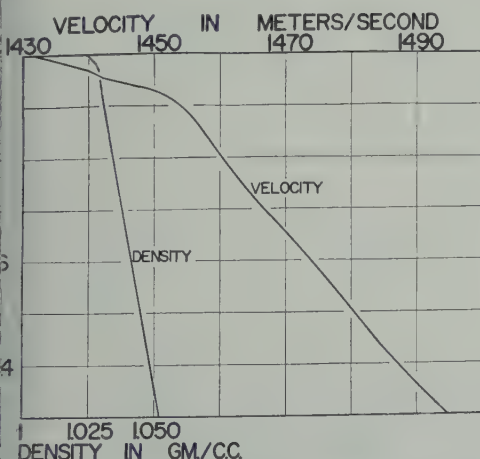


Fig. 6. Vertical sound velocity and density profiles computed from the temperature and salinity profiles shown in Figure 5.

velocity and density profiles shown in Figure 6 were computed from the tables of Matthews [1939]. The steep positive velocity gradient in the upper 350 m of water is due to the rapid increase of temperature to this depth; the smaller positive velocity gradient below a depth of 350 m is controlled by the hydrostatic pressure.

The normal-mode theory has been applied to the present problem by replacing these two inhomogeneous 'layers' within the water by a series of homogeneous, flat-lying layers, each layer having an appropriate average sound velocity and density assigned to it, based on the velocity and density profiles shown in Figure 6. The thickness of each layer in the upper 350 m of water, where the variation of sound velocity is most rapid, was made less than the minimum wavelength of the observed waves. Below a depth of 350 m the partitioning was made coarser, since the variation of sound velocity is less rapid there than in the upper 350 m of water. A check of the computations showed that the partitioning method used gave a satisfactory representation of the physical situation in the period range of the observed waves. The pack ice was taken into account by assuming a homogeneous, isotropic solid layer with compressional velocity, shear velocity, density, and thickness typical of summer pack ice [Hunkins, 1960]. This representation should be valid in the period range of the observed waves. The wavelengths of the observed waves are more than 10 times the mean ice thickness (3 m) and are generally greater than known irregularities on the boundaries of the pack ice [Oceanographic Atlas, 1958]. No account was taken of the shallow-water segment of propagation path, introduced when Drifting Station Charlie drifted over the Chukchi rise, since this segment amounts to a maximum of 100 km in a total propagation path of over 1000 km.

For model A given in Table 1, dispersion curves relating phase velocity and group velocity to period were computed on an IBM 650 computer with a program developed by Dorman [Dorman, Ewing, and Oliver, 1959; Oliver and Dorman, in press]. Dorman has extended Haskell's [1953] matrix-iteration formulation of the period equation (phase-velocity dispersion) for a multilayered elastic solid to include the case of interbedded liquids and solids, and he has developed a computer program for this formula-

TABLE 1. Parameters Used in Making Calculations for Model A

Layer	Compression Velocity, km/sec	Shear Velocity, km/sec	Density, g/cm ³	Layer Thickness, m
1 ice	2.5	1.4	0.90	3
2 water	1.434	...	1.025	50
3 water	1.437	...	1.028	50
4 water	1.440	...	1.029	50
5 water	1.442	...	1.028	50
6 water	1.446	...	1.028	50
7 water	1.449	...	1.030	50
8 water	1.452	...	1.030	50
9 water	1.458	...	1.031	450
10 water	1.490	...	1.042	800-m depth to ∞

Model B excludes layer 1.
Model C decreases layer 9 to 300-m thickness; layer 10 goes from 650-m depth to ∞ .
Model D increases layer 9 to 650-m thickness; layer 10 goes from 1000-m depth to ∞ .

tion of the period equation which permits rapid computation of phase-velocity dispersion. Group-velocity dispersion is computed directly from the computed phase-velocity dispersion. Dorman's program provides an extremely powerful method for analyzing wave propagation of the type observed in this work, since most continuous velocity and density profiles can be represented by a sufficient number of discrete layers. The computed phase-velocity dispersion curves for model A for the first six normal modes in the period range from about 30 msec to the long-period cutoff for each normal mode are shown in Figure 7. The corresponding group-velocity dispersion curves are shown in Figure 8. The computations were not carried out for periods less than about 30 msec because of a short-period limit in the program at about 30 msec for model A. The long-period cutoff for each normal mode would in general be determined by

the water depth along the transmission path and by the velocity of sound in the sub-bottom sediments [Pekeris, 1948].

To determine the effect of the ice layer on the velocity of propagation of the observed waves and to check the validity of the relatively coarse partitioning used in model A, we computed dispersion curves for the first normal mode for three other models (Table 1). In model B the ice layer was removed from model A. The results obtained for models A and B are compared in Figure 9. The removal of the ice layer has a negligible effect on the computed dispersion curves for model A. Hence the pack ice probably had a negligible effect on the velocity of propagation of the observed waves. In models C and D, the velocity partitioning below a depth of 650 m was changed considerably from that used in model A (Table 1 and Fig. 6). Model C is a poorer representation of the physical situation than model A, and model D is a better representation. The results obtained for models A, C, and D are compared in Figure 9. The changes in velocity partitioning have only a small effect on the computed dispersion curves. Hence the velocity partitioning used in model A is a good representation of the physical situation in the period range of the observed waves, and the propagation of the observed waves is largely controlled by the velocity gradient in the upper several hundred meters of water.

Experimental results and comparison with theory. From a number of records, obtained both while the receiving station was in deep water and while it was in the shallow water over

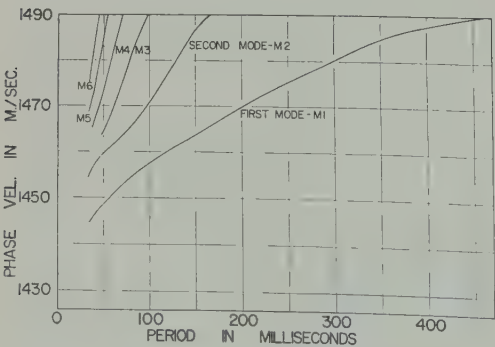


Fig. 7. Phase-velocity dispersion curves for the first six normal modes computed for model A.



Fig. 8. Group-velocity dispersion curves for the first six normal modes computed for model A.

Chukchi rise, dispersion curves relating group velocity to period were plotted for each hydrophone trace and several geophone traces. The experimental group-velocity dispersion curves were obtained by the standard method used in earthquake seismology [Ewing and Press, 1952]. Clearly defined normal modes were found, corresponding to the first and second normal modes of the theory.

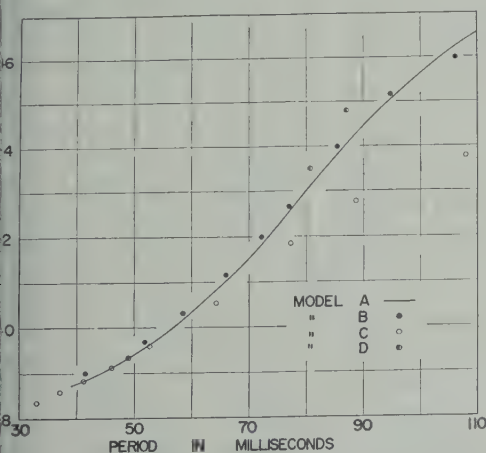


Fig. 9. The effects of the ice layer and the velocity gradient below a depth of 650 m on the first normal-mode dispersion curves in the observed period range. In model B the ice layer was eliminated from model A. In models C and D, the velocity gradient below a depth of 650 m was changed considerably from that used in model A.

In plotting the experimental group-velocity dispersion curves, several sources of experimental error had to be considered. By far the largest source of error was in determining the distance between shot point and receiver. On only a few occasions were astronomic fixes obtained while experimentation was being done. Usually it was necessary to interpolate between fixes obtained before and after the period of experimentation in order to determine the positions of the two stations during this period. The calculated distances are believed to be accurate to within ± 5 km in most cases (± 0.3 per cent of the total distance). The time interval between the shot instant and the arrival of any portion of the wave train on the record was usually determined to within ± 0.5 sec (± 0.01 per cent of the total time interval), and therefore this source of error is negligible compared with the error in the distance determination. Time on the record was read to 1 msec with negligible error. Phase shifts occurring in the receiving system were negligible over the observed period range.

The experimental group velocities as a function of period for the first and second normal modes obtained from the dispersion curves are shown in Figure 10 for a typical record (shot 33, Fig. 1). The theoretical group-velocity dispersion curves for model A for the same two modes in the period range from 30 to 130 msec are also shown in Figure 10. The agreement between theory and

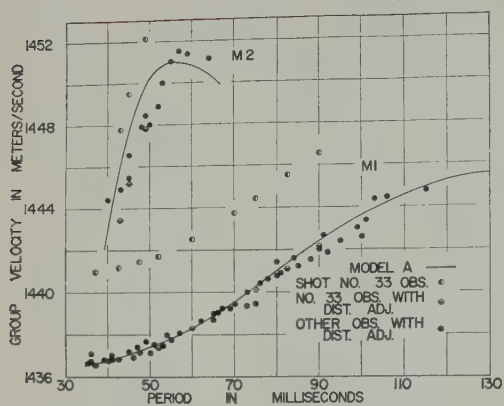


Fig. 10. Comparison of the observed and theoretical group-velocity dispersion curves for the first and second normal modes.

experiment is excellent for both modes. The slight discrepancy in group velocity at any given period is accounted for by the experimental error in the distance determination between shot point and receiver. This is also shown in the figure. An adjustment was applied to the calculated distance for shot 33 which made the observed and theoretical group velocities coincide at a period of 60 msec for the first normal mode (the distance adjustment was -2.5 km for a total calculated propagation path of 1109 km). The adjusted distance was then used to determine the observed group velocities as a function of period for both modes. The adjusted experimental points shown in Figure 10 virtually coincide with the theoretical curves for both modes.

To compare in a systematic way the theoretical group-velocity dispersion curves computed for model A with all the corresponding experimental group-velocity dispersion curves, we applied the same procedure used for shot 33. The calculated distance between shot point and receiver for each shot was adjusted so that the observed and the theoretical group velocities coincided at a period of 60 msec for the first normal mode. This distance was then used to reobtain the observed group-velocity dispersion curves for both normal modes. The distance adjustment was usually within the estimated experimental error for the distance determination between shot point and receiver, and it shifted the experimental group-velocity dispersion curves for both normal modes plotted from any particular record by a nearly constant increment of group velocity

(usually within ± 7 m/sec). Figure 10 shows the experimental points obtained from a number of adjusted group-velocity dispersion curves for records obtained at different times during the course of the experiments. The agreement between theory and experiment is excellent for both normal modes. No significant change was observed in the group-velocity dispersion curves for either normal mode during the experimental period.

On a number of records wave trains were found preceding the waves of the second normal mode and following the waves of the first normal mode. However, since these other wave trains are of short duration and of low amplitude, no accurate group-velocity dispersion curves could be plotted. The dominant periods found in these wave trains (40 to 90 msec) and their corresponding group velocities showed fairly good agreement with those expected from the theory for the third to the sixth normal modes (Fig. 8). These other wave trains apparently consist of a superposition of waves corresponding to portions of the third to the sixth normal modes (Fig. 2).

Phase-velocity measurements were made for the first normal mode from the waves detected by the geophone array (Fig. 1, particularly shot 68). The geophones were used only during the time the receiving station was over the Chukchi rise (Fig. 4). Since the variation of phase velocity over the observed period range is rather small, no accurate phase-velocity dispersion curves could be plotted. However, an average value of phase velocity for the waves of the first normal mode in the period range from 80 to 50 msec is 1550 m/sec. This value is too high to agree with the phase-velocity computations for model A (Fig. 7), which indicates that the sub-bottom sediments on the Chukchi rise had some influence on the propagation of the waves of the first normal mode in the observed period range. (The fact that some decrease in signal strength was apparent for a long segment of shallow-water path also indicates that the sub-bottom sediments had some influence on the transmission of the observed waves.) In an adequate model describing the physical situation for the shallow-water segment of propagation path account must be taken of the positive velocity gradient in the water and the velocity of sound in the sediments (dispersion curves for such a model can be easily computed with

man's computer program). However, no dispersion curves were computed for such a model because of the inadequacy of the phase-velocity dispersion data and because the velocity sound in the sediments was not known.

The amplitude above background noise as a function of period for the first and second normal modes for a typical wave train (the train in Figure 2 shown in Figure 11. Also shown in Figure 11 is the receiving-system response as a function of period for this wave train. The attenuation of periods less than 50 msec, which is indicated by the response curve shown in Figure 11, was necessary for most shots because of the man-made background noise at the receiving station. The attenuation of periods less than 50 msec reduced the amplitude of the waves of the first normal mode for periods less than 50 msec (Figs. 1, 2, and 11), but, on several occasions during the most favorable listening conditions, shots were received with flat receiving-system response in the period range from 2 to 130 msec, and no waves with a period less than about 30 msec were observed. Apparently, irregularities in the boundaries of the pack ice, particularly irregularities on the underside of the pack ice, one of which may extend 30 m below the ice-water interface [*Oceanographic Atlas*, 1958], scatter waves of periods less than about 30 msec so that no coherent interfering wave system is formed. The long-period cutoff at about 120 msec for the waves of the first normal mode and about 70 msec for the waves of the second normal mode (Fig. 11) has not been explained,

although the bathymetry along the transmission path may be important in this connection.

The maximum amplitude of the waves of the second normal mode (Fig. 11) corresponds to an Airy phase [Pekeris, 1948], that is, the group-velocity maximum of the second normal mode (Fig. 10). At a stationary value of group velocity, the range of the sound field varies only as $r^{-5/6}$, where r is the distance between source and detector. At nonstationary values of group velocity, the range dependence of the sound field is r^{-1} . Therefore, at large distances between source and detector, the Airy phases should form a prominent part of the wave train. The wave train shown in Figure 2 has a well-developed Airy phase for waves of the second normal mode. (The waves of the first normal mode may have a stationary value of group velocity at a period of about 30 msec, Fig. 10.)

Apparently, the strong excitation of the waves in the period range from about 35 to 80 msec, which was consistently observed in this work and which is indicated by Figure 11, was enhanced by the bubble-pulse period of the underwater-explosion sound sources. Pekeris [1948] has shown that the pressure amplitude in normal-mode sound propagation is directly proportional to the period spectrum of the acoustic pressure at the source. For an underwater explosion emitting one or more bubble pulses, the period spectrum of the acoustic pressure at the source has a maximum at the bubble-pulse period [see, for example, Goldman, 1948]. Therefore, in normal-mode explosive sound transmission the signal, in general, should be well excited for periods centered about the bubble-pulse period of the explosion source. It was determined experimentally that the explosive charges used in this work emitted at least one strong bubble pulse. The bubble-pulse period of the charges ranged from about 30 to 90 msec, depending on the charge size and the firing depth [Worzel and Ewing, 1948], and therefore occurred in the same period range as the maximum excitation of the long-range signals. This is good qualitative evidence that the bubble-pulse period was of some importance in determining the excitation of the long-range signals.

No computations were carried out for the various normal modes to determine the vertical pressure distribution in the water or the dependence of the pressure amplitude on the shot

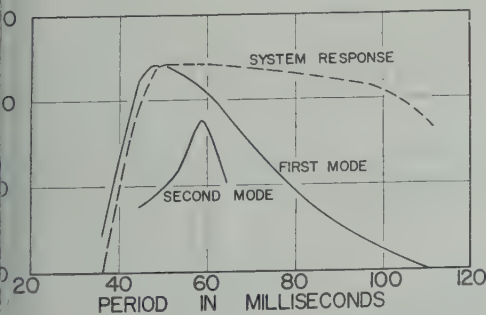


Fig. 11. The amplitudes of the waves of the first and second normal modes above background noise for the wave train shown in Figure 2 and the receiving-system response curve for this wave train. The bubble-pulse period for this shot was 60 msec.

depth [Pekeris, 1948]. The experimental work showed that the pressure level for the observed waves generally increased with depth to 65 m and that the strongest signals were detected from the larger charges fired at the intermediate depths.

To obtain a rough estimate for the range of detection of a 9-lb charge of TNT even with considerable man-made background noise occurring near the detector, we made the following simple calculation:

For the wave train shown in Figure 2, which was detected with a hydrophone at a depth of 65 m, the mean amplitude of the waves of the first normal mode is 15 db above background noise (Fig. 11); this background noise includes the man-made background noise at the receiving station. Taking the distance between shot point and detector to be 1000 km, neglecting attenuation of the waves, assuming that a mean amplitude for waves of the first normal mode 4 db above background noise should be easily detectable, and using the fact that the amplitude of the waves decreases as r^{-1} at nonstationary values of group velocity, we see that the range of detection is about 4000 km. Hence, a similar signal should be detected almost anywhere in the central Arctic Ocean.

As has been discussed by Ewing and Worzel [1948], Sofar sound transmission can be a valuable tool in conducting marine geophysical studies. For example, a navigational system for locating the positions of drifting stations could be the establishment of at least two Sofar stations at known positions and the firing of small bombs at the drifting stations to permit a triangulation calculation to be made. These Sofar stations could also be used to study seismic activity in the Arctic Ocean.

Acknowledgments. This work was carried out under contract AF19(604) 2030 with the Air Force Cambridge Research Center under the direction of Professor J. Oliver. Computing facilities were made available by Watson Scientific Computing Laboratory, Columbia University. Mr. E. P. Kelley of the U. S. Navy Underwater Sound Laboratory, New London, Connecticut, is to be thanked for informing me of the firing schedule of the charges and for supplying the shot instants, charge sizes, and firing depths. Dr. J. Dorman is to be thanked for supplying the program used in the computations

and for instructing me on the operation of the IBM 650 computer. During the instruction period Dr. Dorman obtained a number of phase- and group-velocity solutions for the first and fourth normal modes. Both Professor J. Oliver and Dr. K. Hunkins read the manuscript critically and offered many valuable suggestions during the course of the work.

REFERENCES

- Crary, A. P., Arctic Ice Island Research, *Advances in Geophysics*, 3, Academic Press, New York, 1-39, 1956.
- Dorman, J., M. Ewing, and J. Oliver, Study of shear velocity distribution in the upper mantle by mantle Rayleigh waves, *Bull. Seism. Soc. Am.*, 50, 87-115, 1959.
- Ewing, M., F. Press, Crustal structure and surface wave dispersion, 2, Solomon Islands earthquake of July 29, 1950, *Bull. Seism. Soc. Am.*, 42, 315-325, 1952.
- Ewing, M., and J. L. Worzel, Long-range sound transmission, in *Propagation of Sound in the Ocean*, *Geol. Soc. Am., Mem.* 27, 1-35, 1948.
- Farlow, J. S., III, Reference 58-28 Project I, *Skate Oceanographic Data*, Woods Hole Oceanographic Inst., 1958.
- Goldman, S., *Frequency Analysis, Modulation and Noise*, McGraw-Hill Book Co., New York, 1948.
- Haskell, N. A., Dispersion of surface waves of multilayered media, *Bull. Seism. Soc. Am.*, 45, 17-34, 1953.
- Hunkins, K., Seismic studies of sea ice, *J. Geophysical Research*, 65, 3459-3472, 1960.
- Matthews, D. J., Tables of the velocity of sound in pure water and sea water, *British Admiralty Hydrograph. Dept., Rept.* 282, London, 1939.
- Oceanographic Atlas of the Polar Seas, Part II*, H. O. Publ. 705, U. S. Navy Hydrographic Office, Washington, D. C., 1958.
- Officer, C. B., *Introduction to the Theory of Sound Transmission*, McGraw-Hill Book Co., New York, 1958.
- Oliver, J., and J. Dorman, Exploration of suboceanic structure by the use of seismic surface waves, in *The Sea: Ideas and Observations*, Interscience Publishers, London, in press.
- Pekeris, C. L., Theory of propagation of explosive sound in shallow water, in *Propagation of Sound in the Ocean*, *Geol. Soc. Am., Mem.* 27, 1-117, 1948.
- Tatel, H. E., and M. A. Tuve, Seismic exploration of a continental crust, in *Crust of the Earth*, *Geol. Soc. Am. Spec. Paper* 62, 35-50, 1955.
- Worzel, J. L., and M. Ewing, Explosion sounds in shallow water, in *Propagation of Sound in the Ocean*, *Geol. Soc. Am., Mem.* 27, 1-53, 1948.

(Manuscript received November 21, 1960;
revised April 5, 1961.)

The Velocity of Compressional Waves in Rocks to 10 Kilobars, Part 2¹

FRANCIS BIRCH

*Harvard University
Cambridge, Massachusetts*

Abstract. The measurements of the velocity of compressional waves up to 10 kilobars for some 250 specimens of rock, reported in part 1, are discussed with respect to the effects of porosity, alteration, anisotropy, and composition. The relations of isotropic elasticity are shown to be approximately valid for a number of examples. Reasonable agreement with theoretical values for quasi-isotropic aggregates is demonstrated where comparison is possible. At pressures above a few kilobars, the principal factors determining velocity are density and mean atomic weight; oxides and silicates conform to the same general relations, with a few exceptions. Details of symmetry or crystal structure appear to be of secondary importance. Velocity is an approximately linear function of density for materials having a common mean atomic weight, but is in general not a single-valued function of density alone.

Introduction. The measurements of velocity of compressional waves to 10 kilobars reported in part 1 [Birch, 1960a] provide a basis for a renewed effort to understand the major factors determining this velocity in rocks. In the following pages we examine the roles of porosity, alteration, anisotropy, chemical and mineralogical composition. A few new measurements have been added.

Several troublesome questions concerning the elasticity of rocks can now receive at least partial answers, though many remain.

Emphasis has been placed on correlation with simple physical and chemical variables, with the object of interpreting the seismic velocities of the crust and upper mantle.

Comparison with other measurements. Because of real differences among rocks correctly described as 'granite,' 'gabbro,' and so on, studies by different observers often show large discrepancies for which it is difficult to account. Measurements at 1 atmosphere are especially subject to large differences because of variable porosity, even when made by a single method. In general, the measurement of pulse transmission time is more reliable than are methods which require homogeneous properties ('wedge method,' critical transmission or reflection; see Balakrishna [1958]), though there are several instances in the

present work where peculiarities of propagation may be suspected. Kubotera [1954] gave compressional pulse velocities for 18 samples of granite ranging from 4.09 to 5.89 km/sec; no dependence of velocity upon frequency was found between 50 and 300 kc/s, the range of his transducers. The reasonable agreement with the range of present samples of granite at one atmosphere may be considered to extend the frequency to about 3 Mc/s. Matsushima [1960] published pulse velocities for a biotite granite, for a transducer frequency of 500 kc/s, at pressures as high as 4 kilobars, combined with axial stress; the limiting velocity appears to be about 6.7 km/sec, higher than the mean velocity for any of the granites of the present study, though not very different from some of the individual values. Volarovich and Balashov [1957] gave measurements for several rocks up to 5 kilobars; as their samples were relatively long, the velocity observed was presumably the 'bar velocity,' $(E/\rho)^{1/2}$, rather than the velocity of the compressional wave in an unbounded medium. With correction for the difference between these velocities, their V_P at 5 kilobars would be about 6.2 km/sec for basalt, 6.1 for syenite, 5.1 for dolomite. These values appear to be somewhat low, but the general nature of the pressure effect was similar to that found in part 1.

Auberger and Rinehart [1961] examined the effect of frequency upon velocity for several rocks at ordinary pressure with transducer frequencies between 250 and 1000 kc/s. As the

¹ Published under the auspices of the Committee on Experimental Geology and Geophysics and the Department of Geological Sciences at Harvard University.

sample length was no greater than 3 cm, even for samples having grain dimensions up to 6 mm, some anomalies might be expected. The observed variation of velocity was probably within the experimental error and showed no systematic dependence upon frequency, though differences of as much as 12 per cent were recorded for a sandstone and 10 per cent for a granite. With travel times of the order of 2 to 5 microseconds, the uncertainty of time measurement is likely to be large with transducers having natural frequencies below 1 Mc/s.

Knopoff [1954] found 5.76 km/sec as the compressional velocity in a sample of Westerly granite at 1 atmosphere; this is appreciably higher than the velocities at low pressure in the present Westerly samples. The name 'Westerly granite' is applied, however, to a variety of rocks quarried in this area, and *Knopoff's* sample had a density of 2.66 g/cm³, compared with a mean of 2.619 for the present specimens.

Peselnick and Outerbridge [1961] found no significant change of shear velocity in Solenhofen limestone over the very wide range of frequency from 4 to 10⁷ cps, but noticed differences correlated with density. The velocity for their sample (S-1) having a density of 2.59 g/cm³, 2.9 km/sec at 9 Mc/s, is close to that of *Birch and Bancroft* [1938] for a sample of density 2.605 g/cm³, 2.75 km/sec at about 8000 cps.

A close comparison is possible for several rocks of which specimens cut from our samples were studied by *Hughes* and his collaborators to pressures of about 4 kilobars. The measurements are shown in Table 1. These specimens were supplied before the extreme anisotropy of the dunites had been recognized; the specimen of Balsam Gap dunite was taken by chance in a slow direction, that of the Twin Sisters dunite in a fast direction. In view of the different methods of time determination and other experimental details, as well as of inherent variation from specimen to specimen, the agreement between these independent measurements is reassuring.

Comparisons with seismically measured velocities can be made in a few cases, but they are subject to many qualifications. In the first place, we have virtually no information regarding variations within a body such as, for example, the Quincy granite. In the second place, seismic observations in such a body usually must be

TABLE 1. Comparison of Measurements of Velocity V_P
(Velocity in km/sec; each line gives values for a single specimen.)

Rock	$P(\text{bars}) = 500$	1000	2000	4000	Re
Marble, Danby, Vt.	6.36	6.55	6.63	6.67	1
		6.48	6.53	6.58	4
		6.69	6.76	6.81	
		6.65	6.69	6.77	
Granite, Westerly, R. I.	5.98	6.06	6.12	6.18	2
		5.84	6.02	6.19	4
		5.78	5.89	6.00	
		5.89	6.00	6.11	
Granite, Quincy, Mass.	6.06	6.21	6.30	6.38	2
		6.07	6.16	6.27	4
		6.01	6.06	6.13	2.5
Granite, Barrie-field, Ont.	6.22	6.34	6.38	6.43	1
		6.28	6.35	6.42	4
		6.20	6.27	6.32	6.38
		6.16	6.26	6.32	6.40
Dunite, Balsam Gap, N. C.	7.54	7.63	7.77	7.86	3
		7.52	7.54	7.70	7.85
		7.55	7.70	7.84	7.96
		8.38	8.42	8.49	8.57
Dunite, Twin Sisters, Wash.	8.78	8.87	8.91	8.96	3
		7.86	7.97	8.04	8.12
		8.73	8.78	8.85	8.88
		7.74	7.83	7.92	7.97

1. *Hughes and Cross* [1951].
2. *Hughes and Maurette* [1956].
3. *Hughes and Maurette* [1957b].
4. *Birch* [1960a].

limited to horizontal distances of a few kilometers; propagation is confined to small depths, the range for which the pressure effect is large. Over greater distances and greater depths it is not possible to be sure that other rocks do not constitute some fraction of the path. It is interesting, however, to examine a few of the examples of short-range seismic work in quarries or other reasonably well-known bodies. *Leet and Ewing* [1932] found 4.96 ± 0.02 km/sec for the Quincy granite, to about 3000 feet; the penetration was believed to be less than 200 meters; for the Rockport granite the velocity was 5.08 ± 0.01 km/sec, to about 4600 feet, and in the Westerly granite, 5.00 ± 0.04 km/sec to about 1700 feet. In a later study, *Leet* [1933] found 5.14 km/sec in Rockport granite, to 6300 feet. These values are all fairly consistent with the measured values

small specimens at megacycle frequencies, at pressures; a similar comparison for the velocities of shear waves [Birch, 1938a] leads to the same conclusion, except that the laboratory values were for frequencies of the order of 10^4 cps. These comparisons also support the idea that the pressure effect observed in the laboratory has a counterpart under natural conditions, with the corollary that strong upward refraction is to be expected within a few kilometers of the surface for most rocks [Birch, 1938a, 1958; Herrin and Richmond, 1960].

Short profiles in the Bethlehem gneiss by Kruger and Linehan [1941], all but one unreversed, gave velocities of 3.54, 4.51, 7.7, 3.64 (reversed), 4.6 km/sec; the three specimens studied in the laboratory from a single large rock collected by Dr. Kruger gave 3.6, 4.9, and 4.4 km/sec with a mean of 4.4 km/sec at low pressure. The agreement is reasonable, except for the high velocity of 7.7 found at one locality for a profile parallel to the direction of foliation. The experimental work gives no suggestion of so great a dependence on orientation, and it seems unlikely that 7.7 km/sec represents a true velocity of propagation in this rock.

Though samples are lacking of other bodies of granite in which similar short profiles have been studied, the velocities found seismically by other investigators are consistent with the laboratory work; Weatherby, Born, and Harding [1934] found velocities increasing from 4.54 to 5.46 km/sec in the Tishomingo granite, Arbuckle Mountains, Oklahoma, as the distance to the shot point increased from 100 to 2500 feet. Brockamp [1935] found 4.8 km/sec in granite near Rönne, Denmark, and Gutenberg [1937] found 5.2 km/sec for granite near Yosemite, California.

Reich [1950] gave 6.5 km/sec for gabbro, in West Prussia, for a depth of penetration of 1200 meters. Katz [1955, p. 324] obtained 6.63 km/sec for near-surface trajectories in the anorthosite of Tahawus, N. Y.; the mean value for the sample from Tahawus is 6.73 at 10 bars. Nikitin [1949] mentioned 5.5 to 6.5 km/sec for diabase at shallow depth. A more thorough search of the literature would probably yield other examples.

Porosity. Earlier work [e.g. Adams and Wilton, 1923; Zisman, 1933a, b, c; Birch and Croft, 1938, 1940; Hughes and others, 1950 and later] has shown that pressure affects the

elastic constants of rocks first by reducing porosity and eventually, as pressure is increased, by an intrinsic effect upon the crystalline components. Because of porosity, the effective cross section for carrying an external load is less than the apparent cross section; application of pressure through an impermeable covering reduces the intergranular spaces and increases the effective cross section and the effective elastic constants. At the same time, stress concentrations at areas of contact increase to the point where crushing may take place, frequently revealed by permanent changes when the pressure is reduced.

In typical holocrystalline igneous rocks, the porosity is of the order of tenths of 1 per cent, and exists as thin wedgelike openings between grains. Presumably the grains were once in solid contact over their surfaces, except perhaps for entrapped fluid films; changes of temperature and stress have brought about a degree of misfit. Under pressures of the order of 1 kilobar, solid contact is approximately restored, and above this point the pressure effect is close to the intrinsic one. This is the interpretation of the characteristic shape of the curve of velocity versus pressure for the igneous rocks.

In sedimentary rocks the porosity is usually of a different kind: first, it may be large, of the order of 20 to 30 per cent or more; second, it exists as interstices between more or less rounded grains which have never been in solid contact with one another except at localized areas considerably smaller than the surfaces of the grains. Application of pressure through an impermeable cover increases the load on these areas of contact and produces elastic deformation, crushing, and increase of modulus, just as in the igneous rocks, but it is virtually impossible to eliminate the porosity by application of pressure alone at ordinary temperatures. This has been shown directly by Hughes and Cooke [1953] for several sandstones; the porosity, initially nearly 20 per cent, was reduced at most about 7 per cent of this value at 1 kilobar, with the pressure effect evidently diminishing as pressure increased. The velocity in porous sandstones remains well below the value for a compact aggregate of quartz even to 10 kilobars [see Bridgman, 1918, p. 264, for porosity after exposure to 30 kilobars]. Quartz is especially refractory, but aggregates of even so weak a material as rock salt will not reach grain densities at pressures of this order.

Somewhat similar behavior may be noted for lavas having a glassy matrix in which small cavities have been formed by expansion of steam; these are practically uncollapsible, and the effect of externally applied pressure is correspondingly small [for example, see the results for andesite in *Hughes and Jones, 1950*].

In recent studies, fluid pressures have been applied to the pore spaces of sedimentary rocks as well as to the external surface [*Wyllie, Gregory, and Gardner, 1958*]. The result is to counter-balance part of the external pressure, the net effect being about the same as for a single external pressure equal to the difference.

It has been shown [*Tocher, 1957; Matsushima, 1960*] that simple compression in the direction of propagation raises V_p nearly as much as does hydrostatic compression of the same magnitude, whereas the velocity of propagation in directions normal to the direction of simple compression is little changed. These experiments are qualitatively consistent with the hypothesis of pore closure stated above. Unlike hydrostatic compression, which may be increased indefinitely, the magnitude of simple compression is limited by the compressive strength; for many purposes, however, simple compression may offer a more convenient method of reducing porosity for velocity determinations.

Even in the igneous rocks, a small amount of porosity may persist at the highest pressures, with the result that pressure coefficients of velocity may remain somewhat higher than would be found with perfectly compact aggregates. Several samples show 'abnormally' high pressure coefficients between 6 and 10 kilobars, notably the Bushveld pyroxenite (bronzitite) for which the mean change for this interval is about twice as great as for the other ultramafic rocks; most of this abnormality comes from a single sample.

For a few monomineralic rocks, comparison may be made with the theoretical elastic constants or velocities computed for perfectly compact aggregates from the properties of the single crystals. These comparisons are considered in more detail below; it appears that differences which might be attributed to residual porosity at 10 kilobars do not exceed a few per cent, and they may result from other causes.

Anisotropy. For a thorough investigation of anisotropy, it would be necessary to study the

uniformity of velocity among specimens having the same orientation as well as the differences in different directions. The differences found in three mutually perpendicular directions may arise from variations of composition on the scale of the specimens as well as from a systematic variation with direction. It is therefore remarkable that some of the largest differences are in the dunites which are nearly monomineralic; since compositional differences are practically excluded, the differences must be traced to some degree of orientation of the dominant component, olivine, and to the anisotropy of the olivine crystal.

At low pressures, differences of porosity are systematically associated with orientation and may introduce anisotropy, but at high pressures, where porosity is virtually suppressed, anisotropy is a measure of nonrandom orientation of crystal grains. At high pressures, the greatest difference among the three directions rarely exceeds 2 or 3 per cent for the granites, granodiorites, anorthosites, and gabbros; the diabases are isotropic within a few parts per thousand. By contrast, the greatest difference at 10 kilobars reaches 10 to 15 per cent for the dunites, 1 to 5 per cent for the pyroxenites. At 1 atmosphere, differences as large as 10 per cent or more are found for some of the granites and dunites, several per cent for some diabases. These differences may be related to original orientations in the stress field, or to differential porosity resulting from the relief of unequal pressures.

The differences found for schistose rocks are smaller than might have been expected. The conspicuously banded gneisses show greater differences of 2.9 and 5.4 per cent at 10 kilobars compared with 24 and 22 per cent at the low pressure. Thus the difference at low pressure is a consequence of looseness normal to the banding rather than of crystal orientation. The oriented crystals, principally micas, constitute only a minor fraction of the volume, and the major components, quartz and feldspar, must be fairly randomly oriented. For the six samples of chlorite schist, the greatest difference is 44 per cent at 1 bar, 7.6 per cent at 10 kilobars. Though one sample was oriented in such a way that the propagation would be approximately normal to the schistosity, in other cases the schistosity is not clearly marked and the greatest difference may not have been found. Other comparisons

TABLE 2. Anisotropy in Ultramafic Rocks and in Various Schists and Gneisses

Rock	$P = 10$ bars			$P = 10$ kilobars		
	V_P , km/sec		Diff., % of mean	V_P , km/sec		Diff., % of mean
	Highest	Lowest		Highest	Lowest	
oxenite, Cal.				8.20	7.82	5
nzitite, Stillwater	7.58	7.20				
nzitite, Bushveld	6.2	5.0	5	7.89	7.79	1
zбургite, Bushveld	7.3	6.6	21	8.13	7.80	4
ite, New Zealand	7.9	7.2	10	8.05	7.82	3
ite, Balsam Gap, N. C.	7.9	7.2	9	8.43	7.66	10
ite, Addie, N. C.	8.0	6.4	23	8.69	8.00	8
ite, Twin Sisters	7.9	7.3	8	8.51	7.91	7
ite (hortonolite)	8.3	7.2	14	8.95	8.07	10
ite, Webster, N. C.	7.0	6.6	6	7.57	7.19	5
ite, Webster, N. C.	7.0	6.9	1	7.87	7.63	3
(altered)	6.3	5.5	13	6.93	6.62	5
entinites						
hetford, Que.	5.8	5.5	5	6.15	5.91	4
udlow, Vt.	5.7	4.0	36	7.33	6.56	11
antigorite)						
udlow, Vt.	6.6	6.2	6	6.94	6.79	2
alifornia	5.9	5.8	2	6.35	6.29	1
rtzite, Mont.	5.8	5.3	9	6.46	6.26	3
e (Cambridge)	5.81	4.97	15	6.39	5.96	7
rite schist	5.9	3.8	44	7.36	6.82	8
schist (2)	5.0	4.8	4	7.01	6.93	1
nolite schist	7.32	5.62	26	8.00	7.01	13
a schist	6.5	4.6	33	6.91	6.31	9
phibolite, Mont.	7.31	6.09	18	7.66	6.83	11
ss						
elham, Mass.	3.7	2.9	24	6.43	6.25	3
ell Gate, N. Y.	5.6	4.5	22	6.64	6.26	6
Bethlehem), N. H.	4.9	3.6	30	6.43	6.17	4

shown in Table 2. Measurable differences in at 10 kilobars for some of the schists, but are much smaller than at low pressure.

The appreciable anisotropy found for all the ites, in striking contrast with the igneous is in general, including the pyroxenites, lends t to the idea reached by a number of ogists [Turner and Verhoogen, 1951, p. 242 eq.] that these rocks have reached their ent positions by a process of 'cold intrusion.' t there is a preferred orientation of crystal in these samples may be demonstrated by usual optical method. I am indebted to Priestly Toulmin III for studies of several ons of the Twin Sisters dunite, which show ked concentrations of the a axis in the tion of the highest velocity. Subsequent urements by Verma [1960a, b] on an olivine tal of composition close to that of the Twin rs dunite show that the velocity in the a

direction is 9.87 km/sec, in the b direction 7.73 km/sec, and in the c direction 8.65 km/sec. These observations are qualitatively consistent with one another. The degree of orientation throughout samples as large as the present ones can hardly be found by the methods of structural petrology; it is much less laborious to measure velocities, which provide averages for large numbers of crystals. The properties of olivine may, however, be especially favorable for the velocity method, the greatest difference of velocity reaching about 25 per cent of the mean velocity. In quartz, by contrast, the greatest difference is only about 10 per cent of the mean velocity, so that a greater degree of orientation is required to give a significant difference of velocity. Elimination of porosity by the application of pressure is also essential to the success of this method for finding directions of orientation.

A crude theory may be developed to give an

indication of the degree of orientation in the Twin Sisters dunite, based on the velocities in the three principal directions as given by Verma. Suppose the proportions of path length in a given sample are x along the a direction, y along the b direction, z along the c direction; with $x + y + z = 1$. The corresponding velocity is $1/V = x/9.87 + y/7.73 + z/8.65$; this may be plotted as contours on a triangular diagram representing the proportions x, y, z . As it turns out, the velocity for $x = y = 0.50, z = 0$, is 8.66, nearly equal to the velocity in the c direction. The contours are thus straight lines parallel to the perpendicular from $z = 1.00$ to $x = y = 0.50$.

The velocities for the Twin Sisters samples are not exactly consistent with this simple model, which gives a mean value of 8.66 km/sec instead of 8.42. In order to show so low a velocity as 8.07 (Twin Sisters 3), the concentration of b axes in the direction of the specimen axis must be fairly high with a corresponding concentration of the a axis in the direction of specimen 2.

Alteration. Few rocks are entirely free from alteration of the original minerals, and in some kinds of alteration the products have physical properties differing greatly from those of the parent. The alteration of olivine to serpentine has a large effect upon velocity, as olivine with a mean velocity of about 8.5 km/sec is replaced by serpentine with a velocity of about 6 km/sec. This appears to be a major source of variation among the dunites. The Twin Sisters dunite is

the least serpentinized of those studied and has the highest velocity, the mean value of 10 km/sec, bars being about 1 per cent lower than that of gem-quality olivine of nearly the same Mg/Ca ratio (Table 8).

Hess [1959] plotted velocity versus density for serpentine-olivine compositions, ranging from unaltered dunite to serpentine; the degree of serpentinization for intermediate compositions was not indicated. A similar plot for the present measurements, at 10 kilobars, shown in Figure 1, suggests that serpentinization may have a greater effect on velocity than on density. This is to be expected from a simple summing up of properties. Let y_i be the proportion by volume of component i having density ρ_i and velocity V_i . Then the density of the aggregate is $\rho = \sum y_i \rho_i$. The velocity is the length divided by the time of transit. Suppose each path of length L includes a proportion of component i equal to y_i ; the time of travel is then $\sum Ly_i/V_i$ and the mean velocity $V = (\sum y_i/V_i)^{-1}$. Table 3 shows values computed in this way for theoretical serpentine-dunite aggregates at 10 kilobars. The relation between velocity and density is not quite linear; the deviation at the 50 per cent point reaching 0.2 km/sec. While this curve agrees somewhat better with the experimental values for the dunites than does the linear relation, the departures are still appreciable.

Hess's plot does not include values for the iron-rich dunites or peridotites, which fall to the

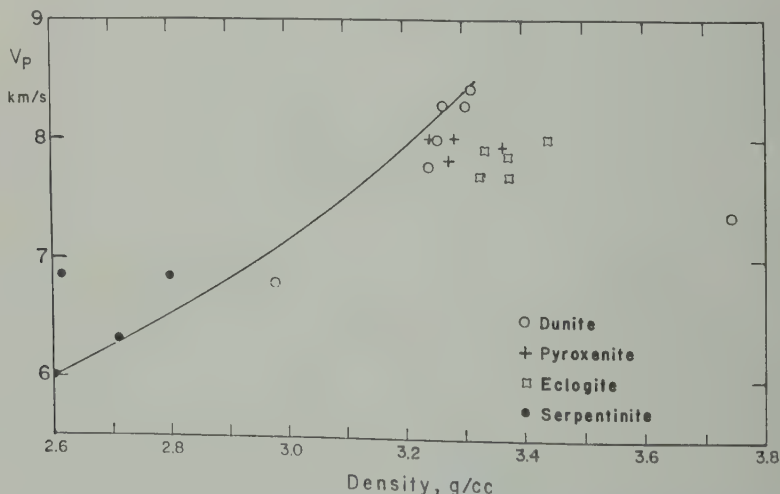


Fig. 1. Velocity at 10 kilobars versus density for ultramafic rocks and serpentinites. The curve represents the calculated values of Table 3 for ideal serpentine-olivine aggregates.

TABLE 3. Density and Velocity in an Ideal Serpentine-Olivine Aggregate

Proportion of serpentine by Volume, %	Density, g/cm ³	Velocity, km/sec
0	3.324	8.50
10	3.252	8.16
25	3.143	7.70
50	2.962	7.03
75	2.781	6.48
100	2.600	6.00

at of the line (see below). It also appears that hornblende has a notably higher velocity than pyroxene; I am indebted to Professor Hess for the distinction between these two serpentinites. Other studies of serpentines and serpentinitized rocks are needed for a satisfactory delineation of these effects.

In the granitic rocks small degrees of alteration appear to have relatively minor effects on density and velocity; the usual products, sericite and kaolin, probably have nearly the same values for these properties as do the feldspars they replace. There seems to be a curious inverse relation between the amount of alteration and the amount of initial change of velocity with pressure, which suggests that slightly altered rocks have lower porosities than fresh or less altered ones. This conclusion is based on preliminary determinations of water content of rocks (water driven off between 100° and 200°C) by Mr. Peter Bell. Relative measurements of the quantity of water given off by gram samples, pulverized to pass through 20-mesh, were made by observing color changes in a tube of indicating silica gel (Davison Chemical Company, IG-327, 0-4% RH). By this test, six granites examined, three were relatively 'wet' by comparison with the other three. The initial velocities, in kilometers per second, for the 'wet' group are as follows: Hyderabad A, 5.7; Lehigh, 6.1; Barriefield, 5.7. For the 'dry' group, they are: Chelmsford, 4.2; Rockport, 5.0; Stone Mountain, 3.7. Optical examination also indicates that the Stone Mountain granite is the least altered. The extreme difference among these samples at 10 kilobars is 0.35 km/sec, so that the effect of alteration, if this is indeed the chief cause for the differences, is most important at low pressure. The rocks of the 'wet' group are about 2 per cent denser than those of the 'dry'

group, and they are older (Precambrian versus Paleozoic). The relationships among these factors have still to be disentangled.

Alteration has not yet been studied with reference to velocity in the mafic rocks; conceivably it may be related to certain anomalies which will be discussed below.

Relations among elastic constants. The elastic properties of rocks are usually discussed in terms of the theory of isotropic elasticity, in which only two independent elastic constants are required for a complete description of elastic behavior. Any pair of elastic constants suffices to determine all the others, with the aid of relations shown in Table 4. An isotropic material remains isotropic under hydrostatic compression, and these relations continue to hold, but with values dependent upon the pressure and, of course, temperature [Birch, 1938b]. Rocks are at best quasi-isotropic on the macroscopic scale; the properties are averages for numbers of highly anisotropic crystals; application of hydrostatic pressure to the boundaries of a specimen does not result in hydrostatic pressure on the individual grains, and it is not evident that the compressibility, for example, which determines the velocity of compressional waves is necessarily identical with the compressibility found from gross changes of volume under pressure. Observations of Young's modulus, Poisson's ratio, or velocities at ordinary pressure may furthermore be disturbed by the effects of porosity, for which the classical theory makes no allowance. Consequently, large discrepancies are usually found when the 'constants' are calculated from different sets of quantities measured at low pressures. Opportunities for comparison have been few, since most investigators have measured no more than two constants, while at least three are required for this purpose.

A notable exception is the work of Ide [1936], who combined his own observations of the resonant frequencies of cylinders of rocks with those of Zisman [1933a, b, c] of E and σ for the same specimens. His Table 2, of which a portion is given in Table 5, shows Poisson's ratio as determined by three independent methods, with the use of the formulas of isotropic elasticity. Fair agreement is obtained for two unusually compact rocks, the Vinalhaven diabase and the Sudbury norite; for the others, the discordance is marked.

TABLE 4. Connecting Identities for Elastic Constants of Isotropic Bodies.
 K = bulk modulus; E = Young's modulus; μ = shear modulus;
 β = compressibility = $1/K$; λ = Lamé's constant; σ = Poisson's ratio;
 ρ = density; $R_1 = V_P/V_S$; $R_2^2 = K/(\rho V_S^2)$; $R_3^2 = K/(\rho V_P^2)$.

K	E	λ	σ	ρV_P^2	$\rho V_S^2 = \mu$
$\lambda + 2\mu/3$	$\mu \frac{3\lambda + 2\mu}{\lambda + \mu}$...	$\frac{\lambda}{2(\lambda + \mu)}$	$\lambda + 2\mu$...
...	$9K \frac{K - \lambda}{3K - \lambda}$...	$\frac{\lambda}{3K - \lambda}$	$3K - 2\lambda$	$3(K - \lambda)/\mu$
...	$\frac{9K\mu}{3K + \mu}$	$K - 2\mu/3$	$\frac{3K - 2\mu}{2(3K + \mu)}$	$K + 4\mu/3$...
$\frac{E\mu}{3(3\mu - E)}$...	$\mu \frac{E - 2\mu}{3\mu - E}$	$E/(2\mu) - 1$	$\mu \frac{4\mu - E}{3\mu - E}$...
...	...	$3K \frac{3K - E}{9K - E}$	$\frac{3K - E}{6K}$	$3K \frac{3K + E}{9K - E}$	$\frac{3KE}{9K - E\mu}$
$\lambda \frac{1 + \sigma}{3\sigma}$	$\lambda \frac{(1 + \sigma)(1 - 2\sigma)}{\sigma}$	$\lambda \frac{1 - \sigma}{\sigma}$	$\lambda \frac{1 - 2\sigma}{2\sigma}$
$\mu \frac{2(1 + \sigma)}{3(1 - 2\sigma)}$	$2\mu(1 + \sigma)$	$\mu \frac{2\sigma}{1 - 2\sigma}$...	$\mu \frac{2 - 2\sigma}{1 - 2\sigma}$...
...	$3K(1 - 2\sigma)$	$3K \frac{\sigma}{1 + \sigma}$...	$3K \frac{1 - \sigma}{1 + \sigma}$	$3K \frac{1 - 2\sigma}{2 + 2\sigma}$
$\frac{E}{3(1 - 2\sigma)}$...	$\frac{E\sigma}{(1 + \sigma)(1 - 2\sigma)}$...	$\frac{E(1 - \sigma)}{(1 + \sigma)(1 - 2\sigma)}$	$\frac{E}{2 + 2\sigma}$
$\rho(V_P^2 - \frac{4}{3}V_S^2)$	$\frac{9\rho V_S^2 R_2^2}{3R_2^2 + 1}$	$\rho(V_P^2 - 2V_S^2)$	See below.

$$2\sigma = (R_1^2 - 2)/(R_1^2 - 1) = (3R_2^2 - 2)/(3R_2^2 + 1) = 4(3R_3^2 - 1)/(3R_3^2 + 1).$$

An indication of the accord to be expected for materials which more nearly satisfy the conditions of isotropy and compactness is given by the values for copper and steel. These samples were not in fact shown to be isotropic, and some of the difference may come from effects of grain elongation and orientation; the gross differences found for most of the rocks, however, may fairly be ascribed to porosity. It may thus be anticipated that a similar test in which measurements at pressures of the order of a few kilobars are used will show better agreement.

Various comparisons at 4 kilobars are shown in Table 6, which contains the material of an earlier table [Birch and Bancroft 1938, Table 10,

p. 126], supplemented by the new measurements of V_P and data for a few other rocks. The measurements of V_P are for different specimens of the same samples which furnished the specimens for V_S and β , except for the marble, quartzite, and Westerly granite. The mean for three specimens of Danby marble has been combined with V_S for a single specimen of Proctor marble; both are nearly pure calcite, and the 'observed' compressibility (β) is that of calcite as given by Bridgman [1928]. The mean V_P for three specimens of Montana quartzite has been combined with the mean V_S for two specimens of a Pennsylvania quartzitic sandstone; these are nearly pure quartz, and the 'observed'

TABLE 5. Poisson's Ratio at Ordinary Pressure by Different Methods, after Ide

Rock	Sample	Static	$E/2G-1$	$1/2-E\beta/6$
Granite				
Quincy, surface	3		0.040	0.338
Quincy, 100 ft	2		0.069	0.309
Quincy, 235 ft	4		0.130	0.333
Quincy, 235 ft	5	0.117	0.160	
Lockport 100 ft 'hardest way'		0.106	0.180	0.354
Lockport 100 ft 'easiest way'		0.097	0.144	
Albite, Naalhaven	1	0.271	0.270	
	2	0.258	0.260	0.244
	3	0.275	0.259	
Albite, Sudbury	3	0.236	0.230	
	4	0.224	0.210	0.205
Obsidian, French Creek	2	0.125	0.160	
	3	0.152	0.230	0.317
Quartzitic sandstone	1	0.112	0.105	
	2		0.025	0.215
Albite, Pennsylvania	2		0.285	0.330
Albite, Vermont	1	0.166	0.138	
	2	0.146	0.226	0.400
	3	0.185	0.144	
Obsidian			0.370	0.342
Albite			0.270	0.287

compressibility is that of quartz, as given by *Idgman* [1928]. The mean V_P for three specimens of a new sample of Westerly granite has been combined with the V_S of a single specimen of another sample of Westerly granite, of somewhat higher density, and the 'observed' compressibility is given by *Adams and Williamson* [1923] for still another specimen. In the earlier work the practice of systematically averaging measurements for three orthogonal specimens has not been adopted, so that the values of V_S are usually less representative than are the measured values of V_P . Nevertheless, except for albite, the previously calculated values of V_P are within about 4 per cent of the new observed values. Determinations on the same samples might reduce these discrepancies still further, but they do not much exceed the differences in different directions in the same samples.

From the measured velocities, assuming isotropic elasticity, we may calculate the quantity β , and thence the compressibility β . This may

be compared with directly measured values. Those in parentheses have been taken from the literature, as indicated; the others are based on linear compressibilities of single specimens, as given by Birch and Bancroft. The discrepancies are larger in this comparison than in the comparison of V_P ; the errors are multiplied in taking the difference of the squared velocities, as much as five times or so if the two velocities are wrong in opposite directions. The outstanding discrepancies are for albitite (27 per cent) and syenite (40 per cent); for the latter V_S seems too small. In most instances, the observed static compressibility is higher than the compressibility calculated from the velocities; this may mean that the ratio V_P/V_S is systematically too high, or that some systematic error affects the compressibility measurements, especially of the more siliceous rocks. The static compressibility is derived as the slope of a curve, usually of second degree in the pressure, fitted to observations of change of length or of volume. While a curve of this form usually represents the data with adequate precision, it is conceivable that the real change follows a more irregular curve that has appreciably different values of slope. Another possibility is a difference in the averaging process between the static measurement and the propagation of short waves. No convincing explanation of this difference in compressibilities other than accumulation of errors of measurement and of effects of anisotropy and inhomogeneity can be offered at present. The agreement is notably better for the basic and ultramafic rocks than for the more siliceous ones.

A final comparison is given in terms of Poisson's ratio (σ). This may be obtained from measured V_S and β , as in Birch and Bancroft (column 7), or from measured V_P/V_S (column 8). The relatively high values, about 0.3 or more, for the feldspathic rocks appear to be real. The lowest values, except for quartzite, are for the quartz-rich rocks and for the pyroxenites. The low value for quartzite is in agreement with the predictions from aggregate theory (next section); the values for the granites are intermediate between those for quartz and feldspars, as are those for the basic rocks between the values for pyroxenites and feldspars. Thus at least a qualitative account can be given. The best values are probably those of column 8 derived from the velocity ratios.

TABLE 6. Elastic Parameters at 4 Kilobars

Rock	V_P , km/sec		V_S , km/sec	K/ρ , (km/sec) ²	β §, mb ⁻¹		σ	
	obs.*	calc.†	obs.†	calc.‡	obs.†	calc.	calc.†	calc.
Marble, Vt.	6.72	6.51	3.49	28.9	(1.39)	1.28	0.30	0.3
Quartzite	6.22	6.08	4.00	17.4	(2.51)	2.18	0.12	0.1
Granite								
Westerly	6.10		3.49	21.0	(1.98)	1.82		0.2
Quincy	6.30	6.08	3.62	22.2	1.92	1.72	0.23	0.2
Rockport	6.39	6.24	3.59	23.6	1.85	1.62	0.24	0.2
Albitite	6.40		3.45	25.1	(1.93)	1.52		0.2
Anorthosite								
New Glasgow ¶	6.82		3.50	30.2	(1.4)	1.22		0.2
Anorthosite								
Stillwater**	7.04		3.68	31.5		1.15		0.2
Syenite								
Ontario	6.70	6.05	3.36	29.8	1.69	1.21	0.27	0.2
Tonalite**	6.48		3.64	24.3		1.49		0.2
Diabase, Md.	6.84	6.96	3.83	27.2	1.16	1.22	0.28	0.2
Gabbro, Mellen	7.13	6.96	3.71	32.5	1.14	1.05	0.30	0.2
French Creek	7.11	7.15	3.98	29.4	1.13	1.11	0.27	0.2
Bronzitite								
Stillwater**	7.71	7.83	4.59	31.4	0.96	0.97	0.25	0.2
Bushveld	7.75	7.86	4.55	32.5	0.89	0.94	0.25	0.2
Dunite								
Balsam Gap	8.13	8.05	4.57	38.3	0.83	0.80	0.26	0.2

* Part 1 [Birch, 1960a] and new measurements.

† Birch and Bancroft [1938, 1940], except β for calcite and quartz [Bridgman, 1928]; for Westerly granite Adams and Williamson [1923]; for albite, Yoder and Weir [1951]; anorthosite (labradorite) Adams and Gibson, [1929]. V_P and σ calculated from V_S and β .

‡ $K/\rho = V_P^2 - \frac{4}{3}V_S^2$, with observed V_P and V_S .

§ $\beta = 1/K$.

¶ From $2\sigma = (R^2 - 2)/(R^2 - 1)$, with observed V_P and V_S ; $R = V_P/V_S$.

¶ New sample. V_S from PSP.

** Dimensions corrected for compression.

The velocity ratios may be used to find the dependence of Poisson's ratio upon pressure for some of these rocks. Table 7 shows values to 4000 bars, plus a few to 10,000 bars. The shear velocity was determined in these latter cases only to 9000 bars, and has been extrapolated to 10,000 for the bracketed values. There is a tendency for σ to increase slightly with pressure, but by a barely significant amount. The values at 1 atmosphere are generally discordant, reflecting the effects of porosity.

Rocks as elastic aggregates. Like the metals of technology, rocks are aggregates of elastically anisotropic crystals. Samples containing large numbers of grains, randomly oriented, may, as shown above, be macroscopically isotropic despite low symmetry of individual crystals and practically indeterminate internal stresses and strains. For a valid average we require a reasonably high

ratio between sample dimensions and grain size, and, when wave propagation is involved, suitable relations among sample size, grain size, and wavelength. In certain coarse-grained rocks, the crystals are longer than the wavelength at megacycle frequencies, and the possibility of anomalous propagation arises. It may be imagined that some of the energy, traveling by a longer 'faster' path, arrives with a velocity greater than the average; the method of observing the first detectable arrival might then give this anomalously high velocity. This might account for what seem to be high values for the syenite, gabbros, and possibly the albitite.

The syenite was restudied with three sets of transducers having resonant frequencies of about 2.7, 1.0, and 0.4 Mc/s. In this rock, the high frequency components of the pulse are damped out in transmission, and the transmitted pulse

TABLE 7. Poisson's Ratio from V_P and V_S at High Pressure
 $R = V_P/V_S$, $2\sigma = (R^2 - 2)/(R^2 - 1)$

$P(\text{kilobars}) =$		1	2	4	6	10	Notes
nite Vesterly	R	1.75	1.76	1.75			1, 3
	σ	.258	.262	.258			
quincy	R	1.73	1.73	1.74			1, 3
	σ	.249	.249	.253			
ockport	R	1.76	1.77	1.78			1, 3
	σ	.262	.266	.269			
tite	R	1.84	1.84	1.85			2, 4
	σ	.290	.290	.294			
rthosite	R	1.90	1.90	1.91	1.91	(1.91)	2, 3
	σ	.308	.308	.311	.311	.311	
alite	R	1.78	1.78	1.78	1.78	(1.79)	2, 3
	σ	.269	.269	.269	.269	.273	
nite	R	1.99	1.99	1.99			1, 3
	σ	.331	.331	.331			
base	R	1.79	1.79	1.79			1, 3
	σ	.273	.273	.273			
aryland							
bro ellen	R	1.92	1.92	1.92			1, 3
	σ	.314	.314	.314			
rench Creek	R	1.78	1.78	1.79			1, 3
	σ	.269	.269	.273			
zittite							
illwater	R	1.67	1.67	1.68	1.68	(1.69)	2, 3
	σ	.220	.220	.225	.225	.230	
shveld	R	1.66	1.68	1.70			1, 3
	σ	.215	.225	.235			
ite	R	1.76	1.77	1.78			1, 3
	σ	.262	.266	.269			
alsam Gap							

1. *Birch and Bancroft* [1938], V_S .
2. *Birch and Bancroft* [1940], V_S .

3. *Birch* [1960a], V_P .
4. New measurement, V_P .

the same with all of these transducers—a wave with slow rise time. The peak amplitude of the first rise increases as the pulse width is increased up to about 3 microseconds; this means that energy in phase with the earliest arrival continues to come in for this length of time. The time of the first arrival is independent of the transducer frequency, within the poor resolution for such a pulse shape. It seems likely that in material of this kind, the shortest waves, which might take paths of shorter-than-average length, are so badly scattered that they do not arrive with appreciable energy; the transmitted energy is in the form of waves long enough not to be lost by scattering and also long enough to give a reasonable average of the transmission details of transmission are evidently

complex. In single crystals, the propagation of plane waves is related to the elastic constants through the Christoffel equation [*Love*, 1927, p. 288; *Mason*, 1958, p. 368] which gives three velocities as roots of a cubic equation for each direction of the normal to the wave front. Only for special cases of symmetry and direction can waves of compression (displacement normal to wave front) be clearly distinguished from shear waves (displacement tangential to wave front). The propagation through a random aggregate of crystals consequently involves propagation in mixed modes which defy detailed analysis. Averaging of various kinds must suffice, subject to experimental confirmation that the relations for an isotropic medium are satisfied on the macroscopic scale.

Of the methods that have been proposed for

TABLE 8. Calculated and Observed Velocities in Aggregates

Material	V_P , km/sec			V_S , km/sec		
	Calculated		Observed 4 kb	Calculated		Observed 4 kb
	Voigt	Reuss		Voigt	Reuss	
α quartz ¹	6.22	5.95	6.22 ⁹	4.21	3.94	4.00 ¹⁸
Calcite ²	6.64	6.17	6.72 ¹⁰	3.73	3.23	3.49 ¹⁹
			6.67 ¹¹			3.21 ¹¹
Aragonite ³	5.92	5.64	5.90 ¹²	3.71	3.53	4.57 ²⁰
Olivine ⁴	8.56	8.40	8.32 ¹³	4.98	4.88	4.54 ²¹
						4.90, 4.8
Garnet 1 ⁴	8.47	8.47		4.77	4.77	
Garnet 2, ⁴	8.52	8.52	7.99 ¹⁴	4.77	4.77	
Spinel ⁴	10.08	9.77		5.86	5.46	
Periclase ⁵	9.55	9.45		6.01	5.90	
Corundum ⁶	10.89	10.79	10.4 ¹⁵	6.45	6.35	6.3 ¹⁵
Magnetite ⁷	7.39	7.39	6.99 ¹⁶	4.20	4.19	
Hematite ³	6.53	6.45	7.74 ¹⁷	4.23	4.18	
Rutile ^{4,8}	9.43	8.96		5.43	4.87	

Notes

¹ Cady [1946, p. 137].² Bhimasenachar [1949].³ Voigt [1928, p. 761].⁴ Verma [1960b].⁵ Bhagavantam [1955].⁶ Wachtman and others [1960].⁷ Doraiswami [1947].⁸ Birch [1960b].⁹ Montana quartzite.¹⁰ Marble, Danby, Vt.¹¹ Danby marble [Hughes and Cross, 1951].¹² Hot springs deposit, Mexico.

Where no reference is cited, the value is from Birch [1960a] or unpublished.

¹³ Twin Sisters dunite.¹⁴ Crushed and altered single crystal.¹⁵ Artificial aggregate, AD-99.¹⁶ Ore, Port Henry, N. Y.¹⁷ Fibrous aggregate.¹⁸ Quartzitic sandstone, Pa. [Birch and Bancroft, 1938].¹⁹ Marble, Proctor, Vt. [Birch and Bancroft, 1938].²⁰ Dunite, Balsam Gap, N. C. [Birch and Bancroft, 1938].²¹ Twin Sisters dunite [Hughes and Maurette, 1957a].²² Twin Sisters dunite [Verma, 1960a; two different specimens at about 10 kilobars].

averaging the elastic constants in order to obtain the static elastic constants of random aggregates, Hill [1952] showed that those of Voigt [1928] and Reuss [1929] lead to upper and lower limits, respectively, the difference being a measure of anisotropy of the crystal. Voigt averaged the elastic constants (c_{ij}) over all directions; Reuss averaged the elastic compliances (s_{ij}) over all directions. Other possibilities come to mind, such as averaging the velocity of the fastest mode over all directions, or the reciprocal of the velocity. Where the Voigt and Reuss values differ little, a good estimate may be expected.

Of the rock-forming minerals, complete sets of elastic constants exist for quartz, calcite, aragonite, corundum, olivine, magnetite, hematite, and a few garnets. The Voigt and Reuss values are shown in Table 8 for ideal isotropic aggregates of these minerals, together with

measured values at 4 kilobars for rocks consisting chiefly of these minerals. At this pressure the effect of porosity is largely overcome, with the correction for the intrinsic pressure effect still no greater than a per cent or so. The comparison has been made in terms of velocities since these have been directly determined for rocks. The velocities for the aggregates have been calculated by forming the two constants K (bulk modulus) and μ (shear modulus) by the aggregate theories and then forming the velocities. Densities are not always given by investigators concerned with elastic constants; when not known, they have been assumed to be theoretical densities, which may be higher than the actual ones. For later use, a few values are included for aggregates that have not yet been studied.

Various defects of the natural aggregates

be noticed. The aragonite aggregate is represented by a single sample; though three samples were cut from the block of sinter, two proved to be largely calcite. The third was chiefly aragonite, shown by the X-ray diffraction pattern and the density. The velocity is within the expected range, but there is no proof that this sample is isotropic.

The comparison for olivine is affected by the presence of serpentine, especially in the Balsam dunitite. Alteration is also present in the other sample; this is an aggregate in the sense that it is made up of many small pieces, but, it was cut from a large garnet showing well-developed crystal faces, a high degree of orientation probably exists. The chemical analysis leads to a formula (molar) $\text{Al}_{17}\text{Py}_{15}\text{Gr}_5\text{Sp}_4$; this is close to that of Verma's garnet No. 2.

Verma's measurements on two garnets of gem quality show that the velocities depend very much upon direction. This may be shown by relating the anisotropy factor, $2c_{44}/(c_{11} - c_{12})$, which equals unity for an isotropic medium. For Verma's garnets, this factor equals 0.96 for No. 1 (spessartite-almandite) and 0.98 for No. 2 (almandite-pyrope). Thus the value for any direction should be close to the mean value. The difference of 5 per cent in Table 8 is probably a measure of the degree of alteration in the sample.

The corundum aggregate has a bulk density of 3.82; thus it has an apparent porosity of about 4 per cent, which is practically unaffected by pressure. For an aggregate of higher density, obtained through the courtesy of Dr. H. G. Coes, Jr., the velocity was found to be 7.8 km/sec at ordinary pressure. Four sets of measurements are available for corundum. The ratio $(c_{11}/c_{33})^{1/2}$ ranges from 1.10 [Bhimasenachar, 1949] to 1.01 [Wachtman, Tefft, Lam, and Stinchfield, 1950]. The change of velocity with direction is remarkably small according to the latter determinations.

The Port Henry magnetite contains enough heavy density material to reduce the density from a theoretical value of 5.18 to 4.866. The density of the single crystal is not given. The measured density in the ore is 6 per cent below the theoretical value, slightly less than the discrepancy between actual and theoretical densities. The anisotropy factor for magnetite is 1.12 [Doraiswami, 1950] or 1.22 [Voigt, 1928].

The largest discrepancy is for hematite. Voigt's sample was described as 'specular hematite' ('eisenglanz') from Norway; no density was given. From Voigt's elastic constants, the compressibility may be computed as 10.3×10^{-7} per bar; this is nearly twice as large as the value directly determined by Madelung and Fuchs [1921] for hematite from Elba with a density of 5.16. These authors gave 10.8×10^{-7} per bar as the compressibility for another sample of Fe_2O_3 ('roteisenstein,' density 4.9); this is close to Voigt's value. The compressibilities of magnetite and of ilmenite are 6×10^{-7} per bar.

The present sample was metallic, black, fibrous hematite, probably from Cumberland, England; its bulk density was 5.01, instead of the theoretical 5.26. A single specimen was cored from this, with its axis in the direction of the fibers. Examination by Professor C. S. Hurlbut, Jr., showed that this direction is that of the c axis, so that the velocity should be approximately $(c_{33}/\rho)^{1/2}$. According to Voigt, this would be about 6.6 km/sec, instead of the observed 7.8. With Voigt's values no great difference of velocity should be found in other directions, so this high value would remain unexplained. Further confirmation was obtained by measurements on a small prism of the hematite aggregate by McSkimin's interferometric method at about 10 Mc/s [McSkimin, 1950]. The velocities in three orthogonal directions were 7.27, 7.28, and 7.81 km/sec, at 1 atmosphere, the density of this small piece being 5.11 g/cm³. The high value is in the direction of the fibers, and it agrees well with the corresponding value for the large sample when compressed. It seems likely that the true mean value for hematite is between 7.5 and 7.8 km/sec. A new determination for the single crystal is in progress. One might expect to find the ratios for different directions very similar to those for corundum, which has the same symmetry and structure and nearly the same axial ratios of the unit cell.

The dunites are notably anisotropic. Table 8 shows values obtained on individual samples by Verma [1960a] by observation of the transformed pulse, PSP. The significance of these values is not clear, since, if the medium is not isotropic, PSP does not have a unique travel time; furthermore, the direction of propagation of the shear wave is not along the axis of the sample. Verma found that the six values of Poisson's ratio

corresponding to the principal axes of the olivine crystal range from 0.113 to 0.338. The value for the ideal isotropic aggregate is 0.244.

These comparisons leave the impression that where the materials are comparable the agreement between the aggregate values and those of the single crystals is within the expectable limits. No gross errors from residual porosity or other peculiarities of the natural aggregates are indicated. The single crystals for which values are available are, however, those of relatively high symmetry; as is shown above, some questions remain concerning the feldspars.

Dependence upon composition. The tendency for velocity to increase with density has been amply demonstrated [Adams and Williamson, 1923; Adams and Gibson, 1926, 1929; Adams, 1931; Birch and Bancroft, 1938, 1940; Hughes and Cross, 1951; Hughes and Maurette, 1956, 1957a, b] and a simple correlation has frequently been postulated for the interpretation of seismic data. With the more extensive sampling now available, it is clear that proportionality holds only within specified subgroups. The following discussion will be limited to relations at 10 kilobars, but much the same conclusions may be reached with the values at 4 or 6 kilobars, once the confusing effects of porosity are largely eliminated. Velocities and densities uncorrected for changes of dimensions under pressure (the values of part 1, Tables 5 and 6) will be used, unless otherwise specified. At 10 kilobars, these corrections are less than 3 per cent for the density and 1 per cent for the velocity; but they

are systematic, being largest for the rocks of lowest velocity.

Mean velocities and densities, corrected for the change of dimensions, are shown in Table 9 for the granites and for the basic rocks. The granitic rocks include the two granitic gneisses and the quartz monzonite; the rock of highest density in this group is the Latchford granite ($\rho = 2.683$). The mean values differ little from the earlier means for a smaller group [Birch, 1958, p. 160]. Within the group of granitic rocks a tendency for velocity to increase with density may be discerned, but the correlation is weak with $r^2 = 0.32$. The other parameters of a least squares line of the form $V = a + b\rho$ are shown in Table 15. The range is from 6.12 to 6.34 km/sec, the standard deviation from the line is 0.08 km/sec.

A difference of velocity of about 5 per cent is found between the means for the diabbases and the gabbros. Disregarding the Holyoke diabase, the mean for 4 diabbases (12 specimens) is 6.30 km/sec, and the 12 individual values are between 6.81 and 6.98. For the 9 specimens of gabbro and norite, the mean is 7.24 km/sec; the values are between 7.11 and 7.36. The density has about the same range in each group. Petrologically the groups are not well separated: French Creek gabbro or 'norite' has a diabasic texture and is somewhat finer in grain than the Keweenaw diabase. The Holyoke diabase falls well below either group with respect to velocity but has a normal density. The explanation of these differences is still uncertain, though

TABLE 9. Average Values of Velocity and Density Corrected for Dimensional Changes

P (kilobars) = 0.01		0.5	1	2	4	6	
Granitic rocks	15 rocks	$V_P^* = 5.02$	5.93	6.12	6.21	6.30	6.34
	43 specimens	$\rho^\dagger = 2.651$	2.651	2.658	2.664	2.674	2.683
Diabase	5 rocks	$V_P = 6.46$		6.71	6.74	6.78	6.81
	15 specimens	$\rho = 2.989$		2.994	2.997	3.004	3.011
Gabbro, norite	3 rocks	$V_P = 6.4$		7.02	7.06	7.12	7.16
	9 specimens	$\rho = 2.988$		2.993	2.996	3.003	3.010
Diabase, gabbro norite	8 rocks	$V_P = 6.44$		6.83	6.86	6.91	6.94
	24 specimens	$\rho = 2.989$		2.994	2.997	3.004	3.011

* V_P in km/sec.
† ρ in g/cm³.

TABLE 10. Additional Measurements on Feldspar Rocks

Rock		Density, g/cm ³	Velocity, km/sec						
			$P^* = 0.01$	0.5	1	2	4	6	10
Albite	1	2.616	6.16	6.28	6.33	6.41	6.50	6.56	6.63
	2	2.616	6.03	6.16	6.22	6.27	6.35	6.40	6.47
	3	2.612	6.02	6.11	6.16	6.25	6.34	6.38	6.46
Mean		2.615	6.07	6.18	6.24	6.31	6.40	6.45	6.52
Anorthosite	1	2.704	6.71	6.71	6.75	6.78	6.82	6.84	6.87
New Glasgow,	2	2.712	6.50	6.55	6.62	6.66	6.72	6.77	6.83
See	3	2.707	6.42	6.67	6.71	6.75	6.80	6.83	6.86
Mean		2.708	6.54	6.64	6.69	6.73	6.78	6.81	6.85
Anorthosite	1	2.722	6.23	6.64	6.75	6.81	6.87	6.90	6.97
Whiteface	2	2.710	6.17	6.55	6.63	6.70	6.77	6.81	6.86
N. Y.	3	2.705	6.43	6.63	6.69	6.75	6.82	6.84	6.90
Mean		2.712	6.28	6.61	6.69	6.75	6.82	6.85	6.91

P in kilobars.

is likely that chemical differences account for part of the discrepancies; this is considered fully below.

Several new samples consisting mainly of oligoclase have been added to those of part 1; new measurements are given in the usual form in Table 10. Two different samples called 'albite' have been studied at various times; they are distinguished by different densities arising from different amounts of dark minerals from different compositions of the feldspar. The rock called 'albite' in part 1 should have been designated 'oligoclase' and will be so designated in the following discussion. The rock now called 'albite' is the same one for which the shear velocity was reported [Birch and Bancroft 1940; Birch, 1943], though for a different set of specimens. The anorthosite from New Glasgow, New York, is similar to the rock studied by Adams and Coker [1906, p. 50]; a chemical analysis published by Osborne [1949, p. 102] has been reserved for later use. The 'Whiteface' anorthosite was collected by M. G. Simmons at the base of Whiteface Mountain near 'The Flume,' on the West Branch of the Ausable River, Lake Placid quadrangle, New York.

With the anorthosites and oligoclase of part 1, there are now seven rocks consisting mainly of oligoclase feldspar for which velocities and densities have been measured. A plot of V_P at 10 kilobars versus density for these rocks shows a nearly linear relation, with a standard deviation of only 0.03 km/sec (Table 15). This suggests

that differences of texture and grain size have little effect on velocity; the range of mean grain size is from about 0.5 mm for the New Glasgow anorthosite to about 2 mm for the Tahawus anorthosite (with occasional grains to 1 cm or more). The composition of the feldspars ranges from nearly pure albite (An_3) to bytownite, and, as density varies nearly linearly with anorthite content, velocity also must be nearly proportional to anorthite content.

In an effort to improve the values for the feldspar component alone, corrections have been applied for the heavy mineral content, which reaches about 12 per cent by volume in several cases. This content was determined by separation in liquids, and also by calculation from densities, with fair agreement in most instances (Table 11). The feldspar densities were found by flotation in mixtures of bromoform and monobromo-naphthalene; compositions were found from the indices of fused samples [Larsen, 1909], according to the tables given by Foster [1955] and by Schairer, Smith, and Chayes [1956, p. 195]. These studies were carried out by Peter Bell. The densities and indices of the glasses are self-consistent, except for the Whiteface sample, for which the density appears to be too low. The potassium content, not yet determined, may be appreciable [see Buddington 1939, p. 30, and other analyses in Table 14].

The plot of velocity versus density is less regular for the corrected feldspar components alone (Fig. 2) than for the rocks; the standard

TABLE 11. Density, Composition, and Velocity (10 kilobars) for Plagioclase Feldspars

Rock	Density, g/cm ³		Index of Feldspar Glass	Proportion of Heavy Minerals by Volume, %		An, mole %	V _P , km/sec	
	Rock	Feldspar		From densities	By separa- tion		Rock	Feldspar
Albite	2.615	2.613	1.4904	0.3	0.3	3	6.52	6.53
Oligoclaseite	2.687	2.622	1.4970	8.3		12	6.76	6.67
New Glasgow	2.708	2.694	1.5379	0.6	1.7	59	6.85	6.83
Whiteface	2.712	2.669	1.5300	5.9	7.4	50	6.91	6.80
Tahawus	2.768	2.676	1.5285	12.7		49	7.02	6.92
Stillwater	2.770	2.735	1.5640	5.3	8.3	88	7.10	7.00
Bushveld	2.807	2.719	1.5532	12.9	12.6	76	7.21	7.11
Albite (extrapolated)		2.61				0		6.53
Anorthite (extrapolated)		2.76				100		7.21

deviation from the least-squares line is 0.06 km/sec, or nearly 1 per cent of the velocity. Probably the assumptions on which the corrections are based cannot be relied upon for greater precision. The velocities at 10 kilobars for the pure end members must be close to 6.5 km/sec for albite and 7.2 km/sec for anorthite.

The velocities so found for the feldspars may be combined with the velocities found for the pyroxenes to give a fair account of the velocities in the gabbros. Again only two components are considered, the feldspar with velocity as given by the corrected line, and a heavy component,

taken as having a density of 3.4 g/cm³ and velocity 7.9 km/sec for all cases. The proportion of heavy component is found from the density. The results are shown in Table 12. When the same procedure is applied to the diabbases, the calculated velocities continue to lie close to 6.5 km/sec, in all cases higher than the measured velocities. A single example is given.

The notable departure from a single-value dependence of velocity on density is illustrated in Figure 3, where the (uncorrected) 10-kilobars velocities have been plotted against density (1 bar) for all the silicate rocks, including metamorphic rocks, and for oxides of iron and titanium. Values are also indicated for quartz isotropic aggregates of periclase, spinel, corundum, rutile, several garnets, α quartz and magnetite, and magnetite, calculated from single-crystal constants (Table 8). The apparent disorder of this representation is reduced on examination of the composition of the substances for which the points deviate most widely from the main sequence. The points at highest density are for the iron and titanium ores; the intermediate group is for iron-rich silicates and rutile. This suggests the possibility of a correlation with two principal variables, density and iron content, or more generally, heavy mineral content.

To avoid consideration of the individual effect of all of the chemical components, we shall characterize the chemical composition in terms of the mean atomic weight which has been shown to be a significant physical parameter for silicates.

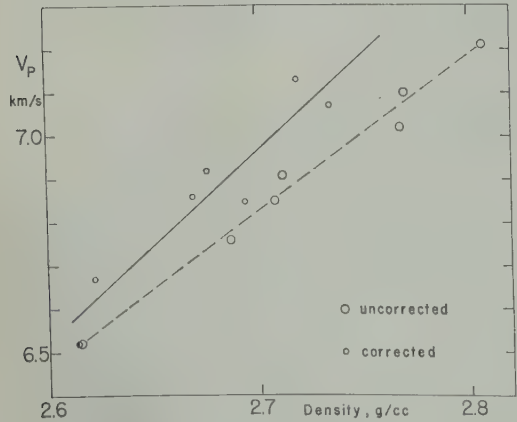


Fig. 2. Velocity at 10 kilobars versus density for rocks composed mainly of plagioclase feldspar. The large circles represent measurements on the rocks. Small circles are for the feldspar components alone, after correction for the content of heavy minerals.

TABLE 12. Observed and Calculated Velocities for Mafic Rocks at 10 Kilobars

Rock	Density, g/cm ³	Anorthite Content of Feldspar, mole %	Proportion of Feldspar, % by Volume	Velocity, km/sec	
				Observed	Calculated
bro					
len	2.931	60	67	7.21	7.18
ite					
hveld	2.978	60	60	7.28	7.25
bro					
ch Creek	3.054	65	50	7.23	7.36
base					
reville	2.976	55	60	6.93	7.24

h, 1952, p. 256]. The iron-free common
ate minerals have mean atomic weights
mula weight divided by the number of
icles in the formula) close to 20 (Table 13).
only relatively abundant elements which

TABLE 13. Mean Atomic Weight of Minerals

	Ideal Compositions	<i>m</i>
soberyl	BeAl ₂ O ₄	18.14
umene	LiAlSi ₃ O ₆	18.60
ite	Mg(OH) ₂	19.44
entine	Mg ₃ Si ₂ O ₅ (OH) ₄	19.80
rite	Mg ₅ Al ₂ Si ₃ O ₁₀ (OH) ₈	19.85
	Mg ₃ Si ₄ O ₁₀ (OH) ₂	19.96
ophyllite	Mg ₇ Si ₈ O ₂₂ (OH) ₂	20.02
tz	SiO ₂	20.03
atite	MgSiO ₃	20.08
ophane	Na ₂ Mg ₃ Al ₂ Si ₈ O ₂₂ (OH) ₂	20.09
erite	Mg ₂ SiO ₄	20.10
pe	Mg ₃ Al ₂ Si ₃ O ₁₂	20.15
lase	MgO	20.16
e	NaAlSi ₃ O ₈	20.17
erite	Mg ₂ Al ₄ Si ₅ O ₁₈	20.17
te	NaAlSi ₃ O ₆	20.21
ite	Al ₂ SiO ₅	20.25
l	MgAl ₂ O ₄	20.32
ndum	Al ₂ O ₃	20.39
opite	KMg ₃ AlSi ₃ O ₁₀ (OH) ₂	20.86
ovite	KAl ₃ Si ₃ O ₁₀ (OH) ₂	20.96
oclase	KAlSi ₃ O ₈	21.40
hite	CaAl ₂ Si ₂ O ₈	21.40
e	Ca ₂ Al ₃ Si ₃ O ₁₂ (OH)	21.63
side	CaMgSi ₂ O ₆	21.65
ularite	Ca ₃ Al ₂ Si ₃ O ₁₂	22.52
itoid	Fe ₂ Al ₃ Si ₂ O ₁₀ (OH) ₄	22.90
stonite	CaSiO ₃	23.23
artite	Mn ₃ Al ₂ Si ₃ O ₁₂	24.75
ndite	Fe ₃ Al ₂ Si ₃ O ₁₂	24.88
ndite	Ca ₃ Fe ₂ Si ₃ O ₁₂	25.40
silite	FeSiO ₃	26.38
	TiO ₂	26.63
ite	Fe ₂ SiO ₄	29.11
ite	FeTiO ₃	30.35
ite	Fe ₂ O ₃	31.94
ite	Fe ₃ O ₄	33.08

produce appreciable deviations from this number
in common minerals are calcium, titanium, and
iron. The deviation from 20 to 21 is usually a
crude measure of iron content. The mean atomic
weight of most common rocks is between 20 and
22. This may be calculated from the chemical
analysis: if m_i is the mean atomic weight of
oxide i , and x_i the proportion by weight of this
oxide in the rock, then the mean atomic weight
of the rock is $m = (\sum x_i/m_i)^{-1}$. Some typical
analyses and the corresponding values of m are
given in Table 14. The mean atomic weight
ranges from about 21 for granites to about 22
for the common mafic igneous rocks; it is close
to 21 for iron-poor dunites but reaches 24.3 for
hortonolite dunite, 24.1 for the almandite garnet,
30.8 for titaniferous magnetite. These numbers
have been calculated for the rocks for which
chemical analyses are available and are attached
to the corresponding points (indicated by open
circles) in Figure 3.

Straight lines of the form $V = a + bp$ have
been fitted by the method of least squares to
various groups of points; the parameters of these
lines are given in Table 15. If all points are used
except those for the iron- and titanium-rich
samples ($m \geq 24$), the standard deviation is 0.33
km/sec for 65 points, with a correlation coefficient
of 0.93, or $r^2 = 0.87$ (solution 5); that is, 87
per cent of the variation of velocity in this
group may be accounted for by correlation with
density. The diabases, gabbros, and eclogites
show a distinct tendency toward higher densities
for a given velocity; these are omitted in the
other solutions, except in solution 7, which is for
these basic rocks only. Solutions 1 and 2 are for
the same groups of samples, all having m between
20 and 22; for solution 1, the velocities and
densities are uncorrected for the change of

TABLE 14. Chemical Analyses and Mean Atomic Weights (*m*)

Rock	SiO ₂	Al ₂ O ₃	Fe ₂ O ₃	FeO	MgO	CaO	Na ₂ O	K ₂ O	H ₂ O+	TiO ₂	P ₂ O ₅	MnO	<i>m</i>	Ref.
Granite	72.2	14.4	0.9	1.0	0.4	1.4	3.3	5.5	0.4	0.3	0.1		20.9	1
Westerly, R. I. (G-1)														
Granite	74.9	11.6	2.3	1.3	.1	.4	4.3	4.6	.3	.2			20.9	2
Quincy, Mass.														
Granite	77.6	11.9	.6	.9		.3	3.8	5.0	.2	.3			20.6	3
Rockport, Mass.														
Granite	73.4	14.4	.1	.7	.3	1.1	4.0	5.1	.4	.3	.6		20.7	4
Stone Mt., Ga.														
Gneiss	72.5	13.3	1.9	.6	.4	1.8	3.6	3.9	1.5	.3	.1		20.8	5
Pelham, Mass.														
Granite	69.6	15.4	2.7	n.d.	tr	1.8	5.4	4.3	1.0				20.8	25
Barre, Vt.														
Quartz monzonite	63.9	15.4	1.9	3.1	2.2	4.3	2.8	4.2	0.7	0.7	.2		21.2	26
Butte, Mont.														
Augite syenite	55.8	14.7	2.6	9.0	1.0	4.6	4.6	4.8	.8	.7	.3		22.1	6
Anorthosite	53.7	27.2	.3	1.4	.5	11.3	3.8	.7	.8	.1			21.1	7
New Glasgow, Ont.														
Anorthosite	47.5	32.3	.7	.4	.4	16.0	1.9	.4	.2		.2	.2	21.3	8
Bushveld														
Gabbro	47.6	22.5		8.7	7.4	9.7	2.8	.3	.5	.4	.1	.1	21.8	6
Mellen, Wis.														
Diabase	52.3	15.2	1.9	8.6	6.5	11.0	2.1	.7	.6	1.1	.1		22.0	1
Centreville, Va. (W-1)														
Diabase	52.7	14.1	2.0	9.8	6.4	9.4	2.6	.9				.4	22.0	9
Holyoke, Mass.														
Diabase	51.3	15.1	1.1	9.3	8.0	11.4	2.0	.3	.4	.8	.1	.2	22.0	10
Frederick, Md.														
Diabase	52.5	15.1	.8	10.7	5.2	6.9	5.5	1.4	1.8	1.0			21.8	27
Cobalt, Ont.														
Diabase	49.9	16.3	n.d.	13.5	6.2	6.6	1.8	2.3	.8	1.5	.2		22.2	28
Sudbury														
Gabbro	52.8	13.0	.3	8.7	10.0	11.9	1.6	.5	.3	.8	.1	.1	21.8	6
French Creek, Pa.														
Jadeite	58.5	23.5	.5		.8	1.3	13.6	.3	.2				20.4	11
Japan														
Jadeite	59.3	24.8	.3	.2	.3	.8	14.1	.2					20.4	11
Burma														
Bronzite	54.7	1.8	.5	9.2	30.2	2.2	(Cr ₂ O ₃ = 0.5)		.5	.1		.2	21.2	12
Stillwater														
Bronzite	55.4	1.6		9.4	32.5	0.5	(Cr ₂ O ₃ = 0.7)			.1	.2	.2	21.0	13
Bushveld														
Harzburgite	41.2	1.2	4.0	8.2	34.4	1.4	.2	.3	5.2	.3	(NiO = 0.4)		21.7	14

Rock	SiO ₂	Al ₂ O ₃	Fe ₂ O ₃	FeO	MgO	CaO	Na ₂ O	K ₂ O	H ₂ O +	TiO ₂	P ₂ O ₅	MnO	m	Ref.
Dunite	40.9	.1		8.3	50.1				.2	(NiO = .3)	.2		21.0	15
Webster, N. C. (olivine only)														
Dunite	39.5	.9	.7	7.6	48.8	(Cr ₂ O ₃ = 1.0)			.9		.3	.1	21.1	16
Mt. Dun, New Zealand														
Dunite	38.4	.6	1.6	6.6	51.5	.1					.3	.1	20.9	17
Balsam Gap, N. C. (olivine)														
Dunite	40.6	.1		8.0	50.6	.1	.1		.1	.1	.3	.1	20.9	16
Twin Sisters, Wash. (olivine)														
Olivine (peridot)	41.2			8.0	49.7	.1		(NiO = 0.5)				.1	20.9	18
Burma														
Dunite (hortonolite)	36.7	1.6		38.0	22.2	.5	.3					1.1	24.3	19
Bushveld														
Eclogite	48.7	11.7	1.4	6.8	16.7	13.9	.4	.2	.1	(Cr ₂ O ₃ = .2)	.2		21.7	20
Sunnmøre, Norway														
Eclogite	48.6	14.0	3.5	9.4	6.6	11.9	3.9	.2	.6	1.1	.3	.3	22.2	21
Healdsburg, Cal.														
Garnet (almandite-pyrope)	39.3	22.1	0.7	19.6	11.5	6.2				.1	.4	.4	22.6	24
Gore Mt., N. Y.														
Garnet (grossularite)	39.1	19.6	3.7	1.7	.2	34.9			.1	.2	.4	.4	22.8	22
Conn.														
Garnet (almandite-pyrope)	36.3	20.2	.1	32.0	4.8	2.0						1.7	24.1	11
Garnet (No. 1 [Vernia] sp-al)	35.4	21.0		19.1	.1	.4				2.5		23.8	24.9	18
Garnet (No. 2 [Vernia] al-py)	36.3	21.0		37.1	3.6	1.5						.4	24.3	18
Magnetite ore	1.2	1.6	65.7	12.0	.5	.2	.1		.7	16.3	.5	.5	30.9	23
Magnet Heights, Bushveld														

References

1. Mean values [Fairbairn and others, 1951, p. 37].
2. Warren [1913, p. 227].
3. Washington [1898, p. 793].
4. E. S. Shepherd [Goranson, 1932, p. 228].
5. G. Steiger [Washington, 1917, p. 169].
6. F. A. Gonyer [Birch and Bancroft, 1938, p. 73].
7. W. H. Herdsman [Osborne, 1949, p. 102].
8. E. G. Radley [Daily, 1928, p. 732].
9. G. W. Hawes [Washington, 1917, p. 771].
10. E. S. Shepherd [Adams and Gibson, 1929, p. 713].
11. J. Ito, new analysis.
12. T. Kameda [Hess, 1960, p. 62].
13. H. G. Weall [Daily, 1928, p. 730 (#2)].
14. J. Moir [Daily, 1928, p. 730].
15. M. D. Foster [Ross, Foster, and Myers, 1954].
16. Reed [1959].
17. F. A. Gonyer [Ross, Shannon, and Gonyer, 1928, p. 545 (#2)].
18. J. Ito [Vernia, 1960b, p. 760].
19. A. McA. Johnston [Wagner, 1929, p. 60], also Hall [1932, p. 325 (II)].
20. [Eskola, 1921, p. 30].
21. W. Herdsman [Borg, 1956, p. 1574].
22. Aggar and Krieger [1932].
23. Hall [1932, p. 351 (XV)].
24. Levin [1950, p. 534].
25. W. C. Day [Washington, 1917, p. 751].
26. H. N. Stokes [Washington, 1917, p. 359].
27. N. L. Bowen [Washington, 1917, p. 447].
28. T. L. Walker [Washington, 1917, p. 769].

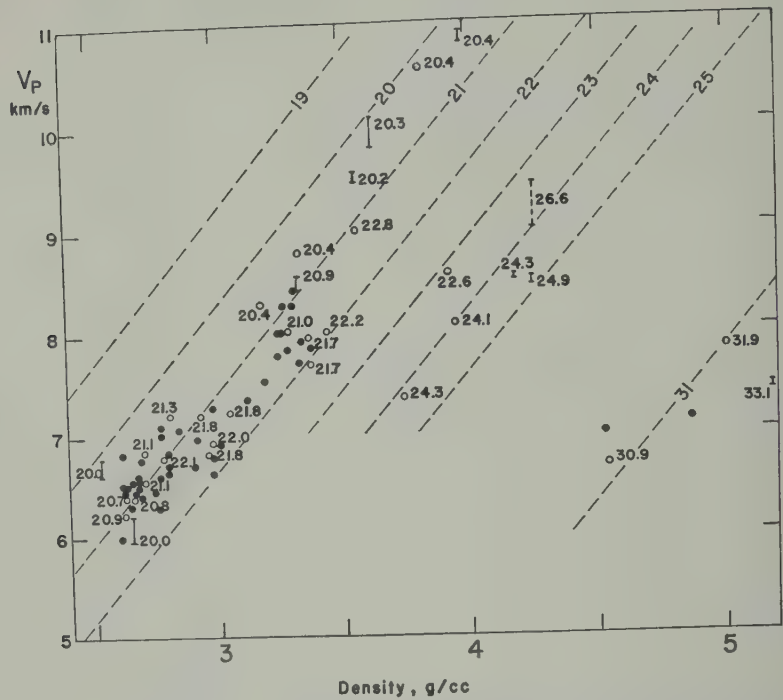


Fig. 3. Velocity at 10 kilobars versus density for silicates and oxides. Values calculated from single-crystal elastic constants are indicated as vertical lines (Table 8). The numbers attached to open circles are mean atomic weights (Table 14). Dashed lines suggest variation for constant mean atomic weights.

TABLE 15. Parameters of Least-Squares Solutions, of the Form $V_P = a + b\rho$ (V_P in km/sec, at 10 kilobars, ρ in g/cm³; uncorrected for changes of dimensions unless otherwise noted; σ = standard deviation of velocity; r = correlation coefficient.)

Solution	Data	n	a , km/sec	b , km/sec	σ , km/sec
				g/cm ³	
1	$m \approx 21$	45	-1.34	2.92	0.31
2	Corrected V and ρ , Same points as in 1	45	-1.87	3.05	0.26
3	$m \approx 21$, but with single crystal values	47	-2.01	3.16	0.26
4	Corrected ρ , same as 3, minus 1 point	46	-2.55	3.31	0.28
5	All except $m \geq 24$	65	-0.98	2.76	0.33
6	Granites	15	-0.30	2.54	0.08
7	Diabase, gabbro, eclogite	18	-1.00	2.67	0.22
8	Like 5, but corrected ρ	61	-1.14	2.78	0.31
9	Anorthosites, whole rock	7	-2.78	3.56	0.03
10	Plagioclase only	7	-4.94	4.41	0.06

sions under pressure, while for solution 2 solutions have been applied. In solutions 3 and 4, values for quasi-isotropic aggregates of base, spinel, and corundum have been deduced, and some of the other points have been omitted.

The slopes of these lines (b) are close to 3 km/sec per g/cm³; the standard error of the slope is more than 1 per cent of its value except for the granites only (solution 6) and the basic rocks only (solution 7). None of these lines is based exclusively on samples having identical mean atomic weights, and many individual discrepancies may be noted. As a first approximation, however, the correlation with density and mean atomic weight holds remarkably well over a wide range of velocity and density. The standard deviation of velocity being about 0.3 km/sec, the standard deviation of density is about 0.1 g/cm³; that is, if the velocity is known and the mean atomic weight is assumed to be in the range of the common rocks, the estimate of velocity should be correct to within 0.1 g/cm³ two-thirds of the time. (The specific effect of temperature is disregarded for the present). A wider range of composition must be considered, as in the discussion of the upper mantle, where margins of uncertainty expand, especially at higher densities. Because of the scarcity of alk-forming elements lighter than sodium, the line for $m = 20$ probably sets a lower limit to the density of any large terrestrial volumes, for oxides and silicates of beryllium and lithium will be found to give points in the shaded area. Toward the high densities, it is difficult to set a general limit short of the iron

metamorphic rocks have been treated together with the igneous rocks; separate solutions are not significant differences for samples having the same presumed mean atomic weight. The chemical data for the metamorphic rocks are scarce, however, and analyses should probably be obtained. In the computation of mean atomic weight of minerals containing hydroxyl, each group has been counted as a single mineral of atomic weight 17. In consequence, the formulas of some of these minerals (serpentine, chlorite, talc) have mean atomic weights below 20; the real minerals normally contain enough iron to raise this figure to 20 or

Though the data for the iron-rich rocks are evidently insufficient for the determination of lines, they may be used to indicate the position of lines for m equal to 24 or 25, and m equal to 30, on the assumption that these lines have the same slope as the well-determined line for $m \approx 21$. Thus Figure 3 is covered by a family of parallel lines of constant m ; within limits, any point in this figure may conceivably be realized either by simple mixtures of minerals or by replacement of light elements by heavy ones in solid solutions.

There are several notable exceptions: rutile and grossularite deviate widely from the position to be expected for their densities and mean atomic weights. The calcium-rich plagioclase rocks have either higher velocities or lower densities than are consistent with the present hypothesis. With these exceptions, there are few points which depart by more than one unit of mean atomic weight from their hypothetical positions. The insignificance of the details of crystalline structure, in comparison with the parameters of density and mean atomic weight, is striking.

It is likely that some variation of slope takes place as m varies; examination of a similar diagram for metals, based on studies with strong shocks, shows a tendency for the slope $(\partial V/\partial \rho)_m$ to decrease as atomic weight or number increases. Within the relatively small range of atomic weight, 20 to 30, represented in the present work, the change of slope is probably not large.

Possibly half of the difference between diabases and gabbros may be accounted for in terms of the chemical analyses (Table 14); the Mellen gabbro and the French Creek 'gabbro' were analyzed by Gonyer, the Frederick diabase by Shepherd, and the Centreville diabase by the 30 cooperating analysts of the study by *Fairbairn and others* [1951]. These analyses permit calculation of the mean atomic weights of these rocks (see below) as 21.8 for the two gabbros and 22.0 for the two diabases. At the same density, rocks differing by one unit in mean atomic weight show a difference of velocity averaging about 0.7 km/sec; in terms of these analyses, a difference of about 0.14 km/sec is to be expected, the gabbros having the higher velocities. The degree of reliance to be placed on the chemical analyses is a matter of much uncertainty, especially when different rocks have been analyzed in different laboratories; the real differences may be still

greater and may account for the whole difference in velocity. Even though errors of analysis may to some extent offset one another in the calculation of mean atomic weight, different analyses of the same rock, diabase W-1 [Fairbairn and others, 1951], yield values of m ranging from 21.9 to 22.1. Thus differences of this order are probably not significant unless the analyses have been made by the same analyst and by consistent procedures. For comparison, analyses by H. N. Stokes of samples of the Butte, Montana, quartz monzonite from four different localities show no significant differences, the four values of m falling between 21.13 and 21.20 [Washington, 1917, pp. 247, 359].

Isostructural lines may also be sketched in, roughly at right angles to the lines of constant m . For the olivine structure, we may connect a point for normal dunites ($m = 21$) with the point for the hortonolite dunite ($m = 24.3$) and prolong this line to an estimated end point for fayalite ($m = 29$) with a density of 4.3 and extrapolated velocity of 6.5 km/sec. An allowance has been made for serpentinization of the hortonolite dunite. Similarly, a line for the spinel structure should connect the points for ordinary spinel and for magnetite, and so on. Some of these lines may be useful for the estimation of velocity in hypothetical compounds not available for measurement.

With the exceptions noted, and with an appreciable scatter arising from neglected characteristics, the velocity in the silicates and oxides is a function of two principal variables, density and mean atomic weight. These variables may be combined to form a single parameter, ρ/m , which is proportional to the reciprocal of the mean volume per atom and ranges from about 0.10 for open structures such as quartz and albite to about 0.20 for corundum, the most tightly packed oxide. The correlation is much less close between velocity and ρ/m than between velocity and density for constant m , but it is better than the correlation between velocity and density alone, most of the points, including those for the iron-rich materials, now falling within about 0.5 km/sec from the best straight line. This does not provide an escape from the ambiguity of the velocity-density dependence, but it serves to bring out the basic importance of packing density. The ratio ρ/m is closely related to Fairbairn's [1943] 'packing index,'

which can be correlated with a number of physical properties. If the mean volume of atoms per gram atom is denoted by \bar{v} , the Fairbairn's packing index f is proportional to $\bar{v} \rho/m$; it has the advantage of being a dimensionless number, a simple ratio of volumes. For most of the common silicates, \bar{v} is nearly constant and f is nearly proportional to ρ/m . Thus a plot of velocity versus f shows much the same degree of correlation as does that of velocity versus ρ and materials such as α quartz which are anomalous on one plot are also anomalous on the other. Neither parameter is sufficient for distinguishing between albite and anorthite, for example; on the other hand, the ratio ρ/m gives a fair indication of difference between diopside and forsterite, whereas the packing index is the same for both. Neither parameter includes any allowance for individual peculiarities of chemical composition or of crystal structure. The simple concept of packing density goes far, however, to bring order into the physical properties of complex silicate structures; in these, as in the oxides, the most important feature is the oxygen ion, accounting for nearly half of the volume. It may be remarked that the measurements for three glasses given in part I also fall in appropriate positions on Figure 1, though they are not plotted and have not been used in the least-squares solutions.

Along a line of constant mean atomic weight, density changes only because the mean volume per atom changes. This change reflects different types of structure (albite to jadeite) or different compositions having different equilibrium densities (albite to anorthite). It is tempting to infer that if the density is changed by compression, for a given substance, the velocity varies in much the same way with the density as it does for these structural and compositional changes; in other words, that the lines of constant m show the relation of velocity to density for compression of any of the materials whose points fall on this line. As the experimental points for the line of $m \approx 21$ reach from a density of about 2.6 to a density of nearly 4, this would represent a degree of compression not yet available directly for these materials.

There is little experimental evidence available which to compare such an inference. The change of velocity between 6 and 10 kilobars are roughly consistent with the slope of the lines of Figure 1, but these changes are known only to one-f

cracy. The only experiments at much higher pressures are those of *Hughes and McQueen* [1958]; curves of density versus pressure are given for shock-wave conditions for samples of albite and gabbro to pressures of some 700 kilobars. To obtain velocities from the published data, it is necessary to take derivatives of the pressure-density function, but it is clear from the scatter of the experimental points that the derivatives will be highly uncertain. The published curve for the dunite leads to a virtually constant velocity under shock-wave conditions of 6.0 km/sec, a result which seems implausible. Measurements of the gabbro show much scatter and possibly a phase change, but a marked increase of velocity accompanies the increase of pressure at the higher pressures. These pioneering experiments suggest unexpected difficulties in the application of shock-wave techniques to rocks, but they offer promise of eventually supplying data at the relevant pressures.²

The changes of velocity associated with change of phase are also of considerable interest. Several examples may be seen in Figure 3. Albite transforms to jadeite plus quartz at a pressure of 10 kilobars (at about 200°C) after compression of 12 per cent; the contraction on phase change is about 17 per cent, and the velocity is about 10 per cent higher in the jadeite-quartz aggregate than in the albite. On the transformation of albite to eclogite, the change of density is again about 15 per cent, as contrasted with a contraction of a few per cent for the diabase to eclogite of between 10 and 20 kilobars. Structural changes are of interest in connection with the interpretation of the variation of seismic velocities in the 'transition region' between depths of some 300 and 900 km and at various discontinuities. The spinel form of Mg_2SiO_4 has an important role in the explanation of the transition region [*Birch*, 1952, p. 274; *Ringwood*, 1958a, b, c]. If the density of this phase is 3.55 g/cm³ [*Ringwood*, 1958b], its velocity will be in the neighborhood of 9.5 to 10 km/sec (at 10 kilobars, ordinary temperature). An application of

these measurements to the problems of the transition layer and the mantle will be found elsewhere [*Birch*, 1961]. It cannot be taken for granted that all phase changes will follow the lines of constant m ; for example, in the transformations, α quartz to β quartz (and calcite to aragonite), the denser phase appears to have the lower velocity. It seems likely, however, that closer packing will normally increase velocity and density together, as suggested by most of the data.

The measurement of velocity for diabase glass completes a study begun many years ago at the suggestion of Reginald A. Daly. In earlier work [*Birch and Law*, 1935; *Birch and Bancroft*, 1942], measurements of compressibility and of the velocities of longitudinal and torsional waves in thin bars were used to find the velocity V_P . The present large sample was cored from the same chilled melt of Westfield (Holyoke) diabase from which the older samples W1 and W2 were made; its density is 2.750 as compared with 2.807 and 2.798, probably because of a greater proportion of vesicles in the larger piece. The velocity V_P as inferred for W1 and W2 had the values 6.51 and 6.36 km/sec at ordinary temperature and pressure, to be compared with the direct measurement of 6.30 km/sec (part 1). This is close to the value, 6.45 km/sec, derived from the compressibility of a natural basaltic glass by *Adams and Gibson* [1926]. The effect of pressure is negligible up to 10 kilobars, and a temperature of 600°C reduces the velocity by about 4 per cent. Thus the earlier conclusion that there can be no major subcrustal layer of vitreous basalt is substantiated. The low-velocity layer of *Gutenberg* [1959] has a minimum velocity of about 7.8 km/sec. If this represents vitreous material, the composition must be very different from that of basalt.

Acknowledgments. The assistance of H. H. Hess, C. S. Hurlbut, Jr., Loring Coes, Jr., Peter Bell, M. G. Simmons, and Priestley Toulmin, III, in various aspects of this investigation is gratefully acknowledged.

REFERENCES

- Adams, Frank D., and Ernest G. Coker, An investigation into the elastic constants of rocks, more especially with reference to cubic compressibility, *Carnegie Inst. Wash. Publ.* 46, 69 pp., 1906.
 Adams, L. H., The compressibility of fayalite and the velocity of elastic waves in peridotite with different iron-magnesium ratios, *Gerlands Beitr. Geophys.*, 31, 315-321, 1931.

- Adams, L. H., and R. E. Gibson, The compressibilities of dunite and of basalt glass and their bearings on the composition of the earth, *Proc. Natl. Acad. Sci. U. S.*, **12**, 275-283, 1926.
- Adams, L. H., and R. E. Gibson, The elastic properties of certain basic rocks and of their constituent minerals, *Proc. Natl. Acad. Sci. U. S.*, **15**, 713-724, 1929.
- Adams, L. H., and E. D. Williamson, The compressibility of minerals and rocks at high pressures, *J. Franklin Inst.*, **195**, 475-529, 1923.
- Agar, W., and P. Krieger, Garnet rock near West Redding, Connecticut, *Am. J. Sci.*, **24**, 68-80, 1932.
- Auberger, Michel, and John S. Rinehart, Ultrasonic velocity and attenuation of longitudinal waves in rocks, *J. Geophys. Research*, **66**, 191-199, 1961.
- Balakrishna, S., Velocity of compressional waves in some Indian rocks, *Trans. Am. Geophys. Union*, **39**, 711-712, 1958.
- Bhagavantam, S., Elastic properties of single crystals and polycrystalline aggregates, *Proc. Indian Acad. Sci. A*, **41**, 72-90, 1955.
- Bhimasenachar, J., Elastic constants of corundum, *Current Sci. (India)*, **18**, 372-373, 1949.
- Birch, Francis, Travel times for shear waves in a granitic layer, *Bull. Seism. Soc. Am.*, **28**, 49-56, 1938a.
- Birch, Francis, The effect of pressure upon the elastic parameters of isotropic solids, according to Murnaghan's theory of finite strain, *J. Appl. Phys.*, **9**, 279-288, 1938b.
- Birch, Francis, Elasticity of igneous rocks at high temperatures and pressures, *Bull. Geol. Soc. Am.*, **54**, 263-286, 1943.
- Birch, Francis, Elasticity and constitution of the earth's interior, *J. Geophys. Research*, **57**, 227-286, 1952.
- Birch, Francis, Interpretation of the seismic structure of the crust in the light of experimental studies of wave velocities in rocks, in *Contributions in Geophysics in Honor of Beno Gutenberg*, Pergamon Press, New York, pp. 158-170, 1958.
- Birch, Francis, The velocity of compressional waves in rocks to 10 kilobars, 1, *J. Geophys. Research*, **65**, 1083-1102, 1960a.
- Birch, Francis, Elastic constants of rutile, *J. Geophys. Research*, **65**, 3855-3856, 1960b.
- Birch, Francis, Composition of the earth's mantle, *Geophys. J.*, **4**, 1961.
- Birch, Francis, and Dennison Bancroft, The effect of pressure on the rigidity of rocks, *J. Geol.*, **46**, 59-87 and 113-141, 1938.
- Birch, Francis, and Dennison Bancroft, New measurements of the rigidity of rocks at high pressures, *J. Geol.*, **48**, 752-766, 1940.
- Birch, Francis, and Dennison Bancroft, The elasticity of glass at high temperatures, and the vitreous basaltic substratum, *Am. J. Sci.*, **240**, 457-490, 1942.
- Birch, Francis, and Russell R. Law, Measurement of compressibility at high pressures and high temperatures, *Bull. Geol. Soc. Am.*, **46**, 1250, 1935.
- Borg, Iris, Glaucophane schists and eclogites, Healdsburg, California, *Bull. Geol. Soc. Am.*, **1563**-1584, 1956.
- Bridgman, P. W., The failure of cavities in crystals and rocks under pressure, *Am. J. Sci.*, **45**, 268, 1918.
- Bridgman, P. W., The linear compressibility of thirteen natural crystals, *Am. J. Sci.*, **10**, 296, 1928.
- Brockamp, B., Seismische feldarbeiten in Deutschland, *Beitr. Geophys.*, **44**, 211-212, 1935.
- Buddington, A. F., Adirondack igneous rocks and their metamorphism, *Geol. Soc. Am. Mem.*, **7**, 5 pp., 1939.
- Cady, W. G., *Piezoelectricity*, McGraw-Hill Book Co., New York, 1946.
- Daly, Reginald A., Bushveld igneous complex, the Transvaal, Shaler Memorial Series, *Geol. Soc. Am.*, **39**, 703-768, 1928.
- Doraiswami, M. S., Elastic constants of magnetite, pyrite, and chromite, *Proc. Indian Acad. Sci.*, **25**, 413-416, 1947.
- Eskola, P., On the eclogites of Norway, *Videnskapselskapets-Skrifter I, Mat. naturv. Kl.*, **1**-118, 1921.
- Fairbairn, H. W., Packing in ionic minerals, *Geol. Soc. Am.*, **54**, 1305-1374, 1943.
- Fairbairn, H. W., and others, A cooperative investigation of precision and accuracy in chemical spectrochemical and modal analysis of silicate rocks, *U. S. Geol. Survey Bull.*, **980**, 71 pp., 1951.
- Foster, Wilfred R., Simple method for the determination of the plagioclase feldspars, *Am. Mineralogist*, **40**, 179-185, 1955.
- Goranson, E. W., Some notes on the melting of granite, *Am. J. Sci.*, **23**, 227-236, 1932.
- Gutenberg, B., On some problems concerning seismic field methods, *Beitr. angew. Geophys.*, **125**-140, 1937.
- Gutenberg, B., Wave velocities below the Mohorovicic discontinuity, *Geophys. J.*, **2**, 348-352, 1951.
- Hall, A. L., The Bushveld igneous complex of the Central Transvaal, *Union S. Africa Geol. Soc. Mem.*, **28**, 560 pp., 1932.
- Herrin, Eugene, and Jean Richmond, On the propagation of the Lg phase, *Bull. Seism. Soc. Am.*, **197**-210, 1960.
- Hess, H. H., The AmSoc Hole to the earth's mantle, *Trans. Am. Geophys. Union*, **40**, 340-345, 1959.
- Hess, H. H., Stillwater igneous complex, Montana, *Geol. Soc. Am. Mem.*, **80**, 1960.
- Hill, R., The elastic behavior of a crystalline aggregate, *Proc. Phys. Soc. London A*, **65**, 349-352, 1952.
- Hughes, D. S., and C. E. Cooke, Jr., The effect of pressure on the reduction of pore volume in consolidated sandstones, *Geophysics*, **18**, 298, 1953.
- Hughes, D. S., and J. H. Cross, Elastic wave velocities at high pressures and temperatures, *Geophysics*, **16**, 577-593, 1951.
- Hughes, D. S., and H. J. Jones, Variation of elastic

- moduli of igneous rocks with pressure and temperature, *Bull. Geol. Soc. Am.*, **61**, 843-856, 1950.
- Ghies, D. S., and C. Maurette, Elastic wave velocities in granites, *Geophysics*, **21**, 277-284, 1956.
- Ghies, D. S., and C. Maurette, Variation of elastic wave velocities in basic igneous rocks with pressure and temperature, *Geophysics*, **22**, 23-31, 1957a.
- Ghies, D. S., and C. Maurette, Détermination des vitesses d'onde élastique dans diverses roches en fonction de la pression et de la température, *Rév. inst. franç. pétrole et Ann. combustibles liquides*, **12**, 730-752, 1957b.
- Ghies, D. S., and R. G. McQueen, Density of basic rocks at very high pressures, *Trans. Am. Geophys. Union*, **39**, 959-965, 1958.
- John M., The elastic properties of rocks: a correlation of theory and experiment, *Proc. Natl. Acad. Sci. U. S.*, **22**, 482-496, 1936.
- Leuz, Samuel, Seismic study of crustal structure in Pennsylvania and New York, *Bull. Seism. Soc. Am.*, **45**, 303-325, 1955.
- Loeff, L., Seismic wave velocities in Westerly granite, *Trans. Am. Geophys. Union*, **35**, 969-973, 1954.
- Miller, F. C., and D. Linehan, Seismic studies of dykes and intrusives in western New Hampshire, *Bull. Geol. Soc. Am.*, **52**, 633-648, 1941.
- Mooney, A., Determination of elastic wave velocities in rocks by means of ultrasonic impulse transmission, *J. Phys. Earth*, **2**, 33-38, 1954.
- Neuen, Esper S., The relation between the refractive index and the density of some crystallized silicates and their glasses, *Am. J. Sci.* (4), **28**, 233-274, 1909.
- Olson, L. D., Velocity of elastic waves in granite and gabbro, *Physics*, **4**, 375-385, 1933.
- Olson, L. D., and W. M. Ewing, Velocity of elastic waves in granite, *Physics*, **2**, 160-173, 1932.
- Olson, S. B., Genesis of some Adirondack garnet gneisses, *Bull. Geol. Soc. Am.*, **61**, 519-566, 1950.
- Olson, A. E. H., *A Treatise on the Mathematical Theory of Elasticity*, Cambridge University Press, 33 pp., 1927 (also Dover, New York, 1944).
- Reich, H., and R. Fuchs, Kompressibilitätsmessungen an festen Körpern, *Ann. Phys.*, **65**, 289-309, 1921.
- Reid, W. P., *Physical Acoustics and the Properties of Solids*, Bell Lab Series, D. Van Nostrand Co., New York, 1958.
- Shimizu, Shogo, Variation of the elastic wave velocities of rocks of the process of deformation and fracture under high pressure, *Disaster Prevention Research Inst. Bull.* **32**, 1-8, Kyoto, Japan, 1960.
- Simkin, H. J., Ultrasonic measurement techniques applicable to small solid specimens, *J. Acoust. Soc. Am.*, **22**, 413-418, 1950.
- Stoll, V. N., Recording of converted refracted S_2P_1 waves for the purpose of computing the elastic constants of diabase covered by alluvium, *Bull. (Izvest.) Acad. Sci. USSR, Geophys. Ser.*, **8**, English ed., 794-803, 1959.
- Osborne, F. F., Coronite, labradorite, anorthosite, and dykes of andesine anorthosite, New Glasgow, P. Q., *Trans. Roy. Soc. Canada*, **43**, 85-112, 1949.
- Peselnick, Louis, and W. F. Outerbridge, Internal friction in shear and shear modulus of Solenhofen limestone over a frequency range of 10^7 cycles per second, *J. Geophys. Research*, **66**, 581-588, 1961.
- Reed, J. J., Chemical and modal composition of dunite from Dun Mt., Nelson, New Zealand, *J. Geol. Geophys.*, **2**, 916-919, 1959.
- Reich, H., Geologische Ergebnisse der seismischen Beobachtungen der Sprengung auf Helgoland, *Geol. Jahrb.*, **64**, 243-266, 1950.
- Reuss, A., Berechnung der Fließgrenze von Mischkristallen auf Grund der Plastizitätsbedingung für Einkristalle, *Z. angew. Math. u. Mech.*, **9**, 49-58, 1929.
- Ringwood, A. E., The constitution of the mantle I, Thermodynamics of the olivine-spinel transition, *Geochim. et Cosmochim. Acta*, **13**, 303-321, 1958a.
- Ringwood, A. E., The constitution of the mantle II, Further data on the olivine-spinel transition, *Geochim. et Cosmochim. Acta*, **15**, 18-29, 1958b.
- Ringwood, A. E., The constitution of the mantle III, Consequences of the olivine-spinel transition, *Geochim. et Cosmochim. Acta*, **15**, 195-212, 1958c.
- Ross, C. S., E. V. Shannon, and F. A. Gonyer, The origin of nickel silicates at Webster, North Carolina, *Econ. Geol.*, **23**, 528-552, 1928.
- Ross, C. S., M. D. Foster, and A. T. Myers, Origin of dunites and of olivine-rich inclusions in basaltic rocks, *Am. Mineralogist*, **39**, 693-737, 1954.
- Schairer, J. F., J. R. Smith, and F. Chayes, Refractive indices of plagioclase glasses, *Ann. Rept. of Director Geophys. Lab.*, 195-197, 1955-1956; *Carnegie Inst. Wash. Year Book* **55**, 1956.
- Tocher, Don, Anisotropy in rocks under simple compression, *Trans. Am. Geophys. Union*, **38**, 89-94, 1957.
- Turner, F. J., and J. Verhoogen, *Igneous and Metamorphic Petrology*, McGraw-Hill Book Company, New York, 1951.
- Verma, R. K., Elasticity of several high-density crystals, Thesis, Harvard University, 1960a.
- Verma, R. K., Elasticity of several high-density crystals, *J. Geophys. Research*, **65**, 757-766, 1960b.
- Voigt, W., *Lehrbuch der Kristallphysik*, B. G. Teubner, Leipzig, 1928.
- Volarovich, M. P., and D. B. Balashov, Study of velocities of elastic waves in samples of rock under pressures up to 5000 kg/cm², *Bull. (Izvest.) Acad. Sci. USSR, Geophys. Ser.*, (English ed.), **3**, 56-69, 1957.
- Wachtman, J. B., Jr., W. E. Tefft, D. G. Lam, Jr., and R. P. Stinchfield, Elastic constants of synthetic single crystal corundum at room temperature, *J. Research, NBS*, **64 A**, 213-228, 1960.
- Wagner, P. A., *Platinum Deposits and Mines of South Africa*, Oliver and Boyd, Edinburgh and London, 326 pp., 1929.
- Warren, C. H., Petrology of the alkali-granites and porphyries of Quincy and the Blue Hills, Mass.,

- U. S. A., *Proc. Am. Acad. Arts and Sci.*, 49, 203-331, 1913.
- Washington, H. S., The petrographical province of Essex County, Mass., 1, *J. Geol.*, 6, 787-808, 1898.
- Washington, H. S., Chemical analyses of igneous rocks, *U. S. Geol. Survey, Profess. Paper* 99, 1201 pp., 1917.
- Weatherby, R. B., W. T. Born, and R. L. Harding, Granite and limestone velocity determinations in Arbuckle Mountains, Oklahoma, *Bull. Am. Assoc. Petrol. Geol.*, 18, 106-118, 1934.
- Wyllie, M. R. J., A. R. Gregory, and G. H. F. Gardner, An experimental investigation of factors affecting elastic wave velocities in porous media, *Geophysics*, 23, 459-493, 1958.
- Yoder, H. S., and C. E. Weir, Change of free energy with pressure of the reaction nepheline + albite = 2 jadeite, *Am. J. Sci.*, 249, 683-694, 1957.
- Zisman, W. A., Young's modulus and Poisson's ratio with reference to geophysical applications, *Proc. Natl. Acad. Sci. U. S.*, 19, 653-665, 1933a.
- Zisman, W. A., Compressibility and anisotropy of rocks at and near the earth's surface, *Proc. Natl. Acad. Sci. U. S.*, 19, 666-679, 1933b.
- Zisman, W. A., Comparison of the statically and seismologically determined elastic constants of rocks, *Proc. Natl. Acad. Sci. U. S.*, 19, 680-686, 1933c.

(Manuscript received March 27, 1961.)

The Use of Gravity Methods to Study the Underground Structure and Impact Energy of Meteorite Craters

M. J. S. INNES

Dominion Observatory, Ottawa, Canada

Abstract. Gravity data have been used to calculate the mass deficiency and hence the amount of shattered rock under the Deep Bay, Brent, and Holleford craters. The results show good agreement with the crater model computed by Rottenberg as combined with the depth/diameter ratios of Baldwin for meteorite impact craters. The zone of complete rupture is shown to extend to a depth of approximately one-third of the crater's diameter, and impact energy values, derived from energy of crushing, are 6.5×10^{23} ergs, 2.1×10^{24} ergs, and 8.7×10^{25} ergs for Holleford, Brent, and Deep Bay, respectively.

INTRODUCTION

After the discoveries of the New Quebec crater [Feen, 1950], the Brent crater [Millman, 1951], and the Holleford crater [Beals, Ferguson, and Lindau, 1956], all located in the Canadian Shield and having characteristics that strongly suggest meteoric origin for all three, attention was drawn to a large circular water-filled depression known as Deep Bay which forms the southern part of Reindeer Lake in northern Saskatchewan. A preliminary investigation [Innes, 1957], all the evidence from geological and geophysical observations supported the hypothesis that Deep Bay, too, was formed by impact and explosion of a meteorite, perhaps during the Mesozoic. Gravity observations taken in the vicinity of the rim, now deeply eroded and evident only in the height of land that forms the headwaters of short streams emptying into the bay, revealed a gravity 'low' associated with the feature. In this paper, the results of recent gravity measurements are presented which strengthen the hypothesis that the Deep Bay, Brent, and Holleford craters were all formed by similar processes and (2) provide an estimate of the total volume of rock deformed during the cratering process, thus leading to an estimate of the minimum energies involved in their formation.

ESTIMATION OF SHATTERED ROCK ON THE BASIS OF OBSERVED GRAVITY

Gravity data and crater dimensions. Gravity observations of the craters at Brent [Millman, 1951], Deep Bay [Clark, Willmore, and Innes, 1960] and

Holleford [Beals, 1960; Beals, Innes, and Rottenberg, 1960] indicate the presence of circular negative gravity fields associated with both these craters. These observations (Figs. 1 and 2) were interpreted as being a consequence in part of the sedimentary rock filling the craters and in part of the presence of crushed and fragmented rock due to meteorite impact and explosion. Since these ideas received satisfactory confirmation from diamond-drilling operations, it seemed reasonable to apply similar gravity techniques to a study of the Deep Bay crater.

During the winter of 1959 a program for training observers to make gravity measurements on sea ice in the Canadian Arctic provided the opportunity for further gravity work at Deep Bay. Because of the instability of the ice, a Worden gravimeter with greater than usual damping characteristics and a specially constructed eyepiece for averaging the readings was employed with much success. Most of the measurements were made on days during which the wind velocities seldom exceeded 10 mph, and temperatures ranged between $\pm 10^\circ\text{F}$. Under these ideal winter conditions, observations could be completed in about 5 minutes, and uncertainties were less than 0.5 scale division, or 0.2 mgal. Tests carried out under more severe conditions on a day unsuitable for aircraft operations, during which wind velocities ranged from 20 to 30 mph with gusts up to 40 mph or greater, showed that, by averaging the observations over longer periods of 10 to 12 minutes, an accuracy of 0.7 mgal is possible.

Some 45 stations, established on the ice at

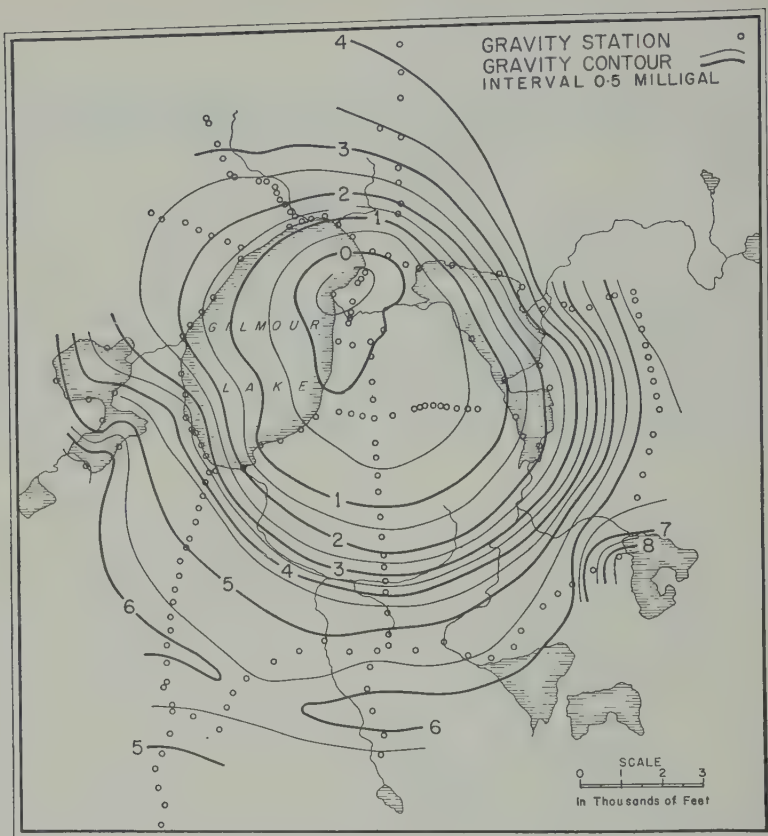


Fig. 1. Bouguer gravity anomaly map of Brent crater.

Deep Bay, provide a clear picture of the gravitational field. The results (Fig. 3), which confirmed the earlier work, indicate a circular gravity minimum of 30 mgal with contours generally concentric with the circular margin of the bay. Corrections for depths of water and terrain reduce the gravity minimum to 20.1 mgal. This corresponds to an average outward gradient of about 5 μ gal/mile, indicating that the maximum depth to the top of the disturbing masses is shallow, less than 3 miles.

The interpretations of negative gravity fields for the Brent and Holleford craters have been largely confirmed by the results of the diamond-drilling program. It would therefore appear that gravity methods can be applied with some confidence to the data for Deep Bay. The original rim diameter of Deep Bay is estimated to be about 40,000 feet, or 7.57 miles, which, on the basis of Baldwin's [1949] formula relating crater depths with diameter, places the floor of

the crater at a depth of 2100 feet below the surface of the bay. The sedimentary fill would account for about 3 to 5 mgal of the anomaly depending upon its density; thus 15 to 17 mgal would have to be explained by the underlying brecciated zone. If the mean density of the latter is similar to the density of the breccia obtained from drill core samples at Brent, which seems likely because both craters are underlain by granitic gneisses of much the same composition and density, it follows that the deformed zone under the Deep Bay crater extends to depths between 7000 and 12,000 feet.

Mass deficiency and its application to the estimation of the mass and volume of fragmented rocks. Statistics resulting from these investigations are given in Table 1. The peak gravity anomaly associated with each crater (column 3) increases (negatively) with increasing diameter. As has been mentioned, the negative gravity anomalies reflect the low-density sedimentary material

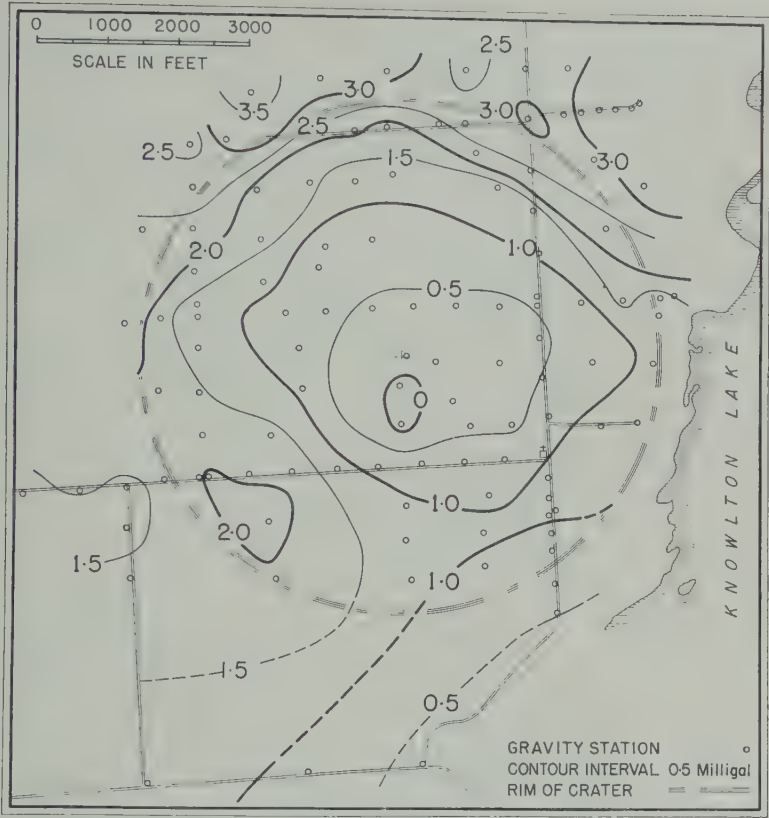


Fig. 2. Bouguer gravity anomaly map of Holleford crater.

g within the craters and the low-density
mental rocks or breccia which are the
ducts of explosion and underlie the craters'
rs. Radial uparching of the surrounding rocks
consequence of upward-directed forces acting
ng their formation may contribute to the
tive gravity field. However, the contribution
to uplift is not large, as the density determi-

nations of the sediments and breccia associated
with both the Brent and the Holleford craters
indicate that the anomalies can be accounted for
almost totally by these materials.

The diminution in mass from normal crustal
conditions, or the mass deficiency ΔM , due to
the presence of these low-density materials, can
be estimated by direct integration of the gravity

TABLE 1. Dimensions and Gravity Data for the Holleford, Brent, and Deep Bay Craters

1) Crater	(2) Diameter, ft	(3) Maximum Gravity Anomaly (Δg), mgal	(4) Mass Deficiency (ΔM), grams	(5) $\Delta M/D^3$, g/ft ³	(6) Mass of Breccia and Sediments, grams	(7) Volume of Breccia and Sediments, ft ³
Holleford	7708 (2349 m)	-2.2	$3.4 \pm 0.2 \times 10^{14}$	7.4×10^2	3.84×10^{15}	5.29×10^{10}
Brent	11,500 (3505 m)	-5.5	$9.2 \pm 0.3 \times 10^{14}$	6.0×10^2	1.35×10^{16}	1.91×10^{11}
Deep Bay	40,000 (12,192 m)	-20.1	$2.1 \pm 0.2 \times 10^{16}$	3.3×10^2	3.10×10^{17}	4.38×10^{12}

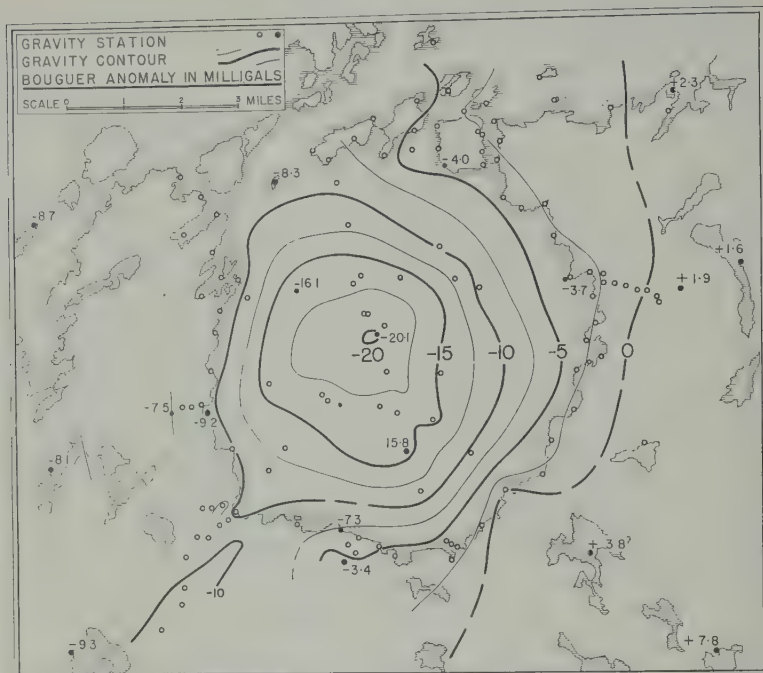


Fig. 3. Bouguer gravity anomaly map of Deep Bay crater.

anomalies. The method [Hammer, 1945] is based on Gauss's theorem,¹ in that the surface integral of the gravity anomaly, taken over an infinite horizontal plane, is proportional to the mass alone and is independent of its form and shape. The method has the added advantage that no assumptions need be made about the densities of the disturbing masses. Column 4 gives the total mass deficiency for each crater obtained by integration of the gravity anomaly maps in Figures 1, 2, and 3. The integration was carried out at least twice for each crater, and departures from the mean values listed in the table provide a measure of the uncertainty in the process of integration. The greatest error in the ΔM values stems, perhaps, from the difficulty in estimating normal background values, but errors from all sources should not exceed 10 per cent.

As one might expect the total rock deformation in a meteorite crater to be directly proportional to the third power of the crater's dimensions,

$$\int_S \Delta g \, dS = 2\pi\gamma \sum \Delta M.$$

Δg is the gravity anomaly for an element of surface area dS , and γ is the gravitational constant.

It is of interest to examine how ΔM varies with crater diameter. The ratios $\Delta M/D^3$ (column 5) show that the third-power rule is not strictly true and suggest that ΔM increases with diameter at a rate somewhat smaller than D^3 . It is found that the mass deficiency can very well be represented by the relation

$$\Delta M = 6.52 \times 10^4 D^{2.50} \text{ grams}$$

where D is the crater diameter in feet. Although based upon only three samples of experimental data, this exponential relation seems hardly fortuitous and qualitatively would seem to be a strong argument, independent of geological and topographical considerations, that these craters have been formed by similar physical processes.

Density of rocks within and surrounding craters. To calculate the total mass and volume of the rocks giving rise to the negative gravity fields, it is necessary to know the mean density of the sedimentary and fragmental rocks and also the mean density of the country rocks surrounding the craters.

The densities associated with the Brent craters are well known. Numerous measurements of surface samples and bulk determinations by

TABLE 2a. Densities for the Brent Crater Sedimentary Rocks

Footage	Number of Determinations	Density	
		Range, g/cm ³	Mean, g/cm ³
0-100	18	2.27 to 2.71	2.553
0-211	23	2.21 to 2.68	2.526
1-311	20	2.42 to 2.72	2.503
1-411	16	2.41 to 2.76	2.573
1-511	20	2.41 to 2.49	2.459
1-611	20	2.34 to 2.55	2.432
1-711	20	2.30 to 2.72	2.514
1-811	23	2.41 to 2.62	2.495
1-851	8	2.28 to 2.65	2.429
1-851 feet	168	2.21 to 2.76	2.501

TABLE 2b. Densities for the Brent Crater Fragmental Rocks

Footage	Number of Determinations	Density	
		Range, g/cm ³	Mean, g/cm ³
-951	24	1.99 to 2.52	2.378
-1051	22	1.99 to 2.61	2.367
-1151	20	2.29 to 2.54	2.423
-1251	21	2.17 to 2.49	2.337
-1351	20	2.31 to 2.56	2.435
-1451	20	2.31 to 2.49	2.391
-1561	24	2.42 to 2.74	2.557
-1661	20	2.37 to 2.53	2.441
-1761	22	2.35 to 2.71	2.462
-1861	20	2.29 to 2.56	2.425
-1961	20	2.31 to 2.61	2.456
-2061	20	2.41 to 2.59	2.507
-2161	15	2.47 to 2.62	2.508
-2261	20	2.47 to 2.65	2.548
-2361	20	2.53 to 2.71	2.577
-2461	20	2.44 to 2.60	2.506
-2561	20	2.33 to 2.50	2.400
-2661	20	2.23 to 2.47	2.345
-2761	20	2.31 to 2.66	2.535
-2861	20	2.53 to 2.72	2.612
-2961	20	2.43 to 2.65	2.569
-3061	20	2.51 to 2.69	2.615
-3161	19	2.41 to 2.73	2.648
-3261	20	2.44 to 2.69	2.637
-3361	20	2.51 to 2.72	2.659
-3461	20	2.55 to 2.69	2.623
-3491	7	2.59 to 2.67	2.624
2640	534	1.99 to 2.72	2.498

gravity profile method [Millman and others, 1960] show that the mean density of the country rocks in the vicinity of the Brent crater is about 2.67 g/cm³. Table 2 gives the densities obtained from drill core samples from a 3500-foot hole put down near the center of the crater. Although there is a wide range in density within each 100 foot of core, from the top to the bottom of the hole, the mean densities show conclusively that both the sedimentary and fragmental rocks are responsible for the negative gravity field. The sedimentary rocks, which extend from the surface to a depth of 851 feet, range in density from 2.21 to 2.76 g/cm³ and have a mean value of 2.501 g/cm³. The table shows that the sedimentary rocks decrease slightly in density with increasing depth.

Fragmental material and gneiss breccia were encountered below the sedimentary rocks and continued to a depth of 3491 feet (the bottom of the hole). The breccia consists of fragments of granite gneiss, similar in composition to the granitic rocks surrounding the crater. The fragments vary in size from small particles to large blocks several feet across. The fragmental rocks range in density from 1.99 to 2.72 g/cm³, and mean values for each 100 feet of drilling show a gradual increase from about 2.37 g/cm³ near the top of the zone to about 2.63 g/cm³ at the bottom of the hole. As the mean density of the rocks forming the lower part of the hole is slightly less than the mean density of the surrounding gneisses (2.67 g/cm³), it would appear that this drill hole does not completely penetrate the rupture zone. The mean density of all determinations of the breccia is 2.498 g/cm³. There is therefore very little difference (about 0.1 per cent) between the mean density of the sedimentary and that of fragmental rocks; for the purpose of analysis, 2.50 g/cm³ is the value adopted for each of them. Based upon the attraction of the infinite layer, these drilling and density results indicate that about 24 per cent of the total anomaly field is due to the sedimentary rocks within the crater and the remainder to the underlying breccia.

Table 3 gives a summary of the density determinations for the drill cores from the Holleford crater [Beals, 1960]. Although drilling did not penetrate to the bottom of the breccia zone in the hole nearest the center of the crater (hole 1), the results should provide a fairly reliable estimate of the mean density of the rocks

TABLE 3. Densities for the Holleford Crater

TABLE 3.—Densities				
Drill Hole	Footage	Number of Deter- minations	Density	
			Range, g/cm ³	Mean, g/cm ³
(a) Sedimentary Section, Holleford Crater				
1	0-725	28	2.27 to 2.73	2.563
2	0-495	22	2.16 to 2.76	2.569
Mean				2.565
(b) Fragmental Rocks, Holleford Crater				
1	725-1128	14	2.37 to 2.79	2.563
(c) Country Rocks, Holleford Crater				
2	495-1430	36	2.69 to 3.19	2.840
3	0-422	21	2.64 to 2.79	2.708
Mean				2.791

responsible for the gravity anomalies. The sedimentary rocks from drill holes 1 and 2 range in density from 2.16 to 2.76 g/cm³, the mean value being 2.565 g/cm³. The fragmental rocks, the longest section of which extends from a depth of 725 feet to 1128 feet in hole 1, have densities ranging from 2.37 to 2.79 g/cm³, the mean value being 2.563 g/cm³.

It is seen that, as for Brent, the sedimentary and fragmental rocks at Holleford, although highly variable in density at all levels, have almost identical mean densities. A value of 2.564 g/cm³, therefore, would seem to be a representative density of both the sedimentary and fragmental sectors of the crater. It should be pointed out that the almost identical densities found for the breccia and sedimentary rocks in each of these craters is coincidental, as there appears to be no obvious reason why this should be so.

Less certain, however, is the value to be adopted for the mean density of the country rock at Holleford. The crater lies in an area near the edge of the Canadian Shield. Heavy Ordovician limestones and dolomites, which occupy the uppermost part of the crater, form a thin mantle on the rim and to the south of the crater. Numerous measurements show that these rocks have a mean density of 2.70 g/cm³. Precambrian rocks outcrop to the north of the crater and consist of (i) granite gneiss having a mean density of 2.74 g/cm³ and (ii) crystalline limestones having a mean density of 2.80 g/cm³. As too little is known about the relative abundance of the three kinds of rock in the vicinity of

the crater to assign weights with confidence, it was considered that the most probable value for the mean density of the country rocks might be provided by those sections of the drill core from holes 2 and 3 that lie outside the sedimentary and breccia zone of the crater. As indicated in Table 3, the mean density of samples over a range in depth of about 1400 feet is 2.791 g/cm³, and this value will be adopted for the analysis that follows.

The Deep Bay crater lies in an area underlain by granite gneiss quite similar in composition and density to the country rocks near the Brent crater. As no drilling has been done at Deep Bay, the densities observed at Brent will be used for analysis of the gravity data for Deep Bay.

Mass and volume of the breccia and sedimentary rocks. The total mass and volume of the breccia and sedimentary rocks responsible for the gravity anomalies are given in columns 6 and 7 of Table 1. These have been calculated from the mean densities obtained in the preceding section and from the following relations:

$$\text{Total mass} = \sigma_b / (\sigma_e - \sigma_b) \Delta M \quad (1)$$

and

$$\text{Total volume} = \Delta M / (\sigma_e - \sigma_b) \quad (2)$$

where ΔM is the mass deficiency given in column 4 of Table 1, σ_b is the mean density of the fragmental and sedimentary rocks, and σ_e is the mean density of the country rocks.

ALTERNATIVE ESTIMATE OF CRATER STRUCTURE ON THE BASIS OF CRATER THEORY

General consequences of Rottenberg's theoretical work. To justify these results (columns 6 and 7 of Table 1) quantitatively would require a direct calculation, from first principles, of the mass and volume of breccia produced in a crater of given dimensions; but, unfortunately, the mechanisms of crater formation have proved too difficult a problem for complete solution. As a result of recent analytical investigation of this problem by Rottenberg [Beals, Innes, and Rottenberg, 1960], however, it is now possible to estimate the volume of the ruptured zone of a meteoritic crater with some confidence. It was shown that for meteoric impact into granite gneiss the depth of broken rock beneath the original plain, in the direction of penetration, is very nearly equal

one-third of the crater diameter. We thus have two points located on the surface separating the zones of rupture and fracture which fix the limits of the volume of the breccia; one point on this surface is obviously near the center of the crater, and the other may be identified by the crater's rim (see Fig. 4). It should be mentioned here that 'rupture zone' and 'crushing zone' used interchangeably throughout this paper refer to that region of the crater in which the shattered and broken rocks are completely disassociated from their original position. The 'fracture zone,' on the other hand, is the region immediately surrounding the rupture zone. Although the rocks in this zone are highly fractured and show evidence of having been uplifted, they are essentially *in situ*.

This new information, together with the assumptions that (i) Baldwin's empirical formulas relating rim diameter D , rim height E , and crater depth d are valid and (ii) that both the crater floor and the lower boundary of the breccia zone have the shape of a paraboloid of revolution, leads to the following equations which permit predictions of the volumes associated with crater formation.

The volume of the crater below the original plain will be given by the volume of the paraboloid

$$V_c = (\pi/8) D^2(d - E) \quad (4)$$

The volume of fragmental material² left in the crater will be, analogously,

$$V_b = (\pi/8) D^2(D/3 + E - d) \quad (5)$$

² A working formula for the volume of breccia in cubic feet is $\log V_b = -0.8301 + 2.3760 \log D + 2.385 (\log D)^2 - 0.0234 (\log D)^3$.

The total volume of the country rock ruptured by the exploding meteorite will be equal to the volume of the crater below plain, plus the volume of the fragmental rocks left in the crater, or

$$V_t = V_c + V_b = (\pi/24) D^3 \quad (6)$$

It should be emphasized at this point that V_t is defined as the volume below the original plain that is deduced from the outer limit of crushing (rupture) and is sometimes referred to as the true crater volume; this is in contrast to the crater volume below the rim, which in most investigations is considered to be proportional to D^2d .

Crater structure as a function of diameter. The volumes V_c , V_b , and V_t are plotted as functions of crater diameter in Figure 5. Although each shows a progressive change in volume with increasing diameter, it will be noticed that their respective rates differ. The total volume of country rock ruptured by the cratering process, V_t , increases simply as the cube of the diameter and is shown as a straight line in the logarithmic plot. On the other hand, both the volume of the breccia, V_b , left in the crater and the crater volume below plain, V_c , increase at different rates; this of course reflects the dependence of the formulas on Baldwin's relation which shows that, with increasing size, crater depth increases at a slower rate than the diameter. Baldwin's diameter-depth curve, which is superimposed in Figure 5, clearly illustrates this progressive change in crater form.

It is also implicit from these formulas that the volume of fragmental material, V_b , increases more rapidly with the increasing crater size than does crater volume, V_c . In other words, the

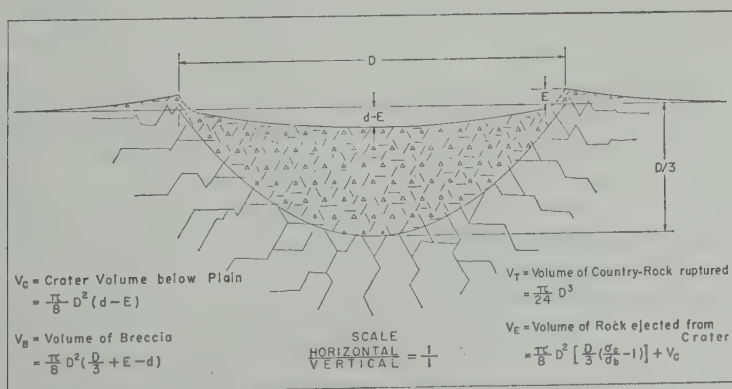


Fig. 4. Cross section of a typical crater.

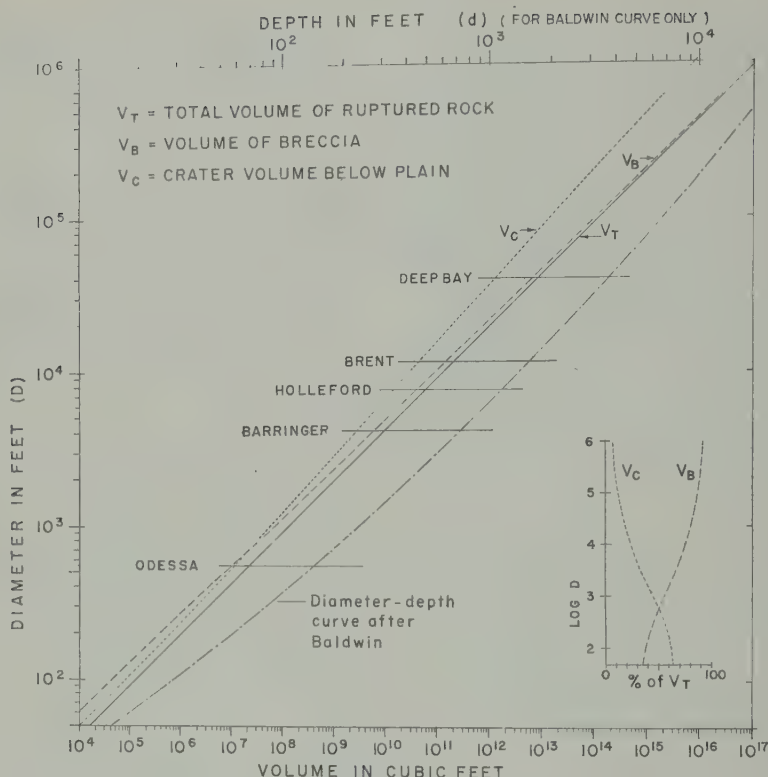


Fig. 5. Relationships of crater depths and volumes to crater diameters.

larger the crater, the greater is the proportion of ruptured material that falls back into the crater. This is clearly illustrated in Figure 5, which also shows, for comparison, V_b and V_c plotted as percentage of the total volume V_t of country rock ruptured during the cratering process. It is seen from equations 4 and 5 that, when the crater dimensions are such that $D < 6(d - E)$, then $V_c > V_b$. For larger craters the volume of the fragmental material is always the greater.

An explanation for this has been given recently by Charters [1960], who points out that, if it is assumed that the volume of rock crushed by impact is proportional to the kinetic energy of the meteorite and that a fixed fraction of the energy is available for lifting and ejection, it can be shown that the height to which the broken rock will be lifted is the same, regardless of the size of the projectile. Thus a smaller proportion of the fragmental material produced by the impact explosion is ejected as the craters become larger.

The above formulas (equations 4, 5, and 6)

have been used to predict the volumes given in columns 2, 3, and 4 of Table 4 for the Holleford, Brent, and Deep Bay craters. It is seen that for craters of these dimensions the predicted volumes of the breccia, V_b , are 3 to 5 times greater than the corresponding crater volumes, V_c , and represent from 73 to 84 per cent of the total volume of the ruptured rock.

Analytical expression of Schröter's rule. While the volumes V_c , V_b , and V_t are estimated simply from the crater dimensions, densities of the rock before and after rupture are needed in the estimation of the volume of the fragmental rock ejected from the crater. Letting these, as previously, be represented by σ_c and σ_b , respectively, the country rock fragmented by the explosion, V_t , will suffer an increase in volume amounting to $V_t[(\sigma_c/\sigma_b) - 1]$, and the volume of fragmental material ejected to form rim materials will be given by

$$V_e = \frac{\pi}{8} D^2 \left[\frac{D}{3} \left(\frac{\sigma_c}{\sigma_b} - 1 \right) + d - E \right] \quad (7)$$

TABLE 4. Mass and Volumes of Fragmental and Sedimentary Rocks

(1) Crater	(2) Crater Volume (V_c) below Plain, ft ³	(3) Fragmental Rock in Crater (V_b), ft ³	(4) Volume of Country Rock Ruptured (V_t), ft ³	(5) Fragmental Rock Ejected from Crater (V_e), ft ³
Holleford	1.57×10^{10}	4.42×10^{10}	5.99×10^{10}	1.95×10^{10}
Brent	4.63×10^{10} (3.02×10^{10})	1.53×10^{11} (1.52×10^{11})	1.99×10^{11} (1.82×10^{11})	5.98×10^{10}
Deep Bay	1.33×10^{12}	7.04×10^{12}	8.38×10^{12}	1.90×10^{12}

Note: For the Brent crater volumes in parentheses are based on drilling results.

This simply states that the volume of rock ejected by the exploding meteorite is equal to the increase in volume of the country rock due to rupture plus the volume of the crater below the surrounding plain.

It follows that the total mass of rock ejected from the crater will be given by

$$M_e = V_t(\sigma_c - \sigma_b) + V_c\sigma_b \quad (8)$$

$$M_e = V_c\sigma_c + V_b(\sigma_c - \sigma_b) \quad (9)$$

Equations 7 and 9 may be considered as working formulas of Schröter's rule, quoted by Baldwin [1949, p. 114] as follows: 'For each crater the part of the material above the surface is approximately equal to the volume of the interior depression below the surface.' It is pointed out, however, that equations 7 and 9 indicate that both the volume and the mass of rock ejected from the crater are greater than the volume and mass of country rock that would just fill the crater below the original plain.

This excess volume and mass depend primarily upon the change in density of the country rock due to rupture and constitute a significant portion of all material thrown out of the crater. Estimates of the volumes of fragmented rock ejected from the three fossil craters are given in column 5 of Table 4; they are based upon the mean densities given previously. It will be noticed that these volumes are from 20 to 45 per cent greater than the crater volume below plain. As compaction and lithification would tend to have increased the density of the breccia since it was first fragmented, the estimates may be taken as lower limits of the total volume of rock ejected from these craters. Finally, it should be men-

tioned that the volume of a meteorite crater's rim will usually be greater than the volume of ejected materials as estimated by equation 7. This follows because no account is taken of the uplift of the surrounding rocks due to upthrusting and to the expansion within the fractured zone. At the Deep Bay crater, for example, although it has been deeply eroded and although the fragmental material has long since been swept away by glaciers and other agents of erosion, bedrock portions of the original rim still stand sufficiently high to have a marked effect in controlling the drainage pattern in the immediate vicinity of the crater [Innes, 1957].

COMPARISON OF OBSERVATIONAL AND ANALYTICAL RESULTS

Gravity surveys. It now remains to examine how well these predicted volumes compare with the observational data. We first consider the evidence from the gravity surveys. Column 7 of Table 1 gives the combined volume of the fragmental and sedimentary rocks in each crater, based entirely on measurements of rock densities and the gravitational field associated with each crater. All these fossil craters have suffered erosion, the amount depending on their age and environment. It is difficult to judge just how much erosion has taken place, and there remains considerable uncertainty about the original level of the surrounding country and, to a lesser extent, about the original crater diameters. However, as there is clear-cut evidence that all three craters have sedimentary rocks covering their floors, and as the outer limits of brecciation, at least for two of these craters, Brent and Deep Bay, may be established reasonably well by surface observation, it is obvious that the greater part of the low-density material

(the sediments and breccia) have escaped erosion (see Fig. 4). The volumes indicated by the gravity measurements (column 7, Table 1) should therefore have approximately the same magnitudes (if different, they should be smaller) as those predicted for the total volume of shattered rock given in column 4 of Table 4.

The agreement between the observed and predicted values is excellent (within 10 per cent) for both the Brent and the Holleford craters. For the Deep Bay crater, however, it is found that the volume estimated from the gravity data is only about 50 per cent of the predicted value. This difference is also indicated in equation 1, in which it was found that the mass deficiencies associated with these craters increase with increasing crater size as $D^{2.5}$, rather than D^3 as has been predicted.

At this stage of the investigation it is believed that not too much significance should be attached to the lack of agreement in the data for Deep Bay, which could be attributed to several causes. It has already been mentioned that there may be error in ΔM for Deep Bay, arising from uncertainties in eliminating regional effects, and that further investigation may show that the discrepancy stems, for the most part, from incorrect density assumptions in estimating the total volume. As is indicated in equations 2 and 3, a relatively small error in σ_a or σ_b , or both, would produce a considerable error in the total mass and volume of rock estimated from the gravity data. It will be recalled that the Deep Bay result has been deduced on the assumption that the rock densities involved are similar to those at Brent. Although this assumption seems logical enough, as far as the breccia and country rock are concerned, it is possible that the sedimentary rocks deep within the crater have densities that differ significantly from those used in the reduction. The final answer to the problem must await the results of a diamond drilling program now being planned for the Deep Bay crater.

Drilling results. Other observational evidence was, of course, obtained from the drill hole put down near the center of the Brent crater. This drilling penetrated 851 feet of sedimentary strata, to the original crater floor, and about 2650 feet of the underlying fragmental rocks. As far as can be judged the bottom of the hole just about reaches the lower boundary of the

ruptured zone. The drilling, therefore, provides an independent measurement of both the volume of the sedimentary rocks within the crater, or its present volume, and the volume of the breccia. The volumes based on the drilling results are shown in parentheses in the appropriate columns of Table 4.

The basin enclosing the sedimentary rocks at Brent is well defined topographically by an almost perfect circle [Millman and others, 1960] having a diameter of 9500 feet. For a maximum thickness of 851 feet at the center of the crater it is found that the sedimentary rocks occupy about 3.02×10^{10} ft³. The assumption, as before, is that the breccia zone has a surface diameter of 11,500 feet and depth at center equal to the depth of the drill hole, or 3500 feet, leads to a value of 1.82×10^{11} ft³ for the total volume of sedimentary and fragmental rocks and 1.52×10^{10} ft³ for the fragmental rocks alone. The volume of breccia and sedimentary rocks indicated by the drilling is therefore in excellent agreement (within 5 per cent) with the volume deduced from the gravity data. It also agrees (within 10 per cent) with the estimate of the total volume of country rock ruptured (column 4) during the formation of the crater.

Important also is the result that the volume of sedimentary rocks indicated by the drilling is about two-thirds of the volume of the original crater below plain (column 2) and that the volume of the breccia is almost in exact agreement with the predicted value given in column 3. This result, as one might expect, is due to the upper portions of the crater being affected more drastically by erosion than the underlying breccia zone. It should be pointed out, however, that complete agreement should by no means be expected, as this could result only if the elevation of the drill hole collar were known precisely in relation to the original level of the surroundings before crater formation. However, these results are considered to hold considerable significance because they show that the actual volumes of the sedimentary and fragmental rocks at Brent agree both in magnitude and in proportion with the volumes predicted for a crater of this size. It would be disturbing if, for example, it was found that in this best-studied crater the volume of sedimentary material (which provides an estimate of the original crater volume below plain) is several times greater than the volume

the breccia. Unfortunately, a similar comparison cannot be carried out for the Holleford crater because of the lack of drilling information at its center.

Summary of structural information. Figure 6, which has been drawn with identical vertical and horizontal scales, summarizes the topographical and structural details that have been determined from this and previous studies of these craters. A typical gravity anomaly profile for each crater is also shown for comparison. The present topographical relief of the craters is given by the solid lines; the original crater profiles, based on the general characteristics of explosion craters [Baldwin, 1949], are shown by the broken lines.

It will be noted that very little of the original rim has escaped erosion, which is not surprising considering the great age of these craters—at

least 70 m.y. for Deep Bay and 700 m.y. for the Holleford and Brent craters. On the other hand, it seems likely that the sedimentary rocks now filling these great depressions have tended to preserve their underground structure. Although much has been learned in previous studies concerning the effects of the impact and explosion of meteorites, attention has been focused chiefly on the surface effects, the resulting crater, the rim, and the fragmentation of surface rocks. The present investigation, on the other hand, shows that the disturbed zones extend to great depths that are proportional to the diameter of the crater, and it emphasizes the important fact that a major proportion of the deformational effects of the explosion underlie the floor of the resulting crater.

In concluding this section it can be said that gravity surveys carried out over these three

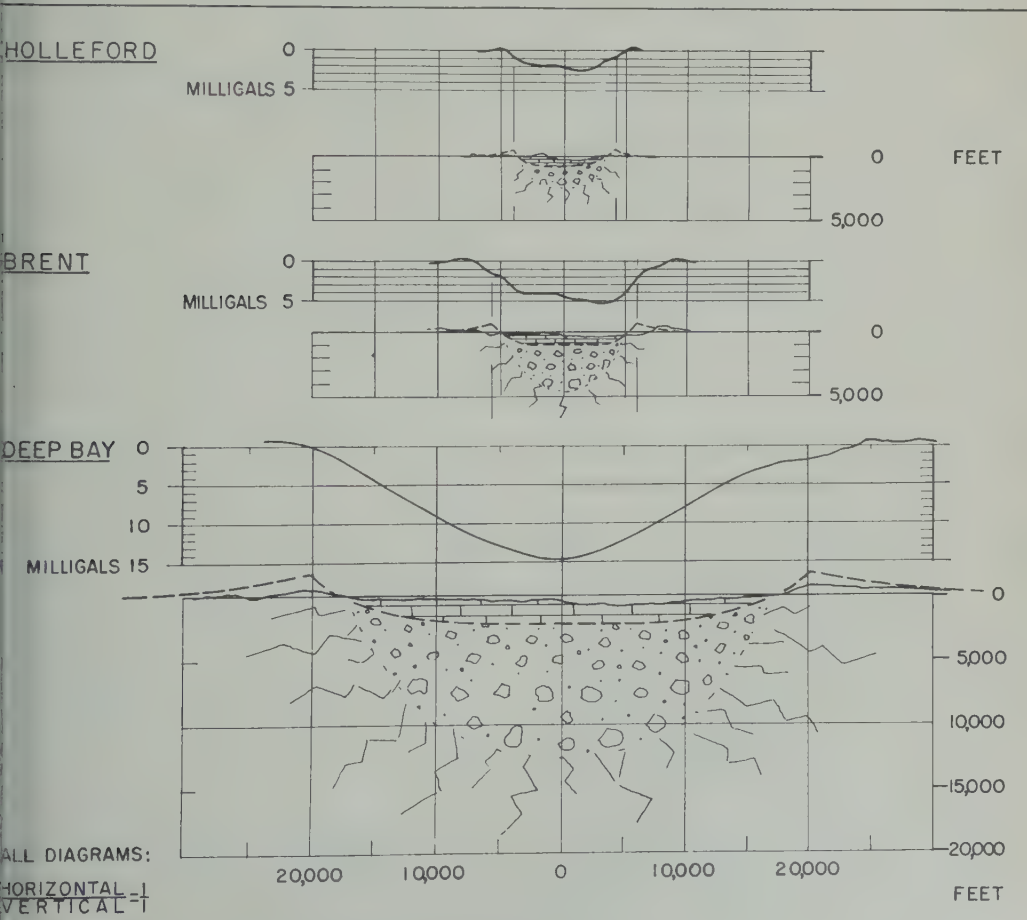


Fig. 6. Cross sections of craters.

fossil craters show that, within the limits of error in reducing the data, the total volume of the country rock ruptured during their formation increases, with increasing crater size, very nearly as the cube of the diameter. This confirms Rottenberg's analytical development, which showed that the depth of rupture due to meteoritic explosion in granitic rocks is about equal to one-third of the diameter of the resulting crater. The drilling results at the Brent crater confirm this conclusion and show that the volume of breccia is several times greater than the volume of sediments now occupying the crater. The general agreement between observation and prediction is extremely good, leaving little doubt that these three craters were formed by meteorite impact and explosion.

ENERGY CONSIDERATIONS

Energy consumed in fragmentation of the country rock. Since no mathematical treatment based upon first principles is available, the problem of estimating the kinetic energies and masses of crater-forming meteorites is not easily handled, and estimates are usually based upon extended extrapolations [Wylie, 1943; Baldwin, 1949; Rinehart, 1950; Hill and Gilvarry, 1956] from comparatively small explosions, or upon the direct calculation of the amounts of work done in crushing and ejecting the rock [Öpik, 1958; M. S. Macphail, personal communication, 1959]. But there have been no experimental data to demonstrate that such extrapolations are valid over the whole range of energies—from those released in small TNT explosions to the tremendous energies that must have been available to produce these three fossil craters and other meteorite craters of similar or larger dimensions.

As the gravity investigation has provided observational evidence for the amount of rock brecciation during the cratering process, it is possible to estimate with some confidence the minimum energies required for their formation, by direct calculation of the amount of work required to crush and fragment the rock. What is required is a good estimate of the average amount of work required to crush rock under the confining pressures existing in the upper part of the earth's crust by an explosive-initiated high-amplitude wave. For this, it would seem that no better value is available than might be obtained from the results of controlled under-

ground nuclear experiments. In the Rainier event [Johnson, Higgins, and Violet, 1959] rock was crushed to a radial distance of 130 feet from the point of detonation of the explosion. The energy consumed in crushing was estimated to be about 47 per cent of the total prompt energy released, equivalent to about 6.4×10^7 ergs/g. This combined with the volumes of fragmental rock associated with the three fossil craters, as estimated from the gravity surveys (column 7, Table 1), should provide a firm estimate of the minimum energies required to form these craters. The same value combined with equation 6 leads to the following general relation for the energy consumed in brecciation during the cratering process:

$$E_{(\text{crushing})} = 2.39 \times 10^{11} D^3 \sigma_c \quad \text{ergs} \quad (10)$$

for the crater diameter D in feet, or

$$E_{(\text{crushing})} = 8.44 \times 10^{12} D^3 \sigma_c \quad \text{ergs} \quad (11)$$

for the crater diameter D in meters. σ_c , as before, is the mean density of the country rock.

The solid curve in Figure 7 illustrates equation 10 for the general case, assuming a normal crustal density of 2.67 g/cm³. The crushing energies estimated for six North American craters of probable meteoric origin are listed in column 6 of Table 5. The energies shown by the triangles in Figure 7 are based on the gravity data. The largest disagreement with predicted values (about 50 per cent) is for the Deep Bay crater, but, as previously explained, until more investigation is carried out this result cannot safely be interpreted as evidence for a departure from the cube law for the higher energy ranges. It is satisfactory, however, that the sense of the departure is in a direction that suggests a less efficient transfer of energy for the larger craters.

Total meteorite energy and mass. Although the energies given by equation 10 seem reasonable enough and may be safely taken as the minimum energy requirements to produce craters explosively on impact, the estimates of total meteorite energy in column 6 of Table 5 and illustrated by the broken curve in Figure 7 are not so certain. The estimates of total energy, which are about twice the energy required for crushing alone, are based on the assumption that the proportions of the total available energy³ that go into heating

³ Total available energy per gram of crushed rock at Rainier was about 1.38×10^8 ergs.

TABLE 5. Table of Energies Predicted for Six North American Meteorite Craters

(1) Crater	(2) Diameter, ft	(3) σ_{cs} g/cm ³	(4) Total Mass Ruptured, grams	(5) Crushing Energy, ergs	(6) Meteorite Energy ergs	(7) Mt	(8) Meteorite Mass, tons ($V = 20$ km/sec)
Odessa	550	2.6	1.60×10^{12}	1.03×10^{20}	2.19×10^{20}	5×10^{-3}	120
Barringer	4,150	2.6	6.89×10^{14}	4.44×10^{22}	9.44×10^{22}	2.3	5.2×10^4
Holleford	7,709	2.79	4.74×10^{15}	3.05×10^{23} (2.47×10^{23})	6.49×10^{23}	16	3.6×10^6
New Quebec	11,290	2.67	1.42×10^{16}	9.14×10^{23}	1.95×10^{24}	47	1.0×10^6
Brent	11,500	2.67	1.50×10^{16}	9.66×10^{23} (8.69×10^{23})	2.06 ± 10^{24}	50	1.1×10^6
Deep Bay	40,000	2.67	6.34×10^{17}	4.08×10^{26} (2.01×10^{26})	8.69×10^{26}	2100	4.9×10^7

Note: Energy values in parentheses (col. 5) are based on gravity analyses.

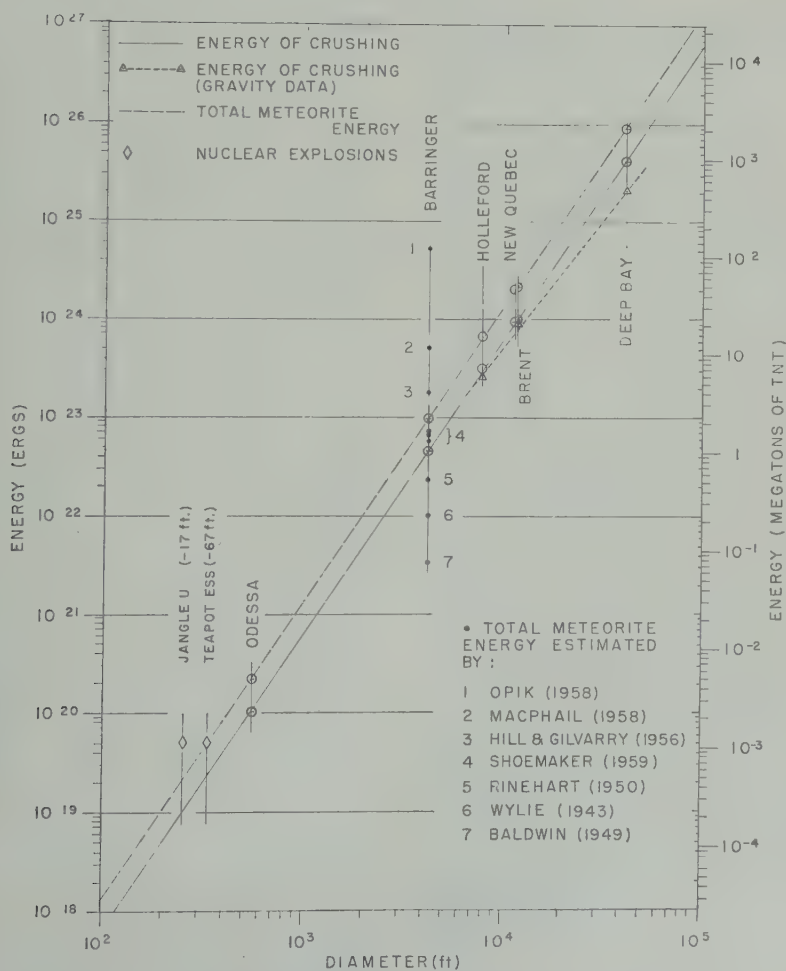


Fig. 7. Relationships between meteorite energy and crater diameter.

crushing, fracturing and elastic effects, etc., in meteorite crater explosions are the same as in the underground nuclear explosions and are given by

$$E_{\text{meteorite}} = 5.08 \times 10^{11} D^3 \sigma_c \text{ ergs} \quad (12)$$

For ready comparison with the results of other investigators, the total meteorite energies are also given in units of megatons of TNT equivalent¹ (column 7) and the corresponding meteorite masses for an impact velocity of 20 km/sec (column 8). If spherical, such meteorites would have diameters that are about 1/40 or 1/56 of the diameter of their resulting craters, depending on whether the meteorites are of stone with a density of 3.0 g/cm³ or of iron with a density of 7.8 g/cm³.

Until a great deal more is known about the partitioning of energies released on impact of high-velocity bodies, other than making comparisons with the results of other investigators, there is very little that can be said about the accuracy of these estimates. Although there may be important differences, it is assumed here that impact explosions are no less efficient in rupturing rock than confined nuclear explosions are and that the partitionings of energy are the same. Recently, data have been published [Johnson, Higgins, and Violet, 1959] for two craters, Teapot-Ess, about 335 feet in diameter, and Jangle-U, 250 feet in diameter. Both were formed by nuclear explosions having energy yields of 1.2 kilotons. The depths from surface to the detonation points were, respectively, 67 and 17 feet. Data for these explosions are shown by the diamond symbols in Figure 7, in which it will be seen that the energy for the Teapot-Ess crater is almost identical with the value predicted by the scaling curve for a meteorite crater of this size. As the Teapot-Ess crater has been shown [Shoemaker, 1959] to be structurally similar to the Barringer crater, this result lends considerable support to the validity of the assumption that the partitionings of the energy of impact explosions do not differ significantly from those in confined nuclear explosions. It should be mentioned that both the Teapot-Ess and Jangle-U craters were formed from shots fired in alluvium, and the meteorite craters under discussion are in hard rock. The comparison may

still be approximately valid, however, since crater dimensions seem to be remarkably insensitive to the properties of the material.

As many studies dealing with this problem of estimating the energies of crater-forming meteorites have been carried out for the Barringer crater, the results of a number of these have been included in Figure 7. That the problem is a difficult one is obvious from the wide disagreement in the results, the extreme values of which differ by more than three orders of magnitude. The value of the energy predicted in Table 5 is slightly larger than the result obtained by Shoemaker [1959] by direct cube-root scaling from the Teapot-Ess crater.⁵ It is of interest to note that energies estimated by scaling from high explosives form a group (points 5, 6, and 7 of Fig. 7) that are generally smaller than those estimated by the scaling curve. It has been pointed out by Shoemaker that scaling energetically from chemical explosions leads to an underestimation of the energies of meteorite craters because their initial pressures are lower than those of nuclear explosions, in which a significant portion of the energy is used in melting the rock.

On the other hand, the estimates by M. S. Macphail (personal communication, 1959) and Öpik [1958], both obtained by direct calculation of the energy consumed in crushing and ejection, are, respectively, one and two orders of magnitude greater than is predicted here, largely because in both these studies it is assumed that a much greater proportion of the total available energy is necessary for ejection of materials, heating, seismic effect, etc. Macphail estimates the energy consumed in fragmenting the rock at the Barringer crater on the basis of evidence from ore-crushing experience. It was found that a modern crushing mill requires about 2.7×10^8 ergs/g to crush 'average' rock to 3-inch size and about 4.1×10^8 ergs/g to pulverize it. Macphail estimated that about 10 per cent of the fragmental material at Barringer consists of rock flour, which leads to 6.5×10^7 ergs/g for an average value of the energy required for rupture. Although this is in good agreement with the value assumed in this investigation, Macphail considered the energy consumed in fragmentation

¹ 1 megaton (Mt) of TNT equivalent = 4.2×10^{22} ergs.

⁵ Although a diameter of 4150 feet has been used here, Shoemaker's illustration suggests that 3800 feet might be more appropriate for the original diameter of the crater, which would reduce the estimate to 7.3×10^{22} ergs.

represent only about 6 per cent of the total energy available. Öpik [1958] used a value of 0.5×10^6 ergs/g for the energy of crushing and assumed that it represented only about 3 per cent of the shock energy. However, the success of equation 12 in predicting the dimensions of the Teapot-Ess crater suggests that both these estimates are too large.

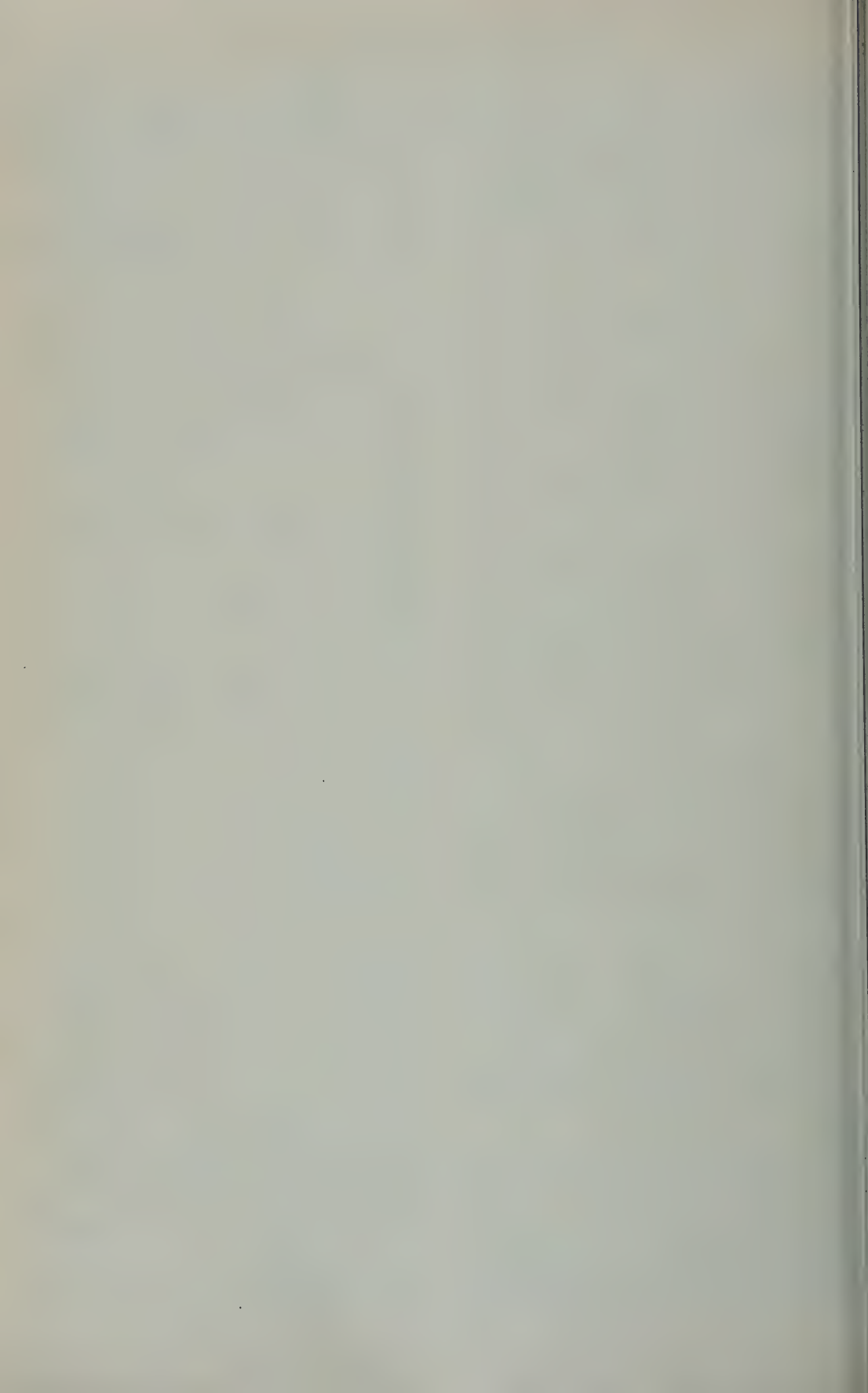
Finally, some remarks might be in order regarding the use of cube-root scaling in predicting energies. Equations 10 and 12 follow this conventional law, which merely states that the volume of rock affected is proportional to the energy released. Wylie [1943], Baldwin [1949], Rinehart [1950], and others have estimated the energy and mass of the meteorite that formed the Barringer crater on the assumption that the crater volume is directly proportional to the energy released by the incident meteorite. Though Rostoker [1953], LaPaz [1952], and others have questioned this assumption, Hill and Gilvarry [1956], in a detailed investigation of this subject, pointed out that evidence from controlled explosions tends to confirm this proportionality, which in turn implies that Baldwin's both-diameter relationship is inconsistent with cube-root scaling. In an attempt to overcome this difficulty, these authors developed methods for determining the energy yield of a meteorite by means of modified scaling laws that are consistent with the Baldwin relation and at the same time preserve different features of cube-root scaling. However, it seems probable that the extremely restricted range of the cratering experiments would hide any tendency for the connection between energy and crater volume to become other than linear. It is considered, therefore, that in our present knowledge no better estimate can be made of the energy than that obtained by assuming that the total volume of rock disrupted (as given by equation 6) is directly proportional to the kinetic energy of the meteorite. It is clear from the foregoing that this assumption is consistent both with Baldwin's diameter-depth relationship and with cube-root scaling.

Continued geophysical and structural studies of fossil meteorite craters, coupled with comprehensive drilling programs, offer a splendid opportunity not only to improve our knowledge of the early history of the earth but also to provide important information about the effects of impact explosions for the higher energy ranges.

Acknowledgments. It is a pleasure to thank Dr. C. S. Beals, Dominion Astronomer, who has taken a keen interest in this work and has given valuable advice. I acknowledge the able assistance of Mr. D. K. Smith with the winter gravity observations at Deep Bay and of Mr. L. W. Sobczak with the density measurements for the Brent crater. I am also grateful to Dr. J. A. Rottenberg and Mr. A. C. Hamilton for critically reading the manuscript.

REFERENCES

- Baldwin, R. B., *The Face of the Moon*, University of Chicago Press, Chicago, 1949.
- Beals, C. S., A probable meteorite crater of Precambrian age at Holleford, Ontario, *Publs. Dominion Observatory*, 24, no. 6, 1960.
- Beals, C. S., G. M. Ferguson, and A. Landau, Analogies between lunar and terrestrial topography, *J. Roy. Astron. Soc. Canada*, 50, 203-250, 1956.
- Beals, C. S., M. J. S. Innes, and J. A. Rottenberg, The search for fossil meteorite craters, *Current Sci. (India)*, 29 (6 and 7, June and July), 205-218 and 249-262, 1960.
- Charters, A. C., High speed impact, *Sci. American*, pp. 128-140, October, 1960.
- Fielder, G., How craters are formed, *Discovery*, 18, 45, 1957.
- Hammer, Sigmund, Estimating ore masses in gravity prospecting, *Geophysics*, 10, 50, 1945.
- Hill, J. E., and J. J. Gilvarry, Application of the Baldwin crater relation to the scaling of explosion craters, *J. Geophys. Research*, 61, 501-511, 1956.
- Innes, M. J. S., A possible meteorite crater at Deep Bay, Sask., *J. Roy. Astron. Soc. Canada*, 51, 235-240, 1957.
- Johnson, G. W., G. H. Higgins, and C. E. Violet, Underground nuclear detonations, *J. Geophys. Research*, 64, 1457-1469, 1959.
- LaPaz, L., Meteoroids, meteorites, and hyperbolic meteoritic velocities, in *Physics and Medicine of the Upper Atmosphere*, chapter 10, University of New Mexico Press, 1952.
- Meen, V. B., Chubb crater, Ungava, Quebec, *J. Roy. Astron. Soc. Canada*, 44, 169, 1950.
- Millman, P. M., Editorial note, *Sky and Telescope*, 11, 9, 1951.
- Millman, P. M., B. A. Liberty, J. F. Clark, P. L. Willmore, and M. J. S. Innes, The Brent crater, *Publs. Dominion Observatory*, 24, 1960.
- Öpik, E. J., Meteor impact, *Irish Astron. J.*, 5, 14, March 1958.
- Rinehart, J. S., Some observations on high speed impact, *Popular Astron.*, 58, 458, 1950.
- Rostoker, Norman, The formation of craters by high speed particles, *Meteoritics*, 1, 11-27, 1953.
- Shoemaker, E. M., Impact mechanics at Meteor Crater, Arizona, *U. S. Geol. Survey, Open File Rept.*, July 1959.
- Wylie, C. C., Calculations on the probable mass, of the object which formed meteor craters *Popular Astron.*, 51, 97, 1943.



The Origin of Folding in the Earth's Crust

V. V. BELOUSSOV

*Institute of Physics of the Earth
Academy of Sciences of the USSR, Moscow*

Abstract. In the light of recent special study, folding phenomena represent the reaction of the layered beds of the earth's crust on the differential vertical movements of separate blocks of the crust. It is possible to distinguish the following types of folding. *Block folding* represents the most direct reaction of layers on the vertical movements of the crust's blocks, the most characteristic of this type of folding being boxlike folds. They occur both on platforms and in geosynclines. *Injection folding* is due to the horizontal flow of the more plastic rocks, which are squeezed out from some areas and accumulate in others, where injection or piercement cores are formed. The flow of plastic rocks results from the uneven load of superimposed layers and especially from the fractures that cut these layers. The main places of occurrence of injection folding are foredeeps and tectonic basins. *Metamorphic or deep folding* is connected with the processes of granitization and metamorphism when the density of rocks becomes lower as the result of the impregnation of rocks by volatile substances. Reduced density induces upward flow, as a result of which deep diapirlike structures are formed. The folding of *general crumpling* mostly represents the influence of gravitational forces provoking the sliding of layers down the slopes or the spreading out of the upper parts of the elevated blocks. Such spreading out creates horizontal compressive forces which crumple the adjacent layers into folds. Sometimes the folding of general crumpling is created by the pushing apart under the mechanical influence of injection cores or of deep metamorphic diapirlike structures. The deep folding and the folding of general crumpling occur widely in geosynclinal belts. There are no indications in the phenomena of folding of the existence of general compressional forces in the earth's crust. Horizontal compression exists only as a local phenomenon and is limited to some narrow belts within geosynclines. The causes of horizontal compression are also local. Only vertical movements of separate blocks of the crust exist as primary phenomena.

HISTORICAL INTRODUCTION

Layers of sedimentary rocks are originally laid in the horizontal position, as Leonardo Vinci already knew toward the end of the fifteenth century. In the seventeenth century Nicolaus Steno, in studying the rocks of Toscana, was convinced that the layers he observed tilted from the horizon were moved from the original position by the action of certain mechanical forces [Steno, 1669]. In the eighteenth century V. Lomonosov, while observing the layers of mountain rocks which piled 'like collapsed vaults, one link on the other, on edges, erect, on side,' regarded this irregularity as the deposit of layers as the result of the activity of underground flames which 'rupture the plane lying above and along clefts seek the way into the open. When at large they abandon the fractured joints to their weight which fails to support the broken pieces into straight position in order' [Lomonosov, 1763].

At the end of the eighteenth century the geologists gradually came to distinguish a

certain geometrical regularity in the seeming disorder of the disposition of the layers, observed mainly in mountainous regions. It was noted that the separate parts of the tilted layers could be joined into a series of more or less regular wavelike curves, concave and convex, now known as folds. In size the folds vary from those so small that several can be seen in a piece of rock scarcely as large as the palm of one's hand to tremendous curves several kilometers high.

Considerable progress has been achieved since then in the study of folding formed by the layers of rocks in the earth's crust. In various regions the form of folding has been studied in detail, and many features of the geometry of folding have become known. It has been determined that intensive folding originates in the geosynclines, that is, in the most mobile zones of the earth's crust characterized by the great swing and contrasts of vertical (oscillatory) movements of the crust.

There are two stages in the 'lifespan' of every geosyncline [Beloussov, 1956, 1958, 1959a].

During the first stage the subsidence of the earth's crust is predominant, the geosyncline is a sea basin on the subsiding bottom of which the sediments accumulate many kilometers thick, and the rising zones within the geosyncline have the form of island chains. During the second stage, in contrast to the first, upward motion predominates: new island chains appear which expand and form high ranges; the sea recedes from the geosyncline; and the geosyncline is succeeded by a considerable mountainous relief. The layers crumple into folds mostly during the second stage; the process of folding is closely connected with the development of high elevations within the geosyncline. As the two-stage development of the geosyncline is known to be periodic and to a certain extent synchronic for all continents, certain epochs can be distinguished in the history of the earth when crumpling of layers into folding was most intensive. From the beginning of the Paleozoic era these epochs of strong folding occurred at the end of the Ordovician and the beginning of the Silurian eras (the Caledonian folding epoch), in the middle and upper Carboniferous (the Hercynian epoch), in Paleogene and Neogene (the Alpidic epoch). On the coasts of the Pacific Ocean the last folding epoch developed somewhat earlier, at the end of the Jurassic and the beginning of the Cretaceous periods.

These epochs of folding alternate with periods of comparative calm that coincide in time with the stages of the main subsidence of the geosynclines. The folding that is active during a certain epoch forms its own folded zone on the surface of the earth. In this connection the Caledonian, the Hercynian, and the Alpine folded zones can be distinguished along with other numerous and ancient (pre-Paleozoic) folded zones. The folded zones of different age markedly overlap one another, and the process of folding occurs repeatedly in the same place. Since in the process of geological history the geosynclines become narrower and occupy smaller areas on the surface of the earth the folded zones also shrink: the Alpine folding appears in belts much narrower than the Hercynian folding, the Hercynian has an area less than the Caledonian, etc. As soon as the geosyncline dies out in a certain area, the area forms a platform and does not experience further effective folding. Owing to these circumstances the geological structure

of the platform has two stories distinctly outlined: the lower story is the folded basement of the platform, which was formed and crumpled into folds when the conditions of the geosyncline were still existent; the upper story is the so-called platform cover with undisturbed layering that did not experience severe folding.

The distinctions among different types of folding have been established only in the last few decades [Beloussov, 1945]. The folding which developed in the mountain ridges that formed the geosynclines and which until recently drew so much attention turned out to be only one of the many types of folding. Because of its stretched form of the folds with narrow parallel waves between them this folding is often called linear; and because it entirely covers the territory of the folded zone, leaving no unfolded gaps, it is also called complete or holomorphic.

Another type is the domelike or discontinuous (idiomorphic) folding, which consists of separate uplifts having the form of round or oval domes or elongated swells. These folds range in length from hundreds of meters to scores of kilometers and in amplitude from scores of meters to 1.5 kilometers. Sometimes they form a chain in one constant direction, and sometimes they are scattered in disorder over an area. It is a peculiar trait that between the uplifts the layers are undisturbed, thus making only convex folds and none concave.

Folding of the second type, as well as the complete folding, develops in geosynclines. It occupies the outlying parts of a geosyncline and the parts within it that have a comparative calm development of the oscillatory movements of the crust. For example, the intermountain depressions found in geosynclines between the ridges and on the outskirts of a geosyncline and the foredeeps which divide the geosyncline from the platform, are zones of development of such foldings.

The second type of folding is often observed not only within the geosynclines; it is also found on platforms, mostly on the subsided parts, the so-called 'synclises.' In general, the discontinuous or domelike folding has much wider distribution over the earth's surface than the complete folding, especially during the recent geotectonic cycles.

Whereas the morphology of folding and the history of its development have been studied

re or less satisfactorily, progress in the study of the causes of folding has indeed been slight. We shall not be too far from the truth if we state that during many decades almost nothing has been achieved in this field.

For a long time (the fourth quarter of the nineteenth century and the beginning of the twentieth) the contraction hypothesis of the origin of folding was widely accepted. According to this hypothesis the globe of the earth had contracted, causing the crust to wrinkle. This concept is too well known to need restating here. Its importance derives from its assumption that the activity of the horizontally directed crumpling forces at any given spot causes the most folding, plastic zones of the crust, namely the synclines, to crumple into folds, as if crushed under the pressure of hard platforms drawing toward each other as a vise.

The contraction theory can no longer be considered to meet the demands of modern scientific observations. It cannot interpret the extremely complex, though regular, development of the oscillatory movements of the earth's crust. It fails to explain the discontinued folding in the synclines and on the platforms, since the formation of isolated dome uplifts cannot result from the horizontal shrinking of the earth's crust. Modern calculations of the thermal history of the earth lead to the conclusion that the globe has still heating, or at any rate not cooling (it should not be overlooked, by the way, that the contraction hypothesis was suggested before the discovery of radioactivity, with which the release of heat in the interior of the earth is connected). Many other findings also contradict the hypothesis.

The old contraction theory was followed by other theories about the processes in the interior of the earth which also assumed that folding is the result of horizontal shrinking of the earth's crust, if not over the whole surface of the earth simultaneously then at least over large areas.

For instance, the hypothesis of the drifting continents, which connected folding with the pressure the continents exert on each other when they 'bump together' can be considered one of the theories [Wegener, 1922]. The hypothesis of undercrustal currents is another [Kraus, 1959]. Denying the possibility of the presence in the earth's mantle of slow displacements of material by convection-type currents, the hypothesis

assumes that in the place where the undercrustal current is making a whirl downward it would suck in the part of the earth's crust above it. The central part of the area subsides, the elevated edges approach each other, and the layers of the area are crumpled into folds.

All such concepts associate folding with horizontal compression of parts of the earth's crust. In contrast, some other suggestions were proffered that supported the interpretation of the process of folding by entirely different principles. Foremost among these suggestions is the hypothesis of the gravitational origin of folding [Haarmann, 1930; Bemmel, 1954]. This hypothesis claims that the earth's crust as a whole does not undergo compression, but only slow, wavelike vertical uplifts and depressions. On the slopes of the uplifts the layers of rocks with plastic and creeping properties are in an unstable condition and can slowly flow down under the influence of gravity, though the angles of inclination may be very small. When resisted by rocks which lie lower down along the slope the moving layers ruffle into folds.

These newer concepts considered folding a secondary phenomenon resulting from the vertical oscillatory movements of the earth's crust. They connected the oscillatory movements of the earth's crust with the formation of folding much better than previous theories and overcame difficulties in the explanation of discontinued folding: the separated uplifts that comprise it could be considered the result of the activity of local vertical movements of the earth's crust analogous to its oscillatory movements.

The solution of the problem of the origin of folding was much hindered by an obstacle which would seem strange to workers in other sciences. Even though both the theoretical and the practical significance of the causes of folding was evident, until recently almost no one was specially engaged with the problem. It may have seemed possible that this perplexing problem could be solved more or less by chance along with other problems, perhaps with geological surveys or with the study of the geological structure of certain deposits.

RECENT STUDIES

Only during the last few years have special researches of folding been undertaken by the Institute of Physics of the Earth, the Academy

of Sciences of the USSR, which were headed by the author. The study of the detailed structure and the history of the development of folded zones formed the basis of these researches. Moreover, the natural material for the observations is chosen from the point of view of this problem alone, without the necessity of adaptation to the needs of any other tasks.

Of course, the problem of the origin of folding, like any other large scientific problem, is infinite, and we can hardly expect that it will ever be completely solved. The stages in its solution, however, can certainly be defined; and in this article the author intends to give a brief report of some results obtained during the earliest work upon the problem.

The first and somewhat unexpected result was the conclusion that, during geological surveys of regions with complex folding, the geologist, limited by the given scales of the maps and profiles he is drawing, can almost never reflect in his documentation the folding as it is in reality. He is forced, to a certain extent, to approximate. Often the approximation results in a serious distortion of the real forms and sizes of folds, and the form and the size of the fold are the most important criteria in the understanding of the course of its formation. Owing to this circumstance the special research revealed many peculiarities in the morphology of the folds and their groups that previously had almost escaped notice.

Researches were conducted in various regions of folding of the USSR, but they were mainly concentrated in the Caucasus, where the conditions of work were best. Data dealing with the structure of folding on territories abroad were also applied. The method of simulating the process of folding on small models made of plastic materials (petrolatum, resin, clay, etc.) proved

to be a useful aid in the understanding of many questions about the mechanism of the folding process.

The folds that are observed in nature can be divided not into two, as in earlier classification, but into four types, depending on the immediate mechanisms of their formation. This classification of folds might be called kinematic, because it is based on the character of movements of the layers of the crust of the earth directly resulting in the formation of folds [see also Beloussov, 1959b].

The first and simplest type is *block folding*. The formation of this folding is directly connected with the vertical uplifting of separate blocks of the earth's crust. At a certain depth, for instance, in the comparatively hard basement of the platform, such blocks are bounded by fractures either vertical or almost vertical. Even in the layers of the platform cover, which are more plastic, the uplifting of the blocks can result in the upward arching of the layers without fractures. This arching is called *transverse* because the arching force is applied perpendicularly to the layer.

The most characteristic form for this type of folding is the box form of folds. Often they are asymmetric, with one steep limb and the other gently inclined (Fig. 1). The model shows that when the covering plastic rocks are very thin, the shape of the arching layers changes markedly from the bottom upward, and from boxlike below it gradually becomes a gently arching swell above. It can be supposed that the slight sloping swells and domes in the eastern regions of the Russian platform with the dip of the layers only 1° to 2° are examples of this mechanism of formation. Down below they are associated with the uplifting of blocks of the earth's crust along faults.

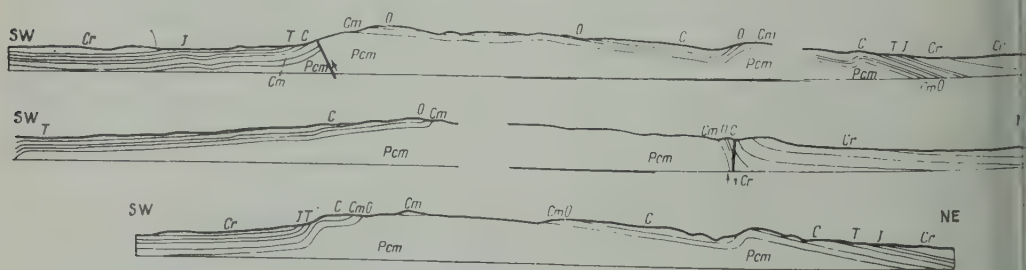


Fig. 1. Examples of box folds of block origin. Box folds in the Rocky Mountains, United States. After Darton.

Block folding is found on platforms and in geosynclines. On platforms the block folding is expressed in its 'purest' form, though the amplitude of folds in the average is less than in geosynclines. Within geosynclines the block folds are more distinctly expressed in the foredeeps and intermountain depressions, but they undoubtedly occur also on the uplifts, where they are often screened by folding of other types.

The second type of folding is *injection folding*.

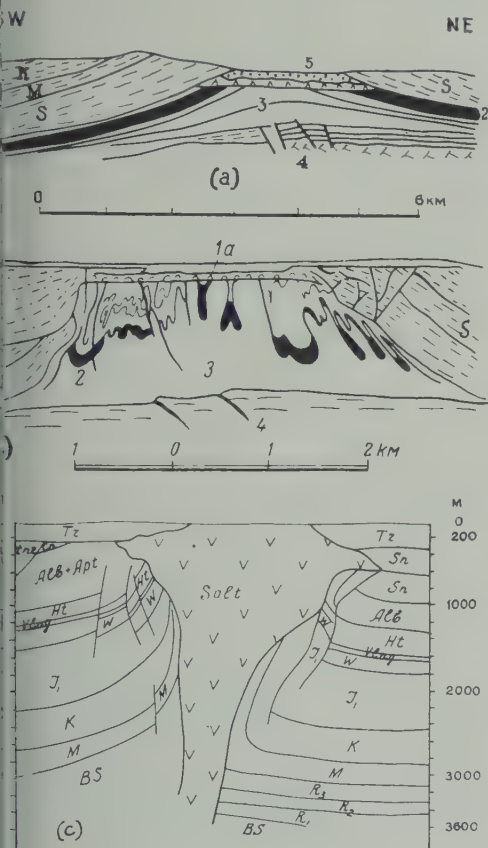


Fig. 2. Injection folds with cores of different ages. (a) Injection core formed by salt in the shape of a lens: 1, 2, 3, salt and gypsum of Permian age; 4, underlying rocks; 5, covering rocks of the Permian age, Hannover region (FRG); after Seidl [1963]. (b) Injection core in the shape of a tree stump formed by salt and anhydrite: 1a, caprock; 2 and 3, salt and anhydrite layers of the Permian age; 4, underlying rocks; 5, covering rocks of the Triassic to Tertiary; after Bentz [1949].

When, in sedimentary formations, a series of especially plastic rocks is deposited, such as salt, gypsum, clays, or thin alternations of clays and marl, under certain conditions such material can start moving. In this process the plastic material flows out from certain locations, and when displaced for a certain distance in the horizontal direction it accumulates in other places. In the areas from which the material flows its quantity lessens and the thickness of the plastic series diminishes; and, correspondingly, in places of compression the series thickens, forming a bulge. Various shapes are observed in such bulges. They may have the form of a lens (Fig. 2a); they often are domelike or resemble swells (Fig. 2b). Frequently the plastic material accumulates in the shape of a column reaching the height of several kilometers with the diameter of hundreds of meters (Fig. 2c). The shape to which the plastic mass is molded depends largely on the structure of layers above and primarily on the existence of fractures in them. The fractures may be used by the plastic material as passages for its movement (Fig. 3). In their turn the overlying layers are affected mechanically by the movement of the plastic material underneath. This plastic material in places of its injection raises the layers above, and these layers, depending on the form of the 'injection core,' arch up either like a dome or like an elongated swell, stretching and cracking while they rise. The plastic material can break the layers above it, intrude into fractures, forming the 'piercement core,' and push the layers aside. At the same time in the places of outflow of plastic material the overlying layers sink down slightly.

Like the first type of folding the injection folds are characterized by distinctly expressed anticlines alternating with wide and gentle subsidences or with wide plots of completely undisturbed layers (Fig. 3).

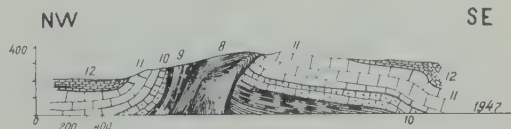


Fig. 3. The fold with clay injection core (the Jura Mountains, France). 8, Clays of the Oxford layer of the Upper Jurassic. 9-12, Higher layers of the Upper Jurassic. The injection core is formed along the fracture in the overlying layers of rocks. After Glangeard and Schneegans [1949-1950].

The internal structure of the injection or piercement core is interesting. If the plastic mass has good layering, the plastic layers of the injection core are often found to be bent into complex and squeezed small folds (Fig. 2b). The general thickness of plastic layers in the location of injection increases as the result of their crumpling into folds, but the thickness of each separate layer remains unchanged. In simpler situations the plastic layers form the symmetric or asymmetric convex fold dipping steeply into the core and becoming progressively gentler on the limbs with distance from the core (Fig. 3).

What are the causes of the underground horizontal flux of plastic rocks with the formation of injection and piercement cores? The general cause is the loss of gravitational equilibrium in the sedimental layers and the urge to restore that equilibrium by redistribution of material.

For example, if rocks with lower specific weight are deposited under rocks with comparatively greater specific weight the distribution is unstable, since rocks have plastic and creeping properties. A slight curve of the discontinuity between the underlying lighter rocks and the covering heavier rocks with the horizontal upper surface of the heavier is sufficient to start the lighter rocks to flowing from places where their upper discontinuity is somewhat lowered (and where, consequently, the overlying layers exercise the greatest pressure) to places of accumulation where the roof of the lighter rocks is elevated and where, therefore, the pressure on them is less. Once the movement begins it develops further: the lighter rocks elevate and the heavier sink down, trying to change places with the lighter ones. If the overlying layers are not cut by fractures, the lighter rocks rise within the heavier in the form of columns. The distance between these columns is much greater than the diameter of each column. On the surface above such columns the upper layers rise up and form domes between which the upper layers quietly subside over extensive areas. But, if the covering layers have linear fractures, the injection core adapts to them and becomes comblike and elongated along the fracture.

The most typical representation of this kind of injection folding is the diapiric dome with a core of salt. The specific weight of salt (2.1) is less than the mean specific weight of most of the sedimentary rocks (2.3). Moreover, salt under

the conditions of pressure from all directions flows freely. Therefore, when a thick salt layer is deposited under sufficiently heavy layers of other sedimentary rocks, the salt endeavors to come to the surface and in doing so forms columns that penetrate into the overlying rocks (Fig. 2c) [Barton, 1925; Nettleton, 1934, 1941; Parker and McDowell, 1955; Trusheim, 1957].

The described reverse distribution of heavy and light rocks (the heavy over the light) is not, however, the necessary condition in the formation of injection folds. The horizontal flow of plastic rocks with their squeezing up in some places can also be observed when their specific weight is equal to that of the covering rocks. This flow of plastic rocks is provoked by the uneven surface pressure on them, which can be caused by the undulating surface relief. Then the plastic rocks under the risings are subjected to heavier pressure than the plastic rocks under the lowering of the relief. All this creates conditions for the squeezing of plastic material from under the risings toward the valleys, where it can be squeezed in the form of injection folds (Fig. 4).

The uneven pressure can also be connected with the presence of fractures in rocks covering the plastic layers. A fracture, especially a large and complicated one, consisting, as it often happens, of a whole series of parallel separate fractures, is the cause of reduction of pressure at the depth, because every fracture is to a certain extent an aperture in the overlying rocks. If the fracture reaches the surface of the plastic layers the material of these layers is drawn to the fracture; it then penetrates into the fracture and rises upward, elevating and pushing aside the neighboring layers (Fig. 3). It is necessary, however, for the weight of the covering layers to be heavy enough to make the plastic layers flow. The accumulation in the fracture zone is

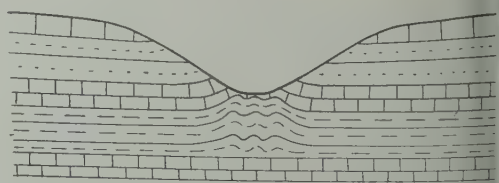


Fig. 4. Diagram of the formation of injection layers under uneven relief. Plastic layers (S) deposited under the watershed and subjected to considerable load are squeezed in the direction of the valley, where they are crumpled into folds.

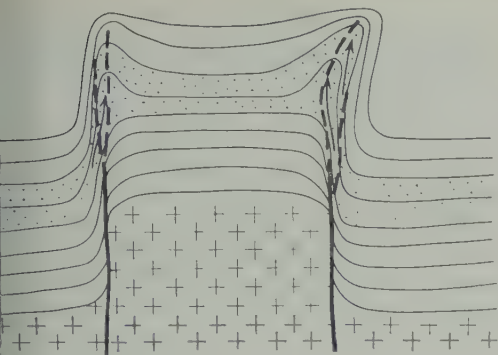


Fig. 5. Diagram of the formation of injection folds above the limbs of the box block fold. The plastic layers are shown by dots; crosses indicate crystalline basement; thick and dotted lines, fractures; arrows, the direction of the flow of plastic material.

doubtedly, largely facilitated by the decrease in the specific weight of the rocks at the expense of the water, often mixed with natural gas, which circulates in the fracture through the altered clay mass. Accumulation could also be promoted by the increased stratum pressure of the water and gas observed in some oil and gas formations.

Probably, these last conditions of the formation of injection folding, in connection with the fractures in the covering layers, occur very frequently in nature.

The connection of injection folding with fractures results in certain interesting peculiarities in the location of the folds. For instance, they are often formed above the steep limbs of the box folds by the pumping up of that limb of the material of some of its plastic layers (Fig. 5). The box folds, as we have stated above, are of block origin. At a certain depth the steep limb of such a fold corresponds to a fracture. But the branches of the fracture also stretch up where

softer rocks make a curve in the form of a box fold. The steep limb of that fold is always pierced by a net of small fractures which create the zone of weaker pressure where more plastic rocks penetrate from below.

It is now established that the large subsidences and uplifts of the earth's crust, that originated as the result of its oscillatory movement, usually do not consist of simple gentle curves of the crust, but on account of its block structure they form steps. Each step is separated from the next by a fracture or by a sharp flexure of the layers. Such fractures or flexures between the steps are favorable locations for the formation of the injection folds above them caused by the squeezing of the plastic material from the steep limb of the flexure upward (Fig. 6).

Injection folds have an extremely wide distribution in nature. Diapiric domes are observed on platforms and especially in the foredeeps of the geosynclines. Elongated in the form of ridges, the injection folds with core consisting mainly of very plastic clays develop in great numbers in the foredeeps and intermountain depressions of the geosynclines. They are found in the Terek foredeep of the Caucasus, in the foothills of the western Alps, and in many other places. They are also often encountered on the structurally complex geosyncline uplifts, where they follow the structural ledges dividing separate steps that complicate the slopes of the uplifts.

On the basis of mechanism of formation, folds of the deep or metamorphic type are very similar to injection folds.

It was noticed long ago [Wegmann, 1930; Eskola, 1949; Kranck, 1957] that the characteristic peculiarity of the structure of comparatively deep zones of the earth's crust, the cross sections of which could be seen on the surface of the deeply eroded crystalline shields

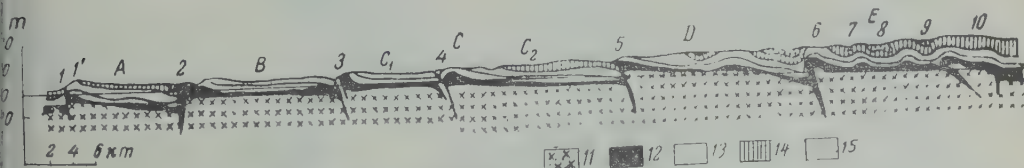


Fig. 6. Injection folds observed in fractures in the Jura Mountains, France. 11, The ancient folded basement. 12, Plastic clays, marls, and gypsum of the Triassic. 13-14, Limestone and marls of the Jurassic. 15, Limestone, marls, and clays of the Cretaceous and Paleogene. The numbers show separate folds; letters indicate individual blocks of the earth's crust divided by fractures. After Glangeard [1949-1950].

like the Baltic Shield (Karelia, the Kola Peninsula, Finland, Sweden), is manifested in the existence of great granitic domes and swells emerging through the surrounding various metamorphic rocks (Fig. 7). In respect to shape and method of formation these domes are analogous to the salt diapiric domes, though they are much larger. It is now agreed by all geologists that the 'fresh' granite originates either by remelting of the granite of earlier formation or by 'granitization,' that is, by production of granite from various sedimentary and metamorphic rocks in the process of partial melting and recrystallization in place. This process is always connected with the impregnation of old granites and other rocks with volatile substances and with the formation of large quantities of hot solutions, vapors, and gases. The saturation of rocks with volatile components reduces the density of these rocks [Eskola, 1950; Bederke, 1953]. Therefore the 'fresh' granite which has not yet finally hardened and is still saturated with volatile substances has lower specific weight than the covering 'dry' metamorphic and sedimentary rocks. This particular circumstance induces the 'fresh' granite to emerge and form domes and columns.

While penetrating into the covering formations the granitic columns elevate the overlying metamorphic rocks and bend them, forcing them to form domes with steep, often vertical, sides. Growing in diameter, the granitic columns press

on the slates that fill the space between the columns and have steep or vertical layering, and squeeze them. This compression of slates between the granitic columns has an irregular distribution: it is stronger in the directions where the distance between the neighboring granitic columns is less, but in the direction where the distance between them is greater there are places that are less compressed. As the result of this process the sets of layers that are subjected to stronger compression are squeezed and stretched and their material flows to more 'spacious' locations between the domes. Here the material accumulates and bends into small, intricate, and irregular folds. It is of interest that such squeezing of material often occurs in the horizontal direction. For that reason the folds that are being formed have vertical axes and are discernible on horizontal cross sections. At the same time during the formation of injection folds on higher levels in the earth's crust the squeezed material is forced upward, and crumples into folds with horizontal axes observed in vertical cross sections. In all probability this peculiarity in the movement of the deeply deposited material is connected with the great resistance, existing in the deep zones of the earth's crust, which the thick overlying layers develop to prevent the movement of the material upward.

The studies by Haller [1955] of the ancient layers of Greenland indicate that the granitic gneiss domes (which are superseded by the

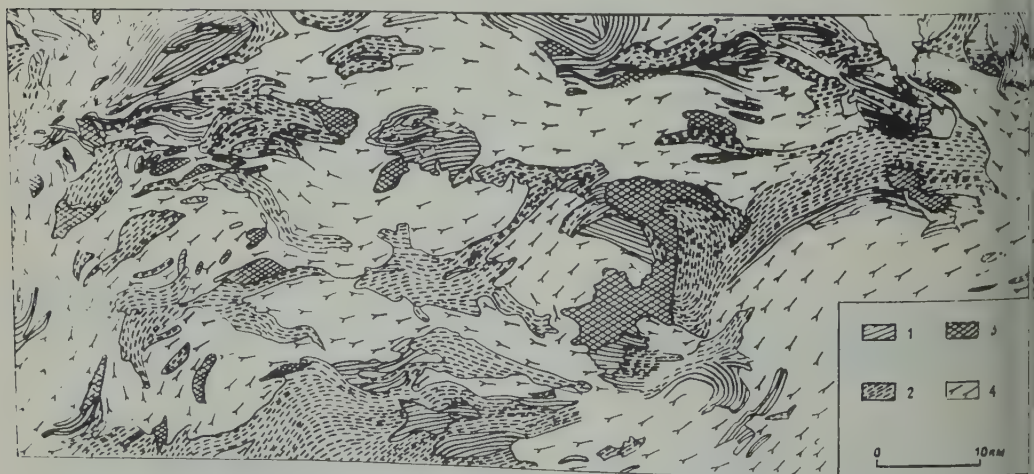


Fig. 7. Granite-gneiss domes in metamorphic slates in the Archean of Finland. 1, Various metamorphic slates of sedimentary origin. 2, Volcanic rocks turned into metamorphic slates. 3, Intrusion of gabbro and diorites. 4, Granite-gneiss (Turku region). After Simonen [1960].

agated swells where the covering layers have fractures that facilitate and guide the movement of the granitic material) often have a very complicated form. 'Visors' protrude from the sides of these domes; they sometimes even look like mushrooms (Fig. 8). Evidently, such domes are formed when the granite during its granitization overcomes strong resistance of the overlying rocks, and at certain levels the material of the domes, not having strength enough to overcome the covering layers or to pierce them, overflows, penetrating into the surrounding rocks horizontally.

It can be added that during the granitization of metamorphic slates are saturated by volatile substances also, and their density decreases. This explains why the slates also endeavor like sponges to rise through the overlying and less metamorphosed layers of the upper zones of the earth's crust. These slates take advantage of the fractures in the upper zones, fill them, and displace the overlying rocks and push them apart. Meanwhile, in the injection zone they themselves collapse into small and closely pressed folds, similar to the folds formed by the salt layers in the core of the diapiric dome.

With these deformations, which occur in 'fresh' granite and in slates that are metamorphosed under the influence of hot solutions and vapors, is called *deep folding*. It is evident that this folding is largely the same as injection folding, the peculiarity of the physicochemical conditions in the deep regions of the crust compel us to recognize it as a separate type.

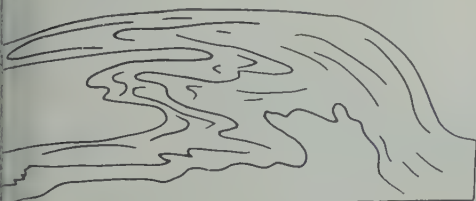
Deep folding is observed not only on ancient crystalline shields but also on deep cross sections of younger folded zones. For example, the so-called Pennine nappes in the Alps could be considered to belong to this type of folding. The nappes are formed by folds which are

steeply inclined at depth but lie flat on higher levels. Their cores consist of granites and gneisses and the limbs of strongly metamorphosed Mesozoic slates. It has been determined that the granites and gneisses, which are mainly ancient (probably Paleozoic), underwent a 'refreshing' process in the Paleogene as the result of the inflow of hot solutions and vapors from the deep layers below [Wenck, 1953]. This process of 'refreshing' and the associated decrease of the specific weight of rocks account for the uplift of folds. The parts of these folds horizontally bent form what we now call the Pennine nappes (Fig. 9).

The last type of folding might be called the *folds of general crumpling*. This is the linear or complete folding which is usually considered to represent the main type of folding within geosynclines. That this folding is observed in geosynclines is true, but the idea that folds of general crumpling predominate in geosynclines is erroneous. In reality, much larger areas of geosynclines are filled by the block, injection, and deep folding taken together. The folds of general crumpling usually form only narrow zones in the parts of the geosyncline where the greatest contrasts in the oscillatory movements are observed, that is, where maximum uplifts and maximum subsidences are in closest proximity.

For instance, over the whole Caucasus region folds of general crumpling make only a narrow zone mostly along the southern slope of the Main Caucasus Range. This zone runs into the axis part of the Range and a little way into the northern slope in the High Daghestan, where deep folding is also present. On the remaining parts of the Caucasus only block and injection folds have developed.

Folds of general crumpling undoubtedly originate from the horizontal compression of a certain part of the earth's crust, or rather of a series of layers. The folds of general crumpling are the folds of the longitudinal bending since the active pressing forces are directed in the plane of the layer. The horizontal compression forces, however, are unquestionably of a strictly local character and have nothing in common with the previously supposed general constriction of the earth's crust, or even of its large areas. The fact that the folds of general crumpling are found in limited areas within the geosynclines, and are



8. The form of a granite-gneiss dome in the ancient rocks of Greenland. After Haller [1955].

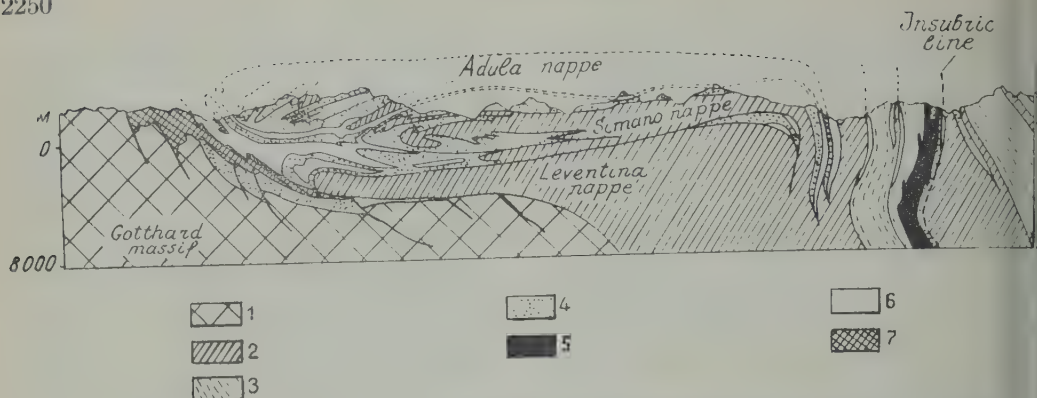


Fig. 9. Pennine nappes in the Alps. 1, Ancient granites of the Gotthard massif. 2, Granite-gneisses of the Pennine nappes, which experienced 'refreshing.' 3, Migmatites—rocks that originated as the result of dispersed penetration of granites into sedimentary rocks. 4, Regionally metamorphosed Paleozoic and Mesozoic rocks. 5, Later magmatic intrusions. 6, Mesozoic sediments on the Pennine nappes. 7, Mesozoic sediments on the Gotthard massif. After *de Sitter* [1956].

surrounded with regions where block and injection folds are developed, strikingly manifests the local character of the horizontal compression forces. Detailed study of the structure of the folded zones ultimately confirms this conclusion.

The observations reveal a number of particular causes which give rise to the local horizontal compression with the formation of the folds of general crumpling. All these causes are related to one another according to their regular connection with certain characteristic peculiarities in the development of the geosynclines.

What are the observed mechanisms of the origin of horizontal compression in the thick series of layers of geosynclines, if analyzed systematically?

The simplest mechanism is the gravitational flowing or sliding of series of rocks down the slopes of the uplifts that develop in geosynclines. Very plastic rocks, such as soft, sodden clays, can flow down the slopes of the uplifts in geosynclines, thus forming gigantic landslides.

Moreover, the clays drag along other rocks which alternate with clays. When meeting an obstruction the clay layers pile up at the lower end of the slope and crumple into folds.

The so-called Helvetian nappes on the northern slope of the western Alps (Fig. 10) are of that origin [*Schneegans*, 1938]. The horizontal displacement of such nappes may be very large—almost as much as 40 km. Such long displacements could not be achieved in a single movement. Evidently, the nappes moved gradually, following the uplift, which elevated and widened within the geosynclines.

Another mechanism of the origin of local horizontal compression is connected with the block structure of the earth's crust. It has already been mentioned that the limbs of the uplifts in the geosynclines usually have a step-fault structure. Each step is formed by a separate block of the earth's crust elevated above the one next to it down the slope and lower than the one just above it. On the crest of the uplift and at its



Fig. 10. The scheme of structure of the Helvetian gravitational nappes in the western Alps. The nappes consist of Mesozoic and Paleogene rocks. The sliding occurred on the plastic rocks of the Paleogene Flysch. After *de Sitter* [1956].

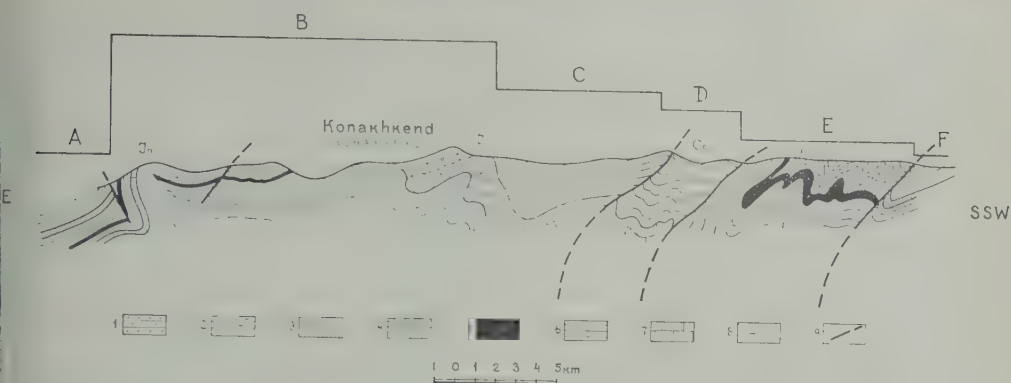


Fig. 11. Schematic profile across the southeastern Caucasus in the region of the Konakhkend village (the Azerbaijan SSR). 1, Miocene. 2, Oligocene. 3, Eocene and Paleocene. 4, Upper layers of the Upper Cretaceous; 5, Coniacian and Turonian layers of the Upper Cretaceous. 6, Lower Cretaceous. 7, Upper Jurassic. 8, Middle and Lower Jurassic. 9, Tectonic faults. The broken line above the profile shows the place of blocks of the earth's crust; A-F indicate separate blocks; In shows injection folding in the scars between blocks A and B, B and C; Cr are the folds of general crumpling which formed on the surface of the lowered block under the pressure of the flowing upper part of the elevated block. After A. M. Shourigin.

the relatively lifted and lowered blocks arrange like a keyboard. The observations show that a relatively elevated block under the force of gravity has a tendency to flow plastically in its upper part in the direction of the neighboring lower block. When the blocks are arranged like a keyboard, all blocks flow in their upper part to one side and down their common slope, toppling one over another in succession. When an isolated block is lifted up and is elevated above both neighboring blocks on either side of it, this block flows on both sides, acquiring the form of a fan (Fig. 11).

In connection with this flow of blocks the upper parts of the vertical faults, which separate the blocks, bend and tilt under the block. Sometimes they even become horizontal. Quite a number of faults that are thought to be overthrusts are really the bent upper parts of the vertical faults.

The upper flowing part of the elevated block lies horizontally on the layers lying on the

surface of the neighboring lower block and crumples them into folds. The results of that pressure may differ, depending on the height of the step, on the degree of flow of the upper part of the elevated block, on the width of the lower block, and on the characteristics of the rocks. The pressure can result in crumpling into folds of only a narrow strip in the immediate vicinity of the ledge, or it can crumple the whole surface of the lower block (Fig. 11).

The next mechanism of crumpling layers into complete folds is connected with the action of the injection folds that push the overlying layers apart. When penetrating into the overlying layers the injection core pushes apart the neighboring layers, which might result in the formation of folds of longitudinal compression on certain areas, that is, local folds of general crumpling (Fig. 12).

The deep injection connected with metamorphic folding has similar efficiency. When the granitized or metamorphosed mass emerges and

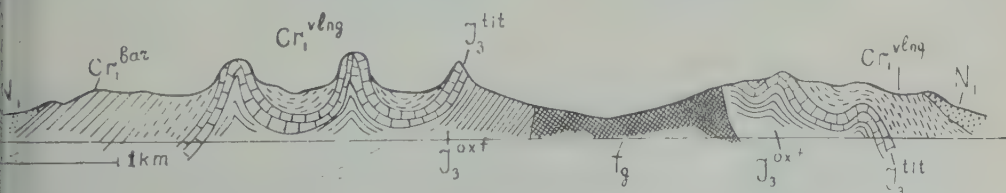


Fig. 12. The injection folds Gigondas in Provence, France. Under the influence of the injection core which drives layers (I_0) apart the neighboring Cretaceous and Jurassic rocks are crumpled into folds. After Goguel [1953].

penetrates into the overlying rocks, it drives them apart and crumples them on certain areas into the folds of general crumpling. Sometimes this effect is not great, but it can be very impressive. It is probable, for example, that many of the folds in the Appalachians have been developed by the horizontal pressure of the enormous granitic domes and of an equally great mass of metamorphic slates rising with the domes, which now constitute the Piedmont plateau (Fig. 13).

The combination of the mechanisms described, which is different in each particular case, results in a certain distribution of the folds of general crumpling within the geosynclines. The gravitational flowing and slidings, the flow of the tops of uplifted blocks, the pushing aside by the injection and deep folds—all these mechanisms have much in common and are inherently connected with the specific conditions in the geosyncline, since they are the results of intensive vertical movement of material in the geosynclines and of the contrasts in the vertical movements and steep dips in the layering of rocks and in relief. That is the reason why the folds of general crumpling develop in geosynclines.

CONCLUSION

Viewing all the different types of folding, we can recognize in them the general reaction of the layered parts of the earth's crust to the vertical displacements of the material of the crust. In different situations this reaction has different degrees of complexity. It is simplest in block folding, when the layers are only uplifted after the movement of the block. It is more complicated in injection folding. On the background of the vertical movements of the blocks the hori-

zontal flow of more plastic series of layers commences, and is followed by vertical injection by way of the fractures formed in connection with the movements of blocks. Finally, the formation of the folds of general crumpling reflects a still more intricate reaction, which includes gravitational displacement along the slope, flow of the uplifted blocks, and the pushing aside force of the injection and deep folds. At the same time the deep folds themselves, though having much in common with injection folds, retain their specific characteristics.

In accordance with this sequence, block folding in their 'pure' form are best developed in the regions with the smoothest and least contrasting oscillatory movements of the earth's crust. These regions are observed on the most undisturbed parts of platforms. Injection folds originate in the somewhat more active tectonic conditions within deep depressions on the platform or in the parts of the geosynclines whose development was not very complicated. The folds of general crumpling reflect the state of the most intensive and contrasting oscillatory movements of the earth's crust.

All specific traits of deep folding are fully displayed when we try to establish the character of the distribution of folds in the vertical cross-section of the earth's crust, when we learn how the shape of folding changes with depth, from one 'story' within the earth's crust to another. The available data allow us to consider the following description as the most probable (Fig. 14).

At the depth of the lowest story is the zone of the granitization and regional metamorphism with its deep folding, the main forms of which are granitic columns. This zone lies at varying

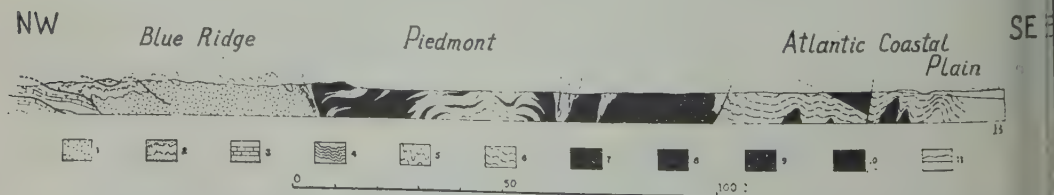


Fig. 13. Crumpling into folds of the Paleozoic rocks of the Appalachians under the influence of the deep granite-gneiss and metamorphic domes which push apart the neighboring layers. 1, Precambrian crystalline rocks. 2, Young Precambrian sedimentary rocks. 3, Paleozoic sedimentary rocks. 4, Metamorphic slates. 5, Granite-gneiss. 6, Mesozoic and Tertiary sediments of the Atlantic coast. Rocks 4 and 5 rising from below pushed aside the Precambrian and Paleozoic rocks. 8, Massifs of weakly foliated acidic rocks. 9, Diorite and gabbro; younger sedimentary rocks. 10, Triassic. 11, Cretaceous and Tertiary. The profile after King [1959].

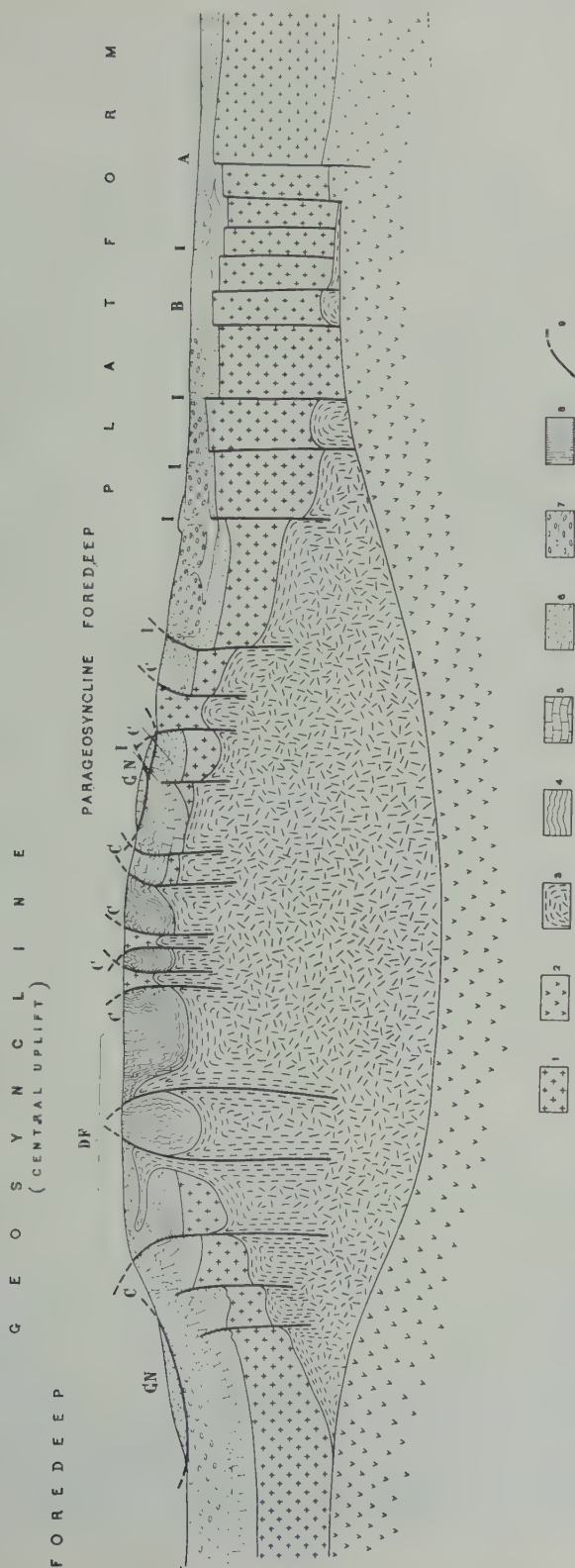


Fig. 14. The general scheme of various types of folding. 1, Granite layer of the earth's crust. 2, Ancient crystalline basement. 3, Young granite-gneisses and migmatites. 4, Sediments of the lower terrigenous formation. 5, Sediments of the calcareous formation. 6, Sediments of the upper terrigenous formation. 7, Sediments of the lagoon and molasse formation. 8, Salt, gypsum. 9, Tectonic faults. *DF*, Deep folding. *C*, The folding of general crumpling. *GN*, Gravitational tectonic nappes. *I*, Injection folds. *B*, Block fold. *A*, A welt of block origin.

depth, probably to about 6-5 km. Above the lowest story lies the story characterized by its block structure. Here the blocks are forced to move up and down to certain levels mainly by the granitic columns and swells of the underlying deeper story. Eventually, the vertical movement of the blocks in the middle story by the mechanisms previously described, results in the formation of block, injection, and general crumpling folds in the upper story.

It is evident that new data convey a more complicated concept of the genesis of folding than the old theory that connected folding with the general contraction of the earth's crust. But at the same time these new concepts are considerably more concrete. They contribute to the classification of folds according to their origin and to the study of conditions of formation of separate natural folds. As long as geologists, consciously or implicitly, applied the contraction hypothesis in their theories, as they did until very recent times, they never thought about the origin of a particular fold which they were studying. And it would have seemed strange to study the origin of only certain folds when the problem of folding was being elucidated for the entire globe. The possibilities and the responsibilities of the geologist now are completely different. Now we can and should study the conditions of formation of each particular fold similarly to the way the geologist studies the conditions of formation of other geological objects: rocks, minerals, fossil organic remnants, etc. The conditions of formation of even near-by folds could be different. Thus a completely new approach is contemplated both in the study of folding of crustal layers and in the methods of their investigation.

REFERENCES

- Barton, D. C., The American salt dome problems in the light of the Roumanian and German salt domes, *Bull. Am. Assoc. Petrol. Geologists*, 9 (9), 1925.
- Bederke, E., Regionalmetamorphose und Granit-aufstieg, *Geol. Rundschau*, 41, 1953.
- Beloussov, V., On types of folding, *Soviet Geol., Collection of papers*, 8 (in Russian), 1945.
- Beloussov, V., Grundfragen der allgemeinen Geotektonik, *Geol. Rundschau*, 45, H. 2, 1956.
- Beloussov, V., Some rules governing the development of the earth's crust, *Endeavour*, 17(68), 1958.
- Beloussov, V., Fundamental features of the structure and development of geosynclines, UGGI, Assoc. seism. et de phys. de l'int. de la terre, *Public. Bureau centr. seism. int., Série A, Travaux scient.*, fasc. 20, Toulouse, 1959a.
- Beloussov, V., Types of folding and their origin, *Intern. Geol. Rev.*, 1 (2), 1959b.
- Bemmelen, R. W. v., *Mountain Building*, The Hague, 1954.
- Bentz, A., *Erdöl und Tektonik*, 1949.
- De Sitter, L. U., *Structural Geology*, McGraw-Hill Book Co., New York, London, Toronto, 1956.
- Eskola, P. E., The problem of mantled gneiss domes, *Quart. J. Geol. Soc. London*, 104, part 4, 1949.
- Eskola, P. E., The nature of metasomatism in the processes of granitization, *Intern. Geol. Congr. 18th session*, part III, London, 1950.
- Glangeaud, L., Le rôle du socle dans la tectonique du Jura, *Ann. soc. géol. Belg.*, 73, 1949-1950.
- Glangeaud, L., and D. Schneegans, Caractères généraux du style jurassien (et des types comtois et haut-jurassien), *Ann. soc. géol. Belg.*, 73, 1949-1950.
- Goguel, J., *Les Alpes de Provence*, Paris, 1953.
- Haarmann, E., *Die Oszillationstheorie*, Stuttgart, 1930.
- Haller, J., Der zentrale metamorphe Komplex von NE Groenland, T. 1., *Medd. Groenland*, 73 (3), 1955.
- King, P. B., *The Evolution of North America*, Princeton University Press, 1959.
- Kranck, E. H., On folding-movements in the zone of the basement, *Geol. Rundschau*, 64, H. 2, 1957.
- Kraus, E., *Die Entwicklungsgeschichte der Kontinente und Ozeane*, Berlin, 1959.
- Lomonosov, M. V., *On Strata of the Earth*, Petersburg, 1763.
- Nettleton, L. L., Fluid Mechanics of salt domes, *Bull. Am. Assoc. Petrol. Geologists*, 18 (9), 1934.
- Nettleton, L. L., Recent experimental and geophysical evidence of mechanics of salt dome formation, *Bull. Am. Assoc. Petrol. Geologists*, 27 (1), 1943.
- Parker, J. J., and A. N. McDowell, Model studies of salt dome tectonics, *Bull. Am. Assoc. Petrol. Geologists*, 39 (12), 1955.
- Schneegans, D., La géologie des nappes de l'Ubaye-Embrunais entre la Durance et l'Ubaye, *Mémoire carte géol. France*, 1938.
- Seidl, E., Beiträge zur Morphologie und Genesis der permischen Salzlagertstätten Mitteldeutschlands, *Z. deutsch. geol. Ges.*, 1913.
- Simonen, A., Plutonic rocks of the Svecofennides in Finland, *Bull. comm. géol. Finlande*, no. 189, 1960.
- Steno, N., *De solido intra solidum naturaliter contracto*, Florence, 1669.
- Trusheim, F., Über Halokinese und ihre Bedeutung für die strukturelle Entwicklung Norddeutschlands, *Z. deutsch. geol. Ges.*, 109, part 1, 1957.
- Wegener, A., *Die Entstehung der Kontinente und Ozeane*, third edition, Braunschweig, 1922.
- Wegmann, C. E., Über Diapirismus, *Compt. rend. soc. géol. Finl.*, 1930.
- Wenck, E., Prinzipielles zur geologisch-tektonische Gliederung des Penninikums im zentralen Tessin, *Eclogae Geol. Helv.*, 46(1), 1953.

Geomagnetic and Solar Data

J. VIRGINIA LINCOLN

Central Radio Propagation Laboratory
National Bureau of Standards, Boulder, Colorado

PRINCIPAL MAGNETIC STORMS

(Advance knowledge of the character of the records at some observatories as regards disturbances)

Observatory (Observer- Charge)	Green- wich date	Storm-time		Sudden commencement			C- figure degree of ac- tivity ⁴	Maximal activity on K-scale 0 to 9			Ranges			
		GMT of begin.	GMT of ending ¹	Type ²	Amplitudes ³			Gr. day	Gr. 3-hr period	K- index	D	H	Z	
					D (6)	H (7)	Z (8)							
(1)	(2)	(3)	(4)	(5)	(6)	(7)	(8)	(9)	(10)	(11)	(12)	(13)	(14)	(15)
L. C. Cravens)	1961	<i>h m</i>	<i>d h</i>		<i>'</i>	<i>γ</i>	<i>γ</i>					<i>'</i>	<i>γ</i>	<i>γ</i>
	Jan. 19	14 41	20 20	s.c.*	-16	-60	+53	ms	20	4,5,6	7	287	1960	970
	Feb. 4	06 00	5 02	ms	4	7	7	164	1530	620
	Feb. 13	02 52	13 21	s.c.*	+5	-4	+5	ms	13	4,5	6	200	990	690
	Feb. 16	00 43	16 19	s.c.*	+6	+50	-14	ms	16	4,5	6	305	1110	780
	Feb. 17	20 27	18 22	s.c.*	-33	+226	-51	ms	18	4,5	7	271	2000	1450
	Mar. 10	07 57	10 22	ms	10	3,4	7	237	1340	1040
	Mar. 13	23 16	15 00	s.c.*	+6	-33	+11	ms	14	4	7	150	1370	860
	Mar. 19	03 ..	20 04	ms	19	5	7	163	1180	847
	Mar. 27	15 03	27 22	s	27	6	8	421	1840	1010
L. C. Clevén)	Jan. 9	07 00	9 19	ms	9	4,5	6	70	380	350
	Jan. 19	14 30	20 22	ms	20	4	7	70	770	680
	Feb. 4	12 00	5 13	ms	4	5,8	6	50	460	480
									5	3	6			
	Feb. 6	01 06	6 17	s.c.*	+1	+40	-5	ms	6	3,4	7	60	640	530
	Feb. 13	02 53	13 18	s.c.	+1	-4	-2	ms	13	3,5,6	6	60	490	400
	Feb. 16	00 44	16 16	s.c.*	-1	+3	-2	s	16	4	8	60	650	660
	Feb. 17	09 00	18 22	s	18	4	8	90	1040	800
	Mar. 5	09 33	6 15	s.c.	-1	+7	+3	s	6	5	8	105	1550	720
	Mar. 10	08 00	10 14	s	10	4	9	135	1280	1250
L. C. Clevén (Sabbén)	Mar. 19	05 00	19 20	ms	19	3	7	60	510	350
	Jan. 8	16 18	9 24	s.c.*	+1	+19	0	ms	9	8	6	30	170	85
	Jan. 19	15 00	20 20	ms	19	7	7	45	210	105
	Feb. 4	13 31	5 09	s.c.*	-4	+10	0	ms	4	7,8	7	50	240	160
	Feb. 13	02 53	13 20	s.c.*	-2	+4	0	m	13	4,6	5	25	135	80
	Feb. 17	10 00	21 24	ms	18	6	7	50	225	155
	Mar. 5	18 00	6 15	m	5	8	5	40	170	95
									6	1,2				
	Mar. 9	13 27	10 19	s.c.*	-5	+38	0	ms	10	3	6	20	220	55
	Mar. 14	00 00	16 16	ms	15	8	6	25	165	80
L. C. Clevén (Gebhardt)	Mar. 18	14 00	20 21	m	18	7				
									19	2,3				
									20	6,7				
	Mar. 27	15 03	28 17	s.c.*	-8	+44	0	ms	27	6	6	30	145	85
												20	135	80
	Jan. 19	12 ..	20 19	m	20	1,3	5	25	110	63
	Feb. 4	13 31	s.c.*	+4*	+15	+2	ms	4	7,8	6	37	154	238
		18 29	5 12	s.c.*	-2	+70*	+13	m	13	4	5	17	102	59
	Feb. 13	02 53	14 03	s.c.	0	+8*	-1	m	16	5	5	19	99	56
	Feb. 16	00 44	16 22	s.c.	+1	+18	-2	m	18	1	6	44	165	94
L. C. Clevén (Gebhardt)	Feb. 17	05 ..	18 22	ms	19	5	5	21	81	33
	Feb. 19	06 ..	23 02	m	19	5	5	21	81	33
	Mar. 5	18 ..	6 14	ms	6	1	6	34	135	120

Approximate time of ending of storm construed as the time of cessation of reasonably marked disturbance movements in the more specifically, when the K-index measure diminished to 2 or less for a reasonable period.
 s.c. = sudden commencement; s.c.* = small initial impulse followed by main impulse (the amplitude in this case is that of an impulse only, neglecting the initial brief pulse); .. = gradual commencement.
 Signs of amplitudes of D and Z taken algebraically; D reckoned positive if towards the east and Z reckoned positive if vertically downwards.
 Storm described by three degrees of activity: m for moderate (when K-index as great as 5); ms for moderately severe (when K as great as 7); s for severe (when K = 8 or 9).

PRINCIPAL MAGNETIC STORMS. Continued

Observatory (Observer-in-Charge)	Greenwich date (2)	Storm-time		Sudden commencement			C-figure, degree of activity ⁴ (9)	Maximal activity on K-scale 0 to 9			Ranges			
		GMT of begin. (3)	GMT of ending ¹ (4)	Type ² (5)	Amplitudes ³			Gr. day (10)	Gr. 3-hr. period (11)	K-index (12)	D (13)	H (14)	Z (15)	
					D (6)	H (7)								Z (8)
Tucson (C. J. Beers)	1961 Mar. 9	h m 13 27	d h 10 18	s.c.*	γ +4*	γ +12	γ -1	ms	10	4	7	47	188	16
	Mar. 13	23 17	16 14	s.c.*	0	+4*	-1	m	14	2	5	24	94	4
	Mar. 19	04 ..	20 02	m	16	1,3
	Mar. 27	15 03	28 16	s.c.*	+5*	-25*	-2	m	19	2,3	5	26	119	5
									27	6,7	5	27	150	3
									28	2				
	Jan. 8	16 18	10 03	s.c.	+1	+4	m	8	6	5	12	84	2
									9	2,3,4				
	Jan. 19	15 ..	20 20	m	20	1,3	5	14	100	3
	Feb. 3	09 08	4 06	s.c.	-1	+24	+1	m	3	4,5,6	4	9	54	2
	Feb. 4	13 32	5 14	s.c.	+1	+9	+1	ms	4	7	6	19	213	5
	Feb. 6	01 06	7 11	s.c.	-1	+14	+1	m	6	3	4	5	47	1
	Feb. 16	00 44	17 11	s.c.	+1	+6	m	16	4,5	5	13	67	1
	Feb. 17	05 ..	18 23	ms	17	4	6	23	190	4
									18	1,3,4				
	Mar. 5	19 ..	6 15	ms	6	1,5	6	19	143	5
	Mar. 9	13 27	10 15	s.c.	+1	+17	+2	ms	10	4	6	12	117	3
	Mar. 13	23 ..	16 15		14	1,2,3,4	5	15	97	3
									15	2,4				
									16	1,3				
	Mar. 18	12 ..	20 23		19	2,3	5	14	82	3
	Mar. 27	15 06	28 10	s.c.	+1	+8	m	27	6	5	13	82	4
	Mar. 31	15 11		s.c.*	+3	+7	+1							
San Juan (M. Vazquez)	Jan. Feb. 4	18 30	No Storms 5 10	s.c.	+0.4	+19	-5	m	4	7	7	7	181	4
	Mar.		No Storms											
Honolulu (C. D. Upham)	Jan. 8	16 17	9 24	s.c.	+	+	+	m	9	4	5	3	90	
	Jan. 18	06 00	20 22	m	20	3	5	6	60	
	Feb. 3	09 08	5 18	s.c.	+	+	+	ms	4	7	6	7	200	
	Feb. 4	18 28		s.c.*	+	+	+							
	Feb. 6	01 06	6 22	s.c.*	+	+	+	m	6	3	5	5	50	
	Feb. 13	02 53	14 02	s.c.	+	+	+	m	13	4,5	5	5	93	
	Feb. 16	00 42	16 23	s.c.	+	+	+	m	16	3,4,5	4	4	83	
	Feb. 17	06 00	19 18	ms	18	1	6	7	190	
	Feb. 17	17 21		s.c.	+	+	+							
	Mar. 5	09 32	6 18	s.c.	0	+2	+2	m	5	7	5	7	170	
	Mar. 9	13 27	10 20	s.c.	+0	+15	+9	ms	10	4	6	17	190	
	Mar. 13	23 00	16 14	m	14	1	5	5	80	
	Mar. 18	12 35	20 02	m	19	2,3	5	6	90	
	Mar. 27	15 03	28 16	s.c.	+0	+17	+7	m	28	3	4	7	65	
	Mar. 31	15 11	3 17	s.c.	+0	+14	+3	m	1	1	4	8	155	
Huancayo (A. Giesecke)	Jan. 7	20 47	9 24	s.c.	0	+24	+2	ms	8	7	6	10	314	
	Jan. 18	12 00	19 02	m	18	5,6,7	5	6	195	
	Jan. 19	10 50	20 21	ms	19	7	6	10	277	
	Jan. 26	06 34	26 21	ms	26	5,6	6	6	141	
	Feb. 3	09 07	3 17	s.c.	-1	+25	+4	ms	3	6	6	8	264	
	Feb. 4	13 31	5 07	s.c.*	+2	+92	+4	ms	4	7	7	10	438	
	Feb. 6	01 06	6 17	s.c.	+1	+20	+4	ms	6	6	6	8	284	
	Feb. 13	02 53	13 23	s.c.	0	+13	+4	ms	13	5,7	6	8	223	
	Feb. 16	00 42	16 22	s.c.	0	+28	+4	m	16	5,6	5	9	198	
	Feb. 17	06 40	18 18	ms	17	6	6	9	384	
	Feb. 20	02 00	21 22	ms	21	5,6	6	7	249	
	Mar. 5	17 51	6 18	ms	6	1	6	8	306	
	Mar. 9	13 27	10 21	s.c.*	+2	+75	+5	ms	10	4,5	6	7	312	
	Mar. 14	00 21	14 21	m	14	6,7	5	5	126	
	Mar. 16	03 09	19 23	m	19	5,6	5	9	274	
	Mar. 27	15 03	27 22	s.c.*	+2	+112	+7	ms	27	6	7	7	343	
Port Moresby (J. A. Brooks)	Jan. Feb. 4	13 31		s.c.	No Storms									
	Feb. 4	18 29	5 13	s.c.	0	+15	+12							
	Mar. 9	13 27	10 17	s.c.	+1	+27	+24	m	4	7	6	11	169	
(No Record 04-07 h March 10).														
								ms	10	4	7	(5)	(310)	(1)

GEOMAGNETIC AND SOLAR DATA
PRINCIPAL MAGNETIC STORMS. Continued

2257

Observatory (Observer- Charge)	Green- wich date	Storm-time		Sudden commencement			C- figure, degree of ac- tivity ⁴	Maximal activity on K-scale 0 to 9			Ranges				
		GMT of begin.	GMT of ending ¹	Type ²	Amplitudes ³			Gr. day	Gr. 3-hr. period	K- index	D	H	Z		
					D	H	Z								
(1)	(2)	(3)	(4)	(5)	(6)	(7)	(8)	(9)	(10)	(11)	(12)	(13)	(14)	(15)	
Manus (M. van Rijk)	1961	<i>h m</i>	<i>d h</i>		<i>'</i>	<i>γ</i>	<i>γ</i>								
	Jan. 7	20 48	10 00	s.c.?	+0.2	+2	+2	m	8	6,7	5	19	122	84	
	(Further abrupt changes at 1617 U.T., Jan. 8)														
	Jan. 15	21 26	16 00	BAY	m	15	8	5	7	43	39	
	Jan. 18	06 ..	19 04	m	18	5	5	22	83	73	
	Jan. 19	13 ..	20 19	m	19	6,7,8	5	25	94	132	
	Feb. 3	09 07	4 00	s.c.	-0.6	+22	+15	m	20	5,6	5				
	Feb. 4	13 31	5 09	s.c.	+3.5	+15	+17	ms	3	5	5	18	64	65	
	Feb. 6	01 06	6 17	s.c.	+1.7	+12	+11	m	4	7,8	6	38	143	195	
	Small initial impulse in D only.														
	Feb. 16	00 44	16 18	s.c.	+0.2	+20	+14	m	6	6	5	28	132	69	
	Feb. 17	05 ..	18 19	m	16	4,5	5	22	120	50	
									m	17	5,7,8	5	28	113	109
	Feb. 20	00 ..	21 00	m	18	1	5				
	Mar. 5	17 ..	6 14	m	20	6	5	19	71	76	
	Mar. 9	13 22	10 18	s.c.*	+1.5	+19	+14	ms	5	7	5	22	89	90	
	Mar. 19	05 ..	20 00	ms	10	4	6	18	211	112	
Mar. 27	15 02	27 21	s.c.	-1.1	+15	+11	ms	19	6	6	22	96	116		
								ms	27	6	6	8	87	79	
Gara (Gregor)	Jan.	No Storms													
	No Record		Jan. 16 0700-2327												
			Jan. 26 1100-2400												
			Jan. 27 0100-0700												
	Feb. 4	13 32	5 12	s.c.	+2	+16	+4	ms	4	7	7	29	164	153	
	Feb. 6	01 06	6 19	s.c.*	-5*	+4	-17*	ms	6	6	6	26	76	175	
	Feb. 13	02 53	14 02	s.c.*	-1*	+3	-3*	ms	13	4,5	6	20	127	147	
	Feb. 16	00 42	16 23	s.c.	-4	+3	-12	m	16	3,4,5	5	23	100	187	
	Feb. 17	06 ..	22 17	ms	17	5	6	27	133	175	
									ms	18	4,5	6			
Mar. 9	13 26	10 13	s.c.*	+1	+20*	+5	ms	10	4	7	29	189	236		
Mar. 27	15 03	28 17	s.c.	+1	+18	+3	m	27	6	5	18	70	120		
Ingi (van der Wal)	Jan. 19	13 30	20 19	m	19	6,7	5	18	146	59	
									20	4,6					
	Feb. 4	13 32	5 12	s.c.	0	+24	+4	ms	4	7,8	6	36	205	130	
	Mar. 9	13 28	10 14	s.c.*	+27*	+5	m	10	4	7	40	253	105	
Riley (Lington)	Jan. 8	16 19	9 14	s.c.	+1	+9	-3	m	9	4	5	18	97	46	
	Feb. 3	09 09	5 10	s.c.	+0.7	+43	-2	ms	4	7	6	18	231	91	
	Feb. 6	01 09	6 18	s.c.*	+23	m	6	3,4	5	15	154	45	
	Feb. 13	02 54	13 17	s.c.	+13	-1	m	13	4	5	20	106	77	
	Feb. 17	05 00	18 15	m	17	5	5	20	188	73	
									18	4	5				
	Mar. 9	13 28	10 14	s.c.*	+0.9	+22	-4	ms	10	4	6	34	185	85	
	Mar. 27	15 05	28 10	s.c.	+1.0	+23	-4	m	27	6	5	14	129	48	

SELECTED GEOMAGNETIC AND SOLAR DATA
Kp, *Ci*, *Cp*, *Ap*, *K_F*, *Rz* and Selected Days
 March 1961

Day ¹	Three-hour Range Indices Kp^2									Prel. ³ Ci	Cp^4	Ap^5	3-hr. Range Indices K_F^6		Prov. R_z
	1	2	3	4	5	6	7	8	Sum				Values	Sum	
1	1+	3-	2o	2-	3+	0+	2-	2+	15+	0.3	0.4	8	1231 3123	16	15
2 q	2+	3+	3-	2-	0+	1-	1+	2o	14+	0.2	0.4	8	2321 1001	10	33
3 Q	3o	1+	1+	1-	1o	1o	0+	0+	9o	0.1	0.2	5	2111 1110	08	44
4 Q	0o	0+	1-	1-	2+	1o	0o	0+	5+	0.1	0.1	3	0100 2101	05	42
5	1o	2o	1o	1+	1-	1+	3+	6-	16+	0.9	0.8	14	1211 1235	16	34
6 D	7-	6o	4o	4+	4+	2-	1o	0+	28+	1.3	1.4	37	6533 4111	24	41
7 Q	0o	0o	0+	1-	1o	1o	2-	2o	7-	0.2	0.1	3	0000 1122	06	31
8 Q	2-	2-	1-	1-	1-	1o	1+	2+	10o	0.2	0.2	5	1211 1012	09	46
9	2o	3-	3-	1o	3+	3o	3o	4-	21+	0.9	0.8	13	2330 3324	20	43
10 D	4o	5-	6+	7o	5o	3o	2-	1+	33o	1.4	1.5	46	4447 4222	29	29
11 q	1-	1+	2-	2-	2o	2-	2+	1o	12+	0.3	0.3	6	0211 2232	13	31
12 q	3+	1-	1o	2o	2-	1-	1-	2+	12+	0.2	0.3	7	3012 2112	12	14
13	3o	2o	3o	2-	2o	3o	2-	2-	18o	0.4	0.5	10	3142 2322	19	27
14 D	4+	5-	4+	4o	3+	4-	4o	2+	31-	1.2	1.2	26	4543 3332	27	46
15 D	2o	4o	3-	4+	5o	3-	3o	5-	28+	1.2	1.2	24	2334 4224	24	42
16	5-	3+	5+	3o	3+	3-	1-	1-	24-	1.1	1.0	20	5353 3211	23	52
17	2+	2+	5-	4o	3-	2-	1o	1+	20o	0.6	0.8	14	2244 3122	20	66
18	2o	1+	1+	0+	3-	4-	4o	3o	18+	0.8	0.7	12	3110 2333	16	51
19 D	2-	5o	6o	4-	5-	5+	4+	4-	34+	1.3	1.4	38	2553 4444	31	40
20	4-	3o	3-	4o	4-	3-	4-	2o	25+	0.9	0.9	17	4224 3221	20	39
21	3o	3+	2-	2o	1+	3o	3o	1o	18+	0.6	0.6	11	3322 2331	19	46
22	3-	4-	4+	3+	2+	2-	1-	0+	19o	0.7	0.7	13	3443 2111	19	55
23	1o	3-	3-	2o	4-	2+	2o	1+	18-	0.6	0.5	10	1332 3222	18	61
24	1+	2+	2-	3+	2+	2o	1+	2o	16+	0.4	0.4	8	1333 2212	17	76
25 Q	2-	0+	1-	1-	2+	1+	1o	1+	9+	0.1	0.2	5	1011 2212	10	64
26	1o	2+	3-	3o	2+	1+	1o	3o	17-	0.5	0.5	9	1332 2123	17	63
27	2o	2o	2+	3-	3-	6o	5-	2-	24o	1.2	1.1	22	2232 2552	23	88
28	4o	4+	4-	3o	3o	3-	2+	1-	24-	1.0	0.9	17	4542 2232	24	90
29 q	1-	1+	1o	2-	2+	1+	2+	1+	12o	0.4	0.3	6	1211 2222	13	94
30	3-	4o	4-	2-	2-	1+	1o	0+	16+	0.6	0.6	10	3343 2121	19	97
31 q	0+	1-	1-	1o	2-	3+	2o	2o	12-	0.4	0.3	6	0101 2332	12	90
Means:										0.65	0.65	14			51.3
No. of days:										31	31	31			31

Notes:

¹ Five quiet days (Q), ten quiet days (Q or q), five disturbed days (D) selected by Committee on Characterization of Magnetic Disturbances, J. Veldkamp, Kon. Nederlandsch Meteorologisch Instituut, De Bilt, Holland.

² Geomagnetic planetary three-hour-range indices *Kp* prepared by Committee on Characterization of Magnetic Disturbances, J. Bartels, Chairman, University, Göttingen, Germany.

³ Preliminary magnetic character-figures, *Ci*, prepared by J. Veldkamp.

⁴ Magnetic character-figures, *Cp*, prepared by J. Bartels.

⁵ Average amplitudes *Ap* (unit 2γ), prepared by J. Bartels.

⁶ Fredericksburg three-hour-range indices *K* (*K*9 = 500γ); scale-values of variometers in γ/mm: *D* = 2.5, *H* = 2.5, *Z* = 3.3) prepared by Robert E. Gebhardt, Observer-in-Charge, Fredericksburg Magnetic Observatory, Corbin, Virginia.

⁷ Provisional sunspot-numbers (dependent on observations at Zurich Observatory and its stations at Locarno and Arosa) prepared by M. Waldmeier, Swiss Federal Observatory, Zurich, Switzerland.

Letters to the Editor

A Photoelectric Analyzer of All-Sky Camera Auroral Photographs

TAKESI NAGATA AND EISUKE KANEDA

Geophysical Institute, University of Tokyo, Japan

seems that quantitative analysis of time of auroral luminosity is a promising approach for research on high atmospheric disturbances in the polar region, especially in connection with the analysis of the simultaneous records of geomagnetic and ionospheric disturbances. Continuous records of the auroral luminosity obtained by a photoelectric photometer will be very useful for this purpose. However, during the IGY/IGC period such photometers were set up in very few places.

On the other hand, it is now possible to have all-sky camera data of auroras observed at about 100 stations over the earth. For the purpose of reducing practically continuous series of variation in auroral luminosity from the IGY all-sky camera data (a series of every 10 seconds photographs), the writers designed and constructed a photoelectric analyzer of all-sky camera auroral photographs, and this apparatus

has proved to work sufficiently well for the above-mentioned purpose.

As shown in Figure 1, the photoelectric analyzer of all-sky camera auroral photographs (ASCA-PA) consists of (a) an optical part, (b) electronic amplifiers, and (c) a recorder. In the optical part, all-sky camera data, copied on 16-mm ciné films, are projected by a 16-mm ciné projector. In the projection, the image of a particular area to be studied and the image of the time signal of the all-sky photograph fall separately on a phototube and a phototransistor, respectively. After magnification by respective d-c amplifiers, the emfs produced in the phototube and in the phototransistor are recorded practically continuously by a pen-writing oscillograph, the former showing variation in the auroral luminosity and the latter the time mark.

By means of a diaphragm in front of the phototube, the average brightness of a specified area

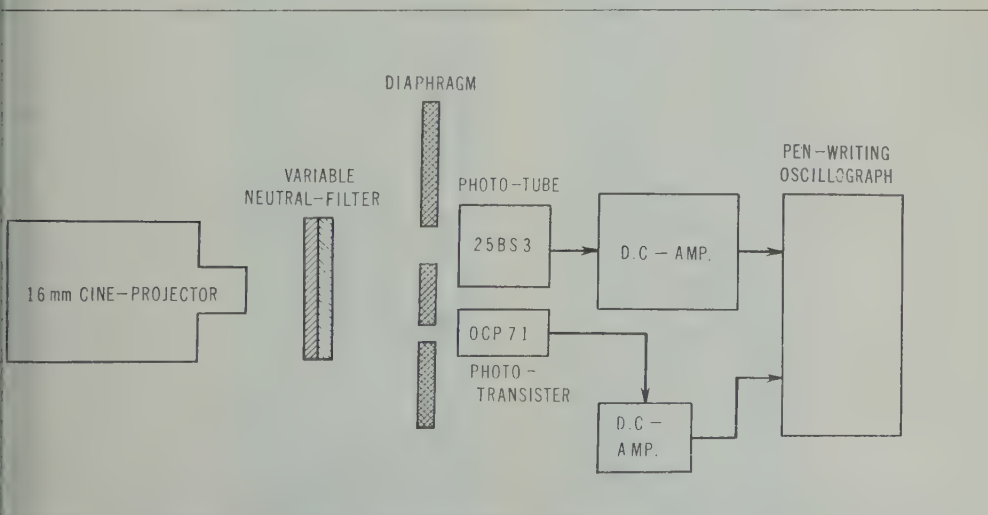


Fig. 1. Block diagram of ASCA-PA.

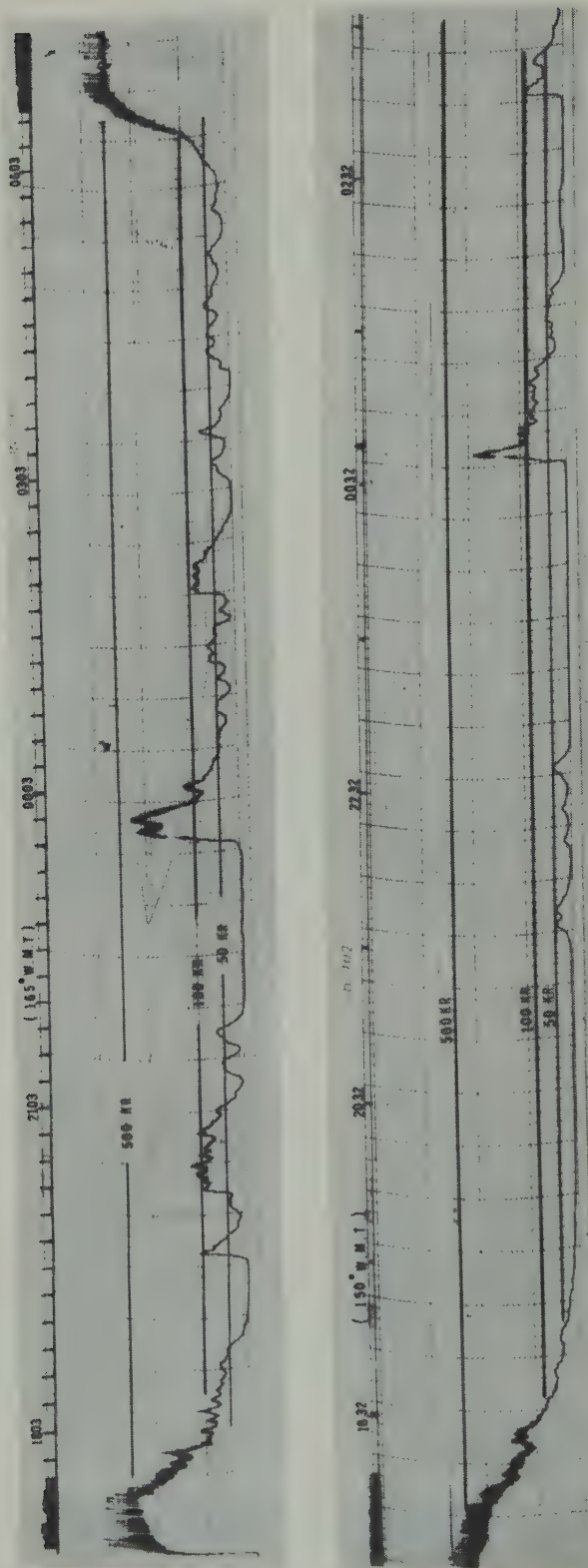


Fig. 2. Examples of records of the photoelectric analyzer of all-sky camera auroral photographs (Feb. 10/11, 1958).

Above A069 Kotzebue ($\Phi = 63.6^\circ\text{N}$ $\Lambda = 242.2^\circ$)
 Below A039 Point Barrow ($\Phi = 68.6^\circ\text{N}$ $\Lambda = 241.0^\circ$)

all-sky is measured. As the standard, a diaphragm for a zenith circular area of 41° in radius of the zenith distance has been adopted in the writers' laboratory. This diaphragm covers a horizontal circular area of 90-km radius of the sphere region 100 km in height, except the shadow circular disk of 19-km radius, which is due to an image of a plane mirror of the camera. For analysis of auroral movement, a diaphragm of much smaller area is used, and for studies of general auroral activities a wider diaphragm (up to 200 km in radius).

A neutral filter consisting of two polaroids, mounted between the diaphragm and the ciné projector, has proved to be very convenient for controlling the sensitivity of the whole apparatus continuously and smoothly.

The time marks are taken through the photomicroprojector from the time marks, either a watch or digits or a $\frac{1}{4}$ -hour lamp, printed on the camera photographs.

In the ASCA-PA actually used in the writers' laboratory, the driving speed of the ciné projector is 12 frames per second, and the running speed of the recording chart paper is 5 mm/sec, giving in about 30-cm-long records corresponding to a whole night's data of all-sky camera photographs (about 9 m long).

Actual records of variation in the zenith luminosity of aurora obtained by the ASCA-PA with the standard diaphragm are illustrated in Figure 2. It will be seen that they give practically

continuous information about auroral luminosity.

An approximate scale for auroral luminosity in the records can be determined by referring to twilight brightness recorded at the beginning (for evening twilight) and at the end (for morning twilight) of a whole night's series of the all-sky camera auroral photographs, since the twilight brightness is, approximately speaking, mainly dependent on the solar depression angle. Practically, it is possible to evaluate the absolute brightness of auroras by referring to the twilight brightness with careful correction for the effect of moonlight. In the photometric studies on auroras, however, a unit of photon flux density, the Rayleigh, or 10^6 photo quanta/cm² sec, has been widely adopted. The luminosity scale in Figure 2 is given in this unit. The transformation from the brightness in the above-mentioned unit (erg/cm² sec sterad) to that in the unit Rayleigh needs several assumptions about the constitution of spectra of aurora and twilight, the wavelength sensitivity of films, etc. The luminosity scale shown in Figure 2, therefore, is estimated to be accompanied by errors within 30 per cent. It seems that this scaling problem requires further studies in detail. Practical problems in detail of the ASCA-PA, including discussion on the scaling method, will be reported in the *Report of Ionosphere and Space Research in Japan*.

(Received April 26, 1961.)

Ring Currents in the Region of the Van Allen Radiation Belts

R. FIEBIG AND H. VOELCKER

*Institut für Reine und Angewandte Kernphysik, Christian-Albrechts-Universität
Kiel, Germany*

By measurements of the earth's magnetic field in the region of the Van Allen radiation belts clear differences between the calculated dipole field and the observed values were found. During the flight of the cosmic rocket Mehta (2/1/1959) an anomaly of the magnetic field at a geocentric distance of about 21,000 km was discovered [Dolginow and Puschkow, 1960]. The shape of this anomaly could be interpreted as being caused by a ring current at the same distance from the earth [Singer, 1960]. An analogous discrepancy between the dipole field and the measured values was observed by the United States satellite Explorer VI in August 1959. Smith, Coleman, Judge, and Sonett [1960] have interpreted the shape of the magnetic field to be based on a ring current of $5 \cdot 10^6$ amp surrounding the earth at a geocentric distance of 60,000 km. The diameter of the current torus was calculated to 6 earth radii.

A theoretical analysis and calculations by the authors about the origin of ring currents in the region of the Van Allen radiation belts will be published in July in *Atomkernenergie*.

The radiation belts have been treated as a plasma contained by the earth's magnetic field. Currents in a plasma like this arise from two causes: inhomogeneities of the magnetic field lead to a particle drift perpendicular to the field and to the gradient of the field strength; inhomogeneities of the particle density lead to the well-known diamagnetic effect, especially on the boundaries of the plasma. In a simple model sufficient agreement was found between the calculated and the observed values of the current strength. The drift velocity was calculated from

Störmer's theory. The obtained current strength are proportional to the unsufficiently known particle densities. An average observed value [Arnoldy and others, 1960] gives a total current of $1.5 \cdot 10^6$ amp for the inner anomaly. The observed magnetic field strength leads to a current of $2.3 \cdot 10^6$ amp.

The outer anomaly may be interpreted by a diamagnetic effect. By means of a statistic of particle orbits based on Störmer's theory quantitative predictions can be made about diamagnetic surface currents. The authors use a model of an idealized radiation belt with monoenergetic particles, constant density within and an ideal slope at the outer boundary of the belt. This theoretical approximation gave a current of $3 \cdot 10^4$ amp. The corresponding current calculated from the observed magnetic anomaly was greater by one order of magnitude. In view of the uncertainty of the measured values the results are acceptable.

REFERENCES

- Arnoldy, R., et al., Measurements of the Van Allen radiation belts during geomagnetic storms, *Space Research, Proc. 1st Intern. Space Sci. Symposium, Nice*, pp. 877-896, 1960.
- Dolginow, S. Sh., and N. V. Puschkow, Magnetic field of the outer corpuscular region, *Proc. Moscow Cosmic Ray Conference*, 3, 30, 1960.
- Singer, S. F., Nature and origin of the earth's radiation belts, *Space Research, Proc. 1st Intern. Space Sci. Symposium*, pp. 797-820, 1960.
- Smith, E. J., P. J. Coleman, D. L. Judge, and C. Sonett, Characteristics of the extraterrestrial magnetospheric system: Explorer VI and Pioneer V, *Geophys. Research*, 65, 1858-1861, 1960.

(Received April 27, 1961.)

Helium, an Important Constituent in the Lower Exosphere

MARCEL NICOLET

*Ionosphere Research Laboratory, Pennsylvania State University
University Park, Pennsylvania*

atmospheric content of He^4 , of the order of $1.13 \times 10^{20} \text{ cm}^{-3}$ [Nicolet, 1957], produced by the radioactive decay of uranium and thorium, is retained in less than 5×10^6 years. A continuous escape of the order of 10^6 He^4 atoms $\text{cm}^{-2} \text{ sec}^{-1}$ can be supported by vertical diffusion in the thermosphere, and the vertical distribution of neutral helium atoms can, therefore, be determined by an application of the diffusive equilibrium. In the homosphere, where the molecular state is prevalent, the ratio of helium and molecular concentrations $n(\text{He})/n(\text{N}_2)$ is equal to 1×10^{-6} . Such a ratio leads to a concentration of $n(\text{He}) = 7.4 \times 10^7 \text{ cm}^{-3}$ at 100 km, where the partial pressure of molecular nitrogen is less than $2.2 \times 10^{-4} \text{ mm Hg}$.

There is clear evidence from theoretical analyses [Nicolet, 1954; Mange, 1955; 1957] and from observations [Meadows and Townsend, 1956; Pukhunkov, 1960] that the transition from the mixing state to the diffusion state for inert gases must occur between 100 and 110 km. An application has been made to helium atoms [Nicolet, 1960] in using the diffusion coefficient defined by Mange [1957; 1961]. The characteristic times of diffusion of helium are 3/2, 1, 1/3, and 1/5 at 100, 105, 110, 115, and 120 km, respectively. The relative concentrations of helium at 105, 110, 115, and 120 km are 1, 1/3, 1/4, and 1/5, if diffusion begins at these altitudes. It is clear from these figures that the concentration of helium can vary by a factor of 5 in the upper thermosphere when the altitude level varies from 105 to 120 km.

Calculations in which thermal diffusion was included were made for various temperature profiles leading to temperatures between 925° and 1600°K at the thermopause. For example, the following concentrations of neutral helium are obtained at an altitude of 750 km:

°K	1250°K	1650°K	2100°K
$n(\text{He}) \text{ cm}^{-3}$	8.6×10^6	1.2×10^8	1.4×10^8

These values correspond to the beginning of

diffusion at 105 km, and if the diffusion level increases up to 120 km, the concentrations must be reduced by 1/5. With the preceding concentrations, the density of neutral helium reaches that of atomic oxygen near 750 km for $T = 925^\circ\text{K}$, near 1000 km for $T = 1250^\circ\text{K}$, near 1250 km for $T = 1650^\circ\text{K}$, and about 1600 km for $T = 2100^\circ\text{K}$.

Such densities show clearly that high densities derived from the rate of change of period of the Echo satellite orbit [Jastrow and Bryant, 1960; Paetzold, 1961; Roemer, 1961] can be explained by the presence of helium. It is certain that atomic oxygen cannot explain the slow decrease of the atmospheric density between 750 and 1500 km, since the temperature that would be required should be greater than 2000°K. Such high temperatures are not acceptable in 1960 for the isothermal region below 750 km. Furthermore, it must be emphasized that the density of the atmosphere above 1000 km cannot be explained by the presence of atomic hydrogen as claimed by Paetzold [1961] and Roemer [1961], since a concentration of the order of 10^4 cm^{-3} , which may be deduced from the observations of Purcell and Tousey [1960] and which is adopted by Johnson [1960], leads to about $2 \times 10^{-20} \text{ g cm}^{-3}$ only. The suggestion of a dust component with a density of $4 \times 10^{-19} \text{ g cm}^{-3}$ at 1600 km [Paetzold and Zschörner, 1961] cannot explain the variations, such as the atmospheric-drag perturbations during the November 1960 events derived by Jacchia [1961], but can be understood in an atmosphere with atomic oxygen and helium. In addition, the complete analysis of the results on the Echo satellite orbit made by Zadunaisky, Shapiro, and Jones [1961] leads to a temperature variation from about 1200° to 1600°K between August 13, 1960, and January 10, 1961. A temperature of the order of 1200°K corresponds to an atomic oxygen-helium atmosphere in which the density decreases by a factor of less than 7 between 1000 and 1500 km.

Since the ionization rate coefficient of He is of the order of $3 \times 10^{-8} \text{ sec}^{-1}$, i.e., 10 per cent of that of atomic oxygen, the total production of He^+ above 500 km may reach values of the order of $2 \times 10^6 \text{ cm}^{-2} \text{ sec}^{-1}$, which must be considered as an escape possibility for helium. Since the total production of O^+ above 500 km and for a temperature of the order of 1500°K should be of the order of $2 \times 10^8 \text{ cm}^{-2} \text{ sec}^{-1}$, one may assume that $n^+(\text{He}) = 10^3 \text{ cm}^{-3}$ when $n^+(\text{O}) = 10^6 \text{ cm}^{-3}$. The vertical distribution of helium ions will be subject to the law of the vertical distribution of ions in electrostatic equilibrium deduced by Mange [1960]. Observations of the positive ion concentration at 1250°K by Hanson and McKibbin [1961] related to the theoretical analysis (at 1500°K) made by Mange [1961] would lead to about 10^4 ions cm^{-3} at 1000 km and 10^3 cm^{-3} at 2500 km. Such concentrations show that helium ions can play a role in the transition region where Hanson and Ortenburger [1961] have considered the variation of the proton and oxygen-ion concentrations.

Finally, it should be pointed out that the presence of several constituents in the neighborhood of 1000 km greatly complicates the problem, since the following scale heights for a temperature of 1750°K are obtained: $\text{H}(\text{O}) = 125 \text{ km}$, $\text{H}(\text{O}^+) = 250 \text{ km}$, $\text{H}(\text{He}) = 500 \text{ km}$, $\text{H}(\text{He}^+) = 1000 \text{ km}$, $\text{H}(\text{H}) = 2000 \text{ km}$ and $\text{H}(\text{H}^+) = 4000 \text{ km}$.

Acknowledgments. The research reported in this work has been sponsored by the Geophysical Research Directorate of the Air Force Cambridge Research Center, Air Research and Development Command under contract AF 19(604)-4563. I am grateful to Mr. G. Kockarts, who has supervised a part of the calculations, and I wish to thank Drs. P. Mange and F. S. Johnson, who have communicated unpublished results to me.

REFERENCES

- Hanson, W. B., and D. D. McKibbin, An ion-trap measurement of the ion density profile above the F_2 peak, *J. Geophys. Research*, **66**, 1667-1671, 1961.
- Hanson, W. B., and I. B. Ortenburger, The coupling between the protonosphere and the normal F region, *J. Geophys. Research*, **66**, 1425-1435, 1961.
- Jastrow, R., and R. Bryant, Variations in the orbit of the Echo satellite, *J. Geophys. Research*, **65**, 3512, 1960.
- Jacchia, L. G., The atmospheric drag of artificial

satellites during the November 1960 event, *Space Research, Second International Space Symposium*, Florence, April 1961.

- Johnson, F. S., The ion distribution above the maximum, *J. Geophys. Research*, **65**, 577-580, 1960.
- Meadows, E. B., and J. W. Townsend, Jr., Rocket measurements of arctic atmospheric ion position above 100 km, *Space Research, Proceedings First International Space Sci. Symposium*, edited by H. Kallmann-Bijl, North-Holland Publishing Company, p. 175, 1960.
- Mange, P., Diffusion processes in the thermosphere, *Ann. geophys.*, **11**, 153, 1955.
- Mange, P., The theory of molecular diffusion in the atmosphere, *J. Geophys. Research*, **62**, 157, 1957.
- Mange, P., The distribution of minor ions in electrostatic equilibrium in the high atmosphere, *Geophys. Research*, **65**, 3833-3834, 1960.
- Mange, P., Diffusion in the thermosphere, *Ann. geophys.*, **17**, 1961.
- Nicolet, M., Diffusion of nitrogen atoms and oxygen molecules in region F, in *Rocket Exploration of the Upper Atmosphere*, edited by R. L. F. Chatterton and M. J. Seaton, Pergamon Press, p. 361, 1961.
- Nicolet, M., The aeronomic problem of helium, *Ann. Geophys.*, **13**, 1, 1957.
- Nicolet, M., The properties and constitution of the upper atmosphere, chap. 2 in *Physics of the Upper Atmosphere*, edited by J. A. Ratcliffe, Academic Press, pp. 17-71, 1960.
- Nicolet, M., Structure of the thermosphere, *International Space Sci.*, **5**, 1, 1961.
- Paetzold, H. K., Die Luftdichte in der irdischen Ionosphäre und Exosphäre, *Naturw.*, **48**, 1961.
- Paetzold, H. K. and H. Zschörner, The structure of the upper atmosphere and its variations from satellite observations, *Space Research, Second International Space Symposium*, Florence, April 1961.
- Purcell, J. D., and R. Tousey, The profile of the hydrogen-Lyman- α , *J. Geophys. Research*, **65**, 370-372, 1960.
- Pukhunkov, A. A., The study of upper atmosphere neutral composition at altitudes above 1000 km, *Space Research, Proceedings First International Space Science Symposium*, edited by H. Kallmann-Bijl, North-Holland Publishing Company, p. 1960.
- Roemer, M., Modell der Exosphäre in Höhe 1000-1700 km berechnet aus den Beobachtungen des Satelliten Echo I, *Mitteilungen der Sternwarte Bonn*, **37**, 1961.
- Zadunaisky, P. E., I. I. Shapiro, and H. M. Smith, Experimental and theoretical results on the structure of Echo I, *Research Space Sci.*, *Smiths. Astrophys. Obs., Special Rept.* **61**, 1961.

(Received May 9, 1961.)

Mainland Beach Changes Due to Hurricane Donna

WILLIAM F. TANNER

*Florida State University
Tallahassee, Florida*

present writer and four of his students carried out a detailed study of the Ten Thousand Islands area of the lower west coast of Florida (see Fig. 1, 'study area'). Field work, including collection of hundreds of sediment samples, was undertaken in June 1960; results of this work will be reported elsewhere. On September 10 and 11, 1960, hurricane Donna moved over Florida. The hurricane crossed the Gulf of Mexico, moved through the middle of the study area, and continued up the west coast almost to Tampa Bay before turning inland. The storm center shifted into the study area at about 0700 September 10, and out at about 1300 the same day. During this 6-hour period the storm center moved less than 50 miles and a great deal of damage was done to roads, causeways, trees, and beaches.

The U. S. Navy made aerial photographs of the lower west coast, from Cape Sable (point 9, see Fig. 1) to Tampa Bay, in October and early November 1960. These pictures, at a scale of 1 : 26,000, were compared with pre-Donna photographs of the same area, at a scale of 1 : 20,000, taken in 1953, 1957, and 1958. The changes observed can be ascribed exclusively to the hurricane. The lapse of time between the two sets of pictures, but it appears highly probable that the storm was responsible for the more pronounced alterations of the shore line. A field trip was made to the area, to inspect the damage at first hand. This confirmed the impression (gained from the photographs) that changes were sharply localized. Serious storm damage was found at eight points (see Fig. 1). Cape Sable (point 9) was not damaged appreciably. At each of the eight points, quantities of sand were either removed or added. This was generally done in connection with the opening or closing of inlets, the reduction or enlargement of small islands, or the lengthening of causeways. Where such changes were made, it was found that the prestorm and poststorm sand levels differed by approximately 5 feet. This is a conservative assumption, considering the small

tidal range, the typical height of beaches above mean water level, and the typical depth of water in the surf zone.

Volume of sand moved, assuming a thickness of 5 feet, was found to lie in the range 5×10^6 to 8×10^6 m³. Rapid transfer of such a volume of sand produces spectacular results at inlets,

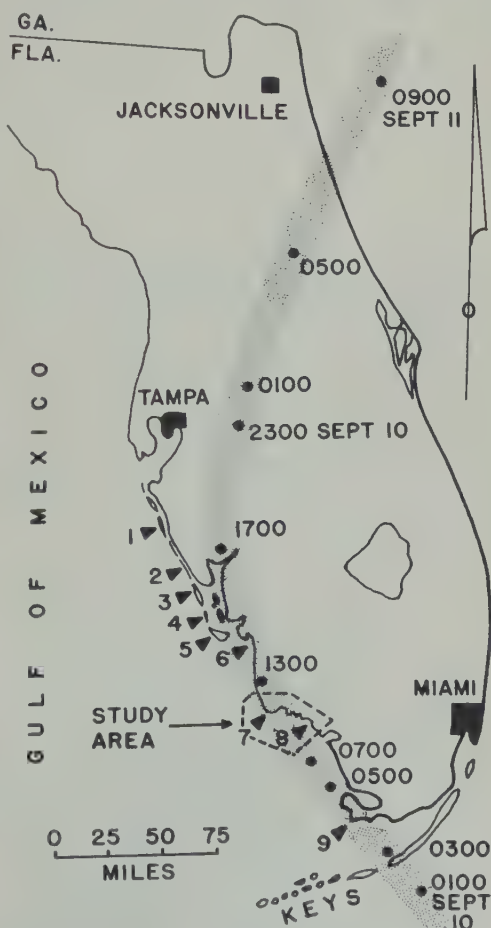


Fig. 1. Map of Florida, showing the path taken by hurricane Donna, the location of the storm center at various times, and nine selected points, eight of which showed beach damage. Four of these are shown in Figure 2.

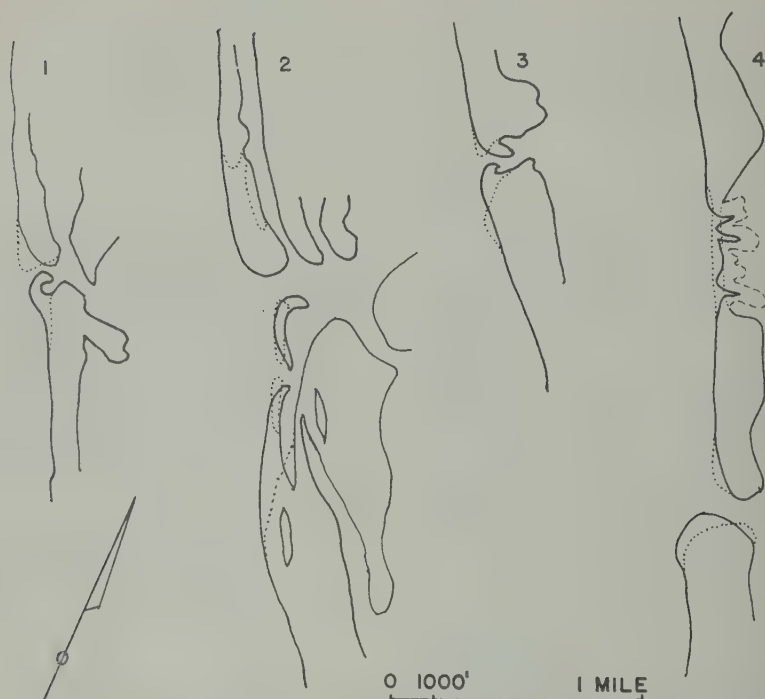


Fig. 2. Maps, traced from aerial photographs, showing beach damage, presumably due to storm waves. The four areas shown are located at points 1 to 4 on Figure 1. Solid lines are present zero contours; dotted lines show prestorm strand lines; dashes outline storm-created wash-over deltas. Dates of prehurricane photography for the four areas are 1957, 1953, 1953, and 1958.

spits, and points. Along a regular stretch of beach, however, uniform transfer of so much sand would probably leave the shore line unaltered. It is therefore assumed that the volume of sand transported past any given exposed point along the lower west coast was of the order of $5 \times 10^6 \text{ m}^3$.

Wave energy can be computed, for a given coast, from wind data, ramp slopes, and breaker heights, or by other means. No computations have been made for the lower west coast of Florida, but a study of other shore lines bounding the southeastern states indicates that the average annual breaker height should be about 20 cm [Tanner, 1960]. An average breaker height of 20 cm suggests an annual transportation rate (past a given point) of about $5 \times 10^4 \text{ m}^3$ of sand [Tanner, 1961]. In other words, hurricane Donna appears to have done 100 years' work, considering the typical energy level thought to prevail in the area. The same volume of sand would represent about 2 years' transportation along a very high-energy coast (for example, one with an annual breaker height about 200 cm).

Inspection of the air photographs and by field examination failed to reveal any evidence of *new* beach ridges. A few small storm beaches were built locally, but these are nothing comparable with the pre-existing ridges of the area. If such an intense storm did not build ridges, the storm wave hypothesis for their construction must be questioned.

Although marked changes occurred locally, the general effect of the storm (as far as sediment transport is concerned) was to speed up, for a short period of time, processes that were operating in the area during less violent weather. Because the general energy level of this stretch of coast is quite low, it may be true that practically all the work done here is performed under severe wave conditions.

REFERENCES

- Tanner, W. F., Florida coastal classification, *Transactions Gulf Coast Assoc. Geol. Soc.*, 10, 259-266, 1960.
Tanner, W. F. Offshore shoals in areas of energy deficit, *J. Sediment. Petrol.* 31, (1), 1961.

(Received April 8, 1961.)

Some Heat-Flow Measurements in the North Atlantic¹

JOHN REITZEL

*Woods Hole Oceanographic Institution
Woods Hole, Massachusetts*

ing the passage of R. V. *Chain* from Ber-
to Helsinki in July 1960, we made four
inations of the flow of heat through the
ottom, in the fashion devised by *Bullard*
We measured the temperature gradient
bottom sediments with thermometers in a
ical probe and found the thermal con-
ty of the sediments near each station
core sample. The results are given in

gradients in this table are based on the
ature differences, extrapolated to long
between two resistance thermometers in
ottom half of a steel probe of 3.2 cm outer
er. These resistors were spaced 2.2 meters
with the lower resistor half a meter above
of the probe. The higher one penetrated
1.8 meters into the sediments at every
as was shown by the rise in its tem-
re over that of a resistor at the top of the
The ocean water about 100 meters above
ottom was taken to give a standard of zero
ature difference along the probe; this
ation is unlikely to lead to more than a
it or two of error in the results.

value of K in the table is an average
conductivity along a core, reduced to
ottom pressure and temperature with the
ions given by *Ratcliffe* [1960]. The aver-
re taken from several direct measurements
n each core by the needle method de-
by *Von Herzen and Maxwell* [1959]
ed by numerous determinations of water

over-all experimental uncertainty in the
w values is estimated to be about ± 12
it, equally divided between uncertainties
radient and in the conductivity. Stations
are about 10 km apart, and both take

tribution 1194 of the Woods Hole Oceano-
Institution.

TABLE 1

Station No.	1	2	3	4
N. Lat.	35°35'	35°35'	51°18'	53°53'
W. Long.	61°08'	61°15'	29°35'	24°05'
Water depth, m	4590	4680	3260	3350
dT/dz , °C/m	.062	.068	>.37	.073
K , 10^{-4} cal/cm sec °C	19.2		>17.	21.0
Q , 10^{-6} cal/cm ² sec	1.20	1.31	>6.2	1.54

their values of K from a single core taken between
them. Part of the discrepancy between the two
is probably due to local changes in thermal
conductivity, and the mean of the two stations,
 1.25×10^{-6} cal/cm² sec, is doubtless the best
estimate of the heat flow in this vicinity. At
station 3, the temperature gradient in the bottom
exceeded the range of the instrument. No core
was taken here, but we can safely suppose that
the conductivity is higher than 17×10^{-4} cal/cm
sec °C, to arrive at a lower limit for the heat flow.

The bottom near stations 1, 2, and 4 showed
very little relief, though it had not the extreme
flatness of a true abyssal plain. Station 3 was
made on the mid-Atlantic ridge, in a small
valley about 50 km northeastward of the main
median valley, which could be plainly identified
on our echo-sounding records. The high heat
flow here is comparable to that observed by
Bullard on the mid-Atlantic ridge at 47°N, as
reported by *Hill* [1960]. A pipe dredge haul near
station 3 brought up yellow mud with large and
abundant shards of fresh volcanic glass, so it is
evident that the excess heat flow here is ac-
companied by volcanism of Pleistocene or
Recent date.

This work has been supported by a WHOI
Associates' Fellowship and by contract Nonr
1367(00) with the Office of Naval Research.

REFERENCES

- Bullard, E. C., The flow of heat through the floor of the Atlantic Ocean, *Proc. Roy. Soc. London A.*, *222*, 408-429, 1954.
- Hill, M. N., A median valley of the mid-Atlantic ridge, *Deep-Sea Research*, *6*, 193-205, 1960.
- Ratcliffe, E. H., The thermal conductivities of ocean sediments, *J. Geophys. Research*, *65*, 1541, 1960.
- Von Herzen, R., and Maxwell, A. E., The measurement of thermal conductivity of deep-sea sediments by a needle-probe method, *J. Geophys. Research*, *64*, 1557-1563, 1959.

(Received May 3, 1961.)

Anisotropic Thermal Conductivity

GENE SIMMONS

Dunbar Laboratory, Harvard University
Cambridge, Massachusetts

The direct determination of thermal conductivity *in situ* is desirable for the accurate estimation of the geothermal heat flow. If material is thermally isotropic, the method using a point source of heat and measuring the gradient at some distance away leads to a determination of the conductivity. However, difficulties are encountered if the medium is thermally anisotropic. The problem is particularly acute in a rather thick layer which has different thermal conductivities in different directions; such common rocks as shales, slates, and some sandstones exhibit directional conductivity.

Consider a right-handed orthogonal coordinate system in x, y, z , with coincident principal conductivities K_x, K_y, K_z . Then, if at the origin we have a point source of heating rate Q , the steady-state temperature is [Nye, 1960, p. 204]

$$T = Q/4\pi KR \quad (1)$$

$$K = (K_x K_y K_z)^{1/2}$$

$$R = (x^2/K_x + y^2/K_y + z^2/K_z)^{1/2}$$

isothermal surfaces are defined by

$$x^2/K_x + y^2/K_y + z^2/K_z = \text{constant}$$

which is similar in shape to the resistivity surfaces. From (1) we obtain the gradients

$$\frac{\partial T}{\partial x} = -\frac{Q}{4\pi K K_x} \frac{x}{R^3}$$

$$\frac{\partial T}{\partial y} = -\frac{Q}{4\pi K K_y} \frac{y}{R^3} \quad (2)$$

$$\frac{\partial T}{\partial z} = -\frac{Q}{4\pi K K_z} \frac{z}{R^3}$$

Measurement of the gradients along the axes (or in three different directions) will therefore enable us to determine the conductivities. In an important practical application, con-

sider a borehole parallel to the z axis in which it is desired to obtain an *in situ* measurement of conductivity to be used (together with a previously measured gradient) in the calculation of heat flow. Let $K_x = K_y \neq K_z$, a likely condition in layered rocks. From equations 2, the conductivities are

$$K_x = -\frac{Q}{4\pi z^2} \frac{1}{(\partial T/\partial z)_{x=0, y=0}} \quad (3)$$

$$K_z = \left[-\frac{Q}{4\pi x^2} \frac{1}{(\partial T/\partial x)_{y=0, z=0}} \right]^2 \frac{1}{K_x} \quad (4)$$

Thus we deduce that a measurement of the thermal gradient along the z axis due to a point source will yield a value for the conductivity in the perpendicular direction and will be independent of the value of the conductivity along the z axis! Yet it is the parallel conductivity that is required for the calculation of the heat flow.

If there were another borehole in the same area, inclined at an angle θ to the z axis, we could perform the same experiment and from the measured gradient, together with K_x (from equation 3), solve for K_z . The expression for the gradient along the inclined hole is

$$\begin{aligned} \left(\frac{\partial T}{\partial S} \right)_{y=0} &= -\frac{Q}{4\pi (K_x^2 K_z)^{1/2} (x^2/K_x + z^2/K_z)^{3/2}} \\ &\quad \cdot \left(\frac{z}{K_z} \cos \theta + \frac{x}{K_x} \sin \theta \right) \end{aligned} \quad (5)$$

where S is measured along the inclined hole.

The use of a point source and the measurement of the thermal gradient to determine conductivity in material with two different principal conductivities requires two nonparallel holes. Since several diamond drilled holes are often drilled in different directions from the same location in the mining industry, it would appear that these offer possibilities for useful measurements.

In an isotropic material, a line source may be advantageously used to determine conductivity [Beck, Jaeger, and Newstead, 1956]. A continuous line source, heating rate Q , parallel to the z axis, and turned on at time $t = 0$ gives

$$T = -\frac{Q}{4\pi K} Ei\left(-\frac{\rho c R^2}{4Kt}\right) \quad (6)$$

where ρ is density, c is specific heat, $R = (x^2 + y^2)^{1/2}$, and

$$-Ei(-\phi) = \int_{\phi}^{\infty} \frac{e^{-u}}{u} du$$

is the exponential integral [Carslaw and Jaeger, 1959, p. 262]. For large times

$$T \approx \frac{Q}{4\pi K} \ln\left(\frac{4\rho c t}{KR^2}\right) - \frac{\gamma Q}{4\pi K} \quad (7)$$

where $\gamma = 0.5772 \dots$ is Euler's constant. But if the material is anisotropic and $K_x \neq K_y \neq K_z$, the substitution

$$x = x'/K_x^{1/2}; \quad y = y'/K_y^{1/2}; \quad z = z'/K_z^{1/2};$$

$$R^2 = x'^2/K_x + y'^2/K_y; \quad K = (K_x K_y)^{1/2}$$

in (7) gives the appropriate solution; namely

$$T \approx \frac{Q}{4\pi(K_x K_y)^{1/2}} \ln\left(\frac{4\rho c t}{x'^2/K_x + y'^2/K_y}\right) - \frac{\gamma Q}{4\pi(K_x K_y)^{1/2}} \quad (8)$$

Thus the conductivity determined by means of a line source parallel to the z axis is the geometric mean of the other two principal conductivities. Perhaps it should be emphasized that this applies to all 'probe' methods inasmuch as the user of probes seem to neglect the possibility of anisotropy. In particular, if $K_x = K_y \neq K_z$, measurements along z will again give only the conductivity in the perpendicular direction.

The main conclusion of this note is that *in situ* conductivity determined in a side-borehole through anisotropic material is not the conductivity parallel to the borehole.

Acknowledgments. I am indebted to Professor Francis Birch for suggesting improvements in the method of presentation and to Dr. E. Herrington for reading this note. The manuscript was completed during the tenure of an NSF fellowship.

REFERENCES

- Beck, A., J. C. Jaeger, and G. Newstead, The measurement of the thermal conductivities of rocks by observations in boreholes, *Australian J. Phys.* **9**, 286-296, 1956.
 Carslaw, H. S., and J. C. Jaeger, *Conduction of Heat in Solids*, 2nd ed., Oxford University Press, London, 510 pp., 1959.
 Nye, J. F., *Physical Properties of Crystals*, corrected 1st ed., Oxford University Press, London, 400 pp., 1960.

(Received April 1, 1961; revised May 2, 1961)

Further Statistics on the Modes of Release of Available Potential Energy

BARRY SALTZMAN¹ AND AARON FLEISHER*Massachusetts Institute of Technology
Cambridge, Massachusetts*

the measurements of the hemispheric spectra
individual pressure change, temperature, avail-
potential energy, and rate of conversion
between available potential energy and kinetic
energy made for each day of February 1959, and
now at the Travelers Research Center, Inc.,
Hartford, Conn.

reported previously in this Journal [Saltzman
and Fleisher, 1960], have been extended to cover
the winter half-year period, January through
March and October through December, 1959.
We present these new results in Tables 1 to 3
and Figures 1 to 7, using the same notation as
was employed in the previous article.

TABLE 1. Mean Values and Standard Deviations of $[\omega]$, $[T]$, $[\omega'^2]$, $[T'^2]$ and $[\omega'T']$ as a Function of Latitude ϕ , for the Winter Half-Year, January through March and October through December, 1959

	80	75	70	65	60	55	50	45	40	35	30	25	20
$[\omega]$	-9	+312	-9	-441	-618	-504	-48	+638	+743	+768	+349	-231	-491
(\pm)	3353	3517	2825	3274	3648	3668	3059	3663	3232	3416	2203	1494	1928
$[T]$	246.84	248.27	249.70	251.13	252.83	254.81	257.54	261.11	265.28	269.31	272.92	275.82	278.30
(\pm)	4.22	3.63	3.19	2.89	2.94	3.12	3.39	3.69	3.77	3.51	3.02	2.24	1.34
$[\omega'^2]$	122	155	189	244	292	428	569	667	760	606	466	279	163
(\pm)	114	94	117	138	155	220	249	255	316	259	245	156	106
$[T'^2]$	20.38	28.24	34.02	37.68	39.66	42.85	43.08	37.88	28.29	18.32	11.43	6.35	3.06
(\pm)	13.01	13.65	12.19	13.17	13.21	15.19	17.43	16.46	12.85	8.86	5.68	3.27	1.37
$[\omega'T']$	-422	-414	-541	-698	-696	-945	-1256	-1453	-1261	-722	-209	+60	+69
(\pm)	604	557	558	569	573	725	764	715	678	581	366	244	149

 $\text{cm}^{-1} \text{sec}^{-3} \times 10^{-4}$.

degrees absolute.

 $\text{cm}^{-2} \text{sec}^{-6} \times 10^{-3}$.degrees absolute)². $\text{cm}^{-1} \text{sec}^{-3} \text{deg abs} \times 10^{-3}$.TABLE 2. Mean Values and Standard Deviations of $2|\Omega(n)|$, $2|B(n)|$, $\Phi(n)$, and $\mathcal{C}(n)$ as a Function of Wave Number n , for the Winter Half-Year, January through March and October through December, 1959

n	1	2	3	4	5	6	7	8	9	10	11	12	13	14	15
$ \Omega(n) _{\phi=45^\circ\text{N}}$	1764	1992	2017	2115	2660	2957	3360	3460	3727	2845	2798	2514	2243	2060	1985
(\pm)	1041	1028	1185	1174	1458	1696	1641	1700	1832	1502	1304	1479	1144	1139	1160
$ B(n) _{\phi=45^\circ\text{N}}$	3.84	3.49	3.19	2.49	2.42	2.18	1.65	1.24	1.05	0.73	0.63	0.52	0.44	0.37	0.31
(\pm)	1.71	1.76	1.42	1.38	1.27	1.18	0.87	0.63	0.48	0.43	0.36	0.27	0.23	0.20	0.17
$\Phi(n)$	379	382	206	121	97	79	45	31	18	11	8	5	4	3	2
(\pm)	175	190	129	74	66	52	32	18	10	7	5	3	2	2	1
$\mathcal{C}(n)$	+137	+336	+267	+273	+330	+473	+382	+308	+227	+120	+73	+42	+25	+17	+9
(\pm)	221	269	273	275	342	402	376	287	215	143	104	81	60	49	39

 $\text{m}^{-1} \text{sec}^{-3} \times 10^{-4}$.

degrees absolute.

 $\text{s cm}^{-2} \text{mb}^{-1} \times 10^3$. $\text{s sec}^{-1} \text{cm}^{-2} \text{mb}^{-1} \times 10^{-3}$.

TABLE 3. Mean Values and Standard Deviations of the Available Potential Energy P , and the Rate of Conversion of Available Potential Energy into Kinetic Energy C for the Region Between 20°N and 80°N

$\bar{P}^* = 6687$	$C_{EST}^{\dagger} = +2671$	
$\sigma = \pm 657$	$\sigma = \pm 792$	
$\bar{P}_Z = 5296$	$\bar{C}_Z = -344$	$\bar{C}_Z(\text{extrap}) = +352$
$\sigma = \pm 555$	$\sigma = \pm 578$	
$\bar{P}_E = \sum_{n=1}^{15} \mathcal{P}(n) = 1391$	$\bar{C}_E = \sum_{n=1}^{15} \mathcal{C}(n) = +3016$	
$\sigma = \pm 361$	$\sigma = \pm 884$	

* $\text{ergs cm}^{-2} \text{mb}^{-1} \times 10^3$.
† $\text{ergs cm}^{-2} \text{mb}^{-1} \text{sec}^{-1} \times 10^{-3}$.

As would be expected, the results based on the longer record display smoother variations with latitude and wave number than those for the single month. In almost all respects the essential features of the winter average conditions were already quite well represented in the February results—hence, most of the comments made in the previous article apply to those shown here. There are, however, two differences from the February values worth noting. These are (i)

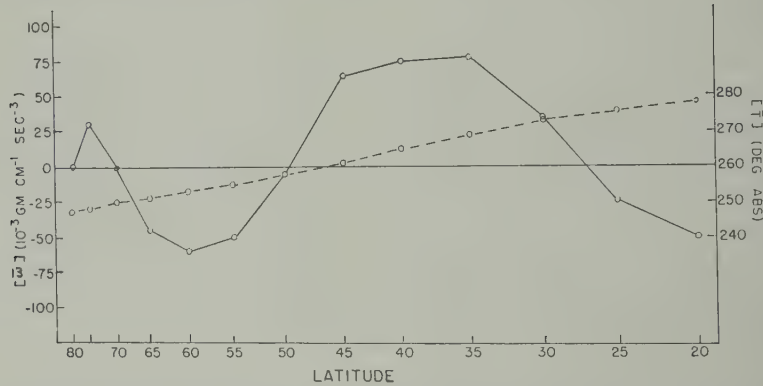


Fig. 1. Mean values of $[\omega]$ (solid curve) and of $[T]$ (dashed curve) for the winter half-year, January through March and October through December, 1959. See Table 1. For the area between 20°N and 80°N $\{[\bar{\omega}]\}$ is $+0.013 \text{ g cm}^{-1} \text{ sec}^{-3}$, which corresponds to a net descending motion of roughly $.02 \text{ cm sec}^{-1}$.

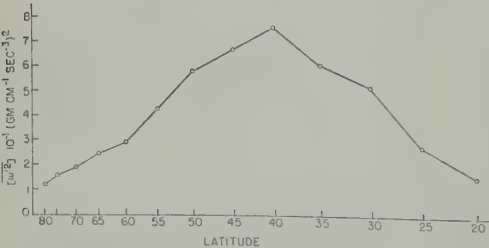


Fig. 2. Mean variance of ω around latitude circles, $[\omega'^2]$, for the winter half-year, 1959. See Table 1.

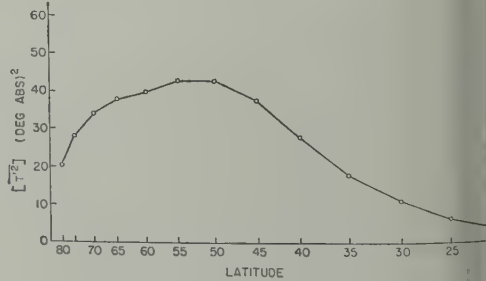


Fig. 3. Mean variance of T around latitude circles, $[T'^2]$, for the winter half-year, 1959. See Table 1.

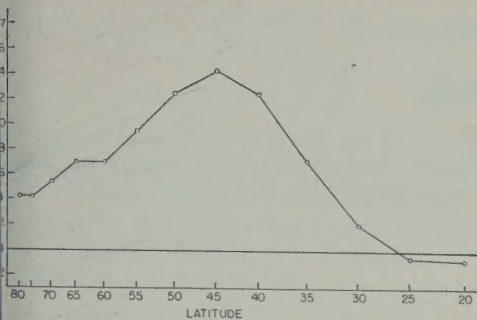


Fig. 4. Mean covariance between ω and T and latitude circles, $-\omega'T'$, for the winter half-year, 1959. See Table 1.

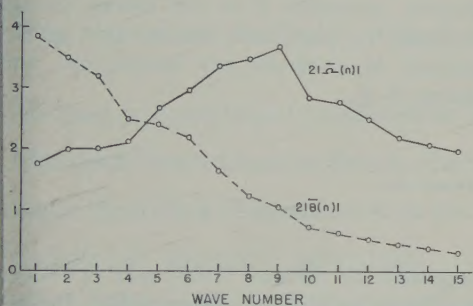


Fig. 5. Mean amplitude spectrum of ω , $2|\Omega(n)|$ (solid line), and of T , $2|B(n)|$ (dashed line), both $^{\circ}\text{N}$ for the winter half-year, 1959. See Table 2.

ward shift of the distribution of $[\omega]$ (Fig. 1) that maximum ascending motion is located at 0°N and maximum descending motion is located at 35°N , in closer agreement with the classical concept of the mean meridional cell pattern, and (ii) the absence of the pronounced maximum of $\Phi(n)$ at $n = 2$, which evidently was an unusual condition for February (see Fig. 6). We apply the same assumption as was used in the previous article (p. 1220) to obtain an estimate of C_z for the entire hemisphere, we use the value C_z (extrap) = $+0.352$ ergs $\text{cm}^{-2} \text{mb}^{-1}$, which is to be compared with the value of $+0.294$ ergs $\text{sec}^{-1} \text{cm}^{-2} \text{mb}^{-1}$ for February.

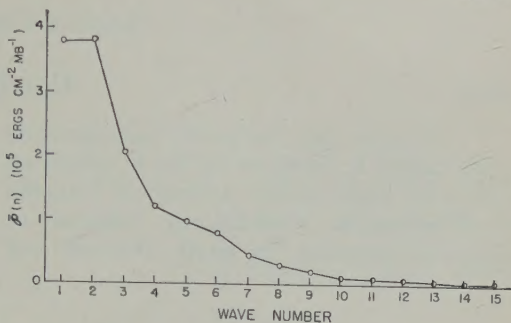


Fig. 6. Mean spectral function for eddy available potential energy, $\Phi(n)$, for the winter half-year, 1959. See Tables 2 and 3.

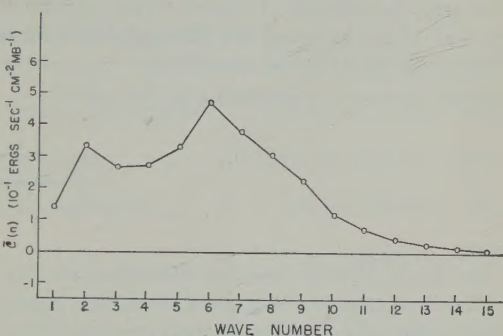


Fig. 7. Mean spectral function for the rate of conversion from eddy available potential energy to eddy kinetic energy, $C(n)$, for the winter half-year, 1959. See Tables 2 and 3.

Acknowledgments. We are indebted to the Joint Numerical Weather Prediction Unit for supplying the basic data and to the M.I.T. Computation Center for providing the IBM 704 computer time and running our program.

This research was sponsored by the Geophysics Research Directorate, Air Force Cambridge Research Center, under contract AF19(604)-6108.

REFERENCE

- Saltzman, B., and A. Fleisher, The modes of release of available potential energy in the atmosphere, *J. Geophys. Research*, **65**, 1215-1222, 1960.

(Received March 17, 1961.)

Corrigenda

Dr. Robert L. Smith would like to correct an error in the paper entitled 'A Theory of Trapping of Whistlers in Field-Aligned Columns of Enhanced Ionization,' by Smith, Helliwell, and

Yabroff, in the March 1960 issue of the Journal. Equation 2, page 818, should read:

$$\mu[N(P), 0] = \mu[N(0), \theta_0] \cos \theta_0$$

The following addition to the paper by P. D. Bhavsar, 'Scintillation Counter Observations of Auroral X Rays during the Geomagnetic Storm of May 12, 1959,' in the March 1961 issue of the Journal, is called to attention by the author:

Add to the caption of Figure 8 (p. 690): spectral equations E is the kinetic energy of electrons in Mev and the relation gives the number of electrons per second per cm^2 energy $> E$.

Dr. R. R. Unterberger has submitted the following amendment and correction to his paper, 'Direct Recording of Small Geomagnetic Fluctuations,' which appeared in the December 1960 issue of this Journal.

Since submitting the above paper, the author learned at the Thirteenth Annual Technical Conference of the Institute of Geophysics held at Berkeley, California, of the commercial availability from Varian Associates of a research rubidium vapor station magnetometer. This information now invalidates the first sentence of the ultimate paragraph of the above paper. Varian's magnetometer is similar to that discussed in the above paper but differs in that it is based on a crossed beam modulation technique

suggested by *Dehmelt* [1957] and developed excellently by *Bell and Bloom* [1957]. Reference to these research workers and their paper should have been included in the published paper.

Also disclosed at the same conference Dr. L. N. Liebermann of Scripps Institute of Oceanography was a Hall effect magnetometer which he has constructed with a reported sensitivity beyond that claimed for any rubidium vapor magnetometer.

Bell, W. E., and A. L. Bloom. Optical detection of magnetic resonance in alkali metal vapor, *Phys. Rev.*, 107, 1559-1565, 1957.

Dehmelt, H. G., Modulation of a light beam by precessing absorbing atoms, *Phys. Rev.*, 160, 1224-1225, 1957.

Dr. Felix Chayes points out that in his paper 'Correlation between Variables of Constant Sum,' published in the December 1960 issue of the Journal (pp. 4185-4193), inequality (17) on p. 4187 is correct but the immediately succeeding discussion of it is erroneous. If the variances are taken as equal, the upper limit of

r_{ij} given by (17) is zero. This limit is erroneously given as +1 in the text. The range $-1 \leq r_{ij} \leq 1$ is of course not '... that characteristic of open data,' so that the opening clause of the following paragraph is also in error, and the entire paragraph may now be deleted without loss.

Contents

(Continued from back cover)

	PAGE
Use of Gravity Methods to Study the Underground Structure and Impact Energy of Meteorite Craters.....	<i>M. J. S. Innes</i> 2225
Origin of Folding in the Earth's Crust.....	<i>V. V. Belousov</i> 2241
Magnetic and Solar Data.....	<i>J. Virginia Lincoln</i> 2255
Letters to the Editor:	
A Photoelectric Analyzer of All-Sky Camera Auroral Photographs	<i>Takesi Nagata and Eisuke Kaneda</i> 2259
Ring Currents in the Region of the Van Allen Radiation Belts	<i>R. Fiebig and H. Voelcker</i> 2262
Helium, an Important Constituent in the Lower Exosphere.....	<i>Marcel Nicolet</i> 2263
Mainland Beach Changes Due to Hurricane Donna.....	<i>William F. Tanner</i> 2265
Some Heat-Flow Measurements in the North Atlantic.....	<i>John Reitzel</i> 2267
Anisotropic Thermal Conductivity.....	<i>Gene Simmons</i> 2269
Further Statistics on the Modes of Release of Available Potential Energy	<i>Barry Saltzman and Aaron Fleisher</i> 2271
.....	<i>R. L. Smith, R. A. Helliwell, and I. W. Yabroff</i> 2274
.....	<i>P. D. Bhavsar</i> 2274
.....	<i>R. R. Unterberger</i> 2274
.....	<i>Felix Chayes</i> 2274

Contents

The National Program for Lunar and Planetary Exploration.....	<i>A. R. Hibbs</i>	2
Characteristics of the Van Allen Radiation Zones as Measured by the Scintillation Counter on Explorer VI.....	<i>Alan Rosen and Thomas A. Farley</i>	2
Cosmic-Ray Production of Low-Energy Gamma Rays.....	<i>Frank C. Jones</i>	2
On the Interplanetary Magnetic Storm: Pioneer V <i>P. J. Coleman, Jr., C. P. Sonett, and Leverett Davis, Jr.</i>		2
Energy Spectrum of Electrons Trapped in the Geomagnetic Field <i>Martin Walt and William M. MacDonald</i>		2
Some Features of Magnetic Storms in High Latitudes.....	<i>David G. Knapp</i>	2
Some Studies of Geomagnetic Micropulsations.....	<i>R. A. Duncan</i>	2
Attempt to Measure Night Helium Glow—Evidence for Metastable Molecules in the Night Ionosphere.....	<i>E. T. Byram, T. A. Chubb, and H. Friedman</i>	2
The Height and Geographical Position of the Red Auroral Arc of April 1–2, 1960 <i>James G. Moore and F. Kirk Odencrantz</i>		2
Some Auroral Observations inside the Southern Auroral Zone.....	<i>J. V. Denholm</i>	2
Equatorial Spread <i>F</i> in Relation to Post-Sunset Height Changes and Magnetic Activity.....	<i>M. S. V. Gopal Rao and B. Ramachandra Rao</i>	2
Theory of Overhead Nonblanketing Sporadic <i>E</i>	<i>Jacques Renau</i>	2
Seasonal and Latitudinal Variations of Air Density in the Mesosphere (30 to 80 Kilometers).....	<i>Roderick S. Quiroz</i>	2
Wind and Temperature Measurements in the Mesosphere by Meteorological Rockets <i>John E. Masterson, William E. Hubert, and Thomas R. Carr</i>		2
On the Deduction of the Vertical Distribution of Ozone by Ultraviolet Spectral Measurements from a Satellite.....	<i>Sean Twomey</i>	2
Stratospheric Aerosol Studies.....	<i>Christian E. Junge and James E. Manson</i>	2
Origin of Radioactive Fallout in the Northern Hemisphere after the Spring Maximum in 1959.....	<i>J. F. Bleichrodt, Joh. Blok, and E. R. van Abkoude</i>	2
Long-Range Sound Transmission in the Arctic Ocean.....	<i>Henry Kutschale</i>	2
The Velocity of Compressional Waves in Rocks to 10 Kilobars, Part 2 <i>Francis Birch</i>		2

(Continued inside back cover)